ORNL-4975

Gas-Cooled Reactor Programs Annual Progress Report for Period Ending December 31, 1973

P. R. Kasten
J. H. Coobs
A. L. Lotts

OAK RIDGE NATIONAL LABORATORY
OPERATED BY UNION CARBIDE CORPORATION FOR THE ENERGY RESEARCH AND DEVELOPMENT ADMINISTRATION

Printed in the United States of America. Available from
National Technical Information Service
U.S. Department of Commerce
5285 Port Royal Road, Springfield, Virginia 22161
Price: Printed Copy $10.00; Microfiche $2.25

ORNL-4975
UC-77—Gas Cooled Reactor Technology

Contract No. W-7405-eng-26

GAS-COOLED REACTOR PROGRAMS ANNUAL PROGRESS REPORT FOR PERIOD ENDING DECEMBER 31, 1973

P. R. Kasten, Program Director
J. H. Coobs, Associate Director
A. L. Lotts, Associate Director

APRIL 1976

OAK RIDGE NATIONAL LABORATORY
Oak Ridge, Tennessee 37830
operated by
UNION CARBIDE CORPORATION
for the
ENERGY RESEARCH AND DEVELOPMENT ADMINISTRATION

Contents

PART II. HTGR DEVELOPMENT PROGRAM

PART IV. GAS-COOLED FAST REACTOR PROGRAM

Foreword

The Gas-Cooled Reactor programs being carried out at Oak Ridge National Laboratory contribute to the development and evaluation of high-temperature gas-cooled reactors (HTGRs) and of gas-cooled fast reactors (GCFRs). These programs, sponsored by the U.S. Atomic Energy Commission (USAEC), include the Thorium Utilization Program (HTGR Fuel-Recycle Development Program), the HTGR Base Program, the HTGR Safety Program, and the GCFR Program. The major effort is in HTGR technology, with emphasis on fuel and fuel-recycle development, and includes fuel fabrication and irradiation testing, head-end processing, fission product behavior, and fuel performance studies. Work is also carried out on the performance of prestressed concrete reactor vessels (PCRVs) under possible reactor conditions. Work in GCFR technology emphasizes development of a core flow test loop to be used in fluid flow and heat transfer studies of GCFR core assemblies; other work involves fission product behavior in a vented fuel element, shielding studies, and system response studies of a steam generator. Close coordination is maintained with General Atomic Company (GAC) relative to their efforts in the design and development of gas-cooled reactors and in HTGR fuel-recycle development.

Major incentives for developing HTGRs are the prospects for economically attractive power production, improved fuel utilization, the potential for obtaining low environmental impact at a diversity of plant sites, the potential for high-temperature direct cycle and process heat applications, and the pertinence of the component technology to GCFRs. The good neutron economy and fuel performance permit high burnup and associated low fuel-cycle costs. The high-temperature capability of the graphite core structure facilitates reactor plant operation at high thermodynamic efficiency, and thus requirements for heat dissipation to the environment are relatively low. Excellent fission product retention by the coated fuel particles leads to coolant circuits with low radioactivity levels. Further, the high exposures attainable with HTGR fuels permit the development of economic fuel recycling. At the same time, the development of fuel-recycle technology is important to the commercial acceptance of HTGRs as economic power producers.

The fuel-recycle effort is part of the national HTGR fuel-recycle development program being carried out by the USAEC at ORNL, GAC, and the Idaho Chemical Processing Plant (ICPP). The objective of the fuel-recycle program is to develop the pertinent technology so that commercial plants for reprocessing and refabricating HTGR fuels can be built and operated economically. The operations to be considered take place between the discharge of spent-fuel elements from the reactor and the return of refabricated fuel elements to the reactor; these include fuel shipping, storage, fuel recovery and purification, refabrication, and waste management. The work involves fuel-reprocessing development, fuel-refabrication development, irradiation testing of refabricated fuels, and fuel-recycle system analyses involving the economics associated with various processes and equipment. The program at ORNL includes development of head-end processing methods for irradiated fuels and associated off-gas cleanup technology, production of microspheres containing recycle-type fuel, microsphere coating technology, recycle-fuel-element fabrication technology, associated equipment and process development, recycle-fuel irradiations, and fuel-recycle evaluation analyses.

The HTGR fuel development work at ORNL is largely concerned with evaluating, understanding, and improving fuel performance and with studying the behavior of certain fission products, including their effects on fuel performance. Coated-particle fuel studies involve irradiation testing, with emphasis on demonstration of satisfactory fuel and materials performance at the

required fuel burnup and fast-neutron fluences, including the testing and development of recycle fuels. In these tests, the High-Flux Isotope Reactor (HFIR) has proved highly useful as an irradiation facility; an in-core facility at the Oak Ridge Research Reactor, also being used provides relatively large volumes for testing fuel bodies.

In work on PCRVs, a thermal cylinder experiment has been completed to study the time-dependent stress-strain behavior of a simulated segment of a PCRV vessel. The prestressing, pressure, and thermal-gradient conditions were those expected under HTGR design conditions; prior to disassembly a built-in heater was activated to simulate a hot-spot condition. The results have been analyzed.

Relative to HTGR safety studies, a fission product technology program has been under way for a number of years that involves the behavior of fission products and of fuel under various circumstances, including abnormal conditions. Included in these efforts is a fission product surveillance program being carried out in the Peach Bottom HTGR, which provides information on fission product behavior in an HTGR environment. These studies were continued for part of the year, with the experimental studies subsequently being transferred to the HTGR Base Program. At present, HTGR safety studies concern analysis of accident sequences and of postulated consequences and assessment of fission product and coolant technology, of core and component technology, and of materials, instrumentation, and containment behavior as they relate to HTGR safety.

The helium-cooled GCFR offers a high breeding ratio, a doubling time of about 10 years, a core conversion ratio of approximately 1.0, and a small reactivity change from loss of coolant. The high core conversion ratio makes possible extended operating periods without refueling and results in low reactivity swings during fuel exposure. Since the fuel performance requirements for this reactor are basically similar to those for the liquid-metal-cooled fast breeder reactor (LMFBR), the GCFR program draws heavily on the fuel development of the LMFBR program. The ORNL fuel work for the GCFR involves irradiation testing of fuel pins. Irradiation test results for a second vented fuel element were obtained during this report period, with encouraging results. Other work being carried out in the GCFR program includes planning and development work on a Core Flow Test Loop (CFTL) to be utilized for heat transfer and fluid flow testing of simulated GCFR fuel assemblies; GCFR shielding studies with emphasis on neutron streaming evaluations; and mathematical modeling of the GCFR steam generator to simulate response under transient conditions.

Work on gas-cooled reactors in also being performed in Europe, with significant efforts being carried out on the HTGR concept by the Dragon Project and by Germany. Associated information pertaining to HTGR research and development work is obtained through the USAEC/Dragon HTGR Agreement and the USAEC/KFA Exchange Arrangement. These exchange programs include information on fuel development, performance and testing, fission product behavior, fuel reprocessing, materials performance, and safety.

The organization of this report is based on an orderly presentation of technical information which largely follows program lines but not completely. The principal exception is Chapter 7, which covers work supported by the HTGR Base Program and the Thorium Utilization Program; the results from irradiation testing and postirradiation examinations of various fuels are better understood when presented in an integrated manner. In general, however, the report presents information associated with specific programs as follows: Thorium Utilization Program, Chapters 1 through 5, 7; HTGR Base Program, Chapters 6 through 11; HTGR Safety Program, Chapters 12 through 17; and GCFR Program, Chapters 18 through 20. The chapters that are associated with the Thorium Utilization Program are organized according to the subtasks identified in the National HTGR Fuel-Cycle Development Program Plan and in 189a No. 10516, the program and budget proposal. Thus, the work on subtask 110, Reprocessing Development, appears in Chapter 1 and work on subtask 120, Reprocessing Prototype Facility, will appear in Chapter 2, although in the reporting period only advisory and review functions were involved and no work is reported. Similarly, work on subtask 210, Refabrication Process Development, appears in Chapter 3, and Chapter 4 presents the progress of design work for subtask 220, Refabrication Prototype Plant. Chapter 5 presents the results of work on subtask 310, Engineering and Economic Studies, while the results from Recycle Fuel Irradiations and Examinations, subtask 230, are combined in Chapter 7 with similar work supported by the HTGR Base Program.

Summary

PART I. THORIUM UTILIZATION PROGRAM

1. HTGR Reprocessing Development (Subtask 110)

The Reprocessing Pilot Plant task 100 is divided into two major subtasks: Reprocessing Development (Chap. 1, subtask 110) and Reprocessing Pilot Plant (Chap. 2, subtask 120). The development subtask is the primary responsibility of General Atomic Company (GAC), but ORNL has a major role in two of the work units (head-end processes and off-gas cleanup), and activity on these units is reported here. The pilot plant subtask is the primary responsibility of Allied Chemical Corporation, and our activity this calendar year was limited to review and comment functions.

1.1 General development. No activity scheduled.

1.2 Head-end reprocessing development. Hot-cell studies of irradiated HTGR-type fuels were continued in small-scale tests aimed at identifying release patterns and distribution of tritium, ^{85}Kr, and various fission products of differing volatilities. Both carbide- and oxide-base fuels were examined, with burnups of about 16 and 35% FIFA respectively. Tritium and krypton releases from the two fuel types differed significantly in that these nuclides tend to be retained in the oxide fuels. The more volatile fission products, such as ruthenium and cesium, were found downstream from the burner in relatively large quantities but were effectively removed by condensation and filtration. An activation product, ^{75}Se, was completely volatilized out of the burner but was condensed in cooler parts of the system.

Calculations and advance planning were done for more sophisticated studies of vapor transport of fission products. Tracer level experiments in contact facilities may be necessary in order to obtain definitive data on certain alpha and beta emitters.

Both experimental and theoretical work was done on the whole-block burner concept. Experimental measurements on a one-sixth-scale unit showed that the concept was feasible in terms of attainable rates and temperature. A theoretical study of burner temperature control by recycle of burner gases suggested that an "adiabatic burner" concept was very desirable. This approach limits reactor combustion temperature by means of the $C\text{-}CO_2$ reaction and should be of value for other burners also (e.g., fluidized-bed burners or shaft furnaces).

1.3 Solvent extraction. No activity scheduled.

1.4 Off-gas cleanup processes. Laboratory studies dealt with three systems: $Kr\text{-}CO_2$, $Xe\text{-}CO_2$, and $CO_2\text{-}I_2\text{-}H_2O$. Work on the distribution of krypton between gaseous and liquid CO_2 was completed. Measurements on the distribution of xenon in CO_2 were started, and the data are reported. As expected, xenon is more soluble in liquid CO_2 than is krypton, by factors of about 4 at $-50°C$ and about 2 at $0°C$. Work was started on the $CO_2\text{-}I_2\text{-}H_2O$ system, and preliminary data indicate that H_2O and I_2 react with each other in liquid CO_2 and that H_2O and CO_2 form a molecular association complex in the gaseous phase.

An experimental engineering facility was designed and built to obtain fundamental engineering data on the KALC process (*k*rypton *a*bsorption in *l*iquid *c*arbon dioxide). The facility, which consists of packed absorption and stripper columns plus associated compressors, is in the final shakedown stage. A computer model was

developed for the CO_2-Kr-O_2-N_2-CO system to help analyze experimental results.

1.5 Product preparation. No activity scheduled.

1.6 Waste treatment and disposal. No activity scheduled.

2. HTGR Reprocessing Pilot Plant (Subtask 120)

During this reporting period, activity at ORNL on this subtask consisted of reviewing design documents for the pilot plant and initiating the preparation of the preliminary system design description of the off-gas cleanup system.

3. HTGR Fuel Fabrication Development

In this step in the HTGR fuel cycle the nitrate solution containing reprocessed ^{233}U is converted, in hot-cell-type facilities, into fuel elements for use in an HTGR. The objective of the national HTGR refabrication development program is to develop technology so that commercial HTGR refabrication plants can be built and operated economically. This goal will be largely met by the design, construction, and operation of the Fuel Refabrication Pilot Plant (FRPP) to be installed in the existing Thorium-Uranium Recycle Facility (TURF) at ORNL. The processes and equipment applicable to remote refabrication in the FRPP will be developed under subtask 210, while the design, construction, and actual operation of the FRPP will be done in subtask 220. Work in subtask 220 is covered in Chapter 4.

Work in HTGR fuel refabrication process development has been going on for a number of years at ORNL. The work this year is reported in sections parallel to the systems of the FRPP. The change to utilize a kernel derived from a weak-acid resin (WAR) instead of a sol-gel-derived kernel was made at the end of this report period; therefore, the sol-gel work is reported under resin loading. The majority of the work accomplished during this report period was in the areas of coating, rod fabrication, and element assembly.

3.1 General development. Work in this area involves the coordination and review of all functions of this subtask and subtask 220, preparation of recycle fuel specifications, and development of material accountability procedures. Activity has primarily been in technical input and review of the design descriptions for the FRPP.

3.2 Uranium feed preparation. No development activities scheduled.

3.3 Resin loading. The change to a kernel derived from WAR was made after this report period was completed. However, the resin development work is reported in this section to conform with the new format, even though that work was supported in part by the base program in 1973. Sol-gel work is also reported in this section.

Resin kernels of the desired size were obtained by wet screening the commercial product received from the manufacturer. A yield of about 25% was obtained in the desired size range. The volume change that resin undergoes through various conversion steps was determined. Initial measurements show that within a loading batch, individual resin kernels are uniformly loaded and that variations from batch to batch are small.

The use of a modified Higgins column for the continuous loading of WAR was successfully demonstrated.

Loading of WAR with both ^{235}U and ^{233}U was carried out successfully using a batch process. Over 500 g of ^{235}U was loaded onto WAR to provide irradiation specimens. In addition, 5 kg of natural uranium was loaded on WAR to provide material for development work on carbonization and coating.

The pulsed nozzle system for preparing sol-gel spheres of uniform size and diameters has continued to operate very satisfactorily. In this system, the breakup of the sol streams is made more uniform by imposing a vibration on the sol at the natural frequency of drop formation. Routine use of the system has consistently given kernels with average diameters within 1% of the predicted value and standard deviations of about 1% of the mean diameter.

Kernels containing ^{233}U and ^{235}U with Th/U ratios of 4.2, 2, 1, and 0 were prepared for irradiation experiments using the pulsed nozzle system. About 300 kg of ThO_2 was prepared for developmental testing.

The Solex sol preparation of $(ThU)O_2$ spheres is the preferred flowsheet for Th/U ratios of 3 to 4.25. This process was demonstrated at a rate of 10 kg/day with excellent results.

3.4 Resin carbonization. In this step in particle preparation, uranium-loaded WAR that has been dried to 110°C is carbonized to UO_2-C intermediate product. Work has just begun in this area.

3.5 Microsphere coating. The engineering-scale coating furnace was upgraded by replacement of the furnace support structure, base, and electrodes. Porous plates of different geometries were evaluated, and a new type of porous plate gas distributor was developed. The buffer coating process was shown to be reproducible. A comprehensive experiment relating process variables to numerous low-temperature isotropic coating properties

was completed, and the result was a much improved understanding of this coating process. A scrubber using liquid perchloroethylene was developed to treat the effluent generated by the carbon coating process.

3.6 Fuel rod fabrication. The principal activities in fuel rod fabrication are dispensing, blending, and loading particles into molds; injection of the matrix into a bed of particles to form a fuel rod; and inspecting and assaying fuel rods.

A system using compression valves to volumetrically dispense particles was developed. With this system, fissile and fertile particles can be dispensed within 0.5% of the average weight specified for a fuel rod.

The approach to blending we have investigated involves splitting the charge required for one fuel rod into ten approximately equal increments and sequentially loading each increment into a fuel rod mold. A mechanized blending device using this technique was designed, constructed, and placed into operation on the laboratory fuel rod machine. Our initial evaluation of this blender has shown that the uranium and thorium content per inch of fuel rod is well within the ±5% target specifications.

The slug injection process for molding fuel has been demonstrated to be suitable in all aspects for the remote fabrication of HTGR and recycle fuel rods. Over 20,000 fuel rods have been made on the laboratory fuel rod machine by this process.

The capability to perform rapid and accurate nondestructive assay of special nuclear materials is an essential part of the FRPP for meeting safeguards and material accountability requirements. Design and development work has been initiated on several devices and techniques to assay the fissile and fertile content of the type of material to be processed in the FRPP. These include (1) ^{252}Cf neutron interrogation devices for active assay of fuel kernels and rods, (2) a calorimeter device for very accurate assay of individual fuel rods, and (3) a passive gamma scanning device for sensing rod-to-rod fissile loading variations.

3.7 Fuel element assembly. The principal activities in fuel element assembly are fuel element loading; carbonization and annealing; end plug, dowel, and poison rod loading; and fuel element inspection. Efforts during this report period have been confined to carbonization and annealing.

A problem of in-block carbonization and annealing has been the increased tendency for particles to be broken during carbonization-annealing and irradiation testing compared with the old process of carbonizing the fuel rods in Al_2O_3 powder. The problem is apparently a result of the difference in pitch carbonization conditions that result in a higher pitch-coke yield. Studies were performed to investigate methods of lowering the pitch-coke yield in in-block carbonization, and it was found that additives to the matrix material would reduce the pitch-coke yield to the desired level. The influence of particle strength on the tendency of particles to break during carbonization and irradiation testing was recognized, and a means of determining particle strength was initiated.

The design of a furnace for the carbonization and annealing of full-size HTGR fuel blocks has begun. This furnace, which is a vertical shaft type capable of 1800°C, will be the prototype of the furnace we expect to use in the FRPP.

3.8 Sample inspection. This task includes development of techniques and equipment necessary for the design and operation of the sample inspection system in the FRPP. Principal development during this period has been in rod and particle inspection.

In rod inspection, a technique was developed for quantitative characterization of the pore structure of fired fuel rods by infiltration of a low-melting metallic alloy into the fuel rod and examination with a quantitative television microscope.

A high-temperature (1500°C) chlorine leach technique was developed for determining broken particle fractions in fired fuel rods. This technique appears capable of determining quantitatively as few as one broken particle in a fired fuel rod.

In particle inspection, an improved singularizer was added to the particle size analyzer. The particle size analyzer continues to look very promising for the measuring of particle diameters at various stages of manufacture. In coating density determination, the differences between the gradient column and mercury displacement values were resolved quantitatively. This led to a new, more precise method for determination of low-temperature isotropic (LTI) coating density. Techniques were developed for characterizing particle shape from the radiograph and for characterizing surface-connected porosity of the LTI coating by nickel impregnation.

3.9 Process control and data handling. The principal activities in this area are involved with application of state-of-the-art control technology to the FRPP. Work in this area is not scheduled to begin before July 1974.

3.10 Waste handling. Work in this area is primarily in developing waste packaging and waste assay methods. During this year, activity has been directed toward formulating a work plan for the waste assay method.

3.11 Materials handling. No development activities scheduled.

4. HTGR Fuel Recycle Pilot Plant Studies

Conceptual design of the HTGR Fuel Refabrication Pilot Plant was started in July 1973. The plant is being designed to process 25 kg of uranium and thorium per day. This is equivalent to about 2.5 fuel elements per day, which would (if operated continuously) supply a reactor such as the Fort St. Vrain with recycle fuel. The unit operations of the pilot plant will vary from 5 to 50% of the anticipated commercial size. The pilot plant, to be installed in the Thorium-Uranium Recycle Facility at ORNL, is being designed for remote operation and maintenance because of the highly radioactive substances to be handled. Phase I of the conceptual design, consisting of detailed criteria, flowsheets, and outlines of system design descriptions, was completed; the conceptual design is scheduled for completion by July 1974.

5. Studies and Evaluation of HTGR Fuel Recycle Systems

Highlights during this reporting period included a detailed assessment of the economic and irradiation performance considerations associated with a change in the reference recycle fissile particle from $(4Th,U)O_2$ to the weak-acid-resin-derived $U{\cdot}O_x{\cdot}C_y$ and a study to optimize the timing of the introduction of fuel reprocessing and refabrication on a commercial basis.

The available economic and performance data on the mixed-oxide and weak-acid-resin (WAR) fissile fuels were accumulated and studied in detail. It was concluded that the WAR system offered the potential for superior irradiation performance, and the sketchy economic data suggested that use of this particle would be no more expensive than the mixed-oxide particle, which was then the reference. Therefore, ORNL and General Atomic recommended to the AEC that the reference particle be changed.

The timing of the introduction of commercial capacity for HTGR fuel reprocessing and refabrication was shown to be somewhat crucial, in that large deviations from optimal timing can lead to greatly increased fuel cycle costs. The study showed that for the presently assumed HTGR construction schedule, calling for the first large reactor to go on line in 1979, commercial reprocessing of spent fuel should begin in 1984 or 1985. Optimal timing was also shown to be somewhat insensitive to changes in some of the important cost parameters, such as uranium ore costs and toll enrichment charges. Another interesting item pointed out by the study is that a delay in the introduction of commercial capacity from optimal is much more costly than early introduction of this capacity.

PART II. HTGR DEVELOPMENT PROGRAM

6. HTGR Fuel Materials Development

The principal objectives of the fuel development program include the preparation and characterization of coated particles and fuel rods for use in irradiation tests designed to demonstrate the performance of fuels at HTGR design conditions or to investigate process latitude and property variations in order to establish specifications. In addition, the development of alternate fabrication processes that offer substantial improvements in fuel performance is emphasized as applicable. During this reporting period, significant developments were made on coating technology, resin-base kernel processing, and extruded fuel rod fabrication.

In coating process development, maintaining athermal conditions during coating runs by use of mixed hydrocarbon gases enabled substantial progress in minimizing property gradients thereby enhancing irradiation performance of pyrocarbon coatings. A commercial product, MAPP gas, which consists mostly of unsaturated hydrocarbons, was shown to have distinct advantages for temperature control during coating runs. Other coating developments consisted of a study of the reduction of undesirable carbon deposits by addition of oxidizing diluents to the coating gas, and the definition of minimum hydrogen-to-silane ratios necessary to maintain acceptable coating properties while maximizing the SiC deposition rate.

Process developments on resin-derived kernels included the definition of acceptable conditions for rapid carbonization (de-volatilization) of the loaded and dried resins and the description of procedures for partial or complete conversion of the carbonized resins to carbide while controlling particle density and the amount of excess carbon. The atmospheric reactivity of all compositions of resin-derived kernels indicated that exposure to moist gases must be prevented.

Studies of alternate fuel rod fabrication processes included preparation of extruded specimens for use in studies of the changes in thermal conductivity during irradiation and the irradiation testing of simulated extruded fuel rods. The extruded fuel rods exhibited anisotropic behavior under irradiation, as expected; diametral shrinkage at moderate fluences was followed by swelling, but the original dimensions were not

exceeded even at exposures exceeding the design fluence.

7. HTGR Fuel Irradiations and Postirradiation Evaluations

7.1 Irradiation Tests in the HFIR Removable Beryllium Facility. During this reporting period, the irradiation of HRB capsules -4 and -5 was completed, and postirradiation examination (PIE) of the fuel was performed. Two items of major interest were revealed in the HRB-4 and -5 experiments. First, there appears to be a problem of mechanical interaction between particle coatings and the matrix material in fuel rods which have been carbonized in block. The bond between the outer LTI coating and the matrix is sufficiently strong that the outer LTI is broken away from the SiC layer as both the coating and the matrix densify under irradiation. This behavior was not noted in fuel rods which had been carbonized in block. Another significant observation was the chemical attack of the SiC layer in the Triso fissile particles (the fuel was Triso WAR UC_2 fissile and ThO_2 Biso fertile) by rare-earth fission products. This was the first observation of this behavior in ORNL irradiation tests, but such behavior has been observed in subsequent tests and in tests conducted by other investigators.

Irradiation and PIE of capsule HRB-6 were also completed. This was the first test in the HFIR of fully enriched fuel. The fissile particles were $(4Th,U)O_2$ with both Biso and Triso coatings and contained both ^{233}U and ^{235}U. This experiment was also the first comparison of the irradiations of these two isotopes of uranium. Both fuels performed well, and no difference could be determined between them. There was no evidence of fission product attack of the SiC layer on Triso-coated particles. Amoeba (kernel migration) was observed in the mixed-oxide fissile particles, and the migration data were added to master plots to supplement data from other experiments.

Capsules HRB-7 and -8 were planned and constructed during this reporting period. The capsules will be inserted into the reactor early in 1974. These capsules were planned before the change in the reference recycle fissile particle was made from $(4Th,U)O_2$ to the weak-acid-resin-derived particle. The capsule contains a variety of fuels, including sol-gel UO_2, weak-acid-resin UC_2, mixed-oxide kernels with different thorium to uranium ratios, and ^{233}U- and ^{235}U-bearing fuels, with both Biso and Triso designs. The performance comparisons between the $(4Th,U)O_2$ and weak-acid-resin particles described in Chapter 5 of this report were based on fuels irradiated separately. In no case was there a comparison of the two fuels irradiated in the same capsule under the same conditions. Such a comparison will be possible with HRB-7 and -8, and the data from this test should shed more light on the decision made recently to change reference fissile particles for the recycle fuel elements.

In addition to the irradiation experiments completed in the HFIR removable beryllium facilities, two additional accomplishments were completed which should greatly enhance our experimental capabilities in the future. Two new facilities have been added to the HFIR to supplement the existing facilities in the removable beryllium reflector. One of these facilities is a moderate flux position in the permanent beryllium reflector, and the second is an out-of-core thermocouple calibration furnace which permits the calibration of HRB capsule thermocouples before, during, and at the end of the irradiation. The permanent beryllium facility is of particular importance because it permits the irradiation of fully enriched pure fissile particles in a neutron flux low enough to reduce the power per particle values to acceptable levels.

7.2 Irradiation Tests in the HFIR Target Facility. Irradiation and PIE of the HT series HT-12 through -15 were completed during the reporting period. These experiments were designed to test various coating designs applied to thoria kernels which were irradiated as loose particles. The results of the experiment were somewhat confusing, in that some samples which were expected to fail did not fail and some samples which were expected to survive failed. In addition, some particle batches which failed at one exposure survived a longer exposure. These results are still being analyzed.

Irradiation and PIE on capsules HT-17 through -19 were also completed. These experiments were designed to investigate the influence of the very important parameter, anisotropy, on particle performance. The experiments were conducted on loose coated thoria kernels, with different coating techniques used to vary the preferred orientation of the LTI coating between 1.0 and 1.7. The general trend noted in examining the results of this experiment is that samples with BAF values greater than 1.1 survived at low temperatures but failed at high temperatures. The low and high temperatures are presently defined as specimen holder temperatures of 900 and 1250°C, but the actual temperatures of the coated particles are several hundred degrees higher.

7.3 Irradiations in the ORR Core Facilities. The ORR core facilities were completed during the reporting period, and irradiation testing was initiated in each. The

C-3 position was used to irradiate the GAC OG-1 experiment, which was designed to test graphite samples. This experiment was completed during the reporting period and the irradiated material returned to GAC for examination.

The E-3 position was utilized for a joint ORNL-GAC coated-particle fuel experiment. The GAC portion of the experiment has been designated P13Q and the ORNL portion OF-1. The entire capsule is also designated OF-1. The upper two-thirds of the capsule is occupied by P13Q and the lower one-third by OF-1. The OF-1 capsule was still under irradiation at the end of the reporting period.

7.4 Irradiation Tests in the ETR Capsule Facilities. All GCR Program irradiations in the ETR were completed prior to the beginning of the reporting period. Postirradiation examination and analysis of the H-capsule experiments were completed during the period, and a topical report was issued.

Postirradiation examination of two ORNL specimens irradiated in GAC capsule P13N was also performed during the reporting period. These specimens contained fuel similar to that irradiated in the HRB-3 experiment described in last year's annual report. There was substantial thermal migration (amoeba) of the SAR fissile particles in these specimens. No such migration was noted in the HRB-3 experiment. On the other hand, no migration of the thoria-containing fertile fuel was noted in P13N, whereas it was noted in HRB-3.

7.5 Recycle Test Elements in the Peach Bottom Reactor. Of the seven recycle test elements (RTEs) initially inserted into the Peach Bottom Reactor, one element (RTE-7) was examined prior to this reporting period. Examination of the second element discharged (RTE-4) was begun during the reporting period. The third element discharged (RTE-2) is awaiting examination, and the remaining four elements will be discharged from the reactor in the fall of 1974. The PIE of RTE-4 had proceeded only to the point of dimensional inspection and visual examination of the fuel rods by the end of the reporting period.

7.6 Nuclear Analysis in Support of Irradiation Experiments. Neutron fluxes and unit reaction rates have been measured for several of the experimental facilities used to irradiate GCR fuels. The following facilities have been studied during the reporting period: peripheral target positions in the HFIR target region (used for HT capsules), the RB-5 and RB-7 facilities in the HFIR removable beryllium region (used for HRB capsules), the VXF-13 facility in the HFIR permanent beryllium region (used for preirradiation of HRB capsules starting with HRB-7), and the C-3 and E-3 facilities in the ORR core (used for fuel and graphite experiments).

7.7 Capsule Thermometry. Experiments have been conducted in four HTGR fuel HFIR irradiation capsules (HRB-3, -4, -5, and -6) to develop improved temperature sensors for the 1000 to 1500°C temperature range. Tungsten-rhenium thermocouples were used to measure fuel center-line temperatures in HRB-3 and -4; rhenium pulse-echo ultrasonic thermometers (UST) were used in HRB-5 and -6. Methods for measuring and correcting for decalibration of the 1200 types of thermometers were developed: thermocouples were corrected by the use of loop resistance measurements, and USTs were corrected by measurements made during reactor shutdown isothermal conditions and by postirradiation calibration updating, using an in-pool whole-capsule calibration furnace. Multijunction, multiloop tungsten-rhenium fuel center-line thermocouples were designed and built for the succeeding experiments HRB-7 and -8.

7.8 Performance Evaluation of Fuels. The H capsules described in Section 7.4 provided some unique problems of performance evaluation. The capsules were irradiated for four cycles in the ETR and removed from the reactor at the end of each cycle. The capsules were accidentally inserted into the reactor upside down at the beginning of the fourth cycle, causing very high temperatures in the half of the capsule designed to operate in the low-flux end of the core. This, plus the lack of instrumentation in the experiment and the very interesting fuel performance characteristics noticed during PIE of the experiment, precipitated a very extensive analysis of this experiment.

8. Prestressed Concrete Pressure Vessel (PCRV) Development

The thermal cylinder experiment is a relatively long-term test of a one-sixth-scale single-cavity PCRV barrel section model under a combination of loadings simulating HTGR operating conditions. The results are used to evaluate the capability of existing analysis methods to determine the stress and strain behavior of complex structural models.

Since termination of the vessel operating period simulation in December 1972, which culminated with an off-design hot-spot test, the model has been disassembled, sectioned, and subjected to post-mortem studies. Although the concrete apparently retained its basic integrity as evidenced by complete absence of structural cracking, the inner row of axial prestressing tendons suffered severe corrosion cracking that led in most cases to failure of one or more wires. The cause of the tendon corrosion and subsequent failure remains to

be identified. During the hot-spot experiment, a small semicircular area of concrete immediately adjacent to the heating element experienced a substantial reduction in strength as determined using a sclerometer.

We have also compared the experimental data from the model stress and strain gages with calculated results obtained using the SAFE-CRACK finite-element analysis computer program. Data obtained from functioning strain gages were in good agreement with each other as well as with calculated results. The analysis generally tended to underestimate heating strains and to overestimate mechanical loading strains. The titanium embedment stress cells behaved inconsistently at times; however, they generally monitored lower stresses than the corresponding values calculated for mechanical loadings. The results of complementary gage evaluations made using companion concrete cylinders are also discussed.

The nuclear moisture probe used to monitor the thermal cylinder model was calibrated at Waterways Experiment Station (U.S. Army Corps of Engineers). Except for a significant loss of moisture from the core region of the model, little if any migration of moisture was monitored during the thermal cylinder experiment.

9. HTGR Structural Materials Investigations

A program was initiated in late 1973 to investigate the properties and behavior of HTGR structural alloys. As presently conceived, the program is divided into four related areas covering high-temperature mechanical properties, welding, structural design methods of HTGR steam-generator and primary-circuit materials, and steam corrosion. Experimental work is in progress in the mechanical properties and corrosion areas.

10. HTGR Fission Product Technology

10.1 Mathematical analysis of fission product release from pyrocarbon-coated particles. Diffusion equations applicable to cesium release from pyrocarbon-coated fuel particles were reviewed. Equations for slab geometry were compared with those for spherical geometry in order to simplify the solution of diffusion problems involving a depleting potential. Equations were also developed to cover the case of a constant potential changing to a depleting potential.

10.2 Postirradiation measurements of cesium release. Annealing experiments on separated components of coated particles revealed that some fraction of cesium is permanently trapped in the kernels during annealing experiments. An unpredictable surge in release rate was also observed during some anneals. An apparatus for removing increments of the coatings in order to obtain concentration profiles has been constructed.

10.3 Status of estimation of cesium release from Biso-coated fuels during irradiation. The fractional release of cesium from reference Biso-coated fertile particles during irradiation was calculated using best estimates of the diffusion coefficient for cesium in the coatings and the expected fuel temperature distribution. This estimate is sufficiently uncertain that more complete limits for HTGR coolant activity must be determined and in-reactor release measurements made before deciding unequivocally that Biso coatings will perform satisfactorily.

11. HTGR Fuel Chemistry

11.1 Mass transport in fuel particles in a temperature gradient. The work during this report period dealt mainly with theoretical and experimental analyses of mass transport effects, such as kernel migration, in HTGR oxide fuels. These analyses were advanced significantly by the availability of experimental measurements of kernel migration from the fuels irradiation program described in Section 7.4. In-reactor experiments with carbide- or nitride-containing UO_2 particles were initiated to evaluate the possible mitigation of kernel migration by these means.

11.2 Gas pressure measurements in coated particles. A program for the measurement of gas pressure and oxygen potential in irradiated fuel particles was developed, and the experimental apparatus was constructed and tested.

11.3 Chemical compatibility of fuel and fission products with coatings. Literature surveys were performed to delineate potential chemical means for improving the retention of cesium, barium, and strontium by oxide kernels.

PART III. HTGR SAFETY PROGRAM

12. HTGR Systems and Safety Analysis

The major activity during the year was preparation of a National HTGR Safety Program Plan in cooperation with the General Atomic Company (GAC). The plan, completed in December, was subsequently divided into two parts and converted into a Planning Guide for HTGR Safety and Safety-Related Research and Development, the latter being identified primarily with the HTGR base program.

Development work was continued on a method for diagrammatic presentation and logical analysis of accident sequences, and a new approach was adopted based on a small number of consolidated initiating events.

A computational model for describing fission product diffusion and transport in HTGR cores was acquired from GAC, adapted for use on ORNL computers, tested, modified and extended in some details, and applied to a few bench-mark problems. It will subsequently be used for analysis of postirradiation measurements of fision product distributions in the Peach Bottom Reactor fuel and primary circuit and for studies of fission product release criteria for large HTGR cores. Also in connection with the observations on Peach Bottom fuel, calculations of fission product inventories were performed and the results compared with experiment.

13. Fission Product Technology

Proposed regulatory restrictions of 15 mrem/year on thyroid dose resulting from release of iodine, if extended to HTGRs, will limit the primary coolant content of iodine to perhaps 36 Ci of ^{131}I. Therefore, some iodine removal from the helium by surfaces is required. Since thermodynamic calculations indicate that surfaces may be oxidized, adsorption isotherms were obtained from measurements of iodine adsorption on Fe_3O_4; these measurements indicate that surface capacity limits could be approached as operation of the reactor continues. Relationships describing iodine exchange between gas and surface indicated that if such processes occurred at useful rates, surface capacity requirements would be usefully reduced. The possibility of removal by deposition of volatile metal iodides was assessed, and it was found that iodide stabilities increased in the order of Ni, Fe, Cr, and Mn. The desorption of iodine adsorbed on iron powder was measured at temperatures up to 600°C. Interpretation in terms of partition coefficients suggested that release during postulated depressurization accidents might be usefully limited.

Iodine and cesium distributions were determined in the Peach Bottom HTGR coolant circuit. Helium leaving the core contains very little organic and dust-borne iodine; these forms appear downstream of the steam generator. Cesium from core II appears to be entering the primary coolant circuit at a rate of about 1 Ci/year after 600 effective full-power days of operation.

14. Primary Coolant Technology

Activity in primary coolant technology has concentrated on the development and use of computational programs as aids in steam ingress analyses. The GOP code, developed at Battelle Pacific Northwest Laboratories, has been adapted for use on a CDC CYBER 74 system; this code is to be employed in an effort to establish the significance of radiolytic reactions on coolant composition using Fort St. Vrain startup data. The OXIDE-2 code, developed at General Atomic Company, has been converted for use on an IBM 360/91; this code will be employed as an aid in the identification of components that are particularly vulnerable to oxidative attack.

15. Confinement Components

The initial effort under this new task area consisted of a preliminary review of recent literature on prestressed concrete reactor vessels and reactor containment structures to provide background material required for the HTGR Safety Program planning guide.

16. Primary-Systems Materials Technology

Study was initiated to identify those areas related to HTGR primary-system structural materials that may have a significant influence on safety. As part of this effort, a report on the status of HTGR metallic structural materials is being prepared. Plans have been developed for the removal and metallurgical examination of selected components of the Peach Bottom prototype HTGR.

17. HTGR Safety Studies for the Directorate of Licensing

This work was initiated in November 1972 at the request of The Gas-Cooled Reactors Branch (GCRB) of the Directorate of Licensing (DOL) in support of their response of licensing applications for HTGR plants. An overall goal of the work was to develop and provide to the GCRB certain analytical methods, usually in the form of computer programs, for use in their evaluations. The effort was redirected in September 1973 by the request to evaluate specific sections of the first general topical licensing report submitted by the General Atomic Company (GAC).

17.1 An adiabatic heatup model. One of the general problems under study required the determination of temperatures throughout the core of the reactor following a complete loss of forced convective coolant flow accompanied by a simultaneous reactor trip. The method developed for this calculation was based on a general multidimensional heat conduction computer program called HEATING that existed at ORNL. The developments necessary for the application of this program to the problem involved a study to determine the best composite representation of the core and the selection of the appropriate initial temperature distributions and boundary conditions. The study progressed through a series of one- and two-dimensional models, and the primary computations were performed using power distributions and dimensions given for the core of the Fort St. Vrain Reactor, since this was the only design for which detailed information was available.

17.2 Coupled conduction-convection model (CCCM). To determine the temperatures developed in the core of the HTGR during periods of forced convective flow, a convective calculation was coupled to the conductive calculations existing in the HEATING program. To incorporate this feature, it was necessary to assume a specific geometric model; this eliminated the ability to specify the general geometric options of the HEATING program and made the calculation specific for this representation of the HTGR core. Calculations were performed for operation under full-power conditions for certain ranges of input parameters. Computations were also performed for the conditions of reduced coolant flow under emergency conditions, and the results were compared with the computed results presented by GAC in the licensing topical report. Agreement was good when the coolant flow was relatively large (the nominal capacity of the core auxiliary cooling systems); however, the single-channel model was unable to predict the redistribution of flow due to buoyancy forces developed at very low flow rates.

17.3 Failure of fuel particles under HTGR operating conditions. In the evaluation of the upper operating limits for the HTGR fuel as specified in the licensing topical report, reviews were made of both the effect of mass transport within the fuel kernel (the "Amoeba" effect) and methods of estimating the stresses developed in the particle coatings as a function of irradiation exposure and temperature. Both of these effects were characterized by specific models, and a review of physical property data and proposed methods of analyses was made. In particular, three existing computer programs – STRETCH, TRISO, and STRESS-2 – were executed, and the resultant predicted behavior was compared, analyzed, and reconciled.

17.4 Sensitivity of HTGR fuel performance to material properties and particle design. As a continuation of the evaluation of the operating limits for the HTGR fuel, a study was made of the sensitivity of HTGR fuel performance as a function of material properties and particle design. The computer program STRESS-2 was used for this evaluation, since it had been shown to produce results that were comparable to the results of the other codes when appropriate input parameters were selected. The analysis indicated that for the Triso particle, with the exception of the PyC irradiation creep and deformation characteristics, the influence of materials properties on predicted performance was small. It was found that design considerations such as the relationship of the kernel volume to buffer volume were most important.

17.5 Analysis of tritium distribution and release in HTGR. A computer program was written to represent the source terms of tritium in an HTGR system. With the specification of diffusion and reprocessing rate constants, the relative movement of the tritium through the system and its inventory as a function of operating history can be calculated.

PART IV. GAS-COOLED FAST REACTOR PROGRAM

18. GCFR Irradiation Experiments

In the joint ORNL-GAC-ANL irradiation testing program for the evaluation of $(U,Pu)O_2$-fueled metal-clad fuel rods for the gas-cooled fast reactor (GCFR), current emphasis is on the testing of fuel rods of the vented-and-pressure-equalized concept, the present reference fuel-rod design for the GCFR. This concept eliminates the large pressure differential across the cladding by venting the fuel-rod interior to a pressure-equalization system and at the same time benefits from information being developed in LMFBR fuel-rod testing programs.

18.1 Description of GCFR-ORR capsule GB-10. The current irradiation test, capsule GB-10, and the preceding one, capsule GB-9, were designed to permit an initial evaluation of the overall performance of the vented-and-pressure-equalized fuel rod. Various aspects of the GCFR pressure-equalization system are also being studied in these tests. The test conditions are typical of those expected for a GCFR fuel rod except for the absence of significant fast-neutron exposure.

Postirradiation examination of the GB-9 fuel rod, which was irradiated at a peak power level of 14.8 kW/ft to a fuel burnup of approximately 54,000 MWd/metric ton of heavy metal, continued at ANL and GAC into calendar year 1973. The GB-9 experiment provided substantial information on the fission product release behavior to be expected from the GCFR vented fuel rod, and the results have been used in many aspects of the GCFR pressure-equalization system design.

The GB-10 fuel rod, similar to GB-9 but designed with greater capability for measuring fission product release and transport, is being operated in three successive peak power steps: 12, 13.5, and 14.8 kW/ft. Sweep line connections to the GB-10 rod permit fission product release measurements under as many as ten different sweep flow modes, including passage of the sweep through the entire rod, which simulates a leak in the cladding of a GCFR fuel pin.

18.2 Results from irradiation testing of capsule GB-10. Steady-state fission-gas release rates have been measured as a function of time at the 12- and 13.5-kW/ft power levels under all the planned sweep flow modes. The fission-gas release behavior observed during the operation of GB-10 to date has been consistent with that observed during operation of capsule GB-9 in that there is a strong continuous release during operation that is quite sensitive to power level and temperature changes. No significant activity bursts have been observed during shutdowns and startups.

Radiation surveys of the GB-10 effluent sweep lines in the reactor pool and valve boxes at reactor shutdown periods have indicated 300 to 700 mR/hr of long-lived activity on the lines and up to 12 R/hr at a junction box where welded couplings exist in the sweep lines. A segment of the effluent sweep line that was removed from the system while installing additional valving read 300 mR/hr. The principal activities found were due to ^{131}I, ^{134}Cs, ^{137}Cs, ^{140}Ba, and ^{140}La.

Other measurements made at the 12-kW/ft power level included fuel-rod flow resistance measurements, iodine-deposition measurements at a fuel burnup level of 18,100 MWd/metric ton, and observations of decay heating in the rod charcoal trap. In the operations to date, we have seen no significant fission product decay heating of the trap. Neutron radiography at 12 kW/ft (burnup of approximately 26,100 MWd/metric ton) showed that the 9-in.-long mixed-oxide fuel column had settled about $^{5}/_{32}$ in.

19. GCFR Steam-Generator Modeling

General Atomic Company personnel have developed and used a digital computer code for simulating various gas-cooled fast breeder reactor (GCFR) system transients. The model of the once-through steam generator used in this code was, of necessity, not very detailed or fine structured. This fact, plus the fact that little computer simulation of once-through steam generators has been done, led to some doubts as to the adequacy of their steam-generator model.

In response to the above-mentioned situation, a very detailed model of the once-through steam generator has been developed on the ORNL hybrid computer. A test transient was run on both computers with similar results.

20. GCFR Core Flow Test Facility

The Core Flow Test Facility for the Gas-Cooled Fast Reactor (GCFR) development program will provide a system in which helium at appropriate flow, temperature, and pressure conditions can be circulated over electric cartridge heaters that simulate a GCFR fuel assembly. The proposed test program will study the response of fuel assemblies to design steady-state and transient conditions. During 1973 the facility requirements were defined, and work on a conceptual design was initiated.

Part I. Thorium Utilization Program

1. HTGR Reprocessing Development (Subtask 110)

K. J. Notz

Reprocessing is that part of the High-Temperature Gas-Cooled Reactor (HTGR) fuel recycle in which spent fuel elements, after cooling about six months, are treated to recover the ^{233}U in a form suitable for subsequent refabrication into recycle fuel. The objective of this subtask is to develop the technology necessary for the design and operation of the HTGR Fuel Reprocessing Pilot Plant (FRPP), which is to be built at the Idaho Chemical Processing Plant (ICPP).

The major steps in reprocessing are head-end reprocessing (unit 1101), which includes crushing, burning particle separation, and dissolution; solvent extraction (unit 1102) to separate the thorium, uranium, and fission products from each other; off-gas cleanup (unit 1103), which involves decontamination from ^{129}I, ^{3}H, ^{220}Rn, and ^{85}Kr; product preparation (unit 1104) to convert the ^{233}U to a suitable form for shipment to the Refabrication Pilot Plant at ORNL; and waste treatment and disposal (unit 1105) to convert the various wastes to a form suitable for eventual disposal. Our scheduled development activity this past year was in the areas of head-end reprocessing and off-gas cleanup.

1.1 GENERAL DEVELOPMENT – 1100 [GENERAL ATOMIC COMPANY (GAC) LEAD]

No activity scheduled.

1.2 HEAD-END PROCESSING – 1101 (GAC LEAD)

V. C. A. Vaughen

1.2.1 Hot-Cell Studies

C. L. Fitzgerald

These investigations, which involve hot-cell burn-leach or burn-grind-burn-leach studies of irradiated HTGR-type fuel specimens, are designed to characterize the behavior of the various nuclides of interest throughout the various stages of processing. Experiments were completed this report period with specimens obtained from a recycle test element[1] (RTE) and recycle fuel test capsules H-1 and H-2.[2]

Recycle test element 7 (RTE-7) was removed from the Peach Bottom Reactor after 252 effective full-power days. The average element burnup was estimated by GAC to be 2.38% FIMA. A peak fast-neutron fluence of $\sim 10^{21}$ neutrons/cm^2 was accumulated.[3] The

1. R. P. Morissette and K. P. Steward, *Recycle Test Element Design, Fabrication and Assembly,* GA-10109 (September 1971).
2. *GCR-TU Programs Annu. Progr. Rep. Sept. 30, 1971,* ORNL-4760, pp. 65–66.
3. *GCR Programs Annu. Progr. Rep. Dec. 31, 1972,* ORNL-4911, p. 116.

fuel combination used in our experiment contained large Triso-coated ThC_2 fertile particles and smaller Triso-coated UC_2 fissile particles (type i), which is a combination quite similar to that used in the Fort St. Vrain Reactor.

Recycle fuel test capsules H-1 and H-2 were irradiated in the Engineering Test Reactor (ETR) to the full design fast fluence of 8×10^{21} neutrons/cm^2 during the period May 1971 through May 1972. The capsules were accidentally inverted during the last quarter of the irradiation period, which caused significant physical damage to a number of the specimens.[4] Of the less damaged specimens from these recycle fuel capsules, those selected for our experiments were H2-2, H2-3, and H2-4. The fuel combinations contained in these specimens are, respectively, UO_2 fissile particles, $(2Th,U)O_2$ fissile particles, and $(4Th,U)O_2$ fissile particles. All contain ThO_2 fertile particles, and all particles are Biso coated. The fertile particles approximate those planned for large commercial reactors. Experiments with H2-3 and H2-4 were completed during this report period.

RTE-7 experiment

Procedure. The primary purpose of this experiment was to obtain fission-gas release data using improved equipment (shown in Fig. 1.1) for gas trapping and filtration of particulates. An earlier experiment with this same fuel was reported last year.[3] The fuel rod was weighed and placed on a bed of −80 mesh alumina in the bottom of the burner assembly and burned using an oxygen flow rate of 100 cc/min. The combustion gases were anlyzed by passing them through (1) a 20-μm pore sintered metal filter and a 0.2-μm pore silver membrane filter, both maintained at 500°C, and then through another 0.2-μm silver membrane filter, a Gelman absolute filter, and molecular sieve traps (for tritium removal), all maintained at ambient cell temperature. The gases were then passed through CO_2, CO, and ^{85}Kr detectors, a CuO oxidizer, and additional molecular sieve traps to ensure complete tritium removal, through a wet test meter, and then into a bag. The burner ash was separated into a +45 mesh (>354 μm) fertile fraction, a +80 mesh (>177 μm) fissile fraction, and a −80 mesh (<177 μm) fines fraction consisting of the alumina and broken particles. The fines fraction was leached twice with Thorex reagent; the fertile and fissile fractions were each ground, burned, and leached twice with Thorex reagent. The +45 mesh fertile fraction was held at 850°C for 2 hr after burning and the +80 mesh fissile fraction was held at 850°C for 10 hr after completion of burning to determine if additional fission products were evolved. During secondary burning of the fertile and fissile fractions, two 20-μm sintered metal filters were used; all other features were identical with the initial burning operation.

4. Ibid., pp. 3–7.

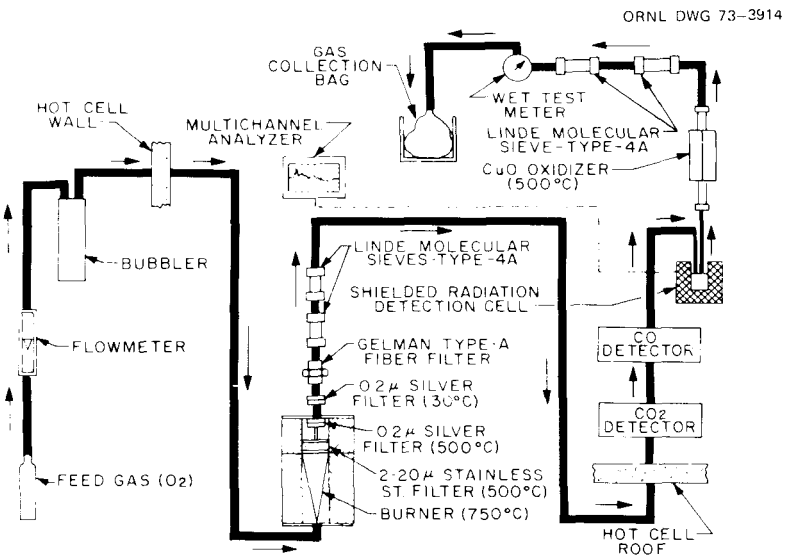

Fig. 1.1. RTE-7 fuel stick burning.

Results. The flowsheet used for the experiment, along with the weights of the materials involved in each operation, is shown in Fig. 1.2. The 10.846-g fuel rod, the second of the $6^1/_2$ rods removed from hole 7, was intact when removed. General Atomic gives the average weight of the stack of rods as 71.2 g, or 10.95 g per rod, in good agreement with our observed weight. We recovered 3.299 g of +80 mesh burned fissile particles and 3.499 g of +45 mesh burned fertile particles (burned down to the SiC coating). These weights correspond with 5.215 and 4.256 g of fissile and fertile particles with the outer PyC intact respectively. The total of these weights (9.46 g) agrees with the stick loading (9.46 g) reported by General Atomic, but the distribution gives an apparent cross-over value of fertile to fissile particles of 5.12%.

Table 1.1 gives the distribution and amounts of thorium and uranium and the uranium isotopic distribution. The cross-over value of fertile to fissile particles based on ^{233}U distribution is 4.45%, which is in good agreement with the value obtained from the weight distribution above. Additionally, the cross-over value of fissile to fertile based on ^{235}U distribution is 0.05%. These data show that ~0.2 g of ThC_2 (SiC coated) passed the +45 mesh screen and was retained with the fissile fraction and that >99.9% of the SiC-coated ThC_2 particles were <45 and >80 mesh. Subsequent thorium analysis of the fissile dissolver solutions indicated only about 3% cross-over, but the internal consistency of the uranium values makes them appear more realistic than the thorium values. This is apparent from the 1.9563 g of thorium recovered from an input of 2.214 g with an estimated 1% burnup. This indicates a thorium material balance of ~90%; the heavy metals distribution shows that the discrepancy is in the fertile fraction. Possible explanations are handling losses or fission product interference with the analytical procedure. The uranium isotopic analyses indicate that 1 to 1.5% of the thorium was converted to ^{233}U and that ~20% of the original ^{235}U fissioned.

Fission-gas release. The amounts of released tritium and ^{85}Kr found during the various processing steps are shown in Table 1.2. The total quantities, expressed as disintegrations per minute, for ^{3}H and ^{85}Kr are 1.8×10^{9} and 1.5×10^{11} respectively. These results differ from those of the previous RTE-7 experiment in two significant respects: more was collected this time and the ^{3}H distribution was different. This increase is due largely to our deliberate efforts to minimize gas losses and to avoid hydrolysis of the thorium and uranium

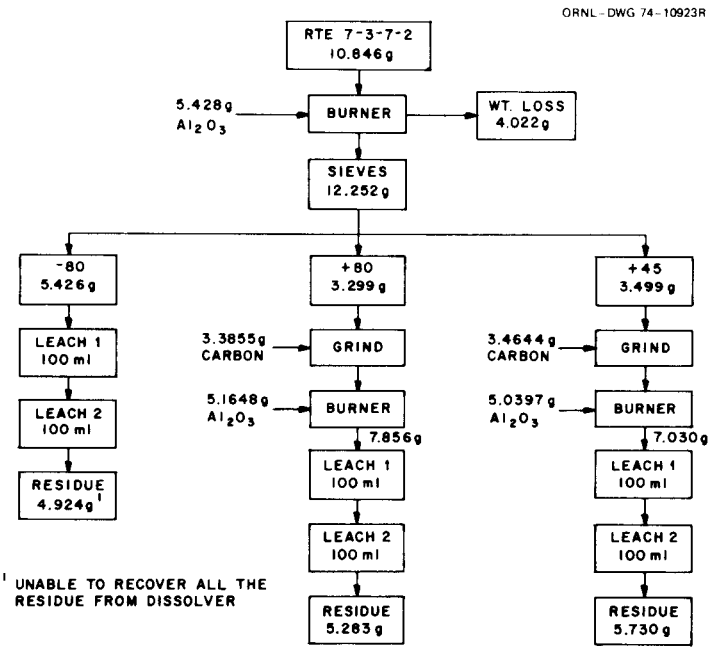

Fig. 1.2. Flowsheet for RTE-7 experiment.

Table 1.1. Uranium and thorium distribution for RTE-7 experiment

Isotope	Preirradiation as charged (g)[a]	Postirradiation			Total
		+45 fraction (g)	+80 fraction (g)	−80 fraction (g)	
^{233}U		0.02295	0.00107	0.00005	0.02407
^{234}U	0.00467	0.00104	0.00456	0.00001	0.00561
^{235}U	0.56620	0.00023	0.45462	0.00031	0.45516
^{236}U	0.00107	0.00001	0.03465	0.00001	0.03467
^{236}U	0.03545	0.00731[b]	0.02133[b]	0.00681[b]	0.03545[b]
Total	0.60800	0.03154	0.51624	0.00718	0.55496
Thorium	2.214	1.87240	0.0708	0.0131	1.9563

[a]Average values based on weights measured during fabrication.

[b]Values based on preirradiation isotopic analyses; all other postirradiation values were measured.

Table 1.2. Fission-gas release in burner off-gas during processing of second fuel rod from RTE-7 (7-3-7-2)[a]

	^{3}H	^{85}Kr
Total (dis/min)	1.746×10^{9}	1.525×10^{11}
Percent of total in:		
Initial burn	26.0	0.129
Fines leach	0.06	0.010
Fertile fraction (+45)	0.06	
Grind	0.06	0.221
Burn	13.23	3.220
Soak	0.21	
Leach	0.02	0.020
Total	13.52	3.461
Fissile fraction (+80)		
Grind	0.01	19.016
Burn	56.47	77.377
Soak (2 hr)	2.24	
Soak (8 hr)	1.66	
Leach	0.04	0.125
Total	60.42	96.518

[a]Designation 7-3-7-2 indicates RTE-7, fuel body 3, hole 7, fuel rod 2.

carbides during the grinding operations. The latter was accomplished by grinding in a closed grinder with a purge of argon–4% H_2. The purge gas was then passed through a hot CuO oxidation unit (to convert the H_2 and any $^{3}H_2$ to water), and the water was removed with molecular sieve traps before the gas was collected for ^{85}Kr analysis.

The ^{3}H distribution is different this time in two respects: more was released during the handling of the fissile fraction, and, of this portion, most was released during the actual burning (and not during a post-burn holding period as before). The new distribution is far more reliable than the prior results because of the special efforts made to collect all the gases this time. Based on the latest data, two points of interest are worth noting. First, a rather large fraction (26%) of the ^{3}H was released during a post-burn holding period. Second, based on ^{85}Kr release, the fraction of broken particles was small, so some other factor must account for the ^{3}H released during initial burning. Thus, one must assume that the ^{3}H associated with the matrix carbon is not due to ternary fission but rather is a result of light element impurities in the matrix and/or is adsorbed from the coolant gas. The ^{3}H holdup during and after the fissile fraction burn may result from chemisorption on uranium oxide and might require long burning times in order to lower the ^{3}H content to acceptable levels for subsequent aqueous processing.

Fission product distribution. The distribution of fission products in the off-gas system is summarized in Table 1.3. The fraction of each nuclide that found its way into the off-gas system ranged from 0.04% for ^{144}Ce to 100% for ^{75}Se. As expected, the fraction of ruthenium was quite high (25.66%), with cesium also fairly high (~6%); ^{75}Se, found only in the matrix carbon, must be an activation product from ^{74}Se, which is present as an impurity. We estimate that 3 ppm natural selenium could account for the observed off-gas activity.[5]

5. C. W. Kee, personal communication.

Table 1.3. Fission product distribution (dis/min) in filter train used in processing second fuel rod from RTE-7

	^{144}Ce	^{106}Ru	^{137}Cs	^{134}Cs	^{95}Zr	^{95}Nb	^{75}Se	^{125}Sb
Matrix burn								
Stainless steel frit 1							7.71×10^5	
Hot Ag filter							8.81×10^3	
Cold Ag filter				No detectable activity				
Gelman filter				No detectable activity				
Line leach	5.14×10^8	1.83×10^7	6.02×10^7	1.20×10^7	4.99×10^6	8.8×10^5		
Total	5.14×10^8	1.83×10^7	6.02×10^7	1.20×10^7	4.99×10^6	8.8×10^5	7.80×10^5	
Fertile burn								
Stainless steel frit 1	1.23×10^7	2.64×10^7	1.37×10^6	2.82×10^5	$\leq 1 \times 10^5$			
Stainless steel frit 2	1.86×10^6	6.64×10^6	5.24×10^4	1.92×10^4	$\leq 2 \times 10^4$			
Hot Ag filter	1.95×10^5	1.16×10^4	1.21×10^4	3.52×10^3	2.19×10^3	8.82×10^3		
Cold Ag filter				No detectable activity				
Gelman filter				No detectable activity				
Line leach	1.44×10^8	4.85×10^8	9.1×10^7	3.09×10^7	2.55×10^6	1.05×10^7		8.6×10^6
Total	1.58×10^8	5.18×10^8	9.24×10^7	3.12×10^7	2.67×10^6	1.05×10^7		8.6×10^6
Fissile burn								
Stainless steel frit 1	8.00×10^8	1.74×10^{10}	3.57×10^{10}	1.18×10^{10}	1.10×10^8	6.02×10^7		9.00×10^8
Stainless steel frit 2	6.94×10^7	1.14×10^{10}	3.79×10^8	1.18×10^8	2.36×10^7	2.39×10^7		4.70×10^7
Hot Ag filter	$\leq 3 \times 10^6$	1.70×10^8	$\leq 4 \times 10^5$	$\leq 2 \times 10^5$	$< 3 \times 10^5$	$< 6 \times 10^4$		$\leq 3 \times 10^5$
Cold Ag filter				Trace of 0.24-MeV gamma activity				
Gelman filter				Trace of 0.24-MeV gamma activity				
Line leach	4.43×10^7	2.98×10^9	4.2×10^7	1.37×10^7	3.00×10^6	4.83×10^6		1.5×10^7
Total	9.17×10^8	3.20×10^{10}	3.61×10^{10}	1.19×10^{10}	1.31×10^8	8.90×10^7		9.62×10^8
Total in off-gas	1.59×10^9	3.25×10^{10}	3.63×10^{10}	1.20×10^{10}	1.45×10^8	1.00×10^8	7.80×10^8	9.71×10^8
Percent in off-gas	0.042	26	6.1	6.0	0.94	0.47	100	2.1

Generally, activity found in the off-gas stream is concentrated in two places: on the first stainless steel frit, where it is trapped with coarser particles (or condensation products), and in the line that joins the hot (500°C) silver filter to the cold (~30°C) silver filter, where it condenses. No significant amounts of activity reached the second silver filter.

H-capsule experiments

Procedure. The general flowsheet for these experiments was burn-leach (i.e., no grinding step needed), and the specific operations were (1) weigh, (2) burn, (3) sieve to separate by size, (4) dissolve, and (5) collect any residues. Emphasis during burning was concentrated on (1) recovery and characterization of volatile and entrained materials in the off-gases and (2) reduction-oxidation cycling intended to force tritium and krypton release. The burner off-gases were analyzed by passing them through a 20-μm sintered stainless steel filter, a five-stage cascade impactor, and a 0.2-μm silver membrane filter, all maintained at 500°C, and then through a water-cooled condenser, another 0.2-μm silver membrane filter, a Gelman absolute filter, and molecular sieve traps (for tritium removal), all maintained at ambient cell temperature. A pre-burn period at 850°C in an inert atmosphere was used in an attempt to desorb any fission gases in the matrix carbon. Two post-burn holds at 850°C were used to determine if fission gases that were not released promptly during burning would be slowly released. All gas streams contained either H_2 or H_2O (via a bubbler) to provide isotopic dilution of tritium. Thus the overall burning operation consisted of six stages:

1. hold at 850°C for 1 hr in Ar–4% H_2 (100 cc/min) prior to burning,
2. burn with wall temperature at 750°C in "wet" air at 300 cc/min for time required (about 4 hr),
3. hold at 850°C for 2 hr in "wet" air at 100 cc/min,
4. hold at 850°C for 8 hr in "wet" air at 100 cc/min,
5. reduction cycle in Ar–4% H_2 at 100 cc/min for 6 hr at 850°C,
6. oxidation cycle in "wet" O_2 at 100 cc/min for 2 hr at 850°C.

Gas samples for ^{85}Kr analysis and molecular sieve traps for $^{3}H_2$ recovery were taken at the end of each of the above stages. The collection plates from the cascade impactor were analyzed radiochemically after examination by a scanning electron microscope, and all filters were analyzed radiochemically.

Selective dissolution of the uranium-bearing fissile fractions was tested by using boiling concentrated HNO_3 prior to dissolution in Thorex reagent. A similar treatment sequence was used for the thoria fertile fractions.

Fuel rod specimens H2-3 and H2-4 were identified by their chemical behavior during processing, since the identification markings on the sample containers were illegible.

Results. The flowsheet used for the experiments is shown in Fig. 1.3. As mentioned previously, inversion of the test capsules during the last irradiation cycle caused significant damage to some of the specimens. These particular specimens consisted of several small pieces and a high percentage of loose powder. Thus, complete fuel rods were not processed, and sample weights were about 80% of a complete rod. Heavy metals recovered show that separation of fertile and fissile fractions with nitric acid was successful in the first experiment (>9.5%) but not in the second. Material balances for the first experiment were poor, which indicates that we did not get a representative portion of the fuel rod (i.e., we obtained a higher percentage of matrix carbon than normal). Weights were reasonable for the second experiment. Isotopic analyses show that about 43% of the original ^{235}U fissioned and that about 1.8% of the thorium was converted to ^{233}U.

Fission-gas release. The distribution of the fission gases ^{85}Kr and $^{3}H_2$ during the various stages of processing for the first two experiments is shown in Table 1.4. These two experiments were on specimens H2-3 (2Th/U) and H2-4 (4Th/U). It is evident from these data that there are differences in the krypton and $^{3}H_2$ release patterns. The significant difference in the ^{85}Kr release is during dissolution of the fissile fraction. The majority of the ^{85}Kr remaining was released with HNO_3 dissolution in the first experiment (2Th/U), whereas Thorex dissolution was required to effect this release in the second experiment (4Th/U). Differences stand out also in the $^{3}H_2$ release, in the pre-burn hold (Ar–4% H_2) and in the reduction cycle (Ar–4% H_2). These differences show that fission-gas release patterns can vary with the Th/U ratio in the fissile particles.

Fission product distribution. The distribution of selected fission products in the burner off-gases for these experiments is shown in Tables 1.5 and 1.6. The bulk of the volatile or entrained material was concentrated on the roughing filter and in the hot (500°C) off-gas lines. The general distribution is similar to previous data. We are still in the process of analyzing the data from the cascade impactor, but preliminary

Table 1.4. Fission-gas release during processing for experiments H2-3 and H2-4 (percent of total collected)

	^{85}Kr		$^{3}H_2$	
	H2-3	H2-4	H2-3	H2-4
Pre-burn soak (Ar–4% H_2)	0.33	0.82	7.04	30.30
Burn (air)	49.22	59.77	64.49	46.20
2-hr soak (air)	8.57	1.51	25.94	3.02
8-hr soak (air)	≤0.79	0.86	1.68	7.36
Reduction cycle (Ar–4% H_2)	≤0.19	0.33	0.40	8.66
Oxidation cycle (O_2)	≤0.09	0.07	0.09	0.52
Fines				
L-1(HNO_3)	*a*	0.03	*a*	0.17
L-2(Thorex)	0.79	1.30	0.002	3.01
L-3(Thorex)		0.06		0.25
Fertile				
L-1(HNO_3)	≤0.21	0.14	0.12	0.27
L-2(Thorex)	18.32	16.37	0.08	0.06
L-3(Thorex)	0.22	0.07	0.03	0.01
Fissile				
L-1(HNO_3)	11.16	0.10	0.03	0.04
L-2(HNO_3)	0.17	0.09	0.05	0.04
L-3(Thorex)	9.61	18.40	0.04	0.07
L-4(Thorex)	0.35	0.08	0.01	0.01
Total	100	100	100	100

[a]Not done.

Table 1.5. Distribution of fission products for specimen H2-3

	^{75}Se	^{95}Zr	^{106}Ru[a]	^{134}Cs	^{137}Cs	^{144}Ce
Total activity, dis/min	7.0×10^3	7.4×10^{10}	2.3×10^{11}	5.5×10^{10}	3.0×10^{11}	3.2×10^{12}
Distribution, %						
Burner ash		99.59	80.88	38.27	48.86	99.88
Stainless steel frit (hot)[b]		0.37	15.49	52.53	43.58	0.10
Off-gas system						
Hot off-gas line[b]		0.04	3.61	9.08	7.46	0.02
Impactor (500°C)		<0.001	0.004	0.08	0.07	<0.001
Hot Ag filter (500°C)	22.6	<0.001	<0.001	<0.001	<0.001	<0.001
Condenser (~20°C)	28.4	<0.001	<0.001	<0.001	<0.001	<0.001
Cold Ag filter (RT)	21.1	<0.001	<0.001	<0.001	<0.001	<0.001
Gelman filter (RT)	27.9	<0.001	<0.001	<0.001	<0.001	<0.001
Cold off-gas line (RT)		0.003	0.02	0.04	0.03	<0.001

[a]Trace amounts (~10^3 dis/min) found in $^{3}H_2$ traps beyond filter system.

[b]The temperature of this frit is somewhere between burner temperature (850°C) and the hot off-gas system temperature (500°C). The hot off-gas line, while nominally at 500°, is probably slightly hotter because of heat carried out of the burner by the hot gases.

Table 1.6. Distribution of fission products for specimen H2-4

	^{95}Zr	^{106}Ru	^{134}Cs	^{137}Cs	^{144}Ce
Total activity, dis/min	2.75×10^{10}	3.87×10^{11}	5.55×10^{10}	2.90×10^{11}	1.87×10^{12}
Distribution, %					
Burner ash	99.27	83.98	42.52	48.62	99.47
Stainless steel frit	0.71	15.89	55.86	50.00	0.16
Hot off-gas line	0.07	0.17	1.32	1.19	0.02
Impactor	0.002	0.03	0.28	0.24	0.001
Hot Ag filter	<0.001	<0.001	<0.001	<0.001	<0.001
Condenser	<0.001	<0.001	<0.001	<0.001	<0.001
Cold Ag filter	<0.001	<0.001	<0.001	<0.001	<0.001
Gelman filter	<0.001	<0.001	<0.001	<0.001	<0.001
Cold off-gas line	0.07	0.03	0.04	0.04	0.07

ORNL DWG 74-10922

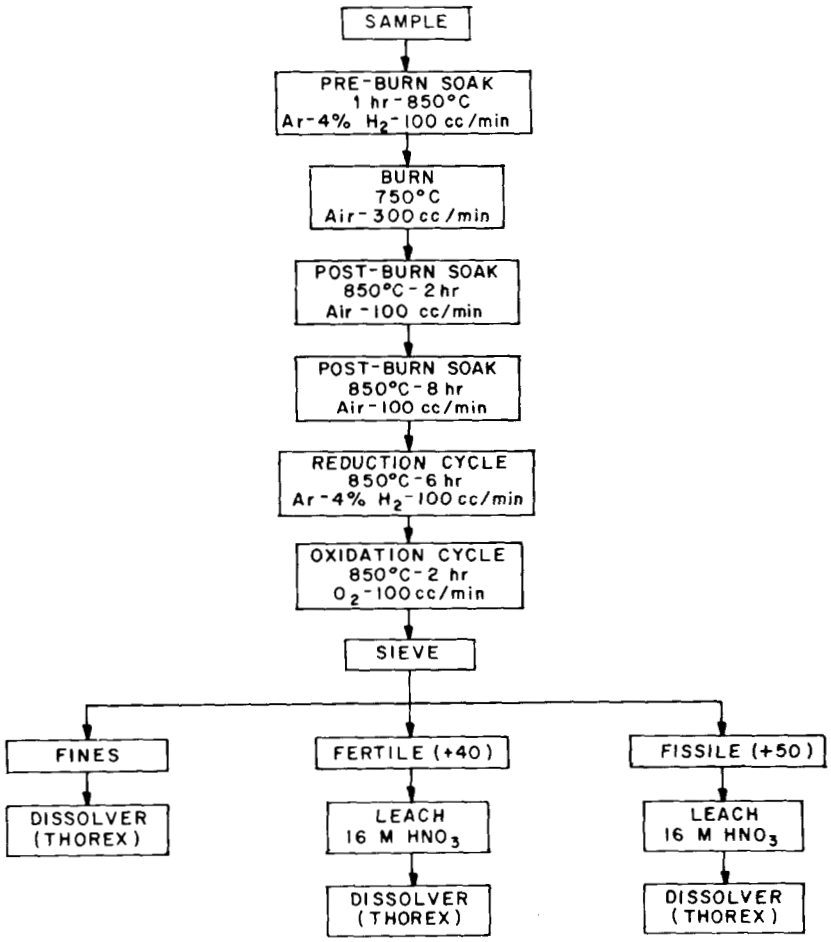

Fig. 1.3. Flowsheet used for H-capsule experiment.

analysis indicates that the composition is uniform for each of the particle size fractions.

1.2.2 Vapor Transport of Fission Products

J. H. Shaffer

In the head-end reprocessing of spent HTGR fuel elements, graphite matrix and particle coating materials will be burned in oxygen and the residual ash processed for the recovery of fissile and fertile materials. Provisions have been made for the decontamination of the burner effluent to remove entrained solids and to separate known gaseous fission products. However, allowable fission product release rates, as established by federal effluent regulation, correspond to very low vapor pressures in the process effluent stream and represent very small fractions of inventory values. Consequently, the available data and potential laboratory methods were assessed to an experimental program for examining vapor transport characteristics of various fission product elements under simulated conditions in the graphite burner.

Necessary fission product decontamination factors for an HTGR fuel reprocessing plant have been estimated on the basis of total volatilization of all fission products entering the plant.[6] Although the graphite burning process will be designed to retain most of the fission products in the residual ash, the values cited for the quantities and specific activities of the various nuclides, process dilution factors, and allowable airborne concentration limits provide a realistic basis for assigning significant vapor transport parameters. Permissible loss rates for the various fission products were calculated using a plant and stack dilution rate of 10^{13} ft^3/day. Vapor transport rates that would result from a process effluent stream of 5.2×10^5 ft^3 per metric ton of heavy metal per day were calculated as hypothetical vapor pressures assuming total gas behavior and monatomic nuclide species. Limiting vapor pressures for each element were calculated from these values and consideration of the relative abundance of each isotope. These values, shown in Table 1.7, indicate that analytical detection levels corresponding to vapor pressures as low as 10^{-10} torr may be required to obtain significant results from an experimental investigation.

The graphite burning process will be accomplished under controlled conditions in order to regulate burner temperatures within limits of 750 to 1300°C. This control will probably be achieved by regulation of graphite and oxygen feed rates into the burner. However, the manner by which this control is achieved may affect fission product transport in the system. Conceivably, excess oxygen in the feed stream could promote oxidation of certain fission products to more volatile valence states. Similarly, a deficiency in oxygen would impose more reducing conditions, which may promote the formation of more volatile suboxide or metallic species.

The thermodynamic feasibility of the events cited above cannot be established with certainty for many of the fission product elements. However, data from which the vapor pressures of both metals and oxides may be estimated have been published for a number of elements of interest to this program. Values calculated for temperatures of 1000 and 1500°K are also shown in Table 1.7. Estimates for vapor pressures of the elements were reported by Margrave,[7] and those for the oxide species were calculated from the compilation by Bedford and Jackson[8] for oxygen partial pressures of 0.1 atm. A preliminary review of these values indicates that certain elements (including cesium, ruthenium, antimony, tellurium, selenium, tin, and silver) may have sufficient volatility under mildly oxidizing conditions at 1000°K to exceed allowable effluent standards. At slightly higher temperatures, uranium volatility may be significant.

The data illustrated above are applicable where pure condensed phases are present. Under burner conditions, the various fission products may have much lower thermodynamic activities owing to their inclusion in condensed phases with urania and thoria in the ash. Under conditions where UO_3 volatility becomes significant, the vapor entrainment of certain of these fission products may also become significant. Consequently, the scope of an applied experimental program should include an appraisal of the effects of condensed phase composition on the relative volatility of solute elements in U_3O_8.

The experimental program will use equipment designed to investigate the volatilities of selected fission product nuclides at temperatures to 1300°C. The experimental procedure, which will employ a transpiration technique, will provide for the measurement of

6. J. W. Snider and R. E. Leuze, *Proc. 12th AEC Air Cleaning Conference, Oak Ridge, Tenn., Aug. 28–31, 1972,* CONF-720823, vol. II, pp. 501–29, January 1973.

7. J. L. Margrave, *The Characterization of High Temperature Vapors,* Wiley, New York, 1967, pp. 478–80.

8. R. G. Bedford and D. D. Jackson, *Volatilities of the Fission Product and Uranium Oxides,* UCRL-12314 (Jan. 20, 1965).

Table 1.7. Vapor pressures of metals and oxides at elevated temperatures

Element	Allowable vapor pressure (torr)	Isotope basis	Vapor pressure of metals (torr)		Vapor pressure of oxides[a]					
					At 1000°K			At 1500°K		
			At 1000°C	At 1500°K	Condensed phase	Vapor specie	Pressure (torr)	Condensed phase	Vapor specie	Pressure (torr)
Pu	5.65×10^{-9}	238	2.1×10^{-10}	1.8×10^{-4}						
Cm	4.96×10^{-9}	244								
Sr	7.68×10^{-7}	90	0.80	4.5×10^{2}	SrO	Sr	4.1×10^{-26}	SrO	Sr	3.58×10^{-3}
						SrO	7.6×10^{-17}		SrO	7.6×10^{-8}
Ce	1.42×10^{-7}	144	1×10^{-12}	6.4×10^{-6}	CeO_2	Ce	2×10^{-58}	CeO_2	Ce	1.4×10^{-32}
						CeO	4×10^{-34}		CeO	1.0×10^{-17}
Cs	7.5×10^{-7}	134	1.6×10^{3}	2.5×10^{4}	Cs_2O	Cs	0.108	Cs_2O	Cs	760
						Cs_2	6.16×10^{-3}		Cs_2	6.61
						CsO	0.465		CsO	369
Th	3.49×10^{-10}	228	1×10^{-20}	2.5×10^{-11}						
Ru	1.84×10^{-7}	106	1×10^{-22}	2×10^{-12}	RuO_2	Ru	3.2×10^{-29}	RuO_2	Ru	6.04×10^{-13}
						RuO	1.11×10^{-20}		RuO	3.39×10^{-8}
						RuO_2	3.09×10^{-14}		RuO_2	1.56×10^{-6}
						RuO_3	9.49×10^{-5}		RuO_3	0.575
						RuO_4	9.12×10^{-4}		RuO_4	4.26
Zr	1.63×10^{-7}	95	1×10^{-21}	1×10^{-11}	ZrO_2	Zr	1.78×10^{-68}	ZrO_2	Zr	5.3×10^{-39}
						ZrO	2.98×10^{-44}		ZrO	6×10^{-24}
						ZrO_2	3.69×10^{-27}		ZrO_2	2.34×10^{-14}
Y	1.47×10^{-7}	91	2×10^{-12}	6×10^{-6}	Y_2O_3	Y	4.24×10^{-54}	Y_2O_3	Y	2.7×10^{-30}
						YO	2.14×10^{-32}		YO	5.87×10^{-17}
U	5.94×10^{-8}	232	1.6×10^{-15}	1×10^{-7}	U_3O_8	U	2.7×10^{-67}	U_3O_8	U	1.2×10^{-37}
						UO	1.6×10^{-41}		UO	$4.65 \times$
						UO_2	3.8×10^{-22}		UO_2	2.06×10^{-10}
						UO_3	3.7×10^{-9}		UO_3	1.37×10^{-2}
Nb	2.64×10^{-7}	95	1×10^{-26}	3.2×10^{-15}	Nb_2O_5	Nb	1.03×10^{-64}	Nb_3O_5	Nb	8.41×10^{-36}
						NbO	8.6×10^{-43}		NbO	3.25×10^{-22}
						NbO_2	3.07×10^{-27}		NbO_2	1.5×10^{-13}
Eu	1.6×10^{-6}	154	0.14	1.6×10^{2}						
Am	1.40×10^{-6}	243	2.5×10^{-6}	6.4×10^{-2}						
Pa	4.1×10^{-7}	233								
Pm	4.8×10^{-6}	147			Pm_2O_3	Pm	2.68×10^{-44}	Pm_2O_3	Pm	3.4×10^{-24}
					Pm_2O_3	PmO	3.53×10^{-20}		PmO	1.1×10^{-11}
Sb	2.22×10^{-6}	125	2.8	1×10^{4}	Sb_2O_4	Sb	5.88×10^{-17}	Sb_2O_3	Sb	1.06×10^{-5}
						Sb_2	1.86×10^{-14}		Sb_2	3.36×10^{-4}
						Sb_4	4.48×10^{-13}		Sb_4	3.01×10^{-4}
						SbO	2.4×10^{-16}	SbO	SbO	2.7×10^{-6}
						Sb_4O_6	6.93		Sb_4O_6	622
Np	1.96×10^{-4}	237								
Sm	1.6×10^{-4}	151	8×10^{-3}	32	Sm_2O_3	Sm	3.3×10^{-43}	Sm_2O_3	Sm	3.6×10^{-23}
						SmO	1.19×10^{-25}		SmO	4.2×10^{-13}
Te	4.04×10^{-7}	127m	$>10^{2}$	$>10^{3}$	TeO_2[b]	Te	4.83×10^{-8}	TeO_2[c]	Te	3.24
						Te_2	2.25×10^{-5}		Te_2	58.7
						TeO	2.33×10^{-10}		TeO	7.2×10^{-3}
						TeO_2	0.122			
Ba	1.74×10^{-9}	137m	0.16	50	BaO	Ba	2.12×10^{-25}	BaO	Ba	1.05×10^{-12}
						BaO	9.35×10^{-13}		BaO	2.57×10^{-5}
Sn	3.18×10^{-8}	123m	4×10^{-8}	2.6×10^{-3}	SnO_2	Sn	1.85×10^{-26}	SnO_2	Sn	2.8×10^{-11}
						SnO	3.27×10^{-14}		SnO	5.8×10^{-4}
Ac	4.15×10^{-10}	225	1.2×10^{-12}	8×10^{-6}						
Bi	1.7×10^{-15}	211	$\sim 10^{-1}$	$\sim 10^{2}$						
Fr	1.7×10^{-16}	221	$>10^{3}$	$>10^{3}$						
Ag	1.9×10^{-7}	110m	5×10^{-6}	0.29	Ag_2O	Ag	5.55×10^{-5}	Ag[c]	Ag	0.256
						AgO	1.09×10^{-12}		AgO	4.37×10^{-7}

[a]Calculated for $P_{O_2} = 0.1$ atm. [b]Solid. [c]Liquid.

species that are transported by potentially reactive gas mixtures of CO_2, CO, and O_2 through a modified effusion-type cell and deposited on a collector plate. Radiotracers will be incorporated in the preparation of starting materials to permit analyses by radiochemical methods.

1.2.3 Experimental Studies of a Whole-Block Burner

P. A. Haas H. Barnert-Wiemer

Experimental studies were made using one-sixth-scale blocks prepared by three axial cuts across corners of the hexagonal HTGR fuel blocks.[9] The principal mechanism of heat removal was by radiation from the graphite to the air-cooled metal burner walls. Since the one-sixth block is not symmetrical, calculations for either correlation of experimental data or theoretical approaches are difficult. The range of allowable gas flow rates was limited by the capacity of the off-gas system. Burning could not be maintained at low O_2 concentrations due to excessive heat losses by both radiation to the walls and by the heat capacity of the diluent gas.

Experimental results with the one-sixth block burner are favorable for continued development of the whole-block burner concept.[9] Oxygen can be reacted with an HTGR fuel block at practical rates for some temperatures in the range of 800 to 1600°C. The exit O_2 concentrations will be low over at least part of this range if the gas is channeled through the coolant holes of axially aligned blocks. The reaction of the fuel blocks for specified burner conditions is reproducible without fluctuations, passivation of the graphite surface, or other unpredictable variations. Together, these results indicate that we can get a practical, reproducible graphite burning rate and a low exit O_2 concentration for some O_2-CO_2 mixtures at some temperatures below 1600°C. The results do not allow us to predict the required temperature or the exit CO content.

An adiabatic flow reactor concept is now recommended with recycle of cooled gas to provide temperature control and heat removal.[10] A simplified model was selected, and computer programs were written to calculate gas compositions and temperatures through the burner. Complete utilization of O_2 or low exit concentrations of O_2 depend on graphite temperatures high enough to produce CO, which reacts with O_2 in the bulk gas. It does not appear practical to operate with both high utilization of O_2 and low exit CO concentration. Instead, the burner conditions should be chosen to clearly favor either moderate concentrations of O_2 or CO in the exit gas. Moderate exit concentrations of O_2 would allow lower graphite temperatures and would probably give the desired burning rates for three axially aligned blocks. Moderate exit concentrations of CO would assure higher burner capacities but would result in higher temperatures and more complex burner control behavior. An experimental adiabatic burner is recommended to verify the calculated results. The general conclusions would also apply to adiabatic fluidized-bed or fixed-bed burners.

1.3 SOLVENT EXTRACTION – 1102 (GAC LEAD)

No activity scheduled.

1.4 OFF-GAS CLEANUP – 1103 (ORNL LEAD)

R. W. Glass

1.4.1 Laboratory Development

R. D. Ackley K. J. Notz A. B. Meservey
J. T. Bell S. R. Buxton

The system Kr-CO_2

The KALC (krypton absorption in liquid CO_2) process is being developed for removing ^{85}Kr from the burner off-gas generated in the head-end reprocessing of HTGR fuel. To provide the basis for process design calculations, the distribution of krypton between gaseous and liquid CO_2 was investigated in the laboratory over the −52.8 to +29.1°C range, as described previously.[11] The results were expressed in terms of a separation factor, Y_{Kr}/X_{Kr}, which is the ratio of the mole fraction of krypton in the gaseous phase to that in the liquid phase and which decreases with increasing temperature (from 29.4 to 1.4 for the above temperature range).

More recently, the effect of adding about 2% Freon-12 (CCl_2F_2) to the Kr-CO_2 system was investigated at −36°C, and the observed separation factor was not affected by the Freon. The laboratory work on the Kr-CO_2 system is complete, and a final report is in preparation.

---

9. H. Barnert-Wiemer, *HTGR Fuel Reprocessing: Preliminary Experimental Studies of a Whole Block Burner*, ORNL-TM-4518 (in preparation).

10. P. A. Haas, *HTGR Fuel Reprocessing: A Whole Block Burner with Recycle of Cooled Gas for Temperature Control*, ORNL-TM-4519 (in preparation).

11. *GCR Programs Annu. Progr. Rep. Dec. 31, 1972*, ORNL-4911, pp. 7–8.

The system Xe-CO_2

The behavior and disposition of xenon in the KALC process are considerably less crucial than for ^{85}Kr because the radioactive fission product xenon isotopes have relatively short half-lives and the cooling times for HTGR fuels are about 150 days. However, obtaining Xe-CO_2 distribution data analogous to those obtained for the Kr-CO_2 system was deemed advisable, particularly in view of the appreciable concentration of stable xenon in the burner off-gas. Accordingly, the separation factors for xenon in CO_2 have been determined over the −55 to +30°C range.

The equipment and experimental techniques were generally the same as those used in the Kr-CO_2 work,[11,12] and the tracer was ^{133}Xe. The only experimental change made during the course of the Xe-CO_2 measurements was the replacement of the single-channel analyzer with a multichannel analyzer, thus giving an improved measurement of the ^{133}Xe 81-keV photopeak. A xenon concentration of about 10^{-4} mole % was used.

The Xe-CO_2 results are presented in Table 1.8 and in Fig. 1.4. The shape of the xenon separation factor vs temperature plot is similar to that previously observed for krypton. As expected (because of the predicted higher solubility of Xe), the xenon separation factors are lower than those for krypton by a factor that varies with temperature. For example, the ratio of separation factors is approximately 0.25 at −50°C, and this ratio increases with temperature and approaches unity near the critical temperature as do the individual separation factors. Some of these results and those for the Kr-CO_2 system were reported at an ANS meeting in November 1973.[13]

There has been some concern that the krypton and xenon separation factors as determined would be biased high if there should be a condensed film on the cylinder inner wall above the liquid level and/or if there should be a mist in the vapor. The cylinder temperatures were uniform in obtaining the results discussed above; that is, the separation factors were determined for the saturated or nearly saturated vapor at equilibrium with the liquid. A group of Xe-CO_2 measurements were performed recently in which the separation factors were determined with the vapor phase at a temperature some 10°C higher than that of the liquid phase. This technique should minimize any film or mist effects. These particular measurements were restricted to the projected temperature range of actual KALC operation, −40 to −20°C. Final calculation of the corresponding separation factor is incomplete, but preliminary values indicate that there are no detectable film and/or mist effects in the earlier separation factors.

Table 1.8. Separation factors for the Xe-CO_2 system

Temperature (°C)	Analyzer used[a]	Photon energy employed[b] (keV)	Separation factor $(Y_{Xe}/X_{Xe})^c$
−54.8	M	81	7.55
−54.4	M	81	7.33
−52.6	M	81	7.15
−50.4	M	81	6.94
−46.2	M	81	5.92
−46.1	M	81	6.01
−36.3	S	>10	4.79
−36.3	S	81	4.80
−26.9	M	81	3.74
−20.6	M	81	3.30
−18.0	S	>10	3.22
−18.0	S	81	3.09
−17.9	S	>10	3.19
−9.3	S	>10	2.78
−9.2	S	81	2.79
−0.2	S	>10	2.34
−0.2	S	>10	2.33
−0.2	S	81	2.35
10.3	S	81	1.94
10.4	S	>10	1.94
10.4	M	81	1.87
19.6	M	81	1.60
20.8	S	81	1.51
20.9	S	>10	1.59
21.0	M	81	1.57
21.1	M	81	1.57
22.0	M	81	1.45
22.9	M	81	1.50
24.9	M	81	1.43
27.0	M	81	1.31
29.1	M	81	1.22
30.0	M	81	1.18
30.5	M	81	1.10

[a] M = multichannel analyzer; S = single-channel analyzer.
[b] Tracer was ^{133}Xe.
[c] Y = mole fraction in vapor phase; X = mole fraction in liquid phase.

12. *GCR-TU Programs Annu. Progr. Rep. Sept. 30, 1972.* ORNL-4760, p. 22.

13. K. J. Notz, A. B. Meservey, and R. D. Ackley, "The Solubility of Krypton and Xenon in Liquid CO_2," *ANS Trans.* 17, 318 (1973).

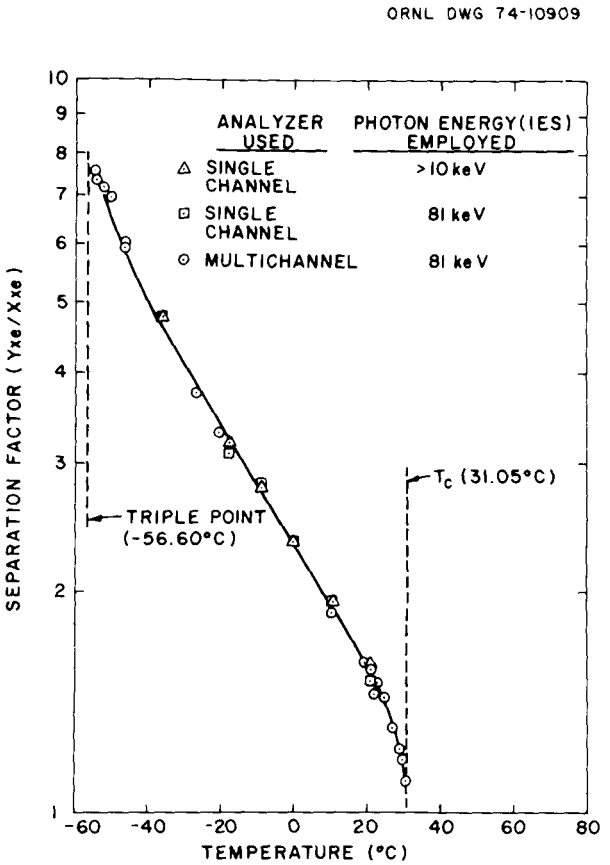

Fig. 1.4. Xenon distribution between gaseous and liquid CO_2.

The system CO_2-I_2-H_2O (Ref. 14)

Preliminary spectrophotometric studies of the chemistry of HTGR fission products in liquid and gaseous CO_2 have shown that I_2 is not very stable in CO_2, that H_2O is associated with CO_2, and that H_2O further decreases the stability of I_2 in the three-component system.

The H_2O-CO_2 binary system was studied to establish techniques for analyzing water in the three-component system. However, early results indicated molecular association of H_2O and CO_2, and a more rigorous investigation was initiated because of the possible entrapment of T_2O in the KALC process. The concentration of water in liquid or gaseous CO_2 can be observed by the intensity of the 1.88-μ absorption band, which is characteristic of the H–O–H structure. The molar absorptivity of this band for H_2O in liquid CO_2 was determined to be 4.0 for the 5 to 25°C range by differential techniques and by combining the literature data for the solubility of H_2O in CO_2 with our observed absorbance data. The vapor-phase association of H_2O with CO_2 was studied by observing the 1.88-μ band for the vapor phase over liquid H_2O at CO_2 pressures of 400 to 900 psi. The amount of H_2O vapor over pure H_2O at these temperatures cannot be detected by these techniques, but the amount of H_2O in the vapor increased with the CO_2 pressure. The data have been interpreted by assuming that the following equilibrium is established in the vapor phase:

$$n\mathrm{CO_2} + \mathrm{H_2O} \overset{K_n}{\rightleftharpoons} (\mathrm{CO_2})_n\mathrm{H_2O}\,.$$

The concentration of H_2O in the vapor phase was assumed to be constant, and the absorbance at 1.88 μ was assumed to represent the $(CO_2)_nH_2O$ species only, because H_2O could not be detected without the CO_2 overpressure. If these assumptions are valid, a logarithmic plot of product concentration vs CO_2 concentration should be linear with a slope of n and an intercept of $\ln K_n'$, where K_n' is the product of the concentration quotient K_n and the H_2O concentration. The logarithmic plots at 15, 25, and 40°C are shown in Fig. 1.5. This analysis indicates that there is molecular association of H_2O with CO_2 and that the association does not disrupt the H–O–H structure of the water. Furthermore, the CO_2/H_2O mole ratio in the vapor-phase association product is indicated to be 1 or 2, depending on the temperature and the CO_2 pressure.

The visible absorption spectrum of I_2 in liquid CO_2 was observed to be similar to that of I_2 in CCl_4 and n-hexane; that is, CO_2 appeared to be a nonpolar solvent for I_2. The I_2 band was at 5141 Å in liquid CO_2, a shift of approximately +20 Å as compared with that in CCl_4. The intensity of the I_2 band decreased with time, indicating that the I_2 was reacting, and the addition of water to the CO_2 increased the rate of I_2 reaction, as shown in the last column in Table 1.9. The concentration of H_2O in liquid CO_2 was monitored by the 1.88-μ band with a molar absorptivity of 4.0; this H_2O band also decreased in the three-component system, indicating that the H_2O was reacting with the I_2.

14. Work reported in this section is supported by the Division of Physical Research and is included in this report because of its direct utility to the Thorium Utilization Program.

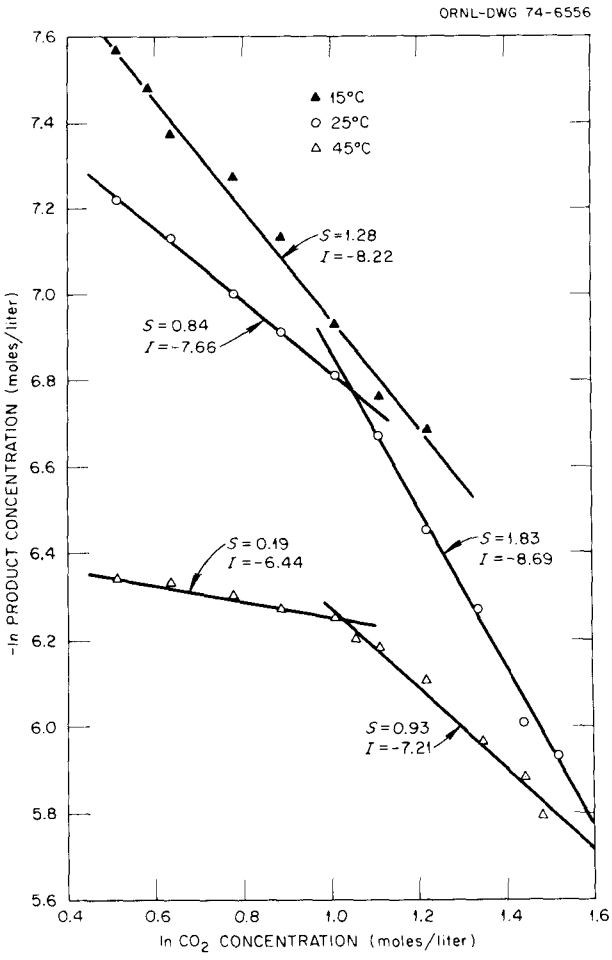

Fig. 1.5. Logarithmic plots of the concentrations of CO_2 and of the CO_2-H_2O association for the vapor-phase reaction of CO_2 at 15, 25, and 45°C.

1.4.2 Engineering Development

R. W. Glass H. W. R. Beaujean[15]
H. D. Cochran D. M. Levins[16]

A process for treating the burner off-gases from HTGR fuel reprocessing plants for the removal of ^{85}Kr is being developed at ORNL. The engineering development utilizes the ORGDP Selective Absorption Pilot Plant and an experimental engineering facility at ORNL (the Off-Gas Decontamination Facility). The design of the ORNL facility was chosen to give a system complementary to the ORGDP pilot plant. The KALC process allows separation of krypton from both light gases (O_2, N_2, CO) and CO_2, with three major separations in a single process. The off-gas decontamination facility allows study of a selected separation with a second column to allow recycle of process streams. The KALC studies in the ORGDP pilot plant will allow study of the entire KALC process. An overall KALC process control system and a proposal to feed only condensed liquid to the absorber are concepts that will be tested.

The KALC process requires three major separations and a fourth, relatively easy, concentration of light gases above the third or stripper separation. In the absorber, nearly all the krypton must be absorbed into liquid CO_2 without absorbing excessive amounts of light gases (CO, O_2, N_2). The light gases, saturated with CO_2 at the absorber conditions but decontaminated of krypton, are discharged. In numerical terms, the liquid/vapor ratio (L/V) must be greater than K_{Kr} and less than K_{O_2} or K_{CO}, where K refers to the equilibrium vapor/liquid distribution for the designated component. In the fractionator, nearly all the light gases must be removed from the liquid CO_2 without removing an excessive fraction of the krypton, and the L/V value must be approximately equal to K_{Kr} and less than K_{O_2} or K_{CO}. The light gases removed from the liquid CO_2 are returned to the absorber feed. In the stripper, the light gases are removed completely from the liquid

Table 1.9. Rate[a] of decreasing iodine concentration in liquid CO_2 at various iodine and water concentrations

Iodine concentration (moles/liter)	Water concentration (moles/liter)	Negative slope of plot of apparent molar absorptivity vs time
$\times 10^{-4}$	$\times 10^{-4}$	$\times 10^{-3}$
2.624	15.9	3.82[b]
		1.48
3.978	19.3	4.44[b]
		2.23
1.974	22.1	5.00[b]
		2.36
2.707	31.4	5.38
4.486	43.1	5.89
6.603	44.9	7.86
4.544	74.8	21.4
5.301	78.1	16.5
29.61		12.3

[a]The rate is expressed as the slope of the plot of the apparent molar absorptivity vs time (in hours).

[b]When two values are given, there were two straight-line segments intersecting at about 11 hr.

15. Guest scientist from KFA Julich.

16. Guest scientist from the Australian Atomic Energy Commission.

CO_2, and the L/V value must be less than K_{Kr}. In order to obtain a high volume reduction (i.e., a high Kr concentration), it is necessary that the fractionator efficiently remove the $O_2 + N_2 + CO$ from the liquid CO_2; also the stripper gas removal rate must be controlled in a manner that produces the desired concentration of krypton in the gas stream leaving the stripper.

Process analyses

Evaluation of the KALC process will proceed in three stages: (1) prediction of the process performance based on selection of a model and theoretical calculations; (2) measurement of process performance during experimental operation of the two development facilities; and (3) analyses of the experimental results to provide general correlations, improved predictions of process performance, and information for process design or scale up.

The development and initial results from an equilibrium-stage model of the KALC process were reported previously.[17] A detailed description of the model and a summary of calculated results have since been reported.[18] These calculations of system performance were useful in assessing the potential impact of upsets in off-gas flow rate and composition on the performance of KALC process operations planned at ICPP. Conclusions are that the moderate upsets anticipated from operations such as burner startup and shutdown can be accommodated by the KALC process if a modest gas holdup volume and recycle capability are included in the process.[19]

A model for computer calculations has been developed to analyze experimental results from the ORNL Off-Gas Decontamination Facility as well as from the ORGDP Selective Absorption Pilot Plant. The model depicts a continuous countercurrent packed column with necessary recognition of varying liquid and vapor flow rates. The calculations yield a value of the volumetric average mass transfer coefficient for each component that best fits the measured inlet and outlet concentrations. Such values of the mass transfer coefficient may be correlated (using the Frossling correlation) and thus form the best basis for scaleup and process design.

Experimental engineering facility

A major step in the development of the KALC process has been the design and installation of an Off-Gas Decontamination Facility at ORNL. The facility consists of two packed columns (one for absorption and one for stripping), compressors for gas recycle, and pumps to provide liquid flow. Standard refrigeration units are used to achieve the nominal −30°C temperature required for processing conditions. The $1\frac{1}{2}$-in.-diam absorption column will be used in conjunction with the 3-in.-diam stripping column to allow study of these operations on a complete recycle basis for gas stream rates of 7 to 10 scfm and liquid rates of 0.5 to 1.5 gpm. The facility is in the shakedown stages, and operations should begin shortly.

One essential measurement during experimental studies in the ORNL Off-Gas Decontamination Facility is the krypton concentrations using ^{85}Kr tracer. The ^{85}Kr concentrations in six feed and product streams from the two columns will be continuously monitored using in-line beta scintillation flow cells. Gas and liquid samples can be withdrawn from points throughout the plant, and collected samples will be counted to determine ^{85}Kr concentration and analyzed for the nonradioactive components. Both absorber and stripper columns have eight sampling points, four liquid and four gas, spaced equidistantly along the columns to enable concentration profiles to be measured. Temperatures, pressures, and flow rates can also be measured throughout the system.

1.5 PRODUCT PREPARATION – 1104 (ALLIED CHEMICAL CORPORATION LEAD)

No activity scheduled.

1.6 WASTE TREATMENT AND DISPOSAL – 1105

No activity scheduled.

17. *GCR Programs Annu. Progr. Rep. Dec. 31, 1972,* ORNL-4911.
18. M. E. Whatley, *Calculations on the Performance of the KALC Process,* ORNL-4859 (April 1973).
19. H. D. Cochran, Jr., and R. W. Glass, *unpublished work.*

2. HTGR Reprocessing Pilot Plant (Subtask 120)

J. W. Snider

The objective of this subtask of the fuel recycle development program is to apply the technology developed under subtask 110 (Reprocessing Development) to a pilot-plant-scale demonstration of the processes and equipment for reprocessing HTGR fuel. Equipment must be designed, built, and operated to demonstrate the following operations:

1. transfer and preparation of fuel elements for reprocessing;
2. crushing of the fuel elements;
3. burning the graphite in a fluidized-bed burner;
4. separation of the fertile and fissile microspheres; crushing the silicon carbide coating on the fissile microspheres;
5. burning the crushed microspheres;
6. dissolution of the uranium and thorium in the burned, crushed microspheres;
7. separation of the undissolved solids (silicon carbide hulls, etc.) from the leachate;
8. separation of the thorium and uranium from the fission products by solvent extraction;
9. separation and purification of uranium by solvent extraction;
10. preparation and packaging the uranium product for shipment and storage as required;
11. demonstration of processes and equipment for iodine, tritium, krypton, and particulate removal from the process off-gas streams;
12. disposal of solid, liquid, and gaseous wastes from the processes.

During the current year, the activity at ORNL on this subtask consisted only of reviewing design documents for the prototype plant as requested by Allied Chemical Corporation and initiating the preparation of the preliminary system design description for the off-gas cleanup system, work unit 1203.

3. HTGR Fuel Refabrication Development (Subtask 210)

J. D. Sease

In this step in the HTGR fuel cycle, nitrate solution containing reprocessed ^{233}U is converted into fuel elements for use in an HTGR. The objective of the HTGR fuel refabrication process development is to develop the technology necessary for the design and operation of the HTGR Fuel Refabrication Pilot Plant (FRPP). The pilot plant, which will be designed for remote operation and maintenance, will require the development of special processes and equipment for this first-of-a-kind nuclear fuel refabrication plant. The objectives of the refabrication development program will be met by

1. establishment of a process flowsheet,
2. development of prototypic equipment components or subsystems,
3. verification testing of prototypic process systems,
4. establishment of operating conditions and procedures,
5. providing a cadre of experienced operating personnel for the prototype plant operation.

Work in HTGR fuel refabrication development[1,2] has been going on for a number of years at ORNL. However, during this report period, renewed interest and increased funding have accelerated the output of this activity compared with previous years. The change to utilize a kernel derived from weak-acid resin (WAR) instead of a sol-gel-derived kernel was made at the end of this report period. This report reflects this change in the reference particle but also covers development work associated with the sol-gel-derived kernels.

The work in refabrication development is subdivided into 11 work units parallel to the function of the pilot plants. These work units are:

1. unit 2100 – general development;
2. unit 2101 – uranium feed preparation;
3. unit 2102 – resin loading;
4. unit 2103 – resin carbonization;
5. unit 2104 – microsphere coating;
6. unit 2105 – fuel rod fabrication;
7. unit 2106 – fuel element assembly;
8. unit 2107 – sample inspection;
9. unit 2108 – process control and data handling;
10. unit 2109 – waste handling;
11. unit 2110 – materials handling.

3.1 GENERAL DEVELOPMENT – 2100 (ORNL LEAD)

J. D. Sease

General development includes activities such as (1) coordination of schedule and funds; (2) technical input to and review of the refabrication pilot plant design description (PDD) and the system design descriptions (SDDs); (3) preparation of recycle fuel product and process specifications; (4) development of the material accountability, nuclear materials safeguards, and criticality control program for the prototype plant; (5) preparation of operating procedures, specification of operating conditions, evaluations of operational results and data; (6) source and special

1. *GCR-TU Programs Annu. Progr. Rep. Sept. 30, 1971,* ORNL 4760.
2. *GCR Programs Annu. Progr. Rep. Dec. 31, 1972,* ORNL-4911.

nuclear materials accountability and preparation of reports as required for materials accountability and materials protection; and (7) preparation of design descriptions and operating procedures for modified process equipment.

3.2 URANIUM FEED PREPARATION – 2101 (ORNL LEAD)

No development activity is scheduled.

3.3 RESIN LOADING – 2102 (ORNL LEAD)

P. A. Haas K. J. Notz J. H. Shaffer

The objective of the resin loading subtask is to develop the process and prototype equipment for loading ion exchange resin with ^{233}U and for drying the loaded resins. A principal advantage of the resin-based preparation of kernels is that many of the critical product properties can be established and controlled for the feed resin before any radioactivity is present. Another advantage of the resin process is that the amount of material that must be processed through resin loading, resin carbonization, and microsphere coating systems is reduced by a factor of 5 when compared with a (4Th-U)O_2 kernel. The resin loading development involves three principal areas: (1) resin feed preparation to supply resin with properties adequate to meet product specifications, (2) uranium feed preparation to convert uranyl nitrate solution from a reprocessing plant into the form required for the resin loading, and (3) resin loading and drying to provide loaded resin suitable for feed to the carbonization furnace.

The decision to change the reference particle from a (4.25Th-U)O_2 sol-gel particle to the WAR particle was made after this report period was completed. Development work on the WAR for this year was supported by the base program but is reported here for uniformity. Also reported in this section is development work that was done for the sol-gel-derived kernel.

Sol-gel processes, which have been under development at ORNL for a number of years, have been used to prepare a variety of thorium and uranium oxide and carbide spheres. The ORNL sol-gel processes for preparing high-density oxide spheres require (1) preparing an aqueous oxide sol; (2) dispersing the sol as drops into an organic fluid, usually 2-ethyl-1-hexanol (2EH), and then removing water from these drops to give solid gel particles; and (3) drying and firing at controlled conditions to remove volatiles, sintering to a high density, and reducing or converting chemically as necessary. Major development this year was in the engineering-scale demonstration of the Solex process for the preparation of (Th-U)O_2 sol and the preparation of microspheres using the sol.

3.3.1 Size Control

Ion exchange resins produced by commercial manufacturers cover a rather wide size range, nominally 20 to 50 mesh. To obtain the correct size for fuel kernel use, the resin is wet screened. We are doing this with an 18-in. KASON unit. Size distribution data for 50 liters of Amberlite ICR-72 (H^+ form) are given in Table 3.1. These results fit a normal probability distribution fairly well, with a mean size of 680 μm and a standard deviation of 100 μm. Various fractions of this size-separated resin were used to prepare irradiation test materials and other test samples of uranium-loaded resin. A yield of 25% was obtained in the size desired for fissile fuel kernels (32 to 38 mesh).

Table 3.1. Size data for 50 liters of Amberlite IRC-72 (H^+ form)

Screen size (μm)	Screen size[a] (mesh)	Volume percent	
		Each fraction	Cumulative
965	22	9.4	9.4
870	24	8.4	17.8
785	26	5.5	23.3
715	28	15.5	38.8
630	32	6.6	45.4
505	38	25.1	70.5
440	44	8.7	79.2
370	50	4.8	84.0
310	60	9.0	93.0
310		7.0	100.0

[a]"Tensile Boating Cloth" screens.

During the various conversion steps involved in processing resin from the as-received Na^+ form to the final product, the resin undergoes a series of volume reductions. These are summarized in Table 3.2.

3.3.2 Uniformity of Loading

Uniformity of kernel composition is important with regard to core physics, accountability, and quality assurance. In terms of uranium loading, uniformity is of concern on at least four levels:

1. within a single resin bead, the uniformity of uranium loading along the radius;

Table 3.2. Volume relationships for Amberlite IRC-72 resin bead kernels[a]

Initial (wet) volume		
Na^+ form	200 ml	790 μ[b]
H^+ form	100 ml	627 μ
Loaded (dry) volume		
At 110°C	76 ml	561 μ
At 130°C	70 ml	556 μ
Fired (final) volume at 1000°C	26 ml	400 μ
Final (fired) weight at 1000°C	53 g	
Particle density		
At 1000°C (70 wt % U)	3.4 g/ml	400 μ
At 1250°C (75 wt % U)	3.7 g/ml	380 μ
At 1750°C (90 wt % U)	5.3 g/ml	317 μ

[a]Loading: 100% of capacity with UO_2^{2+} (3.4 meq/ml wet resin in H^+ form).
[b]Equivalent diameter.

2. within a single loading batch, the uniformity of uranium loading from bead to bead;
3. within a single source of resin, the uniformity of uranium loading from one loading batch to another (or, for continuous column loading, from one time period to another);
4. for a single type of resin, the uniformity in capacity from one batch to another.

We already have information on levels 1 to 3 and can make some reasonable predictions about level 4.

Within a single bead, the uranium density along the radius appears to be constant. Knowledge of resin manufacture and structure would predict this, the relative constancy of percent uranium loaded onto different diameter beads of the same resin provides indirect evidence that this is so, and radiographs of loaded beads confirm it within the limits of capability of this technique. It was shown earlier that "outer shell" loading of uranium, leaving an unloaded center, could be done with WAR in the Na^+ or NH_4^+ form for exchange times of less than 1 hr.[1] Conversely, outer shells could not be obtained with strong-acid resin, with WAR in the H^+ form, or with WAR in Na^+ or NH_4^+ forms for exchange times greater than 1 hr.

The following density data (g/ml) were obtained by W. R. Laing for 24 individual WAR beads that were fully loaded with uranium:

2.093	2.108	2.114
2.097	2.108	2.117
2.101	2.109	2.118
2.104	2.109	2.119
2.105	2.110	2.120
2.105	2.110	2.120
2.105	2.112	2.127
2.107	2.113	2.128

Note: mean = 2.1107, std. dev. = 0.00853, and range = 2.11 ± 0.02 g/ml.

The densities were determined in a gradient column using resin beads that had been sampled at random from about 1 liter of 32/38 mesh resin that had been loaded as a single batch using UO_3. The loaded resin was washed thoroughly to remove any uranyl nitrate and stored wet. Densities were measured on wet beads that had been blotted to surface dryness. Wet beads were used because we were certain that all the internal porosity was fully filled with pure water; had the beads been dried first, there would have been uncertainties introduced from variations in the degree of dryness, the amount of trapped air after immersion in the density gradient column, and the actual density of the column fluid that did penetrate the voids. Since the density of dried beads is about 1.7 g/ml and the volume shrinkage due to drying is about 20%, one can calculate that the wet beads contain about 75 vol % water, which includes the void volume in the dry beads plus the swelling of the resin itself from imbibition of water. From the very narrow range of these data (±1%), one can conclude that both the uranium content and the void volume are constant from bead to bead within a single batch of WAR.

The fourth possible source of variations in loading, due to differences in the exchange capacity of resins from batch to batch, still needs to be investigated.

3.3.3 Continuous Loading

A technique for continuous loading using a modified Higgins column has been demonstrated previously for strong-acid resins, which are able to extract all the uranium from a uranyl nitrate solution.[3]

With WAR, effective loading of uranium is achieved from an acid-deficient uranyl nitrate solution that is obtained by reacting uranyl nitrate with excess UO_3 as

3. *GCR Programs Annu. Progr. Rep. Dec. 31, 1972*, ORNL-4911, p. 31.

follows:

$$UO_2(NO_3)_2 \xrightarrow{UO_3} UO_2(NO_3)_{2-x}(OH)_x ,$$

where x is about 0.6. In batch loading, the uranyl nitrate, UO_3, and resin are mixed together. In the continuous-column method, the acid-deficient uranyl nitrate contacts excess resin and loads only to the degree that yields nearly stoichiometric uranyl nitrate:

$$1.5UO_2(NO_3)_{1.4}(OH)_{0.6} \xrightarrow{\text{excess resin·H}} 0.45R_2UO_2 + 1.05UO_2(NO_3)_2 + 0.9H_2O .$$

The uranyl nitrate effluent is then recycled by recontacting it with excess UO_3. Using the previously described equipment,[2] uranium was loaded onto WAR (Amberlite IRC-72) at the rate of 100 g per hour (in a 1-in.-diam column). The uranium distribution profile over the working length of the column was obtained by sampling the resin every 6 in. and analyzing for uranium content (Fig. 3.1). Although this profile is not nearly as sharp as that obtained for strong-acid resin, it is sufficiently well defined to indicate that full loading can be attained in a reasonable length.

3.3.4 Loading with ^{235}U and ^{233}U

The adaptability of the resin loading method for preparation of HTGR fuels will be influenced by process technology and by possible radiolytic effects on process materials. Process equipment for both primary and recycle fuel preparation must be designed and arranged according to restraints imposed by nuclear criticality considerations. Additionally, equipment used for recycle feed materials must also be suitable for remotely controlled operations. Radiolytic effects on process materials may result in degradation of the resin particles and alteration of the redox potential of the uranyl nitrate feed solution. Evaluations of these possible effects comprise a part of the chemical development program on the resin loading process.

During preceding investigations of the resin loading process, a number of small batches containing approximately 200 g each of highly enriched (93 to 97.6%) ^{235}U were prepared for irradiation experiments. The batch loading procedure for these materials was that routinely used for loadings with normal uranium from acid-deficient uranyl nitrate solution (Fig. 3.2). Without exception, these preparations were free of detectable degradation of either the resin particles or the feed solution. Although these conclusions are based on

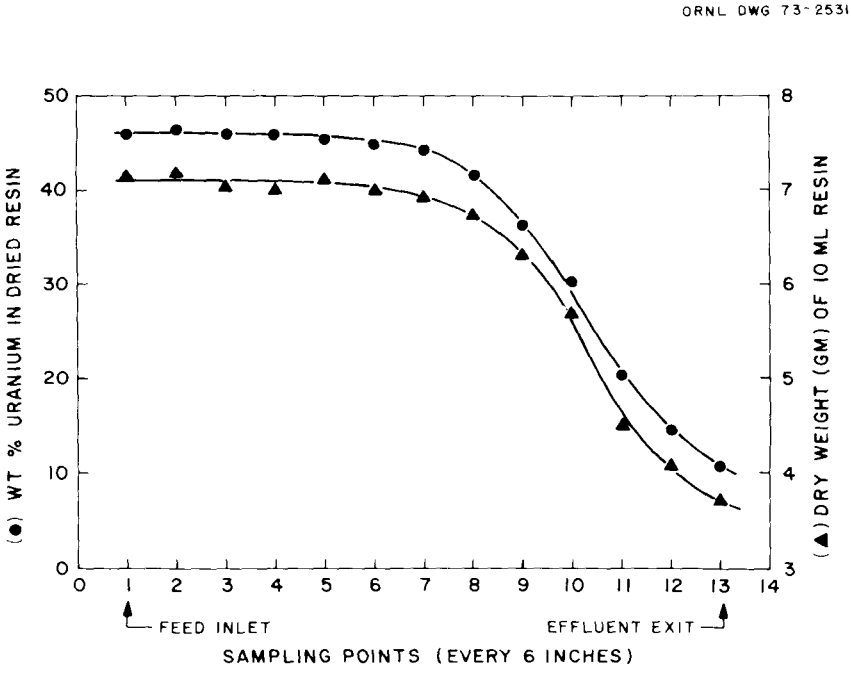

Fig. 3.1. Uranium profile for weak-acid resin loaded in continuous column.

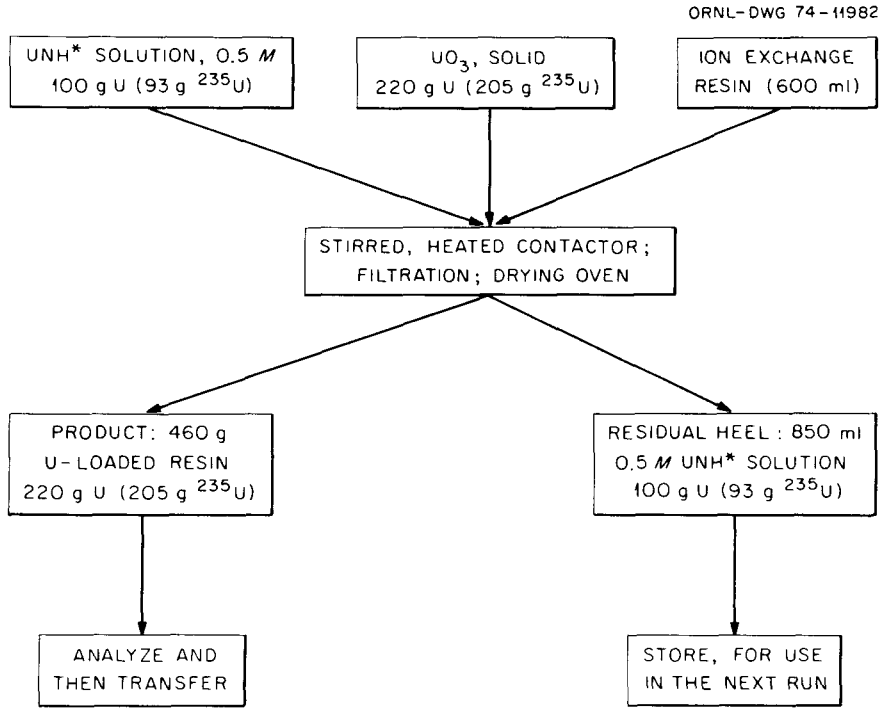

*UNH IS ACID DEFICIENT FROM CONTACTING EXCESS UO_3. THE APPROXIMATE COMPOSITION IS $UO_2(OH)_{0.5}(NO_3)_{1.5}$.

Fig. 3.2. Batch loading of weak-acid resin with ^{235}U.

limited experience, there is no available evidence that the preparation of initial or makeup HTGR microspheres fueled with ^{235}U should be impaired by undesirable radiolytic effects.

However, the suitability of the method for use with recycle fuel requires that the resin loading operation be satisfactorily performed with recovered ^{233}U, with no significant effect on the chemical process or resin particle from the radioactivity of associated ^{232}U daughters. At an early point in the development of the resin loading process, a trial run had been conducted with freshly separated ^{233}U (which contained about 7 ppm ^{232}U). Although the resin was successfully loaded with uranyl ion in the experiment, with no observable degradation, precipitation of the uranium [presumably as a hydrous U(VI) oxide] was noted.[4] Since the precipitated phase had not been observed in previous and subsequent experiments with normal uranium or with solutions enriched in ^{235}U, the phenomenon has been tentatively ascribed to radiolytic effects.

We recently demonstrated that precipitation of the uranium during the loading operation can be eliminated by continuous sparging of the uranyl nitrate solution with oxygen prior to and during the ion exchange process. Whether or not this simple modification is sufficient to avoid the precipitation nuisance under the practical situation in which substantially higher radiation intensities are involved awaits further experimental study.

3.3.5 Preparation of Test Materials

A significant part of the chemical investigative effort associated with resin-based microsphere development has been the preparation of loaded resins for carbonization studies and for irradiation test specimens. During 1973, approximately 10 kg of uranium as uranyl ion was loaded on selected ion exchange resins as

4. Ibid, pp. 28–30.

follows:

Resin	Uranium assay	Uranium loading (g)	Loading method
Amberlite IRC-72	Normal	3500	Batch
Dowex 50	93% ^{235}U	350	Column
Amberlite IRC-72	93% ^{235}U	120	Batch
Amberlite IRC-72	Normal	1170	Batch
Amberlite IRC-72	Normal	400	Batch
Dowex 50	Normal	1850	Column
Amberlite IRC-72	93% ^{235}U	440[a]	Batch
Amberlite IRC-72	Normal	2250[b]	Batch

[a]Two loadings at 220 g each.
[b]Five loadings at 450 g each.

In each case, uranyl ion from uranyl nitrate solution was exchanged with the resin in its hydrogen form. Loadings on strong-acid resin, Dowex 50, were made from stoichiometric UNH solution at concentrations of about 0.05 *M*. Loadings on weak-acid resin, Amberlite IRC-72, were made from 0.3 to 0.5 *M* uranyl nitrate solutions. However, less favorable exchange equilibria for weak-acid resin than for strong-acid resin have required the introduction of acid deficiency in the uranyl nitrate solution to achieve full loading. These laboratory-scale preparations, as well as larger engineering-scale operations, have used the method of adding UO_3 to the uranyl nitrate solution to achieve acid deficiency.[5]

Recycle of this solution in successive batch loading operations requires only the addition of sufficient UO_3 to satisfy the exchange capacity of the resin batch. In larger plant operations, acid deficiency can probably be introduced more satisfactorily by partial denitration of the UNH feed solution by either steam stripping or solvent extraction with an organic amine.

The repeated preparation of these test materials has provided a basis for improving experimental techniques and for examining some chemical equilibria associated with the loading process. Parameters of the resin loading process that may become important to fuel development technology include the controlled partial loading of resin particles and the simultaneous loading of various cations and uranyl ion. Partial loadings of uranyl ion may be a direct method for obtaining variations in density of the carbonized or oxidized particles. The controlled inclusion of other cationic species in the loaded resin may have utility for improving physical properties of the fuel kernel, for fission product retention, and for nuclear performance applications requiring incorporation of a burnable poison with the fissile material.

Two experiments were conducted as a preliminary examination of exchange equilibria in nitrate solution between samarium as Sm^{3+} and uranium as UO_2^{2+} after the latter had been loaded onto WAR (Amberlite IRC-72). In one experiment the resin was loaded nearly to its exchange capacity with uranium (~48 wt % on dried resin); the second corresponded to an approximate 89% uranium loading. Samarium exchange from nitrate solution was examined on 10-ml aliquots of wet resin in a range corresponding to 180 to 730 ppm by weight samarium with respect to uranium. The data were calculated as distribution coefficients

$$\left[D = \frac{\text{(moles solute/gram resin)}}{\text{(moles solute/liter solution)}}\right]$$

and correlated with the reaction

$$2Sm(NO_3)_3 + 3UO_2R_2 \rightleftharpoons 2SmR_3 + 3UO_2(NO_3)_2 \ .$$

Plots of these distributions according to the equation

$$\ln D_U = \tfrac{2}{3} \ln D_{Sm} - \tfrac{1}{3} \ln K_Q$$

by linear regression yielded a value of 0.67 for the slope of each of the two data sets. For a loading that contained 45.9 wt % uranium in the dried resin, the equilibrium quotient K_Q had a value of 0.86 (g/liter); for a loading that contained 42.7 wt % uranium in the dried resin, the equilibrium quotient was 0.68 (g/liter). These results illustrate that simultaneous loading of trace elements with uranyl ion will be strongly dependent on the relative loading of uranium on the resin. Preliminary examinations of equilibria associated with the uranyl ion exchange reaction also show strong dependence on the composition of the uranyl nitrate exchange media. For resin loaded to 70% of its capacity with uranium and in equilibrium with 0.3 *M* UNH solution, the ratio of nitrate ion to uranyl ion is approximately 2.25 (NO_3/U). This value decreases to about 2.00 for fully loaded resin. These tentative results indicate that a more complete understanding of the chemical equilibria associated with the resin exchange reactions may permit more selective process control than can now be realized.

5. P. A. Haas, *HTGR Fuel Development, Use of UO_3 to Load Cation Exchange Resin for Microsphere Preparation*, ORNL-TM-3817 (September 1972).

3.3.6 Sol-Gel Preparation of Microspheres

Pulsed nozzle for size uniformity. In sol-gel preparation of spheres, the formation of sol drops is a critical operation, since oversized and undersized spheres constitute the principal off-specification material. The pulsed nozzle technique that was reported last year has continued to operate very satisfactorily.

In this system, the breakup of sol streams from orifices or capillaries is made more uniform and regular by imposing a vibration at the natural frequency of drop formation. Routine use of the system has consistently given kernels with average diameters within 1% of predicted values and standard deviations of about 1% of the average diameter. Detailed results have been reported.[6] About 300 kg of ThO_2 spheres and smaller amounts of ThO_2-UO_2 spheres were prepared (see Sects. 2.1.2, 2.1.3, and 2.1.4). Thoria spheres of two larger average diameters were prepared to demonstrate results for a wider range of diameters. Diameters calculated from nozzle conditions along with experimental measurements were as follows:

Nozzle type	Predicted diameter (μ)	Measured average diameter (μ)	Standard deviation[a] (μ)
One capillary	595	594	3.7
One capillary	694	680	6.1
One capillary	690	695	5.4
Eight orifices	392	394	14

[a]95% confidence interval, normal distribution assumed.

An increased sol viscosity appears to be favorable to transmission of the vibration to the point of drop formation, but a low sol flow rate as used for a small glove box sphere-forming column is unfavorable.

(Th-U)O_2 and UO_2 sphere preparation with ^{233}U and ^{235}U. ThO_2-$^{235}UO_2$ spheres with Th/U ratios of 4.2, 2, 1, and 0 and ThO_2-$^{233}UO_2$ spheres with Th/U ratios of 4.2, 1, and 0 were prepared for irradiation experiments. Four batches of $^{235}UO_2$ sol (300 g of ^{235}U per batch) and two batches of $^{233}UO_2$ sol (100 g of ^{233}U per batch) were prepared by precipitation peptization and mixed with ThO_2 sol to provide these compositions. The improved procedure for formation of uniform sol drops was used for these preparations. Agreement between the predicted and measured average diameters was good, and the uniformity of size was much better than that of previous small batch preparations but not as good as for routine preparation of ThO_2 spheres.

ThO_2 microsphere preparation. Routine preparation of ThO_2 spheres was continued for about six months to prepare 300 kg of 390- and 500-μ-diam spheres. Three reports provide complete descriptions of our preferred procedures for preparing ThO_2 spheres.[6-8]. The 2-ethyl-l-hexanol (2EH), which is used in microsphere forming, was charged into the engineering-scale ThO_2 forming system in April 1972 and remained in use, with additions only to maintain an inventory of about 200 liters, for an accumulated operation of about 600 kg of ThO_2 spheres without any apparent effects on the sphere formation. Surfactants were added to the 2EH at the rate of 0.6 g of Span 80 and 3 g of Ethomeen S/15 per liter of sol feed for the 390- or 500-μ ThO_2 spheres.

Solex sol preparation and (Th-U)O_2 sphere preparation. The preferred sol preparation flowsheet for Th/U atom ratios of 3 to 4.25 is a continuous solvent-extraction process. The uranium is U(VI) and the sol is ThO_2-UO_3. This process was demonstrated with sphere preparation at the rate of 10 kg (Th + U) per day.[9] The same sol preparation equipment with minor modifications was satisfactory for rates of 1.0 and 1.5 kg (Th + U) per hour, but operation was poor at 2.0 kg (Th + U) per hour.[10] This equipment is critically safe by geometry and has other characteristics that are desirable for remote operation with ^{233}U. The equipment design has been described.[11] This Solex equipment was put into operation to prepare ThO_2-UO_3 sol containing natural uranium and a Th/U ratio of 4. The initial objective was to accumulate a stock of sol and/or gel spheres for studies of gel sphere drying and other refabrication operations. Mechanical operation was excellent, with no difficulties after 20 months without

6. P. A. Haas and W. J. Lackey, *Improved Size Uniformity of Sol-Gel Spheres by Imposing a Vibration on the Sol in Dispersion Nozzles*, ORNL-TM-4094 (May 1973).

7. P. A. Haas, *Process Requirements for Preparing ThO_2 Spheres by the ORNL Sol-Gel Process*, ORNL-TM-3978 (December 1972).

8. P. A. Haas, *Sol-Gel Preparation of Spheres: Design and Operation of Fluidized Bed Columns*, ORNL-4398 (September 1969).

9. C. C. Haws, B. C. Finney, and W. D. Bond, *Engineering-Scale Demonstration of the Sol-Gel Process: Preparation of 100 kg of ThO_2-UO_2 Microspheres at the Rate of 10 kg/day*, ORNL-4544 (May 1971).

10. P. R. Kasten et al., *GCR-TU Programs Annu. Progr. Rep. Sept. 30, 1971*, ORNL-4760, pp. 30–31.

11. J. W. Snider, *The Design of Engineering-Scale Solex Equipment*, ORNL-4256 (April 1969).

use. This startup with a new charge of solvent and a different feed along with some operational errors revealed the importance of some chemical flowsheet criteria; these will be discussed individually. Two approaches to using Solex sols for (Th-U)O_2 spheres with Th/U ratios of 10 were tested.

The electrical conductivity of the sols provides an excellent check on the sol quality with respect to process upsets or the presence of some impurities. Values of 400 to 800 micromhos/cm at 18°C for the dilute (<0.5 *M*) sol product are favorable, while higher values are unfavorable. Any sodium in the sol results in an equal molar increase in the nitrate concentration and increases the sol conductivity. Some of our feed had sodium concentrations of 300 to 400 ppm (Th + U), and this had a detectable effect on the sol conductivity. The new solvent appears to need a better pretreatment than the preliminary acid-caustic-water washes. There has always been excessive solids, or "crud," at the organic-aqueous interfaces when starting with new solvent, but the effects on the product sol were obscured by other startup problems. Apparently these dirty interfaces result in entrainment. We started without a water scrub after the caustic regeneration column, and the entrainment of sodium in the solvent from the regeneration was carrying sodium to the sol and giving high sol product conductivities. Careful analyses showed a detectable, but tolerable, entrainment of sodium for clean interfaces and an excessive entrainment for dirty interfaces. This problem is completely eliminated by using a water scrub contactor after the caustic contactor, and all future operations will use this water scrub. Sol product conductivities are also a sensitive indication of inadequate extraction of nitrate in the first nitrate extraction. This may result from a low solvent flow rate, a low caustic flow rate (with incomplete regeneration of the amine), or inadequate mixing in the regeneration contactor.

Operation of the Solex system with an inadequate flow of free amine results in formation of a precipitate in the digester. This precipitate requires shutdown and cleanout of the system because it cannot be flushed through by simply using normal system flows. This effect was observed once when we accidentally operated with an inadequate caustic flow rate to the amine regeneration contactor. In this case, a large increase in sol product conductivity occurred before precipitation. An agitator speed of 350 rpm in the regeneration contactor may give a borderline mixer efficiency and incomplete regeneration of the amine, and thus is another cause of precipitation in the digestor.

Part of the evaporation of sol was carried out with continuous operation of the evaporator. The takeoff of product was manually controlled, since the sol density control was previously found to be unsatisfactory. Continuous operation appears to be acceptable otherwise.

Previous observations for preparation of ThO_2-UO_3 gel spheres[1,2] were confirmed. The 2EH composition required for fluidized-bed formation of spheres from ThO_2-UO_3 sols varies with the Th/U ratio, the NO_3^-/(Th + U) ratio, and the digestion-aging time of the sol. Generally, both Span 80 and Ethomeen S/15 must be added to the 2EH. Excessive sticking and clustering occur if Span 80 is not present, while Span 80 alone results in nonspherical gel particles. The following conditions have generally resulted in good gel spheres.

1. The sol preparation flowsheet is with countercurrent flow of aqueous and organic and an excess of the organic to give the minimum NO_3^-/(Th + U) ratio and dilute sol conductivities of 400 to 800 micromhos/cm.
2. The sol is digested at ~100°C, usually by carrying out the evaporation for concentration at atmospheric pressure.
3. The concentrated sol is allowed to age at least several days, and preferably for more than a week, before sphere preparation.
4. Approximately equal concentrations of Span 80 and Ethomeen S/15 are used in the 2EH.
5. The total concentration of surfactants and degradation products must be limited to avoid cracking of the gel spheres; ≥0.5 vol % is very likely to cause cracking and ≤0.3 vol % is the preferred concentration.

Ion exchange as part of the 2EH recycle is not useful for the ThO_2-UO_3 sols. The sols do not contain any formate, and the countercurrent sol preparation flowsheet leaves the minimum of nitrate free for possible extraction into the 2EH. The ion exchange degrades the Span 80 into a less effective form, and replacement of the Span 80 results in excessive accumulations of degradation products. Thus the best recycle procedure is simple distillation to remove water and a slow partial replacement of the 2EH inventory to limit degradation products. Batch surfactant additions at the rate of 4 g of Span 80 and 1 g of Ethomeen S/15 per liter of ThO_2-UO_3 sol feed (the surfactants are added to the 2EH) maintained satisfactory column operation for the low-conductivity sols. Cracking of the gel spheres

12. P. A. Haas, internal memorandum, June 1973.

during drying increased noticeably when the cumulative surfactant additions including the initial amounts reached 0.5 vol %. This confirms the need for a 2EH replacement rate of about 2 liters per liter of ThO_2-UO_3 sol or 6 liters per kilogram of ThO_2-UO_3.

The principal requirement for control of drying conditions is to prevent cracking. If the gel spheres in the 2EH slurry discharged from the sphere-forming column are free of cracks, cracking during drying and firing appears to be principally a result of excessive rates of volatilization in the spheres. This occurs from the following three sources of heat.

1. Excessive rates of heatup from externally supplied heat. The critical range is 100 to 180°C, where most of the volatilization occurs. For an individual sphere, relatively high rates, perhaps as high as 10°C/min, would be acceptable. For heat transfer through bulk spheres, the individual sphere rate of heatup can be much higher than the average rate, so the allowable average rate decreases as the quantity of sphere increases.

2. Excessive rates of heatup from burning of the remaining organics or carbon in air during firing. Firing of ThO_2-UO_3 or ThO_2 in air is an effective and simple way of assuring low carbon content and high densities, but drying to $\geq$220°C in steam is necessary to prevent excessive rates of temperature rise and cracking in ThO_2-UO_3 or ThO_2 spheres of 350 or 400 μ fired diameter. Drying to lower temperatures or without steam may leave enough organics and carbon that spheres of this size crack during the burning.

3. Excessive rates of heatup during exothermic reactions in the gel with NO_3^- or U(VI) as oxidizing components and organics as reducing components. The concentration of organics must be stripped to a low value to prevent cracking when this reaction occurs. This effect is not a significant problem for our standard flowsheets for ThO_2 or UO_2; these spheres can always be dried to $\geq$220°C in steam without exothermic reactions.

The third effect is troublesome for ThO_2-UO_3 gel spheres and controls the design of an engineering-scale sphere dryer. For most batches of ThO_2-UO_3 spheres, the exothermic reaction starts in spheres at 170 to 200°C, progresses through the whole dryer over a period of minutes, and causes temperature rises of 100 to 300°C in less than 1 min for an individual sphere. Spheres dried to over 170°C in steam generally undergo the reaction without cracking; spheres not dried to 170°C are likely to crack. When the ThO_2-UO_3 sols have higher NO_3^-/(Th + U) mole ratios than the standard 0.12, the exothermic reactions start at lower temperatures and drying without cracking becomes very difficult.

The recent experimental results with the ThO_2-UO_3 gel spheres confirm these generalizations on drying. For NO_3^-/(Th + U) mole ratios of 0.12 or less and $\leq$0.4 vol % surfactants in the 2EH, gel spheres were dried using a 24-hr drying cycle and fired to give good ThO_2-UO_2 spheres. Temperature excursions occurred for every batch of ThO_2-UO_3 with Th/U = 4, but excessive cracking occurred only for NO_3^-/(Th + U) ratios $>$0.12 or for high surfactant concentrations in the 2EH. Studies are in progress to develop a shorter, or simplified, drying cycle for the ThO_2-UO_3 gel. Use of a high flow rate of recycled argon plus steam did not appear to be adequate to delay or control the temperature excursions. Preliminary tests of heating to 180°C in 2EH are favorable; apparently the exothermic reaction occurs, but the temperature is controlled by heat removal by boiling 2EH.

Our sol-gel processes had been demonstrated for Solex ThO_2-UO_3 sols with Th/U ratios of between 3 and 4.25. The General Atomic Company selection for their reference fuels (commercial plants) may be UC_2 and/or $(ThU)O_2$ with Th/U ratios of 6 to 12 for the fissile particles. Therefore, we tested two approaches for use of Solex sol to prepare $(Th\text{-}U)O_2$ spheres with Th/U ratios of 10.

For one approach, we mixed ThO_2-UO_3 Solex sol with Th/U = 4 with our standard ThO_2 sol to give sol with Th/U = 10. This mixed sol was better for sphere preparation than the Solex sol alone and gave excellent fired spheres. One possible variation of this approach would be to disperse the ThO_2 powder in a dilute Solex sol with a lower (perhaps 2) Th/U ratio. This would minimize the size of Solex equipment and waste and could eliminate the need for Solex evaporations and for minimum NO_3^-/(Th + U) ratios.

In the second approach, we operated the Solex equipment with nitrate feed solutions of Th/U = 10. The dilute sol appearance and conductivity were very good. The evaporated sol was very fluid and could probably be concentrated to a higher (Th + U) molarity than could the sols of Th/U = 4. Analyses showed a high NO_3^-/(Th + U) mole ratio of $\geq$0.20 (as compared with about 0.12 for Th/U = 4). Sphere preparation was not successful, with difficulties in agreement with the high NO_3^- concentration. Large temperature excursions during drying resulted in more than 99% cracking of the gel particles of all batches tested. Both a small distortion and some clustering were troublesome

during formation of the gel spheres. From past experiences, we would expect to alleviate these two sphere-forming problems by evaporating to a higher concentration, but the high nitrate content would still result in excessive cracking during drying.

CUSP system for $^{235}UO_2$ sol preparation. Preparation of UO_2 sols in CUSP equipment with a capacity of 1 and 4 kg of UO_2 per batch has been demonstrated and reported.[13] A system was designed for preparation of 1-kg batches of $^{235}UO_2$ sol. Currently, the processing equipment has been fabricated and installed in a new enclosure, and the assembly is ready for installation in Building 3019. The work remaining to be done by ORNL forces currently progresses on a second priority as craftsmen are available, since no definite program commitment existed. Should a commitment appear and the necessary manpower be allocated, the system could be placed in operation within about 60 days. The plutonia-sol-making and dense microsphere fabrication equipment has been on standby for several years; one of the enclosures (involved in plutonia sol preparation) is in poor condition and should be replaced before operations could resume.

3.4 RESIN CARBONIZATION – 2103 (ORNL LEAD)

D. R. Johnson W. J. Lackey

The objective of the resin carbonization work unit is to develop a process and the prototype equipment for reducing uranium-loaded weak-acid resin kernels to an intermediate UO_2-C product. In the first step of the microsphere coating operation (work unit 2104), the UO_2-C microspheres will be partially converted to UC_2. The resultant fuel kernels will contain approximately 75 mole % UC_2, 25 mole % UO_2, with an excess of carbon. The size and density of the converted fuel kernel are strongly dependent on the process variables during resin carbonization.

The carbonization process consists in fluidizing the loaded and dried resin kernels with an inert gas and then heating the particles to reduce the resin to carbon. A gaseous hydrocarbon reaction product must be swept out of the carbonization furnace and scrubbed to prevent the formation of deleterious tar and soot on the cool surfaces of the furnace. The carbonized resin particles are pyrophoric and must be handled and transferred remotely in an inert atmosphere.

Resin carbonization development will begin in calendar year 1974.

3.5 MICROSPHERE COATING – 2104 (ORNL LEAD)

W. J. Lackey F. C. Davis
W. H. Pechin M. K. Preston
R. S. Lowrie

The objective of the microsphere coating work unit is to experimentally develop the processes and equipment needed to remotely coat HTGR fuel particles. In this regard, we will obtain process and equipment performance data needed for the design and modification of the coating system for the FRPP. Microsphere coating is divided into three areas:

1. particle coating, which consists of kernel conversion and application of porous and dense carbon coatings as well as silicon carbide coatings to fissile fuel particles;
2. coater effluent treatment, in which the effluents from the carbon and silicon carbide coating operations are rendered into a form suitable for disposal;
3. particle handling, which includes particle transfer, storage, classification, weighing, batching, blending, and sampling.

The recently revised coating process flowsheet for the pilot plant is shown in Fig. 3.3. Two identical coating furnaces are planned, each of which will operate independently; that is, the furnaces operate in parallel, and each furnace is capable of depositing all the coating layers desired. This parallel operating scheme, when compared with series operation, reduces the amount of bookkeeping required for characterization and inventory purposes.

3.5.1 Particle Coating

Fluidized-bed-type particle coating equipment and processes are being developed for remote coating of recycled HTGR fuel. The reference recycle fissile particle is of the weak-acid-resin type described in Sect. 3.3.

The uranium-loaded resin particles are carbonized prior to coating, and the desired fraction of the UO_2 is reduced to UC_2. The fuel kernels are then coated with a Triso coating. For particles of this type, about 3 kg of uranium will be coated daily in the Thorium-Uranium

13. B. C. Finney and P. A. Hass, *Sol-Gel Process-Engineering Scale Demonstration of the Preparation of High Density UO_2 Microspheres*, ORNL-4802 (November 1972).

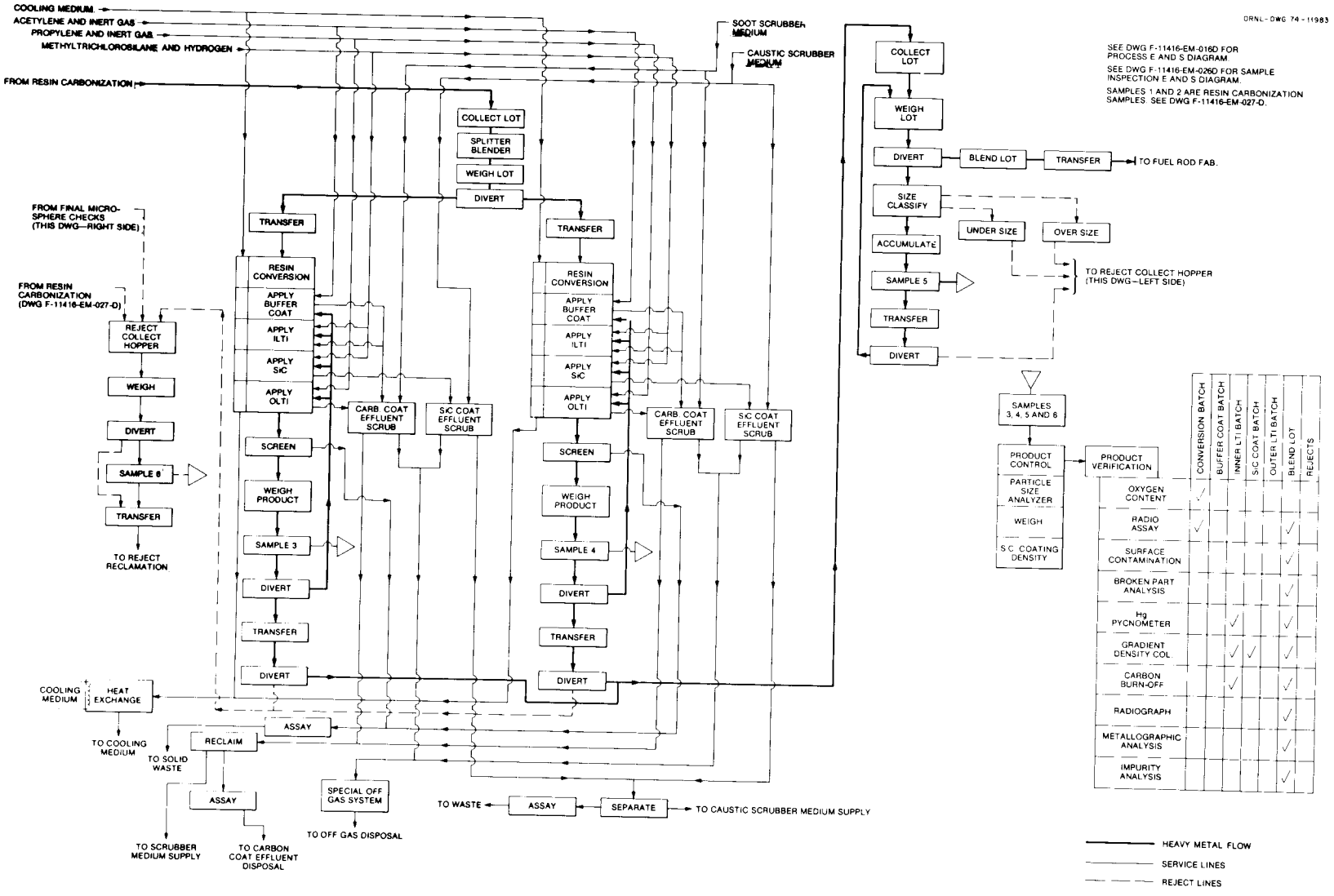

Fig. 3.3. Remote coating process flowsheet.

Recycle Facility (TURF) pilot plant. A developmental engineering-scale coater, described previously,[14,15] has been operational for several years. Major efforts this year consisted in improving several portions of this equipment and obtaining a better understanding of the processes used to deposit both the acetylene-derived porous buffer coating and the propylene-derived dense carbon coating.

Equipment modifications. The major modification to the 5-in.-diam engineering-scale coating furnace was replacement of the furnace support structure, base, and electrodes. An isometric drawing of the modified coater is shown in Fig. 3.4. The cantilevered support and new electrodes allow better access to the lower portion of the coater and thus allow increased flexibility in the design of both the gas distributor and the particle unloading system. The new design eliminates occasional overheating of the electrodes and is more amenable to remote operation and maintenance.

The engineering-scale coater was modified so that a porous plate (frit) type gas distributor could be used in addition to the conventional conical distributor. Porous plates of different geometries were evaluated, and a new type distributor, shown in Fig. 3.5, was developed.[16] The new frit is thought to be superior to previous frit designs for the following reasons.

1. The coating gas(es) is brought near the bottom of the frit by a single water-cooled nozzle, and thus the nozzle and frit holder are as simple as that used with a flat frit.

2. Contrary to a flat frit of uniform thickness, nearly all of the coating gas flows through the six thinned regions of the newly designed frit, and thus the gas velocity is comparatively high. Because of the high gas velocity, heating of the gas within the frit is minimized, and thus decomposition of the gas and plugging of the frit with carbon are also minimized or eliminated. Plugging is also minimized because the thinned region of the frit is at the bottom and is cooled more efficiently by the water-cooled gas injector.

3. Since there are no nozzles protruding through the frit, loss of particles down through such holes cannot occur, and the frit can be used as the bottom of an unloading vessel.

Results to date with frits of the new design have been most encouraging. There has been no measurable increase in resistance to flow of gas through the frits during the course of coating, which indicates that plugging is not occurring. A polished section of a frit that was used to deposit both buffer and low-temperature isotropic (LTI) coatings was examined microscopically, and no carbon deposits were seen in the thinned region of the frit. Deposits were easily seen microscopically in the old type of flat frits. One of the new frits was used for four buffer and four LTI coating runs without experiencing plugging. Some difficulties have been encountered with each of the frits we have worked with. Sealing of the frit in the holder sufficiently to prevent leakage of gas has been troublesome. A new holder is being designed to eliminate leakage. Also, with each of the frit geometries, some particles adhere to the frit. To combat this problem, we are currently fabricating frits with steeper slopes. Properties of carbon coatings deposited using frits are reported in the following section.

The acetylene supply system for the engineering-scale coater and for a second 5-in.-diam coater was modified to allow use of higher acetylene flow rates. Ten acetylene cylinders were connected to a common manifold with a small flash arrester between each cylinder and the manifold. A large flash arrester was located between the manifold and the coater, and a vented relief valve was installed to prevent overpressurization of the manifold. The system is designed to operate at 15 psig in order to prevent the spontaneous decomposition that can occur at higher pressures.

Commercial sources were located for two types of heat shields that should be superior, especially for remote operation, to the molybdenum heat shields currently used in the prototype coating furnace. One type consists of rigidized carbon felt, while the other consists of multilayers of corrugated Grafoil sandwiched between carbon felt. A hollow cylinder of each type, suitably sized for the 5-in.-diam prototype coater, was received from the vendors. Both are sufficiently rigid to be free standing and appear sufficiently rugged for remote handling.

An assessment was made of the economic and technical advantages and disadvantages associated with use of 9-in.-diam coaters in a remote HTGR refabrication plant rather than 5-in.-diam coaters.[17] The larger

14. R. B. Pratt and S. E. Bolt, *Status and Progress Report for Thorium Fuel Cycle Development for Period Ending Dec. 31, 1966*, ORNL-4275, pp. 61–78.

15. W. J. Lackey et al., *GCR-TU Programs Annu. Progr. Rep. Sept. 30, 1971*, ORNL-4760, pp. 45–50.

16. Patent applied for.

17. W. J. Lackey, J. D. Jenkins, and F. J. Homan, *Assessment of Coater Size for the Fuel Refabrication Prototype Plant*, ORNL-TM-4566, in preparation.

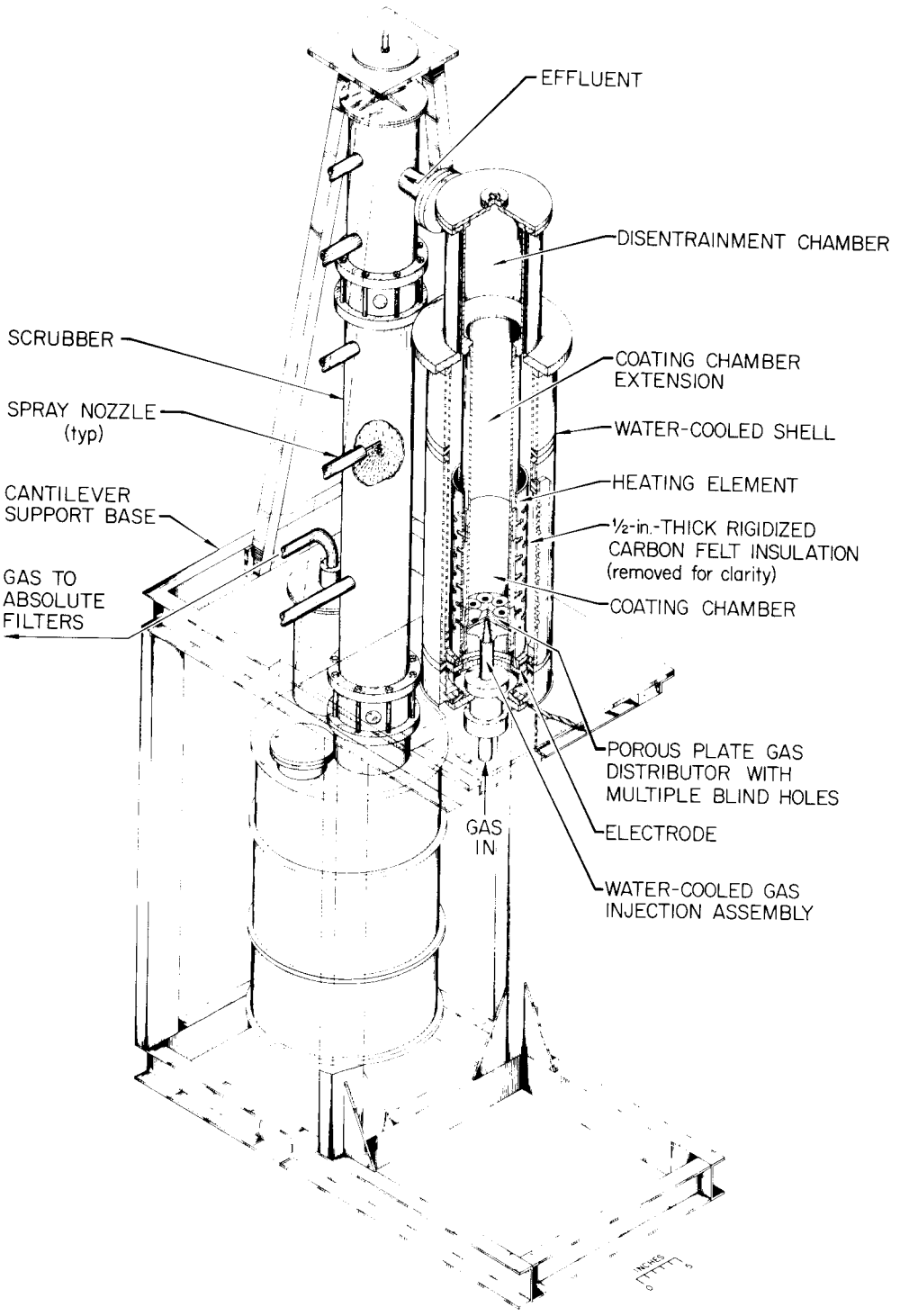

Fig. 3.4. Engineering-scale coating furnance. (The scrubber is described in Sect. 3.5.2).

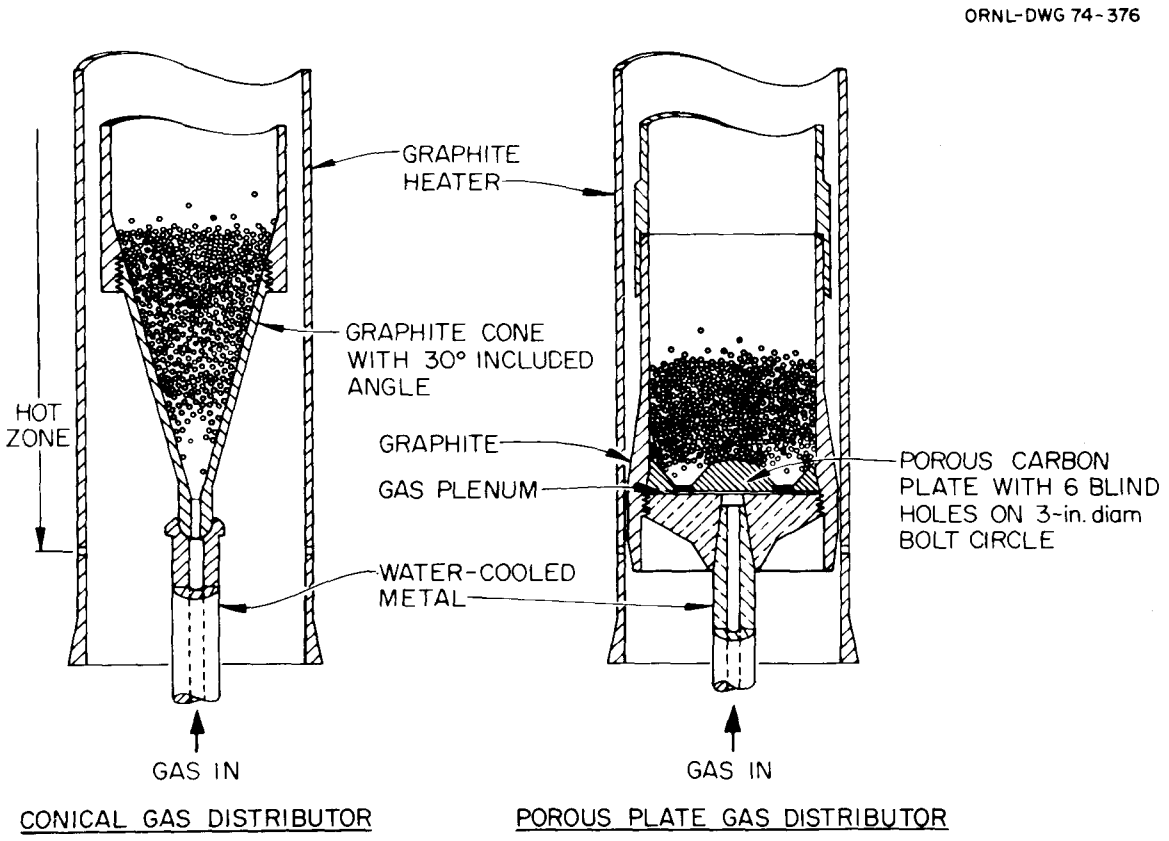

Fig. 3.5. Multiblind hole porous distributor.

coater is clearly favored from the economic standpoint. Since criticality considerations dictate that 9-in.-diam coaters must never be flooded with hydrogenous materials, the furnace coolant and soot scrubbing media cannot be water or any other hydrogenous material. Suitable alternative materials that are not good moderators appear to be available. Development of a 9-in.-diam coater to the state currently existing for the 5-in.-diam engineering-scale coater was estimated to require about \$1 million and $2\frac{1}{2}$ to 3 years.

Process development. The first coating deposited for either Biso- or Triso-coated particles is a porous carbon buffer layer. One function of the buffer layer is to provide void space for accommodation of fission gases and fuel swelling. Therefore, the buffer coating density and thickness must be controlled to ensure that ample void space is available. A method was developed whereby the quality of one buffer coating run could be compared with another having different values for density and coating thickness standard deviation. The method is based on the assumption that a buffer thickness of less than 65 μm provides inadequate void volume for a particle that has a buffer density of 1.1 g/cm^3 and a kernel diameter of 350 μm. This is thought to be a reasonable value for the critical void volume, since for a particle batch having a buffer density of 1.1 g/cm^3, an average buffer thickness of 100 μm, and a batch thickness standard deviation within 15 μm, it can be shown that 1% of the particles will have less than the critical void volume.

The model was developed with Biso-coated particles in mind, but the conclusions reached concerning the relative quality of different buffer coatings are equally valid for Triso-coated particles. Particle batches are rated by calculating and comparing the percentage of particles per batch that have less than the critical void volume. The curves in Fig. 3.6 show the values of density and coating thickness standard deviation that yield 0.1, 0.5, 1.0, and 2.0% of the particles with less than the critical void volume. For example, the point

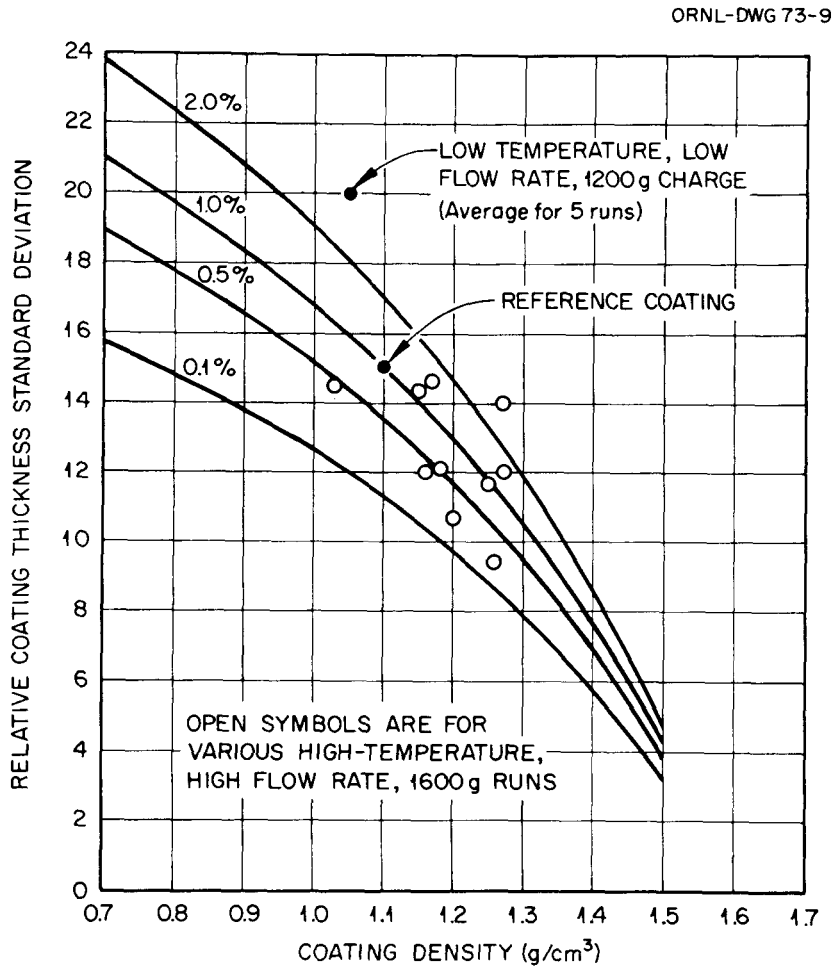

Fig. 3.6. Graph used to compare quality of buffer coating batches. The lines give the percentage of the particles in a batch that have less than the critical void volume defined in the text.

labeled "reference coating" represents a particle batch that has a buffer density of 1.1 g/cm^3 and a coating thickness standard deviation of 15 μm. Note that this point falls on the 1% line, meaning that 1% of the particles have a void volume less than the assumed critical value. Also shown in the figure are data points for several coating runs made with the 5-in.-diam coating furnace using a conical gas distributor. The uppermost point (filled circle) represents five coating runs made using nonideal coating conditions, and the number of particles having less than the critical void volume exceeds 2%. On the other hand, each of the open circles represents a coating run made using various improved conditions, namely, higher temperatures and higher acetylene flow rates. Note that the high-temperature and high-flow-rate runs yield improved coatings even though the charge was larger. These data points for the improved conditions scatter about the 1% line and are thus generally equal in quality to the reference coating. This graph illustrates a phenomenon that was generally observed for the buffer coating process; that is, as the process variables were altered in a manner that resulted in a lower value for the coating thickness standard deviation, there was a concurrent increase in coating density. This interaction makes it necessary to use a method such as that described here when the quality of two or more buffer batches is being compared.

Figure 3.7 gives results for additional buffer coating runs made with a conical gas distributor. Line 1 shows that as the diluent flow rate is increased, the coating thickness uniformity improves but the coating density simultaneously increases. The net result is that the product quality is virtually independent of the diluent flow rate. (Although not shown in the graph, product quality is improved by increasing the acetylene flow rate.) Lines 2 and 3 of Fig. 3.7 show that product quality is improved slightly as the charge is reduced from 3.2 kg to 800 g.

Figure 3.8 gives the results for buffer coatings deposited using porous-plate-type gas distributors of various geometries. The results are rather independent of geometry and cluster about the 1 and 2% lines. The properties are amazingly similar to those obtained with the conical distributor, especially when one considers that the gas and particle flow patterns and velocity are so dissimilar for the two types of distributors.

The excellent reproducibility of the buffer coating process was demonstrated by making 12 nominally identical runs. The coating conditions were as follows: kernel = 350- to 420-μm-diam ThO_2, temperature = 1475°C, acetylene flow rate = 5 scfm, helium flow rate = 2 scfm, time = 12 min, and coating chamber = new single inlet 30° included angle cone per run. The more important coating properties are summarized in Table 3.3. The overall impression to be gained from studying the data is that each coating run yielded a high-quality product that varied only slightly from one run to another, even though a large charge (3200 g) was used. The coating density varied from a minimum of 1.125 to a maximum of 1.147 g/cm^3, which is trivial, considering that the specification will likely be 1.1 ± 0.2 g/cm^3.

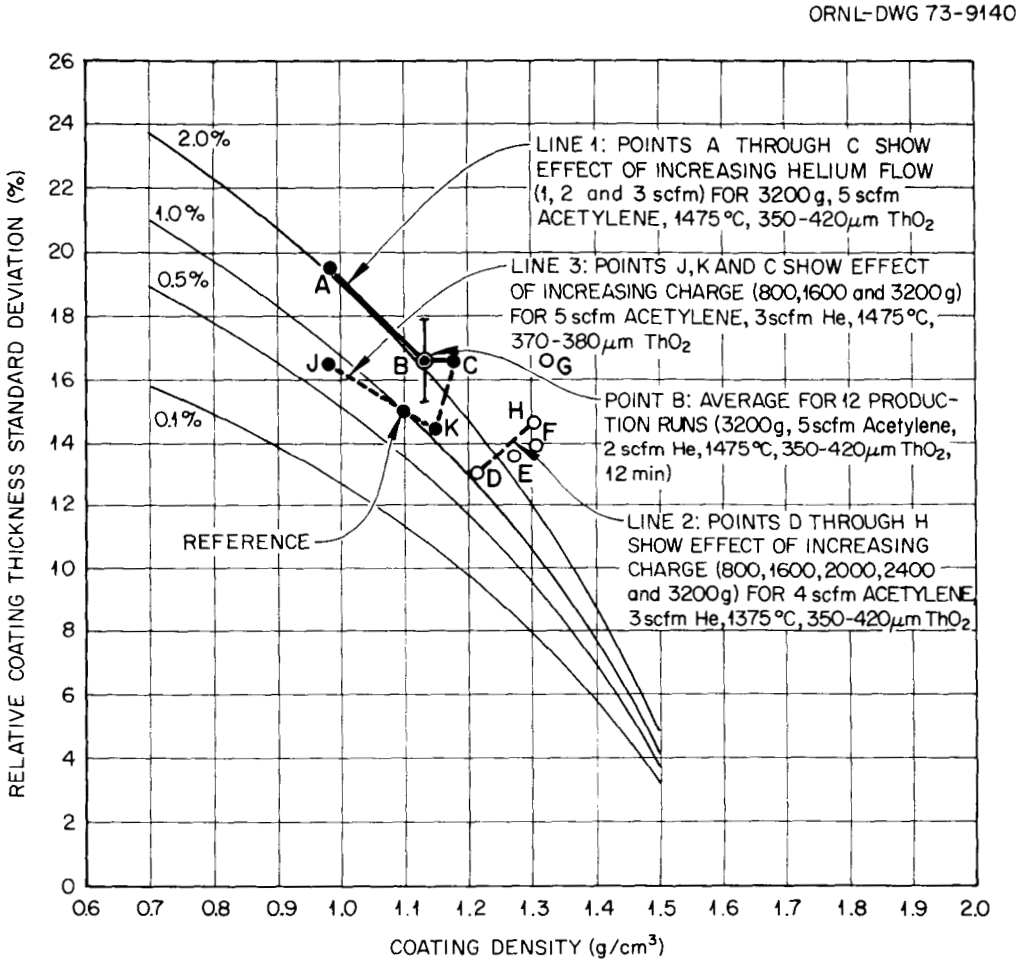

Fig. 3.7. Effect of diluent flow rate and charge on the quality of buffer coatings.

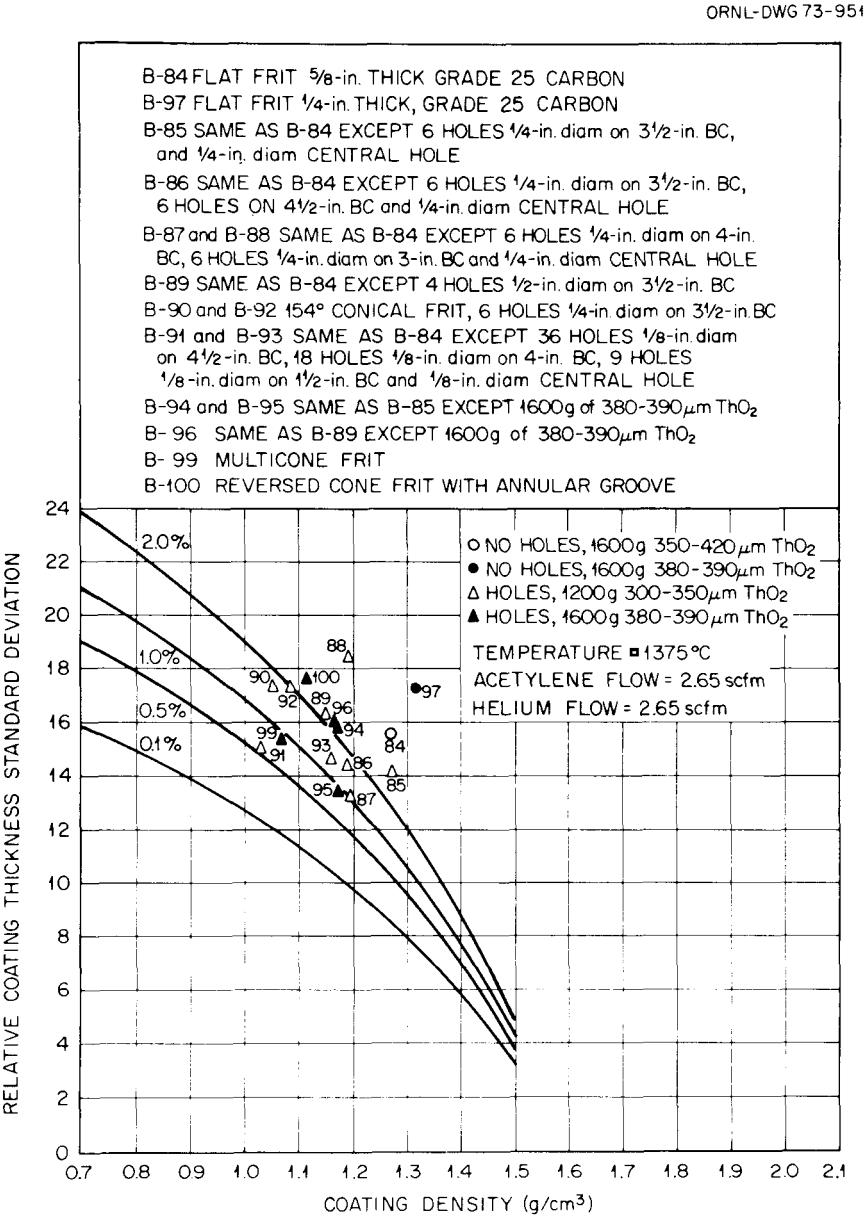

Fig. 3.8. Quality of buffer coatings deposited using various geometries of porous plates.

The minimum and maximum average coating thicknesses of 98.5 ± 3.3 and 107.5 ± 3.3 μm are also strikingly similar. Other points of interest include the following.

1. Coating densities calculated by two different methods were in excellent agreement. The method that utilized burnoff and mercury density measurements was slightly more precise than the method that utilized burnoff and radiograph measurements.

2. The efficiency of utilization of the input carbon was 53.0 ± 0.4%.

3. On the average, 99.95 ± 0.06% of the input kernel weight was recovered.

Now shift attention to the isotropic carbon coating derived from propylene, the so-called LTI coating. A large number of carefully controlled LTI coating runs were conducted using the 5-in.-diam coating furnace to determine the influence of propylene flow rate,

Table 3.3. Buffer production runs

Run No.	Coating density (g/cm^3)	Coating thickness (μm)	Coating thickness standard deviation (%)
A-273	1.147	98.5[a]	13.1[a]
A-275	1.130	107.3	17.7
A-277	1.126	107.5[b]	16.7
A-278	1.133	102.3	17.8
A-279	1.132	102.9	19.2
A-280	1.125[a]	103.6	17.8
A-281	1.130	100.6	14.0
A-282	1.141	103.7	14.5
A-283	1.130	103.1	20.0[b]
A-284	1.138	105.1	17.0
A-285	1.135	100.5	16.6
A-286	1.138	99.8	14.9
Av	1.134 ± 0.004	102.9 ± 1.8	16.6 ± 1.3
Ref.	0.9–1.3		15

[a]Minimum.
[b]Maximum.

temperature, charge, and presence vs absence of a helium diluent on the coating properties and process. Properties that were characterized in detail were (1) coating density; (2) coating thickness and standard deviation; (3) microstructure; (4) surface characteristics, such as roughness and depth to which the coatings were permeable; (5) percent open porosity; (6) fraction of broken coatings; (7) particle shape; and (8) particle strength. Process responses of interest were efficiency, coating rate, extent to which carbon infiltration increased the buffer coating density, and loss of particles. Most of the LTI coating runs were made using the conical gas distributor. Results pertaining to a porous plate distributor are identified as such. The more important results are summarized below.

The fraction of defective LTI coatings, as measured on the as-coated particles using the chlorine leach technique, was strongly related to LTI coating thickness. This correlation is shown in Fig. 3.9 for particle batches prepared using wide ranges in coating temperature, propylene flow rate, and charge. It should be clear that the thin coatings resulted from the use of unusually low temperatures, high flow rates, and/or high charges; and higher quality particles having thin coatings could presumably be made by using more conventional coating conditions. Nevertheless, these data clearly point out the importance of coating thickness. With these same particle batches, the particle crush strength was found to increase with coating thickness. Also note in Fig. 3.9 that the fraction of defective particles was reduced by in-place annealing. This in-place annealing was conducted in the coating furnace immediately after depositing the LTI coating, and the particles were allowed to cool only after annealing. Since in-place annealing reduced the fraction of defective particles by factors of 20 and 30 for the two cases shown in Fig. 3.9, it is assumed that the coatings are stressed in the as-deposited condition, and additional stresses imposed during cooling result in exceeding the fracture stress in the case of unannealed particles. Additional evidence that the as-deposited coatings are stressed is that the crush strength is increased by annealing. There is some evidence that the properties of the buffer coating influence the failure fraction, thus indicating mechanical interaction between the buffer and LTI coatings. This evidence is preliminary, but note in Fig. 3.9 that the defective fraction is higher for both the cone and frit when the buffer was a composite batch (batches used to make the composite ranged in buffer density up to 1.4 g/cm^3) as compared with the case where the buffer had a density of 1.1 g/cm^3.

More nearly spherical particles were produced by increasing the propylene flow rate and by decreasing the temperature and charge. Additional analysis showed that the influence of propylene flow rate and charge was attributable to a variation in deposition rate and that all that was needed to predict particle shape was deposition rate and temperature, as shown in Fig. 3.10. Addition of a helium diluent to the propylene resulted in a slight improvement in particle shape, but other detrimental effects (lower efficiency and greater blow-over of particles out of the furnace) offset any slight benefit derived from use of a diluent.

We determined the effect of process variables on the depth to which LTI coatings were permeable as measured by the nickel carbonyl technique described in Sect. 3.8. Note in Fig. 3.11 that when the charge or temperature was altered so as to give a higher deposition rate, the depth to which the coatings were permeable increased. However, when the propylene flow rate was altered to give a higher deposition rate, the permeable depth surprisingly decreased. When a helium diluent was added to the propylene, the permeable depth was decreased to values varying from 40 to 70% of that for coatings applied similarly, except without the diluent. Annealing of the particles reduced the permeable depth only a small amount.

Loss of material during coating as a result of particles being blown out of the furnace or as a result of particles

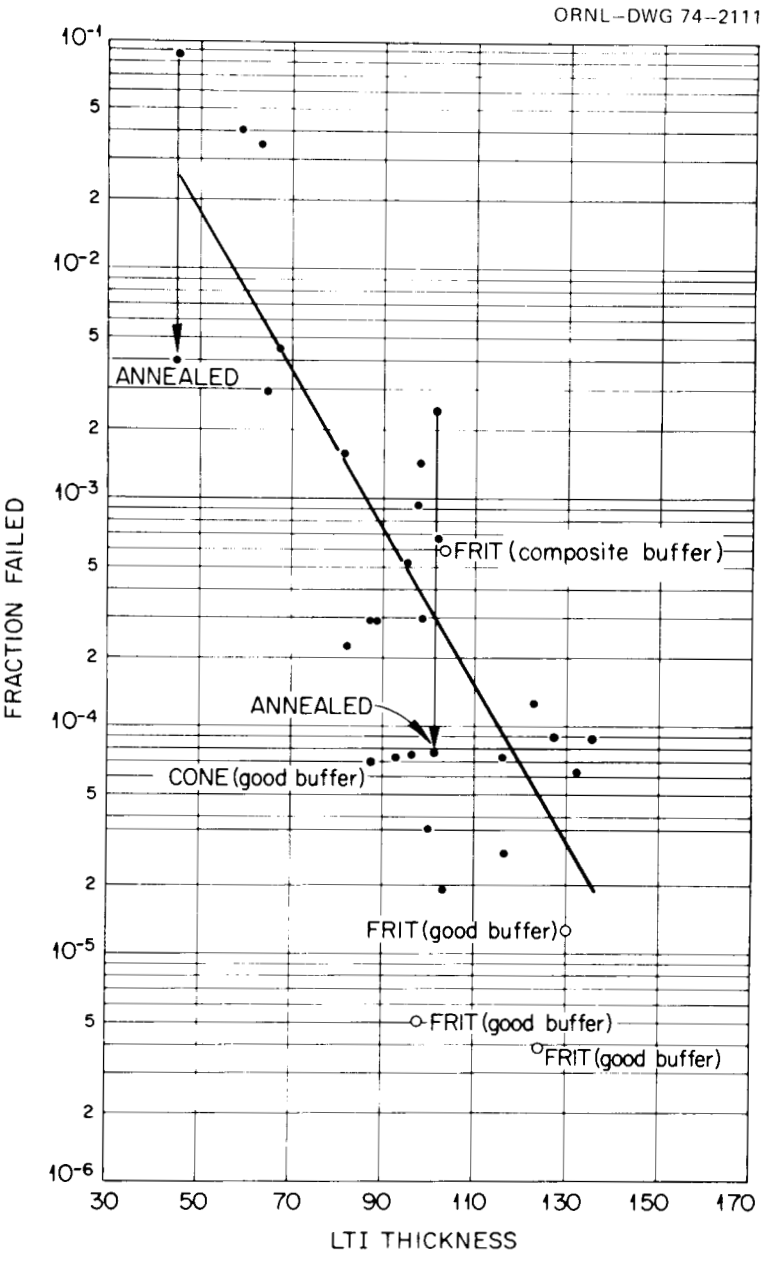

Fig. 3.9. Influence of LTI coating thickness on the fraction defective for as-coated Biso particles.

adhering to the sooty graphite coater components was higher than desired. The average loss of heavy metal was 0.7% when no diluent was used and about 2% with a diluent. Loss of material was enhanced by large charges and high gas flow rates.

For a wide range of operating conditions, the coating bulk density, that is, the corrected gradient density as described in Sect. 3.8, ranged from 1.75 to 1.95 g/cm^3. Coating density increased with increasing temperature (temperature of outer surface of coating chamber), reached a maximum, and decreased with further increase in temperature. At the higher temperatures, the dependence of density on temperature was strongest for lower propylene flow rates. At 1450°C, the coating

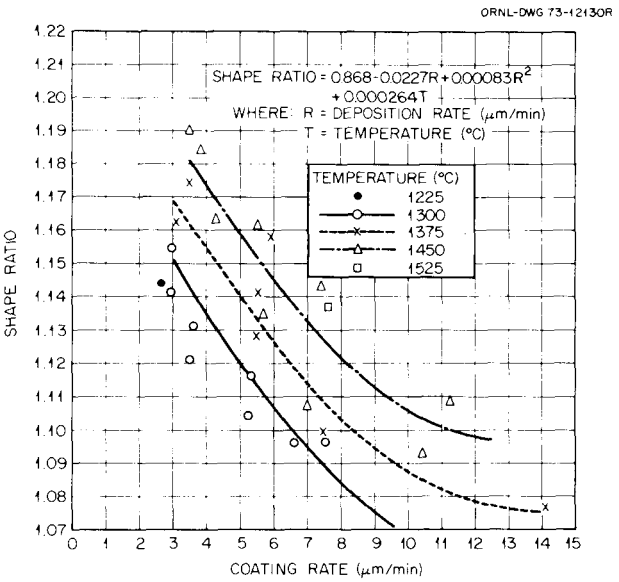

Fig. 3.10. Correlation of particle shape to coating rate and temperature.

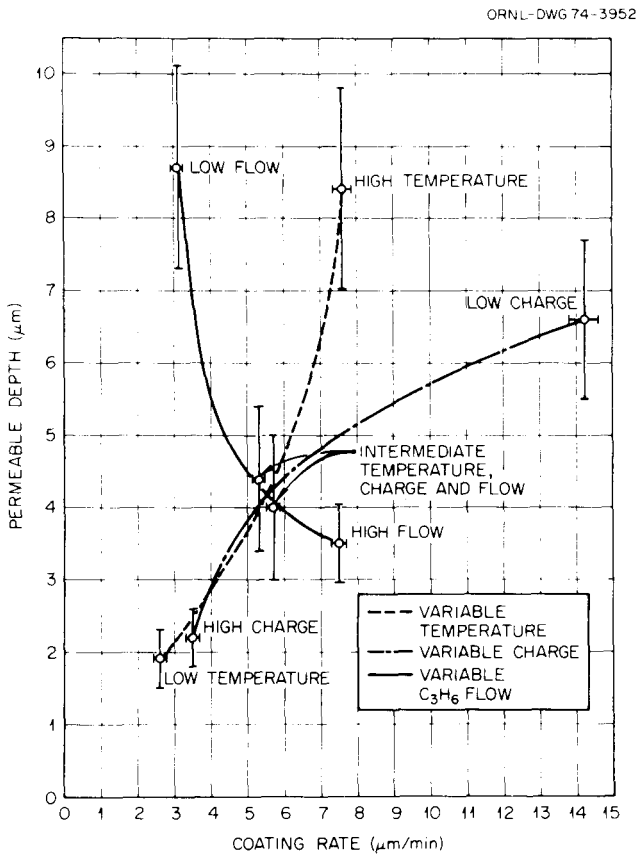

Fig. 3.11. Influence of process conditions on the depth to which the LTI coating is permeable.

density increased on increasing the propylene flow rate from 2.5 to 4.7 scfm, while at 1300°C, the density decreased with increasing flow. For duplicate coating runs, the average spread in coating density was 0.01 g/cm^3, indicating that sufficiently good reproducibility can be obtained.

A 2-μm-thick sealer layer previously applied to the buffer-coated particles did not prevent carbon from infiltrating the buffer coating during deposition of LTI coatings. The extent to which the density of the buffer layer was increased was greatest for runs at low temperature and high propylene flow rates. The increase in buffer density varied from near zero to a maximum of 0.15 g/cm^3, with 0.08 g/cm^3 being average. There was no close correlation with either coating rate or LTI coating density.

The surface texture of Biso-coated particles, as observed with the scanning electron microscope at magnifications up to 10,000X, was relatively unchanged, even when the coating temperature, propylene flow rate, and charge were varied over wide ranges. Neither did the addition of helium noticeably affect the surface morphology. The surface area of Biso-coated particles as measured by the BET technique was about 50 times the geometric area and was reduced by about 20% on annealing 30 min at 1800°C.

Initial information allowing comparison of the product produced with a cone to that produced using a porous-plate-type gas distributor was obtained. Positive aspects of the porous plate, when used to deposit LTI coatings, are that Biso-coated particles are more spherical and the efficiency with which the propylene is utilized is higher when compared with a cone. With a frit, the loss of particles as a result of blow-over may be lower, but loss of particles as a result of adherence to coater components is greater. For constant process conditions, the depth to which the LTI coating is permeable is slightly larger for particles made using a frit. Numerous additional comparisons, including the applicability of a frit for deposition of SiC coatings, must be made before final selection of the type of gas distributor to be used in the pilot plant.

3.5.2 Coater Effluent Treatment

The NaOH scrubber that will be used to remove the HCl from the effluent generated during deposition of

SiC coatings was described previously.[18] We have now designed, fabricated, and tested a somewhat similar scrubber for removing soot and condensable hydrocarbons from the effluent present during deposition of carbon coatings and during carbonization of resin particles. The new scrubber is shown in Figs. 3.4 and 3.12. Basically, the scrubber consists of a tower that forces the effluent to be contacted by sprays of liquid perchloroethylene. Perchloroethylene (C_2Cl_4), a nonhydrogenous, nonflammable organic solvent, wets the soot and dissolves the condensable organic vapors. The resulting slurry is capable of holding appreciable quantities of soot, that is, >100 g/liter. The gas entering the scrubber is at about 600°C, and thus the perchloroethylene is pumped through a heat exchanger to maintain the temperature in the lower portion of the tower and in the reservoir at about 25°C in order to minimize loss of solvent by evaporation. The scrubber has been used successfully for deposition of buffer and LTI coatings and for resin carbonization.

3.5.3 Particle Handling

A particle sampler consisting of a ten-stage conical riffler was designed and fabricated, and evaluation was begun. With ten stages, the sampler ideally removes 1/1024 of a particle batch. Initial tests show that the sample is unacceptably biased toward large particles. Since the orifice size above the cone as well as the relative position of the stages are suspect, modifications are in progress.

A continuous gyratory screen-type particle size classifier was set up for use with both coated and bare particles. The screen diameter is 18 in., and the material throughput is high. Use of this equipment will determine its suitability for remote use as well as expedite size classification of particles needed for various development efforts.

3.6 FUEL ROD FABRICATION – 2105 (ORNL LEAD)

R. A. Bradley J. E. Rushton
J. D. Jenkins M. G. Willey

The purpose of this work is to develop processes and equipment suitable for fabricating about 8000 fuel rods per day in the FRPP. The fuel rods, which are $\frac{1}{2}$ or $\frac{5}{8}$ in. in diameter and 2 to 3 in. long, contain mixtures of fissile and fertile coated particles and graphite shim particles bonded by a matrix of pitch binder and graphite filler.

The principal activities in fuel rod fabrication are dispensing, blending, and loading particles into molds;

18. W. J. Lackey et al., *GCR Programs Annu. Progr. Rep. Dec. 31, 1972,* ORNL-4911, pp. 33–42.

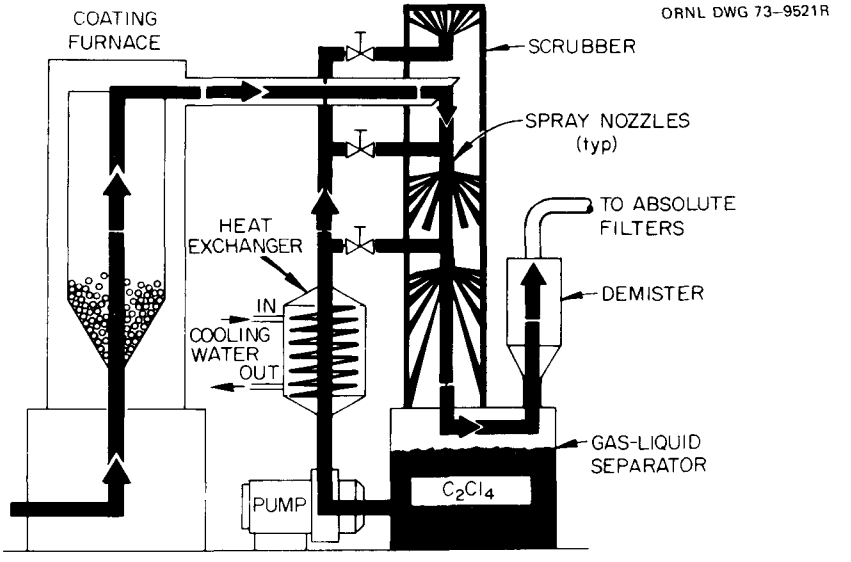

Fig. 3.12. Perchloroethylene scrubber for removing soot and condensable hydrocarbon liquids and solids from the effluent generated during the carbon coating processes.

injecting the matrix into a bed of particles to form a rod; and inspecting and assaying fuel rods.

3.6.1 Particle Dispensing, Blending, and Loading

The particle dispensing, blending, and loading system must be capable of rapidly dispensing precisely controlled quantities of fissile, fertile, and shim particles and blending and loading them into the mold in such a manner that they are distributed uniformly throughout the fuel rod. Our goal for dispensing fissile and fertile particles is to control the amount of uranium and thorium in individual rods to ±1 and 0.5% respectively. Our target specification for blending is that the variation in heavy-metal content per inch of fuel rod be <5%.

We have developed a system using compression valves to volumetrically dispense the particles. This system is illustrated in Fig. 3.13. The compression valve consists of a section of elastomer tubing enclosed in a container such that pneumatic pressure can be applied to the outside of the elastomer tubing. When pressure is applied, the tubing collapses, thus closing the valve. Venting the air pressure opens the valve and allows the particles to flow from a hopper through the compression valve into a collector tube with an adjustable measured volume. After the collector tube is filled, the compression valve is closed, and the particles are emptied from the collector tube through a valve at its base.

The volumetric dispensing system installed on the laboratory automatic fuel rod machine has three sets of hoppers, compression valves, and adjustable collector tubes – one each for fissile, fertile, and shim particles. The three types of particles can be dispensed simultaneously or sequentially.

We have evaluated the use of this system for volumetrically dispensing particles using both bare ThO_2 particles and Biso-coated particles. Closely sized, nearly spherical bare ThO_2 particles were used in preliminary experiments to eliminate the effect of particle shape, particle size distribution, and particle-to-particle density variations on the precision of the dispensing system. The precision with which particles could be dispensed was determined by volumetrically dispensing 100 samples from a hopper in such a manner that ten groups of ten samples each were obtained uniformly along the length of the hopper. At the beginning of each test, the hopper contained about 2 kg

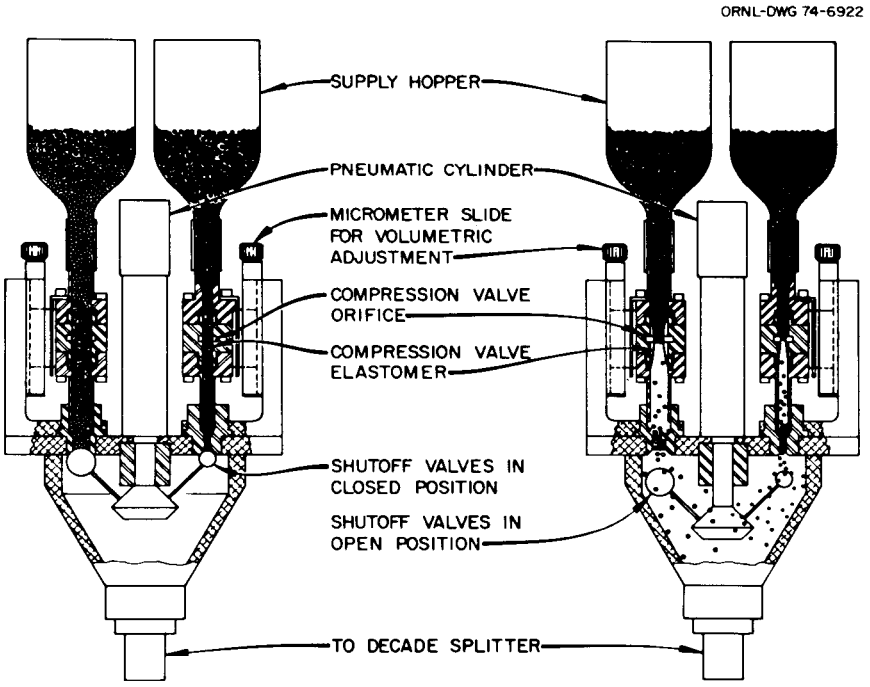

Fig. 3.13. Automatic volumetric particle dispensing system.

of bare ThO_2 particles or about 1 kg of Biso-coated particles. The relative standard deviation of the 100 samples (i.e., the standard deviation expressed as a percent of the mean) was used to indicate the precision with which particles could be dispensed. The results obtained with Biso-coated particles followed the same qualitative trends as those obtained with bare ThO_2 particles.

We found that the ratio of the inside diameter of the compression valve and volumetric collector tube to the mean particle diameter was an important variable. As illustrated in Fig. 3.14, the relative standard deviation decreased slightly as the diameter ratio was decreased from 20 to about 9. As the diameter ratio was decreased from about 9 to 6, the relative standard deviation increased sharply. This increase in the relative standard deviation is attributed to bridging of the particles, causing variations in the packing efficiency.

We also found that the precision with which particles are dispensed is affected by the elastomer pressure, that is, the pneumatic pressure applied to the outside of the elastomer compression valve. As shown in Fig. 3.15, the relative standard deviation decreases as the elastomer pressure increases. For the $^3/_8$-in.-ID valve used to dispense fertile particles (750–850 μm), the optimum pressure is about 35 to 45 psi; for the $^3/_{16}$-in.-ID valve used for fissile particles, the optimum pressure is about 50 to 60 psi.

The precision with which various weights of fissile and fertile particles can be volumetrically dispensed with the system installed on the laboratory automatic fuel rod machine is shown in Table 3.4. The range of weights of fissile and fertile particles per fuel rod is expected to be about 1 to 1.5 and 6 to 14 g respectively. The weight will depend on the coated particle design, fuel rod size, and fuel loading per element. With the volumetric dispensing system presently in use, these amounts of fissile and fertile particles can be dispensed with a relative standard deviation of $\leqslant$0.5 and 0.3% respectively.

The approach to blending that we have investigated involves splitting the charge required for one fuel rod into ten approximately equal increments and sequentially loading each increment into the fuel rod mold. Although the fissile, fertile, and shim particles within any one increment may not be perfectly blended, the relative amounts of fissile, fertile, and shim particles in any increment will be about the same as in any other increment. This splitting technique was selected because it is the most positive way of assuring that the fissile

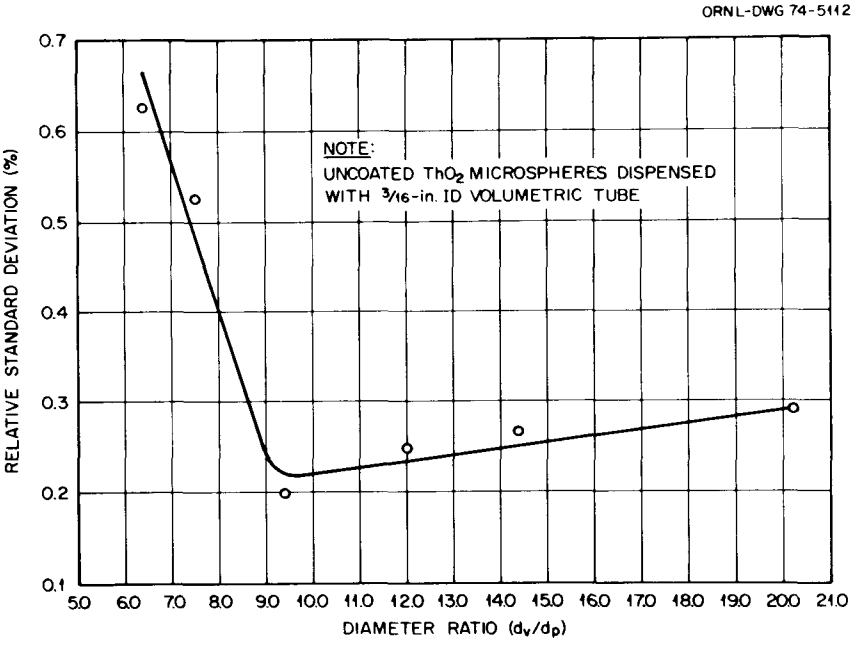

Fig. 3.14. Effect of diameter ratio on relative standard deviation.

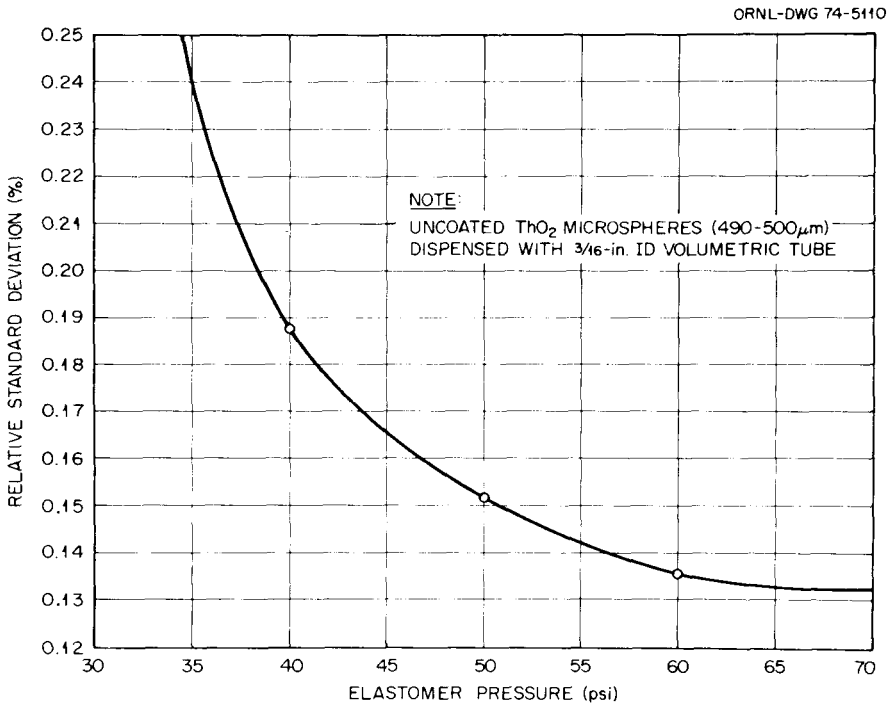

Fig. 3.15. Effect of elastomer pressure on relative standard deviation.

Table 3.4. Precision with which various weights of fissile and fertile particles can be volumetrically dispensed

Particle type	Mean sample weight (g)	Relative standard deviation (% of mean)
Fissile (500–550 μm)	0.669[a]	0.69
	0.854	0.60
	1.031[b]	0.49
Fertile (750–850 μm)	5.311[a]	0.32
	6.877	0.23
	8.502[b]	0.20

[a]Minimum volume obtainable with present valve.
[b]Maximum volume obtainable with present valve; maximum volume can be increased by replacing insert in valve.

and fertile particles are distributed along the entire length of the fuel rod. Preliminary evaluation of this blending technique was reported previously.[19]

We installed a system on the laboratory fuel rod machine for automatically splitting a charge of particles and incrementally loading them into the fuel rod mold. This system is illustrated in Fig. 3.16. Evaluation of the system operated in an automatic mode continues to show that the uranium and thorium content per inch of fuel rod is well within the ±5% target specification. The system is still under evaluation to determine the degree of homogeneity achievable on a finer scale (i.e., less than 1 in.).

3.6.2 Fuel Rod Molding

The slug injection process for molding fuel rods and an automatic machine for fabricating fuel rods by this process were described previously.[19] To form a fuel rod, a preformed slug of matrix is inserted into the mold containing particles, the mold is heated to melt the matrix, and then the matrix is injected into the bed of particles by applying pressure to the top punch. After cooling to ambient, the fuel rod is ejected from the mold.

The laboratory automatic fuel rod machine is a rotary index table to which 24 cylindrical molds are attached. Each mold is indexed through a series of operating stations that load and heat the mold, inject the matrix, cool the mold, and eject the molded fuel rod.

19. R. A. Bradley et al., *GCR Programs Annu. Progr. Rep. Dec. 31, 1972*, ORNL-4911, pp. 44–56.

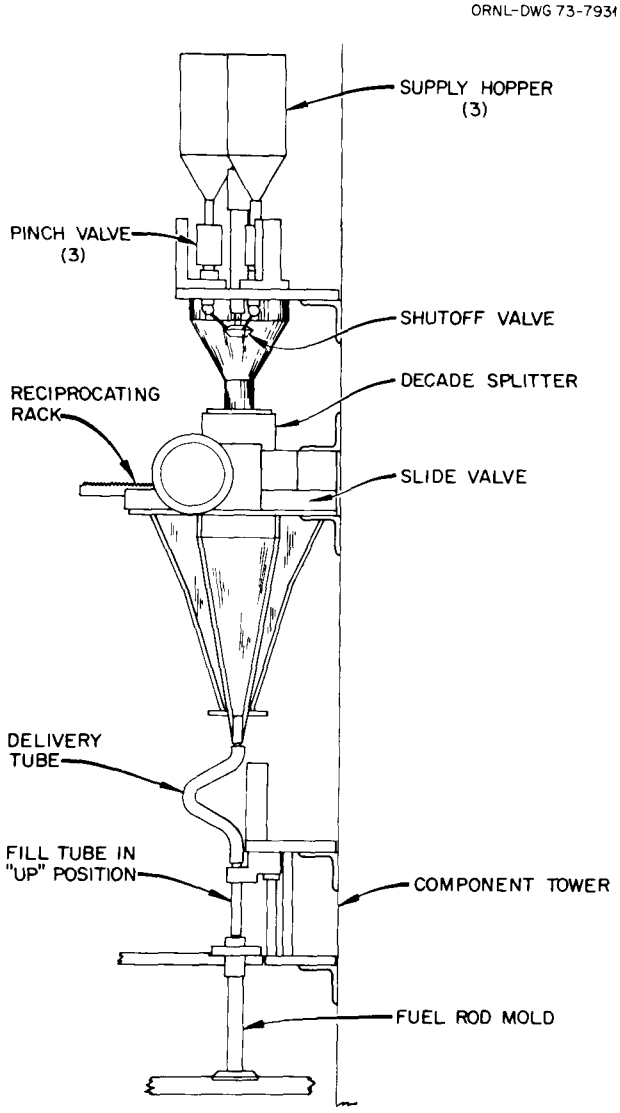

Fig. 3.16. Automatic particle dispensing and blending system.

During this report period, we installed the automatic particle dispensing and blending system described in the previous section on this machine.

Our evaluation of the slug injection process indicates that it is suitable in all aspects for the remote fabrication of HTGR recycle fuel rods. Our experience in fabricating more than 20,000 fuel rods on the laboratory automatic fuel rod machine provides confidence that the fuel rod fabrication system being designed for the FRPP will perform satisfactorily.

3.6.3 Fuel Rod Inspection and Assaying

The capability for performing rapid accurate nondestructive assay of special nuclear materials is an essential part of the TURF demonstration program. Special nuclear materials assay is necessary to ensure that AEC safeguards and accountability requirements are being met during plant operation, to provide quality control and quality assurance information on the facility output, and to maintain real-time material balance control on material in process, both for process control purposes and to ensure criticality safety.

Nondestructive assay of fissile and fertile materials can be achieved by either of two basic techniques (passive and active). In the passive technique, the inherent radioactivity of the material of interest or some companion isotope is used as an indicator of the presence of the material; in the active technique, the sample is interrogated by some penetrating radiation and the resulting induced activity used to measure the material content. We intend to utilize both types of techniques for the assay of fissile and fertile materials in the TURF facility.

Design and development work has been initiated on several devices and techniques to assay the fissile and fertile content of the types of material to be processed through TURF. These include (1) two ^{252}Cf neutron interrogation devices for the active assay of fuel rods and fuel kernels, (2) a calorimeter device for the very accurate assay of individual fuel rods, (3) a passive gamma scanning device for sensing rod-to-rod fissile loading variations, (4) a collimated gamma scanning device to detect inhomogeneous fissile loading distributions in individual fuel rods, and (5) a technique for using conventional radiographs in conjunction with a Quantimet image analyzer to determine the homogeneity of heavy-metal loading in fuel rods. The status of each of these is discussed in more detail below.

^{252}Cf active neutron interrogation devices. The verification of total fissile material content in the refabricated fuel rods will be made with an in-line nondestructive assay system. The assay equipment consists of a ^{252}Cf neutron source surrounded by heavy water for neutron moderation. The fuel rods are assayed by irradiating them with thermal neutrons from the californium irradiator and detecting the fission neutrons emitted from the fissile material in the rods.

A cross-sectional diagram of the ^{252}Cf irradiator is shown in Fig. 3.17. Fuel rods from the fabrication line are fed into a revolving rod carriage located between the heavy-water moderator and the polyethylene reflector. As the rod carriage rotates, the fast-neutron detectors

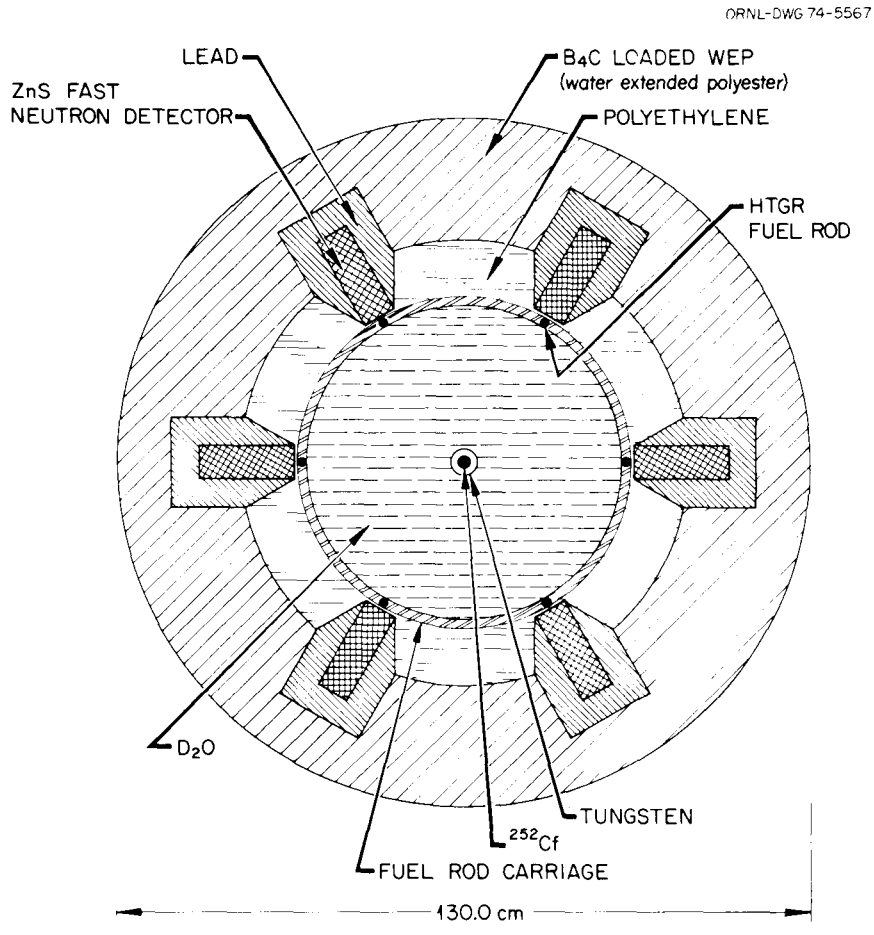

Fig. 3.17. HTGR fuel rod assay system.

count the fission neutrons that are induced by the thermal irradiation. The fissile content of a rod or group of rods is determined by comparison with fuel rod standards.

The nuclear design of engineering-scale equipment for this assay device is under way. The nuclear calculations to study the effect of different moderator materials and geometries on the ^{233}U, ^{235}U, and ^{232}Th fission rates have been completed. The calculated count rates per gram of ^{233}U and ^{232}Th for the device are shown in Fig. 3.18 as a function of radius. The neutron source for these calculations is 1 mg of ^{252}Cf, which has a neutron emission rate of 2.3×10^9 neutrons/sec. Also shown in the figure is the ratio of ^{232}Th to ^{233}U count rates for a fuel rod with a Th/U ratio of 10. The results shown in Fig. 3.18 demonstrate that at the fuel rod carriage position, the sensitivity to ^{232}Th is negligible compared with ^{233}U, so that the neutron count rate is due only to the fissile material in the rod and to fast unmoderated neutrons from the source.

Further nuclear calculations are in progress to determine an irradiator configuration that optimizes the signal-to-noise ratio of the neutron detectors, the ^{252}Cf source strength, and the selection of neutron detectors. A series of experiments is planned to study the suitability of three types of fast-neutron detectors for the in-line assay system.

Calorimeter assay device. One problem with all nondestructive assay devices is that they require calibration using samples of known fissile and fertile content. The fissile or fertile content of the calibration samples must be known to a greater degree of accuracy than that demanded during routine assay of the process material. Currently, such accuracy can only be achieved

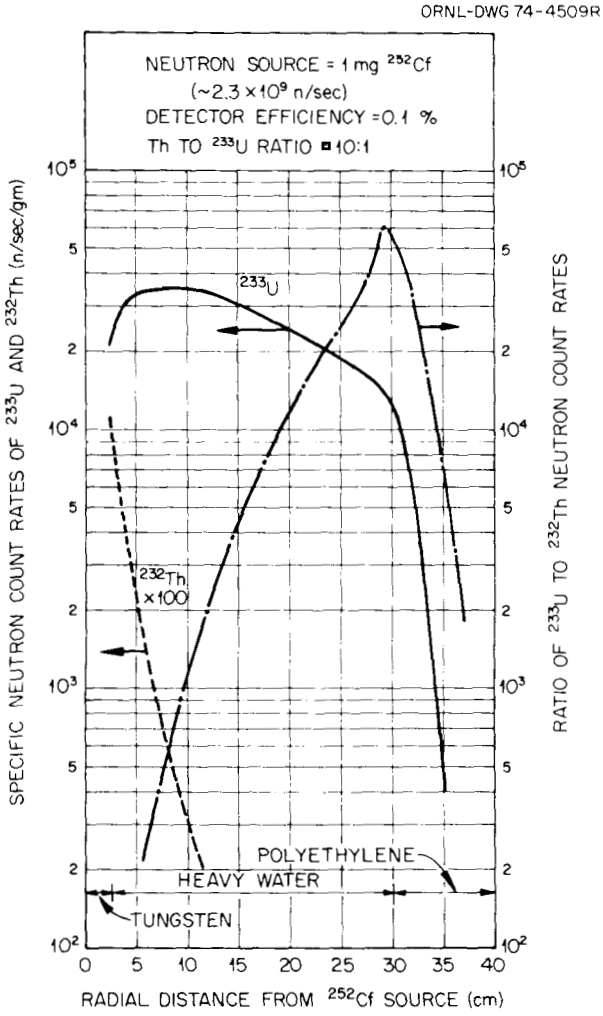

Fig. 3.18. Specific neutron count rates and count rate ratios of ^{233}U and ^{232}Th irradiated in the ^{252}Cf assay device.

by wet chemistry, which unfortunately results in the destruction of the sample.

Calorimetry (i.e., measuring the heat output of a radioactive sample either from its own spontaneous decay or from fissions induced in the sample by neutrons from an external source) provides an alternative nondestructive method of potentially great accuracy for determining fissile content. However, such a technique suffers from a very low throughput capacity because of the long times necessary to attain thermal equilibrium.

We have completed calculations which indicate that calorimetric techniques are feasible for assaying fuel rods containing ^{233}U and ^{232}Th. A device has been designed (Fig. 3.19) that will assay such material by measuring the temperature rise of the sample and sample holder, relative to an isothermal container, due to fissions induced in the sample by neutrons from a californium source. In the device pictured, the upper heater is maintained at the same temperature as the sample holder to eliminate conductive heat loss along the hanger. All heat loss must therefore be by radiation to the container walls, allowing the relatively small heat generation rate (~2 × 10^{-5} W assuming a 100-μg californium source and 0.25 g of ^{233}U in the sample) to result in an induced ΔT of approximately 5°C, well within the limits of accurate detection.

The mechanical design of the calorimeter device is essentially complete, and construction of a test unit is imminent.

Passive gamma scanning device. One problem in assaying ^{233}U-^{232}Th reprocessed fuel is the inherent high gamma background present in the samples due to the unavoidable contamination by ^{232}U and its gamma-active daughters. This gamma activity is a function of both the concentration of ^{232}U in the ^{233}U and the length of time elapsed since the uranium was purified to remove the decay daughters. Because of the time dependence of the ^{232}U daughter activity, this signal cannot be used for an absolute indicator of uranium content. However, on a given fuel batch with a common processing history, the ^{232}U daughter activity does provide a strong signal that will allow rapid comparison of the uranium loading of individual rods relative to other rods in the same batch.

The mechanical and nuclear design of such a device has been initiated.

Collimated gamma homogeneity inspection device. One possible technique for determining the distribution of fissile and fertile material within a fuel rod nondestructively is to scan the rod for axial variations in gamma activity. This can be done by moving the rod past a collimator slit and measuring the fluctuations in the transmitted gamma activity.

A positioning device exists to traverse and rotate a fuel rod past a collimator slit in a controlled manner. We are currently modifying the electronic controls of this device to make it compatible with existing counting equipment. We intend to test the technique by scanning neutron-activated rods to determine fissile material distribution and unactivated rods to determine fertile material distribution.

Quantitative radiograph examination by Quantimet. Radiographs of fuel rods clearly show the heavy-metal fuel kernels within the rod. The calculations we have completed indicate that quantitative information on

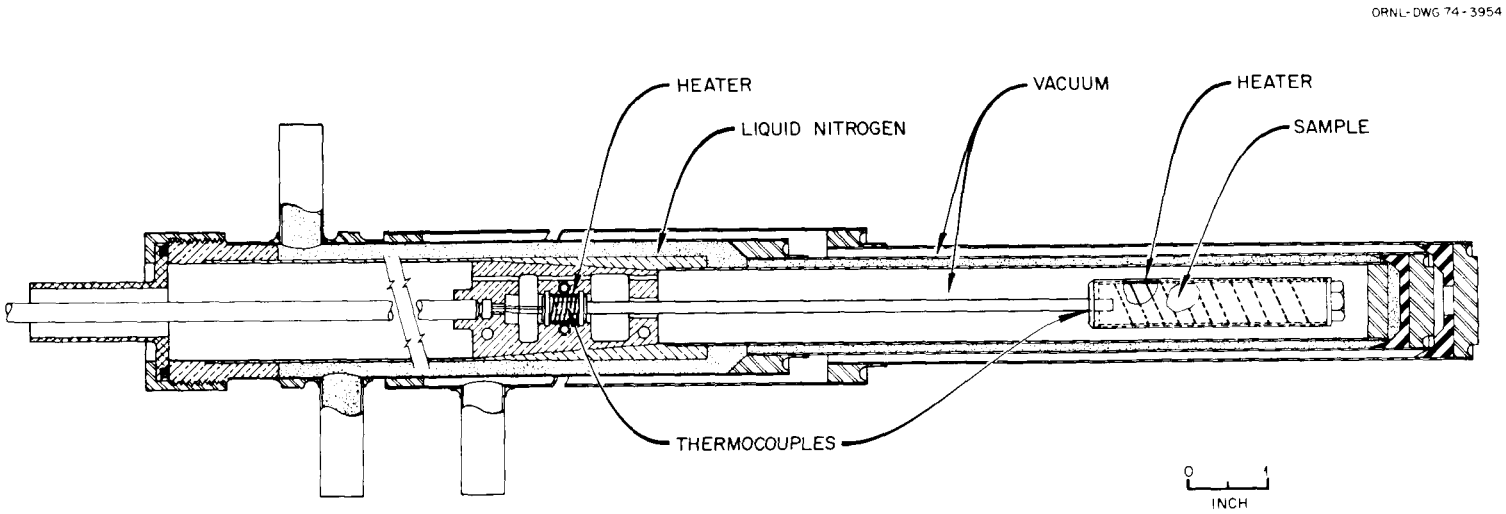

Fig. 3.19. Assay calorimeter.

fuel particle distribution within a rod and total heavy-metal loading can be obtained by scanning such radiographs with a Quantimet image analyzer to determine the ratio of projected kernel area to total rod area on the radiograph. The total projected kernel area can be related directly to heavy-metal loading, and, by scanning the rod in increments, information can be obtained on loading homogeneity.

Preliminary experiments using the Quantimet facility at Y-12 confirm our calculations and indicate that the technique is promising.

3.7 FUEL ELEMENT ASSEMBLY – 2106 (ORNL LEAD)

A. J. Caputo

The fuel element fabrication development work is divided into four areas: (1) fuel element loading, in which green (unfired) fuel rods are loaded into the fuel element block; (2) carbonization and annealing, in which the loaded fuel element block is heated to about 1000°C to carbonize the pitch binder of the fuel rods and then annealed at 1800°C to remove residual volatiles and stabilize fuel rod dimensions; (3) end plug, dowel, and poison rod loading, in which poison rods are loaded into the element and graphite plugs and dowels are placed in the fuel holes and dowel holes and cemented into place; and (4) fuel element inspection, in which the assembled element is inspected and prepared for shipment to the reactor (or stored). Effort during the year has been confined to the carbonization and annealing area of this work.

3.7.1 In-Block Carbonization and Annealing

After the green fuel rod is molded by the slug injection process, it is heated to 1000°C to carbonize the pitch binder. However, since the pitch is thermoplastic, the rod must be supported during carbonization to prevent dimensional distortion. In the past, fuel rods have been supported during carbonization by packing them in aluminum oxide or graphite powder. Although this provides adequate support for dimensional stability, the remote fabrication of fuel rods would be greatly facilitated if this step could be eliminated. It has been proposed that the green fuel rods be loaded directly into the graphite fuel element block and carbonized and annealed in situ.

Accelerated irradiation tests have revealed a potential problem associated with this in-block carbonization technique. The HRB-4 and -5 irradiation tests (see Sect. 7.1.2) showed that a rod carbonized in packed Al_2O_3 powder gave acceptable results, but an identical rod carbonized in a graphite tube (to simulate in-block carbonization) gave unacceptable results and contained many fuel particles with broken outer coatings (Fig. 3.20) of pyrolytic carbon (LTI) after irradiation. Examination of comparable as-fabricated rods showed that the rods carbonized in Al_2O_3 had a low pitch coke yield (26%) and a very porous matrix microstructure, but the rods carbonized in-tube had high pitch coke yields (39%) and a much denser matrix microstructure. Examination of the as-fabricated fuel rods showed no completely broken coatings from either mode of carbonization, but several fuel particles in the rod carbonized in the graphite tube showed the initiation of tears in the outer coating (Fig. 3.21). It appears that as the matrix shrinks during carbonization, there is a mechanical interaction of the matrix and the surface of the fuel particle outer coating. Since in-tube carbonization results in higher pitch coke yields, more shrinkage, and a denser structure than in-powder carbonization, there is enough matrix-particle interaction to initiate tears in the coatings during in-tube carbonization but not during in-powder carbonization. Additional shrinkage during the irradiation tests can cause the tears to propagate until actual breakage occurs.

A study of the in-block carbonization process was initiated to more clearly understand the matrix-particle interaction, with the ultimate goal of performing in-block carbonization without damaging fuel particles and thus produce fuel rods which, from past irradiation tests, would be expected to give acceptable irradiation test results. Since the past irradiation tests indicated that acceptable test results were associated with low pitch coke yields (about 25%) and a uniform and porous matrix microstructure, the initial phase of the study was to determine the in-block processing conditions that would produce these characteristics.

In order to lower the pitch coke yield of the standard matrix (71 wt % Ashland A-240 pitch and 29 wt % Asbury 6353 natural flake graphite filler), the two primary process conditions studied were heating rate and atmosphere used during carbonization to 800°C. Since the thermogravimetric (TGA) analysis of the A-240 pitch showed that 97.5% of the weight loss occurs between 250 and 650°C, a group of carbonization runs was made using an argon atmosphere at various heating rates (1 to 10°C/min) between 250 and 650°C but with a constant, rather fast (5°C/min), rate from room temperature to 250°C and from 650 to 800°C. This included a run at the highest heating rate possible (approximately 100°C/min) obtained by placing the fuel rods into a furnace that was already at a

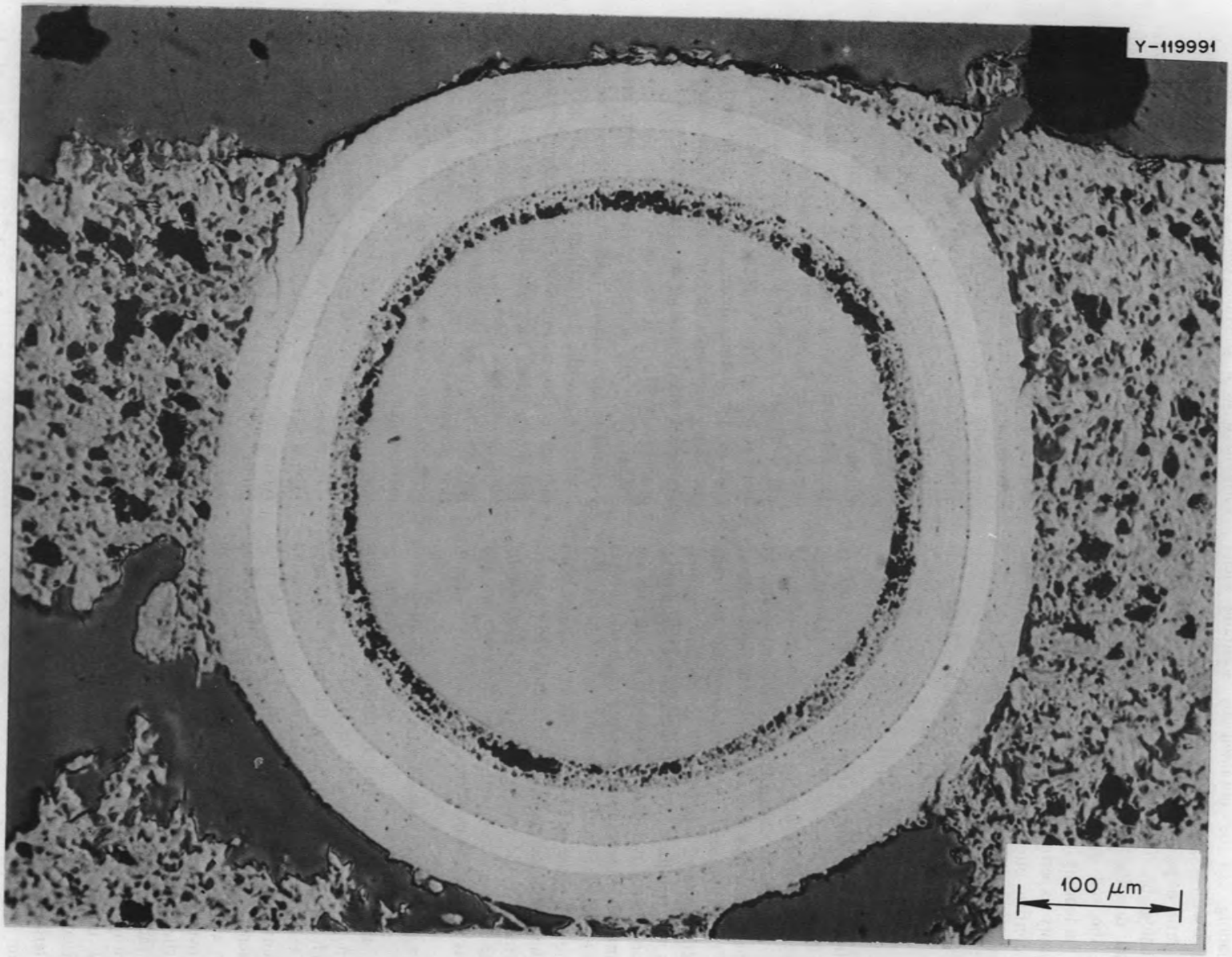

Fig. 3.20. Unirradiated Triso-coated particle showing tears in outer isotropic coating caused by particle-matrix interaction. 300×

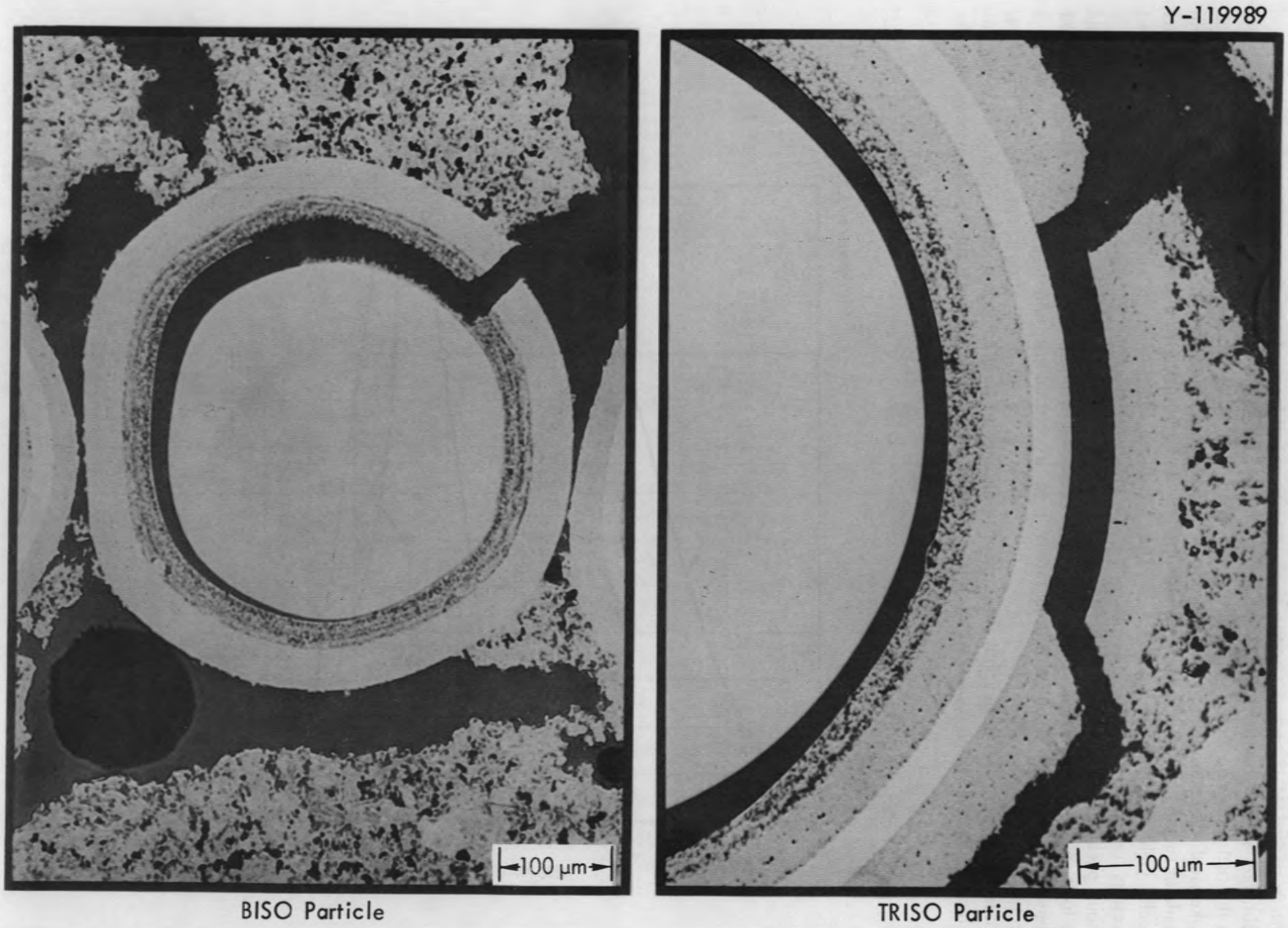

Fig. 3.21. Coatings broken during irradiation because of matrix-particle interaction. The fuel rod that contained the particles shown was carbonized in a graphite tube. Irradiated to 3.6×10^{21} neutrons/cm^2 (>0.18 MeV).

temperature of 650°C. In each run, rods were carbonized both in packed Al_2O_3 powder and in graphite tubes (to simulate in-block carbonization). After carbonization, the fuel rods were annealed at 1800°C and the pitch coke yield was determined. A second group of runs was made in vacuum at similar heating rates, with the pitch coke yield results shown in Fig. 3.22. The significant results for these runs are listed below.

1. Fuel rods packed in Al_2O_3 powder in an argon atmosphere have an overall low pitch coke yield, and it only increases from 15 to 22% when the heating rate is increased from 1 to 10°C/min.

2. Fuel rods in graphite tubes in an argon atmosphere have the highest overall pitch coke yield, but it decreases from 45 to 35% when the heating rate is increased from 1 to 10°C/min.

3. The major effect of heating rate, both in argon and in vacuum, is obtained at 10°C/min, with only a small additional effect obtained by heating at ~100°C/min.

4. Carbonizing in a graphite tube in vacuum further reduced the pitch coke yield (at 10°C/min) to about 25%, which was one of the goals of the investigation.

Although carbonization in vacuum produced the desired low pitch coke yield, it is not as easily adapted to a continuous, remotely controlled process in a hot-cell as an inert atmosphere process. Therefore, another method of lowering the pitch coke yields but still maintaining an inert atmosphere process was the

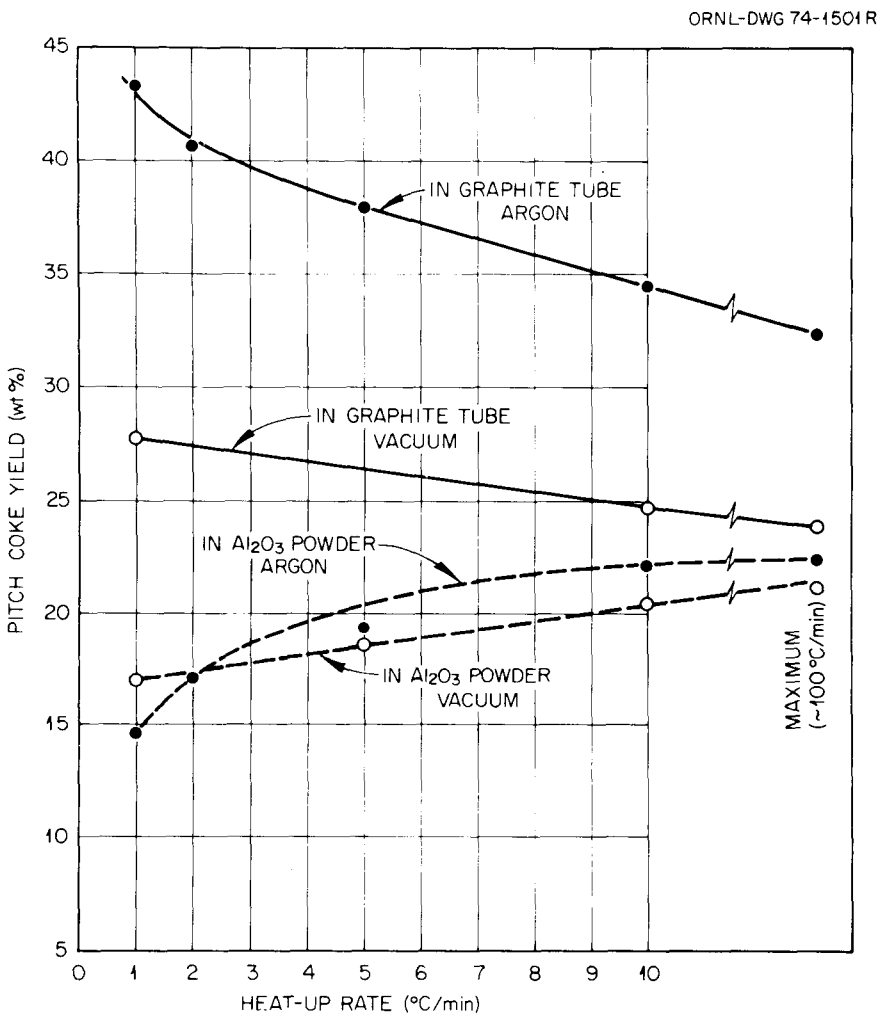

Fig. 3.22. Carbonization of HTGR fuel rods using Ashland A-240 pitch.

use of binders other than the reference Ashland A-240 pitch. Alternative binders studied included (1) Ashland A-170 pitch, (2) mixtures of A-240 and A-170, and (3) A-240 with additives that have very little coke yield. These additives included an internal lubricant, a lightweight oil, and an Ashland commercial product, APO oil. All fabricated fuel rods were carbonized (both in Al_2O_3 powder and in tube) in a common run in an argon atmosphere at a heating rate of 6.7°C/min. A summary of the resulting pitch coke yields is shown in Fig. 3.23. The significant results shown by the data are listed below.

1. In-tube carbonization using the reference A-240 pitch gave a coke yield of about 34%.
2. In-tube carbonization using mixtures of A-240 and A-170 reduced the coke yield to about 27%.
3. In-tube carbonization using A-170 alone reduced the coke yield to the goal of 25%.
4. In-tube carbonization using A-240 with various amounts of any one of the additives gave coke yields in the range of 27 to 31%.
5. Carbonization in Al_2O_3 powder produced the same general results except at an overall lower coke yield level.

From the data, it is apparent that the pitch coke yield from in-tube carbonization in an argon atmosphere can be reduced to the 25% level by using A-170 pitch. Again, this is close to the desired goal, but only irradiation tests could demonstrate if it is low enough. If lower yields are desired, they could be obtained by using either A-170 with additives or A-240 with more than one additive.

In addition to low pitch coke yields, another goal of the in-block carbonization study was to produce the uniform, porous matrix microstructure previously obtained from carbonization in packed Al_2O_3 powder. The difference in the matrix microstructure from these two carbonization techniques is shown in Fig. 3.24. In the heating rate studies, the pitch coke yields were reduced from ~45 to ~35%, but this did not significantly alter the matrix microstructure. However, the tests performed under vacuum reduced the coke yields to the 25% level previously obtained in packed Al_2O_3 powder in argon. Under these conditions, the matrix microstructure also approached that previously obtained in Al_2O_3 powder, that is, a uniform and porous structure. This similarity in structure is shown in Fig. 3.25. Although processing under vacuum is not planned, it is

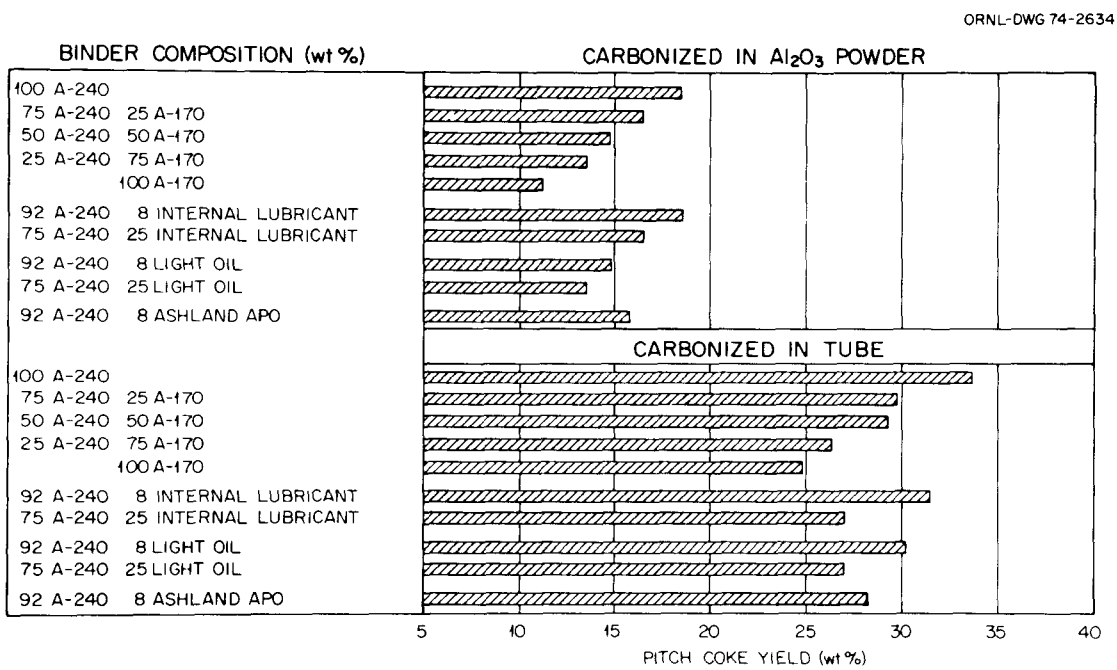

Fig. 3.23. Pitch coke yield of fuel rods made with various binder materials.

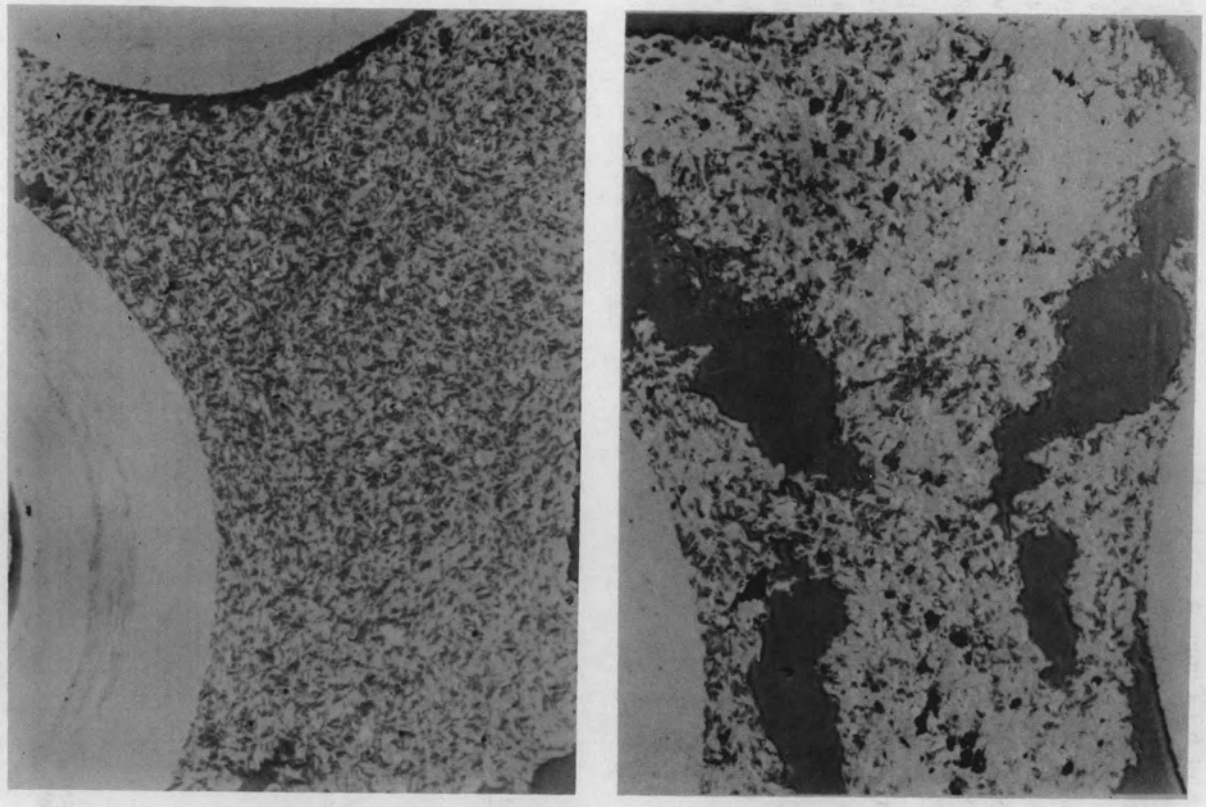

Fig. 3.24. Matrix microstructure of HTGR fuel rods carbonized in an argon atmosphere.

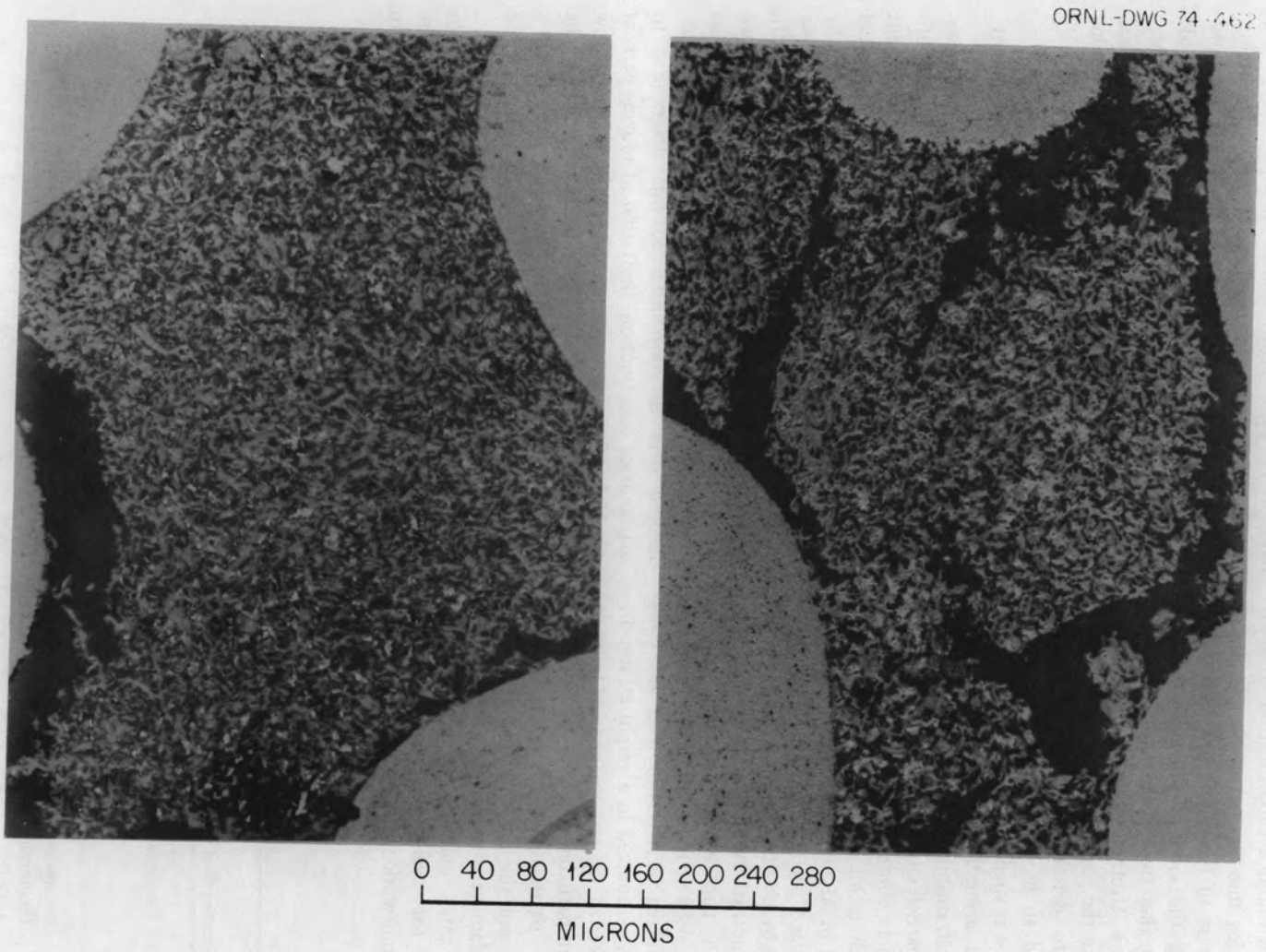

Fig. 3.25. Matrix microstructure of HTGR fuel rods carbonized in vacuum.

encouraging to demonstrate that the matrix microstructure can be obtained from in-block processing similar to that from Al_2O_3 processing.

As mentioned previously, the ultimate goal of this study was to perform in-block carbonization without damaging fuel particles due to matrix-particle interaction. The initial phase of the study approached the problem by reducing the amount of interaction by making the matrix weaker (low pitch coke yields and porous microstructure). Another approach to the problem would be to make the particles stronger. This part of the study was to determine what fuel particle strength was required to prevent damage due to this interaction. Progress was made toward this goal. Fuel rods were fabricated using fuel particles of varying rupture strengths (mean rupture strength determined by breaking individual particles in a small Instron tester) whose damaged particle content had been determined by the chlorine leach technique (see Sect. 3.8). The rods were carbonized in Al_2O_3 powder and in graphite tubes, and the damaged particle content of the fired rods was determined by chlorine leach. The results (as shown in Table 3.5) indicate the following.

1. The unannealed particles with lower rupture strengths (3.97 and 4.88 lb) showed some damaged particles when carbonized in Al_2O_3 powder and considerably more when carbonized in a graphite tube. In both cases, the weaker of the two unannealed batches showed more damaged particles.

2. The annealed particles had higher rupture strengths (7.13 lb), and the chlorine leach failed to detect any particle damage due to in-block carbonization even at high pitch coke yields. The rupture strength technique for evaluating coating quality appears promising, and work will continue in this area to determine the rupture strength required for in-block carbonization without damaging fuel particles.

Future work will be directed toward an increased understanding of the matrix-particle interaction and its relation to coke yield, matrix structure, and fuel particle damage. As mentioned previously, unacceptable irradiation tests were experienced with rods that only had the initiation of tears in the as-fabricated rod. Detection of these partially torn coatings of a statistically significant level is not possible at this time. Thus, irradiation testing will have to be done to complete the evaluation of the in-block carbonization process.

3.7.2 Large-Scale In-Block Carbonization Equipment

Work to date has been confined to in-tube carbonization that can only simulate in-block conditions. Modifications are being made to adapt laboratory equipment to use at least small portions of typical large fuel element blocks. The use of full-size blocks will not be possible until the large carbonization furnace (now being designed) is fabricated and installed in TURF. In order to be economical for a future commercial-size plant, a continuous-operation-type furnace appears most attractive. The vertical position design appears favored over the horizontal position design due to materials of construction, limitation of moving parts at the high operating temperature (1800°C), and the low maintenance and remotely operable requirements of the hot cell. Thus a continuous, vertical-type furnace is being designed within the vertical space limitations (22 ft) of the hot cell.

The furnace will be resistance heated and will use four individually controlled zones to obtain a temperature gradient up to 1800°C followed by a cooling zone to

Table 3.5. Damaged fuel particle content of fired fuel rods

Starting fuel particles[a]			Fired fuel rods			
			Carbonized in Al_2O_3 powder		Carbonized in a graphite tube	
Batch No.	Condition	Rupture strength[b] (lb)	Pitch coke yield (wt %)	Number of damaged particles	Pitch coke yield (wt %)	Number of damaged particles
J-421	Unannealed	3.97	18.2	16	32.7	39
J-422	Unannealed	4.88	17.2	7	32.3	26
J-409	Annealed	7.13	22.3	2	35.4	2

[a]Chlorine leach analysis of each batch of starting fuel particles showed up to two damaged particles per amount of particles equivalent to a fuel rod.

[b]Mean rupture strength determined by breaking individual particles in a small Instron tester.

reduce the temperature before unloading. To load the furnace, the fuel element block will be placed into a loading canister, placed on top of the furnace, and added to the column of blocks in the furnace as required. The column of blocks moves downward in a nearly continuous manner, and, when a cooled block reaches the unloading chamber at the bottom, it is unloaded to make room for another block to be loaded at the top of the furnace. The most serious design problems are to obtain the required high temperature followed by rapid cooldown and the design of the rather large valves required for the passage of the fuel element blocks within space limitations. Operational problems will include the fact that the heating rate for the large blocks may vary both across the diameter and along the length. Such a variation would affect the coke yield. The variation in porosity known to exist between the center and the periphery of the large block will also affect the coke yield. Present in-tube carbonization with only an 8-in. fuel column in the tube has shown that a rod that is only one rod removed from the end of tube has a coke yield about 4% higher than the end rod (typically 37 vs 33%). The magnitude of the problem with a full-scale block is expected to be even greater, since the fuel column will be 30 in. long.

A considerable portion of future work will be directed toward scaling up the carbonization equipment and process to handle the large fuel element blocks. Equipment limitations will limit the first step of this to just portions of blocks. As mentioned previously, present small-scale work has indicated many variables will be affected by the scaleup to the large fuel element blocks.

3.8 SAMPLE INSPECTION – 2107 (ORNL LEAD)

W. H. Pechin

This work unit consists of the development work required for design of the sample inspection system of the FRPP. Devices and techniques must be developed to assure that representative samples are selected. Statistical work is required to determine sampling levels that will provide adequate assurance for the data generated. Candidate inspection and analytical techniques must be tested to ensure that they measure the desired attribute with sufficient precision and accuracy. Techniques will be modified as required to be more suitable for the shielded gove box operations required in the FRPP.

3.8.1 Fuel Rod Inspection

Microstructure. Since metallographic examination is a rather qualitative evaluation subject to personal bias, work was initiated on a technique to obtain a quantitative measurement of the matrix microstructure. The rather porous fuel rod (~40%) is infiltrated (at ~200°C and 4000 psi) with a low-melting metallic alloy that fills both the macro- and microporosity of the graphite matrix. The relative percentages of each pore type are determined by examination with a quantitative television microscope. Careful polishing of the sample is required to allow the dark surfaces of the graphite or fuel particles to be distinguished from the light surfaces of the metal-filled pores.

Broken particle fraction. A major problem in the fuel characterization is the determination of the damaged (broken or cracked) fuel particle fraction. Previously, the damaged particle fraction was determined by the acid leach technique. For green rods, the pitch was dissolved in pyridine, while fired rods were deconsolidated by electrochemical means prior to leaching. However, the procedure was slow, the deconsolidation step had the potential for damaging particles, and penetration of a very fine crack by the acid solution was questionable.

High-temperature chlorination with gaseous chlorine has been demonstrated to convert exposed heavy metal in damaged fuel particles to the volatile chlorides that can be quantitatively recovered and spectrophotometrically measured. This technique was evaluated by comparison of the amount of heavy metal leached with the number of defective particles detected by microscopic analysis prior to chlorination. At 1000°C, chlorination of samples (10–12 g) of loose particles (approximately equal to 20,000 particles or a fuel stick loading) required 4 to 6 hr to effect quantitative recovery of the exposed thorium, whereas 16 to 48 hr was required for the quantitative chlorination (1000°C) of annealed fuel sticks (matrix density, excluding open porosity, equal to 1.1 g/cm^3 and 40% open porosity) that were doped with 1 to 10 broken particles. At 1500°C, the time required to chlorinate annealed fuel sticks and obtain quantitative recovery of the exposed thorium is reduced to 3 to 6 hr.

The chlorination technique was found to work with rods fired in packed Al_2O_3 having a low coke yield and with rods fired in carbon tubes having a high coke yield.

3.8.2 Particle Inspection

Particle size analyzer. We have continued the development of the electronic particle size analyzer, which is expected to be the major source of process control data for particle coating in the refabrication pilot plant. By repeated measurement of single particles, this instrument was found to have a standard deviation of

approximately 2 μm. A new particle singularizer was developed to ensure that only a single particle could be in the light beam at any one time, thus ensuring an accurate count. This singularizer (Fig. 3.26) is a rotating evacuated drum that picks up particles individually on holes in the drum. As each hole reaches the proper position with respect to the analyzer delivery tube, an air jet position inside the drum dislodges the particle from the hole and drives it into the delivery tube. Although this unit operates at a slower particle feed rate than the jet pump singularizer previously used, it works with a much wider range of particle size and allows the use of vacuum to move the particles through the sensor unit. The advantage of using vacuum to move the particles is that small vent holes can be placed in the sensor block to prevent the buildup of dust on the photocell or the optics.

New hardware was designed and fabricated for the particle size analyzer to allow the incorporation of a rotating plastic disk with various sized dots to serve as a secondary standard. When not in use, the disk is positioned with a cutaway portion in the light beam. Figure 3.27 shows this equipment with the supporting metal block omitted for clarity.

Coating density. In another area of work, two different techniques for measuring the density of LTI

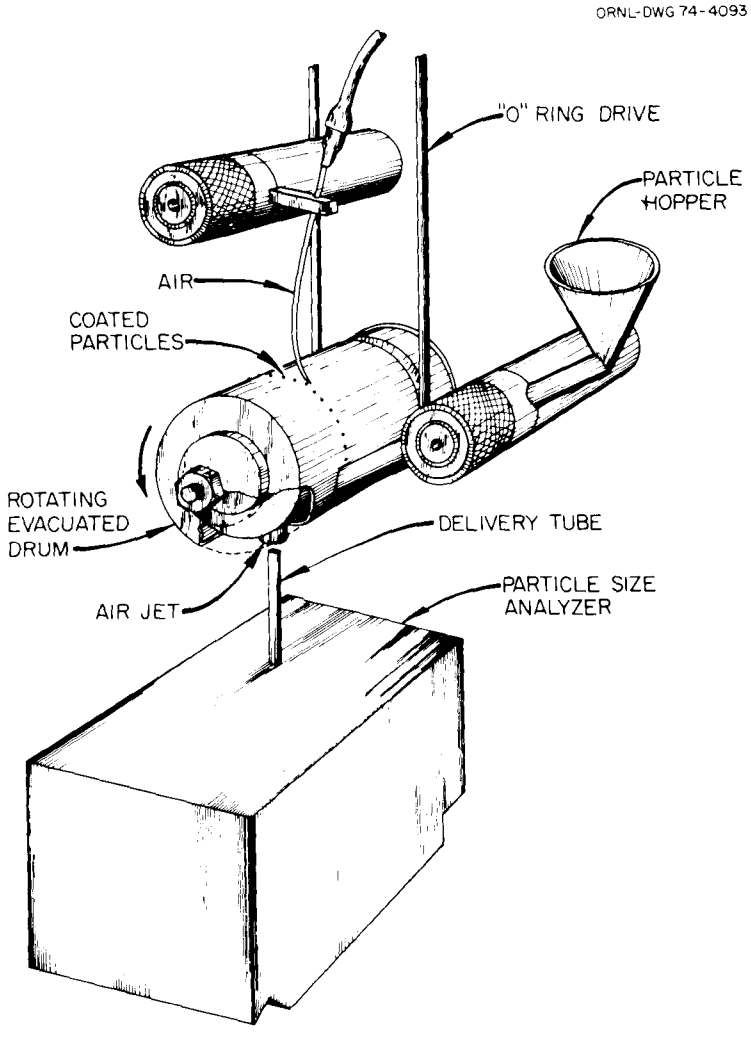

Fig. 3.26. Particle singularizer.

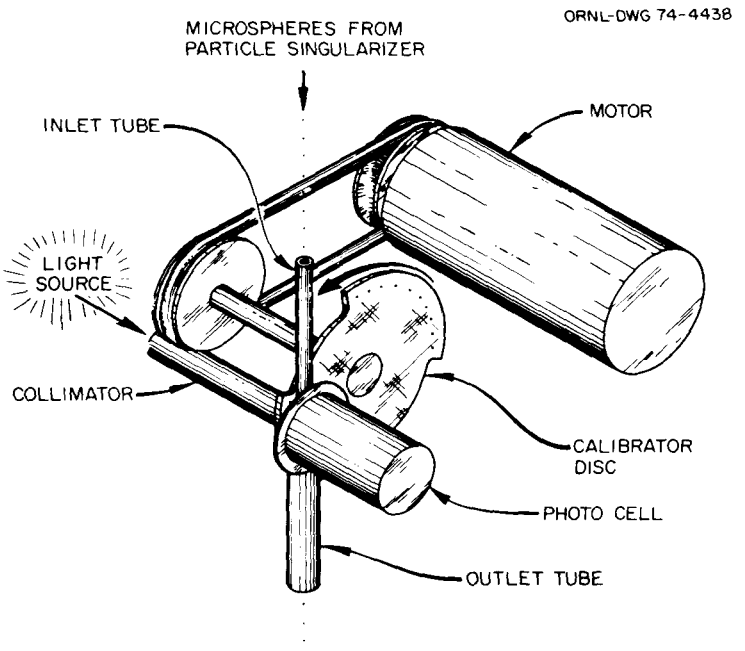

Fig. 3.27. Particle size analyzer.

coatings were evaluated and compared. The two techniques are (1) gradient density, where a fragment of an LTI coating is placed in a column of liquid having a known density gradient from top to bottom, and (2) calculation using the before- and after-coating particle density as determined by low-pressure (250 psi) mercury pycnometry and the percent carbon before and after coating as determined by combustion in air or oxygen. The gradient density technique gives a higher value than the mercury pycnometer burnoff technique. We speculated that the reason was the gradient density liquid filled the open pores of the coating, thus yielding a value higher than the actual bulk density. A quantitative understanding of the bias has been obtained.

The LTI coating was determined for ten batches of particles[20] with LTI coatings deposited directly over ThO_2 kernels to eliminate any confusion caused by infiltration of the buffer coating during deposition of the LTI coating. A comparison of columns 2 and 3 in Table 3.6 shows that the gradient density is invariably higher than the density determined by the low-pressure mercury pycnometer burnoff technique. The open porosity values in column 4 were calculated using the carbon content and particle densities as determined by mercury pycnometry, using pressures of 250 and 15,000 psi, and are thus a measure of the open porosity penetrated by 15,000 psi of mercury. Assuming that the liquid in the gradient density column penetrates these same pores, one can use the open porosity and the gradient density values to calculate the bulk density. The calculated bulk density values given in column 5 agree very closely with the densities obtained by the mercury pycnometer burnoff technique. This excellent agreement gives confidence that the mercury pycnometer burnoff technique is accurately measuring the bulk coating density and that the gradient density values can be corrected if the percent porosity is also measured. Since carbon infiltration of the buffer during deposition of the LTI coating leads to erroneously high density values from the mercury pycnometer burnoff technique, the density obtained by correcting the gradient density for open porosity will be the preferred technique for most Biso-coated particles.

Although previous results have shown a correlation between density and percent open porosity, there are exceptions which make it necessary to measure the open porosity of each sample. For example, samples J-353 and J-358 of Table 3.6 have appreciably different bulk densities (1.895 vs 1.812), but the gradient densities are nearly identical since the coatings have widely different values of percent open porosity.

20. Provided by R. L. Beatty.

Table 3.6. Comparison of LTI coating density measurement techniques

Sample No.	Gradient density (g/cm^3)	Mercury pycnometer (250 psi) and burnoff (g/cm^3)	Open porosity (vol %)	Corrected gradient density[a] (g/cm^3)
J-349	1.712	1.642	3.973	1.644
J-350	1.817	1.759	2.407	1.773
J-351	1.502	1.441	3.379	1.451
J-352	2.013	1.998	0.888	1.995
J-353	1.946	1.895	2.641	1.895
J-354	1.720	1.649	4.455	1.643
J-355	2.044	2.040	0.349	2.037
J-356	1.905	1.873	1.834	1.870
J-357	1.628	1.583	2.691	1.584
J-358	1.948	1.812	6.627	1.819

[a]Corrected gradient density = (1 – vol % open pores/100) gradient density.

Particle surface porosity. During the process of bonding HTGR fuel particles into fuel rods, a carbonaceous bond is formed between the surface of the fuel particles and the rod matrix. During heat treatment and irradiation, the matrix shrinks, and if the particle-matrix bond is too strong, the coating can be torn. Since torn coatings are very undesirable, the strength of the particle-matrix bond is of great interest. The strength of this bond is suggested to be related to the roughness and/or porosity of the outer layer of the pyrocarbon coating.

A method was developed for characterizing the nature of the surface of coated particles. Of particular interest was the depth to which the carbon coatings were permeable, since this could be important in determining the strength of the particle-matrix bond. In this method, the open pores of the particles are impregnated with nickel by removing all gases from the open pore under a vacuum (about 10 μm Hg), introducing nickel carbonyl vapor at a pressure of 1 atm, and decomposing the carbonyl at the surface of the particles heated to about 150°C with subsequent deposition of nickel on the wall of the open pores. Upon examination of a metallographically polished cross section, it is possible to determine the depth to which the pores were interconnected with the surface, since all open pores contain metal deposits. Figure 3.28 is an illustration of particles treated by this technique.

Particle shape. A technique was developed for quantitatively measuring the shape of coated particles. The index of merit, termed "shape ratio," is obtained by dividing the coating thickness on one side of a particle by the thickness on the side that is diametrically opposite. The large thickness is always placed in the numerator, so that the shape ratio is greater than unity. The average value obtained from measurements on 50 to 100 particles is used to characterize a particle batch. Such values, along with macrographs showing the appearance of particles from eight particle batches, are shown in Fig. 3.29. A comparison of the shape ratio values with the visual appearance shows that the shape ratio is a meaningful measure of particle shape or faceting. Further evidence that the shape ratio accurately reflects particle shape is that a correlation was shown to exist between shape ratio and particle packing fraction.

3.9 PROCESS CONTROL AND DATA HANDLING – 2108 (ORNL LEAD)

R. A. Bradley B. C. Duggins

The purpose of this work unit is to develop process control and data handling technology necessary for the design and operation of the HTGR FRPP. Previous work in this area has been conducted and reported as an integral part of the work on individual work units (e.g., fuel rod fabrication or microsphere coating).

The use of a computer system for the operation of the pilot plant appears to be mandatory, particularly for material accountability as it relates to safeguards and criticality control, for quality control calculations, for quality assurance records, and for supervisory control of alarm conditions. Development work is required to apply industry-developed instrumentation and computer interfacing technology to the FRPP.

The instrumentation and data handling industry will be surveyed to determine the state of the art in control

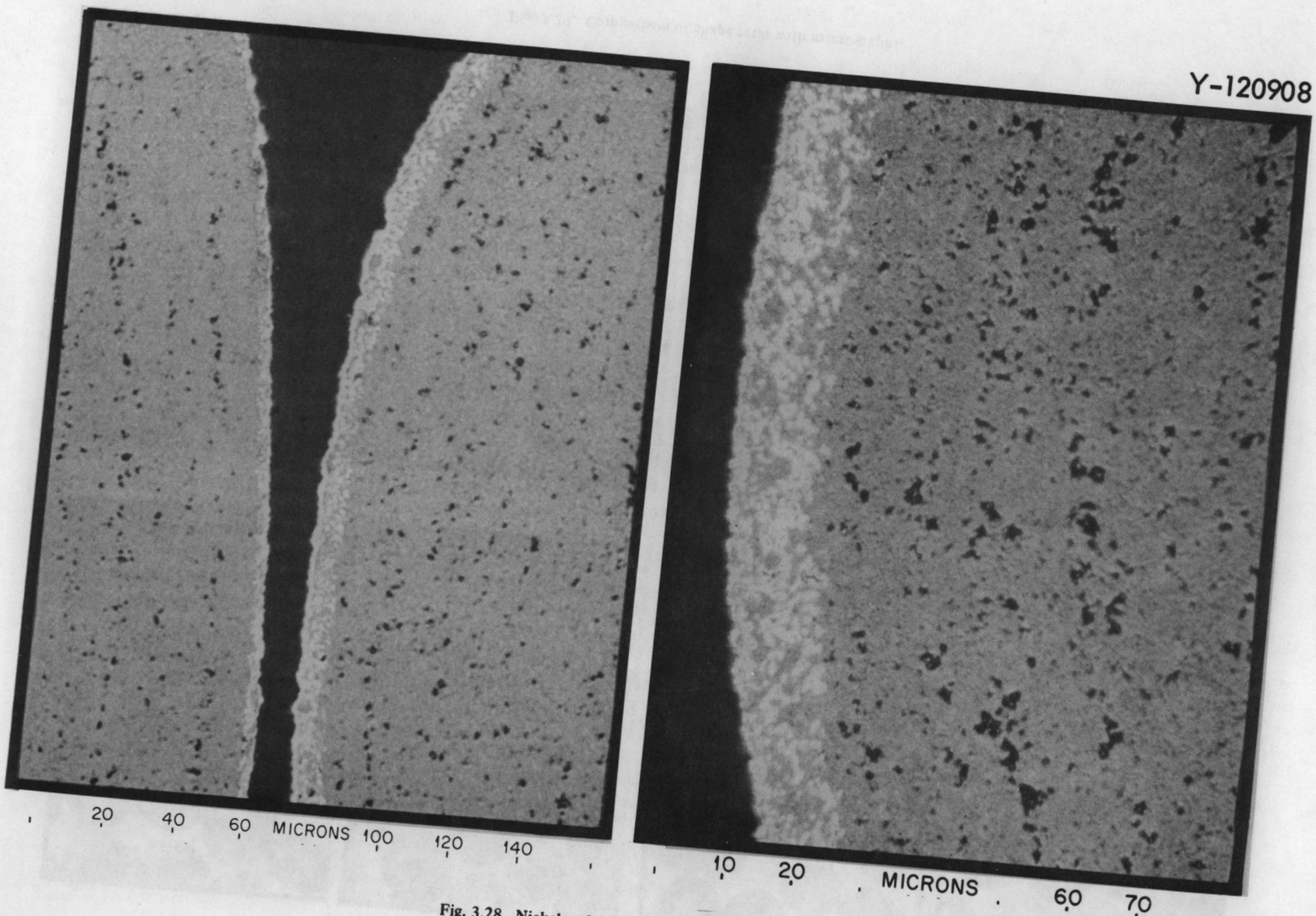

Fig. 3.28. Nickel carbonyl treated LTI coating.

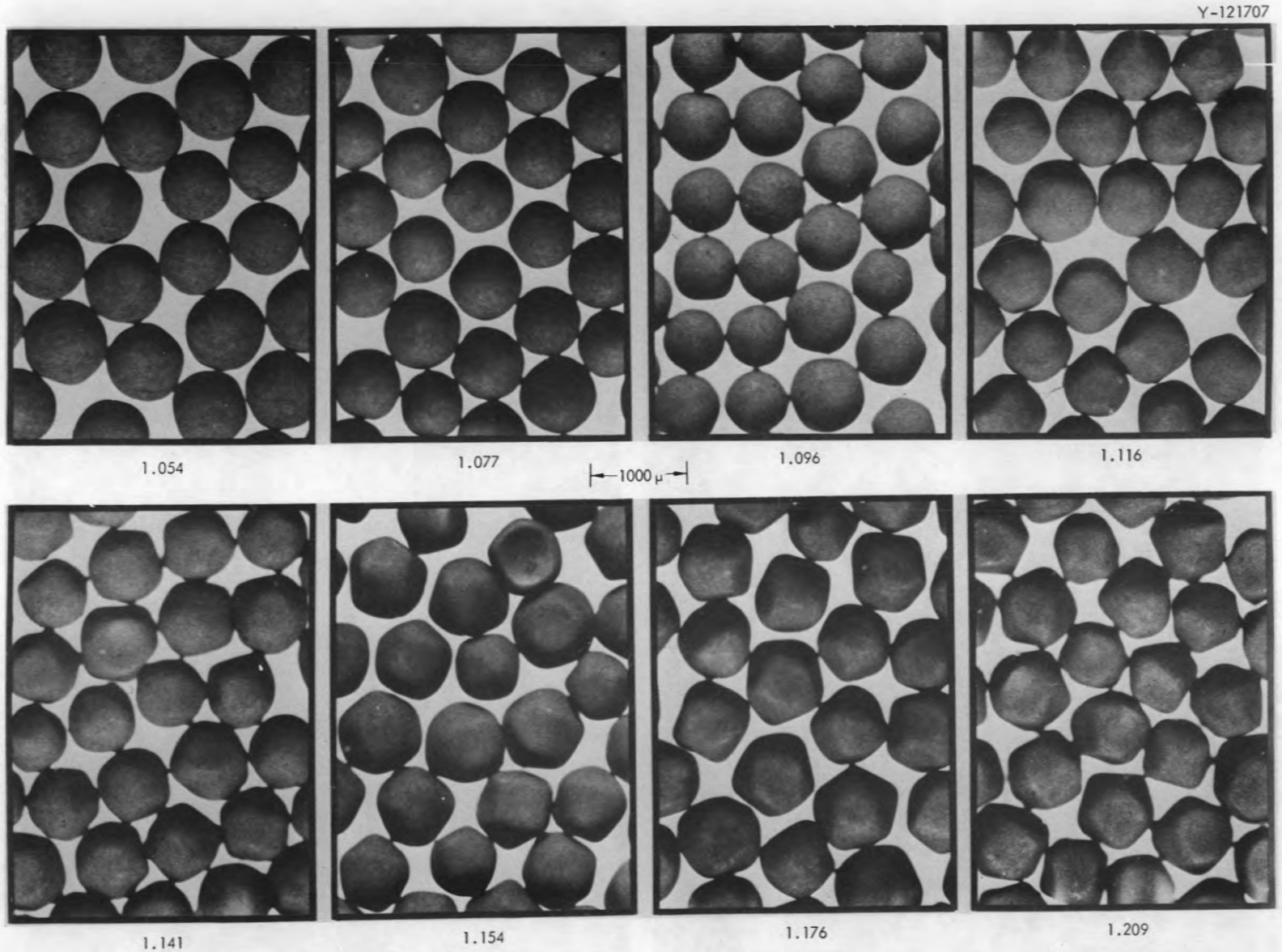

Fig. 3.29. Comparison of shape ratio with macrographs.

technology. Characteristics of the control system will be developed in terms of redundancy and synchronization of control operations and data acquisition. A control software package will be developed to test the fundamental concepts. This package will be applied to a selected system to determine adequacy of the concepts and performance characteristics and to enable projections of requirements in terms of specifications for the final design of the process control system design.

3.10 WASTE HANDLING – 2109 (ORNL LEAD)

J. D. Jenkins

The objective of this work unit is to develop the waste handling technology necessary for the design and operation of the FRPP. The work in this area has been primarily in the development of waste packaging and waste assay methods. This work included selection of standard waste containers to facilitate waste handling and assay requirements, development of remote container sealing and leak-testing techniques, determination of waste compaction requirements and methods, and bagging techniques for transferring of waste out of the hot cell. Equipment for these operations is being designed.

Waste assay is necessary to meet the nuclear material accountability and safeguards requirements. Techniques are being developed for assaying the various types of waste.

Current plans are to assay solid, high-fissile-content waste (i.e., reject product) with a calorimeter device located in one of the processing cells. For low-level solid waste, a separate system based on gamma scanning of the ^{233}U decay daughters is being considered. During this year, activity in waste assay has been directed toward formulating a work plan.

3.11 MATERIALS HANDLING – 2110 (ORNL LEAD)

No development activities are scheduled.

4. HTGR Fuel Recycle Pilot Plant Studies

J. W. Anderson[1] F. C. Davis

The HTGR Fuel Recycle Pilot Plant demonstration will be the culmination of the HTGR fuel recycle development program. The work has been divided between two plants: the Reprocessing Pilot Plant and the Refabrication Pilot Plant. The demonstration will establish the technical feasibility of fabricating HTGR fuel elements in a remotely operated facility using highly radioactive feed materials recovered from spent reactor fuel. The pilot plant demonstration will verify the practicability and reliability of the equipment and process designs, provide a demonstration of operating and maintenance methods and procedures, provide process data and design information necessary for scaleup to commercial plant sizes, provide data and information on nuclear safeguards and criticality control, and indicate those areas in which additional development work may be needed. During the past year, the conceptual design of the Refabrication Pilot Plant equipment was begun; it is scheduled for completion during FY-74.

4.1 REPROCESSING PILOT PLANT DEMONSTRATION

J. W. Snider

4.1.1 Evaluation of Idaho Facilities

The HTGR Prototype Fuel Processing Facility, as conceptually designed, will occupy portions of four existing facilities plus a new facility.[2] The facilities and their functions are described below.

1. The crushing, burning, classification, dissolution, and SiC hull handling will be done in cells 1, 2, 3, and 4 of Building 640. A mechanical crane, to be constructed atop cell 2 under the Rover Program, will be used for fuel element handling.

2. The acid-thorex (solvent extraction) process will be located in cells A, C, and D of Building 601.

3. Analytical functions will be performed in Building 627.

4. Product loadout will be performed in a new facility (Building 656) located south of Building 640. Portions of the heat-removal and ventilation systems of Building 640 will be located within this facility.

5. The off-gas process will be located in the middle cell of Building 604.

4.1.2 Off-Gas Treatment and Decontamination System Design Criteria

The off-gas flowsheet is based upon the following process steps: (1) iodine removal using lead and silver zeolites, (2) radon removal using molecular sieves, (3) tritium removal using molecular sieves, and (4) krypton removal using the KALC process.

There are to be two off-gas systems for the process off-gas streams: one for all head-end process steps up to and including the dissolver and hull washing and another for all remaining process steps.

4.2 REFABRICATION PILOT PLANT

F. C. Davis

Process flowsheets and equipment and system diagrams for the ten processing systems to be located in the pilot plant were prepared. These flowsheets and diagrams reflect the latest advancements under subtask 210. Detailed critical-path schedules were prepared to enumerate all the activities necessary to produce the conceptual design for each processing system. Ten system design description outlines and one plant design

1. Present address: Project Management Corporation, CRBR, Oak Ridge, Tenn.

2. *Environmental Impact Study on HTGR Fuels Reprocessing Facilities, National Reactor Testing Station, Idaho,* WASH-1534 (January 1974).

description outline were prepared. Section 1 of each of these documents, the Functional and Design Requirements, was in preparation to serve as a basis for the conceptual design of the equipment within the system.

Conceptual design of the equipment has been progressing at a rate to complete the effort by July 1, 1974. Items requiring additional development efforts are being identified and related to subtask 210.

4.2.1 Schedule and Status

The conceptual design studies for the Fuel Refabrication Pilot Plant were continued at a low level during the first half of this reporting period. Efforts continued in preparing process flow diagrams and equipment and systems diagrams for each of the ten major systems in the plant: (1) uranium feed, (2) resin loading, (3) resin carbonization, (4) microsphere coating, (5) fuel rod fabrication, (6) fuel element assembly, (7) sample inspection, (8) process control and data handling, (9) waste handling, and (10) materials handling. Each of these systems was arranged into subsystems and components of related equipment items.

The engineering efforts were substantially increased during the last half of the reporting period. Phase I of the conceptual design, consisting of detailed criteria preparation, completion of the process flow diagrams, completion of the equipment and systems diagrams, and preparation of outlines of the system design descriptions, was initiated to be completed in 1974. Conceptual design of equipment was begun to be completed by July 1974.

4.2.2 Overall Plant Conceptual Design

Preliminary plans and procedure documents have been prepared and circulated for review and comment. These documents cover design procedures, document control, document review and approval procedures, document revision procedures, external review procedures, subtask 220 organization and responsibilities, etc. These documents are presently being used to serve as a basis for timely and efficient operation of the conceptual design activities.

The necessary modifications and additions to TURF, Building 7930, to efficiently house and operate the pilot plant are being studied. This includes areas for a sample inspection laboratory, an instrument room to house the various instrument racks and panels, and an area for the computer facilities necessary to operate the pilot plant.

4.2.3 System 1 – Uranium Feed

Chemical flowsheets have been prepared for the uranium feed system. These flowsheets schematically indicate the process flows and flow rates, identify equipment items, and show equipment relationships and the interfaces with other systems.

4.2.4 System 2 – Resin Loading

The resin loading system has recently replaced the sol preparation system as the process to demonstrate the production of fuel kernels in the pilot plant. Chemical flowsheets and equipment data sheets had been prepared for the sol preparation process. The conceptual design work on the resin loading system is being initiated by preparing flowsheets and equipment and systems diagrams.

4.2.5 System 3 – Resin Carbonization

The resin carbonization system has recently replaced the microsphere preparation system as the process to prepare microspheres for the ensuing processes in the prototype plant. Chemical flowsheets and equipment data sheets had been prepared for the microsphere preparation process. The conceptual design work on the resin carbonization system is being initiated by preparing flowsheets and equipment and systems diagrams.

4.2.6 System 4 – Microsphere Coating

The precoating and postcoating equipment items have been conceptually designed. These items include fuel particle hoppers, diverter valve, size classifier, shape classifier, weighers, sampler, and the lot blender. The conceptual design of a typical coating furnace and its peripheral equipment is in progress. This includes the furnace, the fuel particle unloading mechanism, the scalping classifier, and a scrubber to treat the effluent gas generated during the coating operations. Equipment arrangement layouts are being prepared to study the relationship of equipment, the viewing limitations through the hot-cell windows, the limitations of the remotely operated manipulators, and the interfacing with other systems.

4.2.7 System 5 – Fuel Rod Fabrication

All the subsystems that comprise the fuel rod fabrication machine have been conceptually designed. The designs of the fuel rod transfer subsystem, the fuel rod integrity inspection subsystem, and the fuel rod assay subsystem are in progress. Equipment arrangement layouts are being prepared to study the various

subsystem relationships, the viewing limitations through the hot-cell windows, the limitations of the remotely operated manipulators, and the interfacing with other systems.

4.2.8 System 6 – Fuel Element Assembly

The equipment items necessary to perform the many steps in fuel element assembly have been identified and are in various stages of conceptual design. The fuel element loading machine, the intercell transfer unit, and the load verification and end plug insertion unit have been conceptually designed. Conceptual designs of the other units are in progress.

4.2.9 System 7 – Sample Inspection

The units necessary to perform the inspection of the fuel particles, the fuel rods, and the fuel element assembly sample have been identified. This list has been altered since the reference fuel has changed from $(Th,U)O_2$ particles to UC_2-UO_2 particles derived from uranium-loaded resins.

4.2.10 System 8 – Process Control and Data Handling

The requirements for power control, sensor, and data handling and storage are being identified to determine the needs of the process control and data handling system. Each of the other systems in the pilot plant are being analyzed to determine their power consumption and instrumentation requirements. Appropriate sensors and control systems are being designed into the processing equipment subsystems to provide proper interfacing with this subtask.

4.2.11 System 9 – Waste Handling

Each of the process systems in the pilot plant have been analyzed to determine the amount and type of waste materials that will be produced. The capability of the existing TURF facility to handle wastes is being studied to determine the additional equipment that will be necessary to service the pilot plant process. A fuel reject rate is being estimated for each system in the pilot plant and the type of fuel rejects that would be expected. These estimates will be used to direct the conceptual designs of packaging and assaying equipment that will be necessary.

4.2.12 System 12 – Materials Handling

Each of the process systems in the pilot plant have been analyzed to determine the type and amount of materials to sustain operations. These materials include feed and support materials to the process, scrap and off-specification materials generated by the process, and the products coming from the process. The needs determined by this study are being compared with the capabilities of the existing TURF facility to determine the additional requirements that must be provided. Plans and procedures are being formulated to perform a thorough check-out of the existing in-cell crane and manipulator system. This system must be made operational to handle process equipment being installed in the cells for development testing.

5. Studies and Evaluation of HTGR Fuel Recycle Systems

F. J. Homan A. L. Lotts

The objectives of this task and the plan for attaining these objectives, stated in last year's annual report,[1] remain the same.

5.1 EVALUATION OF HTGR RECYCLE PROCESSES

D. A. Dyslin

Some of the computer programs that are needed to perform process trade-off studies have been written. These are BAL (material balance), CEP (capital cost), and TCP (total capital cost). The BAL program calculates the heavy-metal flow through the recycle plant as a function of reject rates in the various processes; CEP calculates the capital cost of each individual process block as a function of heavy-metal throughput for that process; and TCP calculates the total capital cost for a plant using the output from BAL and CEP.

In addition to capital costs, the hardware and operating costs need to be estimated. To accomplish this, the BAL program will be expanded to include material balance calculations for materials other than heavy metals such as gases and graphite blocks. This expanded BAL program will be used for establishing hardware cost estimates, and its output will also be used to estimate operating costs. Computer programming for hardware and operating costs, which has begun, will be followed by comparison cost studies of commercial recycle plants.

5.2 COMPARISON OF CANDIDATE RECYCLE FUELS FOR THE HTGR

F. J. Homan

5.2.1 General

The mixed $(Th,U)O_2$ fuel with a 4.25:1 thorium-to-uranium ratio is currently the reference recycle kernel for the HTGR.[2] Recent evidence of poor dimensional stability of this kernel at high temperatures and temperature gradients has caused some concern as to whether this particle will perform adequately. This concern has resulted in consideration of several other candidate fuels for use in recycle fuel elements. Among the alternatives are oxides, carbides, and oxycarbides of uranium derived from weak-acid resin (WAR); the strong-acid-resin-derived UOS system; and mixed thorium-uranium oxides with higher thorium-to-uranium ratios than the current reference kernel. These alternatives must be compared with the present reference particle on the basis of both irradiation performance and economics. The present irradiation data are not adequate to show a clear-cut advantage of one system over another; only estimates of recycle economics are currently available, since no HTGR recycle facility of any size has been built or operated. However, irradiation tests in progress and others in the planning stages should significantly clarify the performance picture. Detailed cost estimates are being made which should provide valuable guidance on the relative costs of fabricating candidate recycle fuels.

1. J. W. Anderson and A. L. Lotts, *GCR Programs Annu. Progr. Rep. Dec. 31, 1972,* ORNL-4911, p. 63.

2. *National HTGR Fuel Recycle Development Program Plan,* ORNL-4702 (Rev. 1, April 1973), p. 18 (in press).

It is important that a reference kernel be selected from the potential candidates as soon as possible. Equipment is presently being designed for installation in the Thorium-Uranium Recycle Facility (TURF), which is to be a pilot plant for a large commercial fabrication facility for recycle fuels. Planning and equipment development for the TURF is strongly dependent on the fuel system to be processed there. Since equipment is scheduled for installation in the TURF beginning in July 1976, the reference fuels should have already been confirmed.

This report describes present knowledge on the economics and performance of the candidate recycle fuels. This will provide a foundation upon which new information can be added to facilitate a timely selection of a reference system for TURF.

5.2.2 Economics

The overriding economic consideration related to the choice of particle for recycle fuels is the amount of material that must be processed in the shielded portion of the refabrication plant. To demonstrate this point, capital cost estimates will be presented for a combination reprocessing-refabrication facility that is capable of supporting a 45,000-MW(e) HTGR economy. Gulf General Atomic (GGA) has estimated the throughputs and capital cost associated with such a facility,[3] so this discussion will serve the dual purpose of comparing the economics associated with candidate recycle fuel kernels and linking our economic estimates to those made by Gulf.

Gulf's estimates of the throughputs for the combination facility are given in Table 5.1. Since we are not interested in the reprocessing part of this facility at the present, we will only estimate the cost of a facility sized to reprocess 307 metric tons of heavy metal per year. The estimate of $41 million is based on an equation described in Refs. 4 and 5.

Fuel element fabrication involves four major steps: (1) kernel preparation, (2) coating, (3) fuel rod fabrication, and (4) fuel element assembly. These steps are basically the same as those used in fabrication of fresh fuel, except that they must be accomplished in heavily shielded facilities using remote techniques. Capital and operating costs are therefore decidedly higher for recycle fuel than for fresh fuel fabricated in a contact facility. It would therefore appear logical to minimize the amount of material that must be processed in the shielded portion of the refabrication plant in order to minimize the amount of equipment and space.

Capital cost estimates[6] for the four stages of HTGR fuel refabrication are given in Figs. 5.1 to 5.4. These figures have been used to estimate the cost of refabricating HTGR fuel for the 23 recycle elements at the

3. *HTGR Base Program Quart. Progr. Rep. Aug. 31, 1971,* Gulf-GA-A-10784, pp. 15–48.

4. *Reactor Fuel Cycle Costs for Nuclear Power Evaluation,* WASH-1099, p. 92 (December 1971).

5. F. J. Homan, "Timing the Utilization of Recycle Fuels in High-Temperature Gas-Cooled Reactors," submitted to *Nuclear Technology.*

6. J. W. Anderson and J. P. Jarvis, *"Commercial Recycle Plant Studies – Process Evaluations,"* unpublished data.

Table 5.1. Data for recycle plant capacity [45,000-MW(e) economy]

Process	Annual capacity (metric tons)				
	Number of fuel elements	^{233}U	^{235}U	Th	Total
Reprocessing	38,880	14	5	288	307
Refabrication					
From recovered ^{233}U	12,645				
From recovered ^{235}U	3,690				
Through coating					
^{233}U mix		14		50	64
^{235}U mix			5	11	16
Assembly					
^{233}U mix	12,645	14		101	115
^{235}U mix	3,690		5	29	34

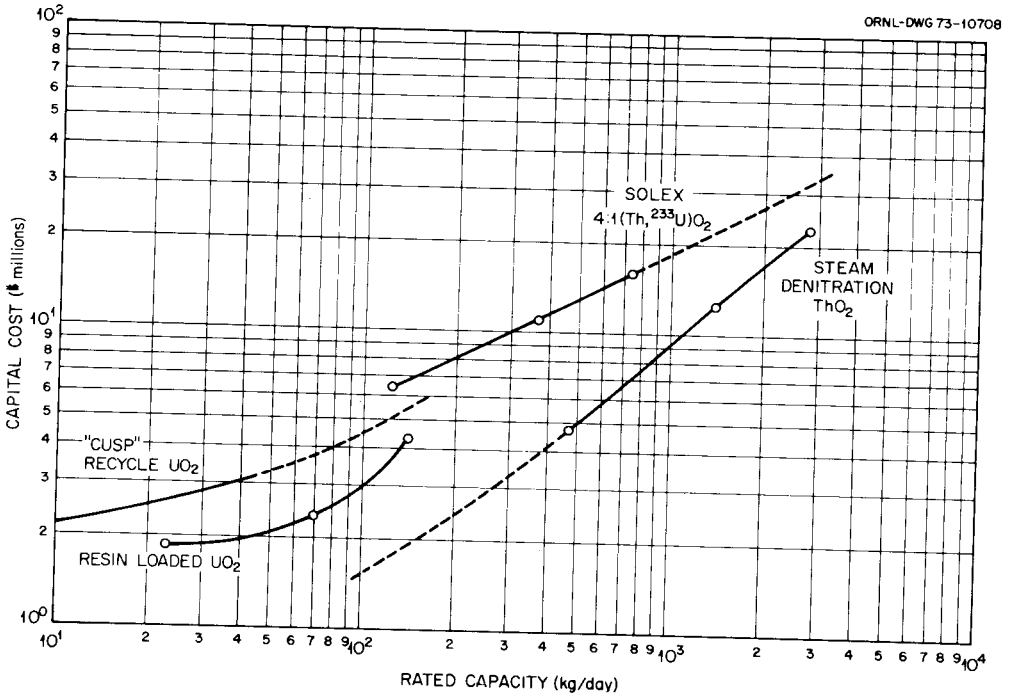

Fig. 5.1. Kernel preparation capital costs.

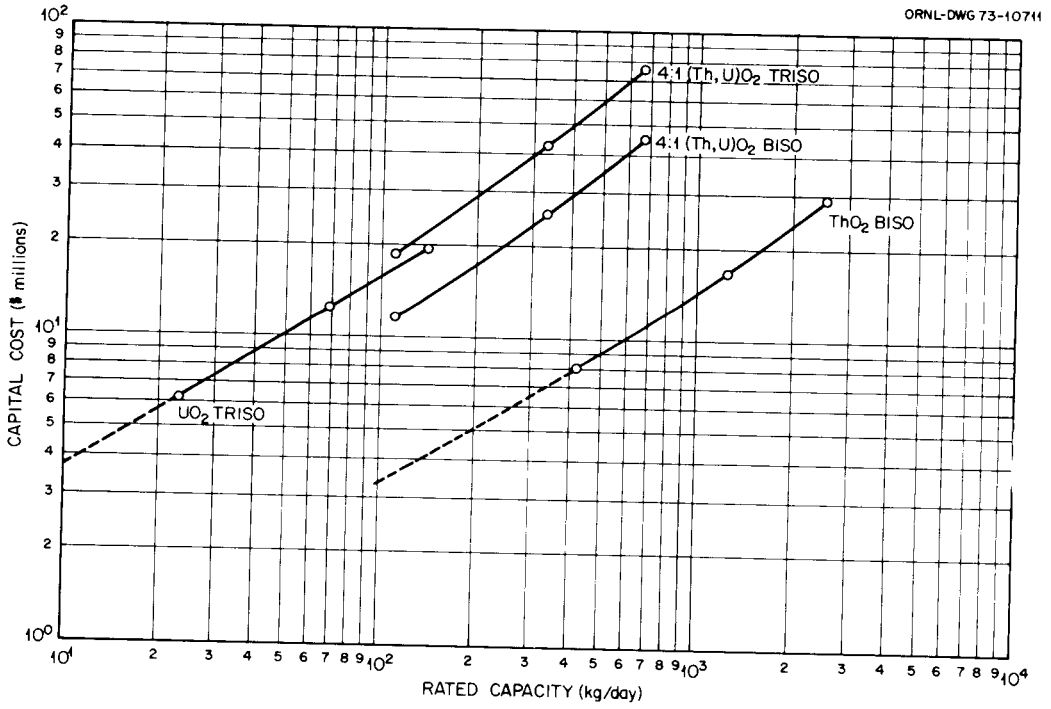

Fig. 5.2. Coating capital costs.

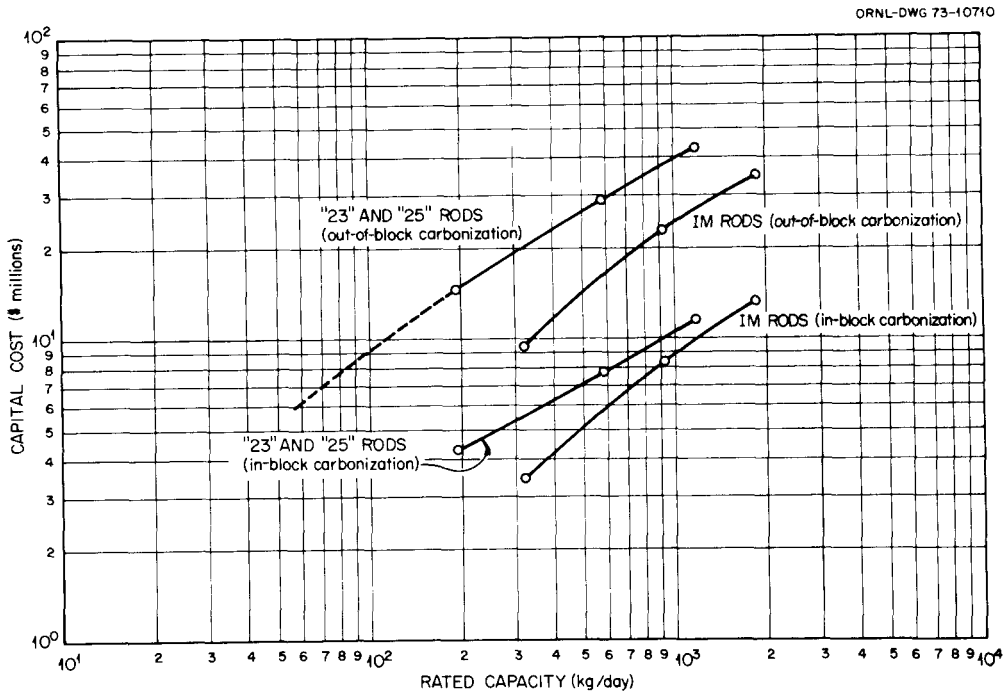

Fig. 5.3. Fuel rod fabrication.

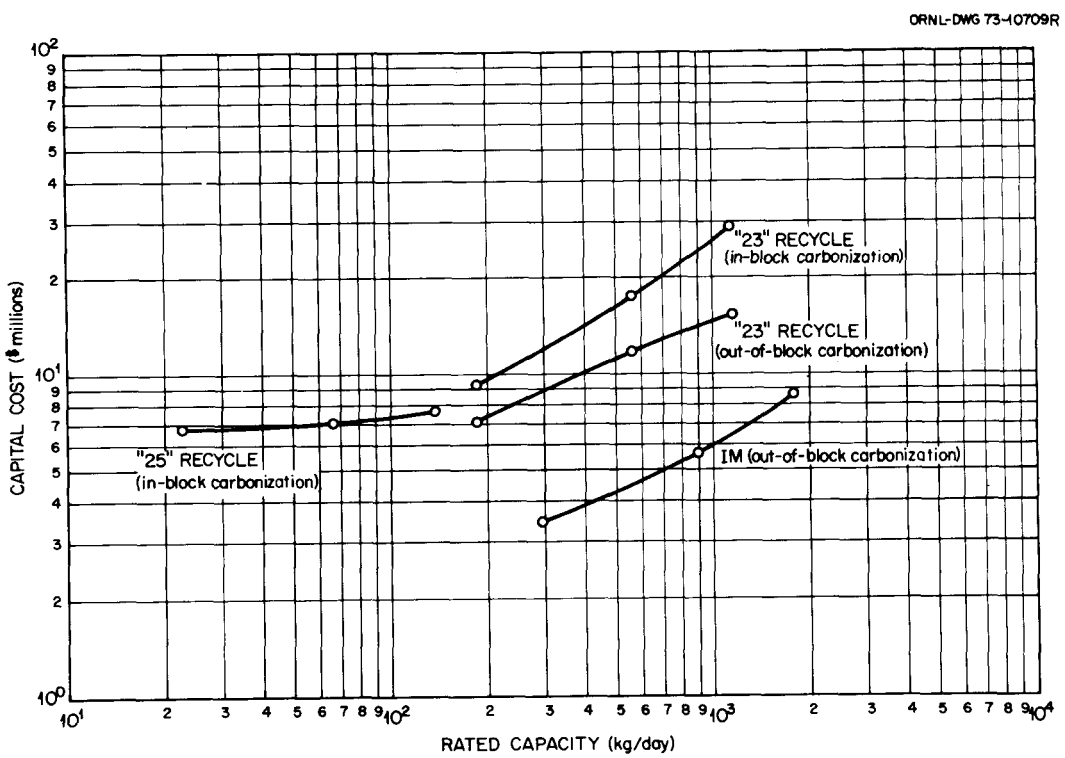

Fig. 5.4. Fuel element assembly.

rate of 115 metric tons of heavy metal per year, as specified in Table 5.1. A load factor of 0.8 has been assumed for the refabrication plant, which means approximately 290 operating days per year. At this rate, the plant must be capable of processing about 400 kg of heavy metal per day.

The throughputs for the shielded and contact lines for refabrication of ^{233}U-bearing recycle elements are given in Table 5.2 for 4:1, 8:1, and WAR 0:1 particles.

Table 5.2. Throughputs for candidate recycle kernels[a]

	Metric tons/year			Kilograms/day		
	4:1[b]	8:1	0:1	4:1	8:1	0:1
Shielded line						
Uranium	14	14	14	48	48	48
Thorium	56	101	0	193	348	0
Total	70	115	14	241	396	48
Contact line						
Thorium	45	0	101	155	0	348
Total	115	115	115	396	396	396

[a]Applies to refabrication of ^{233}U-bearing recycle elements for a 45,000-MW(e) HTGR economy.

[b]Thorium-uranium ratio in recycle fissile particle; 0:1 is the WAR-derived UO_2 kernel.

It is immediately obvious that the economics of the 0:1 particle should be favorable because so little of the material need be processed in the shielded line, whereas the 8:1 particle requires that all the heavy metal for the ^{233}U-bearing fuel elements be processed in the shielded line.

Capital cost estimates derived from the throughputs from Table 5.2 and the cost curves from Figs. 5.1 to 5.4 for the different steps are given in Table 5.3 for the kernel compositions being considered. The results of this study show a $90 per kilogram advantage for the WAR kernel over the 8:1 kernel and a $58 per kilogram advantage of the WAR kernel over the 4:1 kernel, assuming all the kernels are Triso coated. When the 8:1 or 4:1 kernels are assumed to be Biso coated, the cost advantage for the WAR kernels (still Triso) is reduced to $38 and $24 per kilogram respectively. Whether commercially refabricated HTGR fuel will be of the Triso or Biso design has not been established yet. The reference 4:1 design is Biso coated, but it is anticipated that the TURF will be built with the capability of applying Triso coatings. There is some feeling among those working in the coated particle fuel area that commercially reprocessed fuel will require a Triso coating as well to maintain a "clean" coolant circuit. Even so, the capital cost estimates given in Figs. 5.1 to

Table 5.3. Refabrication capital costs[a] for 23 recycle elements

	Cost ($ × 10^6)				
	4:1		8:1		UO_2 WAR
	Triso	Biso	Triso	Biso	Triso
Kernel preparation					
Fissile	8.9	8.9	11.5	11.5	5.5
Fertile	2.0	2.0	0.0	0.0	3.7
Coating					
Fissile	33.0	20.0	49.0	29.0	9.8
Fertile	4.2	4.2			7.0
Fuel rod fabrication[b]	6.2	6.2	6.2	6.2	6.2
Assembly[b]	14.0	14.0	14.0	14.0	14.0
Total	68.3	55.3	80.7	60.7	46.2
$/kg[c]	177	143	209	157	119
Δ $/kg	58	24	90	38	
Δ %	49	20	76	32	

[a]Applies to equipment for 23 recycle element refabrication line for a 45,000-MW(e) HTGR economy.

[b]Assumes in-block carbonization.

[c]Assumes 30%/year fixed charge rate and 400 kg/day for 290 days/year.

5.4 reflect substantial economic advantages for the Triso WAR particle over the 4:1 or 8:1 Triso fuels and also a significant advantage over the 4:1 or 8:1 Biso fuels.

As shown later in this chapter, the capital cost estimates presented here are in reasonable agreement with GGA estimates for a combined reprocessing-refabrication facility capable of supporting a 45,000-MW(e) HTGR economy. Even so, it should be pointed out that there are some inadequacies in the present analysis. For instance, should the 8:1 particle be used, there would be a one-particle system, and the blending step (which is part of the fuel rod fabrication procedure) could be omitted. This would also save an inspection step. Presumably, blending of the thoria fertile particle with the WAR Triso fissile particles would be more difficult (and therefore more expensive) than blending fertile and 4:1 fissile particles. Subtle points such as this are not considered in the calculations presented in Table 5.3.

5.2.3 Performance

Both the reference 4:1 $(Th,U)O_2$ particle and the WAR UO_2 and UC_2 particles have been tested under irradiation. All particles have shown good performance at low temperatures, and the 4:1 particles have shown the tendency to migrate at elevated temperatures and temperature gradients. However, because of the uncertainty associated with the operating temperatures and temperature gradients of the experiments in which these particles were tested, positive conclusions about their suitability for recycle application have not been made. To date, the WAR and 4:1 $(Th,U)O_2$ particles have not been tested in the same experiment to give quantitative comparisons of their performance under identical irradiation conditions. This experiment will be accomplished in the HRB-7 and HRB-8 capsules to be inserted into the HFIR in January 1974. The 8:1 $(Th,U)O_2$ particle will be tested in these capsules as well.

In order to set the stage for the anticipated results from HRB-7 and HRB-8, a review was conducted of all irradiation experiments in which the three candidate recycle particles described above were tested. This information is systematically presented in Tables 5.4 and 5.5. Some additional comments on performance of these candidate particles are given below.

Reference 4:1 $(Th,U)O_2$ recycle fuel

As indicated in Table 5.4, four of the ten 4:1 specimens contained in HRB-1 were examined metallographically. There was no evidence of the amoeba effect in any of them, although there was some slight discoloration on one side of the particles examined from sample 6A. In the highest temperature rod (5A) there was no evidence of amoeba, although amoeba was noted in UO_2 kernels operating at similar temperatures in nearby specimens.

There were approximately 24 fuel rods in RTE-7 containing reference 4:1 (two fuel bodies, two holes per body, and six rods per hole). Metallography has been performed on rods from 7-5-2; and their appearance was excellent, as would be expected from this low exposure and operating temperature. No additional metallography is planned.

The 48 fuel rods containing 4:1 fuel from RTE-4 have not been metallographically examined. Several rods will be examined in the future, but, because of the low operating temperature and exposure, the fuel is expected to look good.

Extensive information is available on 4:1 fuel from the H capsules.[7] There were six samples containing 4:1 fuel: four rods and two loose beds. Rod H-1-4 operated at surface and center-line temperatures of approximately 1050 and 1420°C, respectively, for 97 effective full power days (EFPD) and at surface and center-line temperatures of approximately 900 and 1200°C, respectively, for an additional 39 EFPD. The maximum temperature gradient in this rod was approximately twice that expected in a large HTGR, but the maximum center-line temperature was approximately that in an HTGR. The rod fragmented into two pieces when removed from the capsule, but the particles survived the irradiation in good condition. Of the forty-two 4:1 particles in the plane of the polish, the only coating failures observed were for particles that had fabrication defects (i.e., were coated without a buffer layer). A small amount of kernel migration was observed. No migration was observed in 5 particles from the plane of polish, and migration from 2 to 43 μm was observed in 23 of the particles.

Rod H-1-10 operated at very high surface and center-line temperatures for the last 39 EFPD of the test. The calculated surface and center-line temperatures during this time were 1480 and 2150°C respectively. This center-line temperature was much greater than the 1400°C maximum temperature expected in an HTGR, and the temperature gradient was about three times the maximum gradient in an HTGR. Because of

---

7. R. A. Olstad et al., *An Irradiation Test of Candidate HTGR Recycle Fuels in the H-1 and H-2 Capsules*, ORNL-TM-4397 (July 1974).

Table 5.4. Summary of ORNL experimental data on reference 4:1 (Th,U)O_2 recycle fuel

Experiment	Sample identification	Fast fluence (neutrons/cm^2), $E > 0.18$ Mev	Burnup (% FIMA)		Design[a] (μm)	Density[a] (g/cm^3)	Irradiation temperature (°C)	Remarks
			Fissile	Fertile				
		x 10^{21}						
HRB-1[b]	1A	4.0[c]	9.8	0	195/37/20/33/53			
	1B	4.0	9.8	0	195/37/20/33/53			
	1C	4.0	9.8	0	195/37/20/33/53		770	No metallography
	3A	6.6	12.7	5.9	195/37/20/33/53			
	3B	6.6	12.7	5.9	195/37/20/33/53		1150	Metallography
	4A	7.3	13.8	7.1	195/37/20/33/53		1400[d]	Metallography
	5A	8.0	14.9	8.2	195/37/20/33/53		1130	Metallography
	5B	8.0	14.9	8.2	195/37/20/33/53			No metallography
	6A	7.4	14.0	7.4	195/37/20/33/53			Metallography
	6B	7.4	14.0	7.4	195/37/20/33/53		1140	No metallography
HRB-6	1A	e	e		350/100/30/25/40	?/1.15/1.95/3.2/1.95	e	4.25:1 (Th,U)O_2 Triso ^{235}U
	1B				350/100/30/25/40	?/1.15/1.95/3.2/1.95		4.25:1 (Th,U)O_2 Triso ^{235}U
	3A				350/100/80	?/1.15/1.95		4.25:1 (Th,U)O_2 Biso ^{233}U — No metallography yet
	3B				350/100/90	?/1.15/1.95		4.25:1 (Th,U)O_2 Biso ^{235}U — No metallography yet
	3C				350/100/80	?/1.15/1.95		4.25:1 (Th,U)O_2 Biso ^{233}U — No metallography yet
	3D				350/100/90	?/1.15/1.95		4.25:1 (Th,U)O_2 Biso ^{235}U — No metallography yet
RTE-7[f]	7-6-1[g]	n1	n2.4		355/74/135	10.1/1.1/1.92	900–1050	
	7-6-2	n1	n2.4		355/74/135	10.1/1.1/1.92	980–1150	No metallography
	7-5-1	n1	n2.4		355/74/135	10.1/1.1/1.92	900–1050	
	7-5-2	n1	n2.4		355/74/135	10.1/1.1/1.92	980–1150	Metallography on fuel rod number 2; appearance of particles is excellent
RTE-4[f]	4-3-1 to -8	n1.5	n3.5		343/72/73	10.1/1.1/1.94	925–1230	No metallography yet
H Capsules[h]	H-1-4	6.3	8.2		355/74/135	10.1/1.1/1.92	1420[i]	Only failures noted in single plane of polish viewed were due to fabrication defects
	H-1-10	5.4	8.6		355/74/135	10.1/1.1/1.92	2150	Very high temperatures during fourth cycle; extensive damage at center of rod
	H-1-6	8.6	8.6		355/74/135	10.1/1.1/1.92	1670	Loose particles; amoeba-related failures
	H-2-4	7.5	7.5		355/74/135	10.1/1.1/1.92	1430	Not examined – sent to Chemical Technology Div. for reprocessing studies
	H-2-10	8.3	8.3		355/74/135	10.1/1.1/1.92	1800	Center badly damaged due to very high temperature during last cycle
	H-2-6	8.2	8.2		355/74/135	10.1/1.1/1.92	1690	Loose particles; not examined

[a] Values are for kernel/buffer/1 PyC/SiC/0 PyC coatings respectively.

[b] J. L. Scott et al., *An Irradiation Test of Bonded HTGR Coated Particle Fuels in an Instrumented Capsule in HFIR*, ORNL-TM-3640 (March 1972).

[c] The fluences reported by Scott et al. (see footnote *b*) are lower than this. This experiment was irradiated for eight cycles in the RB facility of the HFIR. Subsequent to removing it, information became available that indicated that 11 cycles were required to achieve full fast fluence exposure. Therefore, the analysis was done based on 11 cycles to full fluence. Later still additional evaluations of the HFIR core indicated that eight cycles in the RB facility achieved full exposure, so the numbers represented here reflect this.

[d] Temperatures for HRB-1 were calculated from readings from thermocouples adjacent to fuel rods. Center-line temperatures were calculated by assuming a fuel rod conductivity of 3.0 Btu hr^{-1} ft^{-1} (°F)$^{-1}$ and a radial gap of 0.004 in. Fuel rod 4B was composed of a resin binder, and the matrix debonded rather badly during the irradiation. Therefore, the thermal conductivity of the fuel rod may have been as low as 1.5 Btu hr^{-1} ft^{-1} (°F)$^{-1}$ (a value associated with loose beds of particles). This change in the bed conductivity increases the calculated fuel center-line temperature from 1230 to 1430°C.

[e] Details must await completion of postirradiation analysis.

[f] E. L. Long, Jr., R. B. Fitts, and F. J. Homan, *Fabrication Report for ORNL Fuel Irradiated in the Peach Bottom Reactor and Postirradiation Examination Report for Recycle Test Elements 7 and 4* (in publication).

[g] For the recycle test elements (RTEs) the sample identifications read n1-n2-n3, where n1 is the RTE number, n2 is the fuel body number, and n3 is the hole number.

[h] R. A. Olstad et al., *An Irradiation Test of Candidate HTGR Recycle Fuels in the H-1 and H-2 Capsules*, ORNL-TM-4397 (July 1974).

[i] These temperatures represent the maximum calculated for the fuel rod center line during the irradiation. This experiment was complicated by a nonintentional inversion of the capsules during the last of four irradiation cycles. See footnote *b* for additional details on fuel operating temperatures.

Table 5.5 Summary of ORNL experimental data on WAR recycle fuel

Experiment	Sample identification	Fast fluence (neutrons/cm²) $E > 0.18$ Mev	Burnup (% FIMA)	Design[a] (μm)	Density[a] (g/cm³)	Irradiation temperature (°C)	Remarks
		$\times 10^{21}$					
HT-8[b]	1401 (IRC 50)	9	*c*	300/0/74	?/0/1.94	1050[d]	Loose particles, UC dioxidized (~0.5% 0); no failure
	1142 (IRC 50)	8		350/0/74	?/0/1.95		Loose particles, UC 7–8% 0; 5% failure
C1-28[e]	F 1482	*f*	*f*	445/29/65	2.5/1.5/2.02	1000[g]	Desulfurized strong acid resin; 2% failure
	H 1488			460/19/67	1.9/1.5/2.02	1000	Desulfurized strong acid resin; 0% failure
HRB-4 and -5	1A	*c*	*c*	366/45/30/30/30	6.2/0.95/1.94/3.21/1.89	*c*	UC_2 Triso
	1B						UC_2 Triso
	1C						UC_2 – No low melting alloy observed
	3A						UC_2 Triso (Low melting alloy observed; microsphere analysis planned)
	3B						UC_2 Triso
	3C						UC_2 Triso
	3D						UC_2 Triso
HRB-6	1C4						$^{233}UO_2$ (Triso) (Loose particles in specimen 1C; no postirradiation examination yet available)
	1C5						$^{233}UC_2$ (Triso)
	1C6						$^{233}UO_xC_y$ (Triso)

[a] See footnote *a* of Table 5.4.

[b] D. M. Hewette II, R. B. Fitts, C. B. Pollock, J. I. Federer, and J. L. Scott, *Effect of Neutron Irradiation on Loose and Bonded Particles Coated with Pyrolytic Carbon and Silicon Carbide* (in publication).

[c] Details must await detailed postirradiation analysis of the experiment.

[d] These temperatures represent design values for the graphite holders. The temperatures of the coated particles were considerably higher, and more representative temperatures must await detailed analysis of the experiment.

[e] C. B. Pollock, "Coated Particle Development," *GCR-TU: 71–5,* p. 1 (April 1971); M. T. Morgan, R. L. Towns, and L. L. Fairchild, "Postirradiation Examination and Analysis of the C1-28 Experiment," *GCR-TU: 72-22,* p. 35 (September 1972); and M. T. Morgan, R. L. Towns, and L. L. Fairchild, "Postirradiation Examination and Analysis of the C1-28 Experiment" (in preparation as ORNL report).

[f] No postirradiation analysis performed on this experiment.

[g] Represents maximum temperature reached. Duration at this temperature was short.

these severe thermal conditions, the center of the rod was badly damaged and a large amount of kernel migration (50 to 260 μm) was observed. A core was formed in the center of the rod, and the adjacent particles were converted to a mixture of carbide and graphite phases.

Rod H-2-10 also operated at very high temperatures during the last irradiation cycle. The calculated surface and center-line temperatures were 1100 and 1800°C, respectively, and the temperature gradient was about three times the maximum gradient in an HTGR. As in rod H-1-10, the center of the rod was badly damaged and a large amount of kernel migration (16 to 240 μm) was observed.

Sample H-1-6, which consisted of loose particles, operated with calculated surface temperatures of 900 to 1000°C and center-line temperatures of 1500 to 1700°C during the test. Several particles in this sample failed by the amoeba effect, and the presence of some coating fragments and bare kernels indicated pressure vessel failures as well. The kernels in this sample showed more fission-gas bubbles than the kernels irradiated in bonded rods at comparable calculated temperatures, indicating that the temperatures calculated for the loose particle bed may be too low. Rod H-2-4 was not examined metallographically, but was sent to the Chemical Technology Division for reprocessing studies; loose bed H-2-6 was not examined.

WAR-derived fuel

Very little quantitative information is available on the irradiation performance of the WAR particles. The tests in which these particles have been irradiated have not yet been well analyzed, and calculation of temperatures in WAR particles is complicated by the shrinkage of the particle away from its coating, leaving a sizable gas gap. The kinetics of this shrinkage are not known.

Although no amoeba migration has ever been noted in WAR particles, some disquieting behavior was noted in HRB-4. In four of the five samples examined metallographically, the kernels appeared molten, possibly due to rare-earth fission product attack on the silicon carbide layer, resulting in introduction of silicon into the kernel, which forms a low-melting (about 985°C) uranium-silicon alloy. This behavior was noted only in HRB-4 (recall that HRB-4 and -5 are sister experiments, with HRB-5 being in the reactor to half the maximum HTGR neutron exposure and HRB-4 being in the reactor to full fluence). Since HRB-4 operated to about 25% FIMA in the fissile particles, whereas HRB-5 had only about half that burnup, there may be some threshold level of fission product concentration before this behavior occurs. Molten kernels were apparent in about 30% of the particles viewed in the four specimens polished. It should also be noted that this behavior was not noted in specimen 1C. Since this specimen had a higher thermal conductivity matrix (an extrusion, whereas samples 3A through 3D were slug injected) and therefore lower temperatures, there must have been fuel at the temperature of particles at the surface of the slug-injected rods, where molten kernels were noted.

5.2.4 Conclusion

From this review of ORNL irradiation data on the reference 4:1 recycle particle and the WAR particle, it can be concluded that adequate performance is still to be demonstrated for both particles. Additional analyses are needed on the irradiations that have already been accomplished, and the data from HRB-7 and -8 need to be studied in detail. These latter experiments also contain samples of the 8:1 kernel, which have never been tested at ORNL. In addition, irradiation data from other sites should be included in the review for completeness.

5.3 ECONOMICS OF TIMING OF HTGR FUEL RECYCLE

F. J. Homan

Preliminary work in this area was described in the last annual report.[8] Since then, the work has been expanded and published in the open literature.[9,10] The highlights and results of the study are presented here.

This study was made to determine the economically optimum time to begin reprocessing and refabrication of HTGR fuel as a function of the size of the HTGR economy. It is obvious that storing the spent fuel instead of recycling it immediately increases the amount of virgin ^{235}U needed and also introduces the requirement for storage facilities for the spent-fuel blocks. On the other hand, to begin recycle operations immediately would be uneconomic because of the very small size of the reprocessing and refabrication facilities

8. F. J. Homan, *GCR Programs Annu. Progr. Rep. Dec. 31, 1972*, ORNL-4911, p. 71.

9. F. J. Homan, "Timing the Utilization of Recycle Fuels in High-Temperature Gas-Cooled Reactors," *Nucl. Technol.* 21(1), 5–15 (January 1974).

10. F. J. Homan, "Timing the Use of Recycle Fuel in the HTGR," *Trans. Amer. Nucl. Soc.* 17, 314–15 (November 1973).

involved. The study sought to find a balance between these two opposite effects to minimize the cost of electricity produced by the HTGR economy assumed. The method of cost calculation and description of fuel cycle steps[9] need not be repeated here, and yearly tabulation of the reactor startup schedules for the HTGR economies considered was given in the last annual report.[8] The economic assumptions used in the final study were the same as those described in the last annual, except that an inflation rate of 5%/year was added, using 1978 as a base year.

The results of the study showed that 1984 or 1985 was the optimum time to begin fuel reprocessing. This is shown in Fig. 5.5, where the penalty for early or late reprocessing (compared with optimal timing) is plotted against initial reprocessing date. Note the steep increase in penalty for the larger HTGR economies. Summaries of the present-worthed fuel cycle component costs and levelized unit costs for reprocessing, fabrication, and refabrication are given in Tables 5.6 and 5.7 respectively.

On completion of a study like this, one could question whether the critical size of an HTGR economy before recycle should be considered at all. This question was resolved by successively truncating the 124-reactor economy; the results for the various truncated economies are given in Table 5.8. Note that recycling reduces fuel cycle costs in an economy as small as two large reactors [1160 MW(e)], but the savings ($26 million) is considerably less than the levelized cost of the research and development effort to develop recycle capabilities (about $85 million).

Another interesting item that evolved from the study was the influence of increased costs of separative work on HTGR fuel cycle costs. Since the cost of enriched uranium represents the major portion of these costs, the projected increases in the cost of separative work units (SWU) anticipated for private enrichment will have considerable impact. The results of the study are summarized in Table 5.9 and Fig. 5.6. It is interesting

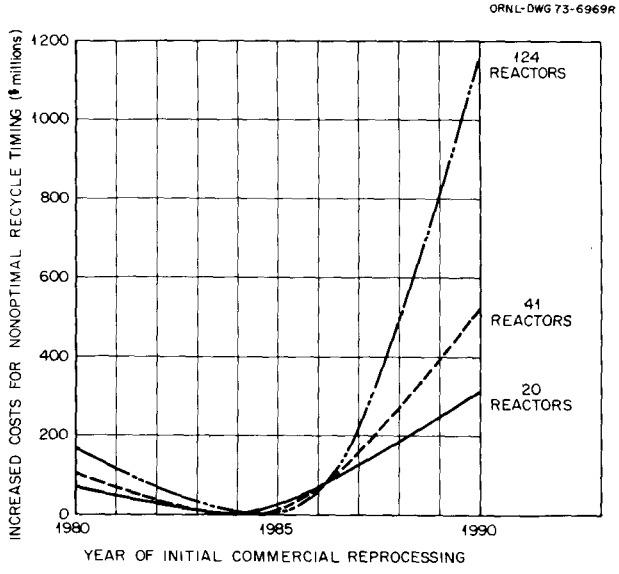

Fig. 5.5. Cost penalties for nonoptimal recycle timing.

Table 5.6. Present-worthed fuel cycle costs for different recycle schemes for the 41-reactor build schedule

Time for initial reprocessing	Cost[a] ($ × 10⁹)									
	Reprocessing	Fabrication	Refabrication	Block storage	Thorium	Shipping	Uranium	Credits	Total	Levelized cost[b] (mills/kWhr)
1980	0.31154	0.33298	0.57993	0.22462	0.03463	0.17929	3.5588	0.18568	5.0361	1.0536
1981	0.29647	0.33293	0.56284	0.22553	0.03590	0.17929	3.5607	0.18528	5.0083	1.0478
1982	0.28038	0.33281	0.54125	0.22629	0.03710	0.17020	3.5614	0.18503	4.9735	1.0405
1983	0.26902	0.33282	0.52228	0.22844	0.03826	0.17924	3.5669	0.18333	4.9536	1.0364
1984	0.25413	0.33297	0.50319	0.23022	0.03936	0.17930	3.5780	0.18095	4.9362	1.0327
1985	0.24017	0.33328	0.48418	0.24402	0.04040	0.17931	3.5962	0.17809	4.9394	1.0334
1986	0.22879	0.33532	0.46071	0.29875	0.04107	0.17932	3.6335	0.17448	5.0030	1.0467
1987	0.21868	0.34594	0.43052	0.36256	0.04304	0.17933	3.6889	0.17109	5.0968	1.0663
1988	0.20815	0.34812	0.41122	0.43140	0.04296	0.17934	3.7590	0.16695	5.2132	1.0907
1989	0.19048	0.35041	0.39172	0.49562	0.04384	0.17935	3.8414	0.16239	5.3304	1.1152
1990	0.18372	0.35293	0.37149	0.55825	0.04468	0.17937	3.9243	0.15951	5.4552	1.1413

[a]Present worthed to Jan. 1, 1978, using a 10% discount factor.
[b]Levelized over 45 years assuming 100% plant factor.

Table 5.7. Levelized unit processing costs for 41-reactor build schedule

Time for initial reprocessing	Cost[a] ($/kg)			Cost ($/block year)
	Reprocessing	Fabrication	Refabrication	Block storage
1980	78.27	89.12	377.01	519.64
1981	74.50	89.07	366.16	519.12
1982	70.48	89.02	352.19	517.88
1983	67.69	88.93	340.34	512.91
1984	64.04	88.77	329.19	501.91
1985	60.74	88.50	319.11	499.47
1986	58.86	88.21	309.70	473.46
1987	57.38	89.72	289.65	456.60
1988	55.78	88.70	297.46	448.06
1989	52.19	87.48	298.41	435.78
1990	51.52	86.29	299.96	423.83

[a]Per kilogram of heavy metal.

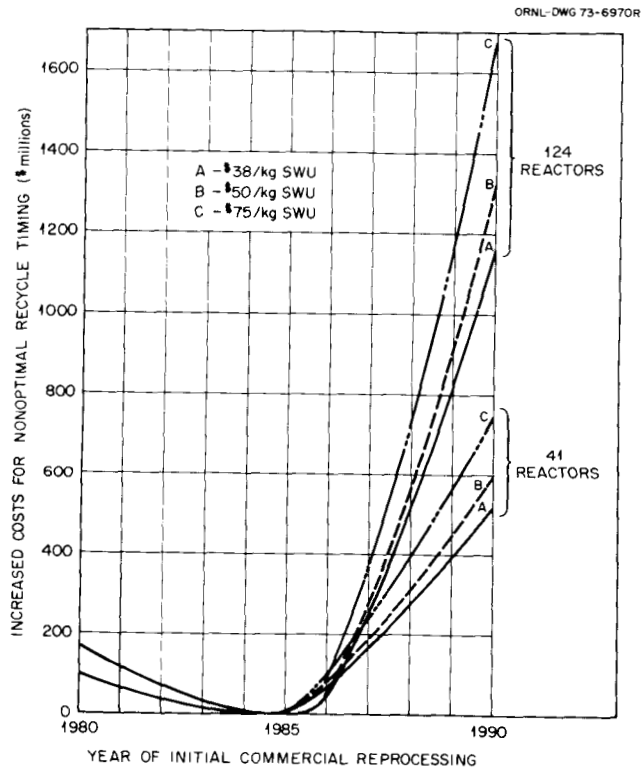

Fig. 5.6. Influence of toll enrichment charges on cost penalties.

Table 5.8. Summary of calculations for all build schedule

	Reactors built											
	1	2	3	4	9	16	26	39	124	254	20	41
Optimum year for initial reprocessing	None	1982	1982	1983	1981	1982	1983	1983	1985	1986	1984	1984
Present-worthed fuel cycle costs, $ × 10^9	0.39029	0.61723	0.79017	0.96882	1.6640	2.5452	3.7204	5.1255	12.919	22.501	2.7630	4.9362
Levelized cost, mills/kWhr	2.5846	2.0936	1.8014	1.6633	1.3130	1.1673	1.0870	1.0332	0.93565	0.90143	1.1336	1.0327
Individual costs for optimum strategy, $ × 10^9												
Reprocessing		0.0961	0.112	0.121	0.182	0.211	0.236	0.267	0.357	0.441	0.195	0.254
Fabrication	0.0805	0.0877	0.104	0.119	0.168	0.222	0.289	0.357	0.685	1.04	0.221	0.333
Refabrication		0.150	0.167	0.175	0.257	0.323	0.400	0.518	0.954	1.43	0.342	0.503
Block storage	0.139	0.0558	0.0691	0.0942	0.100	0.140	0.199	0.231	0.467	0.718	0.152	0.230
Thorium	0.00160	0.00261	0.00387	0.00519	0.0107	0.0186	0.0293	0.0417	0.114	0.196	0.021	0.039
Uranium	0.163	0.225	0.333	0.452	0.947	1.63	2.57	3.71	10.3	18.7	1.83	3.58
Shipping	0.00566	0.0111	0.0165	0.0219	0.0457	0.0818	0.128	0.186	0.518	0.930	0.091	0.179
Credits		0.0104	0.0156	0.0201	0.0488	0.0831	0.129	0.189	0.522	0.934	0.091	0.181
Levelized unit costs, $												
Per kilogram of heavy metal												
Reprocessing		406	316	263	173	117	84	65	31	21	96	64
Fabrication	467	374	299	253	169	130	107	92	63	53	115	89
Refabrication		1631	1218	1001	635	464	366	327	216	179	442	329
Per block/year, block storage	653	1242	1071	911	801	639	526	478	357	302	617	502
Size of first plant												
Metric tons/year												
Reprocessing		19	28	39	76	136	225	331	1,040	2,132	168	344
Fabrication	39	50	89	128	236	361	544	708	1,652	2,815	267	539
Refabrication		9	13	17	37	65	105	158	492	997	81	163
No. of blocks, block storage	13,676	5151	7256	13,108	10,717	18,789	35,255	42,389	126,557	245,483	22,675	41,817
Costs with no reprocessing												
Present worthed, $ × 10^9	0.39029	0.64356	0.88705	1.1227	2.1758	3.5081	5.2629	7.3809	19.046	33.187	3.8539	7.1021
Levelized, mills/kWhr	2.5846	2.1828	2.0223	1.9275	1.7169	1.6089	1.5376	1.4878	1.3794	1.3295	1.5812	1.4859

to note that while the penalties associated with non-optimal timing increase drastically with increased SWU costs, the optimum date for initial commercial reprocessing remains about the same.

Table 5.9. Variation in fuel cycle costs with separative work charges[a]

Time for initial reprocessing	Levelized cost (mills/kWhr)								
	20 Reactors			41 Reactors			124 Reactors		
	$38/kg SWU	$50/kg SWU	$75/kg SWU	$38/kg SWU	$50/kg SWU	$75/kg SWU	$38/kg SWU	$50/kg SWU	$75/kg SWU
1980	1.1622	1.3226	1.6565	1.0536	1.2138	1.5479	0.94800	1.1081	1.4418
1981	1.1537	1.3141	1.6482	1.0478	1.2081	1.5424	0.94406	1.1042	1.4379
1982	1.1441	1.3047	1.6393	1.0405	1.2008	1.5351	0.94081	1.1010	1.4348
1983	1.1372	1.2983	1.6339	1.0364	1.1969	1.5312	0.93817	1.0986	1.4327
1984	1.1336	1.2954	1.6326	1.0327	1.1938	1.5291	0.93623	1.0969	1.4317
1985	1.1440	1.3073	1.6475	1.0334	1.1953	1.5318	0.93565	1.0969	1.4327
1986	1.1617	1.3274	1.6725	1.0467	1.2102	1.5498	0.93906	1.1011	1.4388
1987	1.1862	1.3551	1.7070	1.0663	1.2324	1.5772	0.95276	1.1166	1.4580
1988	1.2092	1.3817	1.7412	1.0907	1.2599	1.6114	0.97212	1.1384	1.4850
1989	1.2359	1.4123	1.7796	1.1152	1.2881	1.6475	0.99475	1.1642	1.5171
1990	1.2620	1.4420	1.8171	1.1412	1.3179	1.6851	1.0192	1.1924	1.5531

[a]Underscores indicate minimums.

Part II. HTGR Development Program

6. HTGR Fuel Materials Development

J. H. Coobs J. L. Scott
W. P. Eatherly

The objectives of the fuel element development program continue to be (1) to demonstrate HTGR coated particles and fuel rods to full fluence and burnup of the reactor; (2) to develop alternative fabrication processes with better economics, performance, and recycle capability than reference materials; and (3) to develop advanced fuels with higher temperature capability than the reference materials. During the past year the major emphases have been placed on the first two.

In the area of coated particles, the principal effort has been the continued development of the process technology and characterization of kernels produced from the weak-acid ion exchange resins, including irradiation testing. For fuel rod studies, almost the entire effort has been to produce samples for irradiation testing. Difficulty in fabricating the samples for thermal conductivity measurements has delayed this irradiation experiment considerably.

6.1 COATING DEVELOPMENT

6.1.1 Carbon Coating Process Development

R. L. Beatty

Carbon coating process development work was concentrated in two problem areas related to deposition of dense low-temperature isotropic (LTI) coatings. The basic process used for deposition of LTI coatings, which currently employs high concentrations of propylene, has been shown capable of producing coatings with good irradiation stability. This process, or a modification of it, is thus a likely candidate for continued development and application to HTGR fuel production. However, two features of the process cause operational difficulties that should receive attention: the large amount of energy absorbed in the fluidized bed and the undesirable carbon deposits formed in the coating chamber.

Minimizing energy absorption during fluidized-bed coating. The LTI coating process was originally developed using propane, which could be handled fairly well in a 1-in. coater. However, the energy absorption due to the heat capacity and endothermic decomposition of propane rendered process scaleup impracticable. Substitution of propylene for propane reduced this energy absorption by approximately one-half, and subsequent development has employed propylene almost exclusively. However, the heat absorbed in the bed, which is on the order of 3 kW for each 1 cfm of propylene flow

$$\left(\text{entirely due to } \int_{\text{Room temp.}}^{\text{Dep. temp.}} C_p \, dT\right) ,$$

may still impose a practicable heat transfer limitation on process scaleup.

From a process engineering viewpoint, an athermal coating process (i.e., one which neither absorbs nor generates power) would be desirable. The controlling

consideration, of course, is that the process must yield a suitable product. Of the readily available inexpensive hydrocarbons, only acetylene produces an excess of energy when heated from near room temperature to the coating temperature and decomposed in the fluidized bed. Saturated hydrocarbons decompose endothermically in addition to the energy required to heat them to the coating temperature. Propylene decomposes nearly athermally but absorbs considerable energy in being heated to the coating temperature as mentioned earlier. This suggests the possibility of compensating part of the propylene heat absorption by preheating it. Another approach to attaining an athermal coating process is to blend acetylene in appropriate amounts with energy-absorbing hydrocarbons.

Blends of acetylene and an energy-absorbing hydrocarbon can easily be formulated to provide an athermal coating process. However, a concern is that acetylene decomposes much more rapidly than any of the other hydrocarbons, and carbon from the two source gases is not likely to be deposited in the same region of the bed. This may or may not be detrimental to coating homogeneity, but products of such a process must be examined carefully.

To select the most appropriate hydrocarbon for blending with acetylene and to choose the best coating conditions for the mixture, it would be useful to have data on deposition rates and coating properties produced by the individual species. Since there was no available information on use of acetylene in high concentrations for deposition of high-density coatings, a few experiments were conducted with acetylene as the only carbon source. Coating variables examined were deposition temperature and dilution with hydrogen, helium, and hydrogen-helium mixtures. It was found that high-density coatings can be deposited at reasonably high rates from acetylene. The effect of increasing deposition temperature was to increase rate and efficiency while reducing density in most cases. This correlates with results of LTI coating studies with other hydrocarbons. Addition of hydrogen had an effect similar to that of lowering the deposition temperature. This is expected if addition of a reaction product retards rate-controlling steps in carbon formation. Also, as expected, the deposition rate and efficiency and coating density for acetylene diluted with helium were shifted to a lower temperature relative to deposition from propylene or propane. Addition of hydrogen to acetylene seemed to adjust its performance to correspond closely to that of propylene diluted with inert gas. Thus, it appears that acetylene can be controlled for independent use as a source of high-density coatings.

The primary interest in acetylene for deposition of dense coatings, however, is in blending it with another hydrocarbon such as propylene to obtain a workable bed heat balance. If hydrogen were added to the mixture to retard decomposition of the acetylene, the propylene decomposition probably would be similarly retarded. In this case, homogeneity of coating reactions through the bed may not be improved at all. Therefore, the workability of acetylene-propylene mixtures must still be considered questionable, and the mixing approach must be evaluated by direct experiment with very careful product characterization. This study serves only to show the relevant behavior of acetylene independently.

Although acetylene can provide the extra needed energy, it is much less convenient than gases that can be handled as bulk liquids under their own vapor pressures. Other species that produce a net energy gain in a coater include allene and methylacetylene, both of which are very expensive and somewhat unstable in pure form. However, these gases can be obtained in stabilized form in a relatively inexpensive commercial product known as MAPP gas.

MAPP is a trademark of Airco, Inc., and stands for methylacetylene-propadiene (allene). MAPP gas was originally developed by Dow Chemical Company and is now sold by Airco Welding Products as a substitute for acetylene in industrial cutting and welding. MAPP gas is handled as a pressurized liquid in cylinders or bulk in the same manner as propane. It is specified as containing, in the liquid phase, a maximum 68 mole % combined methylacetylene-propadiene and a minimum 24 mole % propane, butane, and isobutane (in combination), with the remainder being propylene and butadiene. The alkanes act as stabilizers to prevent decomposition in the absence of oxygen. The net result is a coating gas that is calculated and verified experimentally to produce only about half the bed cooling effect of propylene. Experiments have shown MAPP deposits to be indistinguishable from propylene deposits when allowance was made in coating chamber wall temperatures to produce the same actual average bed temperatures. MAPP gas is now being used routinely for deposition of LTI coatings in laboratory coaters because it allows better temperature control than is possible with propylene. MAPP coatings on inert and fertile particles are currently being irradiated.

Reduction of carbon deposited on furnace parts. The second major problem mentioned for LTI coating deposition was that of reducing undesirable furnace

deposits that form during application of carbon coatings. The carbon deposits in various forms and amounts throughout the graphite fluidization tube, but from the standpoint of tube reuse or, in the worst cases, of simply completing a run, two areas are particularly troublesome: a very hard deposit builds up near the bottom of the bed and soot accumulates on the wall above the bed. To some extent the hard buildup can be controlled by gas inlet nozzle design and by its position relative to the hot zone. However, the soot deposited above the bed accompanies all low-temperature (below about 1800°C) coating processes we have studied. In the case of buffer coatings, a very light soot is deposited on all surfaces from the top of the bed to the soot filter. In the case of dense isotropic (LTI) coatings, a heavier soot condenses on all surfaces from the top of the hot zone to the filter. These soot accumulations severely restrict the number of coating runs that can be made before a shutdown is required for cleanup.

Addition of oxidizing diluents to the coating gas has been studied as one approach to reducing soot deposition. Both air and CO_2 in concentrations from 50 to 80% were used to replace argon dilution of propylene in deposition of LTI coatings with limited success. We have found no detrimental effects of the oxidizing species on coating properties, and there appear to be no safety problems with these mixtures as long as the propylene concentration in air is kept well above 10%, approximately the explosive limit. The three diluents were compared for a deposition temperature of 1325°C as follows. At 50% diluent in propylene, there was no significant difference in argon, air, or CO_2 in deposition efficiency or in carbon deposited at any point in the system. The CO_2 resulted in slightly higher particle coating density, about 2.00 g/cm^3 compared with about 1.95 g/cm^3 with air or argon. As the diluent concentration was increased from 50 to 80%, argon had little effect on any of the measured parameters. Increasing air concentration from 50 to 80% caused a gradual efficiency decrease from 39 to 21%, a marked decrease in the amount of carbon buildup in the cone but little effect on soot deposits, and a decrease in coating density from above 1.95 to about 1.82 g/cm^3. Increasing CO_2 from 50 to 70% resulted in some efficiency decrease, although not as great as with the same amount of air; little effect on cone deposit but a marked reduction in upper tube soot accumulation; and no significant effect on density. The CO_2 was not used above 70% because the graphite coating tube was being severely oxidized above the bed.

The following conclusions have been drawn from these experiments on deposition of LTI carbon coatings from propylene.

If dilution less than 50% is desired, there was little difference to the system or the product whether the diluent was argon, air, or CO_2. The only significant advantage in being able to accommodate an oxidizing diluent might be in replacing an argon supply by an air compressor.

If there is primary interest in reducing the hard carbon deposited at the bottom of the fluidized bed, as might be the case with a porous plate system, dilution with air may be of great benefit. The optimum air concentration in propylene for this purpose appears to lie in the range 60 to 75%. The exact reduction in undesirable carbon formation obtained by using air rather than argon would depend on system design, but may be more than 75%.

If primary interest lies in reducing soot deposition in the coating chamber above the bed, CO_2 dilution affords significant gain, possibly as much as a 75% reduction compared with a like amount of argon. The optimum CO_2 concentration appears to be about 60 to 75%. Employing the upper part of this range would require an oxidation-resistant tube wall such as SiC.

6.1.2 SiC Coating Process

J. I. Federer

A silicon carbide (SiC) coating is applied to HTGR fissile and fertile particles to prevent or minimize migration of fission products to the outer surface of the particles during service at reactor operating temperatures. The SiC coating is applied to a fluidized bed of particles as one of a series of coatings, being preceded and followed by pyrolytic carbon (PyC) coatings. The reactant gases used to produce SiC coatings are methyltrichlorosilane (CH_3SiCl_3), H_2, and an inert gas such as argon or helium as needed for fluidization. (Other silanes could be used to prepare SiC coatings, but CH_3SiCl_3 has been adopted for this application.) Batches of HTGR particles are coated with SiC and PyC in similar coatings furnaces using similar methods. One important way in which the SiC coating process differs from the PyC coating process is the coating rate. Coatings of SiC are applied at a rate not exceeding about 0.3 μm/min, while PyC is applied at rates of 10 μm/min or more. Silicon carbide is applied at the lower rate for at least two reasons: (1) a fear that inferior coatings (porous or nonstoichiometric) will be obtained

at coating rates above 0.3 μm/min and (2) a practical limitation on the flow rate of reactant gases in the proper proportion that can be used to fluidize a bed of particles. Stated another way, coating rate alone may not affect coating quality greatly, but the composition of reactant gases used to obtain high coating rates may not produce high-density SiC. The relation observed in the present study between coating characteristics and the composition of coating gases is described as follows.

Experiments were conducted in which the coating temperature was held constant at 1550°C while the silane flux (flow rate of CH_3SiCl_3 per unit area of particles) and the volumetric hydrogen-to-silane ratio were varied. The conditions and some results of these experiments are shown in Table 6.1. The results show that (1) the coating rate increased almost in direct proportion to the flux and (2) the density increased with increasing ratio. A coating rate of about 4 μm/min was obtained for a flux of 1.0 cm^{-3} min^{-1} cm^{-2}, the highest used, and the density of the coating exceeded 99% of theoretical density, thereby offering proof that high coating rate and density can be simultaneously obtained. The high rate and density were obtained with a hydrogen-silane ratio of 11 (8.3% silane in the total mixture). At the lower fluxes of 0.075 and 0.3 cm^{-3} min^{-1} cm^{-2}, coatings having 99% or more of theoretical density were obtained at hydrogen-silane ratios greater than about 15. These results indicate a dependence of density on ratio and flux. This dependence is illustrated in Fig. 6.1 by the as-polished sections of coatings prepared at ratios of 5 to 25. At the lowest ratio (highest concentration of silane in the reactant gases), the coating had a rough surface and a relatively large amount of grown-in porosity. Coatings prepared at progressively higher ratios had smoother surfaces and a decreasing amount of grown-in porosity. These results are in essential agreement with those of other investigators.[1,2]

Table 6.1. Conditions and results of SiC coating experiments

Conditions		Characteristics	
Flux (cm^{-3} min^{-1} cm^{-2})	H_2: CH_3SiCl_3	Rate (μm/min)	Density (% of theoretical)
0.075	16	0.38	
0.075	16	0.37	98.7
0.07	16	0.33	98.8
0.075	16	0.34	99.2
0.075	18	0.33	
0.075	23	0.32	99.4
0.075	25	0.37	99.8
0.07	39	0.41	99.8
0.3	5	1.39	<98
0.3	10	1.54	<98
0.3	14	1.58	<98
0.3	26	1.36	99.7
0.3	25	1.33	99.7
0.5	6	2.39	<98
0.5	12	2.38	98.7
1.0	11	4.20	99.3
1.0	12	4.06	

At a low silane ratio of 5, the porosity is quite gross, as shown in Fig. 6.1; however, at higher ratios, numerous small pores lie on randomly spaced layers parallel to the surface of the coating. Alternate dense layers and relatively thin porous layers exist through the thickness of the coating. The most obvious reason for the occurrence of porosity is that one or more coating conditions change temporarily. We suspected that liquid silane, which had condensed in the water-cooled injector of the coating tube, was occasionally swept into the fluidized bed. When this occurred, the hydrogen-silane ratio was temporarily lowered, which resulted in a band of porosity in the coating. When the injector temperature was raised to approximately the boiling point of silane, the porosity did not occur under the same conditions that had produced porosity in other coatings. This observation amply demonstrated the necessity for a known and constant flow rate of silane and hydrogen.

The results that have been presented show that coating rate increases almost in direct proportion to silane flux and that a certain minimum hydrogen-silane ratio is necessary for preparation of dense coatings. These conditions impose a restraint on coating rate. For a given surface area to be coated, a certain minimum silane flux is required to achieve the desired coating rate; however, the hydrogen flow rate necessary to maintain a hydrogen-silane ratio that produces dense coatings may eject particles out of the coating tube. This condition was closely approached in the experiment in which SiC was deposited at approximately 4 μm/min; in fact, the ratio could not have been further increased without losing particles. Fortunately, dense coatings can be prepared at a sufficiently high rate that the SiC coating step does not have to be as slow relative

1. T. D. Gulden, *Deposition and Microstructure of Vapor-Deposited Silicon Carbide*, GA-8275 (Dec. 1, 1967).
2. E. H. Voice and D. N. Lamb, *The Deposition and Structure of Pyrolytic Silicon Carbide*, DP Report 677 (October 1969).

PHOTO 3102-74

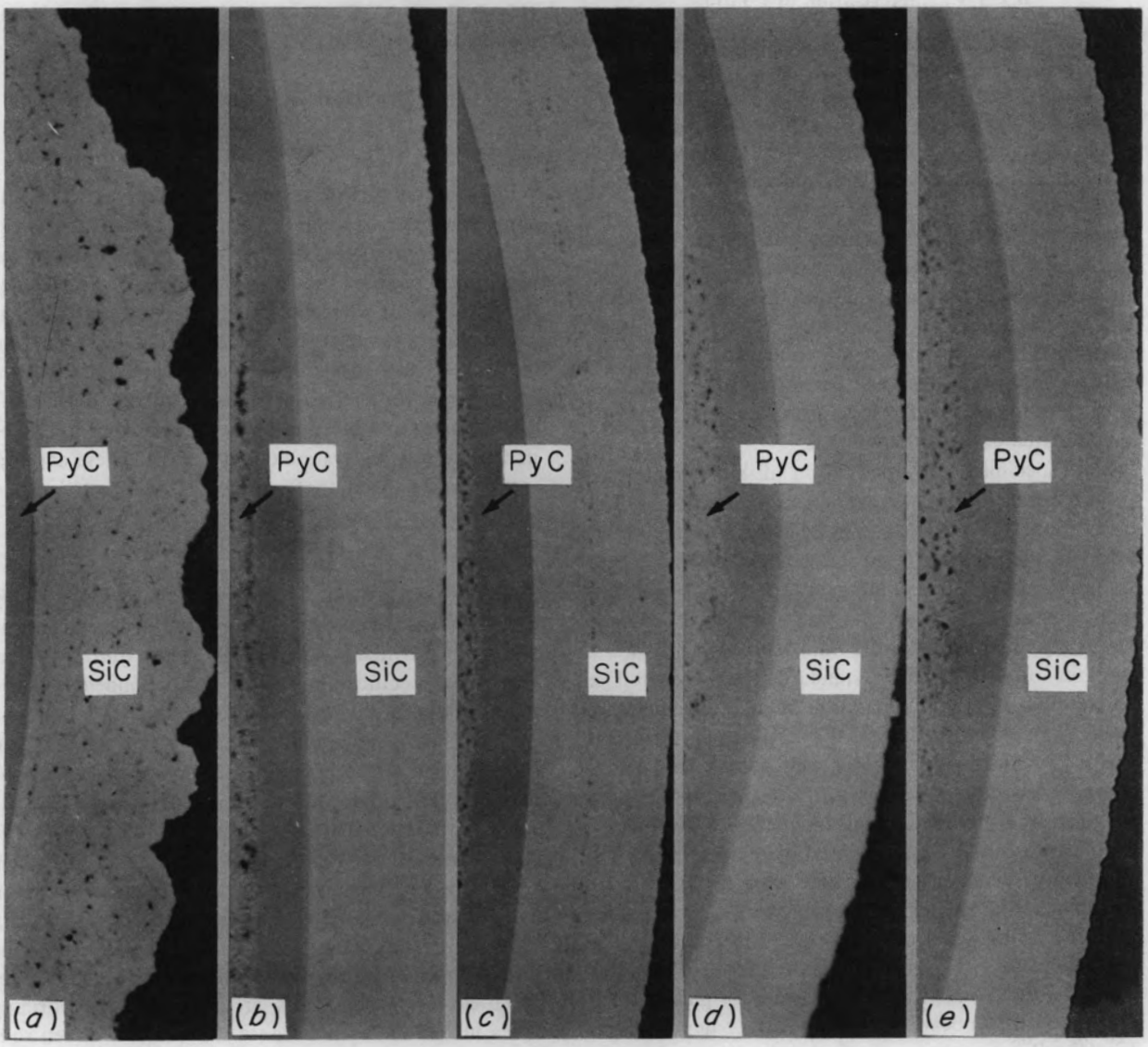

Fig. 6.1. Effect of H_2:CH_3SiCl_3 ratio on the amount of porosity in SiC coatings. Coating temperature, 1550°C; CH_3SiCl_3 flux, 0.3 cm^{-3} min^{-1} cm^{-2}. As polished. 500×.

to the PyC coating steps as is currently practiced. This tentative conclusion is contingent upon being able to reproduce the above conditions in product-size coating furnaces.

6.1.3 Characterization of Coatings

R. L. Beatty E. S. Bomar

The optical (OPTAF) method is favored for monitoring anisotropy in pyrolytic carbon coatings because it can be applied directly to microsphere coatings, while the commonly used x-ray method (BAF) requires flat strip specimens. Thus OPTAF is preferable because preparation of flat specimens by coating small disks or plates along with each batch of microspheres on a routine basis is impractical. Also, the degree to which the disk coating is representative of the microsphere coating is always a point of concern. However, the OPTAF measurements must be calibrated against x-ray BAF determinations if results are to be correlated with accumulated data and experience.

Flat specimens stripped from disks coated in a fluidized bed are the logical choice for the OPTAF-BAF calibration. The flat strips can be measured directly by both techniques and can be compared with corresponding microsphere coatings by the OPTAF measurements. Also, the appropriate range of anisotropies can be readily obtained from the fluidized-bed coatings.

A set of OPTAF-BAF standards was prepared in conjunction with the preparation of coated particles for irradiation experiments HT-17 through HT-19 (see Chap. 7). Since the purpose of these tests was to compare coatings of varied anisotropies, the coating runs involved provided a convenient vehicle for fabrication of the required set of flat-plate specimens. The anisotropy specimens in this case were deposited onto POCO graphite plates 0.310 $in.^2$ × 0.030 in. thick fluidized along with the particles. The coatings were removed from the graphite substrate as 0.200-$in.^2$ plates and x rayed. Each plate was placed in a collimated x-ray beam with the plane of deposition at 13° (the Bragg angle for the first-order basal reflection) to the beam. This produces a diffraction ring with a radial integrated intensity that is proportional at given angular positions to the number of crystallites with basal planes aligned parallel to the corresponding angle in the specimen. Absorption corrections must be made to maintain the proportionality over the full 0 to 90° span, but absorptions at the 0 and 90° positions are nearly identical. Thus, a BAF analytical technique developed by Tassone[3] can be applied to the 0 and 90° relative intensities without significant correction. This method was used for convenience and to avoid uncertain absorption corrections. The x-ray films were scanned with an optical microdensitometer at the 0 and 90° positions, and BAF values were obtained from the ratio of integrated intensities. Measurements on the HT-17 through HT-19 specimens showed BAF values ranging from 1.00 to 1.73.

6.2 BONDED FUEL DEVELOPMENT

R. L. Hamner J M Robbins

The major effort during the past year was devoted to supporting the irradiation testing program (see Chap. 7). In some instances, significant process alteration was required to produce the desired samples. These included development of seven-hole fuel rods formed by intrusion bonding for loose-particle sample holders, devising techniques for producing slug-injected rods with a central hole for thermometry and a molded-in identification mark, and attempting to extrude rods to a fixed matrix density but variable fuel loading. These developments are discussed briefly below.

6.2.1 Intrusion Bonding

A fuel-containing bed holder to support loose coated particles was required for the HRB-6 experiment in HFIR to provide proper temperatures during irradiation. The specifications called for a bonded fuel rod 2.25 in. long and 0.490 in. in diameter, with a 0.090-in. central thermocouple hole with six 0.070-in.-ID surrounding holes in a hexagonal array for containing the particles. The holder was to be a close-packed bed (62 vol %) of coated particles with a matrix of 40 wt % Airco-Speer RC-4 graphite filler in Ashland 240 pitch. A special die design was used that provided for seven wooden rods around which the particles and matrix were contained. After carbonizing the specimens, the residue from the rods was removed, leaving the holes specified. Metal mandrels are preferred for forming holes in bonded rods because the use of wooden rods results in a more irregular hole; however, long specimens, even with one hole, are difficult to remove from the mandrel because the pitch shrinks slightly against it upon cooling after intrusion. The poor fuel distribution observed in the holder was attributed to the fact that only about three particle diameters separate the wooden rods used to generate the holes, thus leaving little space for blending the particles into the mold.

---

3. G. Tassone, *Carbon* 8, 387–88 (1970).

Nevertheless, sound bodies adequate for the purpose were fabricated.

6.2.2 Slug Injection

The matrix material for the slug-injection process is nominally 28.5 wt % Asbury NF 6353 graphite in A-240 pitch. It has been the practice at ORNL to hot mix the filler and pitch without benefit of an inert atmosphere. However, the A-240 pitch is very susceptible to oxygen pickup, which increases the coke yields and, in turn, leads to matrix-coating interaction during carbonization, especially if done in-block. We attempted to eliminate this variable by slurry blending the matrix in benzene at room temperature and then evaporating the benzene in vacuum at 90°C. However, benzene is apparently difficult to remove completely from the pitch, since specimens formed from the vacuum-treated matrix were very inferior. There was evidence of sticking to the punches, and the matrix had large holes apparently caused by evolution of the benzene. All further development work has been done with the normal hot-mixed matrix.

The homogeneous blending of fuel and inert particles for fuel rods having a close-packed particle bed is sometimes a problem, especially if there are three or more types of particles having different densities and sizes. The method used at ORNL by the Fuel Cycle Engineering and Technology Group is to blend with a decade splitter, which divides the charge into ten small increments before they are loaded into the mold. For irradiation experiments HRB-7 and HRB-8, fissile, driver, fertile, and inert particles were required. When the ratio of the low-density inert particles to the remainder was about 0.5, good blending was obtained by a "once-through" blend. However, when this ratio was increased to about 1.5, the blend was grossly nonuniform. Blending twice produced very satisfactory results.

In the preparation of close-packed bonded rods, it is desirable to keep the injection pressure as low as possible to prevent damage to coated particles. The viscosity of the matrix, particle size, large differences in particles sizes, and length all affect the pressure required for injection. For irradiation experiments HRB-7 and HRB-8, coated particles nominally 800 and 500 μm in diameter were specified for 0.8-in.-long specimens. Injection was easily accomplished at 500 psi using only one size of particle (800 μm). We prepared specimens with both sizes of particles having volume ratios, large to small, of 50:50 and 75:25. Specimens having these blends could not be formed at 500 psi but were not difficult to form at 800 psi and a temperature of 175°C. Acid leach of particles from the green rods showed the fraction of heavy metal leached to be 1 to 5 $\times 10^{-5}$, well under the acceptable limit of 1×10^{-4}.

Specimens for irradiation experiments HRB-7 and HRB-8 were also specified to have a central hole for thermocouple placement. The hole was formed by extending a metal mandrel through the punches, particle bed, and matrix slug before heating and injecting the matrix. There was some difficulty in removing the specimen from the mandrel without distortion until a small resistance heater was designed to warm the mandrel to about 50°C. There was considerable difficulty in separating the top punch from the mandrel because of the matrix that had exuded between the mandrel and the inside diameter of the punch. They could be separated only by heating the punch to about 100°C after removal of the specimen from the mandrel or by soaking in a solvent for an extended period of time. It was also desirable to imprint an orientation-identification mark on one end of the specimen so that dimensional measurements could be made at the same locations before and after irradiation. This was accomplished by machining a small ridge on the bottom punch which left an indentation on the bottom of the specimen as shown in Fig. 6.2. Normally, the bond between the specimen and punch would be broken by twisting the punch around the mandrel. However, to prevent damage to the specimen because of the ridge on the punch, it was necessary to design a device for pushing the mandrel away from the bottom punch. This proved readily possible and, as can be seen from the figure, the identifying mark is clearly visible.

6.2.3 Extrusions

Our extrusion development during this period was directed toward preparing specimens to specified dimensions, matrix densities, and particle volume loadings for irradiation testing. The flowsheet for our process was presented previously.[4] In the process where large quantities of material are extruded on a semiproduction scale, the binder, without diluent, is blended directly with the other components in an 8-quart V-blender fitted with an intensifier bar rotating at a slow speed to aid in mixing without particle breakage. It should also be noted that a mix containing coated particles is deliberately made wetter than desirable for unfueled graphite extrusions so it can be extruded at

4. R. L. Hamner and J M Robbins, *GCR Programs Annu. Progr. Rep. Dec. 31, 1972,* ORNL-4911, pp. 85–88.

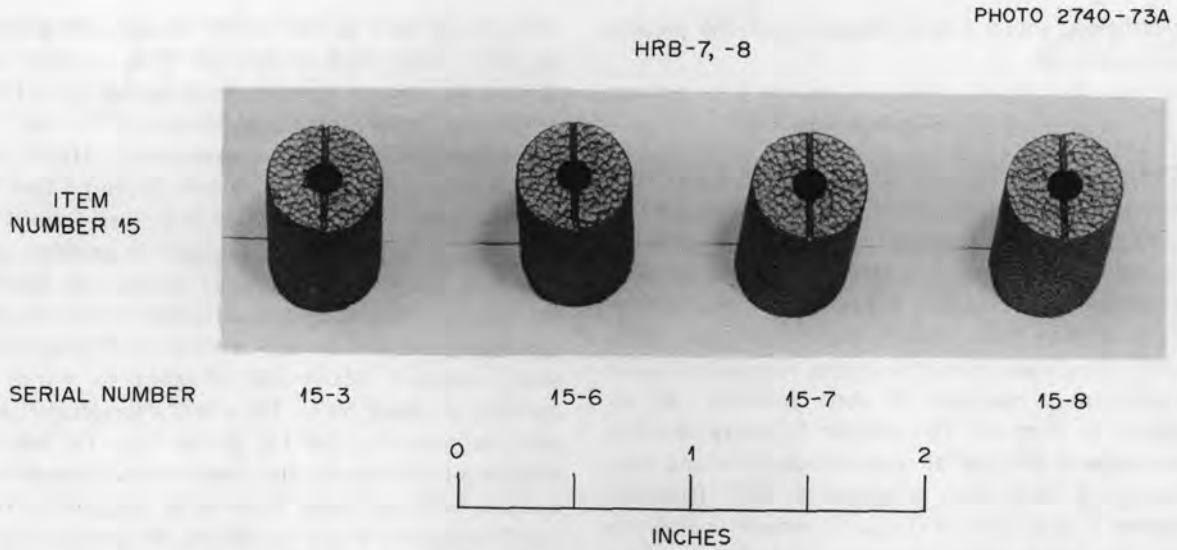

Fig. 6.2. Specimens formed by slug injection with thermocouple hole and orientation-identification mark.

low pressures and thus reduce the chance of particle breakage. In the preparation of irradiation test specimens, only small quantities of coated particles are available, and preparation of large batches of mix requires a prohibitive amount of coated particles. Since no suitable equipment is available for mixing small batches without particle breakage, this operation is performed carefully by hand using acetone as a diluent. The components are mixed as a slurry until the acetone is evaporated. This had led to a problem of reproducibility of the consistency of the mixes from batch to batch, with a consequent variability in matrix densities.

Graphitized Robinson coke (−200 mesh) was the filler selected for most of the extrusion development because it is conducive to fabricating an isotropic body for good irradiation resistance. Thermax, a spherical carbon black that tends to lower the binder requirement for extrusion, was substituted for the Robinson filler in amounts varying between 15 and 24 wt %. Varcum (prepolymerized furfuryl alcohol) was used as binder for all extrusions.

One series of planned irradiation experiments (HT-20 through HT-23) requires pseudo-fueled rods (see Chap. 7); hence the filler materials were heat treated to 2800°C to remove metallic impurities, thereby reducing the induced radioactivity after irradiation. Addition of this heat-treated Thermax caused the green matrix to have a consistency quite different from one in which as-received Thermax was used and required an additional 3 pph of binder. In addition, the extrusions were weak and of poor quality. Since the as-received Thermax was relatively pure and produced good extrusions, all specimens were prepared using this material.

Varcum was used as a binder because of its low viscosity at room temperature. Binder levels used ranged from 23 to 27.5 pph for the filler with an additional 0.09 g of binder per cubic centimeter of coated particles. For unfueled extrusions, the minimum binder level appeared to be 23 to 24 pph; however, for very high particle volume loadings (44% for HRB-6), this was increased to 27 pph to reduce the chance for particle breakage.

For the same matrix composition, higher extrusion reduction ratios generally resulted in a higher matrix density (e.g., for unfueled graphite an increase in reduction ratio from 28 to 42 resulted in an increase in matrix density from 1.6 to 1.7).

For irradiation experiments HT-20 through HT-23, we attempted further to maintain constant matrix densities for extrusions with wide variations in volume loadings by adjusting the reduction ratio and heating rate during carbonization as well as by utilizing in-block and in-vacuum carbonization. Particle volume loadings were varied between 0 and 40 vol %. An increase in volume loading above about 30% resulted in a decrease in matrix density, especially at 40 vol %. Unfueled extrusions, for example, generally resulted in nominal matrix densities of 1.7 g/cm^3, whereas matrix densities of extrusions with 40% volume loading were lowered to 1.5 to 1.6 g/cm^3. The inconsistency in the latter case is

attributed to inconsistencies among the different batches of the same composition because of the acetone addition in blending components. This work is continuing.

Dimensional control was good for extrusions (±0.002 in. OD), provided the binder level was satisfactorily established.

The present acceptable level for exposed heavy metal due to particle breakage during fabrication is 1×10^{-4} fraction of heavy metal exposed per heavy metal contained. Previously, we have been limited to only one method of detecting broken particles, except by metallography, and that was in as-formed green rods whereby the matrix and particles were separated by dissolution of the matrix in pyridine followed by leaching the particles in HNO_3 containing a trace of HF. There was no means of detecting broken particles after final processing at 1800°C. The Analytical Chemistry Division (D. A. Costanzo and J. L. Botts) has done exploratory work to solve this problem with regard to extrusions from which exposed heavy metal cannot be completely leached by the use of HNO_3 because of the high matrix densities. The general approach is to first find some means of separating the particles from the fired rod, examine the particles under a microscope, and then leach with HNO_3 and HF. Extrusions having a matrix density of 1.7 g/cm^3 and a volume loading of 30% Biso-coated ThO_2 particles were used. The first attempt at deconsolidation was by the use of 20% ammonium persulfate in concentrated H_2SO_4. The action of the acid was violent, and although the rod was deconsolidated, the matrix broke down in relatively large pieces, most of which remained bonded to the particles or coating fragments from the particles. About 20% of the particles had badly broken coatings, whereas companion samples submitted to metallography showed no broken coatings. This suggested that the violent action of the process combined with the strong bonding of the matrix caused the particle breakage. Deconsolidation by electrolysis under certain conditions resulted in a fine division and clean separation of the matrix. This was accomplished by deconsolidation in 1 *M* HNO_3 and a current of 0.5 A for 48 hr, using a platinum anode and a graphite cathode immersed in the electrolyte.

A planned irradiation experiment (HT-20 through HT-23) to measure the electrical resistivity, thermal conductivity, and coefficient of thermal expansion before and after irradiation requires that the extrusions be brazed after irradiation to graphite components necessary to make the thermal conductivity measurements. The brazing temperature must fall between the irradiation temperature (900°C) and the maximum temperature at which the thermal conductivity will be measured (700 to 750°C). The lowest temperature braze available, a Ag-Ti-Cu alloy, was satisfactory for the joining operation (G. M. Slaughter and J. J. Woodhouse), but the brazing temperature was too high (950°C). We were successful in meeting the braze temperature specification by first copper plating the ends of the extrusions and the graphite components and then bonding with a silver-copper alloy with a eutectic and flow temperature of 780°C.

6.2.4 Irradiation Results on Simulated Extrusions

C. R. Kennedy

Samples of extruded simulated fuel rods have been irradiated in HFIR up to 2.5×10^{22} neutrons/cm^2 ($E > 50$ keV) at both 715 and 950°C. These samples were made as described above but utilized a mixture of 85% Great Lakes Carbon Corporation X1008 and 15% Thermax as matrix filler. The binder was Varcum, a partially prepolymerized furfuryl alcohol catalyzed with maleic anhydride. The simulated fuel loading was 35% by volume. The final heat treatment was limited to 1800°C, resulting in a matrix density of 1.73 g/cm^3. For comparison, some results from an all-matrix graphite made by the Y-12 Plant and irradiated some years ago are also included. This graphite contained no simulated fuel but was fabricated from the same raw materials. However, it was heat treated to 2800°C and had a final density of 1.9 g/cm^3.

The results of the irradiation are shown in Figs. 6.3 to 6.5. Figure 6.3 compares the length and volume changes of specimens irradiated at 715 and 900°C, Fig. 6.4 compares the fuel rod behavior to the all-matrix material, and Fig. 6.5 shows the effect of irradiation on the shear modulus as measured sonically. The dimensional change data are as expected, with the more rapid volume expansion at 950°C rather than 715°C. The densification is larger than for the all-matrix graphite, resulting from the incomplete 1800°C heat treatment and the lower original density. However, the volume expansion rates are no greater than those for the RY-12-29 material. In fact, there is a slight suggestion that the simulated fuel particles may have moderated the expansion rate. The simulated fuel rods have at least the life expectancy of the all-matrix graphite. This is emphasized by the absence of a decrease in the shear modulus shown in Fig. 6.5. The mechanical integrity of the irradiated fuel rods is at least as good as or better

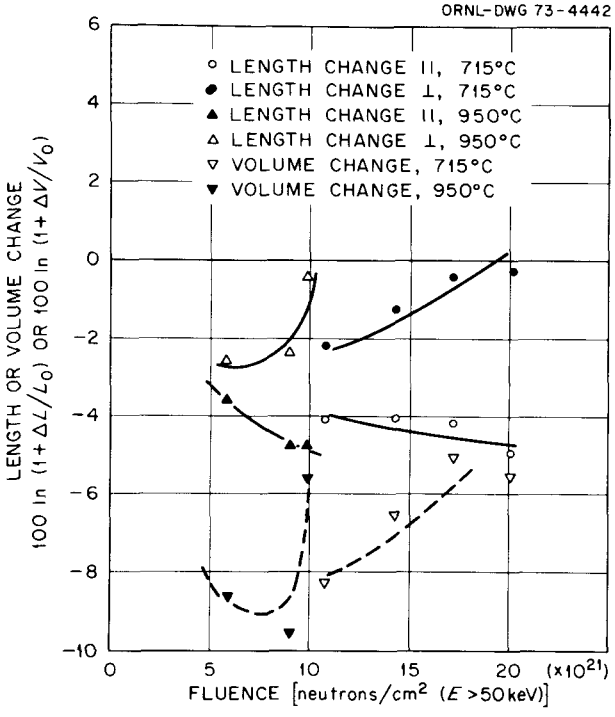

Fig. 6.3. Results of irradiating simulated extruded fuel rods at 715 and 950°C in HFIR.

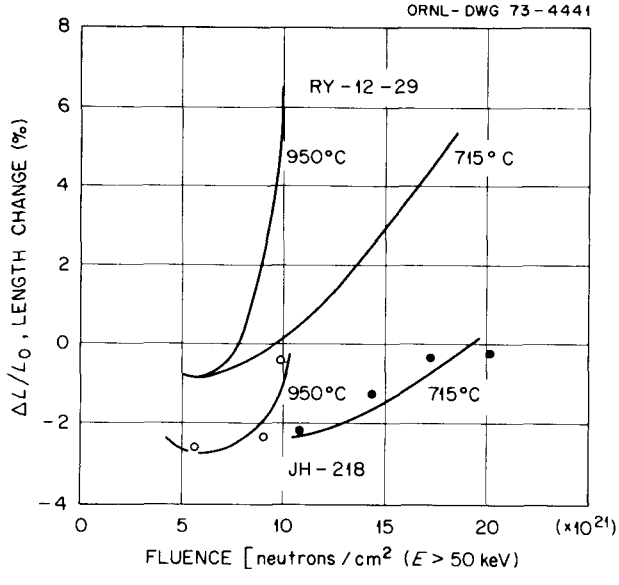

Fig. 6.4. Comparison of dimensional changes in the cross grain behavior of simulated fuel rods (JH-218) and graphite (RY12-29).

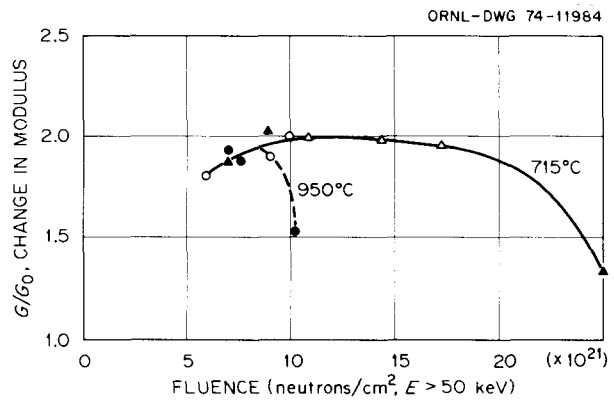

Fig. 6.5. Effect of irradiation on the shear modulus of simulated extruded fuel rods. Closed symbols are all matrix grade RY12-29; open symbols are simulated fuel rods.

than the unirradiated material. The drop in the shear modulus of the all-matrix material indicates that the life expectancy of the fuel rods would not be much greater than 1×10^{22} neutrons/cm^2 at 950°C or 2×10^{22} neutrons/cm^2 at 715°C. Fluences beyond these exposures would result in excessive diametral expansion and interaction with the moderator blocks. However, these fluences are well beyond the design lifetime of the fuel rods.

6.3 RESIN-DERIVED FUEL PARTICLE DEVELOPMENT

C. B. Pollock R. L. Beatty

Fuel particles formed from cation exchange resins are attractive because of simplicity of fabrication and relatively easier quality control in remote fabrication operations. The uranium-loaded beads are dried, carbonized, partially converted to carbide, and finally coated with multilayer coatings similar in design to coatings on other fissile particles. The development work described previously on loading studies[5] and on carbonization, characterization,[6] and irradiation testing of particles derived from weak-acid resin (WAR) was continued during this reporting period. Good results from irradiation testing of WAR fuels and the recognition of performance limitations on $(Th\text{-}U)O_2$ sol-gel kernels led to the adoption, early in 1974, of the

5. K. J. Notz and P. A. Haas, ibid., pp. 27–32.
6. C. B. Pollock and M. D. Silverman, ibid., pp. 90–95.

Triso-coated WAR-derived particle as the reference fissile fuel for the HTGR Fuel Recycle Development Program. Although the decision occurred after this reporting period ended, the work on resin loading and associated resin classification studies is reported in Chapter 3 as part of work unit 2102 for the Fuel Refabrication Process Development. Other development work on carbonization reduction or conversion, characterization, and coating studies on WAR-derived particles is reported here.

6.3.1 Carbonization Studies

Carbonization of uranium-loaded WAR microspheres has previously been shown to be a practicable method of producing fuel particles.[6] The loading and carbonization were shown to be controllable and reproducible, and studies have been extended to determine limits on processing conditions and effects of varying these conditions on product properties. All previous carbonization work had been carried out by programmed heating at 3 to 5°C/min up to 600°C, followed by rapid heating to 1200°C. This procedure resulted in a good product, but accelerating the first stage would be very advantageous from the production-cost standpoint.

To optimize the carbonization process, heating rate experiments were conducted to determine the maximum rate that could be employed without microsphere disintegration and to determine the effects of heating rate on properties. The carbonization rate was gradually increased to about 80°C/min, approximately the maximum heating rate of the furance being used, with the only apparent effect being increased weight loss due to a lower resin coking yield. Microsphere integrity was retained even when the dried resin was poured into a fluidizing tube preheated to 600°C. The heating rate achieved in this manner, about 300°C/min, was limited by the system heat capacities involved. Tolerance of this extreme heating rate in a material that is reduced about 40% in weight and about 70% in volume is apparently due to an extensive system of open porosity. True gel-type resins could not be carbonized at this rate, but Amberlite IRC-72 is produced by a method that retains a continuous network of interconnected porosity. Finally, microspheres were disintegrated by pouring them into a furnace preheated to 1200°C to establish that a limiting rate did exist. Thus from the standpoint of retaining the integrity of uranium-loaded Amberlite IRC-72 microspheres of nominal 600 μm diameter (dried form), the maximum heating rate through the critical (<600°C) carbonization range is greater than 300 but less than 1000°C/min. However, in processing large batches the carbonization rate may be limited by the ability to accommodate the evolved volatiles, although product property considerations may be paramount in any case.

The heating rate through the early stages of carbonization has a significant effect on the density of the carbonized product. Increasing the carbonization rate reduces the resin coking yield, so that the product has a lower carbon content and a higher density. The carbon-to-uranium ratio in the carbonized material varied from about 4 to 6 for heating rates of 300 and 2°C/min, respectively, while respective carbonized kernel densities were about 3.7 and 3.1 g/cm^3. In either case the fuel form is nominally UO_2 dispersed in a porous carbon matrix.

6.3.2 Reduction by Fluidized-Bed Heating

The procedures described above produce oxide fuel that may be used in that form or given further treatment to effect full or partial reduction to the dicarbide. This makes the WAR process unusually versatile; it is particularly attractive, since oxide, carbide, and oxide carbide mixtures are all of interest. The oxide-carbide mixtures are being studied because they offer the possibility of supplying oxygen to tie up lanthanide fission products while avoiding the excess oxygen produced during fissioning in UO_2 fuel. Carbothermic reduction of the carbonized UO_2 microspheres was carried out by heating in a fluidized bed.

Treatment in a fluidized bed effects a controlled reduction [i.e., all particles get the same treatment and the reduction rate is controlled by the specific gas (Ar) flow rate for any given temperature as long as the open-pore network is maintained]. The intimate mixture of UO_2 and carbon, coupled with the short diffusion distances characteristic of fueled resin, results in a reduction rate being controlled by CO removal rather than by solid-state diffusion. As long as the material does not densify enough to close off the porosity network, a large batch (more than a few grams) may be assumed to maintain the equilibrium P_{CO} for a given temperature due to the reaction $UO_2 + 3C \rightarrow UC + 2CO$. In this case the reduction rate is controlled by the specific gas flow rate (argon flow relative to batch size), and the reduction can be stopped at any point to produce desired oxide-carbide mixtures. Full reduction may be carried out at 1800°C in 10 to 20 min, depending on batch size, while partial reduction is best done in the 1600 to 1700°C range to allow better control. If, on the other hand, the material

densifies sufficiently to block the continuous pore network before full reduction is achieved, the reaction becomes diffusion limited and the gas flow rate control does not apply.

The ability to control densification at high temperature is important whether the objective is tailoring particle density or controlling reduction. From the standpoint of reduction control, two problems are encountered if the material densifies or sinters. As described above, the rate is no longer regulated by gas flow, and the bed tends to agglomerate so that the batch is not treated uniformly. Experiments have shown that sintering tendency during reduction is strongly dependent on carbon content and hence on carbonization rate. A material in which reduction can be readily controlled by gas flow is produced by very slow heating, about 2°C/min, through the early stages of carbonization. Particles thus produced have a density near 3 g/cm^3 and comprise a fuel phase dispersed in a nonsinterable carbon matrix. Although the above procedure results in a good product, it is time consuming and may not be optimum.

In order to capitalize on the tolerance of Amberlite IRC-72 for rapid carbonization, experiments were conducted in which the loaded microspheres were successively given a rapid carbonization, a buffer coating, and an 1800°C reduction. This technique avoided the bed agglomeration problem while allowing the CO to be removed rapidly through the buffer. Further, application of the buffer immediately following carbonization fixes the volume inside the coating at the volume of the oxide particle. The buffer does not change dimensions significantly while the fuel is being converted to carbide. In some cases this procedure resulted in a void between the kernel and buffer, while in others the buffer appeared to prevent shrinkage of the kernel during reduction. This kernel shrinkage tendency is, of course, related to carbonization rate as discussed earlier. In either case the free volume associated with the kernel, exclusive of the buffer, is a direct function of kernel mass. This should be advantageous in particle design where a range of kernel diameters and buffer thicknesses must be accommodated. It has not yet been determined whether a uniform, controlled partial reduction can be effected in this manner.

6.3.3 Atmospheric Reactivity

Carbonized fueled resin must be handled in a protective atmosphere prior to coating, but reactivity with laboratory atmosphere varies with the stage of processing. Experiments were conducted in which 1.0-g samples treated at 500, 1200, and 1800°C, respectively, were exposed to laboratory air and the weight gain was monitored as a function of time. After 96 hr, weight gains, in the above order of treatment temperatures, were 7.0, 3.3, and 3.1%, indicating that higher temperature treatment resulted in increased stability. None of the specimens showed physical deterioration during exposure, and the 1200 and 1800°C specimens were returned to approximately their original compositions on reheating. The 500°C specimen, however, partially disintegrated on reheating. These results apply, of course, only to small samples in which there is no significant temperature increase on reaction. Larger batches generate appreciable heat and react more severely unless cooled.

6.3.4 Coating of Resin-Derived Kernels

Coating procedures for resin-based kernels are essentially the same as those for dense kernels except that gas flow rates are reduced to accommodate the lower densities. Coating of resin particles can be done as a separate operation, as with dense kernels, or can be combined with the carbonization treatment discussed above for the buffer. Experiments have shown that combining carbonization, buffer coating, reduction if desired, and dense carbon (LTI) coating in a single operation is a practicable procedure. The major drawback to combining these steps lies in evaluation and meeting quality assurance requirements on the product. Methods are not yet available for determining densities of the kernel or buffer after the coatings have been applied. The important point is that several options are available for preparation of resin-based fuel, and further development is required only for optimization.

Two batches of WAR-derived particles were coated for irradiation testing in experiments HRB-7 and HRB-8. While coating designs have not been optimized to take full credit for the free volume incorporated in the resin kernels, the primary interest in these specimens is to compare their fuel migration behaviors with those of dense oxide and carbide fuels.

7. HTGR Fuel Irradiations and Postirradiation Examinations

J. A. Conlin W. P. Eatherly
J. H. Coobs F. J. Homan

This program supports both the Thorium Utilization (ThU) Program and the Fueled Graphite Development Program. The purpose of the fueled graphite irradiations is to test fuels made in production-scale equipment at exposures up to and exceeding HTGR design conditions of temperature, power density, burnup, and fast-neutron exposure. The purpose of the ThU irradiations is twofold: (1) to provide irradiated fuel for development and demonstration of spent-fuel reprocessing and (2) to demonstrate the adequate performance of recycle fuel elements produced in production-scale equipment. The irradiation facilities utilized for these tests include the Engineering Test Reactor (ETR), the High-Flux Isotope Reactor (HFIR), the Oak Ridge Research Reactor (ORR), and the Peach Bottom Reactor. Although testing in the ETR is now complete and the facility is no longer in use, the results of two ETR tests will be reported here. The ThU irradiations are divided into capsule irradiations and large-scale irradiations. To date, the only large-scale tests conducted have been in the Peach Bottom Reactor.

In addition to the irradiation facilities listed above which are currently in use, two new facilities are to be used in the future. During this report period some planning has been made for irradiations to be conducted in the Fort St. Vrain Reactor and the Dragon Reactor.

The status of all irradiations conducted to date under HTGR programs is included in Tables 7.1 through 7.6.

7.1 IRRADIATION TESTS IN HFIR REMOVABLE BERYLLIUM FACILITY

B. H. Montgomery J. M. Robbins
R. L. Hamner

One type of HFIR irradiation experiment consists of instrumented and gas-swept capsules that are operated in the two removable beryllium (HRB) facilities.[1] These capsules are of moderate size (1.3 in. diam) and have provisions for specimen temperature control by gas mixing and monitoring of fission-gas release by analysis of gas samples. The capsules accommodate fuel specimens in a graphite support sleeve that is geometrically representative of a single fuel channel of a large HTGR fuel element. Fuel loading, temperature, power density, and burnup rate are limited only by the capability of the fuel.

Two new facilities have been added at the HFIR to complement the existing removable beryllium (RB) facilities. One is a moderate flux irradiation facility in a VXF position in the permanent beryllium (PB) reflector. The second is an out-of-core thermocouple calibration furnace which permits the calibration of HRB capsule thermocouples both before, during, and at the completion of the irradiation.

The new facility in the PB reflector permits the loading of fully enriched fissile particles, higher fissile particle densities in the bonded beds (more representative of HTGR fuels), and the attainment of more representative burnup in the HRB capsules. The thermal-neutron flux in the RB position is so high that only low fissile loadings in the particles and low fissile

1. B. H. Montgomery et al., "Irradiation Fuels in the HFIR Removable Beryllium Facilities," *GCR Programs Annu. Progr. Rep. Dec. 31, 1972*, ORNL-4911, p. 98.

Table 7.1. Description and status of HRB irradiation experiments

Experiment	Specimen description	Maximum fast fluence, $E > 0.18$ MeV (neutrons/cm^2)	Maximum particle temperature (°C)	Maximum burnup (% FIMA)		Irradiation schedule		Reference
				Fissile particle	Fertile particle	Start	End	
		$\times 10^{21}$						
HRB-1	Bonded and loose beds of UO_2 and ThO_2 Three types of matrix Experimental fuel rods made by slug injection	5.8	~1400	22	7.7	8/69	2/70	ORNL-TM-3640
HRB-2	Various loose coated particles Experimental fuel rods bonded with various filler materials FSVR production-type fuel rods	10	1200	30	15	12/70	11/71	ORNL-TM-3988
HRB-3	Warm-molded fuel rods with resin-derived and ThO_2 particles Experimental fuel rods made by slug injection Experimental fuel rods prepared by GAC	9	~1600	28	15	1/72	10/72	ORNL-TM-4526
HRB-4	Continuous-matrix fuel rods made by extrusion Experimental fuel rods made by slug injection Experimental fuel rods prepared by GAC	10	1250	30	15	10/72	6/73	
HRB-5	Same as HRB-4	5	1250	16	4.8	10/72	2/73	
HRB-6	Experimental fuel rods made by extrusion Experimental fuel rods prepared by GAC Experimental fuel rods made by slug injection Loose coated sol-gel and resin-derived particles	8	1250	23.8	9.7	2/73	9/73	
HRB-7	Potential recycle fissile fuel candidates, including sol-gel UO_2, weak-acid-resin UC_2, sol-gel $(4Th,U)O_2$ ^{233}U- and ^{235}U-containing particles Experimental fuel rods made by slug injection		~1500			12/73		
HRB-8	Same as HRB-7		~1250			2/74[a]		

[a]Scheduled.

Table 7.2. Description and status of HT irradiation experiments

Experiment	Specimen description	Maximum fast fluence, $E > 0.18$ MeV (neutrons/cm^2)	Maximum particle temperature[a] (°C)	Maximum burnup (% FIMA)		Irradiation schedule		References
				Fissile particle	Fertile particle	Start	End	
		$\times 10^{21}$						
HT-1	Loose ThO_2 particles PyC strips Bonded beds of ZrO_2 particles	6	1100		5	2/68	4/68	ORNL-4266, p. 45 ORNL-4353, p. 28 ORNL-4424, p. 11 ORNL-4508, p. 28 ORNL-TM-3441
HT-2	12 Poco graphite magazines, each containing loose coated particles and PyC- and SiC-coated disk specimens	8	600 800 1100	16	8.3	5/69	9/69	ORNL-4508, p. 16
HT-3	55 bonded bed specimens in 4 Poco grade AXF-5Q graphite magazines 38 specimens – inert coated particles 17 specimens – bonding material alone	8	750 1050			9/68	12/68	ORNL-4353, p. 47 ORNL-4424, p. 25
HT-4	20 bonded bed specimens, inert kernels only	7.5	800 1060			8/69	10/69	CONF-700401, p. 456 ORNL-4508, p.3 ORNL-4589, p. 20
HT-5	Loose particles, ThO_2 and fueled resins Bonded compacts	7.5	840 900 1020	9	5	12/69	2/70	ORNL-4589, p. 22
HT-6	Loose particles and bonded beds containing $^{232}ThC_2$, $^{235}UO_2$, $^{238}UO_2$, and resin-derived kernels		800 1070	18.5	5.2	8/70	10/70	ORNL-4637, pp. 10, 12 ORNL-4760, p. 134
HT-7	Various loose coated particles with inert kernels	9.6	1050			12/70	3/71	ORNL-TM-4551
HT-8	Various loose Triso-coated particles from resin-derived kernels Intrusion-bonded rods with Triso II coated inert kernels Loose Triso and Triso-coated particles from GAC Experimental bonded rods from GAC	9.6	1050	19.4	9.7	5/71	8/71	ORNL-TM-4551
HT-9	Various loose Triso-coated particles with inert kernels	5	1050			3/71	5/71	ORNL-TM-4551
HT-10	Various loose Triso-coated particles with inert kernels; reirradiated from HT-9	14	1050			8/71	12/71	ORNL-TM-4551
HT-11	Test canceled							
HT-12	Biso-coated sol-gel-derived ThO_2 particles coated at ORNL	4	1250		2.9	9/72	10/72	
-13		9	~1550		9.7	10/72	1/73	
-14	Biso-coated sol-gel-derived ThO_2 particles coated at GAC	13	~1550		17.3	11/72	4/73	
-15		16	~1550		21	11/72	5/73	
HT-16	Various carbon coatings on carbon substrates							
	Carbon-coated Eu_2O_3	14	715			2/73	7/73	
HT-17	Large ThO_2 kernels with Biso coatings of varying anisotropy	14.7	900, 1250		2.9	7/73	9/73	
-18		9.5	900, 1250		9.7	7/73	10/73	
-19		14	900, 1250		17.2	7/73	12/73	
HT-20[b]	Slug-injected and extruded fuel rods for thermal conductivity and electrical resistivity measurement Biso-coated carbon particles Experimental graphites		900					
-21			900					
-22			900					
-23			900					

[a]Specimen holder temperature – coated particle temperatures are several hundred degrees higher.
[b]Planned.

Table 7.3. Description and status of ORR irradiation experiments

Experiment	Specimen description	Maximum fast fluence, $E > 0.18$ MeV (neutrons/cm^2)	Maximum particle temperature (°C)	Maximum burnup (% FIMA)		Irradiation schedule		Reference
				Fissile particle	Fertile particle	Start	End	
		$\times 10^{21}$						
A9-7[a]	$(Th,U)C_2$ particles, 3:1 ratio, Triso coating	<0.1	1300	2.0		1 cycle ORR		ORNL-4133, p. 33 ORNL-4036, p. 97
A9-8[a]	Biso-coated sol-gel UO_2 particles	<0.1	1400	9.5		2 cycles ORR		ORNL-4133, p. 36
A9-9	UO_2 and UC_2 with Biso and Triso coatings	<0.1	1000	4.9		1 cycle ORR		ORNL-4133, p. 37, ORNL-4200, p. 48
A9-10	UC_2 with dense two-layer coating	<0.1	1000–1500	8.9		1 cycle ORR		ORNL-4200, p. 48
A9-11	Biso-coated UC_2	<0.1	1000–1500	12.4		1 cycle ORR		ORNL-4200, p. 48
A9-12[a]	Biso-coated UO_2	<0.1	1550-1650	5.1		1 cycle ORR		ORNL-4200, p. 51
A9-13	Sol-gel UO_2, porous carbon coating only	<0.1	700-900	1.2		1 cycle ORR		ORNL-4200, p. 54
A9-14	$(Th,U)O_2$ particles, 3:1 ratio, Biso coated	<0.1	1250	1.8		1 cycle ORR		ORNL-4266, p. 7
A9-15	Biso-coated UO_2 particles in bonded rod	<0.1	1250	35.5		12/67	7/68	ORNL-TM-3361 ORNL-4266, p. 9 ORNL-4353, p. 3
B9-29	Biso-coated UO_2	4 days in reactor	1500			1 cycle ORR		ORNL-4036, p. 99
B9-30	UO_2 with PyC coating	159 hr in reactor	1400	1.8		1 cycle ORR		ORNL-4036, p. 102
B9-31	Sol-gel UO_2 with dense two-layer coating	<0.1	1400	23.4				ORNL-4036, p. 103, ORNL-4133, p. 37

Table 7.3 (continued)

Experiment	Specimen description	Maximum fast fluence, $E > 0.18$ MeV (neutrons/cm^2)	Maximum particle temperature (°C)	Maximum burnup (% FIMA)		Irradiation schedule		Reference
				Fissile particle	Fertile particle	Start	End	
B9-32	Biso-coated sol-gel UO_2	~0.1	1400	26.1		4 cycles ORR		ORNL-4133, p. 42
B9-33[a]	Biso-coated sol-gel UO_2	<0.1	1250	6		1 cycle ORR		ORNL-4133, p. 37
B9-34[a]	UC_2 with PyC buffer, SiC outer coating (no outer carbon coating)	<0.1	1250	7.3		1 cycle ORR		ORNL-4133, pp. 33, 46 ORNL-4200, p. 54
B9-35[a]	Triso I coating on sol-gel UO_2	<0.1	1250	4.6		1 cycle ORR		ORNL-4200, p. 54
B9-36	Uncoated UC_2 (200 particles)	<0.1	700-1200	5		1 cycle ORR		ORNL-4200, p. 54
B9-37[a]	Highly enriched UC_2, PyC buffer, SiC outer coating	<0.1	1700	4.0		1 cycle ORR		ORNL-4200, p. 54 ORNL-4266, p. 9
B9-38	Biso-coated UO_2 three coating thickness	< 0.1	1400	7.8		1 cycle ORR		ORNL-4266, p. 11
B9-39[a]	UO_2 with LTI Biso coating	<0.1	900	13.2		1 cycle ORR		ORNL-4200, p. 56, ORNL-4353, pp. 4–8
B9-40	UC_2 with Triso *I* coating, in bonded rod	<0.1	1350–1700	18		3 cycles ORR		ORNL-TM-3361 ORNL-4353, p. 4 ORNL-4424, p. 6
B9-41	UO_2 with Triso I and Biso coatings and ThO_2 with Biso coatings, all in bonded rods	<0.1	670	22	<10			ORNL-4424, pp. 6–11
B9-42	UO_2 with Triso I and Biso coatings and ThO_2 with Biso, all in bonded rods	<0.1	630	11	<10	2 cycles ORR		ORNL-4424, pp. 6-11
B9-43	Cracked UC_2 and UO_2 particles	<0.1	200–1400 in steps of 200	3.5		1 cycle ORR		ORNL-4508, pp. 12–16

Table 7.3 (continued)

Experiment	Specimen description	Maximum fast fluence, $E > 0.18$ MeV (neutrons/cm^2)	Maximum particle temperature (°C)	Maximum burnup (% FIMA)		Irradiation schedule		Reference
				Fissile particle	Fertile particle	Start	End	
F9-1	Two batches of monolayer UO_2 and UC_2	0.04	1100–1400	49		7/65	7/66	ORNL-4266, p. 22 ORNL-3885, p. 78 ORNL-3951, p. 69 ORNL-4133, p. 60 ORNL-3807, p. 53 ORNL-TM-1427
F9-2	Loose particles, SiC coatings on 2 batches	0.02	1250–1300	25.6–30.7		11/66	7/67	ORNL-4266, p. 24; kernel migration noted ORNL-4200, p. 74 ORNL-4036, p. 79 ORNL-4133, p. 67
F1-1	Bonded 0.385-in.-diam fuel rods (2), fully enriched sol-gel UO_2, ThO_2; P514 resin containing 15 wt % graphite maleic anhydride	0.4	900–1300	43	~1.0	8/67	4/68	ORNL-4200, pp. 77–85 ORNL-4266, p. 24 ORNL-4353, pp. 12–28
C1-28	Experimental fuel rods made by extrusion Various loose coated particles	0.15	1000	11		8/71	12/71	ORNL-4911, pp. 149–52 ORNL–4760, pp. 136–37
OF-1	Experimental fuel rods made by slug injection Specimens carbonized in graphite Specimens carbonized in packed alumina					8/73	10/74[b]	ORNL–4911, pp. 115–16

[a] *Nucl. Appl. Tech.* 8, 417 (May 1970).

[b] Planned.

Table 7.4. Description and status of ETR irradiation experiments

Experiment	Specimen description	Maximum fast fluence, $E > 0.18$ MeV (neutrons/cm^2)	Maximum particle temperature (°C)	Maximum burnup (FIMA)		Irradiation schedule		Reference
				Fissile particle	Fertile particle	Start	End	
		$\times 10^{21}$						
X-basket-1 ORNL-43-89	12 batches of Biso-coated UO_2 and UC_2	0.59 (thermal) 0.067 (fast)	400, 1400	28		6/65	11/65	CONF-660524, pp. 273-91 ORNL-3885, p. 50 ORNL-3951, p. 41 ORNL-4266, p. 43 ORNL-4036, p. 31
X-basket-2 ORNL-43-97	10 batches of Biso-coated UO_2 Sintered UO_2, UC_2, sol-gel UO_2 Sol-gel $(Th,U)O_2$	0.084	400, 1400	25		3/66	8/66	ORNL-3951, p. 31 ORNL-3885, p. 59 ORNL-4266, p. 43 ORNL-4200, p. 37
X-basket-3 ORNL-43-104	4 fuel compositions, 3 types of coatings Sol-gel microspheres with Th/U ratio from 0 to 2		1.4 (fast)	400, 1400	20	2/67	4/68	CONF-700502, pp. 578-81 ORNL-4133, pp. 30, 31
X-basket-4 ORNL-43-98	Various coating designs on mixed-oxide sol-gel microspheres with U/Th ratios of 3.2 and 4.6		1.6	400, 1400	20	9/66	4/68	ORNL-4036, p. 30
X-basket-5 ORNL-43-105	500-μm-diam sol-gel microspheres of ThO_2, 3% UO_2 containing 93% enriched uranium Various coating designs	13 (thermal) 4.2 (fast)	400, 1400		5-12	6/67	8/71	ORNL-4911, p. 124 ORNL-4133, p. 30
H-1, H-2	Bonded beds of main four RTE particle combinations Various loose coated particles	8	>1800	51	<1	6/71	5/72	ORNL-4911, pp. 116, 138
P13N	Warm-molded fuel rods with resin-derived fissile and ThO_2 fertile particles	5.1	1500	66	2.0	11/71	2/73	ORNL-TM-4526 ORNL-4760, p. 115

7.5. Description and status of Peach Bottom irradiation experiments

Experiment	Specimen description	Maximum fast fluence, $E > 0.18$ MeV (neutrons/cm^2)	Maximum particle temperature (°C)	Maximum burnup (% FIMA)		Irradiation schedule		Reference
				Fissile particle	Fertile particle	Start	End	
		$\times 10^{21}$						
RTE-1 (FTE-11)	Candidate recycle	*a*	1260			4/71		ORNL-4589, pp. 11-15;
RTE-2	fuels as bonded beds	2.8	1260	6.3[b]		7/70	9/73	ORNL-TM-4477;
RTE-4	and loose particles	1.5	1260	3.5[b]		7/70	4/72	ORNL-TM-4911,
RTE-5		*a*	1260			7/70		p. 126;
RTE-6		*a*	1260			7/70		ORNL-4760, p. 65
RTE-7		1.0	1260	2.4[b]		7/70	4/71	
RTE-8		*a*	1260			7/70		

[a]Still in reactor at end of reporting period.

[b]Since fissile fuel particles vary from undiluted UO_2 and UC_2 to (Th,20% U)O_2, the burnup numbers are presented in terms of total heavy metal in both fissile and fertile particles.

Table 7.6. Description and status of irradiation experiments conducted in Dragon Reactor and Dounreay Fast Reactor

Experiment	Specimen description	Maximum fast fluence, $E > 0.18$ MeV (neutrons/cm^2)	Maximum particle temperature (°C)	Maximum burnup (% FIMA)		Irradiation schedule		Reference
				Fissile particle	Fertile particle	Start	End	
		$\times 10^{21}$						
DN-5	Pitch and resin-bonded fuel rods containing only Biso-coated ThO_2 (DFR 287/6), sponsored by KFA, 3 niobium capsules irradiated in row 10 of DFR	8	1250		<1.0	8/69	11/69	ORNL-4508, p. 6 ORNL-4637, p. 23
Dragon cooperative experiment	Second and third charges: sol-gel oxide particles with Th/U ratios from 3 to 5; overcoated with resin-graphite mixtures	3	1200	22 (mixed particles)		1/67		ORNL-TM-1601; ORNL-4036, p. 25
MET VII	UC_2, $(4Th,U)O_2$, weak-acid-resin fissile fuel, all Triso coated; Triso-coated fertile ThO_2	4[a]	1230	60[a]	6[a]	1/75	1/79[a]	

[a]Planned.

particle densities in the bonded beds are possible if excessive heat-generation rates are to be avoided. This had made it impossible to test representative fuel compositions or to achieve burnups greater than about 30% FIMA. The PB position has a thermal-neutron flux (as yet not accurately known) of about half that of the RB position. By irradiating an HRB capsule in the PB facility first for about two HFIR cycles, it is possible to burn out about 50% of the initial fissile loading. The capsule can then be transferred to the RB facility, where the high fast-flux exposure and the continuation of the fuel burnup is achieved. By this means we can attain burnups above 50% FIMA with fissile particle loadings in the bed, about twice that possible previously. This arrangement also makes it possible to irradiate particles containing only ^{233}U. Previously, this could only be done if one accepted excessive particle power densities at the start of the irradiation.

The PB facility is similar in configuration to the RB facilities and is completely compatible with them. It employs the same vessel head flanges and capsule-lead-to-HFIR-vessel sealing arrangement. A capsule to be preirradiated in the PB facility is connected to the regular RB facilities instrumentation. After preirradiation, the capsule is transferred from the PB to the RB facilities without the need for disconnecting or reconnecting any of the instrumentation or service lines. The first capsule to be irradiated in the PB facility was HRB-7. The installation, operation, and transfer were quite satisfactory.

The second new facility at the HFIR is an in-pool thermocouple calibration furnace designed specifically for use with the HRB capsules. The furnace (see Fig. 7.1) consists of a pipe into which the capsule can be

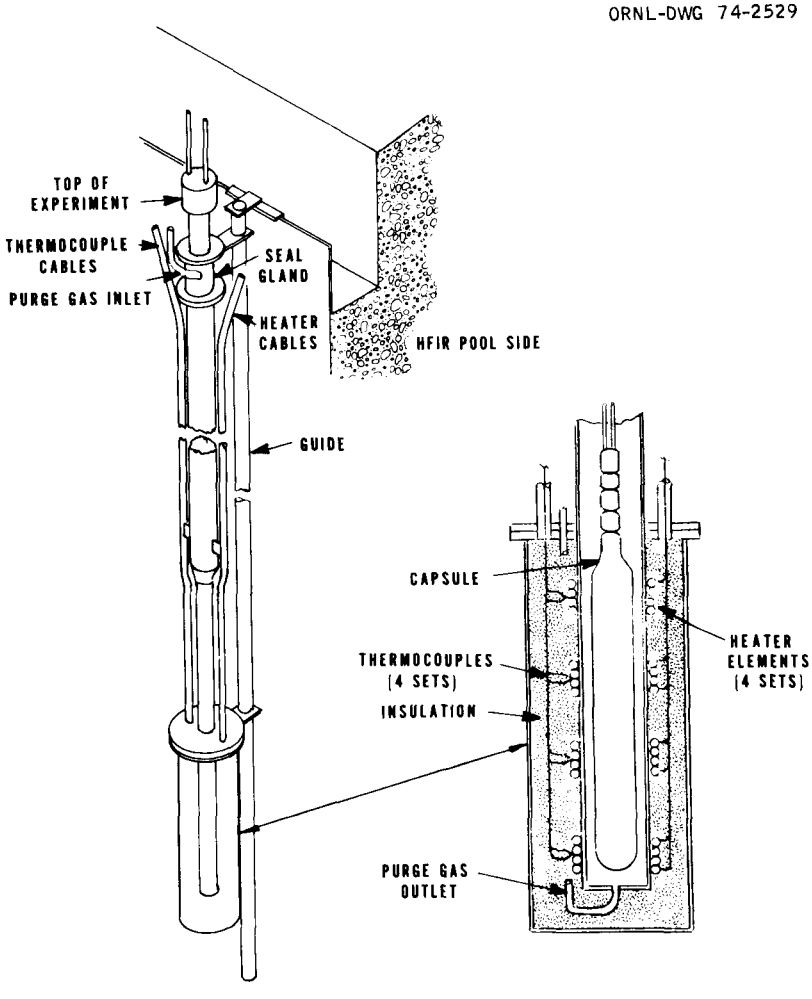

Fig. 7.1. In-pool calibration furnance HRB-X.

inserted. A gland at the top forms a gas-tight seal with the upper end of the capsule leads. The lower end of the pipe has an insulated outer jacket with four sets of heater elements spaced axially along the heated section of the pipe.

To calibrate the capsule thermocouples, the capsule is first removed from the reactor vessel (if the capsule has been under irradiation) and inserted under water in the furnace. After sealing the top of the furnace, the water is blown out of the furnace with helium. The heaters are then turned on, and the capsule thermocouples are calibrated against those of the furnace. Temperatures to 800°C can be achieved, and the temperature gradients of the capsule under irradiation can be simulated by adjusting the axial distribution of power to the four heaters. The 800°C temperature limitation is due to the fact that the entire capsule containment, brazed bulkheads, etc., are all heated to the same temperature. Higher temperatures could jeopardize the capsule containment integrity.

The HRB irradiations conducted during the reporting period are summarized in Table 7.1. Briefly, a topical report was partially completed for HRB-3, and irradiation of capsules HRB-4, -5, and -6 was completed. Postirradiation examination (PIE) was completed on HRB-4 and -5 and partially completed on HRB-6. The HRB-7 and -8 experiments were planned, the capsule design was completed, and fabrication of the fuel for these experiments was begun.

7.1.1 Capsule HRB-3

Irradiation of capsule HRB-3 was described in some detail in the last annual report.[2] Details of this experiment and of an experiment conducted in the ETR with similar fuel are included in a recently completed report.[3] Capsule HRB-3, the first capsule to contain a fuel center-line thermocouple, contained fuel specimens fabricated by both the warm-molding and the slug-injection methods. It was the first ORNL irradiation of HTGR fuel in which kernel migration (amoeba) occurred in the ThO_2 fertile particles. Three of the thirteen ORNL fuel specimens (two warm-molded rods and one slug-injected rod) were examined metallographically. Amoeba of the thoria was observed in two specimens: a very slight migration in one of the warm-molded specimens and considerably greater migration in the slug-injected specimen. No amoeba was observed in the other warm-molded specimen. The combination of a slightly higher heat rate for the slug-injected specimen and the lower thermal conductivity of the slug-injected matrix caused these specimens to operate considerably hotter than the warm-molded specimens.[3]

Superior performance of warm-molded and extruded fuel rods as compared to slug-injected rods operating under similar irradiation conditions has been observed in several subsequent experiments. This is attributed to the higher thermal conductivity of the continuous matrix rods.

7.1.2 Capsules HRB-4 and -5

Capsule HRB-4 (B. H. Montgomery)

Design. The irradiation of the fourth instrumented test (HRB-4) of bonded HTGR coated-particle fuels in the HFIR RB facility was completed on June 26, 1973, after 243.4 days at 100 MW reactor power. The design of this capsule was similar to that of the third capsule[3] of the series, HRB-3, except that the fuel rods were different.

The capsule, shown in Fig. 7.2, was a double-walled water-cooled stainless steel vessel with outside and inside diameters of 1.292 and 0.967 in. respectively. The fuel specimens, which consisted of a series of 0.490-in.-diam bonded fuel rods having a total stack length of 15.32 in., were supported in a one-piece sleeve made of Poco graphite grade AXF-5Q. The design test conditions (1250°C peak fuel temperature and 700°C in the graphite wall at 5.5 kW/ft fission heat rate) were intended to match conditions typical of an HTGR.

Temperatures were monitored by eight sheathed 0.062-in.-diam Chromel/Alumel thermocouples and one bare-wire W–3% Re/W–25% Re central thermocouple. The stainless-steel-sheathed thermocouples were located in axial holes in the graphite sleeve adjacent to the fuel specimens (Fig. 7.3). Six of these thermocouples were coated with a 0.005-in.-thick protective barrier of chemically vapor-deposited tungsten and two were uncoated. The central thermocouple lead wires were threaded through a two-hole 0.062-in.-diam BeO insulator. The junction and lower 2 in. of the insulator were shielded from the fuel surface by a three-layer wrap of 0.0025-in.-thick rhenium foil. The upper fuel specimens (1A, 1B, and 1C; see Fig. 7.3) had a 0.090-in. central hole for this thermocouple. High-purity Fe, Ni, Ti, and Co flux monitors in BeO insulator tubes were located in

2. Ibid, pp. 96–107.

3. F. J. Homan et al., *Irradiation Performance of HTGR Fuel Rods in HFIR Experiment HRB-3 and ETR Experiment P13N*, ORNL-TM-4526 (October 1974).

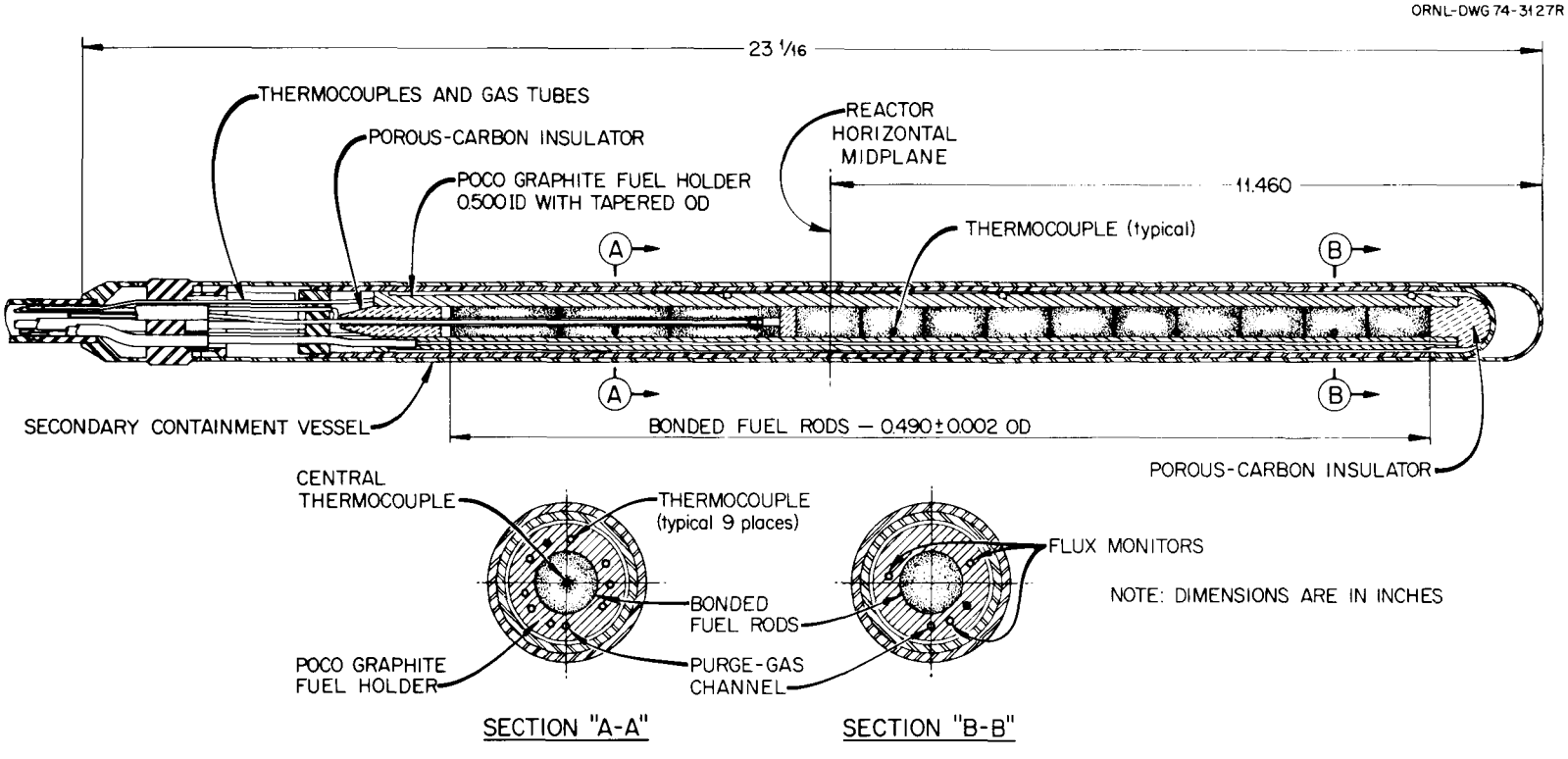

Fig. 7.2. HTGR instrumented capsule HRB-4 for irradiation in HFIR removable beryllium facility.

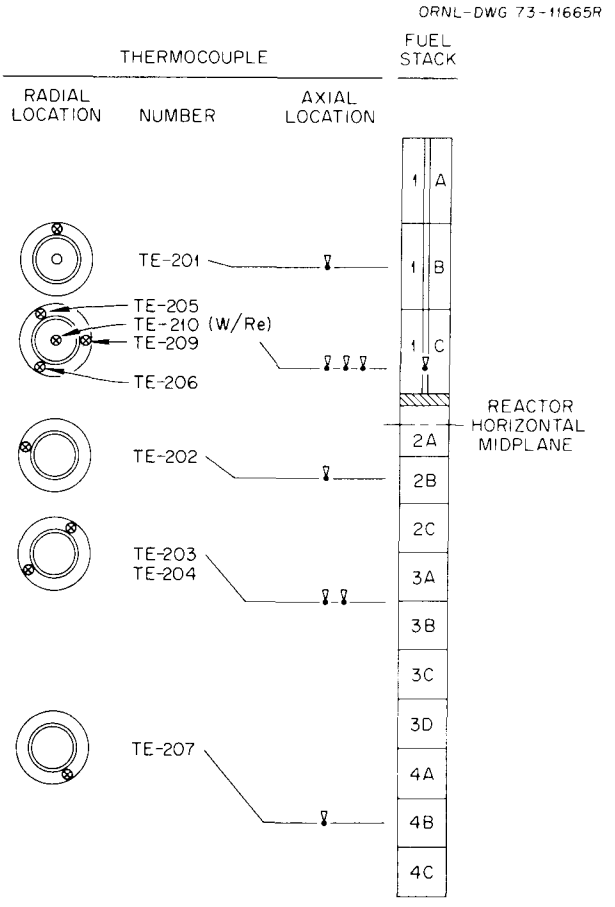

Fig. 7.3. Capsule HRB-4 thermocouple locations.

the graphite sleeve in axial holes similar to those for the thermocouples. The graphite sleeve and the fuel specimens were continuously swept with a 3600-cm^3/hr high-purity helium-neon gas mixture at 1 to 2 atm. Gas samples of the sweep effluent were taken periodically for fission-gas release determinations.

The fuel loadings were increased in the upper end of the capsule to compensate for the loss of the volume created by the central thermocouple hole. Because of the high thermal flux in the HFIR RB facility, the ^{235}U is consumed rapidly (50% in about 16 days at the reactor midplane). To compensate for the loss of fissile material, the ^{232}Th and ^{238}U content of the specimens was adjusted so that the fissile ^{233}U and ^{239}Pu bred in by neutron capture would provide continuing fission power with a minimum of power variation with time (see Fig. 7.4).

The neutron flux and gamma heat, and hence the specimen heat generation, decreases in an approximate cosine function as one moves axially from the reactor midplane. In order to obtain reasonably uniform specimen temperatures with this axially varying heat-generation pattern, we adjusted the thermal resistivity of the radial gas gap between the graphite sleeve and the stainless steel capsule wall inversely with the heat-generation rate. This was accomplished by tapering the diameter of the graphite sleeve so as to increase the gas gap as one moves further from the midplane. The taper was made to provide a constant specimen axial temperature pattern at the beginning of the irradiation. To compensate for overall power variations with time, the composition of the helium-neon sweep-gas mixture which occupies the gas gap was varied to maintain the peak fuel temperature at the design level. However, it must be recognized that neither this nor any other approach can provide uniform temperatures for all specimens with time. The burnup rates and ^{233}U and ^{239}Pu generation rates vary with the flux and hence with axial position. The neutron flux also varies (increases) with time during a given reactor cycle but not in the same proportion for all axial positions. (The percent increase is greater at the ends than at the reactor midplane.) This flux variation with time and position is common to most irradiation facilities and is not unique to the HFIR. We feel that our partial solution to the problem is the best that can be done in this case.

Operation. Capsule HRB-4 was inserted in the RB facility (RB-7) on Oct. 8, 1972, and was irradiated for 11 HFIR fuel cycles (244.0 days at 100 MW reactor power). The irradiation was completed and the capsule removed as scheduled on June 26, 1973. Capsule operation was stable throughout the irradiation, and all test parameters were within design limits. There was, as expected, an initial drop in power as the ^{235}U was consumed, followed by a gradual power buildup which varied with time, axial position, and fuel loading. This is shown graphically in Fig. 7.4, which presents the calculated fission power generated by specimen 2A near the reactor horizontal midplane. The calculated fuel specimen loading, location, isotopic burnup, and fluence (fast and thermal) for each specimen are shown in Table 7.7. Note that the burnup was calculated in percent initial isotope fissioned. To obtain burnup in a particle, the following equation will apply:

$$\%\ \text{FIMA/particle} = \sum_{i=1,n} \frac{(\%\ \text{burnup of isotope } i)}{(\text{initial at. \% of isotope } i)}$$

Table 7.7. Capsule HRB-4 fuel specimen location and loading

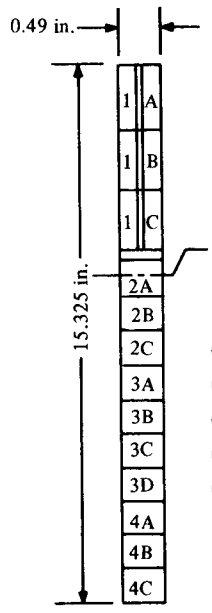

	Length (in.)	Volume (cc)	Fuel loading (g/cc) ^{235}U	Fuel loading (g/cc) ^{238}U	Fuel loading (g/cc) ^{232}Th	Reactor HMP[a] to specimen center (in.)	Percent initial isotope fissioned ^{235}U	Percent initial isotope fissioned ^{238}U	Percent initial isotope fissioned ^{232}Th	Average thermal fluence ($E < 0.414$ eV) (neutrons cm^{-2} sec^{-1})	Thermal fluence ($E < 0.414$ eV) (neutrons/cm^2)	Average fast flux ($E > 0.18$ MeV) (neutrons cm^{-2} sec^{-1})
										$\times 10^{14}$	$\times 10^{22}$	$\times 10^{14}$
1A	1.740	5.1772	0.0049	0.0770	0.1491	5.000	84.0	20.2	9.8	7.49	1.58	3.70
1B	1.743	5.2355	0.0050	0.0791	0.1533	3.250	84.0	23.5	12.3	9.38	1.98	4.35
1C	1.758	5.2624	0.0051	0.0795	0.1540	1.500	84.0	25.9	14.2	10.88	2.29	4.90
Reactor HMP												
2A	1.008	3.1321	0.0042	0.0660	0.1281	−0.125	84.0	26.5	15.0	11.71	2.47	5.00
2B	1.015	3.1609	0.0042	0.0654	0.1270	−1.125	84.0	26.5	15.0	11.80	2.49	4.98
2C	0.990	3.0743	0.0043	0.0673	0.1306	−2.125	84.0	25.0	14.3	11.68	2.46	4.83
3A	0.953	2.945	0.0043	0.0682	0.1321	−3.125	84.0	23.5	13.5	11.20	2.36	4.56
3B	0.953	2.945	0.0043	0.0682	0.1321	−4.125	84.0	21.5	12.5	10.47	2.21	4.24
3C	0.938	2.922	0.0044	0.0687	0.1331	−5.125	84.0	19.0	11.5	9.56	2.01	3.85
3D	0.956	2.978	0.0043	0.0675	0.1306	−6.125	84.0	16.2	9.6	8.50	1.79	3.43
4A	1.000	3.1113	0.0042	0.0665	0.1290	−7.125	84.0	13.5	8.2	7.32	1.54	2.99
4B	1.017	3.1791	0.0041	0.0651	0.1263	−8.125	84.0	10.5	6.5	6.14	1.29	2.50
4C	1.004	3.1228	0.0042	0.0662	0.1285	−9.125	84.0	7.5	4.8	4.90	1.03	1.97

[a]Horizontal midplane.

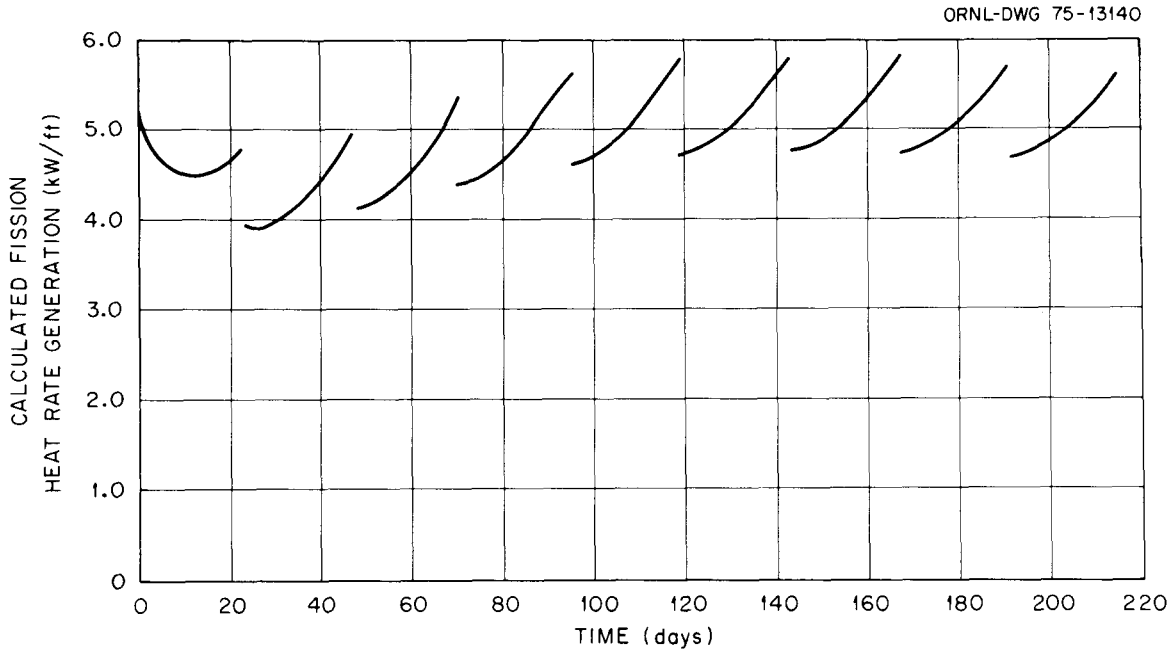

Fig. 7.4. Capsules HRB-4 and -5 fission heat rate for fuel rod 2A.

The burnup and fluence are based on a peak (reactor horizontal midplane) fast flux of 5×10^{14} neutrons cm^{-2} sec^{-1} ($E > 0.18$ MeV) and an average perturbed thermal flux of 1.18×10^{15} neutrons cm^{-2} sec^{-1} ($E <$ 0.414 eV).

The helium-neon sweep-gas effluent was sampled periodically to measure fission-gas release. The ratios of release rate to birth rate (R/B) of selected isotopes vs accumulated irradiation time are shown in Fig. 7.5. The birth rates used in this calculation take into account the depletion of ^{235}U and fissions of bred-in ^{233}U and ^{239}Pu. We first calculated the daily change in isotopic composition of the fuel for each specimen and then the fission product yield from each fissionable isotope.

Typical plots of the time-temperature history for eight of the thermocouples during one HFIR cycle of operation (cycle 87, the fifth cycle of irradiation for capsule HRB-4) are given in Figs. 7.6 through 7.11. Operating temperature was controlled by maintaining TE-207 at 940°C. The short low-temperature indication for all thermocouples at the beginning of each cycle was caused by capsule operation with a 100% helium sweep, which reduces the thermal resistance of the gas between the graphite sleeve and the capsule wall and results in the lower temperatures. The capsule was operated with 100% helium periodically to provide a relative measure of the power generation as a function of temperature without the complication of an uncertain gas conductivity.

The operating history of the HFIR during the time capsule HRB-4 was being irradiated is shown in Table 7.8.

Table 7.8. Capsule HRB-4 operating history

HFIR cycle	Cycle		Operation time (days)	Accumulated irradiation time at 100 MW reactor power (hr)
	Begin	End		
83	10/8/72	10/23/72	15	364.3
84A	10/24/72	11/11/72	18	
84B	11/13/72	11/19/72	5	925.2
85	11/20/72	12/13/72	23	1479.4
86[a]	12/13/72	1/7/73	24	2037.6
87A	1/9/73	1/10/73	1	
87B	1/12/73	2/3/73	21	2577.8
88	2/3/73	2/26/73	23	3119.0
89	2/27/73	3/22/73	23	3664.5
90	3/23/73	4/15/73	23	4213.4
91	4/18/73	5/11/73	23	4764.2
92[b]	5/11/73	6/3/73	23	5310.1
93	6/3/73	6/26/73	23	5854.8

[a]Includes two days at 50 MW.

[b]Within the first three days of this cycle the reactor experienced five momentary power reductions.

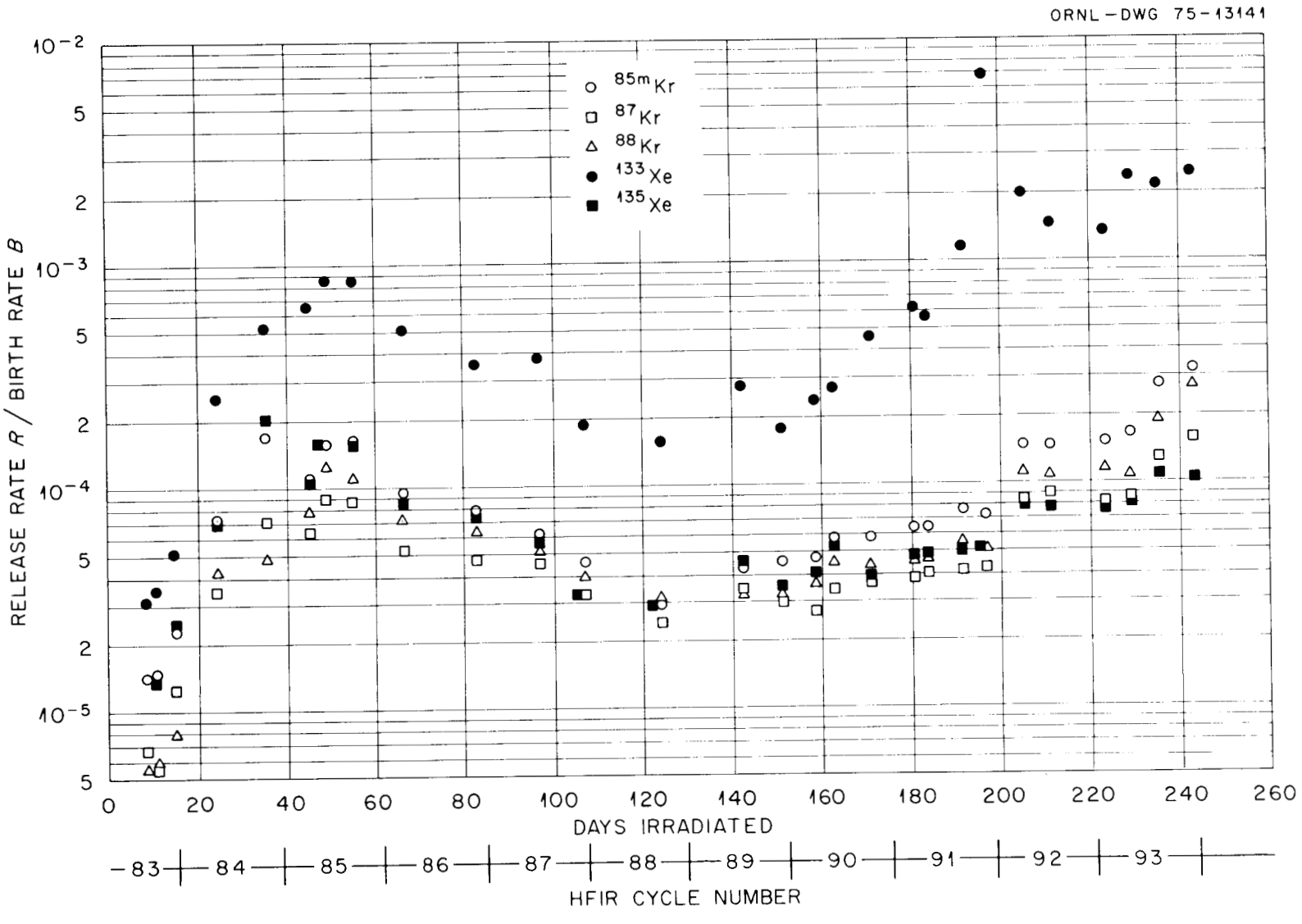

Fig. 7.5. HFIR HRB-4 experiment – fission-gas release/birth ratio vs time (samples 2 through 28).

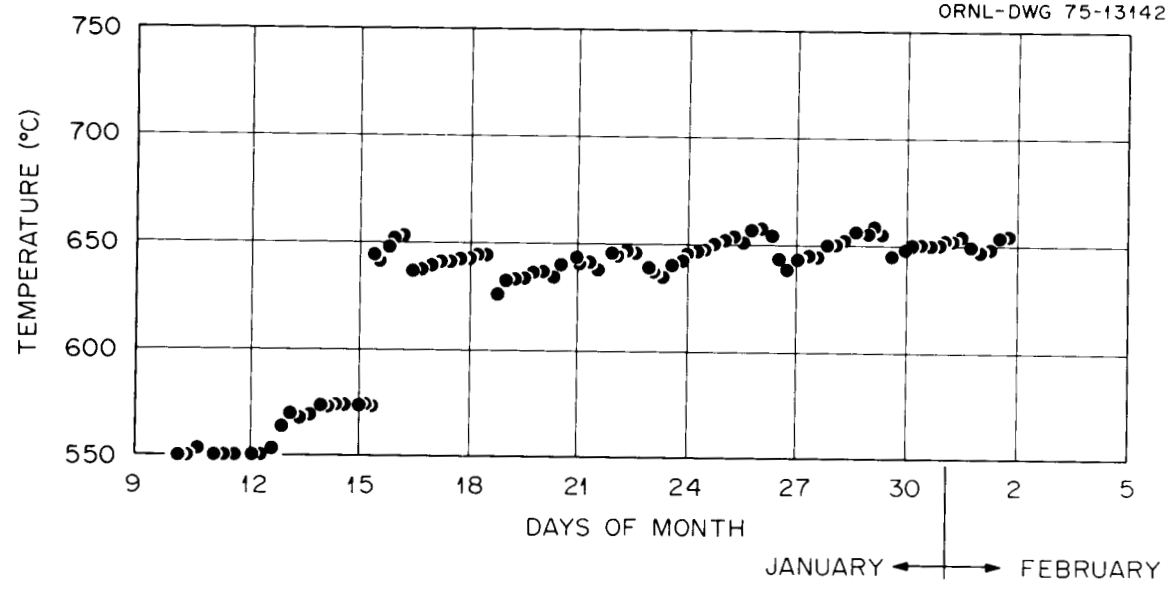

Fig. 7.6. Measured temperature at thermocouple TE-201 in capsule HRB-4 during HFIR cycle 87 – cycle 5 of an 11-cycle irradiation.

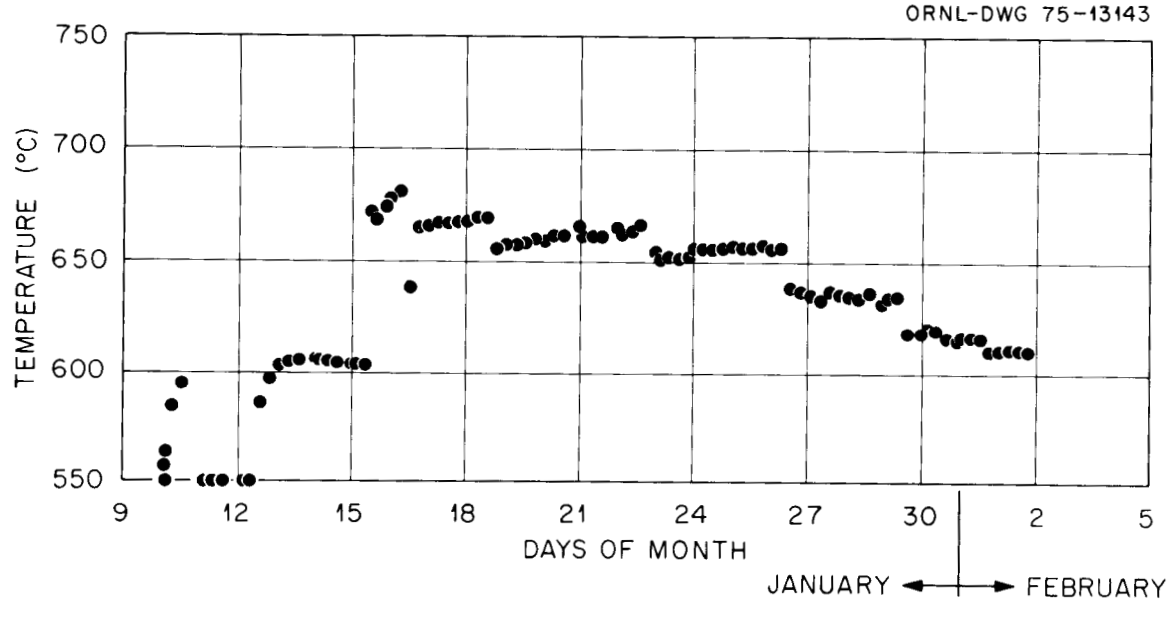

Fig. 7.7. Measured temperature at thermocouple TE-202 in capsule HRB-4 during HFIR cycle 87 – cycle 5 of an 11-cycle irradiation.

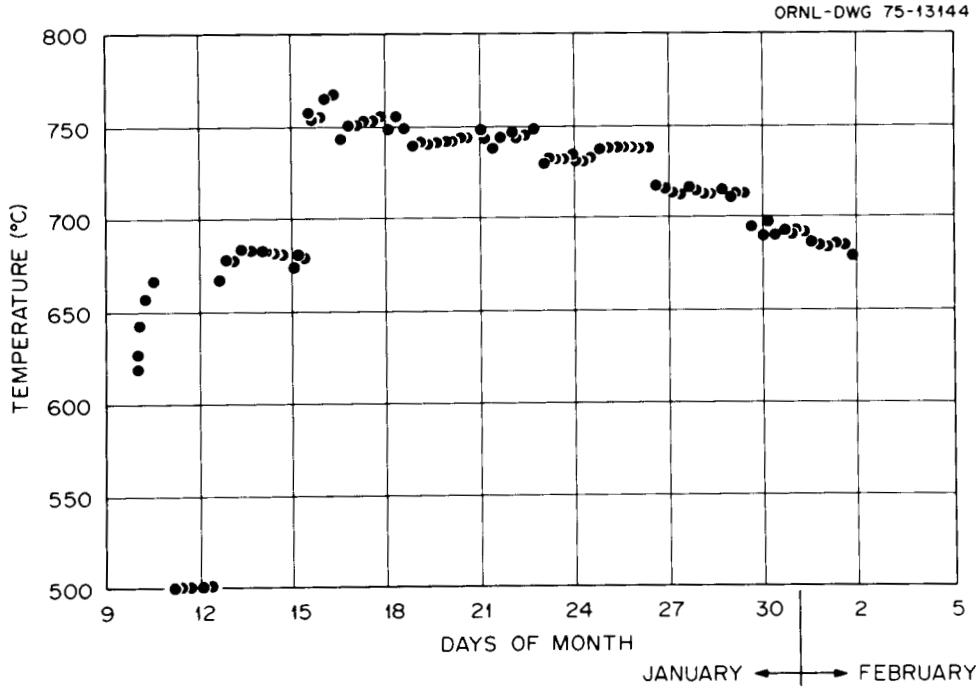

Fig. 7.8. Measured temperature at thermocouple TE-203 in capsule HRB-4 during HFIR cycle 87 – cycle 5 of an 11-cycle irradiation.

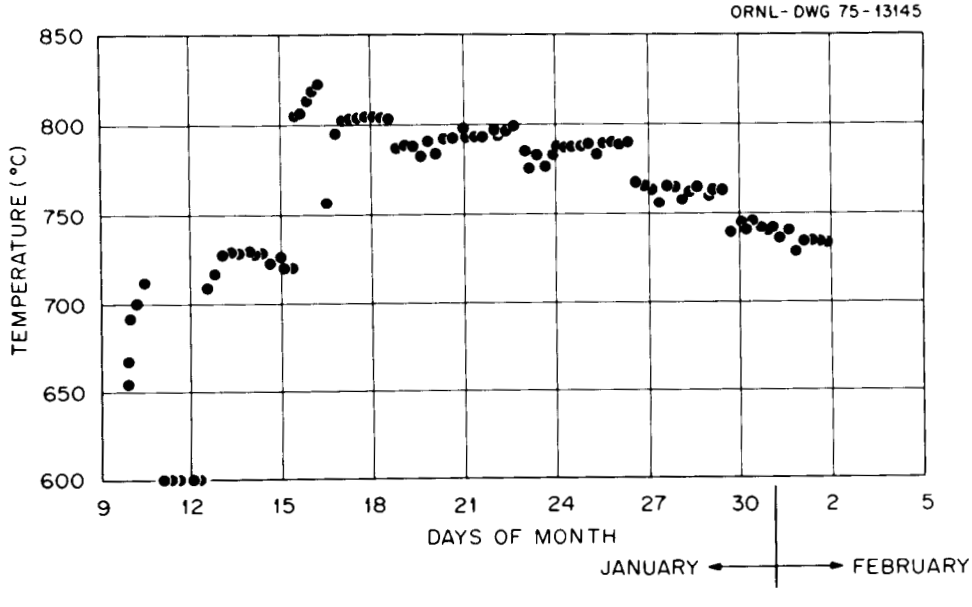

Fig. 7.9. Measured temperature at thermocouple TE-204 in capsule HRB-4 during HFIR cycle 87 – cycle 5 of an 11-cycle irradiation.

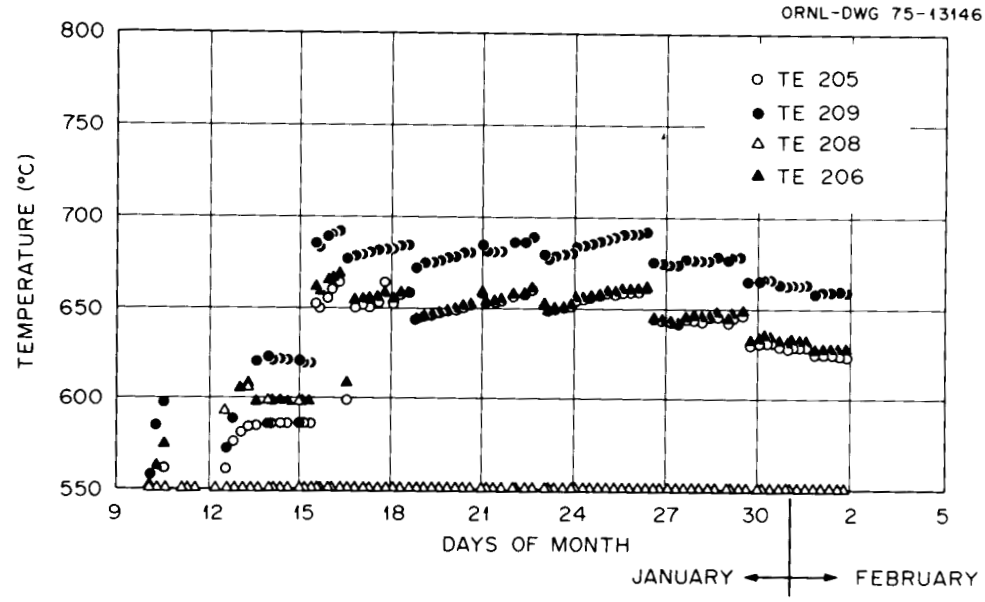

Fig. 7.10. Measured temperature at thermocouples TE-205, -206, -208, and -209 in capsule HRB-4 during HFIR cycle 87 – cycle 5 of an 11-cycle irradiation.

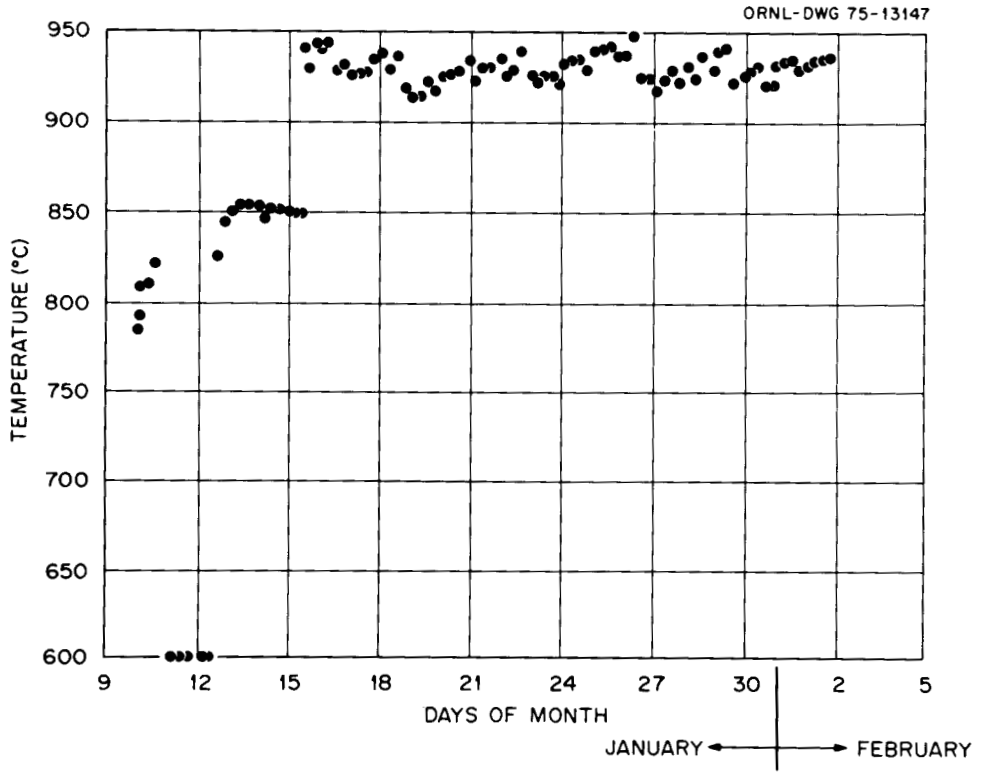

Fig. 7.11. Measured temperature at thermocouple TE-207 in capsule HRB-4 during HFIR cycle 87 – cycle 5 of an 11-cycle irradiation.

Capsule HRB-5

Design. This capsule and the fuel specimens were identical to capsule HRB-4 except that the W/Re thermocouple which monitors the central temperature of bonded-bed specimen 1C had been replaced by an ultrasonic thermometer (see Sect. 7.7). The thermocouple locations in the graphite sleeve, as shown in Fig. 7.12 differ only in the length of TE-104 (located adjacent to the interface of specimens 3C and 3D).

Operation. Capsule HRB-5 was inserted in the RB-5 facility at the beginning of HFIR fuel cycle 83 on Oct. 8, 1972. The capsule was irradiated for five cycles (107.4 days at 100 MW reactor power) to a peak fast fluence of 4.6×10^{21} neutrons/cm^2 ($E > 0.18$ MeV). Due to the similarity of this capsule to capsule HRB-4, the fission heat generation for capsule HRB-4 (Fig. 7.4) applies, except that HRB-5 was irradiated for only 5 HFIR cycles whereas HRB-4 was irradiated for 11 cycles. The fuel specimen loading, location, isotopic burnup, and fluence are given in Table 7.9. The assumptions for these calculations are identical to those of HRB-4.

Samples were taken periodically of the sweep-gas effluent to obtain fission-gas R/B ratios. These are

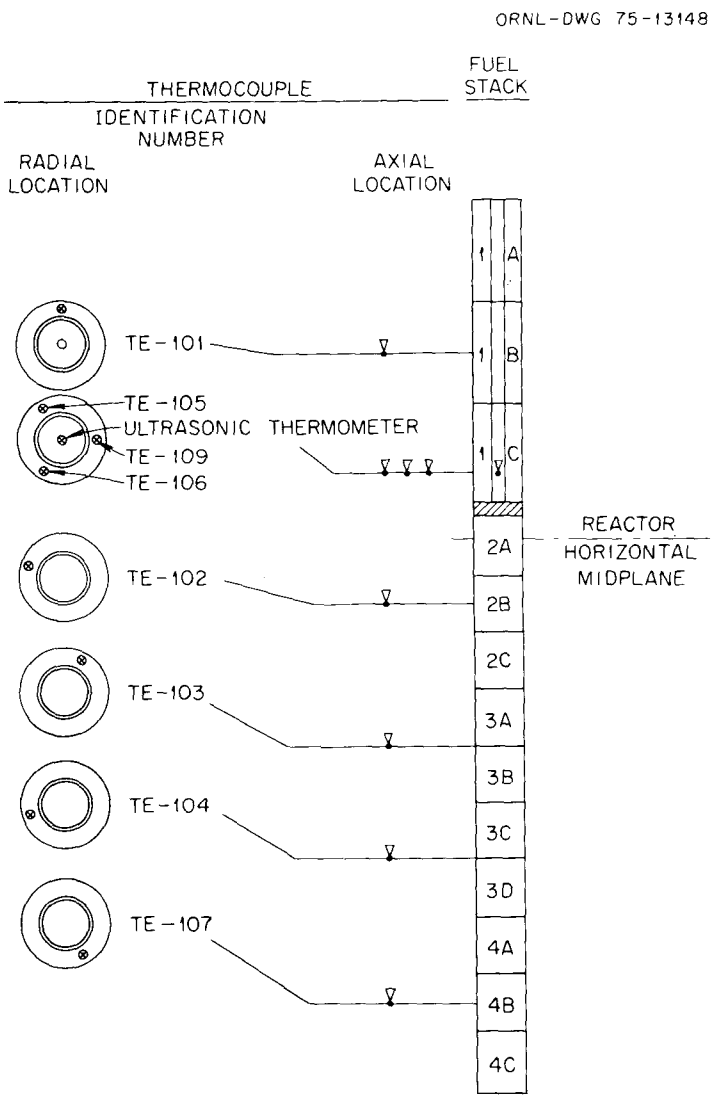

Fig. 7.12. Capsule HRB-5 thermocouple location.

Table 7.9. Capsule HRB-5 fuel specimen location and loading

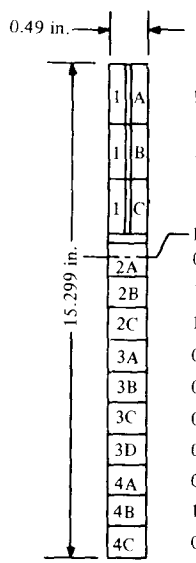

	Length (in.)	Volume (cc)	Fuel loading (g/cc) ^{235}U	^{238}U	^{232}Th	Reactor HMP[a] to specimen center (in.)	Percent initial isotope fissioned ^{235}U	^{238}U	^{232}Th	Average thermal flux ($E < 0.414$ eV) (neutrons cm^{-2} sec^{-1})	Thermal fluence ($E < 0.414$ eV) (neutrons/cm^2)	Average fast flux ($E > 0.18$ MeV) (neutrons cm^{-2} sec^{-1})	Fast fluence ($E > 0.18$ MeV) (neutrons/cm^2)
										$\times 10^{14}$	$\times 10^{21}$	$\times 10^{14}$	$\times 10^{21}$
1A	1.747	5.1980	0.0049	0.0775	0.1502	5.000	82.3	8.5	2.8	7.49	7.0	3.70	3.4
1B	1.746	5.2243	0.0050	0.0783	0.1518	3.250	83.5	10.0	3.7	9.38	8.7	4.35	4.0
1C	1.744	5.2318	0.0050	0.0791	0.1533	1.500	84.0	11.5	4.5	10.88	10.0	4.90	4.5
Reactor HMP													
2A	0.996	3.0995	0.0042	0.0667	0.1295	0.125	84.0	12.0	4.8	11.71	10.8	5.00	4.6
2B	1.005	3.1517	0.0042	0.0656	0.1273	1.125	84.0	11.9	4.8	11.80	10.9	4.98	4.6
2C	1.005	3.1132	0.0042	0.0665	0.1289	2.125	84.0	11.0	4.5	11.68	10.8	4.83	4.5
3A	0.949	2.933	0.0044	0.0685	0.1326	3.125	84.0	10.6	4.4	11.20	10.4	4.56	4.2
3B	0.953	2.945	0.0043	0.0682	0.1321	4.125	84.0	9.5	4.0	10.47	9.7	4.24	3.9
3C	0.952	2.954	0.0043	0.0680	0.1317	5.125	83.8	8.0	3.5	9.56	8.9	3.85	3.6
3D	0.956	2.966	0.0043	0.0677	0.1311	6.125	83.5	7.0	3.0	8.50	7.9	3.43	3.2
4A	0.997	3.1102	0.0042	0.0665	0.1290	7.125	82.5	5.5	2.5	7.32	6.8	2.99	2.8
4B	1.002	3.1461	0.0042	0.0658	0.1276	8.125	81.0	4.0	1.8	6.14	5.7	2.50	2.3
4C	0.997	3.1051	0.0042	0.0666	0.1293	9.125	77.5	2.5	1.0	4.90	4.5	1.97	1.8

[a]Reactor horizontal midplane.

shown in Fig. 7.13 for selected isotopes vs irradiation time.

Operating temperature in the graphite sleeve was maintained between 900 and 940°C on control thermocouple TE-107. A typical set of the measured temperatures during the fifth cycle of operation are shown in Figs. 7.14 through 7.18.

The operating history of the HFIR during the time capsule HRB-5 was in the reactor is given in Table 7.8.

Postirradiation examination of HRB-4 and -5

(E. L. Long, Jr.)

The objectives, design, preparation of test specimens, and operation of capsules HRB-4 and -5 have been reported.[4] The disassembly and examination of the components of these two instrumented capsules were completed during this report period. A brief description of the fuel rods is given in Table 7.10. Two types of ORNL rods were irradiated: three extruded rods (1A, B, and C) and four slug-injected rods (3A, B, C, and D). All the fuel rods contained the same combination of particles; namely, Triso-coated weak-acid-resin-derived (WAR) fissile kernels (95% UC_2), Biso-coated ThO_2 fertile kernels, and Biso- and Triso-coated inert particles. One objective of this experiment was to evaluate the relative performance of fuel rods carbonized in graphite tubes (to simulate in-block carbonization) and to evaluate candidate matrix materials. Three different

4. B. H. Montgomery, J. M. Robbins, and R. L. Hamner, "Capsules HRB-4 and HRB-5 – Capsule Design," *GCR Programs Annu. Progr. Rep. Dec. 31, 1972*, ORNL-4911, pp. 107–11.

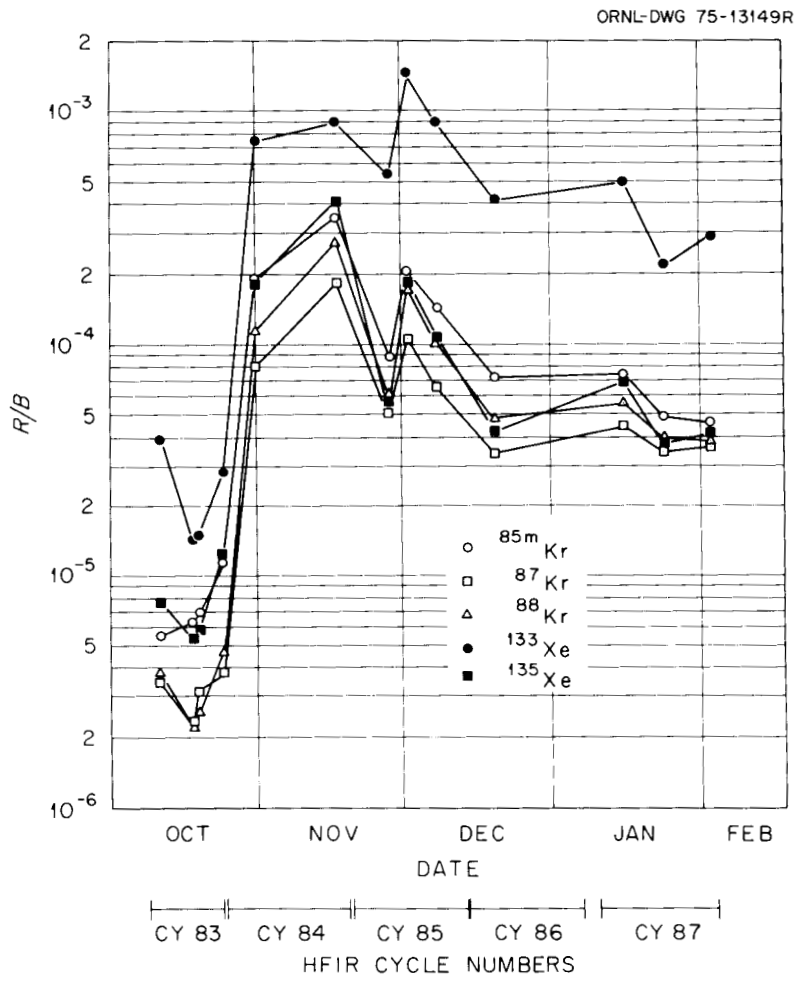

Fig. 7.13. HFIR HRB-5 capsule fission-gas release/birth rate ratio vs time.

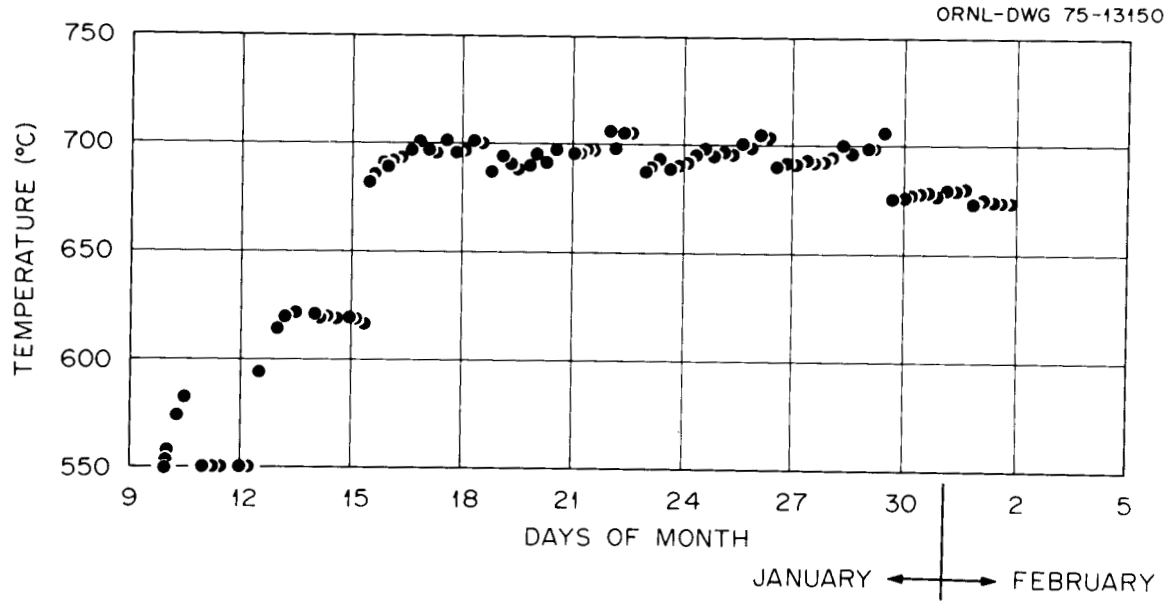

Fig. 7.14. Measured temperature at thermocouple TE-101 in capsule HRB-5 during HFIR cycle 87 – cycle 5 of a 5-cycle irradiation.

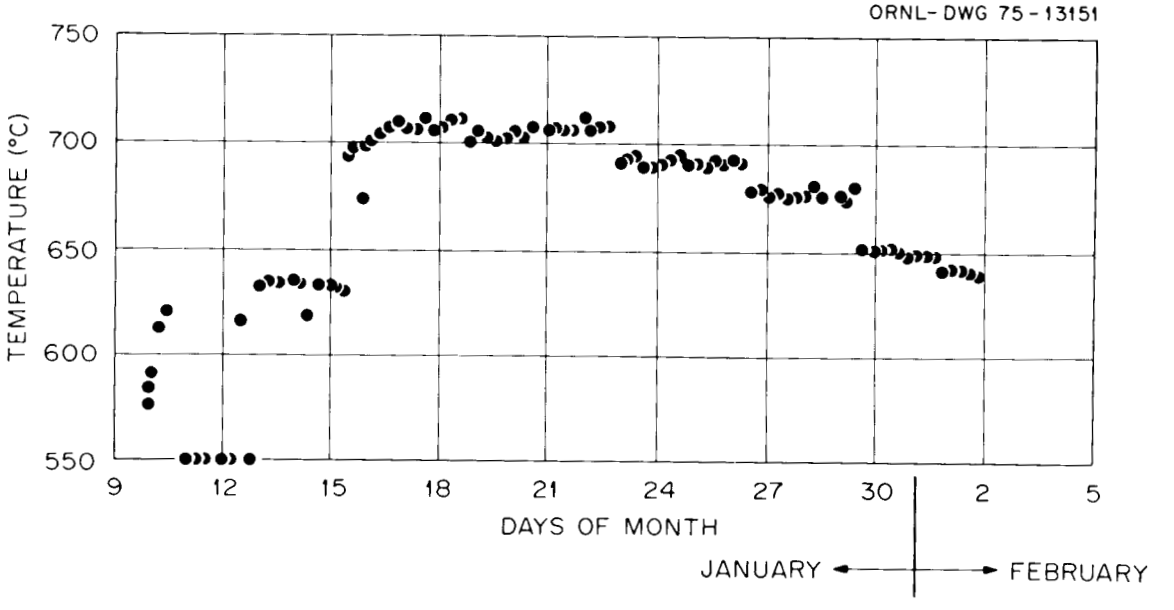

Fig. 7.15. Measured temperature at thermocouple TE-102 in capsule HRB-5 during HFIR cycle 87 – cycle 5 of a 5-cycle irradiation.

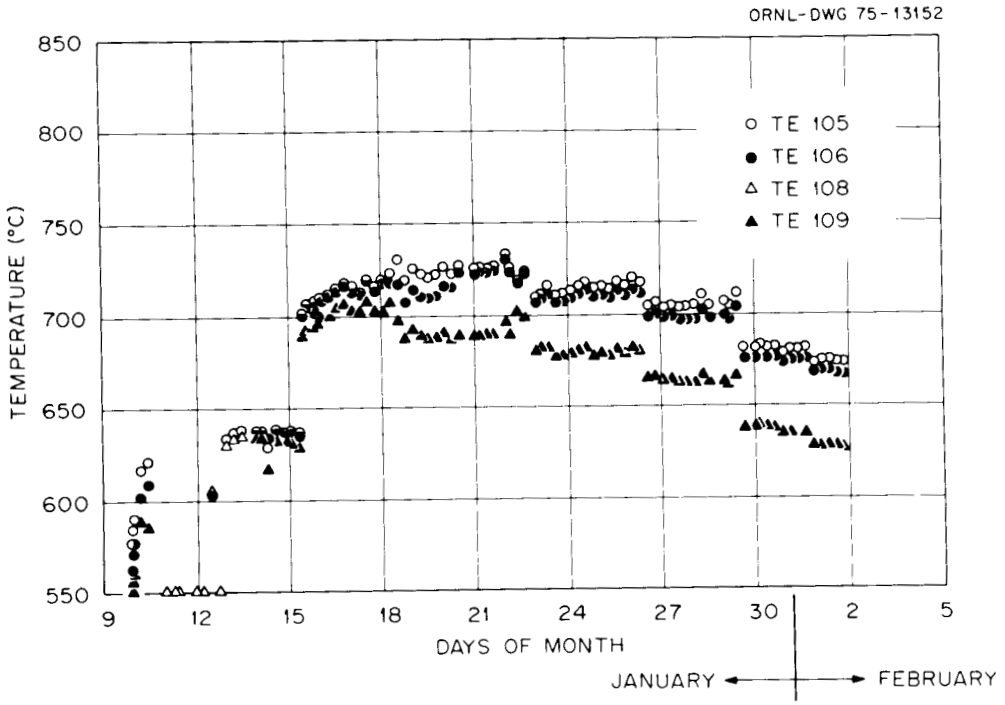

Fig. 7.16. Measured temperature at thermocouples TE-105, -106, -108, and -109 in capsule HRB-5 during HFIR cycle 87 – cycle 5 of a 5-cycle irradiation.

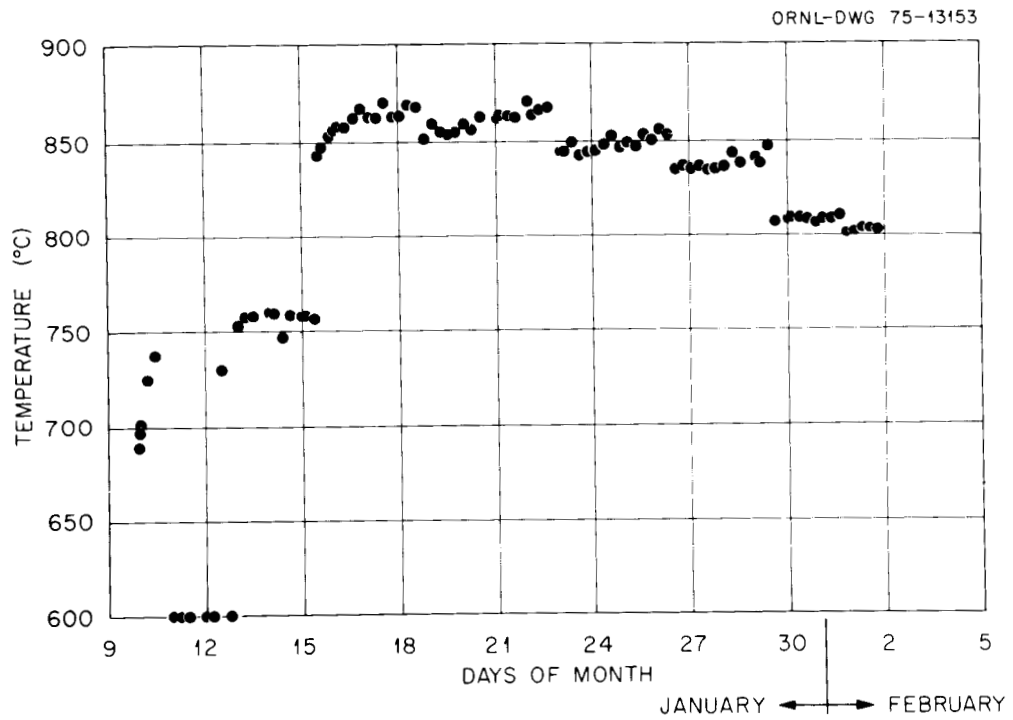

Fig. 7.17. Measured temperature at thermocouple TE-104 in capsule HRB-5 during HFIR cycle 87 – cycle 5 of a 5-cycle irradiation.

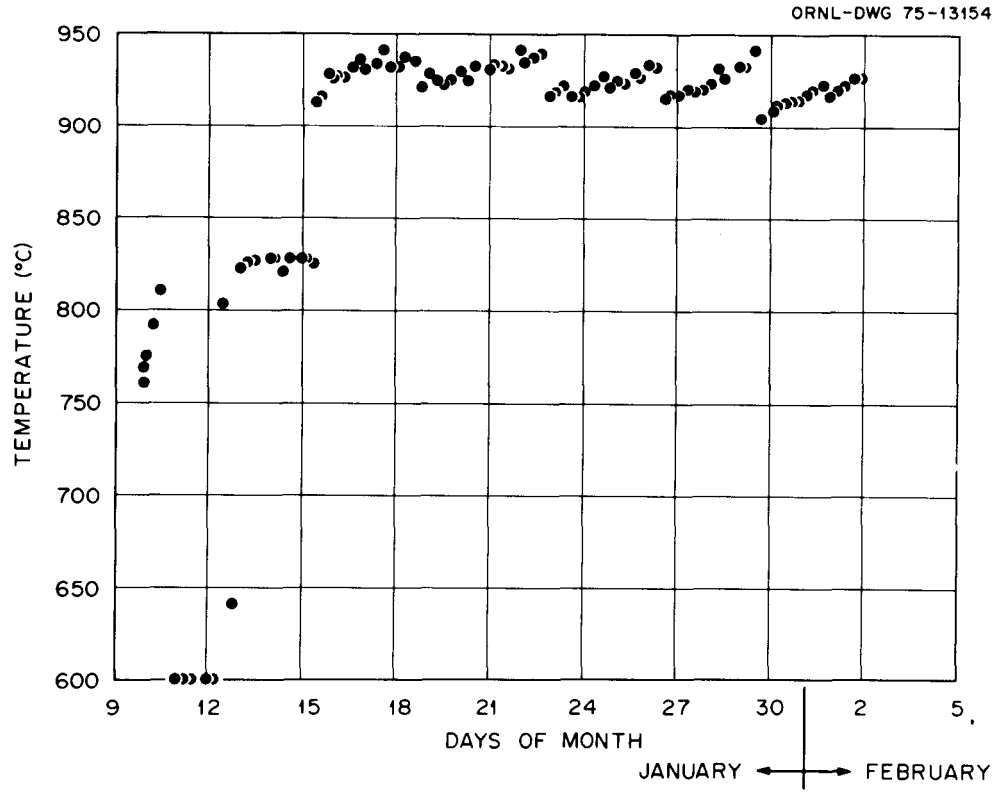

Fig. 7.18. Measured temperature at thermocouple TE-107 in capsule HRB-5 during HFIR cycle 87 – cycle 5 of a 5-cycle irradiation.

Table 7.10. General description of fuel rod specimens used in HRB-4 and -5

Specimen No.	Supplied	Nominal dimensions (in.)		Matrix material	Particle volume loading (%)	Fabrication technique	Carbonization mode
		Diameter	Length				
1A 1B 1C	ORNL	0.490[a]	1.75	Robinson graphitized coke and Varcum	32.5	Extrusion	In covered graphite tray
2A, 4A 2B, 4B 2C, 4C	GAC	0.490	1.0	GAC materials[b]	55–58	Admix	In block (H-327)
3A[c] 3B 3C 3D	ORNL	0.490	1.0		60–62	Slug injection	In packed alumina In block (H-327)

[a]Outside diameter, 0.490; inside diameter, 0.090 in.

[b]GAC's candidates for matrices: 40% RC4 in A240 pitch, 40% GLC in A240 pitch, and 40% GLC 1089 with Thermax in A240 pitch.

[c]Fort St. Vrain reference.

matrices and two different carbonization modes (Table 7.10) are used in fabricating the slug-injection fuel rods.

The arrangement of the fuel rods in the capsules is shown in Fig. 7.2. The three ORNL extruded rods were located at the top of the capsule followed by three GAC fuel rods, the four ORNL slug-injected fuel rods, and three additional GAC rods. Since the GAC fuel rods were returned to their hot-cell facility for examination, there will be no further mention of them in this discussion.

Capsules HRB-4 and -5 were in the HFIR for 5 and 11 cycles respectively. The fuel rods operated at an average design heat rating of 5.4 kW/ft. The fuel rods in HRB-5 reached a peak fast flux of about 5×10^{21} neutrons/cm^2 ($E > 0.18$ MeV) and a burnup of about 16% FIMA in the fissile particles. Fuel rods in HRB-4 reached peak fast fluences and burnups about twice those of the fuel rods in HRB-5. The general appearance of the fuel rods was good; only one rod from HRB-4 (fuel rod 3B) showed evidence of debonding. The resultant correlation of fuel rod dimensional change with fast fluence (>0.18 MeV) is shown in Fig. 7.19. As stated earlier, these fuel rods contained Biso- and Triso-coated particles; the particle volume loading was 60 to 62% for the slug-injected rods and about 30% for the extruded rods. The matrix densities were about 1.7 g/cm^3 for the extruded rods and ranged from about 0.6 to 0.8 g/cm^3 for the slug-injected rods. The onset of anisotropic shrinkage expected in the extruded rods was observed at about 6.5×10^{21} neutrons/cm^2. The surprising result was that the close-packed (slug-injected) rods showed the same anisotropic behavior. A check of the dimensions of the slug-injected green rods vs carbonized vs annealed rods showed no trend toward anisotropic shrinkage. One way to explain this effect would be to assume that the matrices of the slug-injected rods as well as the extruded rods have a preferred orientation; and at fluences above 6.5×10^{21} neutrons/cm^2, Biso coatings will have densified sufficiently that the matrix becomes the controlling factor resulting in anisotropic shrinkage of the slug-injected fuel rods. The continuous matrix of an extruded rod is always the controlling shrinkage factor, since the volume of the rod occupied by coated particles is only about 30%.

Metallographic sections of the slug-injected fuel rods were examined to determine the effect of the carbonization technique on the irradiation performance of the three matrices. No broken coatings were found in the rods containing the Fort St. Vrain (FSV) matrix (3A) or in the one with the experimental matrix carbonized in packed Al_2O_3 (3B). However, a significant number of the pyrolytic-carbon coatings in the rods with the experimental matrices carbonized in graphite tubes (3C and 3D) had failed as a result of particle-matrix interaction. Examples of failed Biso and Triso coatings are shown in Fig. 7.20.

Examination of the as-fabricated rods containing the FSV-type and experimental matrices that were carbonized in packed Al_2O_3 revealed that in each case the matrix was very porous and the individual graphite filler particles were discernible. Matrices of the rods carbonized in graphite tubes were much more dense, and the individual filler particles were not discernible. The denser matrices resulted from higher yield of coke from pitch in the rods carbonized in graphite tubes. The as-fabricated rods with the denser matrices carbonized

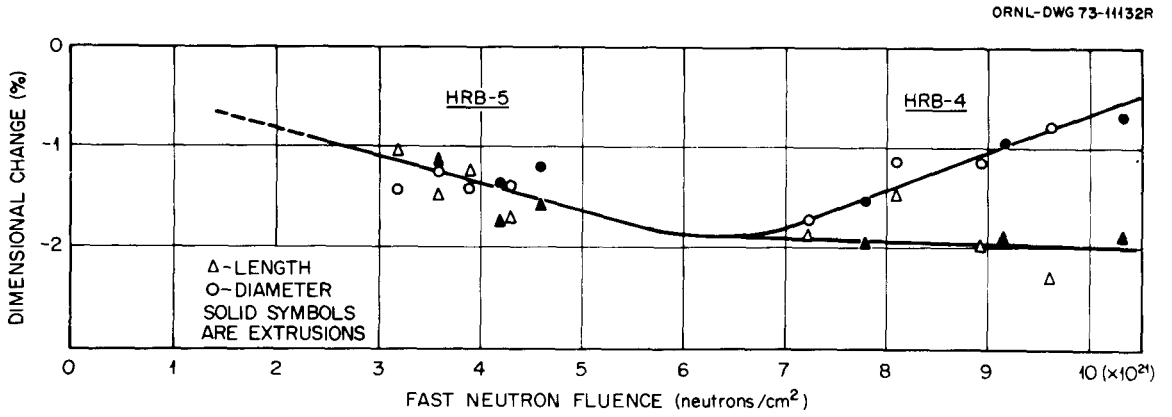

Fig. 7.19. Dimensional changes of fuel rods from HRB-4 and -5 experiments.

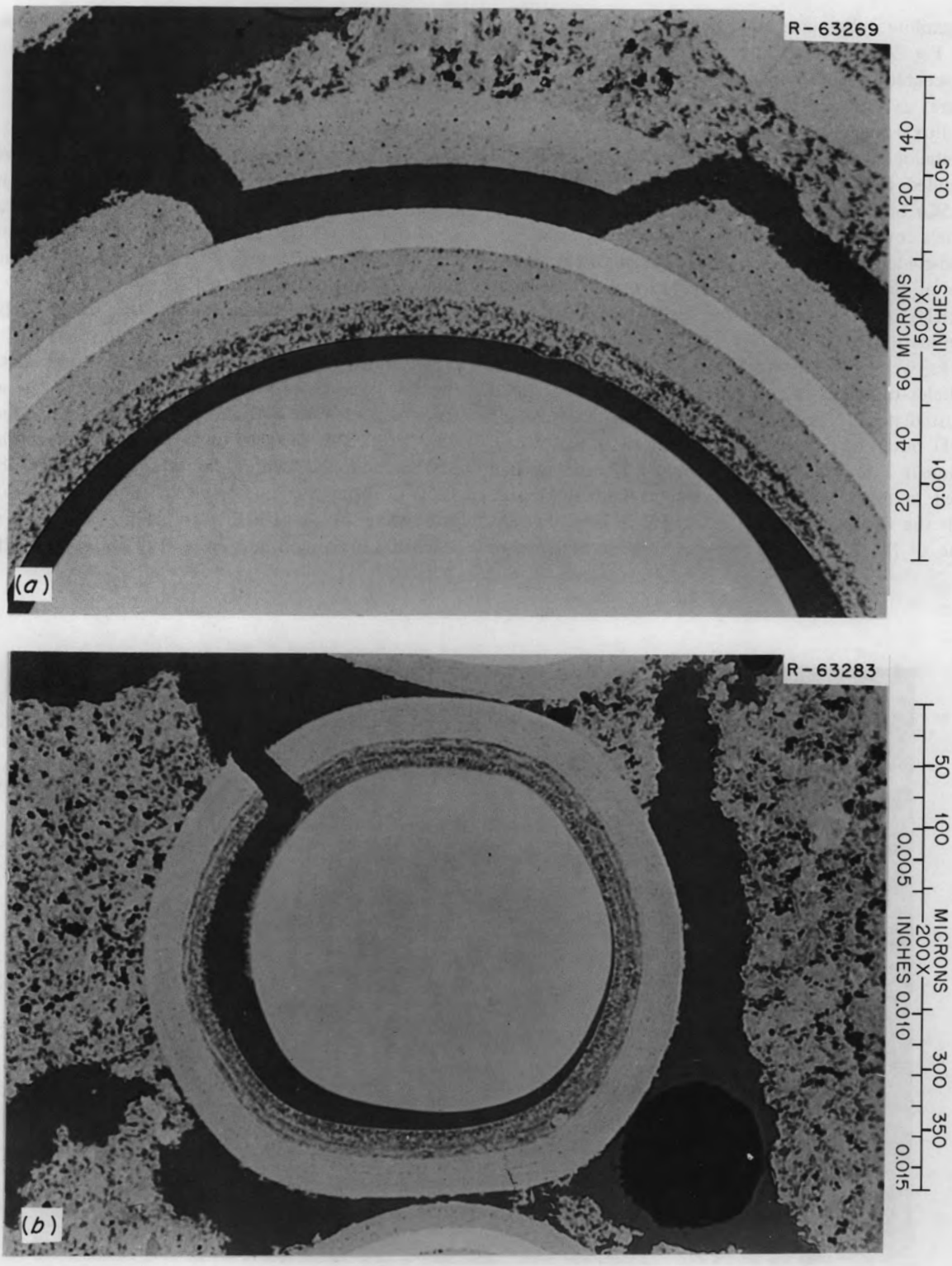

Fig. 7.20. Appearance of (*a*) Triso and (*b*) Biso coatings that failed from matrix-particle interaction in slug-injected fuel rods irradiated in HRB-5.

in graphite tubes contained particles with small tears (see Fig. 7.21) in the outer coatings of the Triso- and Biso-coated particles. These tears initiated coating failure as the matrix and coatings densified with fast-flux damage.

Metallographic examination of sections through the extruded fuel rods revealed that a significant number (~25%) of the SiC coatings on the Triso-coated fissile kernels contained cracks. None of the SiC layers on the Triso-coated inert kernels exhibited cracks. (The thickness of the SiC layer was about 15 μm on the inert particles and 32 μm on the fissile particles.) Close examination of the archive sample revealed that fine cracks were present in the SiC layers on the fissile particles of the as-extruded rods and were exaggerated by irradiation. None of the low-temperature isotropic (LTI) outer layers on the fissile particles had failed, although a few (~2%) of the inner LTI coatings had failed in particles that contained cracked SiC layers. With the exception of one cracked Biso inert particle, none of the Biso-coated particles showed evidence of potential failure. No obvious changes were observed in the matrix as a result of the irradiation test, nor was there any evidence of particle-matrix interaction.

Thus, it appears that in-block carbonization has presented some unexpected problems. Also, there are apparent problems with the extruded fuel rods, since an unacceptable fraction of cracked SiC layers were present in the Triso fissile particles in the as-fabricated condition. Irradiation testing either increased the number of cracked SiC layers or merely enhanced them so that they were much more readily detected.

Metallographic examination of the fissile particles contained in the slug-injected rods that achieved full HTGR fluence revealed several potential problems for the SiC layers. The kernels of the fissile particle were composed of WAR particles that had been converted to 95% UC_2. The surfaces of the fuel rods were about 950°C, and the center-line temperature was about 1250°C during the time of peak fission-heat-generation rate while in the HFIR test facility. The fuel rods reached a maximum burnup level of about 27% FIMA.

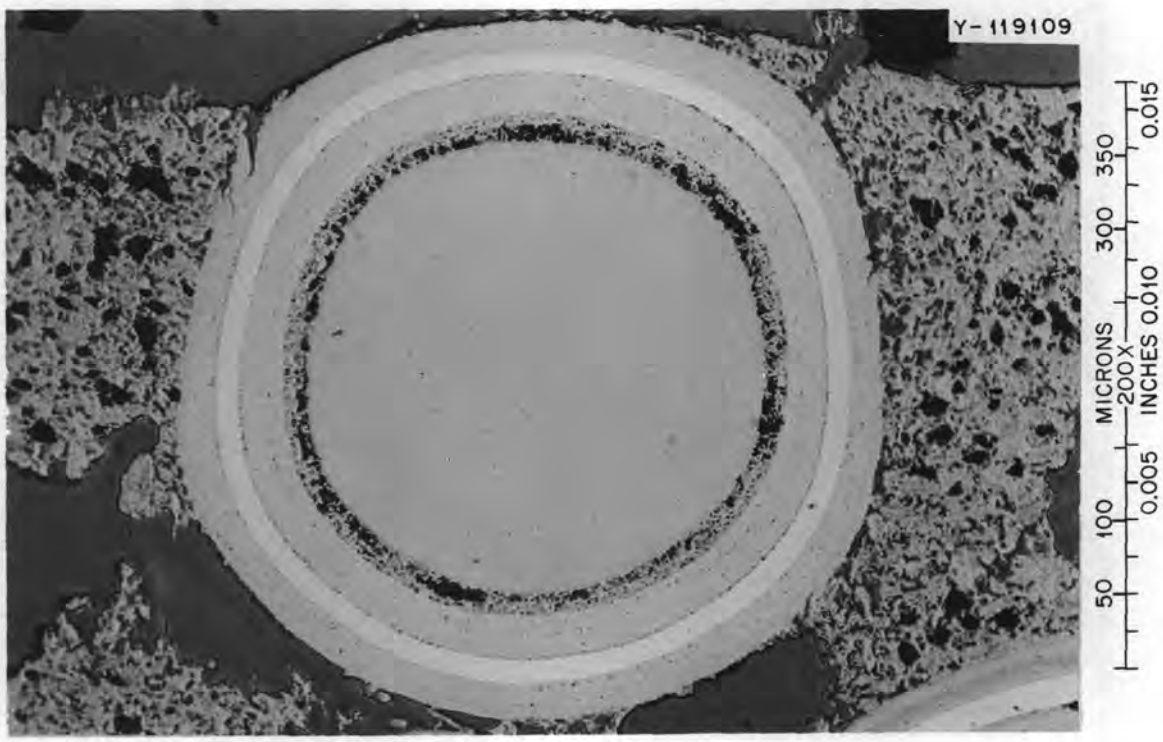

Fig. 7.21. Unirradiated Triso-coated particle in control fuel rod for HRB-4 and -5. (Note small tears in the peripheral region of the outer coating.)

In the relatively small number of fissile particles exposed in the planes of polish, about one-third shows evidence of attack in inner surface regions of the SiC layers. This attack appears as localized regions and is not dependent on the temperature gradient. The attack varied in degree of severity from only slight to complete penetration of the thickness of the SiC. A general degradation of the inner surface of the SiC was also apparent in many of the coated particles. Analysis of a region of attack with the aid of an electron microprobe revealed the fision product palladium to be the culprit. The results of this analysis are shown in Fig. 7.22. Since the attacked regions appeared to have been molten, a check with a palladium-silicon phase diagram showed three eutectics[5] that have melting points below the surface temperature of the fuel rods (15.5% Pd, mp 800°C; approximately 45% Pd, mp 720°C; 58% Pd, mp 850°C). This result would be atypical of HTGR conditions, since the bulk of the palladium present was a fission product from ^{239}Pu and not the ^{235}U (the UC_2 was enriched to about 6% ^{235}U). However, this result could become significant should a decision be made to incorporate plutonium in the HTGR fuel cycle.

In addition to the above problem, about one-fourth of the UC_2 kernels appeared to have been molten and were in intimate contact with the inner LTI coating, and a metallic-like ingot had attacked the SiC coating. Although no SiC coatings had failed as a result, up to one-half the thickness of the SiC appeared to have been dissolved by the metallic-like material; one such particle is shown in Fig. 7.23. The results from an electron microprobe analysis of one of the molten kernels is shown in Fig. 7.24. The rare earths La, Ce, Pr, and Nd were the fission products associated with the localized dissolution of the SiC layer. Note also that uranium was not associated with this reaction zone and that there is no obvious concentration of silicon in the kernel.

The rare-earth fission products were also found concentrated on the inner surface of the cooler side of the SiC coating, as reported in other coated-particle

5. Max Hansen, *Constitution of Binary Alloys*, p. 1126, McGraw-Hill, 2d ed., 1958.

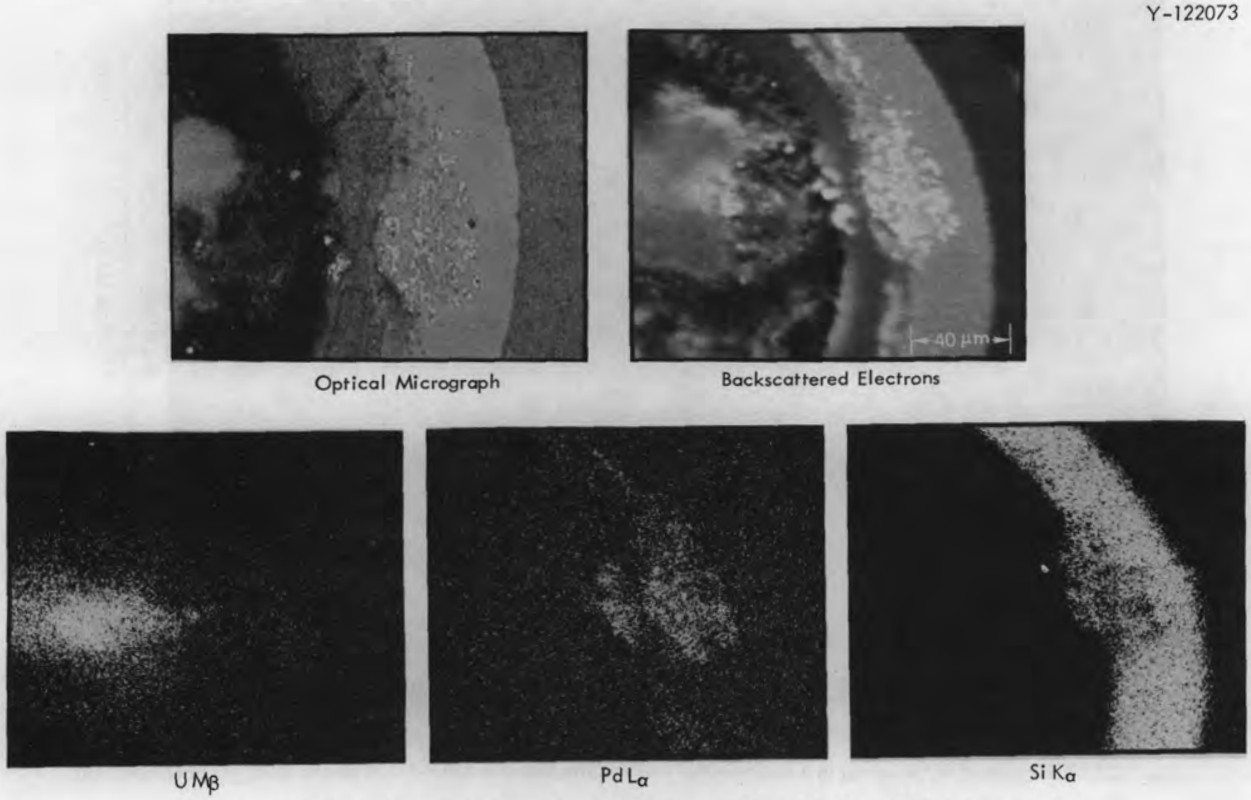

Fig. 7.22. Palladium–silicon carbide reaction in a Triso-coated particle from HRB-4, fuel rod 3A.

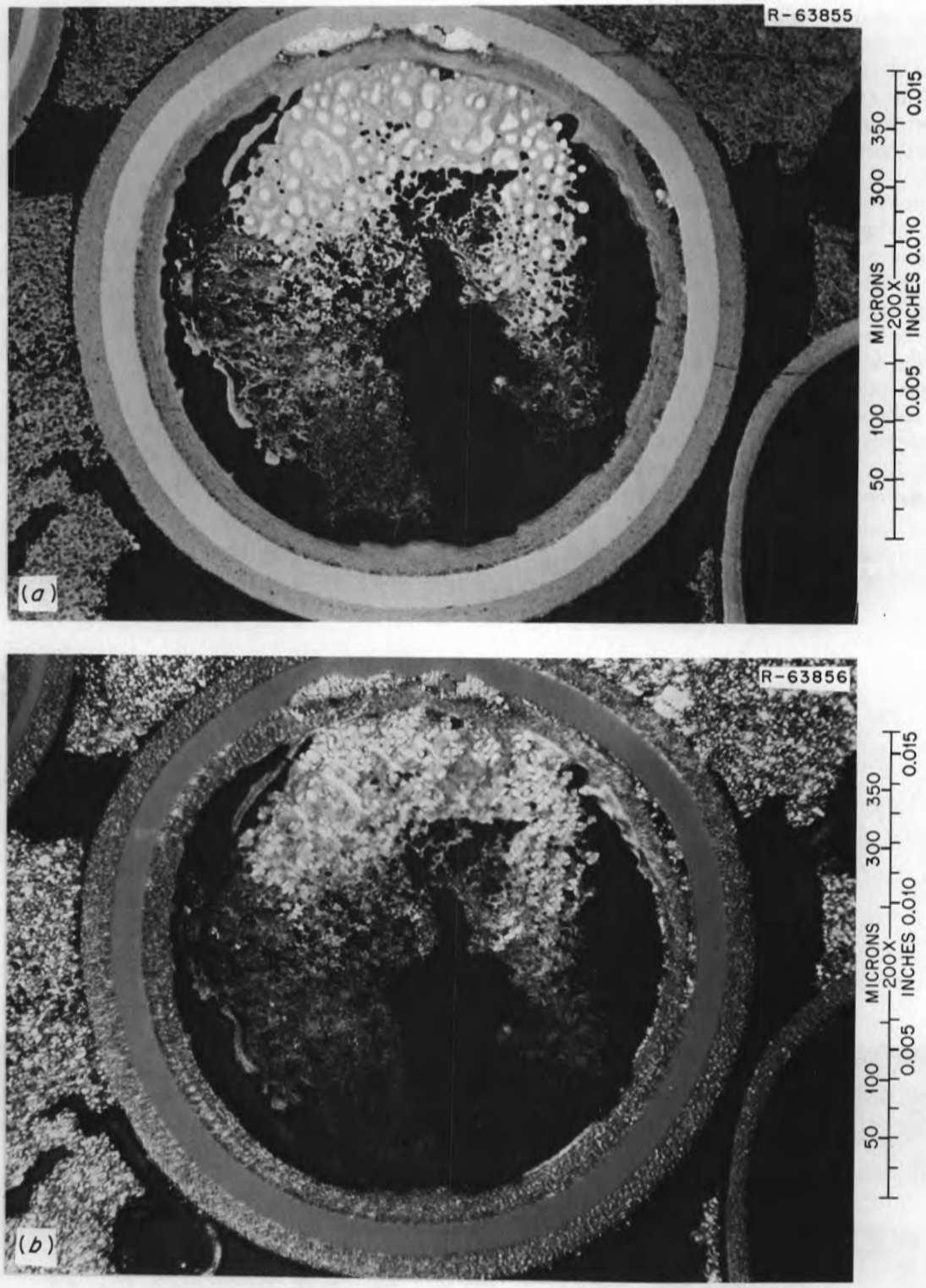

Fig. 7.23. Triso-coated WAR kernel in a slug-injected fuel rod irradiated in HRB-4. (*a*) Bright field; (*b*) polarized light.

systems that have been exposed to a thermal gradient.[6] The presence of the rare earths led to penetration of about half the thickness of the SiC coating. Attacks by both this rare earth and palladium are shown in Fig. 7.25.

6. *HTGR Base Program Quart. Progr. Rep. May 31, 1973,* GULF-GA-A12599, pp. 87–93.

The kernels of the Biso fertile particles in the slug-injected fuel rod 3A from HRB-4 exhibited a slight "amoeba" effect. The ThO_2 kernels had migrated about 20 μm or less. Although there was no measurable movement of the ThO_2 kernels in the other three fuel rods, the densified-buffer recoil zone was noticeably darker on the hot side of the kernel. An electron microprobe analysis failed to detect any chemical

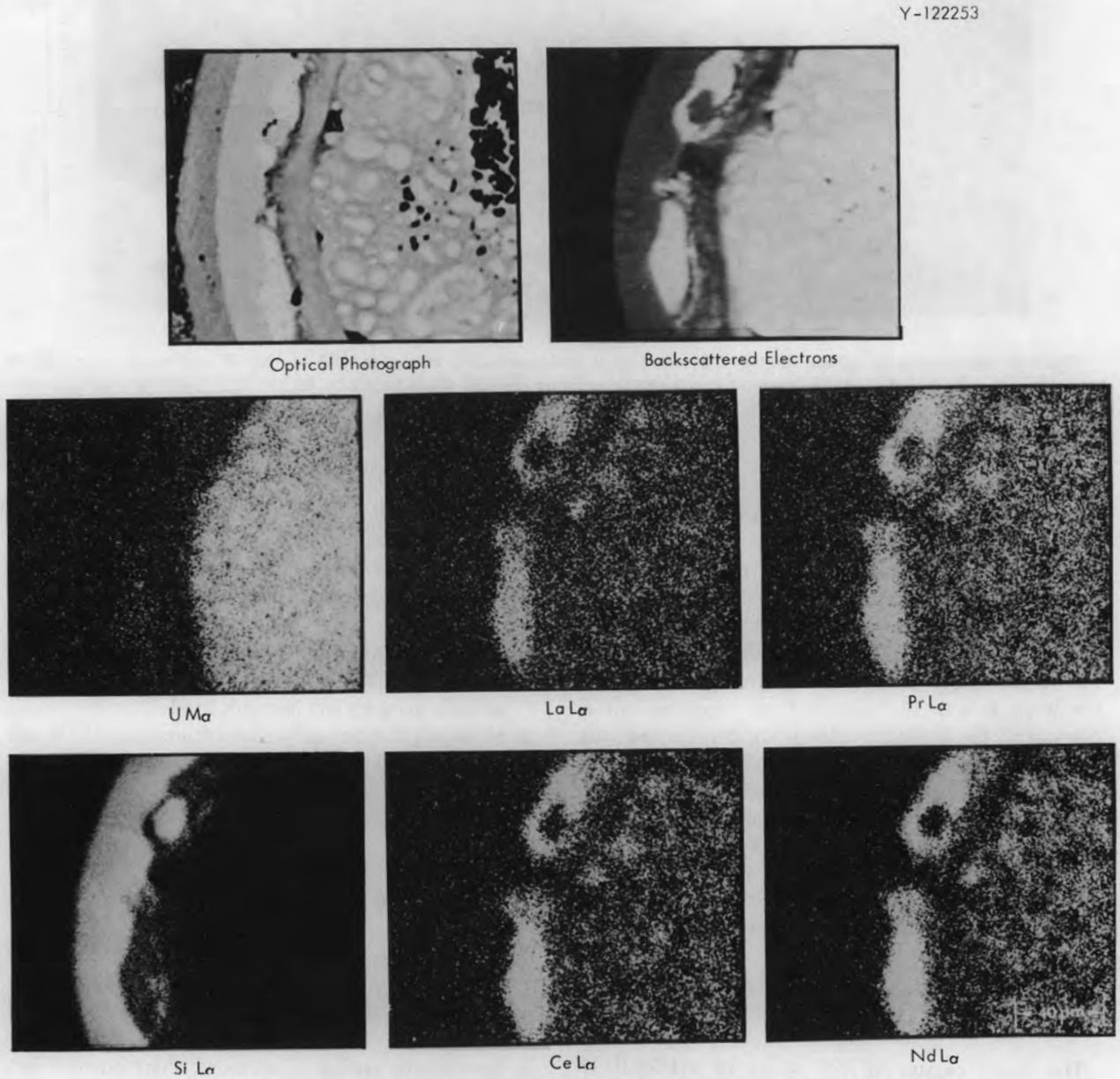

Fig. 7.24. Microprobe results from a molten WAR kernel in fuel rod 3B, irradiation capsule HRB-4.

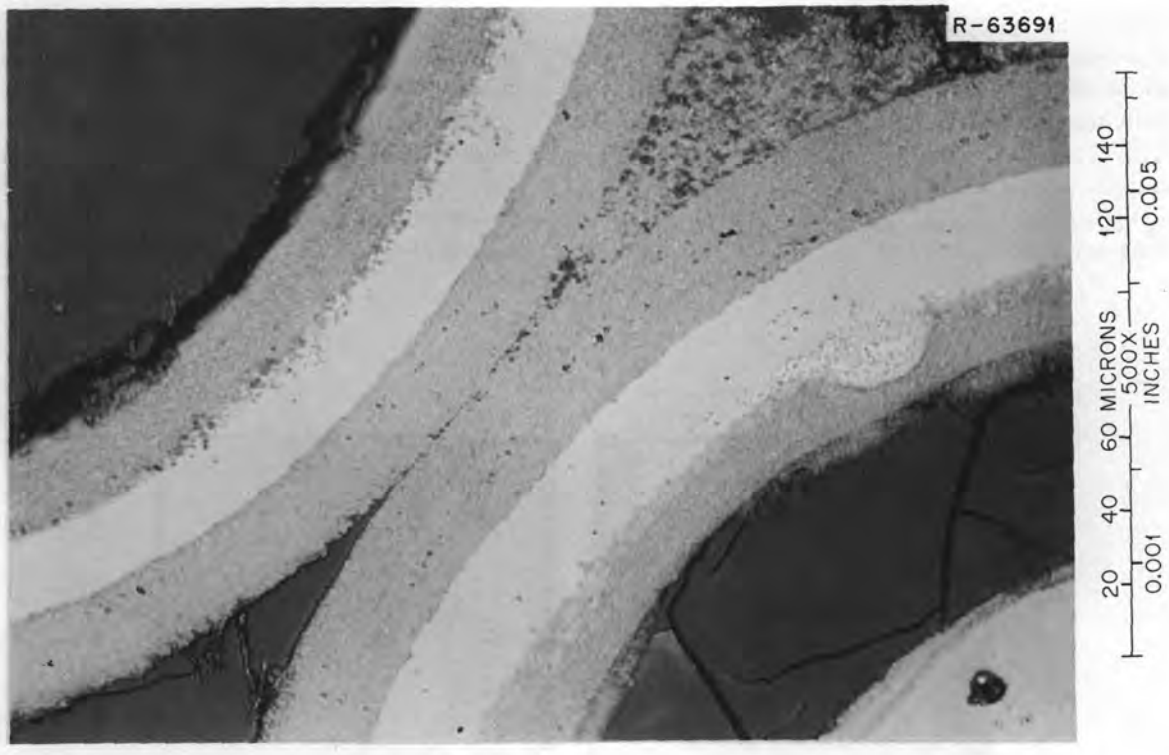

Fig. 7.25. Metallographic section through Triso coatings of fissile particles irradiated in HRB-4. The SiC coating on the left shows the results of attack by rare-earth fission products; the SiC coating on the right shows attack by Pd.

difference between the hot and cold side of the buffer layer.

The extruded rods operated at a higher heat rating and in a higher flux than the slug-injected rods. However, the overall temperature of the extruded rod was lower than that of the slug-injected rods because of the higher matrix density. Metallography showed that the WAR kernels had densified, as expected; but in contrast to the fissile particles in the slug-injected rods, there was *no* evidence of fission product attack on the SiC layers. Although only a relatively few (23) WAR kernels were exposed in the plane of polish, there was no clear evidence that any of the kernels were in the molten state during irradiation. Examination of the fertile particles showed no evidence of the "amoeba" effect or indication of potential failure.

7.1.3 Capsule HRB-6

R. L. Hamner

The sixth capsule in the series of HTGR-HFIR irradiation experiments in the RB facility (RB-5) was inserted in March 1973. The capsule, designated HRB-6, was instrumented and swept with inert-gas mixtures in order to monitor the fuel performance. The experiment had five main objectives as follows:

1. to compare the irradiation behavior of Biso-coated 4:1 (Th,^{233}U)O_2 with Biso-coated 4:1 (Th, ^{235}U)O_2 as loose particles and in bonded rods;
2. to supply samples of particles containing ^{233}U and ^{235}U for study of fission product retention within the coated particles and within a carbonaceous matrix;
3. to determine whether the differing fission product spectra from ^{233}U and ^{235}U affect the carbon transport and kernel migration within coated particles;
4. to further test fueled specimens prepared by extrusion, slug injection, and intrusion bonding for dimensional stability when irradiated to full HTGR fluence;
5. to continue testing of ultrasonic thermometers as a means of measuring center-line temperature.

Capsule HRB-6 was similar to HRB-5 except that the fuel loading consisted only of highly enriched mixed-oxide fissile particles and ThO_2 fertile particles. An ultrasonic thermometer was used to monitor the fuel central temperatures, as in HRB-5, and the column of fuel rod specimens contained 2 extruded rods along with the 11 injection-bonded specimens. The capsule was inserted in the RB-5 facility of the HFIR on Feb. 27, 1973, and operated for 8 cycles (183.4 days at power) to a maximum fast-neutron fluence of 7.9×10^{21} neutrons/cm^2 ($E > 0.18$ MeV).

Examination of the slug-injected fuel rods indicated no significant difference in relative thermal stability of the mixed-oxide fissile particles containing ^{233}U and ^{235}U as shown in Fig. 7.26. Although many of the Biso-coated (Th,^{233}U)O_2 particles failed, the failures were related to the properties of the coating on this batch. Both types of kernel migrated up the temperature gradient a maximum distance of 20 to 25 μm, but no other adverse effects were noted. Comparison of the performance of Biso and Triso (Th,^{235}U)O_2 particles in the extruded rods revealed no significant difference. The appearance and dimensional behavior of the extruded rods after irradiation was very good, as was the case in capsules HRB-4 and -5. Details of the specimen characteristics, capsule operation, and fuel performance evaluation are being compiled in a separate report.[7]

7.1.4 Capsules HRB-7 and -8

R. L. Hamner

The seventh and eighth capsules in the series of HTGR-HFIR experiments in removable beryllium (RB) facilities are scheduled for insertion in early 1974 after preirradiation in a permanent beryllium (PB) facility for two cycles. The preirradiation was considered necessary because of the high initial power densities calculated for the fully enriched fissile particles if placed in an RB facility at the beginning of the experiments. To avoid this, the capsules will be irradiated in the PB facility, where ~50% of the ^{235}U will be burned out before removal to the RB facility. The capsules, designated HRB-7 and -8, are similar to those for previous HRB experiments in that they will be instrumented and swept with inert gases in order to monitor fuel performance and control temperatures. The capsules are identical with regard to types of specimens, but their operation will differ in that HRB-7 is expected to have a fuel center-line temperature of 1500°C while that for HRB-8 is expected to be 1250°C. The overall objective for these experiments is to screen a relatively large number of types of fissile particles for performance at high temperatures and high burnup rates. More specific objectives are given below.

1. To test a theoretical model for amoeba migration. The kernels of primary interest are (1) mixed oxide-carbide derived from sol-gel microspheres, because the two-phase mixture is thought to be more stable than oxide fuel kernels, and (2) uranium oxynitride derived from sol-gel microspheres, because thermochemical calculations suggest improved performance under HTGR conditions of fluence and temperature. A sol-gel UO_2 particle will be used as reference for comparison with the other two particles.
2. To test potential recycle fuel candidates. These include sol-gel UO_2, WAR UC_2, and sol-gel (4Th,U)O_2. Comparisons will be made between ^{233}U- and ^{235}U-bearing particles and between Biso- and Triso-coated particles.
3. To establish the relative stability of mixed-oxide sol-gel particles having thorium-to-uranium ratios of 0, 1, 2, 4, and 8. The latter is of interest also to GAC for first core loadings.
4. To test advanced coating designs from GAC in which ZrC is substituted for SiC in their reference makeup particle.
5. To compare the performance of a WAR UO_2-UC_2 particle to that of the GAC reference makeup particle at very high temperatures.
6. To test mixed-oxide fissile particles prepared in a production-size coater (5 in. diam).
7. To test a multijunction tungsten-rhenium thermocouple for measuring center-line temperatures at different locations in the capsule.

Design

Capsules HRB-7 and -8 are identical and are similar to the capsules HRB-4, -5, and -6. They differ only in the fueled specimens, the graphite sleeve dimensions, and the use of a new central thermocouple concept.

The capsules have 19 fuel specimens each (Fig. 7.27). Instead of adjusting the thermal resistance of the gas gap to compensate for the axial variation in thermal flux, we adjusted the specimen fissile and fertile material content so as to approximate a uniform axial heat generation. With this type of loading it was possible to use a uniform gas gap and eliminate the

7. F. J. Homan et al., *Performance of Extruded and Slug-Injected Fuel Rod Specimens in Capsule HRB-6*, ORNL-TM (in preparation).

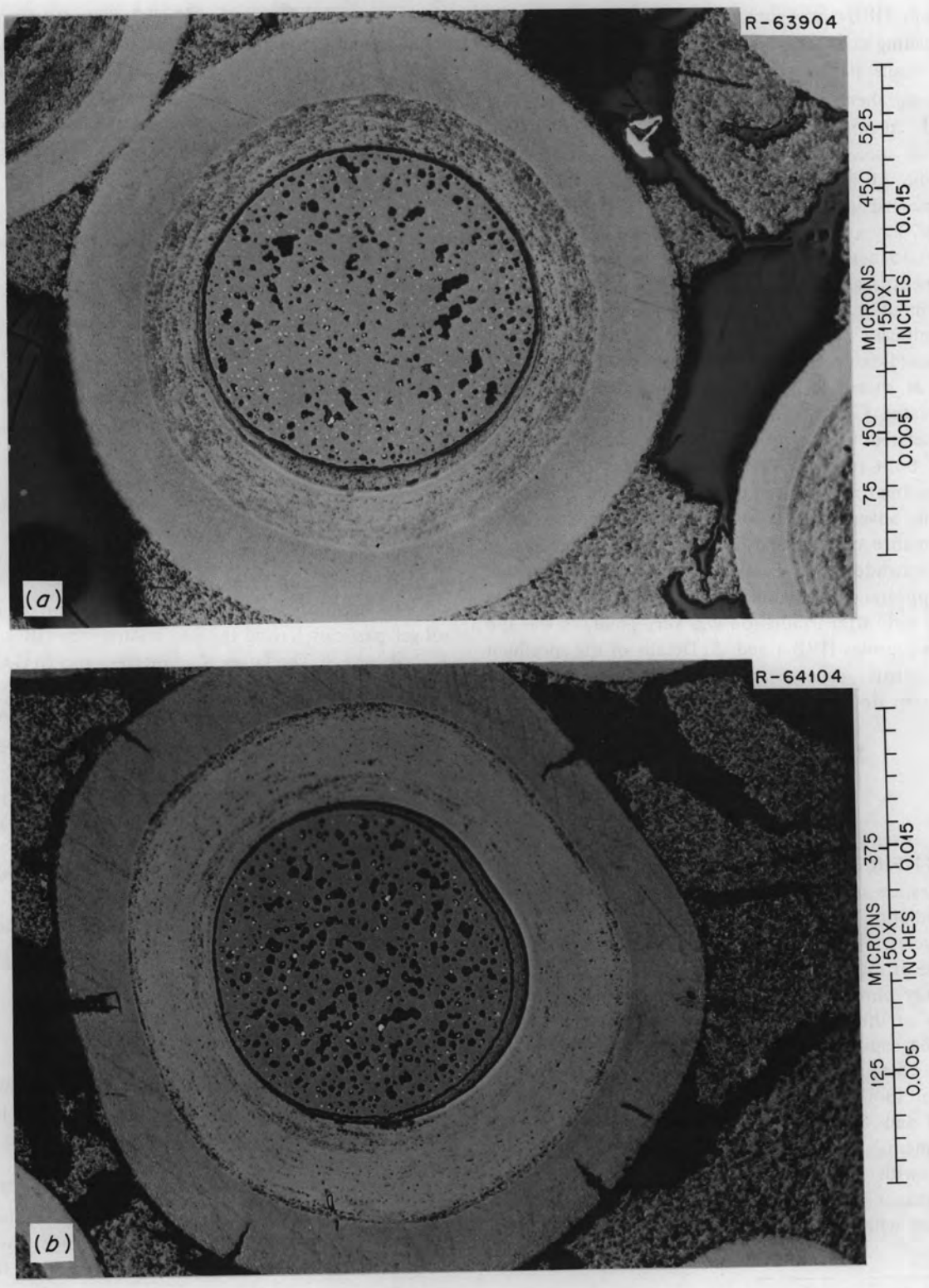

Fig. 7.26. Biso-coated (4Th,^{233}U)O_2 kernels in slug-injected fuel rod specimen 3A irradiated in HRB-6. 100X

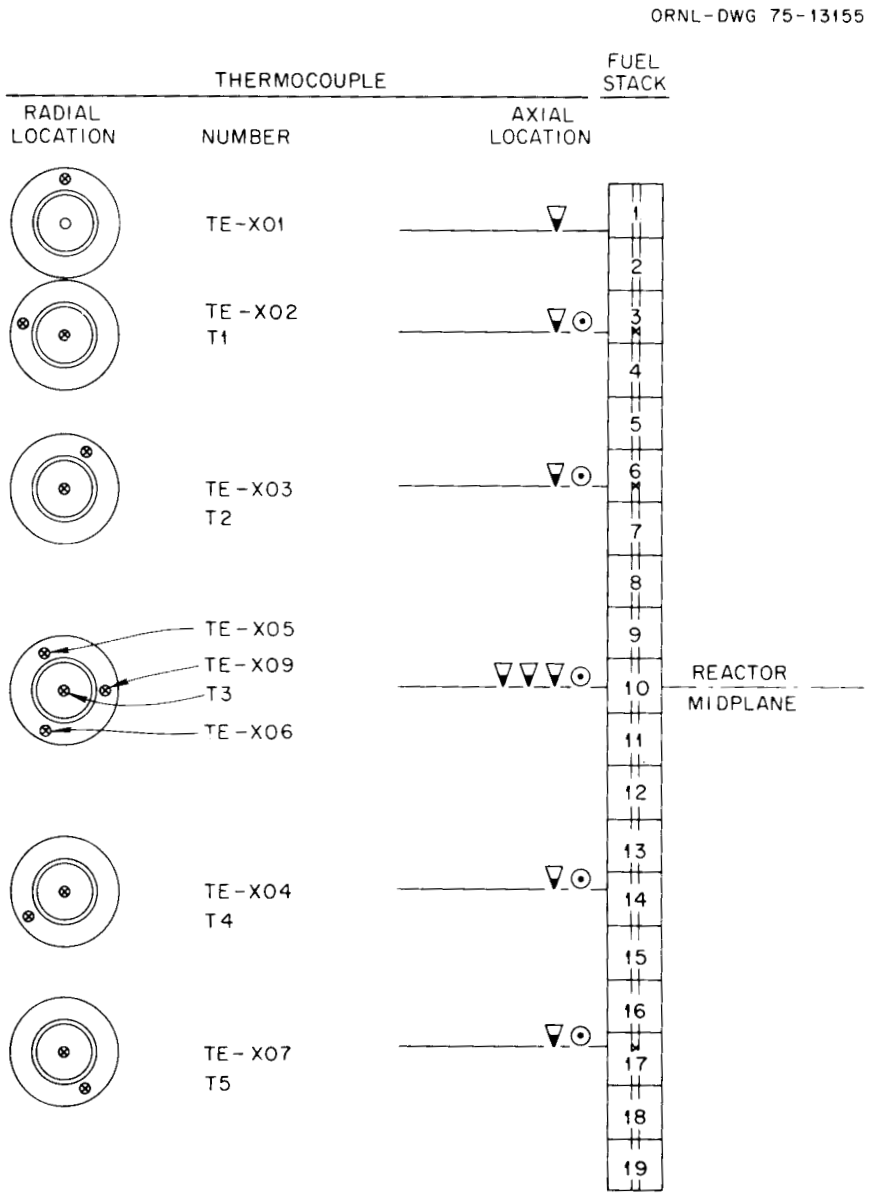

Fig. 7.27. Capsules HRB-7 and HRB-8.

taper on the graphite sleeve. The thermocouple locations are shown in Fig. 7.27. The graphite sleeve thermocouples are stainless-steel-sheathed Chromel/Alumel, as has been the case for the previous HRB capsules. The central temperature is monitored by a special five-junction W–5% Re/W–26% Re thermocouple. All the fuel specimens have a central hole for this thermocouple, and the junctions are distributed over the length of the fuel column. (See Section 7.7 for details.)

The proposed schedule for insertion of each capsule is as follows:

HRB-7: In PB-13 mid-December 1973
Out PB-13 first of February 1974
In RB-7 first of February 1974

HRB-8: In PB-13 first of February 1974
Out PB-13 end of March 1974
In RB-5 end of March 1974

Insertion of HRB-7 in PB-13 was on schedule.

The capsules will be irradiated in the RB facility to a fast fluence of 8×10^{21} neutrons/cm^2 or until a failure of fuel particles as evidenced by bursts of fission-gas release.

Preparation and characterization of test specimens

A brief description of the particles involved, their purposes in the experiments, and their positions in the capsules are given in Table 7.11. The characterizations of all particles after heat treatment at 1800°C are given in Table 7.12. Particles supplied by GAC were not heat treated at ORNL.

Seventeen types of fissile particles are being tested in both experiments. A driver particle, $^{238}UO_2$-UC_2, was included to maintain the desired temperature as the ^{235}U is burned out and until sufficient ^{233}U is

Table 7.11. Fissile particles and positions in HRB-7 and HRB-8 capsules[a]

Position in capsule	Kernel type	Nominal kernel diameter (μm)	Coating type	Purpose in experiment
1	$^{235}UC_2$–1% Th[b]	200	Triso	GAC reference
2	SG (4Th,^{235}U)O_2	350	Biso	Test particle prepared in large coater
3	SG $^{235}UO_2 + U_2N_3$	200	Biso	To study amoeba effect
4	SG $^{235}UO_2 + UC_2$	200	Biso	To study amoeba effect
5	SG $^{233}UO_2$	215	Triso	Potential candidate for recycle; compare with $^{235}UO_2$
6	SG $^{235}UO_2$	200	Biso	Reference for amoeba effect; compare Biso with Triso
7	SG $^{235}UO_2$	200	Triso	Reference for amoeba effect; compare Triso with Biso
8	SG (2Th,^{235}U)O_2	300	Biso	Relative stability; Th:U ratio
9	SG (4Th,^{235}U)O_2	350	Triso	Recycle candidate
10 RHMP	SG (8Th,^{235}U)O_2[b]	500	Triso	Relative stability; Th:U ratio; interest for first-core loadings
11	SG (4Th,^{235}U)O_2	350	Biso	Relative stability; Th:U ratio
12	SG (Th,^{235}U)O_2	250	Biso	Relative stability; Th:U ratio
13	WAR $^{235}UO_2 + UC_2$	400	Triso	Compare with GAC reference makeup particle
14	WAR $^{235}UC_2$	300	Triso	Recycle candidate; compare Triso with Biso
15	WAR $^{235}UO_2 + UC_2$	400	Biso	Compare Biso with Triso
16	WAR $^{235}UC_2$	300	Biso	Recycle candidate; compare Biso with Triso
17	$^{235}UC_2$ with ZrC in coating[b]	200	Triso	Test GAC advanced coating design
18	$^{235}UC_2$–1% Th[b]	200	Triso	GAC reference
19	SG (4Th,^{235}U)O_2	350	Biso	Test particle prepared in large coater
	Other particles – not intended primarily for test			
	WAR $^{238}UO_2 + UC_2$	400	Biso	To maintain temperature after ^{235}U burned out and before heat generation from fertile particle begins
	ThO_2 SG	500	Biso	Fertile particle
	Inert (desulfurized SAR)	500	Biso	Filler particle for volume loading

[a]SG = derived by sol-gel process; WAR = derived from weak-acid resin; SAR = derived from strong-acid resin; RHMP = reactor horizontal midplane.
[b]To be coated by GAC; kernel prepared by GAC's VSM process.

Table 7.12. Characterization of coated particles for HRB-7 and -8

Batch No.	6151-00-035[a]	J-263	OR-2098H	OR-2097H	Pu-303H
Position in capsule	1 and 18	2 and 19	3	4	5
Kernel material[b]	UC_2 – 1% ThC_2[c]	$(4Th,U)O_2$	$UO_2 + U_2N_3$	$UO_2 + UC_2$	UO_2
Uranium content, wt %	18.86	7.25	23.65	24.91	25.5
^{235}U enrichment, at. %	93.15	93.17	93.17	93.17	
^{233}U enrichment, at. %					98.05
Thorium content, wt %	0.19	29.74			
	Mean[d]	Mean	Mean	Mean	Mean
Kernel					
Diameter, μm	196 (16)	353.8 (5.9)	192.5 (4.7)	193.8 (5.8)	226.8 (11.0)
Density, g/cm^3	10.99	9.8	9.9	10.5	10.08
Buffer					
Thickness, μm	99 (10.6)	101.2 (13.8)	70.7 (9.6)	67.6 (8.2)	84.7 (10.9)
Density, g/cm^3	1.07	1.39	1.2	1.19	0.90
Inner carbon coating					
Thickness, μm	33 (3.5)				35.1 (5.7)
Density, g/cm^3	1.92 (NA)				2.0 (ND)
SiC					
Thickness, μm	32 (5.3)				27.1 (1.5)
Density, g/cm^3	3.20 (NA)				3.193 (0.001)
Outer carbon coating					
Thickness, μm	38 (5.0)	91.8 (9.6)	75.6 (7.2)	78.4 (4.9)	40.7 (2.9)
Density, g/cm^3	1.85 (NA)	2.01 (0.007)	2.006 (0.004)	1.998 (0.004)	2.024 (0.005)

Batch No.	OR-2089H	OR-2114H	OR-2094H	OR-2116H	6155-01-020[a]
Position in capsule	6	7	8	9	10
Kernel material[b]	UO_2	UO_2	$(2Th,U)O_2$	$(4Th,U)O_2$	$(8Th,U)O_2$
Uranium content, wt %	22.41	16.99	10.44	6.50	5.23
^{235}U enrichment, at. %	93.17	93.17	93.17	93.13	93.15
^{233}U enrichment, at. %					
Thorium content, wt %			20.79	26.50	43.59
	Mean[d]	Mean	Mean	Mean	Mean
Kernel					
Diameter, μm	195.6 (5.9)	195.9 (5.2)	282.0 (13.2)	360.0 (4.7)	502 (23.1)
Density, g/cm^3	9.97	9.83	10.17	9.8	9.77
Buffer					
Thickness, μm	74.8 (8.6)	85.0 (9.8)	84.5 (7.9)	97.7 (8.7)	106 (17.6)
Density, g/cm^3	1.25	1.28	1.26	1.36	1.24
Inner carbon coating					
Thickness, μm		37.0 (ND)		38.8 (2.9)	32 (4.3)
Density, g/cm^3		2.0 (ND)		2.0 (ND)	1.93 (ND)
SiC					
Thickness, μm		27.3 (1.8)		33.6 (1.9)	34 (6.7)
Density, g/cm^3		3.174 (0.009)		3.205 (0.003)	3.22 (ND)
Outer carbon coating					
Thickness, μm	77.1 (4.7)	46.4 (2.3)	89.0 (6.2)	42.9 (3.0)	42 (6.1)
Density, g/cm^3	2.01 (0.003)	1.977 (0.001)	2.006 (0.003)	2.037 (0.002)	1.81 (ND)

Table 7.12 (continued)

Batch No.	OR-2111H	OR-2090H	OR-2115H	OR-2121H	OR-2106H
Position in capsule	11	12	13	14	15
Kernel material[b]	$(4Th,U)O_2$	$(Th,U)O_2$	WAR UO_2 + UC_2	WAR UC_2	WAR UO_2 + UC_2
Uranium content, wt %	7.24	13.5	19.13	20.03	21.75
^{235}U enrichment, at. %	93.17	93.17	93.18	93.32	93.18
^{233}U enrichment, at. %					
Thorium content, wt %	29.98	13.36			
	Mean[d]	Mean	Mean	Mean	Mean
Kernel					
Diameter, μm	360.0 (4.7)	245.5 (19.0)	385.8 (29.0)	315.3 (29.1)	385.8 (29)
Density, g/cm^3	9.8	8.58	3.18	5.28	3.18
Buffer					
Thickness, μm	95.1 (7.2)	78.5	40.9 (6.8)	74.6 (11.3)	40.9 (6.8)
Density, g/cm^3	1.36	1.28	1.37	1.10	1.37
Inner carbon coating					
Thickness, μm			42.9 (3.6)	36.1 (3.8)	
Density, g/cm^3			2.0 (ND)	2.0 (ND)	
SiC					
Thickness, μm			32.1 (1.9)	28.4 (2.7)	
Density, g/cm^3			3.187 (0.003)	3.188 (0.006)	
Outer carbon coating					
Thickness, μm	94.6 (5.5)	84.4 (7.0)	48.8 (4.0)	49.2 (3.3)	99.0 (7.1)
Density, g/cm^3	2.040 (0.002)	2.008 (0.004)	1.986 (0.005)	1.982 (0.004)	2.003 (0.005)

Batch No.	OR-2120H	6171-63E[a]	J-262	OR-2104H	OR-2079H
Position in capsule	16	17	1–19	1–19	1–19
Kernel material[b]	WAR UC_2	UC_2[c]	ThO_2	WAR UO_2 + UC_2	SAR carbon
Uranium content, wt %	23.66	20.7		29.11	
^{235}U enrichment, at. %	93.32	93.15		0.7	
^{233}U enrichment, at. %					
Thorium content, wt %			54.05		
	Mean[d]	Mean	Mean	Mean	Mean
Kernel					
Diameter, μm	315.3 (29.1)	197 (24)	497.0 (3.2)	426.2 (31.4)	471.5 (24.6)
Density, g/cm^3	5.28		10.0	3.34	1.37
Buffer					
Thickness, μm	74.6 (11.3)	102 (9.5)	84.0 (13.4)	42.3 (7.7)	77.3 (ND)
Density, g/cm^3	1.10	1.00	1.19	1.11	0.95
Inner carbon coating					
Thickness, μm		8.4 (1.2)			
Density, g/cm^3		1.80 (NA)			
SiC[e]					
Thickness, μm		21.0 (0.0)			
Density, g/cm^3		6.5 (NA)			
Outer carbon coating					
Thickness, μm	88.6 (6.6)	65 (3.8)	86.1 (10.9)	83.1 (9.0)	95.3 (6.6)
Density, g/cm^3	1.989 (0.003)	1.73 (NA)	2.008 (0.006)	2.016 (0.006)	1.963 (0.013)

[a] Supplied by GAC.

[b] Kernels derived by sol-gel process unless otherwise noted.

[c] Prepared by GAC's VSM process.

[d] Numbers in parentheses are standard deviations. NA = not available; ND = not determined; WAR = derived from weak-acid resin; SAR = strong-acid resin, desulfurized.

[e] ZrC substituted for SiC.

Table 7.13. Fuel specification loading, location, and flux (capsules HRB-7 and -8)

Length (in.)	Volume (cm^3)	Fuel loading (g/cm^3)			Reactor HMP to specimen center (in.)	Average thermal flux ($E < 0.414$ eV) (neutrons cm^{-2} sec^{-1})	Fast flux ($E > 0.18$ MeV) (neutrons cm^{-2} sec^{-1})
		^{235}U	^{238}U	^{232}U			
						$\times 10^{13}$	$\times 10^{14}$
0.79	2.4412	0.01802	0.15375	0.17334	7.20	61.8	2.95
0.79	2.4412	0.01802	0.15375	0.17334	6.40	70.7	3.31
0.79	2.4412	0.01604	0.11056	0.16648	5.60	79.5	3.66
0.79	2.4412	0.01604	0.11056	0.16648	4.80	88.0	3.97
0.79	2.4412	0.01461	0.08144	0.16062	4.00	95.7	4.28
0.79	2.4412	0.01461	0.08144	0.16062	3.20	102.7	4.55
0.79	2.4412	0.01461	0.08144	0.16062	2.40	109.0	4.78
0.79	2.4412	0.01375	0.06990	0.15758	1.60	114.0	4.92
0.79	2.4412	0.01375	0.06990	0.15758	0.80	117.1	5.00
0.79	2.4412	0.01375	0.06990	0.15758	0	118.0	5.00
0.79	2.4412	0.01375	0.06990	0.15758	0.80	117.1	5.00
0.79	2.4412	0.01375	0.06990	0.15758	1.60	114.0	4.92
0.79	2.4412	0.01461	0.08144	0.16062	2.40	109.0	4.78
0.79	2.4412	0.01461	0.08144	0.16062	3.20	102.7	4.55
0.79	2.4412	0.01461	0.08144	0.16062	4.00	95.7	4.28
0.79	2.4412	0.01604	0.11056	0.16648	4.80	88.0	3.97
0.79	2.4412	0.01604	0.11056	0.16648	5.60	79.5	3.66
0.79	2.4412	0.01802	0.15375	0.17334	6.40	70.7	3.31
0.79	2.4412	0.01802	0.15375	0.17334	7.20	61.8	2.35

generated in the fertile particle to maintain temperature.

The coated particles are contained in close-packed bonded rods formed by slug injection. The matrix materials for all specimens are 28.5 wt % Asbury NF 6353 graphite filler in Ashland grade 240 pitch. Each type of fissile particle was incorporated in separate specimens nominally 0.490 in. OD by 0.8 in. long with a central hole for thermocouple placement. The same fertile, ^{238}U driver, and inert particles were used in all specimens as required for heavy metal and particle volume loadings. Approximately 170 specimens were fabricated for the experiments and for the necessary characterizations and archival samples (see Sect. 6.2.2 for details of fabrication). After final heat treatment at 1800°C, matrix densities were 0.61 g/cm^3 except for the ^{233}U-bearing specimens, which were 0.5 g/cm^3; particle volume loadings were 60%; ^{235}U loadings ranged from 0.014 g/cm^3 at the reactor horizontal midplane to 0.019 g/cm^3 at the capsule extremes; the ^{238}U loadings ranged from 0.72 g/cm^3 at the midplane to 0.159 g/cm^3 at the capsule extremes; and the ^{232}Th loadings varied from 0.160 g/cm^3 at the midplane to 0.178 g/cm^3 at the capsule extremes. Design loading values are given in Table 7.13.

7.2 IRRADIATION TESTS IN THE HFIR TARGET FACILITY

A second type of HFIR capsule is the target, or HT, capsule, which is a small uninstrumented device consisting of an aluminum tube with an external configuration identical to that of a HFIR target rod. The design of typical target capsules has been described previously.[8] These capsules contain small specimens of coated-particle fuels and fuel-element materials in the form of loose particles, bonded fuel rods, pyrolytic-carbon specimens, and experimental graphites. The specimens can be irradiated at temperatures up to 1600°C, depending on the heat flux and specimen type, and to representative HTGR end-of-fuel-life fast-flux exposure in about three months. The test specimens are, in general, contained in cylindrical graphite specimen holders or magazines which occupy the central 20 in. of the capsule. The graphite holders are centered within the capsule by graphite and nickel supports which, in

8. B. H. Montgomery, "Target Irradiation Tests," *GCR-TU Programs Annu. Progr. Rep. Sept. 30, 1971*, ORNL-4760, pp. 134–36.

addition, provide a thermal barrier at the specimen holder ends to minimize axial heat losses.

These capsules have the advantage of low cost and short irradiation time to attain representative exposure. However, the capsules are sealed (thus a gas sweep is not possible) and are not instrumented. Temperatures can only be determined by calculations based on the fission and gamma heat values and capsule geometry and/or deduced by postirradiation evaluation of melt wires or silicon carbide temperature monitors. Also, only small specimens with very small amounts of fissile material can be accommodated.

The HT irradiations conducted during the reporting period are summarized in Table 7.2. Irradiation and PIE on the series HT-12 through -15 and HT-16 were completed. Irradiation of the series HT-17 through -19 was completed and PIE initiated.

7.2.1 Capsules HT-12 through -15

Capsules HT-12 through -15, described previously,[9] were designed to test fertile-type particles with different coating parameters to conditions which would induce predictable failures and thereby establish mineral coating design criteria.

Design

Each capsule contained four tubular graphite specimen holders or magazines. Each holder in turn contained 13 small graphite containers with an annular cavity which held 50 to 75 coated particles each (Fig. 7.28). Two of the tubular holders were designed to develop a 900°C temperature in the particle containers and the other two a 1250°C particle container temperature.

Of the 13 particle containers in each holder, 8 contained fertile particles; the others contained low-enriched UO_2 particles. The type of specimen, ThO_2 and UO_2, were alternated along the capsule length. The UO_2 was added specifically to produce a more uniform power generation and hence specimen temperature over the life of the experiment. It takes considerable time before power generation from ^{233}U bred from the thorium reaches equilibrium. By adding low-enriched UO_2 one can minimize the variation in specimen temperature with time.

9. *GCR Programs Annu. Progr. Rep. Dec. 31, 1972*, ORNL–4911, pp. 113–15.

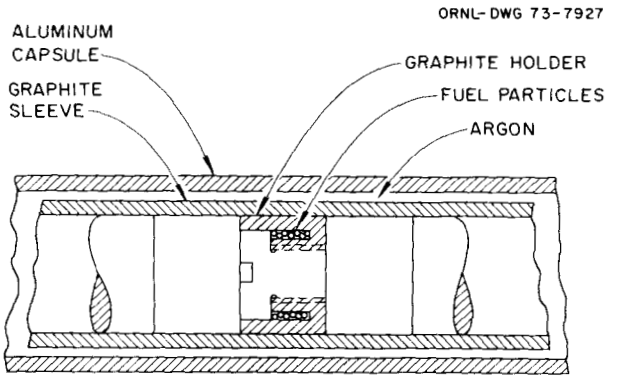

Fig. 7.28. Cross section of HT-12 through-15 coated-particle irradiation capsule.

Operation

Target capsule HT-12 was inserted in target position F-3 on Sept. 10, 1972, and was removed on Oct. 23, 1972, after 38.62 days at 100 MW reactor power. The peak fast fluence was 3.9×10^{21} neutrons/cm^2 ($E > 0.18$ MeV), and the peak fertile particle burnup was 2.9% FIMA.

Capsule HT-13 was inserted in target position G-6 on Oct. 8, 1972, and was removed on Jan. 10, 1973, after 85.5 days at 100 MW reactor power. The peak fast fluence was 8.6×10^{21} neutrons/cm^2 ($E > 0.18$ MeV), and the estimated peak fertile particle burnup was 9.7% FIMA.

Capsule HT-14 was inserted in target position F-3 on Nov. 20, 1972, and was removed on Apr. 15, 1973, after 137.0 days at 100 MW reactor power. The peak fast fluence was 1.4×10^{22} neutrons/cm^2 ($E > 0.18$ MeV), and the estimated peak fertile particle burnup was 17.3% FIMA.

Capsule HT-15 was inserted in target position A-2 on Nov. 20, 1972, and was removed on May 11, 1973, after 159.96 days at 100 MW reactor power. The peak fast fluence was 1.6×10^{22} neutrons/cm^2 ($E > 0.18$ MeV), and the estimated peak fertile particle burnup was 20.3% FIMA.

Table 7.14 gives the fast fluence and fertile particle burnup for each sample holder in each capsule. No attempt was made to calculate the fissile particle burnup. Table 7.15 gives the operating history of the reactor during the irradiation of each capsule.

Table 7.14. Particle fast fluence and fertile particle burnup (capsules HT-12 through -15)

Sample holder No.	Fast-neutron fluence, $E > 0.18$ MeV (neutrons/cm^2)				Fast-neutron flux, $E > 0.18$ MeV (neutrons cm^{-2} sec^{-1})	Distance from holder center line to HMP (in.)	Fertile particle burnup (% FIMA)			
	HT-12	HT-13	HT-14	HT-15			HT-12	HT-13	HT-14	HT-15
	$\times 10^{21}$	$\times 10^{21}$	$\times 10^{21}$	$\times 10^{21}$	$\times 10^{15}$					
1, 52	1.9	4.1	6.6	7.7	0.56	9.199				
2, 51	2.0	4.3	6.9	8.1	0.59	8.909	0.95	4.53	9.56	11.91
3, 50	2.1	4.6	7.4	8.7	0.63	8.626				
4, 49	2.2	4.9	7.9	9.3	0.67	8.344	1.06	5.00	10.45	13.00
5, 48	2.3	5.2	8.3	9.7	0.70	8.601	1.10	5.20	10.90	13.50
6, 47	2.4	5.4	8.6	10.1	0.73	7.779				
7, 46	2.5	5.6	9.0	10.5	0.76	7.496	1.21	5.62	11.67	14.42
8, 45	2.6	5.8	9.4	11.0	0.80	7.214	1.26	5.84	12.05	14.90
9, 44	2.7	6.0	9.7	11.3	0.82	6.931				
10, 43	2.8	6.2	10.0	11.7	0.85	6.649	1.37	6.22	12.75	15.72
11, 42	2.9	6.5	10.4	12.2	0.88	6.366	1.40	6.40	13.08	16.10
12, 41	3.0	6.7	10.8	12.6	0.91	6.084				
13, 40	3.1	6.9	11.0	12.8	0.93	5.801	1.50	6.75	13.70	16.82
14, 39	3.5	7.7	12.4	14.5	1.05	4.199				
15, 38	3.5	7.8	12.5	14.6	1.06	3.909	1.71	7.70	15.30	18.72
16, 37	3.6	7.9	12.7	14.9	1.08	3.626				
17, 36	3.6	8.1	12.9	15.1	1.09	3.344	1.78	7.90	15.67	19.12
18, 35	3.7	8.2	13.1	15.3	1.11	3.061	1.80	8.00	15.82	19.32
19, 34	3.7	8.3	13.3	15.5	1.12	2.779				
20, 33	3.8	8.3	13.4	15.6	1.13	2.496	1.82	8.15	16.10	19.65
21, 32	3.8	8.4	13.5	15.7	1.14	2.214	1.86	8.21	16.21	19.80
22, 31	3.8	8.5	13.6	15.9	1.15	1.931				
23, 30	3.9	8.5	13.7	16.0	1.16	1.649	1.90	8.33	16.42	20.03
24, 29	3.9	8.6	13.8	16.1	1.16	1.366	1.91	8.38	16.50	20.15
25, 28	3.9	8.6	13.9	16.2	1.17	1.084				
26, 27	3.9	8.6	13.9	16.2	1.17	0.801	1.92	8.43	16.60	20.30

Table 7.15. Operational history of capsules HT-12 through -15

HFIR cycle	Begin cycle	End cycle	Days operation	Accumulated irradiation time at 100 MW reactor power (days)
		Capsule HT-12		
82	9/10/72	10/3/72	23	23.44
83	10/8/72	10/23/72	15	38.62
		Capsule HT-13		
83	10/8/72	10/23/72	15	15.18
84A	10/24/72	11/11/72	18	
84B	11/13/72	11/19/72	5	38.55
85	11/20/72	12/13/72	23	74.14
86[a]	12/13/72	1/7/73	24	84.90
87A	1/9/73	1/10/73	<1	85.50
		Capsule HT-14		
85	11/20/72	12/13/72	23	23.09
86[a]	12/13/72	1/7/73	24	46.35
87A	1/9/73	1/10/73	<1	
87B	1/12/73	2/3/73	21	68.86
88	2/3/73	2/26/73	23	91.41
89	2/27/73	3/22/73	23	114.14
90	3/23/73	4/15/73	23	137.00
		Capsule HT-15		
85	11/20/72	12/13/72	23	23.09
86[a]	12/13/72	1/7/73	24	46.35
87A	1/9/73	1/10/73	<1	
87B	1/12/73	2/3/73	21	68.86
88	2/3/73	2/26/73	23	91.41
89	2/27/73	3/22/73	23	114.14
90	3/23/73	4/15/73	23	137.00
91	4/18/73	5/11/73	23	159.96

[a]Includes two days at 50 MW.

Postirradiation examination and analysis

Capsule HT-12. HT-12 was irradiated for two cycles (39 days) in the HFIR to a fast-neutron exposure ranging from 1.9 to 3.9 $\times 10^{21}$ neutrons/cm^2 (>0.18 MeV). When opened, the capsule and magazines were observed to be remarkably free of the sooty material previously found in most target capsules. No evidence of pitting or corrosion on the graphite magazines was observed. This is attributed to the gettering action of zirconium foil disks used between the specimen holders in the magazines.

The ORNL samples performed without failures except for one that had a 24-μm-thick isotropic carbon coating and a flash buffer on a 402-μm-diam kernel. Failure of 55% (41 of 75 particles) was not unexpected and is consistent with assumed values of 25,000 psi tensile strength and a creep rate of 5×10^{-28} psi^{-1} (neutrons/cm^2)$^{-1}$ ($E > 1.86$ eV) in the LTI coating.

Capsule HT-13. HT-13 was irradiated for four cycles (85 days) in the HFIR to a fast-neutron exposure ranging from 4.1 to 8.6 $\times 10^{21}$ neutrons/cm^2 (>0.18 MeV). When opened, the capsule and magazines were observed to be free of soot as in HT-12. However, an important observation from this examination was the degradation and swelling of the Poco graphite sample holders exposed in the high-temperature region. Even though there was no evidence of oxidation or mass transport in the sealed capsule, the graphite was so weak and friable that the screw caps could not be removed without drilling out the threads.

At 1250°C, all ORNL samples with 400-μm-diam kernels and thin coatings for which the calculated stresses exceeded 25,000 psi showed complete or a high rate of failure, while similar samples with conservatively designed coatings survived. One sample (proposed reference) with a 500-μm-diam kernel and a conservative coating design also survived completely, while a similar sample with thinner coatings failed almost completely. At the low temperature, all ORNL samples survived except for 13% failure of one that had an intermediate coating design. With this one exception, the performance of these samples is consistent with assumed values of 25,000 psi tensile rupture strength and a creep rate of 5×10^{-28} psi^{-1} (neutrons/cm^2)$^{-1}$ ($E > 1.86$ eV) in the outer coating.

Capsule HT-14. HT-14 was irradiated for six cycles (137 days) in the HFIR to a fast-neutron exposure ranging from 6.6 to 13.9 $\times 10^{21}$ neutrons/cm^2 (>0.18 MeV). When opened, the capsule and magazines were relatively free of soot and showed no evidence of corrosion. The two low-temperature magazines (design temperature 900°C) were unloaded without difficulty, and the samples of coated particles were easily recovered. However, the two magazines and associated graphite holders in the high-temperature region exhibited extreme swelling. Diametral expansion of sample holders designed to operate at 1250°C was as great as 7.5%. Unloading of these holders was difficult because the graphite was very weak. The extreme swelling nearly closed the gap between magazine and capsule walls, which made the operating temperatures during the latter part of the irradiation lower, but quite uncertain.

The unloading pattern for HT-14 was similar to that of HT-12 and -13. The complete or high survival rates at

the low temperature were anticipated, and the massive failure of all but three samples at high temperature was expected. It is noteworthy that the proposed reference design survived completely.

Capsule HT-15. HT-15 was irradiated for seven cycles (160 days) in the HFIR to fast-neutron fluence exposures ranging from 7.7 to 16 $\times$ 10^{21} neutrons/cm^2 (> 0.18 MeV).

This capsule was withdrawn after seven cycles of irradiation because extreme swelling of the Poco graphite holders and magazines was observed in HT-14 after a six-cycle irradiation. In HT-15, this swelling had completely closed the initial gap between high-temperature magazines and capsule walls, and the capsule had to be slit open to remove the magazines. Diametral expansion of the magazines was more than 6%, and swelling of the sample holders was about 9% at the highest exposure. In addition to the swelling, the sample holders were severely distorted. Many had "hourglass" appearances, having expanded about 4% in the midsection, where the fuel particles were located, and at least 8% at the end cap.

The unloading pattern for HT-15 was similar to that for the previous three capsules. The graphite sample holders in the high-temperature region were very weak and great care was necessary. Of the nine samples of ORNL particles, four survived completely in the low-temperature region and the others had high survival rates. At the higher temperature, the proposed reference design survived well, showing 3% (two particles in 75) failure rate. Table 7.16 is a summary of particle design and survival rates.

7.2.2 Capsule HT-16

Design

HFIR target capsule HT-16 was designed primarily to evaluate the effects of radiation exposure on the physical properties of different graphites. The capsule vessel itself was identical to previous target capsules, but the internal design was different. The specimens consisted of 0.4-in.-diam graphite cylinders with a 0.125-in. central hole and varied in length (12 were $\frac{1}{4}$ in. and 24 were $\frac{1}{2}$ in.). The specimens were mounted

Table 7.16. Results from irradiation of Biso-coated ThO_2 particles in capsules HT-12 through -15

Batch No.	Coated particle design[a]	Holder No.	Survival rate (%)			
			HT-12	HT-13	HT-14	HT-15
At sleeve design temperature 900°C						
OR-1837	402-1-24.4	51	100	100	100	91
OR-1830	402-1-38.1	48	100	100	100	96
OR-1846	402-20.3-21.2	5	100	100	98	100
OR-1826	402-21.4-30.2	45	100	100	81	79
OR-1840	402-24.6-50.1	8	100	100	100	100
OR-1749	402-32.9-36.4	11	100	87	96	87
OR-1838	402-32.3-63.8	42	100	100	100	100
OR-1849	508-79.4-74.7	13	100	100	100	100
OR-1850	508-44.5-48.1	4	100	100	96	94
At sleeve design temperature 1250°C						
OR-1837	402-1-24.4	38	45	0		
OR-1830	402-1-38.1	35	100	0		
OR-1846	402-20.3-21.2	18	100	0		
OR-1826	402-21.4-30.2	32	100	23	11	44
OR-1840	402-21.4-30.2	21	100	100	100	7
OR-1749	402-32.9-36.4	24	100	100	7	100
OR-1838	402-32.3-63.8	29	100	100	97	100
OR-1849	508-79.4-74.7	26	100	100	100	97
OR-1850	508-44.5-48.1	17	100	3	0	0

[a]Numbers give kernel diameter, buffer thickness, and LTI thickness, respectively, in micrometers.

on hollow graphite rods which passed through the central specimen holes. The rods were in turn supported and centered in the capsule by 0.010-in.-thick stainless steel supports.

To minimize axial heat flux from the specimens to the supports and hence axial temperature variation in the specimens, gamma heat suscepters in the form of stainless steel disks were fitted on the graphite rods adjacent to the supports. The heat susceptors were sized such that there would be little or no axial temperature variation in the graphite rod and hence no axial heat flux from the specimen into the rod. All specimens (36 in number) were designed to operate at 700°C. Instead of varying the gas gap (in this case helium) to compensate for axial variation in gamma heat, the hollow support rods were fitted with silicon carbide temperature monitors and tungsten rods distributed so as to produce a uniform axial heat generation over the length of the capsule despite the axial gradient in gamma heat rate.

Operation

Capsule HT-16 was inserted in target position E-7 on Feb. 27, 1973, and was removed on July 29, 1973, after 136.91 days at 100 MW reactor power. The peak fast fluence was 1.39×10^{22} neutrons/cm^2 ($E > 0.18$ MeV). The individual specimen fluence is given in Table 7.17.

Table 7.17. Capsule HT-16 specimen location and fast fluence

Specimen No.	Axial position from reactor HMP (in.)	Average fast flux, $E > 0.18$ MeV (neutrons cm^{-2} sec^{-1})	Fast fluence, $E > 0.18$ MeV (neutrons/cm^2)
		$\times 10^{15}$	$\times 10^{22}$
1075	+9.625	0.487	0.58
1188	+9.375	0.523	0.62
182A	+9.000	0.570	0.67
177B	+8.250	0.670	0.79
176B	+7.750	0.730	0.86
181A	+7.000	0.809	0.96
179B	+6.500	0.857	1.01
940	+5.750	0.925	1.09
1001	+5.250	0.965	1.14
999	+4.500	1.016	1.20
992	+4.000	1.046	1.24
991	+3.250	1.085	1.28
1077	+2.875	1.104	1.30
1190	+2.625	1.115	1.32
980	+2.000	1.140	1.35
979	+1.500	1.157	1.37
182B	+0.750	1.174	1.39
176A	+0.250	1.180	1.39
177A	−0.500	1.177	1.39
1236	−0.875	1.172	1.39
1098	−1.125	1.165	1.38
245	−1.750	1.152	1.36
941	−2.250	1.138	1.35
101A	−3.000	1.108	1.31
129B	−3.500	1.085	1.28
106A	−4.250	1.045	1.24
128A	−4.750	1.013	1.20
129A	−5.500	0.955	1.13
249	−6.000	0.913	1.08
179A	−6.750	0.842	1.00
1238	−7.125	0.805	0.95
1097	−7.375	0.778	0.92
1076	−7.875	0.722	0.85
1189	−8.125	0.692	0.82
1237	−8.375	0.663	0.78
1096	−8.625	0.630	0.74
Magazine	−9.500	0.516	0.61

7.2.3 Capsules HT-17 through -19

J. M. Robbins W. P. Eatherly

Extensive failures of the GAC particles in HT-12 through -15 demonstrated, unequivocally, that the most sensitive parameter in particle coating design is the anisotropy.[9] Consequently, the HT-17, -18 and -19 series was designed as a logical sequence to the earlier series of capsules to better define the behavior of dense pyrolytic-carbon coatings on large ThO_2 kernels as a function of preferred orientation. The preferred orientation was measured by the BAF technique, and attempts will be made to correlate with OPTAF measurements. The preferred orientation was varied between 1.0 and 1.7.

A peripheral experiment involved one particle type with an anisotropy gradient through its outer coating to test the effect of such a gradient. A second particle type was coated using CO_2 instead of argon as the carrier gas. With CO_2, less soot is produced as an inclusion in the coating. The third particle in the peripheral experiment contained a 700-μm kernel (nominal) to help define the largest kernel that it is feasible to use.

Experiment design

This experiment consisted of three HFIR target capsules designated HT-17, -18, and -19 respectively. The format was similar to that of HT-12 through -15 in that the experimental samples were loose coated particles contained in small graphite holders with the entire assembly enclosed by a graphite sleeve. The graphite holders were designed to hold the particles in an annular array. The experiment was designed to test a series of Biso-coated ThO_2 particles at graphite holder surface temperatures of 900 and 1250°C to burnup and fast-neutron exposures up to at least $1\frac{1}{2}$ times the HTGR design requirements. These surface temperatures correspond to particle temperatures of about 1100 and 1500°C respectively. Each capsule contained two samples [except as noted in loading diagram (Table 7.18)] of each of the coating batches being tested. One set of samples was exposed at 1500°C and as near the maximum dose rate around the target midplane as possible. The corresponding set of samples was exposed at approximately 1100°C and at a lower exposure at the ends of the target. Also, 7% enriched uranium was included in each capsule to smooth out heat-generation curves and to maintain a more constant temperature throughout the test. A porous graphite heat shield separated the temperature zones, and a range of flux existed over the experimental samples.

The experiment contained eight particle batches from GAC and ten from ORNL. All measurements and characterization of the GAC particles were performed by GAC. As in HT-12 through -15, the ORNL particles were Biso coatings on large sol-gel-derived ThO_2 kernels. Parameters of the particles are listed in Table 7.19. The ThO_2 kernels and coated particles were carefully sized and thoroughly characterized so that effects of these variables would be minimized.

The ORNL particles were prepared from two kernel batches: nominally 500 and 700 μm in diameter respectively. The buffer and seal coatings were applied to the 500-μm-diam batch by W. J. Lackey of the Fuel Cycle Engineering and Development Group.[10] The outer coating on the 500-μm-diam batch and all coatings on the 700-μm-diam batch were applied by R. L. Beatty of the Carbon Development Group. After the buffer and sealers were applied, the particles were sized on a roller micrometer to eliminate excessively thick or thin coatings. After all coatings were applied, the particles were again sized on a roller micrometer. The sized fraction of the particles with 500-μm-diam kernels was poured over an x-ray holder with 144 holes that captured one particle in each hole. From the radiograph of these 144 particles, 99 were chosen and identified to be tested. The 99 particles were separated in a nonspecific manner into samples of 58 and 41 particles for testing in the high-temperature high-flux region and the low-temperature low-flux region respectively. A similar selection technique was used for the 700-μm-diam kernel batch, except only 16 and 22 particles were selected for testing in the two temperature-flux zones. The smaller number of particles was required because of the larger amount of thorium in the larger diameter ThO_2 kernels. All particles to be tested were heat treated at 1800°C for 30 min in an atmosphere of argon.

After the particles were fabricated, characterized, and heat treated, they were loaded into annular graphite holders and assembled into magazines. All graphite parts except the nickel-bearing positioners were heat treated to 1500°C for 30 min in an argon atmosphere before loading.

Operation

Capsule HT-17 was inserted in target position A-3 on July 22, 1973, and was removed on Sept. 8, 1973, after 46.42 days (two HFIR cycles) at 100 MW reactor

10. See Sect. 3.5.1, this report.

Table 7.18. Loading diagram of particles in HT-17, -18, and -19

Temperature (°C)	Particles	Sample holder	Item No.	Batch No.
900	ORNL (top)			
		2	7	OR-1978T
		4	10	OR-2010T
		5	8	OR-2012ST
		7	5	OR-1987T
		8	6	OR-1972T
		10	3	OR-1986T
		11	4	OR-1985T
		13	2	OR-1967T
		15	10[a]	OR-2010T
		17	8	OR-2012ST
		18	5	OR-1987T
		20	6	OR-1972T
		21	3	OR-1986T
		23	4	OR-1985T
		24	2	OR-1967T
		26	7[b]	OR-1978T
1200	Reactor midplane			
900	GGA (bottom)			
		27	6542-01-013	
		29	6542-01-023	
		30	6542-02-023	
		32	6542-02-033	
		33	6542-16-013	
		35	6542-17-013	
		36	6252-01-023	
		38	6252-01-023	
		40	6542-01-013	
		42	6542-01-023	
		43	6542-02-023	
		45	6542-02-033	
		46	6542-16-013	
		48	6542-17-013	
		49	6252-01-023	
		51	6252-01-023	

[a]This particle will be replaced by item 1, OR-1975T, in HT-19.
[b]This particle will be replaced by item 9, OR-2013ST, in HT-18 and -19.

power. The peak fast fluence was 4.73×10^{21} neutrons/cm^2 ($E > 0.18$ MeV), and the peak fertile particle burnup was 2.88% FIMA.

Capsule HT-18 was inserted in target position E-2 on July 22, 1973, and was removed on Oct. 28, 1973, after 92.94 days (four HFIR cycles) at 100 MW reactor power. The peak fast fluence was 9.48×10^{21} neutrons/cm^2 ($E > 0.18$ MeV), and the peak fertile particle burnup was 9.7% FIMA.

Capsule HT-19 was inserted in target position F-7 on July 22, 1973, and was removed on Dec. 17, 1973, after 139.27 days (six HFIR cycles) at 100 MW reactor power. The peak fast fluence was 1.4×10^{22} neutrons/cm^2 ($E > 0.18$ MeV), and the peak fertile particle burnup was 17.24% FIMA.

Table 7.20 gives the fast fluence and fertile particle burnup for each sample holder in each capsule. No attempt was made to calculate the fissile particle

Table 7.19. Deposition conditions and property measurements on ORNL particles for HT-17, 18, and -19

Batch No.	Deposition conditions[a]			Deposition rate[a] (μm/min)	Measured properties[c]						BAF
					Buffer			Outer Coating			
	Temperature (°C)	Propylene flux ($cm^3\ min^{-1}\ cm^{-2}$)	Propylene concentration[b] (%)		Mean thickness[d] (μm)	Mean density[e] (g/cm^3)		Mean thickness[d] (μm)	Mean density[d] (g/cm^3)		
OR-1975T	1315	4.00	33.3	11.8	68.5 (7.8)	1.19		83.0 (3.5)	1.982	(0.007)	1.00
OR-1967T	1300	2.00	16.7	5.2	75.6 (5.2)	1.19		78.4 (3.7)	2.000	(0.007)	1.05
OR-1986T	1250	1.10	9.2	2.1	69.2 (7.2)	1.19		78.6 (3.5)	2.102	(0.010)	1.10
OR-1985T	1275	1.25	10.4	2.9	71.0 (7.6)	1.19		76.4 (3.9)	2.065	(0.008)	1.12
OR-1987T	1250	0.90	7.5	1.7	72.4 (9.8)	1.19		84.9 (4.3)	2.094	(0.005)	1.17
OR-1972T	1250	1.00	8.4	2.0	69.4 (6.2)	1.19		78.7 (4.3)	2.063	(0.009)	1.22
OR-1978T	1240	0.50	4.2	0.8	69.8 (4.1)	1.19		83.9 (3.6)	2.072	(0.005)	1.73
OR-2012ST	1200–1350	1.50	12.5	3.7	74.1 (6.3)	1.19		100.4 (3.0)	1.919	(0.009)	Gradient
OR-2013ST	1325	4.00	33.3	11.5	80.4 (6.9)	1.19		84.5 (3.9)	2.002	(0.009)	1.00[f]
OR-2010T	1335	9.00	33.3	22.5	96.6 (8.6)	1.08		105.4 (5.4)	1.980	(0.009)	1.00[f]

[a]Outer coating only; buffer coating deposited from acetylene.
[b]Diluted with argon, except OR-2013ST, which was diluted with CO_2.
[c]Summary from MET-CER-DS-2.
[d]Numbers in parentheses are standard deviations.
[e]Calculated, includes seal coating.
[f]Estimated from coating run conditions.

Table 7.20. Fast flux and fluence and burnup for specimens in HFIR target capsules HT-17, -18, and -19

Sample holder No.	Fast-neutron fluence, $E > 0.18$ MeV (neutrons/cm^2)			Fast-neutron flux, $E > 0.18$ MeV (neutrons cm^{-2} sec^{-1})	Distance from holder center to reactor midplane (in.)	Fertile particle burnup (% FIMA)		
	HT-17	HT-18	HT-19			HT-17	HT-18	HT-19
	$\times 10^{21}$	$\times 10^{21}$	$\times 10^{21}$	$\times 10^{15}$				
1, 52	2.24	4.51	6.75	0.56	9.199			
2, 51	2.37	4.74	7.10	0.59	8.909	1.40	5.25	9.91
3, 50	2.54	5.09	7.63	0.63	8.626			
4, 49	2.72	5.44	8.15	0.67	8.344	1.57	5.78	10.83
5, 48	2.83	5.68	8.50	0.70	8.061	1.63	6.05	11.30
6, 47	2.95	5.91	8.85	0.73	7.779			
7, 46	3.07	6.14	9.20	0.76	7.496	1.81	6.53	12.10
8, 45	3.21	6.44	9.64	0.80	7.214	1.90	6.78	12.52
9, 44	3.30	6.61	9.90	0.82	6.931			
10, 43	3.42	6.85	10.3	0.85	6.649	2.03	7.20	13.25
11, 42	3.56	7.14	10.7	0.88	6.366	2.10	7.43	13.60
12, 41	3.68	7.37	11.0	0.91	6.084			
13, 40	3.74	7.49	11.2	0.93	5.801	2.22	7.82	14.21
14, 39	4.23	8.49	12.7	1.05	4.199			
15, 38	4.26	8.54	12.8	1.06	3.909	2.61	8.88	15.88
16, 37	4.35	8.72	13.1	1.08	3.626			
17, 36	4.41	8.84	13.2	1.09	3.344	2.70	9.11	16.27
18, 35	4.47	8.95	13.4	1.11	3.061	2.72	9.22	16.43
19, 34	4.53	9.07	13.6	1.12	2.779			
20, 33	4.55	9.13	13.7	1.13	2.496	2.80	9.40	16.71
21, 32	4.58	9.19	13.8	1.14	2.214	2.81	9.48	16.85
22, 31	4.64	9.30	13.9	1.15	1.931			
23, 30	4.67	9.36	14.0	1.16	1.649	2.85	9.60	17.03
24, 29	4.70	9.42	14.1	1.16	1.366	2.87	9.64	17.12
25, 28	4.73	9.48	14.2	1.17	1.084			
26, 27	4.73	9.48	14.2	1.17	0.801	2.88	9.70	17.24

burnup. Table 7.21 gives the operating history of the reactor during the irradiation of each capsule.

Postirradiation examination

(J M Robbins, W. P. Eatherly)

Capsules HT-17 and -18 have been opened and visually examined; HT-19 will be opened in early 1974. When opened, both HT-17 and -18 were observed to be free of sooty material, as was the case for HT-12 through -15; this is attributed to the gettering action of zirconium foil disks used between the particle holders in each magazine. The graphite particle holders in the low-temperature region from both HT-17 and -18 were removed and opened without much difficulty; however, the magazines in the high-temperature region of HT-18 had to be slit to remove the particle holders, and the holders had to be broken to remove the particles. The graphite holders were observed to break easily and were quite friable; this was not so in HT-17. Table 7.22 shows the survival rates for both ORNL and GAC particles in HT-17 and -18.

The table shows that in HT-17, all the GAC particles survived well except the Triso-coated batch; in HT-18, the GAC particles survived well in the low-temperature zone but began to show some failures at high temperature. Again, the Triso-coated batch failed. No attempt was made to evaluate the GAC particles beyond visual examination; they have been returned to GAC for final evaluation.

The general trend for ORNL particles in HT-17 was that particles with BAFs greater than 1.10 survived at low temperatures and failed at high temperature. An exception was that sample OR-2012ST, with a BAF of

Table 7.21. Operational history of capsules HT-17 through -19

HFIR cycle	Begin cycle	End cycle	Days operation	Accumulated irradiation time at 100 MW reactor power (days)
		Capsule HT-17		
95	7/22/73	8/15/73	23	23.20
96	8/16/73	9/8/73	23	46.42
		Capsule HT-18		
95	7/22/73	8/15/73	23	23.20
96	8/16/73	9/8/73	23	46.42
97A[a]	9/9/73	9/17/73		
97B	9/17/73	10/5/73	26	69.58
98	10/5/73	10/28/73	23	92.94
		Capsule HT-19		
95	7/22/73	8/15/73	23	23.20
96	8/16/73	9/8/73	23	46.42
97A[a]	9/9/73	9/17/73		
97B	9/17/73	10/5/73	26	69.58
98	10/5/73	10/28/73	23	92.94
99	10/31/73	11/23/73	23	116.23
100	11/25/73	12/17/73	23	139.27

[a]Reactor began a programmed reduction in power on 9/14/73 in preparation for the shutdown on 9/17 /73.

Table 7.22. Survival rates for ORNL and GAC particles in HT-17 and -18

Batch No.	Source	BAF or OPTAF[a]	Survival rate (%)			
			HT-17		HT-18	
			900°C	1250°C	900°C	1250°C
OR-2010T	ORNL	1.00	100	100	100	86
OR-1967T	ORNL	1.05	100	0	0	0
OR-2012ST	ORNL	1.08	100	84	0	0
OR-1985T	ORNL	1.12	93	0	0	0
OR-1986T	ORNL	1.10	24	100	0	0
OR-1972T	ORNL	1.22	100	0	0	0
OR-1987T	ORNL	1.17	100	0	0	0
OR-1978T	ORNL	1.73	100	0	0	*b*
OR-2013ST	ORNL	1.00	*b*	*b*	*b*	100
OR-1975T	ORNL	1.00	*b*	*b*	*b*	*b*
6542-01-013	GAC	1.06	100	100	98	91
6542-01-023	GAC	1.10	100	100	54	98
6542-02-023	GAC	1.06	100	100	85	100
6542-02-033	GAC	1.12	100	100	66	19
6542-16-013	GAC	1.07	100	86	93	0
6542-17-013	GAC	1.27	100	100	93	5
6252-01-023[c]	GAC	1.08	0	0	12[d]	12[d]
6252-01-023	GAC	1.08	0	0	0	14[d]

[a]GAC values are OPTAF; ORNL values are BAF.
[b]This particle batch not in this position in this magazine.
[c]Triso-coated particles.
[d]These particles will be checked again for failure at GAC.

1.08, survived better than OR-1967T (BAF 1.05). However, OR-2012ST has an outer coating thickness of 100.4 μm as compared to 78.4 μm for OR-1967T. In HT-18, ORNL particles failed completely except for the new particle (OR-2013ST) and 86% of the particles (OR-2010T) with the large (697-μm-diam) kernels and low (1.00) BAF. The survival of these two particle batches was not unexpected.

Although most of the ORNL particles failed in HT-18, GAC had sufficient survivors to warrant the continuation of capsule HT-19.

7.2.4 Capsules HT-20 through -23

W. P. Eatherly J M Robbins

Important changes may occur in several properties of bonded fuel rods during irradiation. To assess these changes on certain parameters, we have designed an irradiation test series of four HFIR target capsules to measure the change in thermal conductivity, electrical resistivity, thermal expansion, and dimensions of simulated bonded fuel rods as a function of fuel particle volume loading and fast-neutron fluence. The capsules will be irradiated for one, two, four, and six cycles, respectively, at a temperature of 900°C.

The samples for irradiation will be selected on the basis of electrical resistivity measurements. This will ensure that each type of specimen for one capsule will have the same characteristics as the similar specimens for the companion capsules. Also, companion specimens will be selected for preirradiation determination of thermal conductivity and coefficient of thermal expansion. After irradiation, the coefficient of thermal expansion, electrical resistivity, dimensions, and thermal conductivity will be determined. These measurements will be made at temperatures up to 700°C. A mathematical analysis of the data will be made using the following equation:

$$\lambda = \lambda_m \frac{1 - f + f\left(\frac{3\lambda_s}{2\lambda_s + \lambda_m}\right)}{1 - f + f\left(\frac{3\lambda_m}{2\lambda_s + \lambda_m}\right)} ,$$

where

λ = thermal conductivity of the composite,

λ_m = thermal conductivity of the matrix,

λ_s = thermal conductivity of the imbedded particles,

f = volume fraction of imbedded particles.

The above equation assumes a dilute solution of the spherical particles in the carbon matrix and should be valid at the relatively low (<35 vol %) particle loadings of the specimens in this experiment.

Experiment design

Each capsule will contain five bonded fuel specimens with nominal dimensions of 0.4 in. OD, 0.128 in. ID, and 2.0 in. long, symmetrized about the reactor midplane. The remaining space on either end of the capsules will be used to test experimental graphites for possible use as structural parts in gas-cooled reactors. One of the five specimens in the primary experiment will be fabricated by the slug-injection technique and will contain approximately 60 vol % Biso-coated inert particles. This specimen will be positioned about the midplane of the reactor with two of the remaining four specimens on each side of it. These four specimens will be formed by extrusion[11] and will have Biso-coated carbon particle loadings varying from 0 to about 35 vol % in four approximately equal increments. The four extruded specimens will have the same matrix composition and approximately the same matrix density, which is expected to be about 1.65 g/cm^3.

7.3 IRRADIATION TESTS IN ORR IN-CORE FACILITY

K. R. Thoms A. W. Longest

Two high-flux facilities were prepared in the ORR for joint ORNL-GAC irradiation testing. These facilities, which occupy the C-3 and E-3 core positions, are capable of irradiating fully instrumented capsules having temperature control capability achieved by the use of mixed sweep gases. The ORR core loading has been adjusted to produce a fast-neutron flux in these facilities sufficiently high to give representative HTGR exposures of about 8×10^{21} neutrons/cm^2 in one year. One facility, C-3, was occupied by a graphite irradiation capsule designed and fabricated by GAC. The second facility is presently occupied by a joint ORNL-GAC fueled experiment which was designed and constructed principally at ORNL.

7.3.1 Design and Operation of OG-1

The first capsule, designated OG-1, was designed and built by GAC and irradiated in the ORR C-3 position.

11. See Sect. 6.2.3, this report.

The capsule was installed in the ORR on June 18, 1973, and irradiation was terminated on Dec. 2, 1973, after having operated at design temperatures for 3207 hr. This capsule contained 10 graphite crucibles that operated at temperatures ranging from 600 to 1400°C. The 10 crucibles contained a total of about 1200 specimens, some of which were irradiated in previous GAC experiments and some of which will be reirradiated in the next ORR graphite irradiation test, capsule OG-2.

The in-core section of this capsule was divided into two cells; the upper cell contained seven crucibles and the lower cell contained three crucibles. The temperature of each cell was controlled by an independent sweep-gas system of mixed helium and argon. Since this was the first of a series of similarly designed in-core capsules, it served as a proof test of the basic design as well as a basis of support for a previous test[12] performed to estimate the gamma heating rate of the two in-core facilities.

The initial operation of capsule OG-1 was very encouraging. We found that the desired operating temperatures could be obtained easily with approximately the same gas mixture predicted in the thermal analysis. Since the sole source of heat in this capsule was gamma heat, this initial operation confirmed that our prediction of the gamma heating rate in the C-3 core position was fairly accurate.

The most serious problem encountered in the operation of capsule OG-1 was the failure of the thermocouple lead tube. The tube was replaced with tygon tubing, which remained intact during the duration of the test. We found that the resistivity of the reactor pool water is high enough to prevent shorting of the thermocouples even though the top of the hermetic seal to the capsule was completely exposed to the pool water. This hermetic seal prevented the pool water from entering the secondary containment, and therefore the failure of the lead tube proved to be more of an inconvenience than a hazard to the experiment.

The second graphite irradiation test, capsule OG-2, is presently scheduled to be installed in the ORR during the July 14, 1974, shutdown of the ORR.

7.3.2 Design and Operation of OF-1

The joint ORNL-GAC fueled experiment designated OF-1 (GAC designation P13Q) is also divided into two cells, with the top cell (about 15 in. long) containing GAC fuel specimens and the bottom cell (about 8 in. long) containing ORNL fuel specimens. The cells were formed by brazing a nickel bulkhead in the primary containment tube at a point $3\frac{3}{8}$ in. below the reactor midplane. Each cell has its own sweep-gas system allowing independent temperature control and fission-gas release measurements. The entire in-core section of the capsule is shown in Fig. 7.29.

The upper cell, designed and fabricated by GAC, contains three graphite fuel bodies; a typical cross-section is shown in Section A-A of Fig. 7.29. There are three 0.625-in-diam axial holes for fuel rods and three 0.500-in.-diam holes for graphite samples. There is a 0.471-in.-diam hole in the center of each crucible that contains a graphite spine containing thermocouples, dosimetry, and the inlet sweep-gas lines. There are six 0.093-in.-diam holes in the graphite body which also contain thermocouples and dosimetry. There are a total of 17 thermocouples in this cell, including three Chromel/Alumel and 14 tungsten-rhenium (W–3% Re/W–25% Re). The operation of the GAC cell consists in adjusting the sweep-gas mixture to maintain thermocouple K1 (shown in Fig. 7.29) at 750°C.

The lower cell, designed and fabricated by ORNL, contains a single graphite fuel body whose cross section is shown in Section B-B of Fig. 7.29. There are five 0.499-in.-diam holes – one central hole and four peripheral holes. Two of the peripheral holes are to test the in-block carbonization process, while the central holes and the other two peripheral holes are to test the packed-bed carbonized fuel rods. There are ten 0.096-in.-diam holes containing various flux monitors. As can be seen in Fig. 7.29, there are thermocouples in the fuel body web between the peripheral fuel rods and the graphite OD. There are three additional thermocouples in the lower $2\frac{3}{4}$ in. of the fuel body evenly spaced around one peripheral fuel rod. These thermocouples are intended to provide information on the effective thermal conductivity between the fuel center line and the graphite fuel body.

Centering of the graphite fuel body was accomplished by two different methods. At the top end of the fuel body are eight 0.125-in.-diam holes into which "Lucalox" (Al_2O_3) pins were placed. These pins were machined so as to provide essentially point contact with the stainless steel primary containment tube. The bottom end of the fuel body was machined in the shape of an octagon, again providing essentially point contact between the graphite and the primary containment.

Both ends of the fuel body were insulated with 0.500-in.-thick Palarite-C (fibrous carbon) insulation

12. K. R. Thoms, "Irradiation in ORR Core Facilities," *GCR Programs Annu. Progr. Rep. Dec. 31, 1972,* ORNL-4911, pp. 115–16.

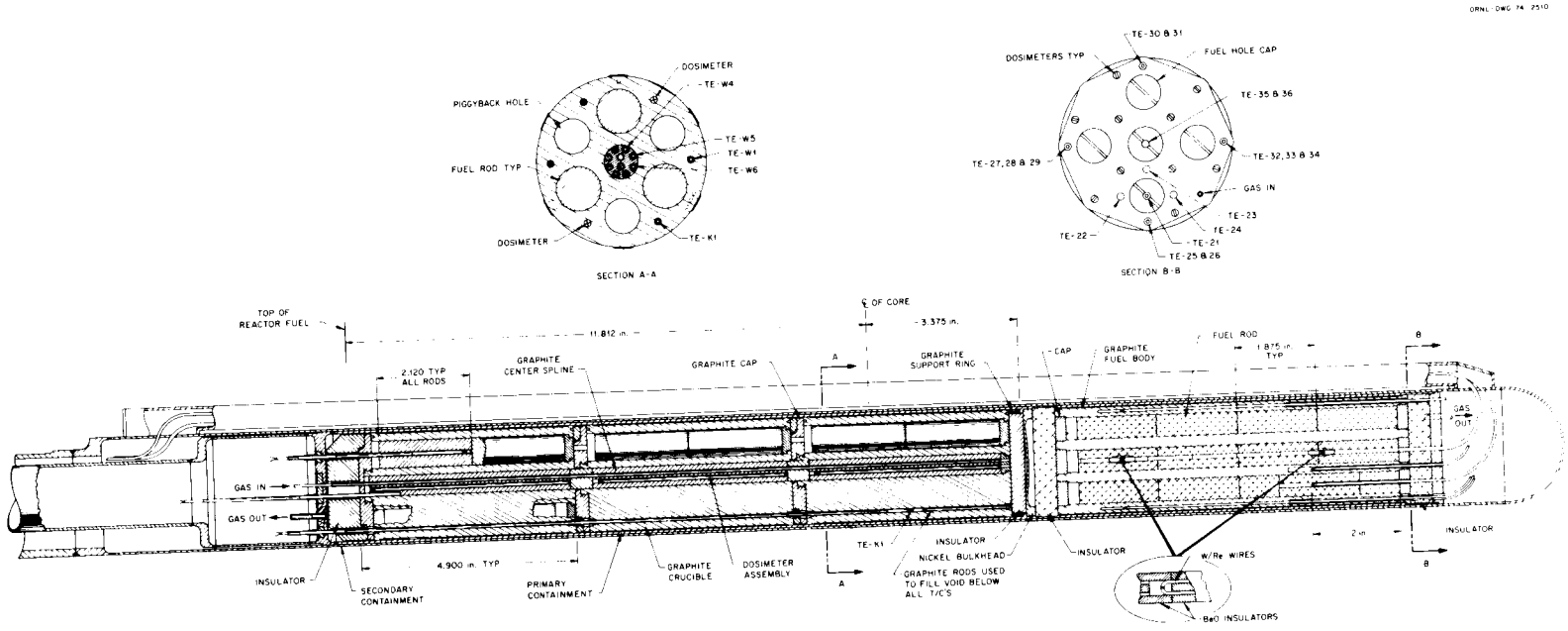

Fig. 7.29. In-core section of capsule OF-1.

disks obtained from Y-12 Development Division. A graphite support ring was placed at the bottom of the fuel body to keep the weight of the fuel body off the Palarite C insulator.

A thermal analysis of the ORNL section of the capsule was made using a combination of three-dimensional and one-dimensional heat transfer calculations. A three-dimensional ($R\theta Z$) temperature distribution calculation was made for the case of normal operating conditions at beginning of life (BOL). The HEATING3 program[13] was used for this calculation, with the capsule represented as shown in Fig. 7.30. Some of the resulting axial and radial temperature profiles are shown in Figs. 7.31 and 7.32. The one-dimensional heat transfer calculations were made to estimate the sweep-gas thermal conductivity variation required to maintain the maximum center fuel stick temperature constant at 1300°C throughout the 300-day irradiation and to estimate the resulting variation of the peripheral fuel stick temperature at a point 2 in. above the bottom of the fuel stick. The results of the one-dimensional calculations, which take into account changes in gas gap thicknesses due to graphite and fuel stick shrinkage with fast-neutron exposure and changes in heat generation rates with time, are shown in Fig. 7.33. A three-dimensional thermal analysis of the GAC section of the OF-1 capsule was performed by GAC.

The OF-1 capsule was installed in the ORR on Aug. 22, 1973, and has operated at design temperature for 2630 hr as of Dec. 31, 1973. Approximately once per week, samples are taken of the sweep gas of each cell and are analyzed for fission products with the aid of a gamma-ray spectrometer. The analysis of the samples from the GAC cell consists in obtaining fission product concentration at the fuel. These results are then reported to GAC, where they are converted to release-to-birth rate ratios (R/B). The analysis of the samples from the ORNL cell consists in determining the R/B value directly. A history of the R/B values for the ORNL cell is presented in Table 7.23.

7.3.3 Preparation of Specimens for OF-1 Irradiation Test

R. A. Bradley W. J. Lackey

The OF-1 irradiation test contained eight types of fuel rods. The test variables included the fissile kernel type (^{233}U or ^{235}U), the size of the coater in which the fissile particles were coated (1-in.-diam laboratory or 5-in.-diam prototype coater), the fuel rod matrix composition, the method of carbonization (packed in Al_2O_3 powder or carbonized in the OF-1 graphite test element), and the fuel rod configuration (solid or annular). The test variables for the eight types of fuel rods are summarized in Table 7.24.

The fertile particles for all rods and the fissile particles for fuel rod types 1, 2, 3, 5, and 6 were coated in the 5-in.-diam prototype coater. The fissile particles for rod type 4 and 7 were coated in a 1-in.-diam laboratory coater; and those for rod type 8, which contained ^{233}U, were coated in a 1-in.-diam coater in the plutonium laboratory. The important characteristics of the coatings of these fissile and fertile particles are summarized in Table 7.25.

All fuel rods contained 20 vol % GCL-1099 graphite shim particles. Pyrolytic-carbon-coated carbon inert particles were added to the fissile, fertile, and shim particles to provide close-packed beds (~62 vol % particle loading).

The solid fuel rods were formed by the slug-injection process on the laboratory automatic fuel rod machine; the annular rods were formed by the same process on a manual press.

The rods were carbonized either in packed Al_2O_3 or in the OF-1 graphite test element as indicated in Table 7.24. In both cases, the carbonization was accomplished by heating at 1°C/min to 500°C, holding 1 hr, and then heating at 5°C/min to 800°C and holding 1 hr. The rods were subsequently heated to 1800°C for 0.5 hr.

The average matrix density and pitch coke yield of each type rod are summarized in Table 7.26. The matrix density is linearly related to the pitch coke yield, which fell into four categories:

1. rods carbonized in graphite element,
2. solid rods carbonized in packed Al_2O_3 in laboratory 254 furnace (types 1 and 4) – 13.7 to 14.6%,
3. annular rods carbonized in packed Al_2O_3 in laboratory 254 furnace (types 5 through 7) – 19.4 to 21.2%,
4. annular rods carbonized in packed Al_2O_3 in alpha laboratory (FCAF) furnace (type 8) – 11.7%.

The differences in pitch coke yield of rods carbonized in packed Al_2O_3 in different furnaces are apparently due to small differences in heating rates.

Metallographic examination of these rods showed that all rods carbonized in packed Al_2O_3 had matrices with

13. W. D. Turner and M. Siman-Tov, *HEATING3: An IBM-360 Heat Conduction Program*, ORNL-TM-3208 (February 1971).

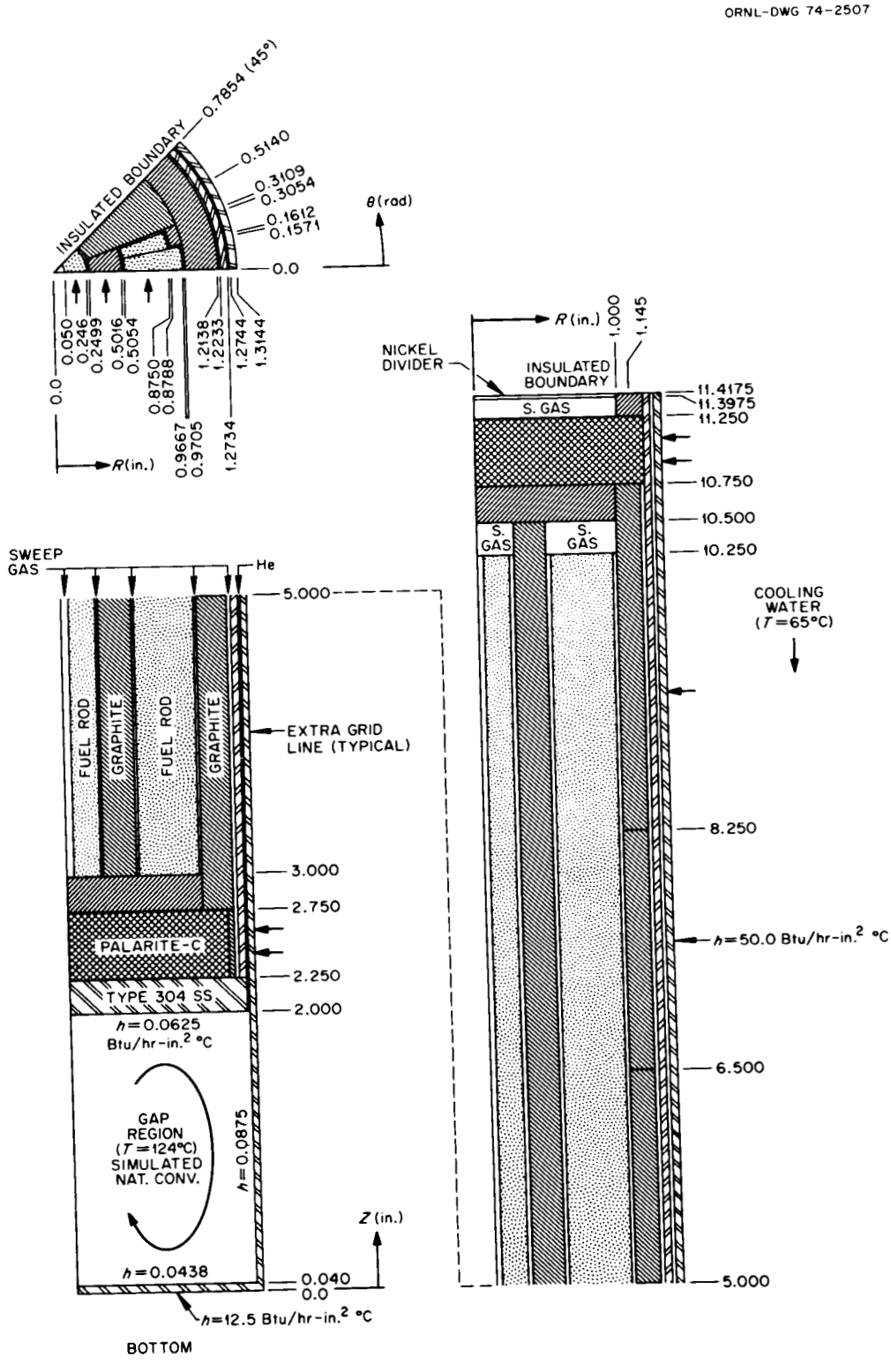

Fig. 7.30. Representation of capsule OF-1 for the HEATING3 program.

Table 7.23. Fission product release data for ORNL cell in capsule of OF-1

Sample No.	Date	Time	Operating time (hr)	Flow rates[a] He/Ne (cc/min)	Temperature (°C)			Fission product release-to-birth rate ratio R/B ($\times 10^{-5}$)				
					TE-21	TE-35	TE-36	^{85m}Kr	^{87}Kr	^{88}Kr	^{133}Xe	^{135}Xe
1-2b-1	8-30-73	0904	19.1	25.0/0	863	925	1110	1.01	0.365	0.442	0.192	*b*
1-2b-3	8-31-73	1028	44.5	11.0/9.1	1000	1045	1235	*b*	1.12	1.35	0.845	0.056
1-2b-7	9-4-73	1447	144	11.0/8.7	969	1000	1180	1.97	0.775	0.900	1.45	0.318
1-2b-11	9-11-73	1010	291	7.5/8.2	989	1020	1195	1.98	0.949	1.31	1.15	0.729
1-2b-14	9-14-73	1052	364	5.0/8.2	986	1019	1187	1.44	0.862	0.907	1.60	0.140
1-2b-16	9-18-73	0952	458	5.0/11.8	1006	1033	1207	1.82	1.18	1.25	3.20	0.183
1-2b-18	9-26-73	1055	647	6.8/8.0	1003	1031	1200	1.94	1.64	1.43	1.76	0.273
1-2b-20	10-5-73	1041	862	5.0/8.0	988	1006	1178	1.78	1.21	0.895	2.30	0.128
1-2b-24	10-18-73	0934	1081	7.5/10.6	1042	1067	1246	2.11	1.36	0.395	2.97	0.248
1-2b-26	10-26-73	1054	1264	6.0/8.3	1030	1050	1238	2.33	1.87	2.16	3.53	0.207
1-2b-29	11-1-73	1021	1409	5.0/11.8	1018	1043	1237	1.55	1.03	1.09	2.11	0.164
1-2b-31	11-15-73	1019	1662	5.0/14.6	1037	1054	1239	2.07	1.10	1.36	1.98	0.164
1-2b-34	11-21-73	1001	1794	6.0/14.5	1034	1048	1224	1.75	1.09	*b*	1.53	0.164
1-2b-36	11-30-73	1251	1997	1.5/7.7	1043	1049	1230	1.58	1.16	1.41	3.37	0.177
1-2b-39	12-13-73	0946	2199	5.0/9.7	1047	1044	1219	2.04	1.43	1.44	3.27	0.114
1-2b-42	12-20-73	0948	2367	2.0/8.7	1040	1029	1210	2.05	1.27	1.39	3.05	*b*
1-2b-44	12-27-73	0915	2529	4.0/8.7	1038	1027	1194	1.74	1.14	1.21	2.30	0.164

[a]During the time period covering samples 1-2b-1 to 1-2b-20, there was a leak in the helium emergency cooling solenoid valve which was estimated to be 5 cc/min. Therefore the helium flow rates reported for these samples are estimated and not actually measured.

[b]The data for these samples were lost through malfunction of analysis equipment.

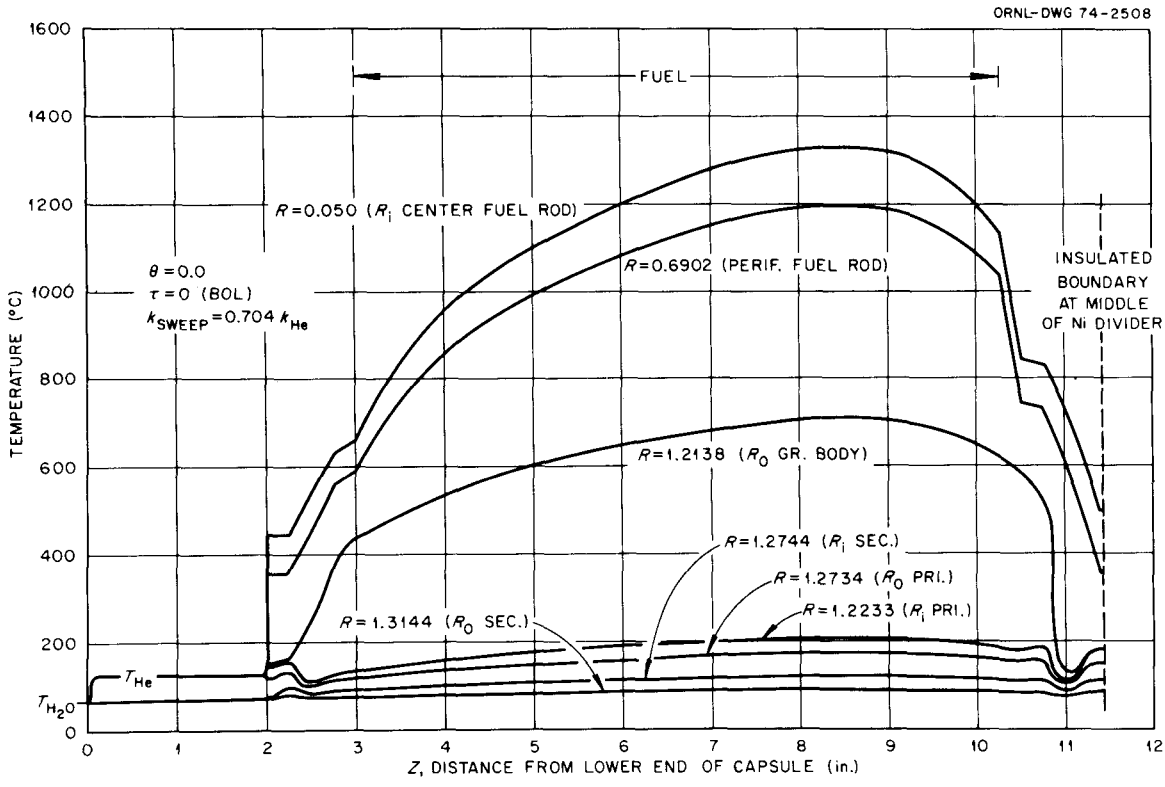

Fig. 7.31. Axial temperature gradients in capsule OF-1 at selected radii.

Table 7.24. Test variables for OF-1 irradiation test specimens

Fuel rod type	Fissile particle type	Matrix filler type	Carbonization method	Fuel rod configuration
1	Prototype coater[a]	Asbury 6353[b]	Packed in Al_2O_3	Solid
2	Prototype coater	Asbury 6353	In graphite element	Solid
3	Prototype coater	GLC 1089[c]	In graphite element	Solid
4	Laboratory coater[d]	Asbury 6353	Packed in Al_2O_3	Solid
5	Prototype coater	Asbury 6353	Packed in Al_2O_3	Annular
6	Prototype coater	Asbury 6353	Packed in Al_2O_3	Annular
7	Laboratory coater	Asbury 6353	Packed in Al_2O_3	Annular
8	Pu laboratory coater[e]	Asbury 6353	Packed in Al_2O_3	Annular

[a]Coated in 5-in.-diam prototype coater – batch J 263.

[b]29 wt % Asbury 6353 natural flake graphite in Ashland A-240 petroleum pitch.

[c]39 wt % GLC 1089 (10–44 μm) graphite powder in Ashland A-240 petroleum pitch.

[d]Coated in 1-in.-diam laboratory coater – batch OR 1977.

[e]^{233}U kernel – coated in 1-in.-diam coater in plutonium laboratory.

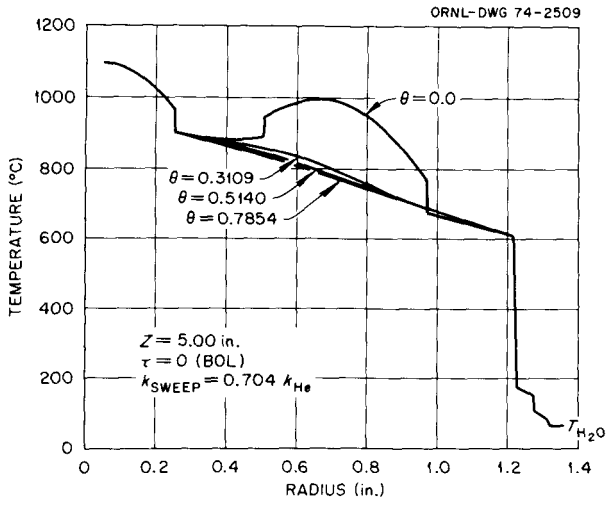

Fig. 7.32. Radial temperature gradients in capsule OF-1 at an elevation 2 in. above bottom of fuel rods.

very open, porous microstructures. This is the type of microstructure that would have been expected based on the pitch coke yield. On the other hand, the microspheres of the rods carbonized in block were much more dense. In the rod containing GLC-1089 carbonized in block (type 3), we found six particles in which the LTI coating was torn, apparently due to a matrix-particle interaction. No tearing was found in the rod containing Asbury 6353 carbonized in block, but from the appearance of the matrix it would not be surprising to see tearing after irradiation.

The results of broken particle analyses are given in Table 7.27. These data indicate that the rod containing GLC-1089 carbonized in block (rod type 3) contained about two broken fissile particles and two broken fertile particles. One annular rod containing Asbury 6353 carbonized in packed Al_2O_3 (rod type 7) also appeared to have about two broken fissile particles.

Table 7.25. Properties of coated particles for OF-1 irradiation test

	Fertile		Fissile			
			5-in.-diam prototype coater		1-in.-diam laboratory coater	Pu laboratory coater
	Unannealed	Annealed	Unannealed	Annealed		
Kernel diameter, μm	496.5 ± 0.6		353.8 ± 1.0		357	350.8
Buffer thickness, μm	84.0 ± 2.7		101.2		93	104.7
Buffer density[a] g/cm³	1.188		1.39 ± 0.05[b]		1.18[c]	1.0
Sealer thickness, μm	3.5		None		None	None
Outer coating thickness, μm	86.1 ± 2.2	82.4	91.8 ± 2.7		106	85.0
Density, g/cm³	1.868[d]	1.921[d]	1.899[d]	1.927[d]	1.96[e]	1.982
Open porosity[f] vol %	4.1	4.3	3.4	4.2		
Deposition rate, μm/min	8.3		7.6			
Particle diameter, μm	839.2 ± 4.9	827.4 ± 5.7	734.8 ± 6.1	717.5 ± 9.6		
Density[g] g/cm³	3.355 ± 0.007	3.415 ± 0.007	2.640 ± 0.007	2.690 ± 0.007	2.44	2.665
U or Th content, g/g particle	0.5405 ± 0.0006		0.3704 ± 0.0006		U 0.0616 Th 0.275	U 0.0561 Th 0.2381
Exposed U or Th,[h] ppm	4, 10	1.1, 1.6	2, 1	22, 39		

[a]Calculated from mercury pycnometry determined particle density before and after coating and wt % carbon determined by burning unless otherwise noted. In the case of the fissile particles, the burnoff results were corrected to account for the increase in O/U ratio during burning.

[b]Sealer not used; calculated from mercury pycnometer particle density, LTI gradient density, kernel density, and kernel and coating dimensions.

[c]Calculated.

[d]Gradient column density corrected by: Corrected gradient column density = (uncorrected gradient column density) (1-P), where P = volume fraction open porosity from mercury pycnometer at 15,000 psi.

[e]Gradient column density (not corrected).

[f]Mercury pycnometer at 15,000 psi.

[g]Mercury pycnometer at 250 psi.

[h]Based on particle weight - two numbers are for duplicate measurements by aqueous HCl leach.

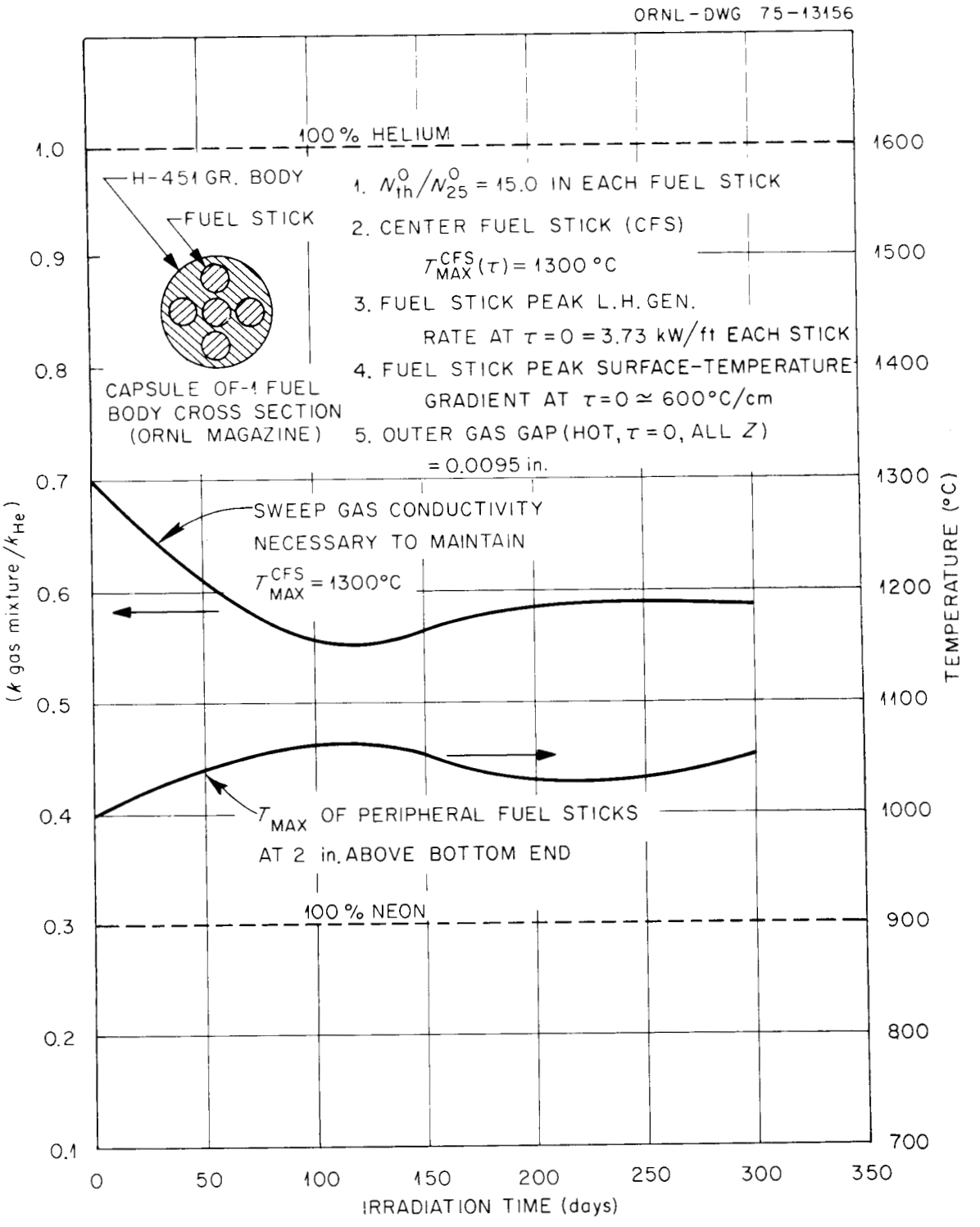

Fig. 7.33. Results of one-dimensional thermal design calculations for ORNL magazine of ORR capsule OF-1.

Table 7.26. Average matrix density and pitch coke yield of OF-1 fuel rods

Rod type	Matrix density (g/cm^3)	Pitch coke yield (wt %)
1	0.473	13.7
2	0.732	44.9
3	ND[a]	ND[a]
4	0.491	14.6
5	0.553	21.0
6	0.540	19.4
7	0.573	21.2
8	0.464	11.7

[a]Not determined due to inability to obtain accurate weights of rods after removal from graphite element.

Table 7.27. Results of broken particle analysis on fuel rods for OF-1

Rod type	Matrix filler[a]	Carbonization method	Heavy metal leached (g)		Fraction (g/g)	
			Th[b]	U[c]	U	Th
			$\times 10^{-6}$	$\times 10^{-6}$	$\times 10^{-4}$	$\times 10^{-4}$
1	29.0% Asbury 6353	Packed Al_2O_3	<13	13	1.1	<0.1
2	29.0% Asbury 6353	In block	8	1	<0.1	<0.1
3	38.5% GLC 1089	In block	1613	68	5.8	10.3
4	29.0% Asbury 6353	Packed Al_2O_3	<8	3	0.24	<0.1
5	29.0% Asbury 6353	Packed Al_2O_3	11	4	0.34	<0.1
7	29.0% Asbury 6353	Packed Al_2O_3	311	79	7.4	1.9
8	29.0% Asbury 6353	Packed Al_2O_3	7	4	0.5	<0.1

[a]Ashland A240 pitch used as binder in all rods.
[b]One fertile particle contains approximately 558×10^{-6} g of thorium.
[c]One fissile particle contains approximately 38×10^{-6} g of uranium and 161×10^{-6} g of thorium.

7.4 IRRADIATION TESTS IN THE ETR CAPSULE FACILITIES

7.4.1 ETR Capsules H-1 and -2

R. A. Olstad

Various aspects of the design, operation, and postirradiation examination of the capsules H-1 and -2 have been reported previously.[14-16] Results of the analysis of the flux monitors in the capsules have also been reported previously.[17] The thermal analysis of these capsules has since been completed, as described in Sect. 7.8.1. Results of the analysis of kernel migration data obtained from this experiment were reported,[18] and a topical report on these capsule irradiation tests has been

14. A. R. Olsen, "Capsule Tests," *GCR-TU Programs Semi-annu. Progr. Rep. Sept. 30, 1971,* ORNL-4637, pp. 110–11.
15. A. R. Olsen and R. B. Fitts, "Capsule Tests," *GCR-TU Programs Annu. Progr. Rep. Sept. 30, 1971,* ORNL-4760, pp. 67–68.
16. A. R. Olsen and R. B. Fitts, "ETR Capsules H-1 and H-2," *GCR Programs Annu. Progr. Rep. Dec. 31, 1972,* ORNL-4911, pp. 116–24.
17. H. T. Kerr, "Nuclear Analysis in Support of Irradiation Experiments," ibid., pp. 138–41.
18. T. B. Lindemer and R. A. Olstad, *HTGR Fuel Kernel Migration Data for the Th-U-C-O System as of April 1, 1974,* ORNL-TM-4493 (June 1974).

issued.[19] The abstract from this report follows:

"Coated HTGR fuel particles were irradiated under severe thermal conditions to high fast fluences (2 to 6 × 10^{21} neutrons/cm^2, >0.18 MeV) and burnups (25 to 45% uranium burnup, <1% thorium burnup) in the ETR in the H-1 and H-2 capsule irradiation test from May 1971 to May 1972. The test was designed to provide samples of irradiated fuel rods for head-end reprocessing studies and to give an accelerated irradiation of the reference recycle fuel particles that are currently being irradiated in the Peach Bottom Reactor in the Recycle Test Element series. Bonded rods of BISO-coated UO_2, $(4.1Th,U)O_2$, $(2.2Th,U)O_2$, or uranium-loaded strong-acid ion-exchange-resin particles mixed with BISO-coated ThO_2 particles and rods of TRISO-coated UC_2 mixed with BISO-coated ThC_2 particles were irradiated. The initial fissile isotope was ^{235}U in all samples. The coated particles were bonded in a close-packed configuration with a carbonaceous matrix to form rods approximately ½ in. in diameter × 2 in. long. Each capsule was surrounded by a hafnium sleeve to decrease the thermal flux in the fuel. About half the samples operated at much above design temperatures during the last of the four irradiation cycles because the capsules were inadvertently irradiated in an inverted position during this period. The calculated center-line temperatures of the bonded rods varied from 900 to 1500°C at the beginning of the test and from 600 to 2600°C at the beginning of the last cycle. Postirradiation examination showed that the rods that operated at normal temperatures throughout the test were largely fragmented or debonded, possibly because of high thermal gradients or because of repeated thermal cycling during the test. The particles themselves survived the irradiation in excellent condition. A small amount of kernel migration was observed in UO_2, $(4.1Th,U)O_2$, and $(2.2Th,U)O_2$ particles in normal-temperature rods but was not observed in the ThO_2 particles. The rods that operated at very high temperatures during the last cycle were severely damaged and contained a central region of reddish powder with no recognizable particles remaining. Substantial migration of the mixed oxide and UO_2 kernels as well as the ThO_2 kernels was observed. None of the carbide or resin-derived particles have been examined metallographically at the time of writing."

A large amount of kernel migration data was obtained from this test because of the relatively high fuel temperatures during normal operation and because of the very high temperatures in some of the fuel rods when the capsules were irradiated in an inverted position. The calculated temperatures have a large uncertainty (see Sect. 7.8) but the relative stability of the different kernel types was well demonstrated in this test. Examples of the relative thermal stability of different fissile and fertile particles at different irradiation temperatures are shown in Figs. 7.34 through 7.37. Figure 7.34 shows a UO_2 kernel which has migrated a small distance into the buffer coating under moderate temperature conditions and a thoria kernel which has exhibited no migration under the same conditions. Figure 7.35 shows a $(4.1Th,U)O_2$ kernel which has migrated a small distance into the buffer coating and, again, a ThO_2 kernel which has exhibited no migration under the same conditions. Figures 7.36 and 7.37 show $(4.1Th,U)O_2$ kernels which have migrated through the particle coatings at high temperatures and temperature gradients and ThO_2 particles which have migrated only partially into the buffer coating under the same conditions. The migration rates observed in this test were correlated with the operating temperatures and temperature gradients, as described in Sect. 11.1.

7.4.2 Postirradiation Examination of ORNL Fuel Rods from ETR Capsule P13N

E. L. Long, Jr.

Two ORNL slurry-blended warm-molded fuel rod specimens were irradiated in two compartments of a five-compartment instrumented ETR capsule (P13N) along with twenty other fuel rod specimens fabricated by GAC. This capsule was designed by GAC as a part of their thermal stability tests; their results are reported separately.[20] The ORNL fuel rod specimens contained the same fuel (strong-acid-resin-derived fissile particles and thoria fertile particles) and were fabricated with the same matrix as the molded rods in HRB-3. The results from the two experiments are thus being reported together.[21] In general, the molded fuel rods in P13N performed as well as those in HRB-3. However, the much higher burnup of the highly enriched fissile particles and the high operating temperatures for a substantial part of the irradiation in P13N combined to produce directional migration of fuel and severe attack by fuel compounds in the SiC layer of Triso coatings. On the other hand, few completely failed coatings were observed, which confirmed the low fission-gas-release data. In addition, no amoeba migration of the fertile particles was observed in P13N, in contrast to HRB-3. Details of the examination and performance analyses are given in Ref. 21.

19. R. A. Olstad et al., *An Irradiation Test of Candidate HTGR Recycle Fuels in the H-1 and H-2 Capsules*, ORNL-TM-4397 (July 1974).

20. *HTGR Base Program Quart. Progr. Rep. Aug. 31, 1973*, Gulf GA-A 12725, pp. 190–234.

21. F. J. Homan et al., *Irradiation Performance of HTGR Fuel Rods in HFIR Experiment HRB-3 and ETR Experiment P13N*, ORNL-TM-4526 (October 1974).

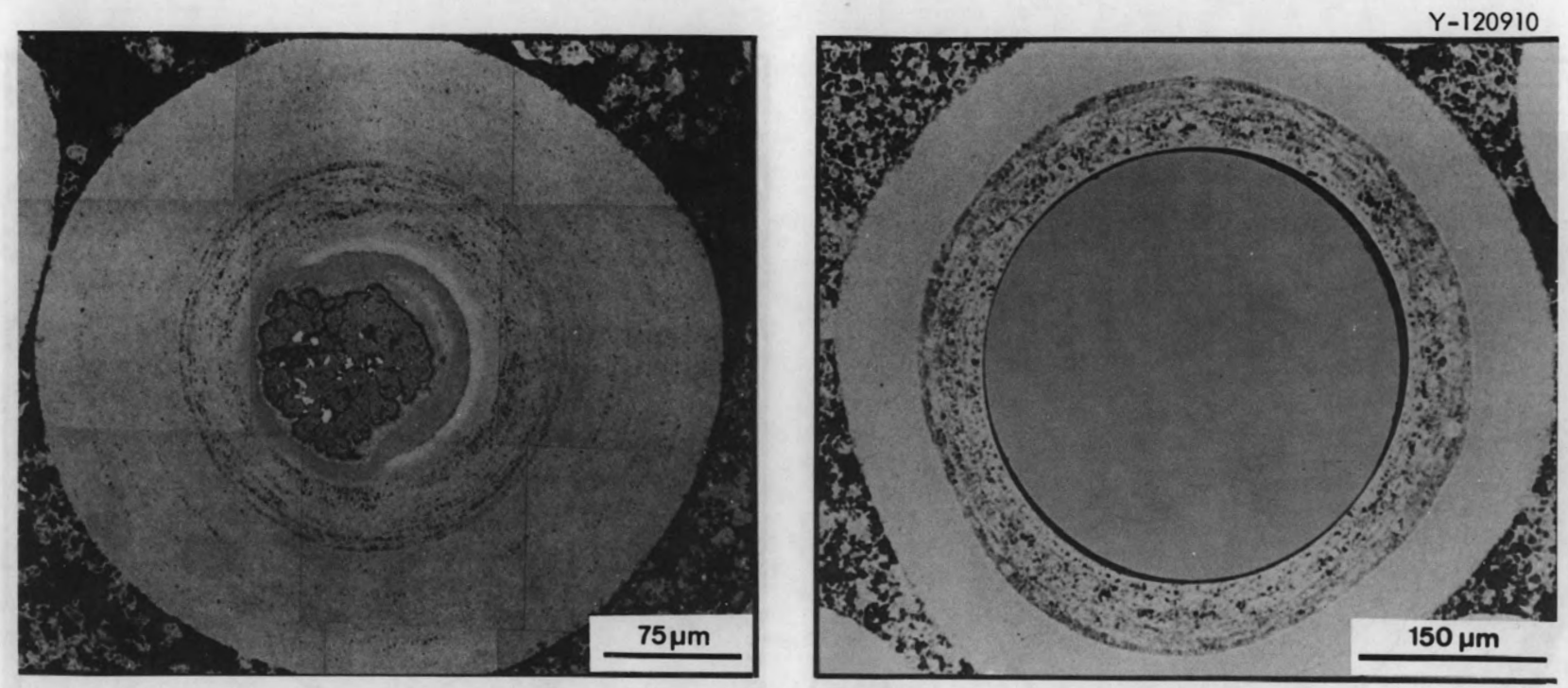

Fig. 7.34. Relative thermal stability of UO_2 and ThO_2 particles irradiated in rod H-1-2. These particles were irradiated for 97 days at ~950°C in a thermal gradient of ~1000°C/cm and attained a fast-neutron fluence of 5×10^{21} neutrons/cm^2. (*a*) UO_2 particle, 33% FIMA burnup; (*b*) ThO_2 particle, 0.2% FIMA burnup.

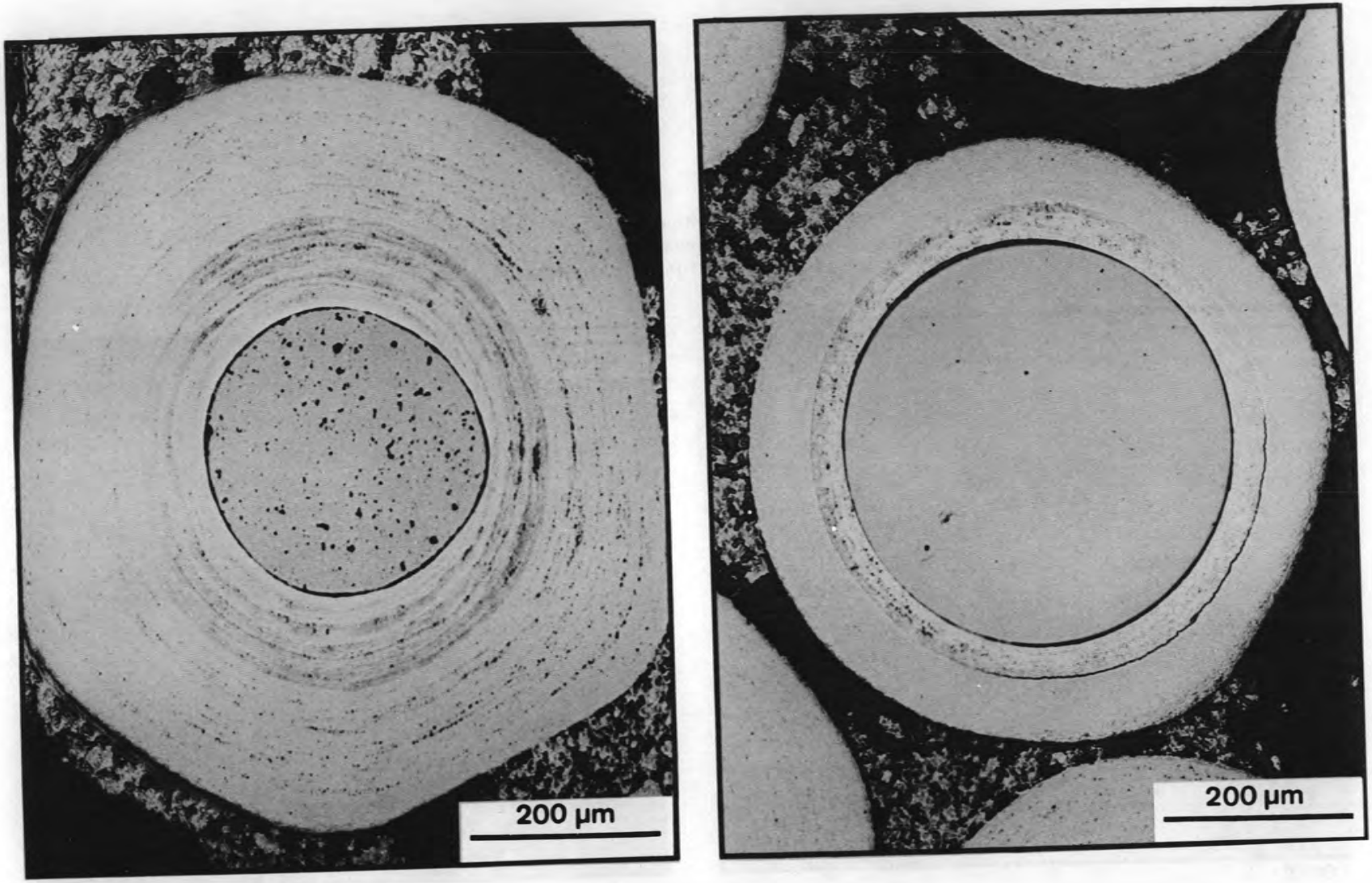

Fig. 7.35. Relative thermal stability of (4.1Th,U)O_2 and ThO_2 particles irradiated in rod H-1-4. These particles were irradiated for 97 days at ~1050°C in a thermal gradient of ~1200°C/cm and attained a fast-neuton fluence of 6.3×10^{21} neutrons/cm^2. (*a*) (4.1Th,U)O_2 particle, 8.2% FIMA burnup; (*b*) ThO_2 particle, 0.4% FIMA burnup.

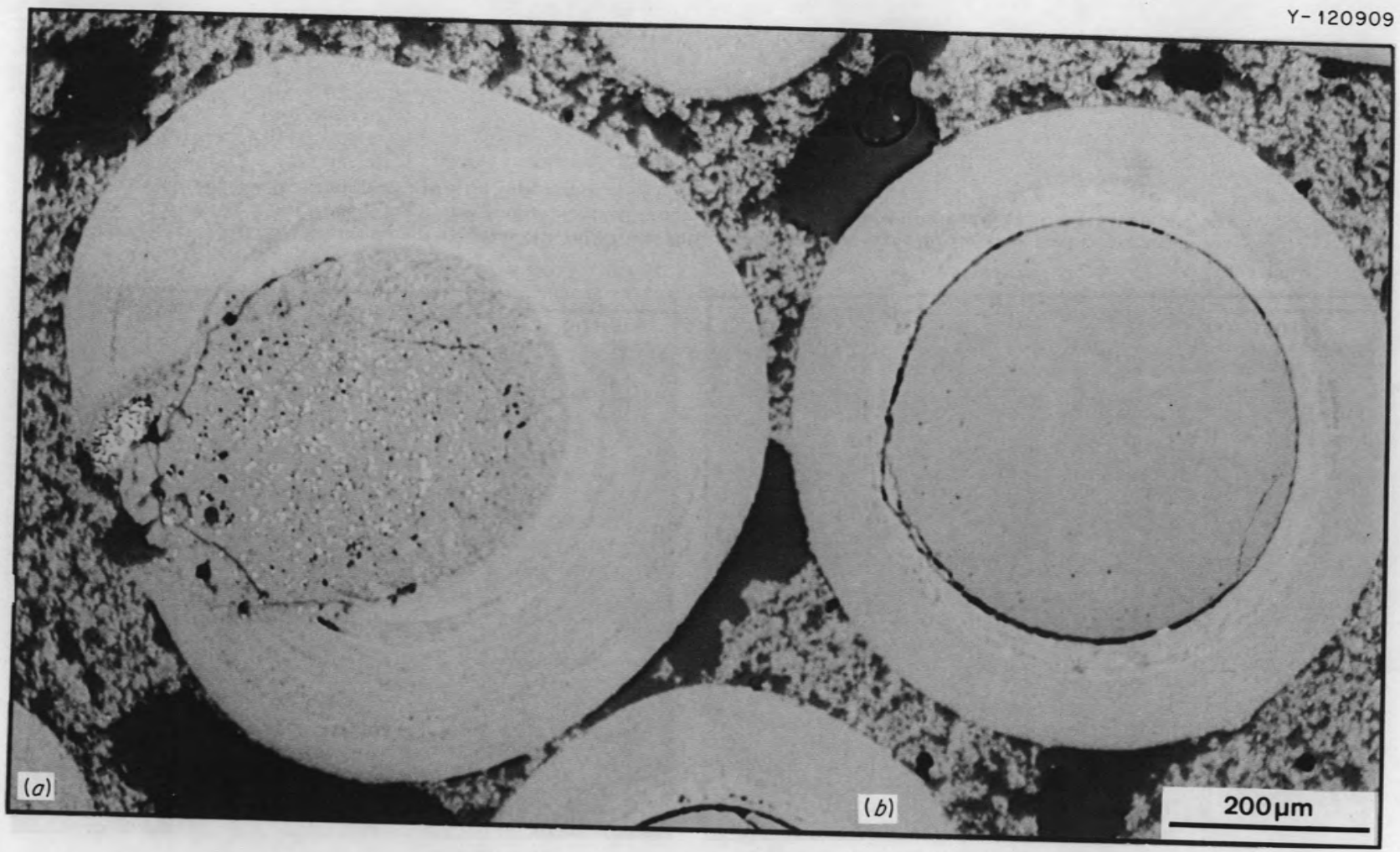

Fig. 7.36. Relative thermal stability of (4.1 Th,U)O_2 and ThO_2 particles irradiated in rod H-2-10. These particles were irradiated for 37 days at ~1350°C in a thermal gradient of ~1700°C/cm and attained a fast-neutron fluence of 5×10^{21} neutrons/cm^2. (*a*) (4.1 Th,U)O_2 particle, 8.3% FIMA burnup; (*b*) ThO_2 particle, 0.3% FIMA burnup.

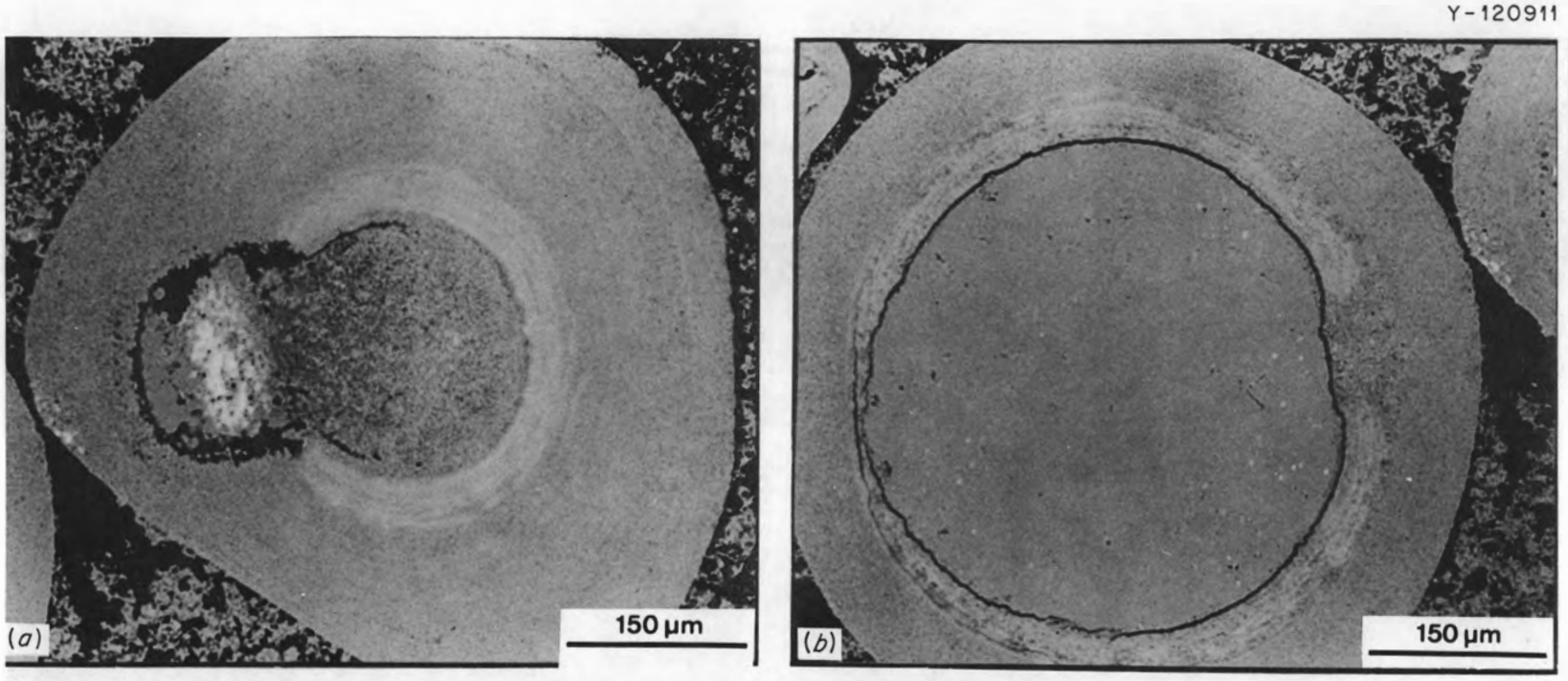

Fig. 7.37. Relative thermal stability of (4.1,ThU)O_2 and ThO_2 particles irradiated in rod H-1-10. These particles were irradiated for 37 days at ~2000°C in a thermal gradient of ~1100°C/cm and attained a fast-neutron fluence of 5.4×10^{21} neutrons/cm^2. (*a*) (4.1Th,U)O_2 particle, 8.6% FIMA; (*b*) ThO_2 particle, 0.4% FIMA.

7.5 RECYCLE TEST ELEMENTS IN THE PEACH BOTTOM REACTOR

E. L. Long, Jr.

A set of seven test fuel elements, known as recycle test elements (RTEs), is being irradiated in the Peach Bottom Reactor. Each RTE contains six 15-in.-long graphite fuel bodies, each of which has eight $\frac{1}{2}$-in.-diam holes to accommodate fuel samples; thus, 48 separate large fuel samples are irradiated in each RTE. These elements were fabricated in a cooperative effort by ORNL and GAC as part of the National HTGR Fuel Recycle Development Program. The elements contain bonded fuel rods and loose beds of particles made from several combinations of fertile and fissile particles of interest for use in the HTGR. The portion of the fuel prepared by ORNL has been described in detail in an ORNL-TM report,[22] which, in conjunction with a GAC report,[23] comprises a complete fabrication description of the test elements.

The irradiation of the first six RTEs began in the Peach Bottom Reactor in July 1970, and the tests have progressed without incident since that time.[24] In April 1971, the first of these elements was discharged from the reactor (RTE-7), and an additional element (FTE-11, previously designated RTE-1) was inserted. After 252 equivalent full-power days of operation, a peak fast fluence of about 10^{21} neutrons/cm^2 ($E >$ 0.18 MeV) was achieved in RTE-7. The second recycle test element (RTE-4) was removed from Peach Bottom in early January 1972 after 384 equivalent full-power days of irradiation. The peak fast fluence exposure was about 1.9×10^{21} neutrons/cm^2, and the average fuel burnup was about 3.5% FIMA.

The results from examination of these two test elements have also been reported in detail.[22] Briefly, the fuel performed very well, as expected at the low exposures, but dimensional data indicated greater irradiation-induced shrinkage of the fuel rods than anticipated from accelerated test data at higher exposures. The reasons for such increased shrinkage may become evident during examination of the remaining test elements. The third recycle element, RTE-2, was removed from the Peach Bottom Reactor in mid-September 1973 after 701 equivalent full-power days, and the postirradiation examination is scheduled to begin in early CY-74. The remaining four recycle test elements will remain in the reactor until the termination of reactor operations, scheduled for fall CY-74.

22. E. L. Long, Jr., R. B. Fitts, and F. J. Homan, *Fabrication of ORNL Fuel Irradiated in the Peach Bottom Reactor and the Postirradiation Examination of Recycle Test Elements 7 and 4*, ORNL-TM-4477 (September 1974).

23. R. P. Morissette and K. P. Steward, *Recycle Test Element Program Design, Fabrication, and Assembly*, GA-10109 (September 1971).

24. *GCR Programs Annu. Progr. Rep. Dec. 31, 1972*, ORNL-4911, Fig. 7.11, p. 104.

7.6 NUCLEAR ANALYSIS IN SUPPORT OF IRRADIATION EXPERIMENTS

H. T. Kerr

Nuclear analysis support required for irradiation experiments generally can be described as follows.

1. Estimates of neutron-induced reaction rates and neutron fluxes are needed during the design of an experimental capsule to determine fuel loadings, heat rates and temperature profiles, neutron fluences, and other design parameters. These estimates are based on information from computational analysis and data from previous experiments.

2. Dosimetry support is available for each irradiation experiment. Dosimeter packages irradiated with the capsule provide activation data for use in evaluating the preirradiation design estimates and in making comparisons with other experiments.

The neutronic characteristics of an experimental capsule are determined primarily by the characteristics of the irradiation facility and to a much lesser extent by the capsule design. For this reason, the primary objective of the nuclear analysis effort has been to completely characterize each irradiation facility. Specific capsule design variations are then evaluated for each irradiation facility. The following facilities are used for GCR program irradiation experiments.

1. The peripheral target positions in the HFIR target region are used for the HT capsules.
2. The RB-5 and RB-7 facilities in the HFIR removable beryllium region are used for the HRB capsules.
3. The VXF-13 facility in the HFIR permanent beryllium region is used for initial low-flux irradiations of some HRB capsules.
4. The C-3 facility in the ORR core is used for GAC experiments. The OG-1 capsule was irradiated in the C-3 facility.
5. The E-3 facility in the ORR core is presently shared by GAC experiment P13Q and ORNL experiment OF-1. However, GAC will assume exclusive use of

the E-3 facility, and two new facilities will be added to the ORR core for ORNL experiments.

The neutronic characteristics which have been determined for each of these facilities are presented below.

7.6.1 Peripheral Positions in the HFIR Target Region

The neutron characteristics in the HFIR target region were established by several computational analyses and experimental efforts. Calculated spatial and time variations of the neutron fluxes within the target region have been substantiated with data from irradiation experiments. Fluxes in the peripheral target facilities are shown in Figs. 7.38 and 7.39 and should be used for analysis of HT capsules. Table 7.28 provides *typical* reaction rate data for the HT capsules.

7.6.2 The RB-5 and RB-7 Facilities in the HFIR Removable Beryllium

Calculated neutron fluxes in the removable beryllium region show large spatial gradients and time variations which result from the close proximity of these facilities to the HFIR core and control plates. Dosimeter data from the HRB capsules and other experiments in these facilities can be interpreted as multicycle averages of the calculated fluxes, but a direct experimental measurement of flux variations in the removable beryllium is extremely difficult and has not been done. Calculated fluxes for the RB facilities are presented in Figs. 7.40 and 7.41, and typical unit reaction rates are given in Table 7.28.

The HRB-3, -4, -5, and -6 capsules were irradiated for five or more fuel cycles and were repositioned in the

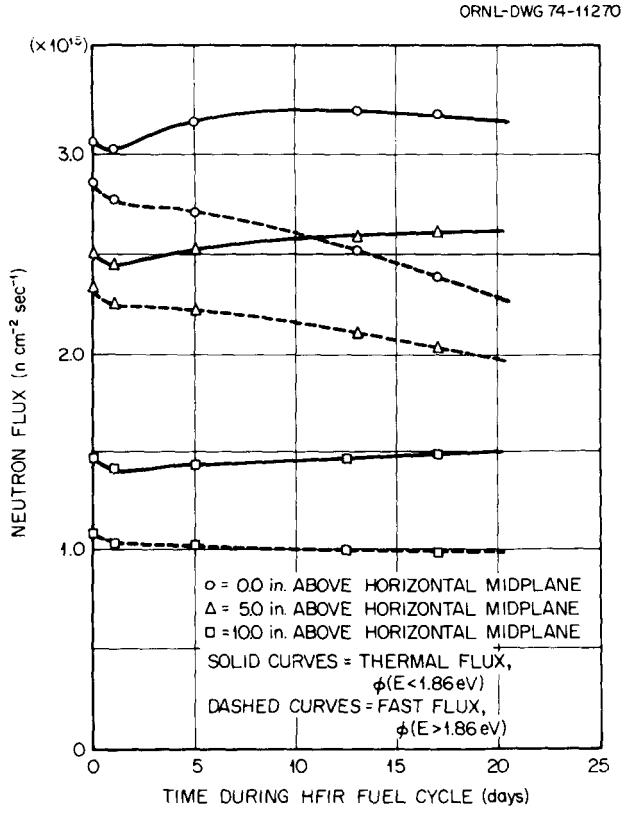

Fig. 7.38. Time-dependent neutron fluxes for three axial positions in the A-2 target facility of HFIR (capsule-dependent perturbations omitted).

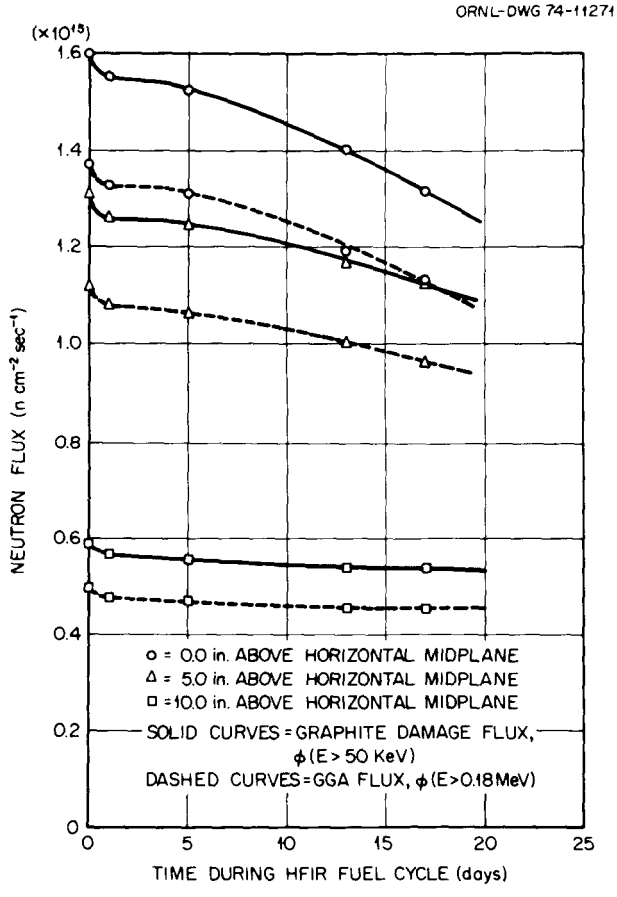

Fig. 7.39. Time-dependent neutron damage fluxes for three axial positions in the A-2 target facility of HFIR (capsule-dependent perturbations omitted).

Table 7.28. Maximum unit reaction rates[a] (10^{-9} reaction/sec-atom) for isotopes in GCR irradiation facilities at ORNL and flux data

Isotope	Reaction	HFIR [100 MW(t)]			ORR [30 MW(t)]	
		A-2 target	RB-5	VXF-13	L-3	L-3
		HT series	HRB series		P13Q and OF-1	OG-1
^{232}Th[b]	n,γ	16.0	11.8	3.5	2.4	2.3
^{233}Pa	n,γ	216	106	35.9	29.1	28.2
^{233}U	n,γ	130	52.8	26.6	11.7	11.3
	n,f	1270	501	272	102	99.2
^{234}U	n,γ	284	124	55.8	31.6	30.7
^{235}U	n,γ	232	93.0	49.6	18.9	18.3
	n,f	1270	482	277	91.1	88.4
^{236}U	n,γ	38.8	17	7.88	8.84	8.57
^{238}U[b]	n,γ	32	18.3	4.0	3.1	3.0
^{239}Pu	n,γ	900	414	216	105	102
	n,f	2070	856	468	197	191
^{240}Pu	n,γ	2100	1026	321	375	364
^{241}Pu	n,γ	840	338	196	73.5	71.3
	n,f	2610	1044	587	221	214
^{59}Co	n,γ	83.5	41.0	20.1	7.60	7.37
^{54}Mn	n,p	0.090	0.017	0.0013	0.0144	0.0140
Neutron fluxes (10^{15} neutrons cm^{-2} sec^{-1})						
$\phi(E > 0.18$ MeV)		1.37	0.49	0.057	0.31	0.30
$\phi(\bar{r})_{tot} = \int_0^\infty \phi(\bar{r},E)\,dE$		5.90	2.60	0.966	1.00	0.97

[a] A unit reaction rate is defined as $\int_0^\infty \sigma(E)\,\phi(E)\,dE$. Values given are typical for GCR target specimen.

[b] These isotopes are strong resonance absorbers, and their reaction rates are very sensitive to capsule design. The values listed are *typical* for GCR capsules.

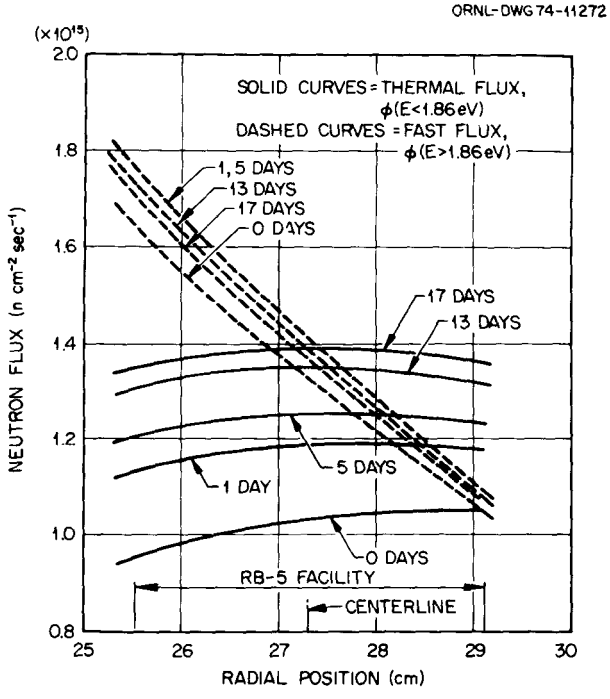

Fig. 7.40. Time-dependent radial profiles of neutron fluxes at horizontal midplane of the RB-5 facility in the HFIR removable beryllium.

facility one or more times during irradiation. Consequently, the activation data from these capsules must be interpreted as a time integral involving neutron fluxes which are orientation dependent. However, uncertainties in the capsule orientation histories produce large uncertainties in the fluxes derived from the activation data. Dosimeter packages in future HRB capsules are designed to eliminate the orientation problem.

7.6.3 The VXF-13 Facility in the HFIR Permanent Beryllium

Neutron fluxes for the VXF-13 facility have not been measured directly, and the fluxes calculated for the permanent beryllium region are strongly dependent on some assumptions in the computational model. Significant effort will be expended during FY-1975 to accurately characterize the VXF-13 facility.

The design of the HRB-7 and -8 capsules required some estimate of the neutron fluxes and reaction rates in the VXF-13 facility. Some activation data were available from dosimeters irradiated at the horizontal midplane of the VXF-7 facility, and the fluxes derived from these data were assumed to be equally valid for the geometrically similar VXF-13 facility. The axial and

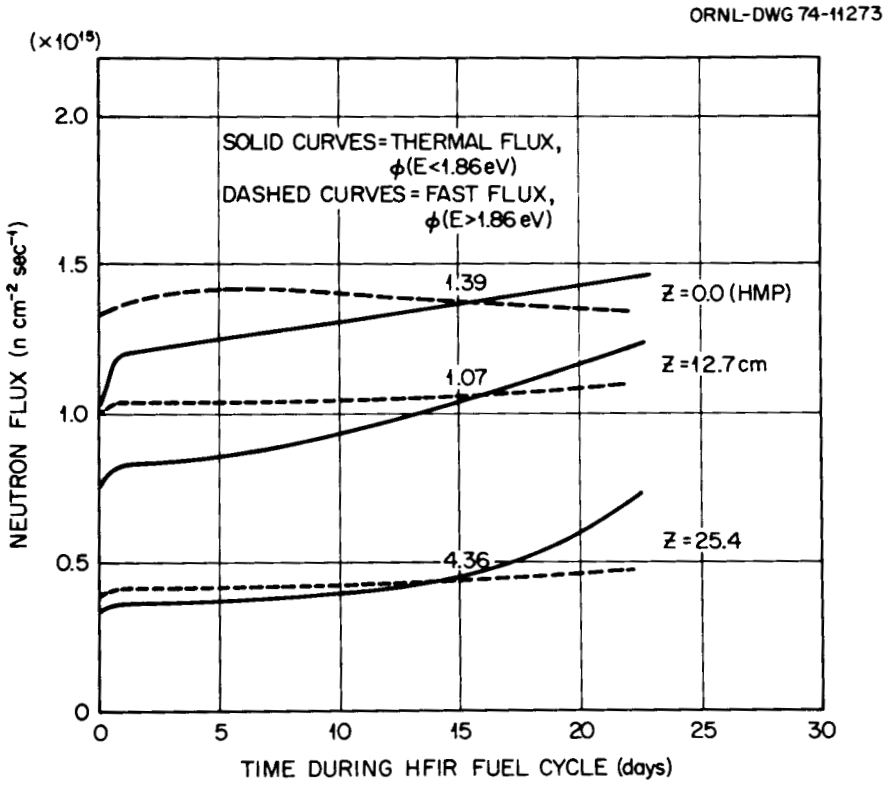

Fig. 7.41. Time-dependent neutron fluxes for three axial positions at a radial position of 27.3 cm in the HFIR removable beryllium.

time dependence of fluxes in the VXF-13 (and VXF-7) position were obtained from computational models and normalized to the experimental data. The resulting fluxes are shown in Figs. 7.42 and 7.43, and preliminary reaction rate data for HRB capsules in the VXF-13 facility are given in Table 7.28.

7.6.4 The C-3 Facility in the ORR Core

The neutronic characteristics of a given ORR core position depend heavily on the relative positioning of fuel elements and beryllium reflector elements in the overall core configuration. Consequently, neutron fluxes for each core lattice position must be determined for each unique core configuration.

The OG-1 experiment was irradiated in the C-3 position of the ORR core configurations shown in Fig. 7.44. The results of computational analyses and dosimetry experiments were combined to determine neutron fluxes in the OG-1 experiment as shown in Fig. 7.45.

7.6.5 The E-3 Facility in the ORR Core

The capsule containing ORNL experiment OF-1 and GAC experiment P13Q was placed in the E-3 facility. Several preirradiation estimates were made of reaction rates and neutron fluxes, and some dosimetry results were obtained from monitors loaded into the E-3 aluminum core piece. Recommended values for neutron fluxes are presented in Figs. 7.46 and 7.47, and reaction rates are presented in Table 7.28. Appreciably more information will be available when the dosimeters are recovered from OF-1.

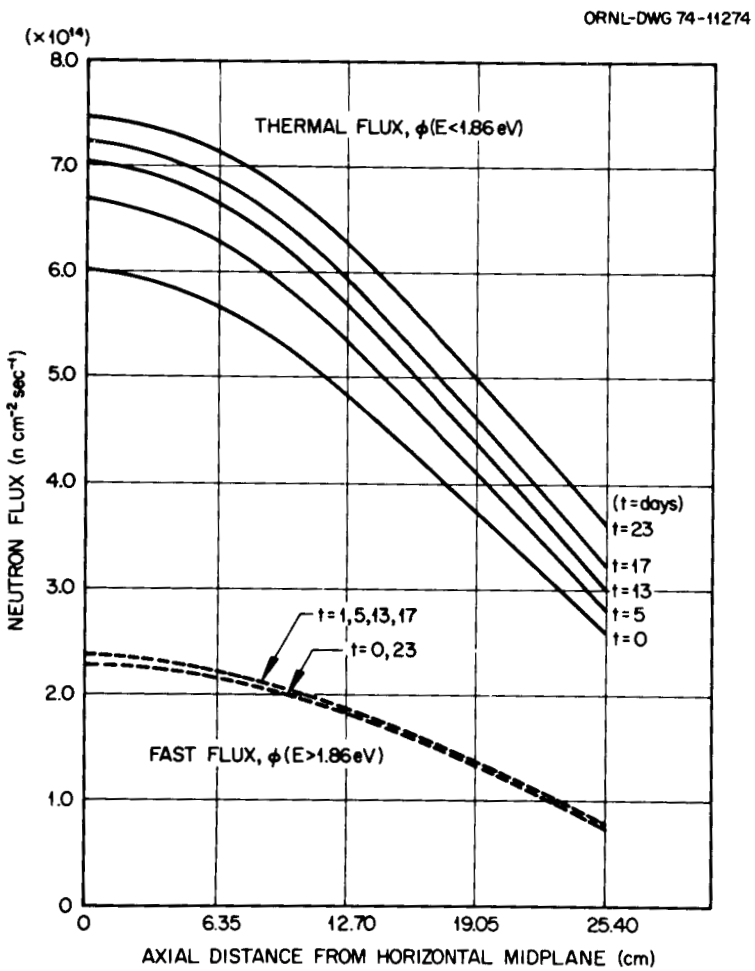

Fig. 7.42. Time-dependent axial profiles of neutron fluxes for the VXF-13 facility in the HFIR permanent beryllium.

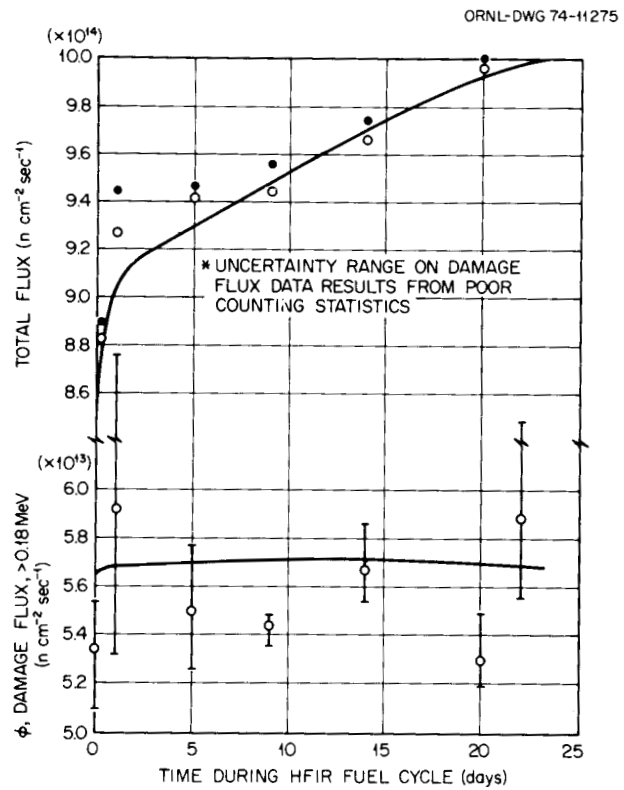

Fig. 7.43. Comparison of calculated and experimentally derived neutron fluxes at the horizontal midplane of the VXF-13 rabbit facility in HFIR permanent beryllium.

ORNL-DWG 74-11276

Pool
W

A-1 Be	A-2 Be	A-3 F	A-4 F	A-5 F	A-6 F	A-7 Be	A-8 Be	A-9 Be
B-1 Be	B-2 F	B-3 F	B-4 C/F	B-5 F	B-6 C/F	B-7 F	B-8 Be	B-9 Be
C-1 Be	C-2 F	C-3 OG-1	C-4 F	C-5 F	C-6 F	C-7 F	C-8 Be	C-9 Be
D-1 Be	D-2 F	D-3 F	D-4 C/F	D-5 F	D-6 C/F	D-7 F	D-8 HT	D-9 Be
E-1 Be	E-2 F	E-3 OF-1	E-4 F	E-5 F	E-6 F	E-7 F	F-8 Be	E-9 Be
F-1 Be	F-2 F	F-3 F	F-4 FF	F-5 F	F-6 FF	F-7 Be	F-8 Be	F-9 Be
G-1 Be	G-2 Be	G-3 Be	G-4 Be	G-5 Be	G-6 Be	G-7 Be	G-8 Be	G-9 Be

S

N

E

Be = beryllium core piece.

F = ORR fuel element.

C/F = partially inserted control rod with a fuel follower section.

HT = hydraulic tube facility.

FF = fuel follower of fully withdrawn control rod.

OF-1 and OG-1 = HTGR irradiation experiments.

Fig. 7.44. ORR core configuration during irradiation of the OG-1 and OF-1 experiments.

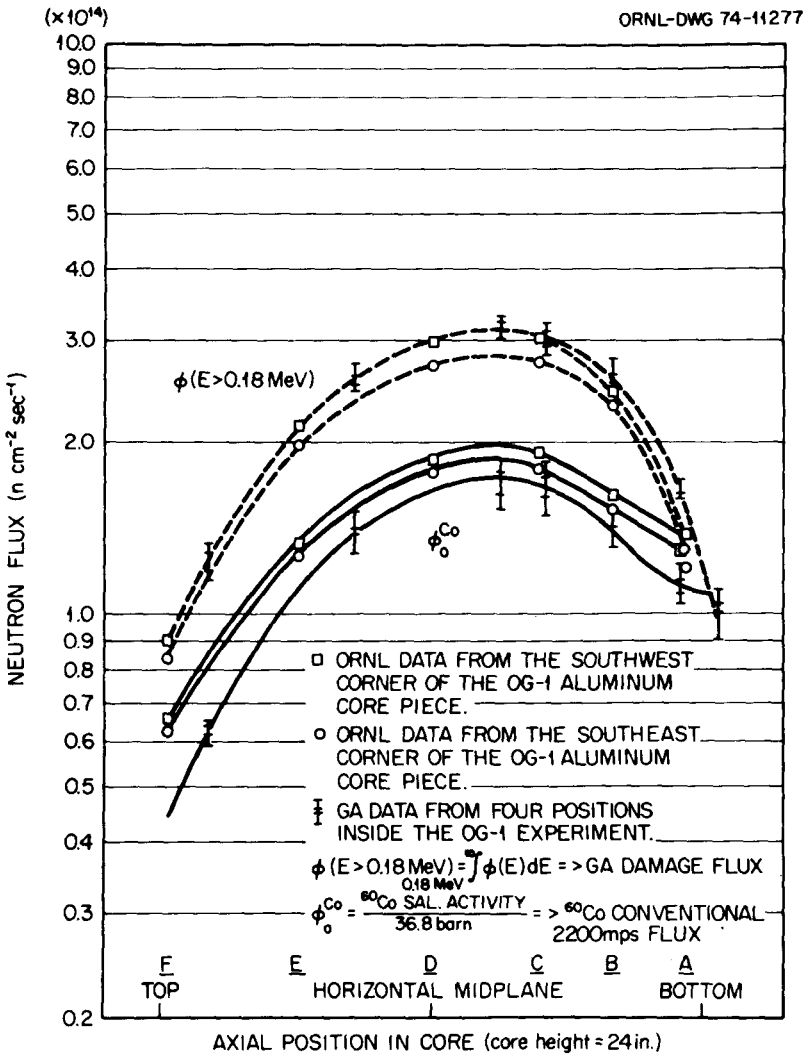

Fig. 7.45. ORNL and GAC flux data for the OG-1 experiment in the C-3 facility of the ORR.

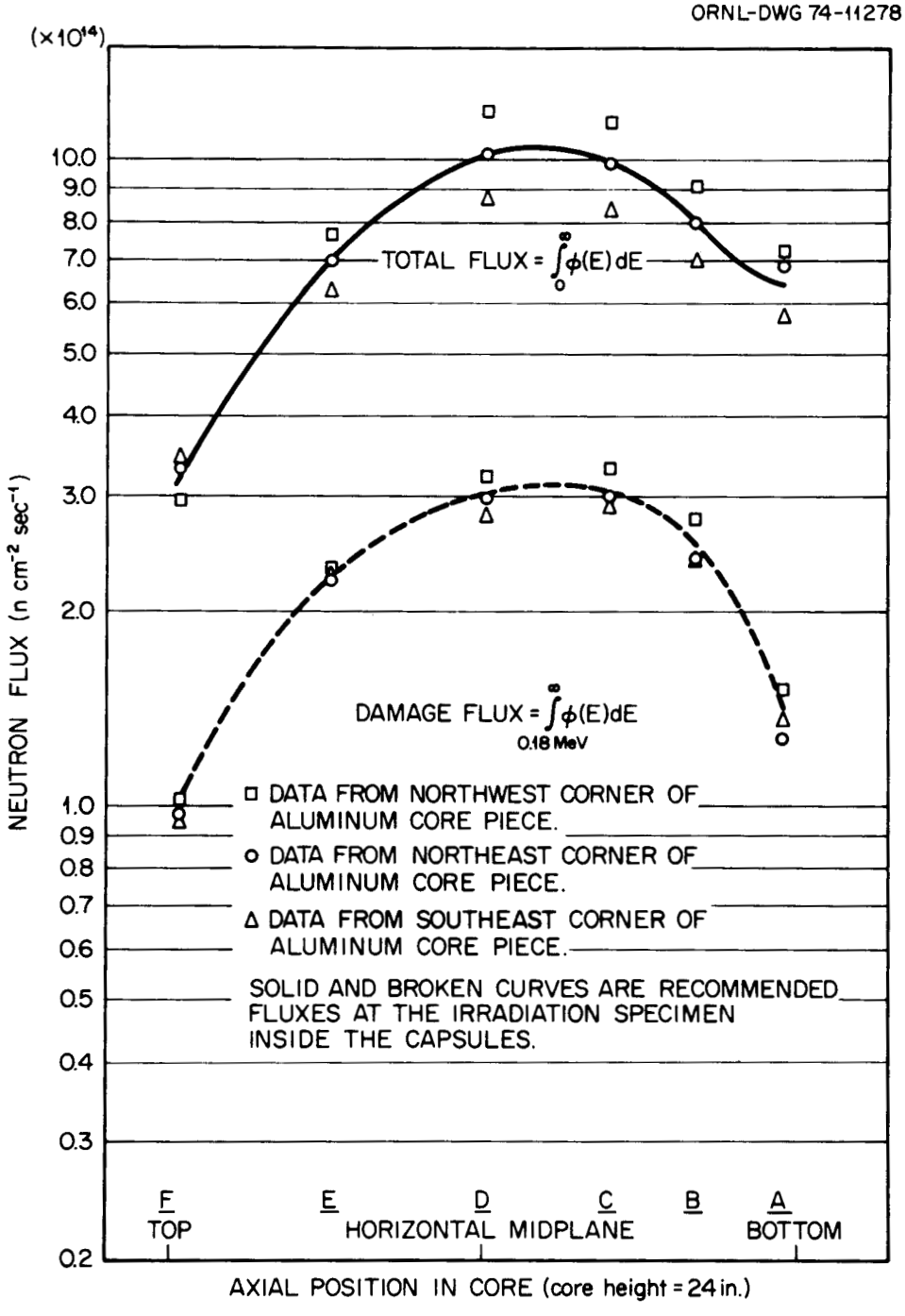

Fig. 7.46. Flux data for the OF-1 (and P13Q) experiments in the E-3 facility of the ORR.

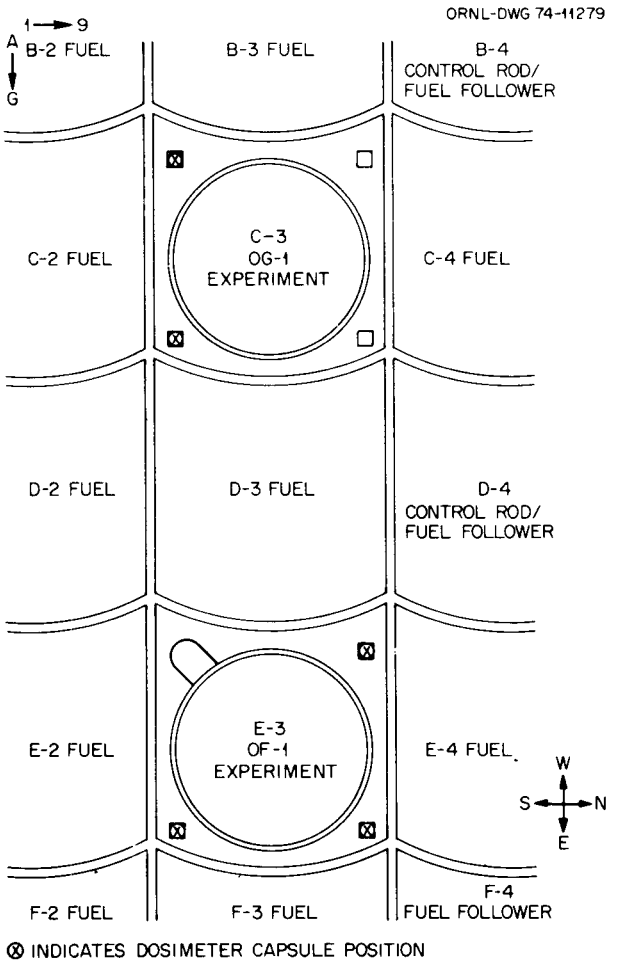

Fig. 7.47. Irradiation experiment positions in ORR core.

7.7 CAPSULE THERMOMETRY

R. L. Shepard R. M. Carroll
J. K. East

7.7.1 HRB-3 Center-Line Thermometry

Design

The fuel center-line temperature in HRB-3 was measured with a W–3% Re/W–25% Re thermocouple made by stripping about 1 ft of the stainless steel sheath and magnesia insulation from sheathed material and replacing the magnesia with hard-fired BeO insulators and an overwrap of rhenium foil. The thermocouple junction (TE-112) was located at the same axial position as three sheathed Chromel/Alumel thermocouples and one sheathed W–3% Re/W–25% Re thermocouple in the peripheral graphite sleeve (thermocouples TE-105, -106, -109, and -108 in Fig. 7.48).

The sheathed W-Re and Chromel/Alumel thermocouple material was brazed through capsule bulkheads and connected to thermocouple extension wire about 10 ft above the fuel, extending about 30 ft to the experiment instrumentation connector at poolside. Heavy copper wire was used for W-Re extension to reduce the total circuit resistance between poolside and the data-collection system. In addition to the usual compensating thermocouple extension wires, a pair of copper wires was attached to the connector terminals on thermocouples TE-108 (peripheral W-Re), TE-109 (peripheral Chromel/Alumel), and TE-112 (central W-Re). These additional wire pairs provided means for passing a small (4 mA) dc current through the thermocouple loop, thereby measuring the loop resistance by subtracting

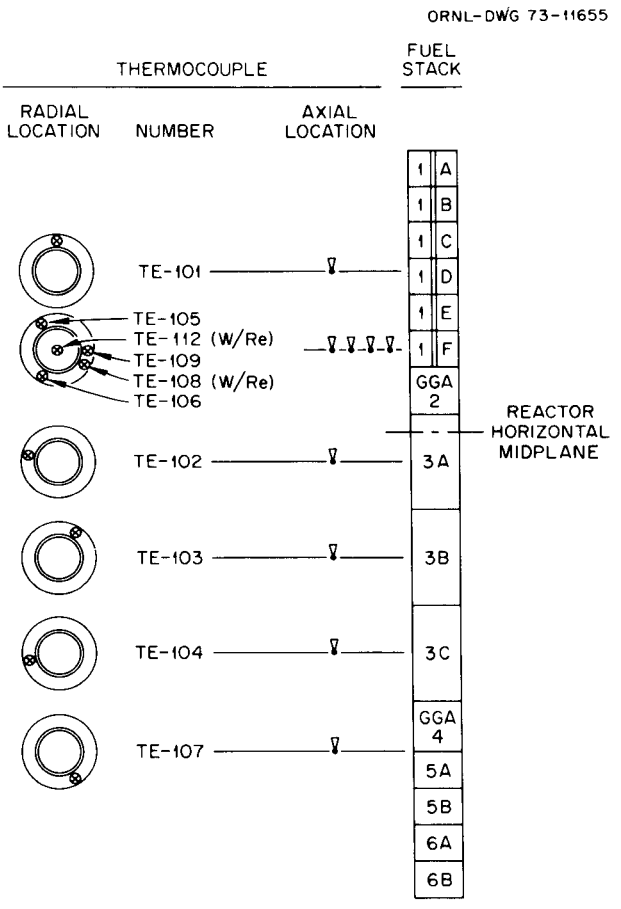

Fig. 7.48. HRB-3 fuel specimen and thermocouple locations.

the thermal emf (no current) from the thermal emf plus IR drop (with current). This loop resistance measurement was performed routinely during the course of the experiment, using the Dextir data system to switch an external current supply and to measure terminal emfs for the three thermocouples. Both forward and reverse dc currents were employed.

Performance

The W–3% Re/W–25% Re center-line thermocouple survived the entire 6100-hr irradiation at temperatures to 1100°C, accumulating a thermal-neutron fluence of about 2.6×10^{22} nvt and a fast (>0.18 MeV) neutron fluence of 7.8×10^{21} nvt in an inert atmosphere but exposed to carbon and fission products. As shown previously,[24] the thermocouple output decreased about 300°C during the 6100-hr irradiation. This decrease in output was accompanied by an increase in loop resistance of 5.4 Ω, or 17% of the total 10-ft-long thermocouple loop. Reduced to that fraction of the thermocouple within the high-flux high-temperature fueled region, this resistance change amounts to several-fold increase.

A plot of values and the measured loop resistance vs the indicated temperatures (Fig. 7.49) taken during the

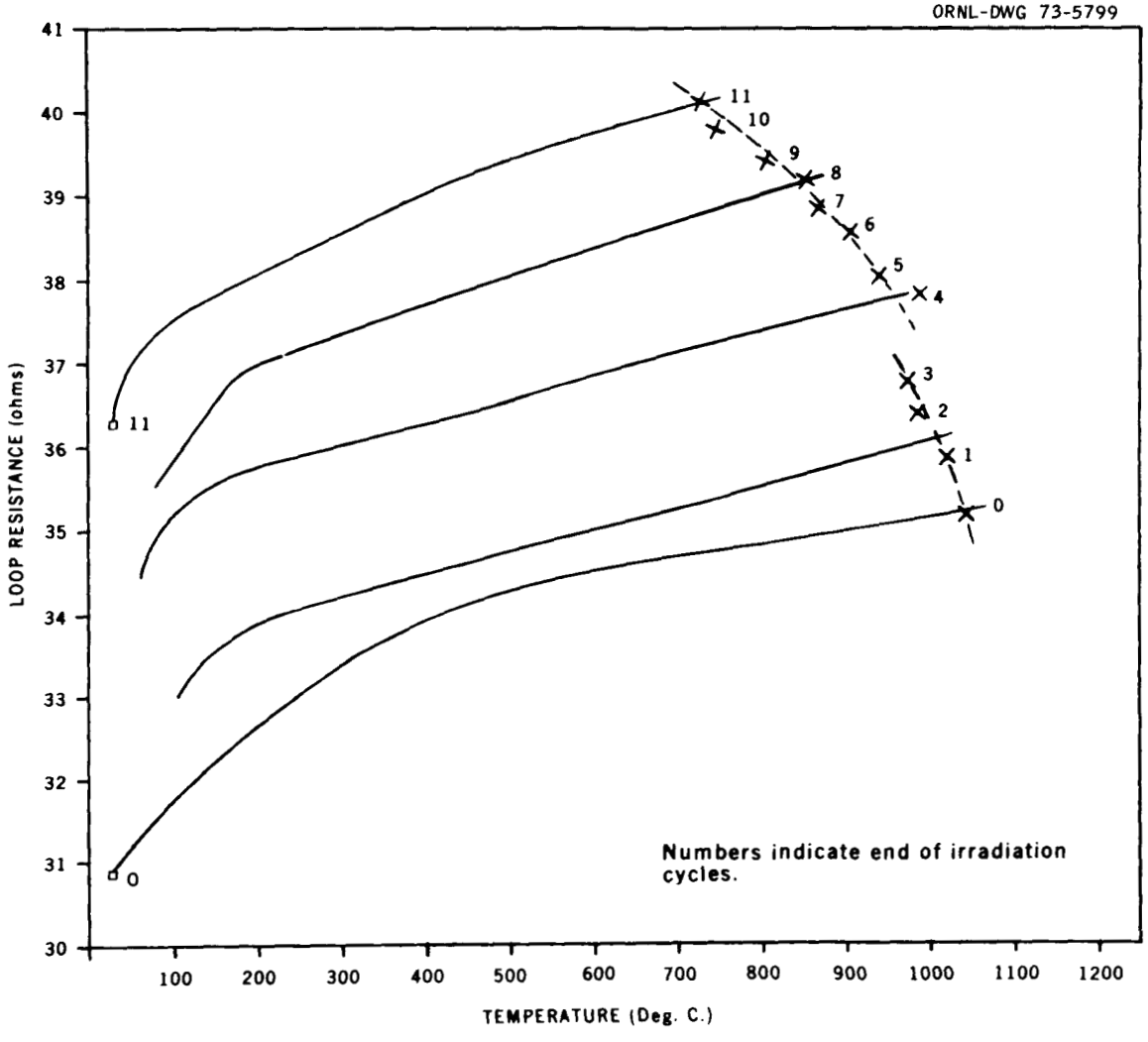

Fig. 7.49. HRB-3 W–3% Re/W–25% Re center-line thermocouple loop resistance vs temperature.

start of 4 of the 11 reactor cycles and the last shutdown shows a progression of the thermocouple condition from one of high output and low resistance to one of reduced output and higher resistance. It also shows the 5-Ω increase in ambient temperature resistance. The dashed line connecting *X*'s identifies the normal operating condition during each cycle and is assumed to denote equal temperatures. If so, this plot shows a shift of thermocouple output of more than 300°C, from the 1100°C indicated initially to about 700°C, at the end of 11 cycles. This evaluation of the thermocouple decalibration agrees to within about 50°C with that obtained from heat production calculations.[24]

Postirradiation examination

The W–3% and W–25% thermocouple wires were retrieved from the HRB-3 capsule in postirradiation hot-cell examinations. Dimensional changes in the wire were clearly too small to account for the large observed resistance changes. Compositional changes, due to calculated W-to-Re transmutation and the separation of a second phase observed in metallographs of the wires, are believed to have caused both the decalibration and resistance increase of the thermocouple wires.

This experiment showed the feasibility of determining that the calibration of the thermocouple was changing by correlating changes in loop resistance and thermal emf, a method independent of any heat production and transfer calculations or assumptions about the true center-line temperature.

7.7.2 HRB-4 Center-Line Thermometry

Design

The W–3% Re/W–25% Re fuel center-line thermocouple for HRB-4 was fabricated from the same materials and by the same method as the one used in the HRB-3 experiment. Sheathed thermocouples in the peripheral graphite sleeve were located in similar positions (Fig. 7.48), except that no sheathed W-Re peripheral thermocouple (TE-108) was used. A significant difference was the connection of the additional loop current-carrying pair of leads. As shown in Fig. 7.50, the 300P/300N current-carrying pair was connected to the thermocouple loop just inside the primary bulkhead, defining a loop about 5 in. long, instead of the 10- to 30-ft-long loop used in HRB-3. Loop resistance measurements made during the course of the irradiation could be made to a precision of better than 0.03 Ω and showed much greater sensitivity to changes in reactor power and to degradation of the thermocouple.

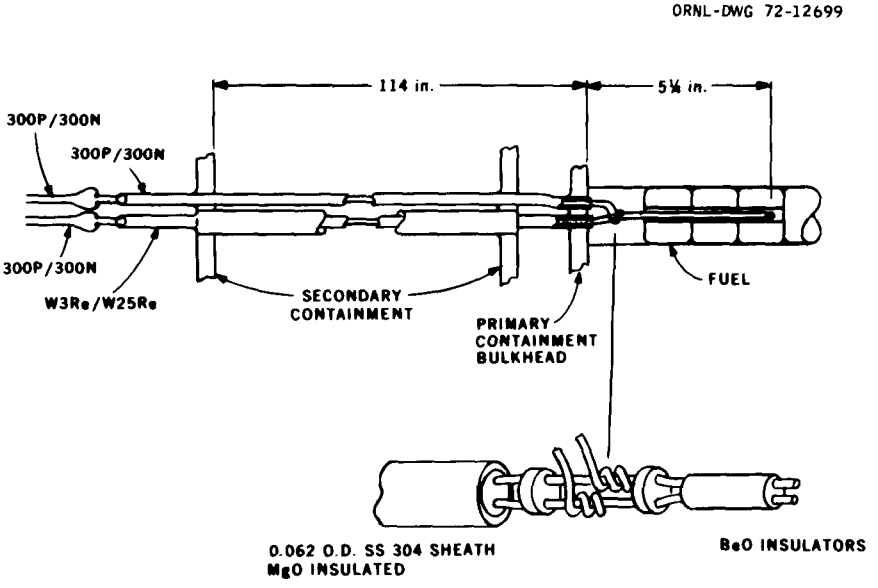

Fig. 7.50. Four-wire W-Re thermocouples in HRB-4.

Performance

The fuel center-line W–3% Re/W–25% Re thermocouple in HRB-4 failed open circuit after 2213 hr at temperatures of 900 to 1000°C during a capsule temperature increase created by adding neon to the helium gas flow. During this irradiation, the thermocouple showed a 75°C decrease in indicated temperature (from 925 to 850°C, assuming constant true center-line temperature) and a 0.6-Ω, or 18%, increase in the thermocouple loop resistance. The resistance increased at an accelerated rate during the 40-hr period preceding the failure, and erratic output was observed in the hour before failure.

The data for loop resistance and indicated temperature for the startup of each of the first four irradiation cycles (to 2011 hr) are plotted in Fig. 7.51. In contrast with HRB-3, these data show straight-line dependence of resistance on temperature (due to the shorter loop used) and permit quantitative estimates to be made of the decalibration. The method assumes that all points on a line perpendicular to the initial (0-hr) resistance-temperature line in fact represent the same true center-line temperature. The decalibration can then be determined graphically for various irradiation times. If such determinations are made, we observe (1) a linear increase in loop resistance at ambient temperature (reactor shutdown) and (2) a linear decalibration rate of about 50°C/1000 hr at an operating (true) temperature of 1100°C. This decalibration rate is about 30% greater than the estimate obtained above by the assumption of constant center-line temperature. When these data are converted from time to fluence and compared with data obtained by Sandefur et al.[25] using copper melting

25. N. L. Sandefur, J. S. Steibel, and R. J. Grenda, *EMF Drifts of Chromel/Alumel and W3%Re/W25%Re Thermocouples Measured In-Pile to High Neutron Exposures*, GULF-GA-A12501 (May 24, 1973).

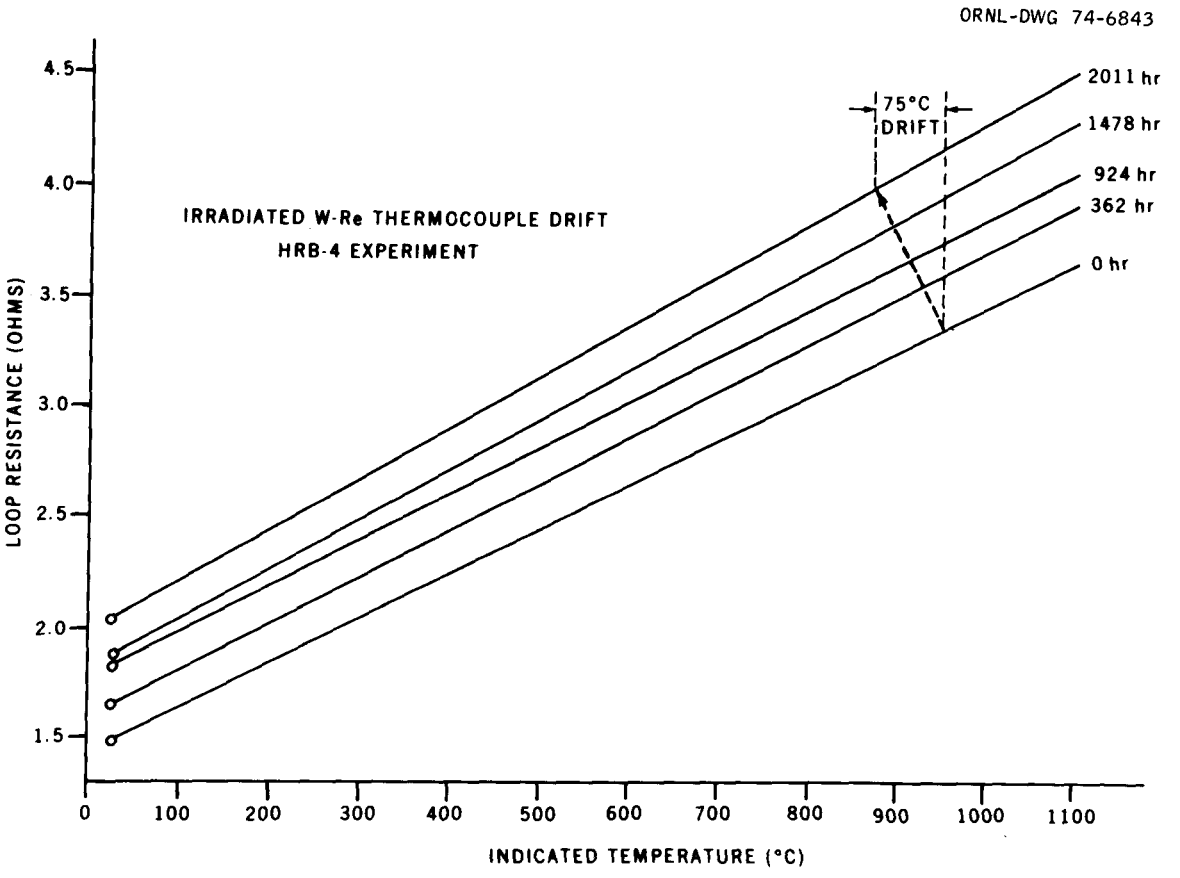

Fig. 7.51. Irradiated W-Re thermocouple drift in HRB-4 experiment.

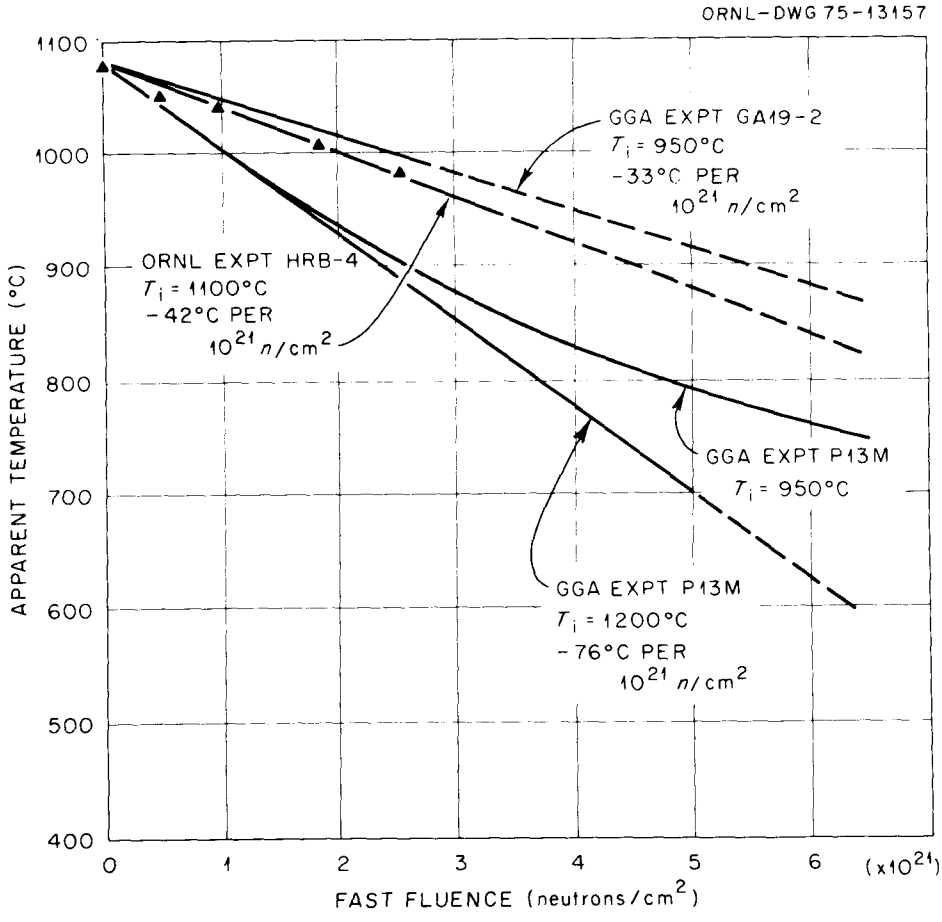

Fig. 7.52. Decalibration of W–3% Re/W–25% Re thermocouple in HFIR experiment HRB-4.

point in-reactor temperature standards, good agreement is obtained (as shown in Fig. 7.52) for irradiations conducted at about the same temperature.

Postirradiation examination

In hot-cell examination of the W-Re thermocouple materials recovered from HRB-4, it was determined that the thermocouple bead had broken off near the weld and that the BeO insulators had lengthened with respect to the thermocouple wires by as much as 3%. Apparently, insulator swelling forced the bead off the thermocouple.

This experiment demonstrated a quantitative correction for irradiated W-Re thermocouple decalibration by accurately measuring thermocouple loop resistance and thermal emf and using a graphical method to obtain true temperatures. The method assumes a normal shift in characteristics with irradiation time.

7.7.3 HRB-5 Center-Line Ultrasonic Thermometry

Design

The 10-ft-long $^1/_{16}$-in.-OD sheathed center-line thermocouple used in capsules HRB-3 and -4 was replaced in HRB-5 by a $^1/_{16}$-in.-OD stainless steel guide tube. This tube contained an ultrasonic lead line terminated by a 2-in.-long rhenium ultrasonic sensor shown in Fig. 7.53. The end of the rhenium sensor was located in about the same position in the fuel capsule as was the thermocouple junction in HRB-4. Containment for the sensor was provided by a welded sensor enclosure terminating the upper end of the guide tube.

ORNL-DWG 72-12697

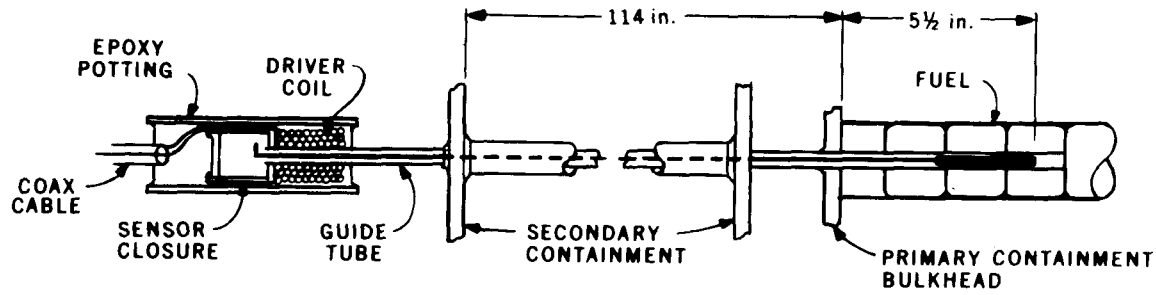

FUEL PIN CENTERLINE INSTALLATION

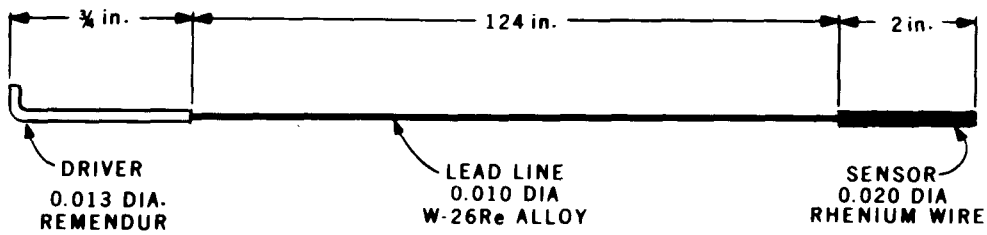

SENSOR LINE

Fig. 7.53. Ultrasonic thermometer in HRB-5.

The ultrasonic thermometer (UST) determines temperature by measuring the time interval between acoustic echos reflected (1) from the joint between the lead line and the sensor wire and (2) from the end of the sensor wire. Thus it measures the transit time in the rhenium wire of a mechanical pulse produced by and then sensed by the driver coil and the magnetostrictive Remendur driver inside the coil. This transit time is a direct measure of the velocity of sound in the rhenium and is a well-known and reproducible function of temperature. Rhenium wire was chosen for the sensor material because it represents a material whose thermal properties are well known to very high temperatures (to 3000°C). Its comparatively large thermal-neutron cross section of 85 b/atom makes it unsuitable for the high thermal-neutron flux environment of the HRB-HFIR experiments, but its tolerance for absorbed carbon is a partially compensating factor in its choice for this experiment.

The complement of sheathed Chromel/Alumel thermocouples in the peripheral graphite sleeve were the same as those used in HRB-4. The 2-in.-long rhenium sensor almost exactly covered the span from TE-101 to the plane of TE-105, -106 and -109.

Performance

The rhenium UST in HRB-5 operated satisfactorily for the entire 2570-hr capsule irradiation at temperatures from 900 to 1100°C, accumulating a thermal-neutron fluence of 1.1×10^{22} nvt and a fast-neutron ($E >$ 0.18 MeV) fluence of $3\,2 \times 10^{21}$ nvt. A pronounced shift in the pulse interval (or transit time) during reactor shutdown isothermal conditions was noted after each 23-day reactor cycle. The points plotted in Fig. 7.54 show a decrease in transit time from about 43 μsec initially to about 40.5 μsec after 2570 hr irradiation, or a 7% decrease. The decrease shows a straight-line dependence on time or fluence. Also plotted in Fig. 7.54 is the initial calibration of the UST (solid line) made before capsule assembly and a final calibration made in the in-pool whole-capsule furnace (shown in

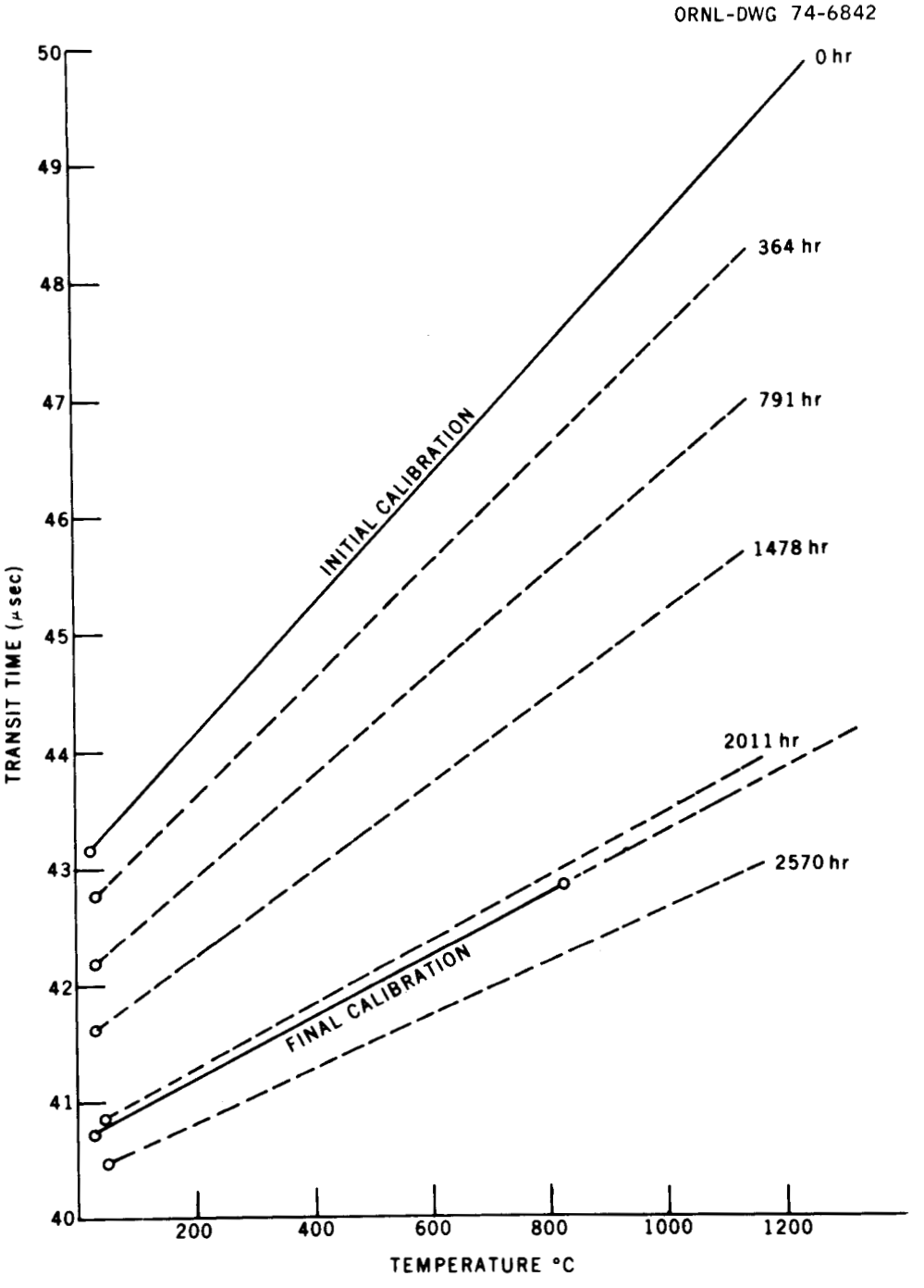

Fig. 7.54. Irradiated rhenium ultrasonic thermometer drift in HRB-5 experiment.

Fig. 7.1) after removing the HRB-5 capsule from its position in the HFIR RB irradiation facility.

The dashed lines interpolated between the initial and final calibration curves in Fig. 7.54 are suggested intermediate calibrations based on the known values of the ambient temperature transit times. Using these interpolated calibration curves, the data obtained during the irradiation may be updated and corrected. Corrections for data taken during 100% helium cooling periods, seven days into each of the reactor cycle, are given in Table 7.29.

Table 7.29. UST center-line thermocouples (100% helium periods)

	Cycle				
	83	84	85	86	87
UST transit time, μsec	47.4	46.6	45.5	44.5	44.0
Uncorrected temp., °C	817	625	450	270	200
Corrected temp., °C	908	910	930	990	1320 (?)
Peripheral temp.,[a] °C	600	600	605	610	632

[a]Average of TE-105, -106, and -109.

An unexplained result occurred at the end of the test. The ambient-temperature value of transit time appeared to shift back (recover) toward its unirradiated value. The shift is opposite to what might have appeared with gradual reduction of decay heat after end of irradiation.

Postirradiation examination

A piece of the ultrasonic sensor line several feet long was recovered intact in the hot cell when HRB-5 capsule was dissected. A mechanical measurement of the W-Re lead line and the rhenium sensor showed no change in diameter of as much as 0.0001 in. The sensor wire was broken and the fractured surface examined with a scanning electron microscope. Numerous voids were visible (Fig. 7.55) at 4000X clustered near grain boundaries. The wire was chemically analyzed and found to contain 50% osmium, having been transmuted from 100% rhenium by the intense thermal-neutron flux. This composition may be predicted by daughter element decay schemes such as that described by Braunton et al.[26] The shift in composition from 100% rhenium to 50% Re + 50% Os should reduce the transit time, as we observed it did, according to data on rhenium-osmium alloys published by Papedakis et al.[27]

This experiment demonstrated the feasibility of using an ultrasonic thermometer, installed as a simple replacement for a thermocouple, to measure fuel center-line temperatures in an irradiation capsule. It also showed the sensitivity of the calibration of the UST to thermal-neutron transmutation of the high-cross-section rhenium sensor material, but provided a means for correcting for the decalibration. The test prompted the fabrication of a unique whole capsule calibration furnace which may be used to verify (or disprove) many ideas about the behavior of irradiated thermometers.

7.7.4 HRB-6 Center-Line Ultrasonic Thermometry

Design

The rhenium ultrasonic thermometer used in the HRB-6 was identical to that used successfully in HRB-5. However, the $^1/_{16}$-in.-OD stainless steel guide tube material was changed and found later to have been of a softer temper and to have been thoroughly cleaned during capsule fabrication.

Performance

The UST sensor worked satisfactorily during capsule fabrication but failed during the first reactor startup and operated only intermittently thereafter during the 4400 hr irradiation at 900 to 1100°C. The difficulty was identified as a pinched guide tube where the flexible portion of the capsule assembly was clamped above the reactor core. Removal from core and straightening the experiment after the second irradiation cycle restored performance of the UST to some degree, and it was possible to make a midterm calibration to 600°C in the in-pool furnace. The calibration obtained falls between the 1478- and the 2011-hr curves in Fig. 7.55 (the calibration curves for HRB-5), apparently too low a value for the transit time for only 1100 hr of irradiation. The data are somewhat suspect, however, due to the severe degradation of the pulse shapes by the kinked line and may well be off in absolute value by several microseconds. An end-of-life in-pool calibration to 750°C was made on HRB-6 following 4400 hr irradiation. It also shows values lower than expected by

26. C. B. J. Braunton, D. N. Hall, and C. M. Ryall, *The Estimation of the Composition and Volume Changes in Noble and Refractory Metal Alloys Due to Neutron Irradiation*, AERE-R5837, Fig. 76 (September 1968).

27. E. P. Papedakis et al., *Ultrasonic Thermometry for LMFBR Systems – Final Report*, NYO-3906-13, p. 113, Fig. 40 (June 1972).

RHENIUM FRACTURE – ARCHIVE MATERIAL
150 X

RHENIUM FRACTURE – ARCHIVE MATERIAL
1000 X

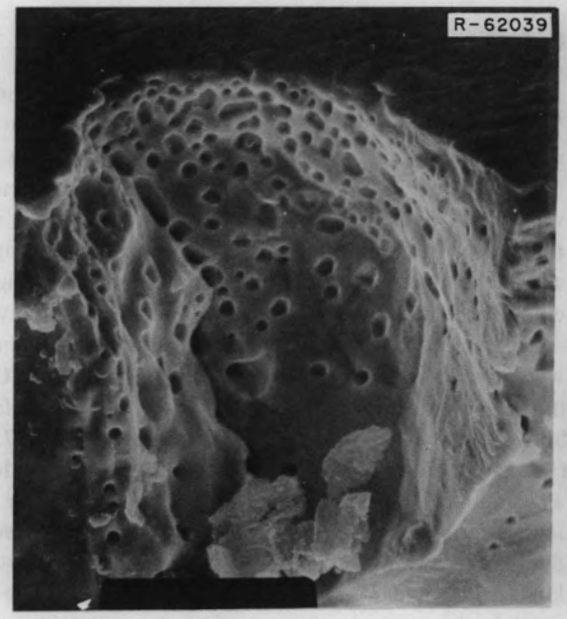

VOIDS IN IRRADIATED RHENIUM 4000 X

VOIDS IN IRRADIATED RHENIUM 1000 X

Fig. 7.55. Rhenium UST sensor from HRB-5.

about 2 μsec, a temperature dependence similar to the first in-pool calibration but steeper than that found for the HRB-5 UST sensor.

Postirradiation examination

Examination of the rhenium sensor recovered in the hot cells from the HRB-6 irradiation capsule again showed an intact but easily broken rhenium wire specimen. Voids clustered near grain boundaries were again observed by scanning electron microscopy. Microhardness measurements made on irradiated and archive rhenium wires showed an increase in hardness from 215 DPH before to 552 DPH after irradiation. A sample has been submitted for chemical composition analysis.

This test demonstrated the vulnerability of the UST to mechanical interference along the acoustic transmission line but suggests that with care such problems can be avoided and satisfactory operation realized as in HRB-5. Calibration shifts were not reproduced well between the two experiments, and further studies would be required before behavior can be predicted with good accuracy. The in-pool furnace offers the possibility of obtaining interim midterm calibrations, at least to 750°C, and thereby confirming the interpolated calibration shifts suggested in the HRB-5 experiment.

7.7.5 HRB-7 and -8 Center-Line Thermometry

Design

A multijunction W-Re thermocouple was developed for use in measuring axial temperature gradients in fuel center-line experiments. This assembly, shown in Fig. 7.56, utilizes three sheathed pairs of W–5% Re/W–26% Re thermocouple wire material brazed through the capsule bulkhead. The stripped wires, about 16 in. long, are insulated with six-hole hard-fired BeO insulators 0.090 in. in outside diameter and joined by wrapping one wire around another to make five thermocouple junctions. One additional pair of sheathed extension wires (G and H) is attached to the main thermocouple loop wires (A and D) so that the loop resistance can be measured. By applying the loop current to successive pairs of wire (G-H, B-C, F-E, C-E, and F-B) and measuring in each case the output of the main loop A-D, resistance may be found for the whole thermocouple loop, two-thirds of the loop, one-third of

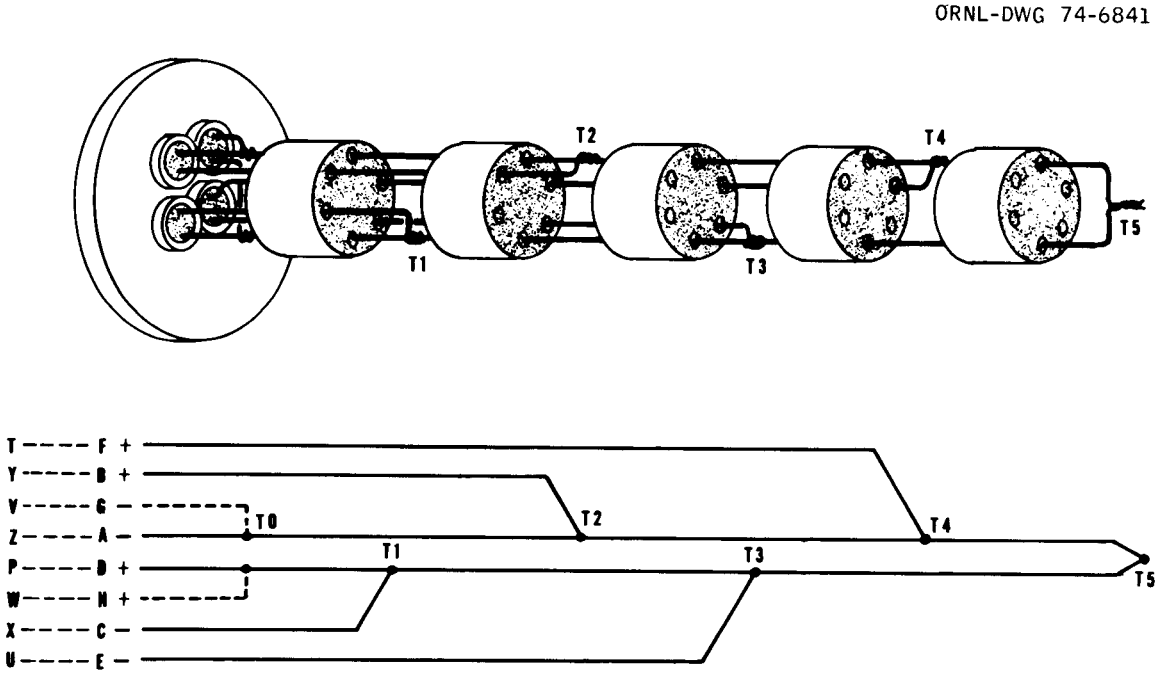

Fig. 7.56. Multijunction multiloop thermocouple.

the loop, and the positive wire (D) and the negative wire (A) individually. The entire assembly was designed to be built, wrapped with rhenium foil to prevent insulator-to-graphite contact, and inserted in a 0.130-in.-ID fuel element stack. Assemblies were fabricated and installed in HRB-7 and -8 experiments scheduled to start irradiation in December 1973 and February 1974.

Performance

The object of this experiment is to be able to measure the temperature gradient along the fuel center-line and along the thermocouple; to measure the effects of time, temperature, and radiation on different portions of the thermocouple; to determine whether the low- or high-rhenium alloy wire is the principal contributor to resistance changes and thermocouple decalibration; and to be able to arrive at a model of thermocouple decalibrations which takes temperature and flux gradients into account.

7.8 PERFORMANCE EVALUATION OF FUELS

R. A. Olstad

A summary and references for this irradiation test are given in Sect. 7.4.1. The thermal analysis of these capsules was complicated because the capsules were uninstrumented and because of the uncertainties in the fission heat rates and gap widths after the capsules were inverted. The temperature calculations were made using the axial profiles of ^{235}U fission rate shown in Fig. 7.57. These profiles were determined from the profiles of thermal flux measured outside the capsules during each cycle by ETR personnel and were normalized to the ^{235}U fission rates measured in the ETR Critical Facility. In the top section of the capsules, the ^{235}U fission rates (fissions/sec per ^{235}U atom) were roughly three times as large after the capsule inversion as before. Similarly, the ^{235}U fission rates in the bottom section of the capsules were much lower after the capsules were inverted than before. It was this large increase in ^{235}U fission rate (or equivalently, the thermal flux) in the top section of the capsule that caused very high operating temperatures and subsequent damage to the fuel during the last irradiation cycle. The reaction rates of the other nuclear transformations were calculated relative to the ^{235}U reaction rate, and the nuclear transformation equations were solved to determine the fuel composition and subsequent fission heating rates during the entire irradiation.

The temperatures that were calculated from these fission heating rates are shown in Figs. 7.58 and 7.59 at the beginning of the first cycle and at the beginning of the last cycle (during which the capsules operated in an

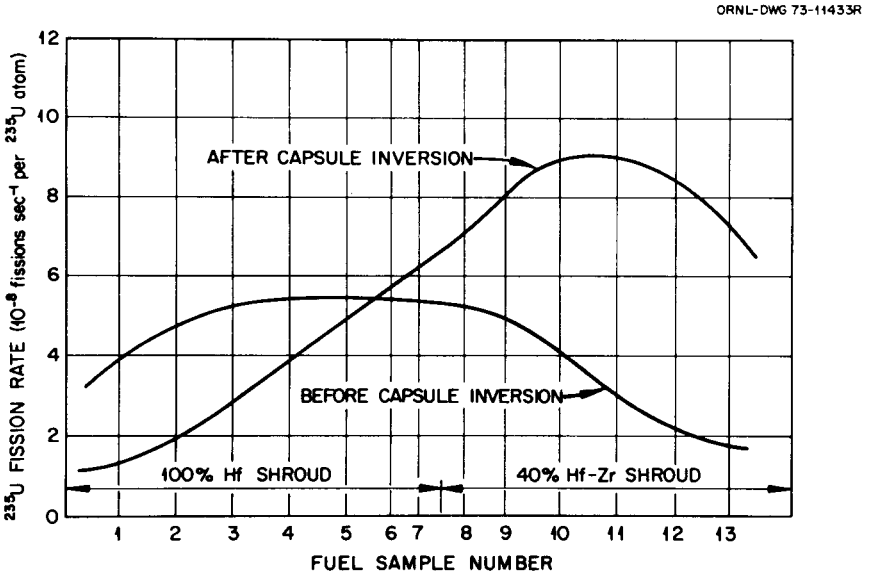

Fig. 7.57. ^{235}U fission rate in H-capsules before and after the capsule inversion.

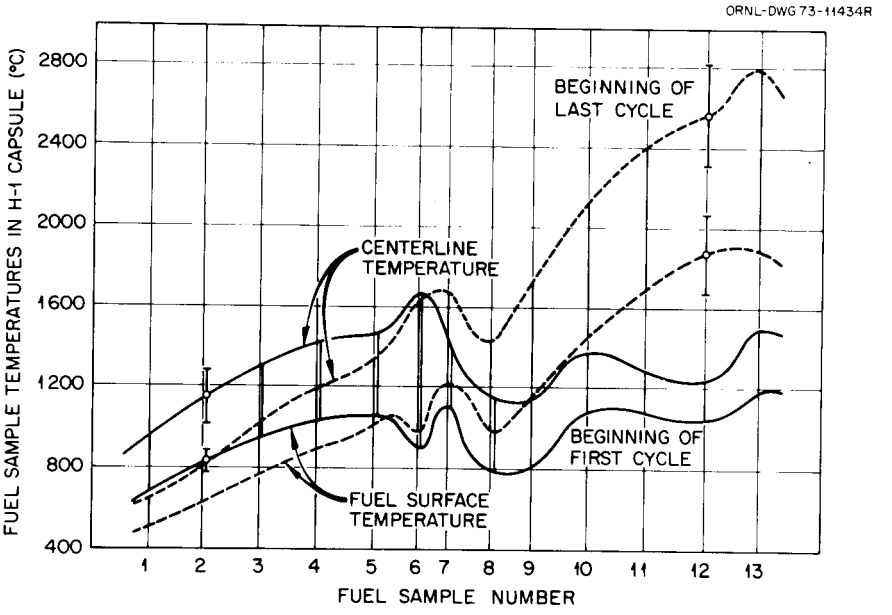

Fig. 7.58. Fuel sample temperatures in H-1 capsule at beginning of first and last cycles.

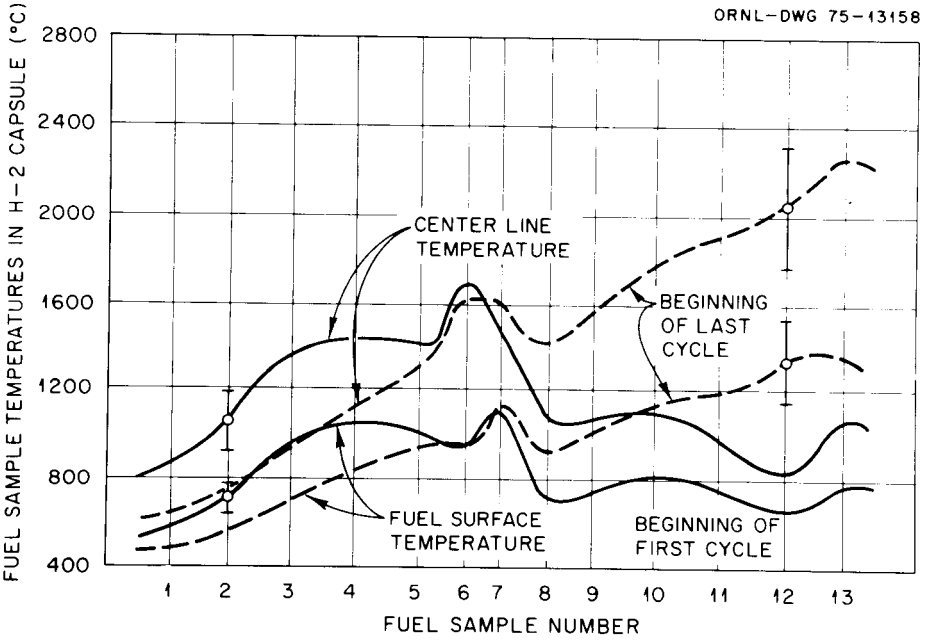

Fig. 7.59. Fuel sample temperatures in H-2 capsule at beginning of first and last cycles.

inverted position). Samples 6 and 13 were blended beds of particles. Since blended beds have a lower thermal conductivity and smaller fuel-graphite sleeve gap than bonded rods, they operated at lower surface temperatures but higher center-line temperatures. The initial center-line temperatures of the bonded rods in the H-1 capsule varied from 950°C for rod H-1-1 to 1450°C for rod H-1-5. However, because of the capsule inversion, the center-line temperatures of rods H-1-10, H-1-11, and H-1-12 were greater than 2000°C during the last cycle. The center-line temperatures of the H-2 samples were generally lower than those of the H-1 samples, both before and after the inversion. The initial center-line temperatures in the rods in both capsules are uncertain by approximately ±100 to ±150°C because of uncertainties in fission heating rates and fuel rod thermal conductivity. The center-line temperatures of the rods that operated at very high temperatures during the last cycle are uncertain by approximately ±250°C because of large uncertainties in the gap between the fuel rods and the graphite sleeves as well as uncertainties in the fission heat rates and fuel conductivity.

The initial temperatures were calculated assuming a bonded-rod thermal conductivity of 0.07 W cm^{-1} $(°C)^{-1}$ and all gaps at their initial values. The temperatures during the last cycle were calculated assuming a rod conductivity of 0.05 W cm^{-1} $(°C)^{-1}$ and assuming that gaps between the graphite sleeves and the stainless steel capsule were at their final values, as determined from postirradiation dimension measurements. The gaps between the bonded rods and the graphite sleeves during the last cycle were assumed to be at their initial values (i.e., 5 mils). This assumption was made because there was a large uncertainty as to whether these gap widths decreased or increased during the irradiation. A gamma heating rate of 15 W/g was assumed in all calculations. The thermal conductivity of the blended beds was assumed to be 0.035 W cm^{-1} $(°C)^{-1}$ throughout the irradiation.

8. Prestressed Concrete Pressure Vessel (PCRV) Development

G. D. Whitman

The major portion of the prestressed concrete reactor pressure vessel development program consisted in the disassembly and examination of the thermal cylinder model and evaluation of experimental data and calculated results. The thermal cylinder experiment was designed to utilize information obtained from the concrete materials characterization, triaxial creep, instrumentation evaluation, analysis methods development, and structural model studies of the PCRV development program. The purpose was to provide reliable test data from a fairly complex cylindrical model for use in evaluating the capability of a finite-element computer analysis in conjunction with small-specimen concrete test data to calculate the type of time-dependent PCRV behavior to be expected in a commercial HTGR power plant.

No further research has been undertaken under the concrete triaxial creep studies; however, the applied loadings have been maintained on the University of Texas long-term creep specimens and strain readings taken periodically. A series of final summary reports are being prepared on triaxial creep studies conducted at the University of Texas and the Waterways Experiment Station, U.S. Army Corps of Engineers. A report is also being prepared on the Waterways Experiment Station concrete moisture migration experiment. Completion of these reports has been delayed both by a lack of available personnel and funding.

8.1 THE THERMAL CYLINDER TEST

J. P. Callahan G. C. Robinson

The thermal cylinder experiment was designed to provide a means for evaluating the present capability to predict temperature and time-dependent stress-strain behavior of a relatively simple prestressed concrete structure using accepted methods of analysis together with laboratory strength and creep test data. The model also provided an opportunity for evaluating long-term stability, accuracy, and reliability of a variety of stress- and strain-measuring devices.

The thermal cylinder model is approximately a one-sixth-scale representation of the central barrel section of a single-cavity-type PCRV such as was employed in the Fort St. Vrain Nuclear Generating Station. The model is 3.75 ft in inside diameter, 4 ft high, and 1.5 ft in wall thickness. Testing of the model was completed in December 1972, and preliminary results were reported.[1] For reference purposes, a schematic representation is shown in Fig. 8.1. The test structure and the model assembly are described in detail in Refs. 2 and 3 respectively.

During this reporting period, we have completed detensioning of the model prestressing, conducted post-mortem studies of concrete cross sections and axial prestressing tendons, and completed an analysis of the model test history.

8.1.1 Analytical and Experimental Results

Thermal cylinder model test. A time-dependent creep analysis of the entire operational history of the thermal cylinder model was conducted using the SAFE-CRACK

1. J. P. Callahan, R. S. Valochovic, and G. C. Robinson, *GCR Programs Annu. Progr. Rep. Dec. 31, 1972,* ORNL-4911, pp. 181–209.

2. J. M. Corum, J. P. Callahan, and M. Richardson, *GCR Programs Semiannu. Progr. Rep. Sept. 30, 1970,* ORNL-4637, pp. 70–71.

3. J. P. Callahan, J. M. Corum, and M. Richardson, *GCR-TU Programs Annu. Progr. Rep. Sept. 30, 1971,* ORNL-4760, pp. 79–91.

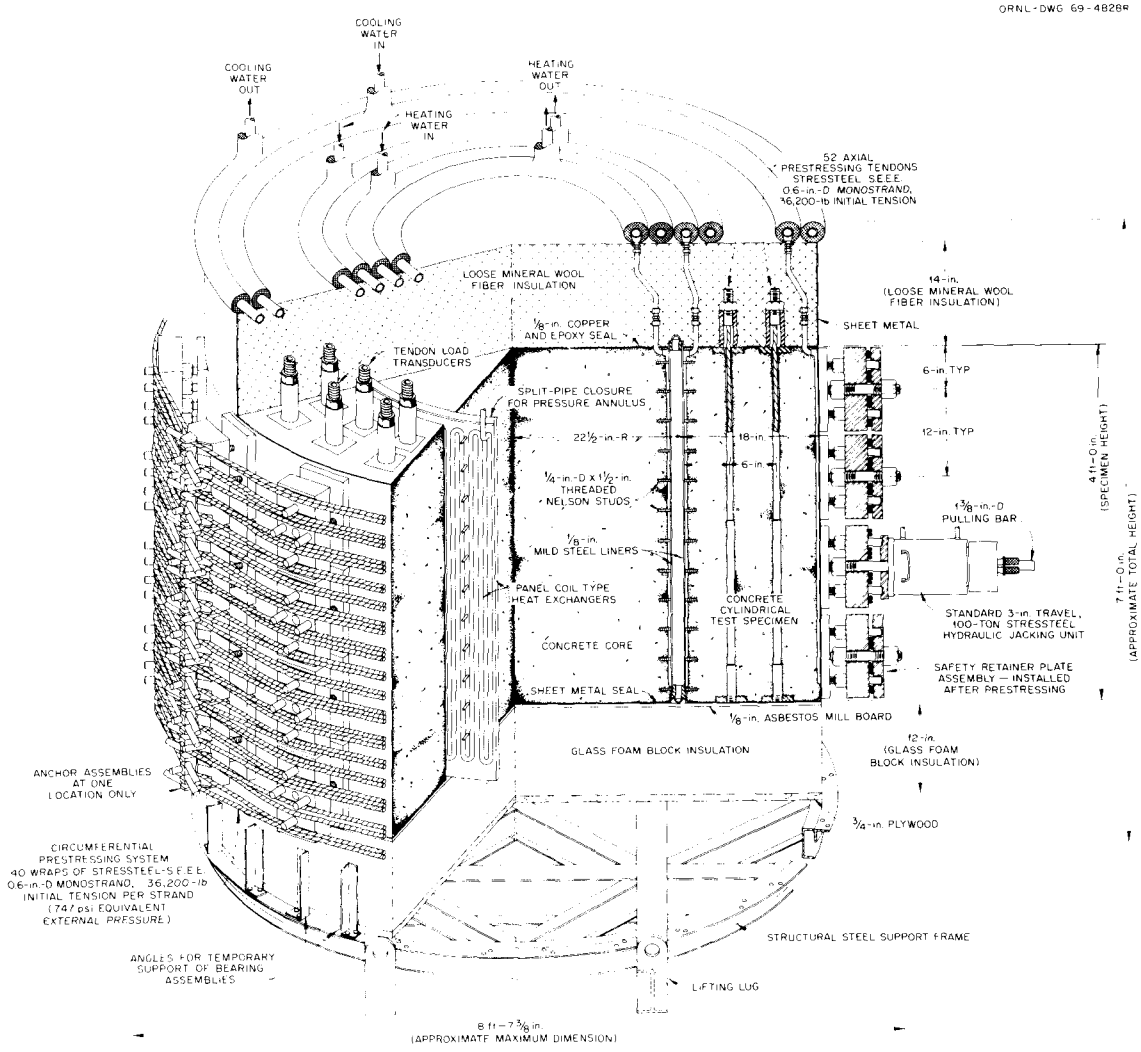

Fig. 8.1. Isometric of thermal cylinder test structure.

computer program[4] together with concrete materials properties data obtained under the overall ORNL PCRV research and development program. The model was analyzed initially[1] for only a portion of its test history and using materials properties data available in the literature for a similar concrete. The complete analysis employed 47 time steps covering 585 days after completion of prestressing.

The analytical model is an axisymmetric thick-walled cylinder having dimensions and geometry of the test model. A total of 564 elements are used, consisting of triangular ring elements to represent the concrete and membrane shell elements to represent the liner or heat exchangers. The circumferential prestressing is represented as uniform pressure applied to the outer barrel section, and the axial prestressing tendons are treated as uniaxial tension elements. Once the specified failure criteria are exceeded, the affected concrete element is allowed to crack, and new stiffness and load matrices are computed in the analysis. The resulting new equilibrium equations are then solved for new displacements.

We have compared the analytical results obtained using SAFE-CRACK with experimental data from the

4. Y. R. Rashid, *Nonlinear Quasi-Static Analyses of Two-Dimensional Concrete Structures*, GA-9994 (Mar. 23, 1970).

thermal cylinder model. Table 8.1 lists the 155 gages included in the model. Although the table indicates percent survival of each gage type, it does not provide an evaluation of gage reliability and accuracy. The remainder of this section discusses the relative performance of the various gages.

The radial positions of the various gages are shown in Fig. 8.2. Generally, the initial letter of the gage designations used in the figure indicates the quadrant in which the gage is located (A, B, C, or D). This is followed by one or two letters or a letter and a number designating the gage type. The first number of the three-number series that follows the letters indicates relative radial position from the inside of the test section, and the last number indicates the orientation (i.e., 1 = axial, 2 = radial, and 3 = circumferential). The middle number is used to further identify individual sensors.

Of the various concrete embedment gages, the single-filament resistance type provided the most consistent and meaningful data. Comparisons of analytical and experimental results for axially and radially oriented gages located in position 1 are given in Figs. 8.3 and 8.4, respectively. In both cases, the prestressing and pressurization strains were overestimated, while strains produced during heatup were underestimated. The behavior of the axial gages during hot-spot heating appears erratic, since a strain jump was recorded shortly after repressurization at 467 days. This effect could have resulted from observed failures of prestressing tendons, as discussed later. The cause of the sharp fluctuations in the analytical results during hot-spot heating will be studied further.

The analytical and corresponding experimental results for gages in the second rosette position are given in Figs. 8.5 to 8.7. The same behavioral trends seen for the gages in position 1 were recorded by these gages as well, with prestressing and pressurization strains being overestimated and heatup strains underestimated. As expected, the recorded strains during hot-spot heating were less deviant, since these gages were farther away from the heated zone (center rosette position of Fig. 8.2). However, significant strain jumps were again monitored by the axial gages, and the analytical curves showed sharp fluctuations during hot-spot heating.

Single-filament-type embedment strain gages were also positioned in the concrete directly adjacent to the hot-spot heaters, as shown in Fig. 8.2 for the "D" section. Figures 8.8 and 8.9 are comparisons for radial and circumferential gages at the hot spot. The prestressing strains agreed exceptionally well for these two gages; although, as seen previously, the initial heatup strains differed significantly from the calculated values, and the experimental pressurization strains were consistently low. With the exception of three questionable calculated data points in Fig. 8.8, the experimental and

Table 8.1. Thermal cylinder test gage survival

Gage type	Letter designation	Total number	Number failed	Percent survival
Embedment gages				
Single filament resistance	EB	47	18	61.7
Vibrating wire				
Type A	D	27	21	22.2
Type B	P	9	3	33.3
Type C	GA	1	1	0
Wound wire resistance		6	1	83.3
Stress cells				
Titanium resistance	T	8	3	62.5
Pressure diaphragm	PSC	6	6	0
Strain gages				
Weldable (liner)		19	6	68.4
Axial tendons	CB	12	3	75.0
Circumferential tendons	CG	8	0	100.0
Load cells				
Axial tendons	TR	12	1	91.7
Total		155	63	59.4

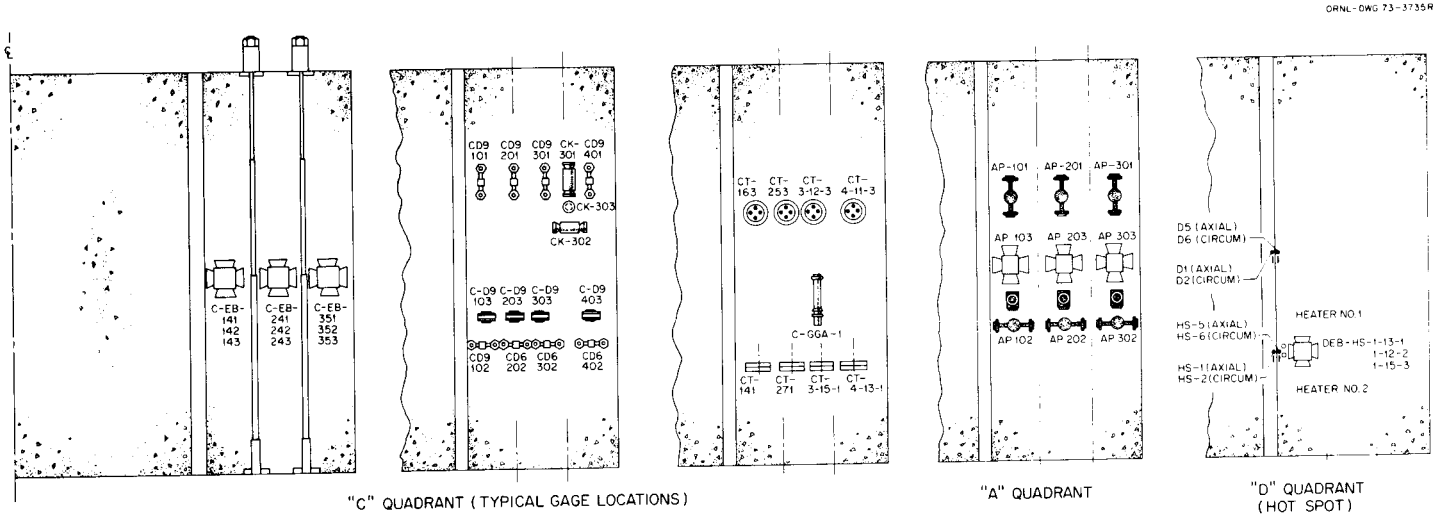

Fig. 8.2. Typical locations of concrete embedment and weldable liner gages.

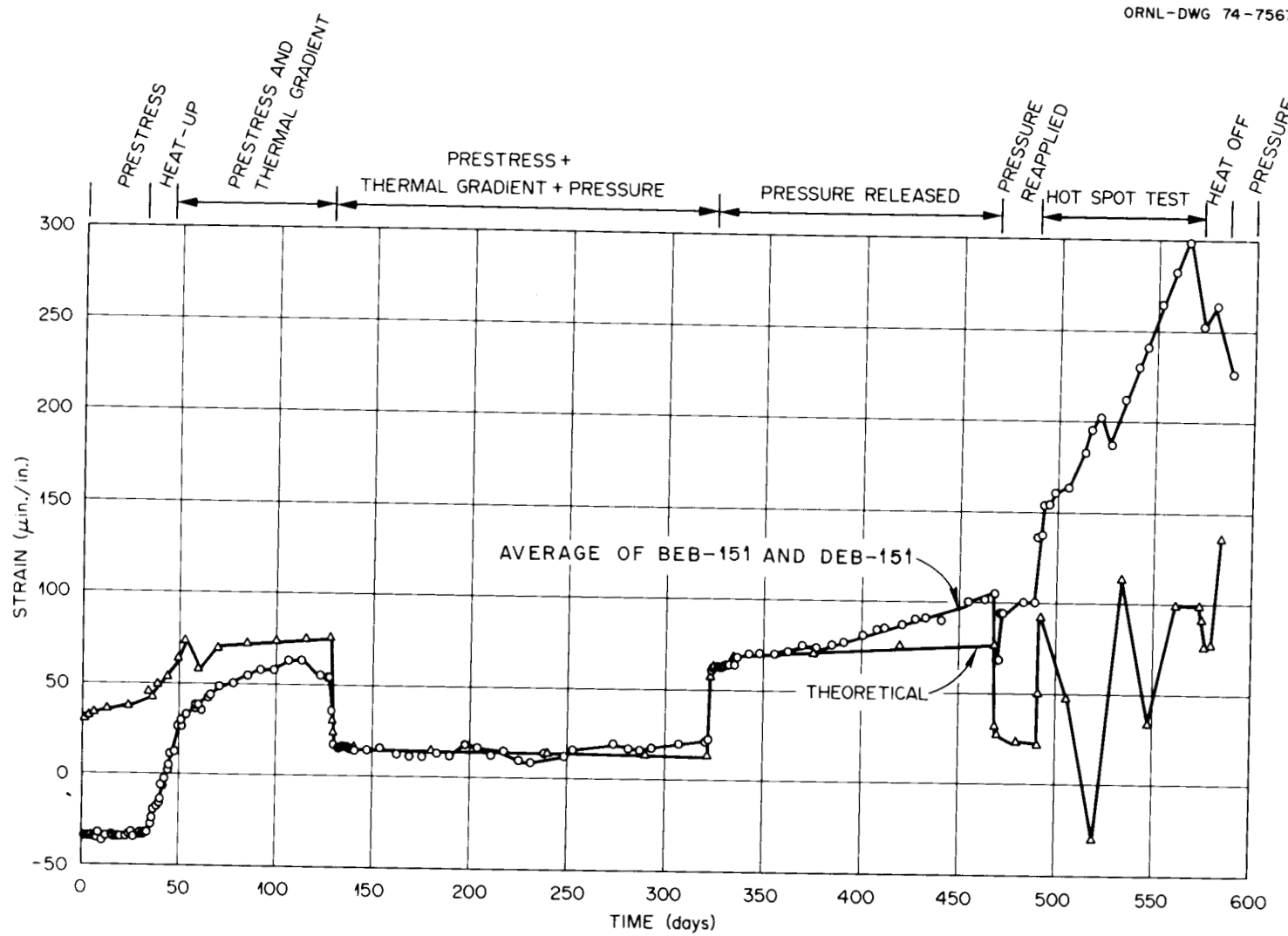

Fig. 8.3. Calculated and experimental results for first-position axial single-filament resistance strain gages.

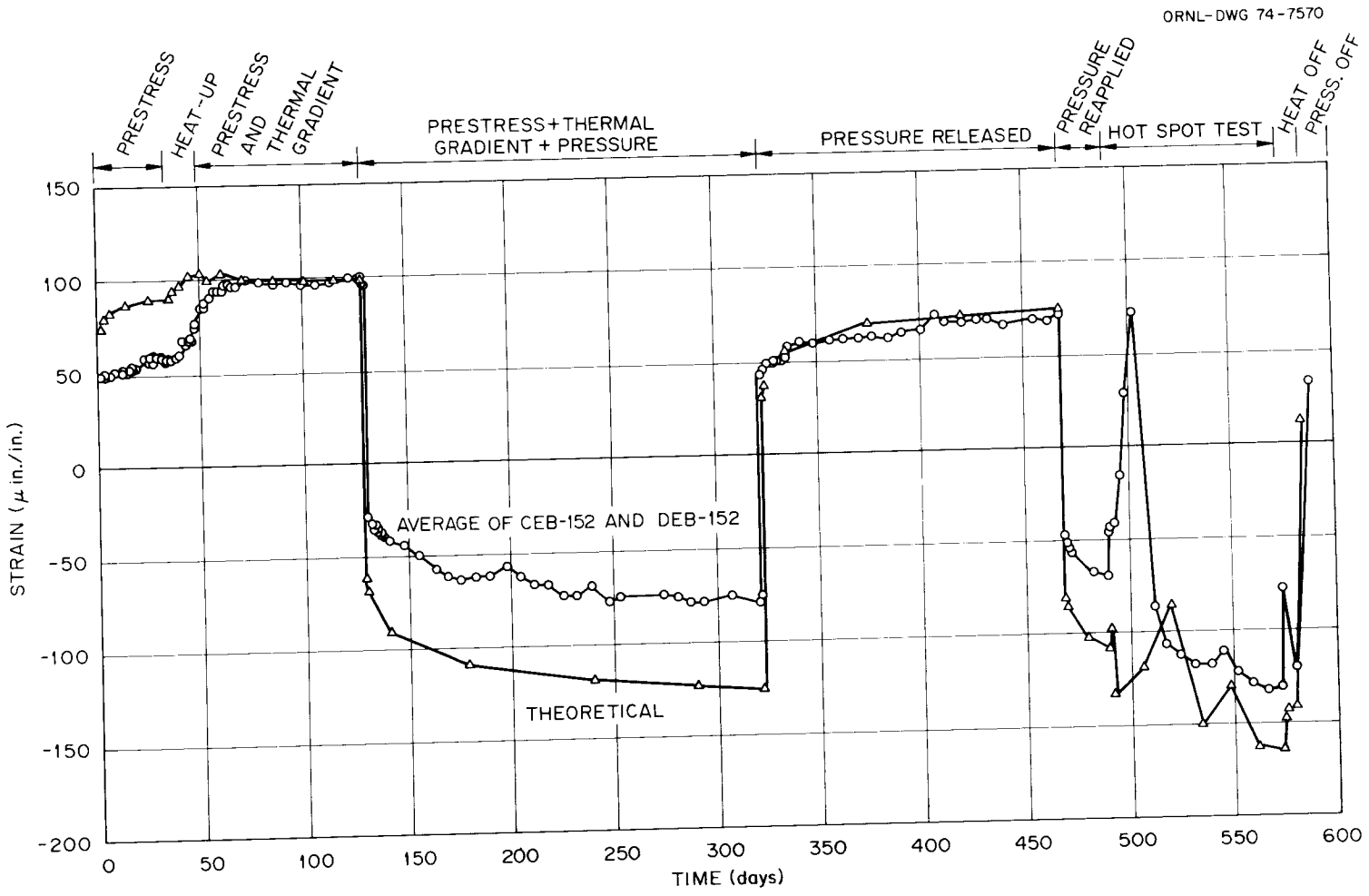

Fig. 8.4. Calculated and experimental results for first-position radial single-filament resistance strain gages.

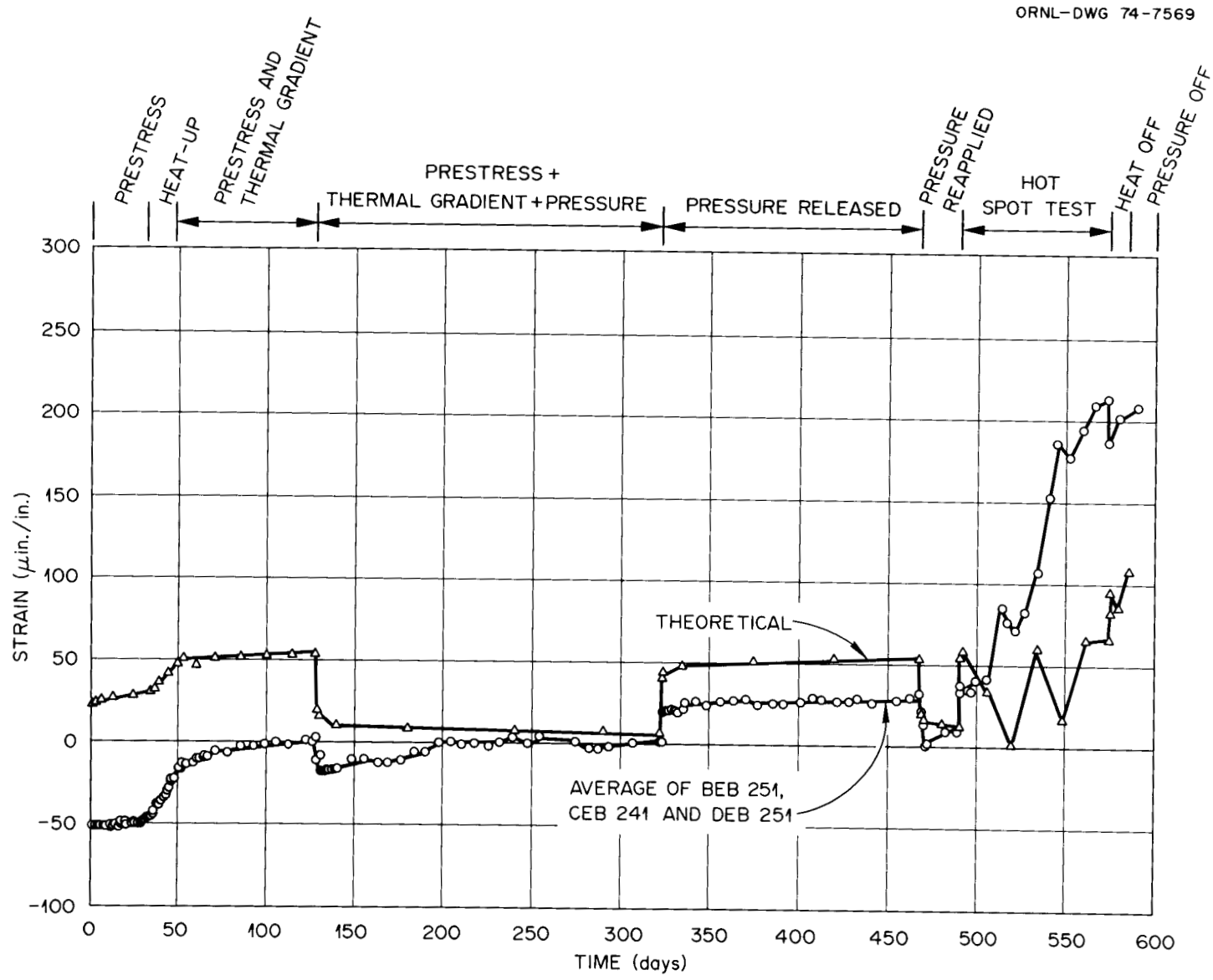

Fig. 8.5. Calculated and experimental results for second-position axial single-filament resistance strain gages.

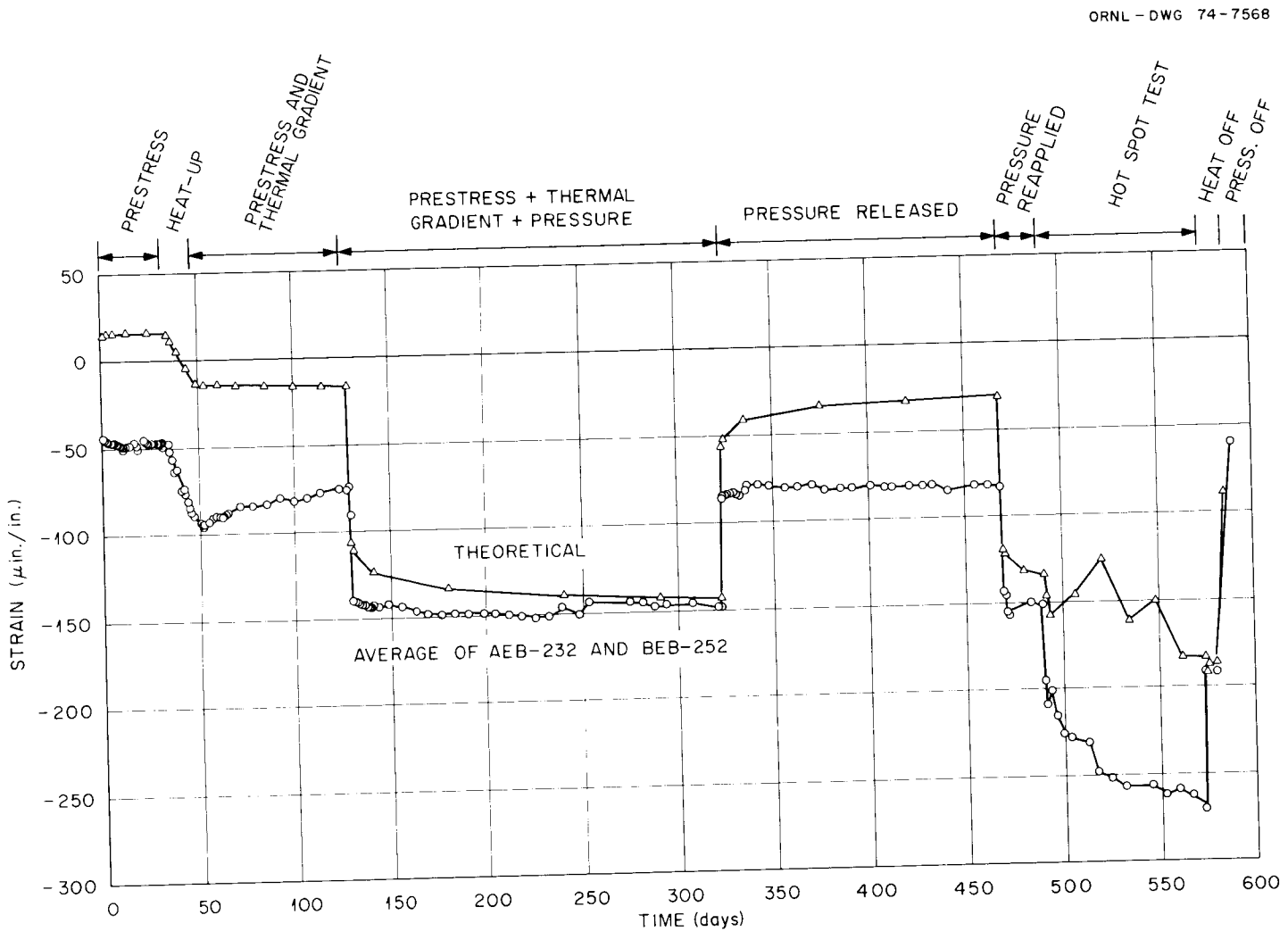

Fig. 8.6. Calculated and experimental results for second-position radial single-filament resistance strain gages.

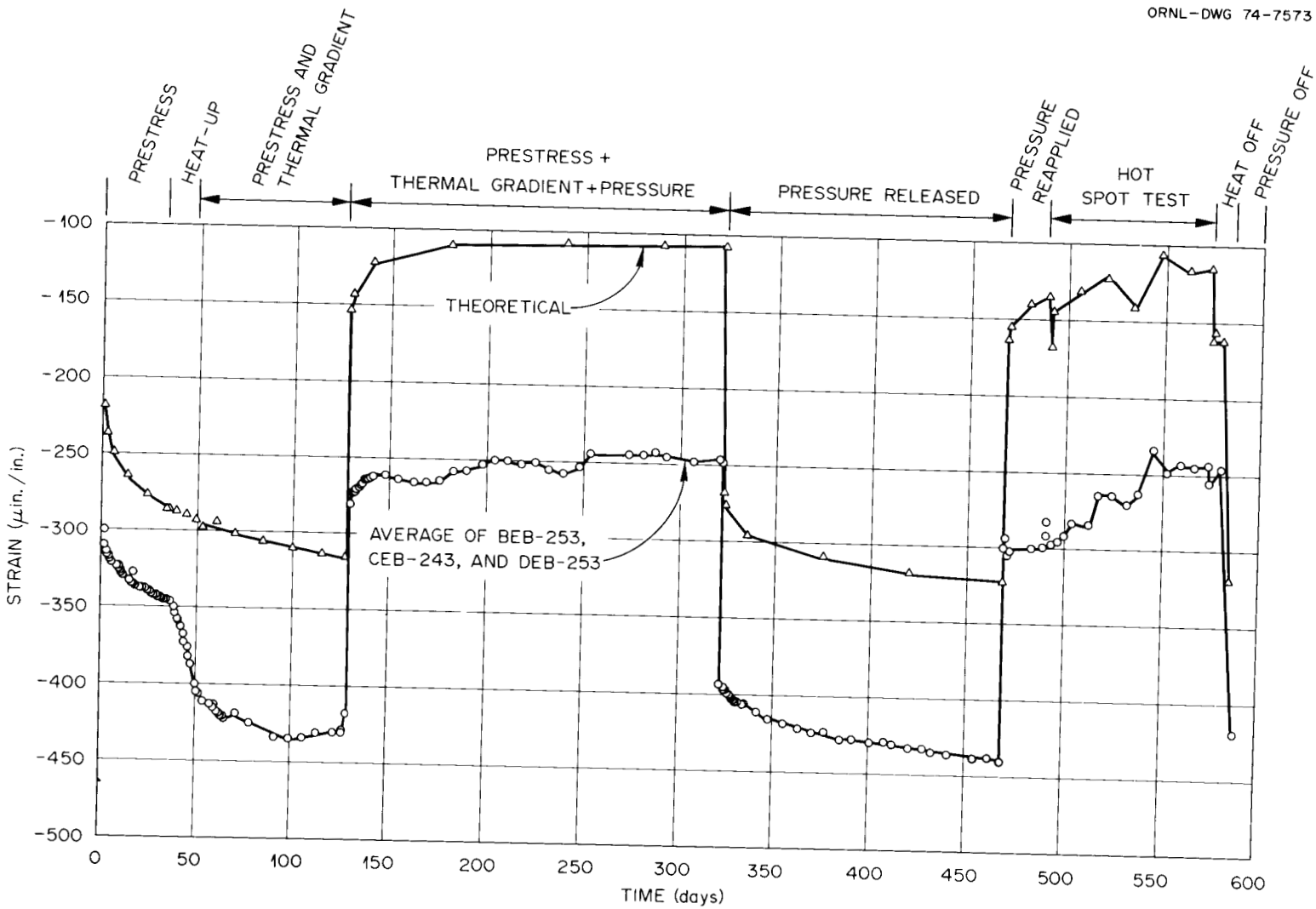

Fig. 8.7. Calculated and experimental results for second-position circumferential single-filament resistance strain gages.

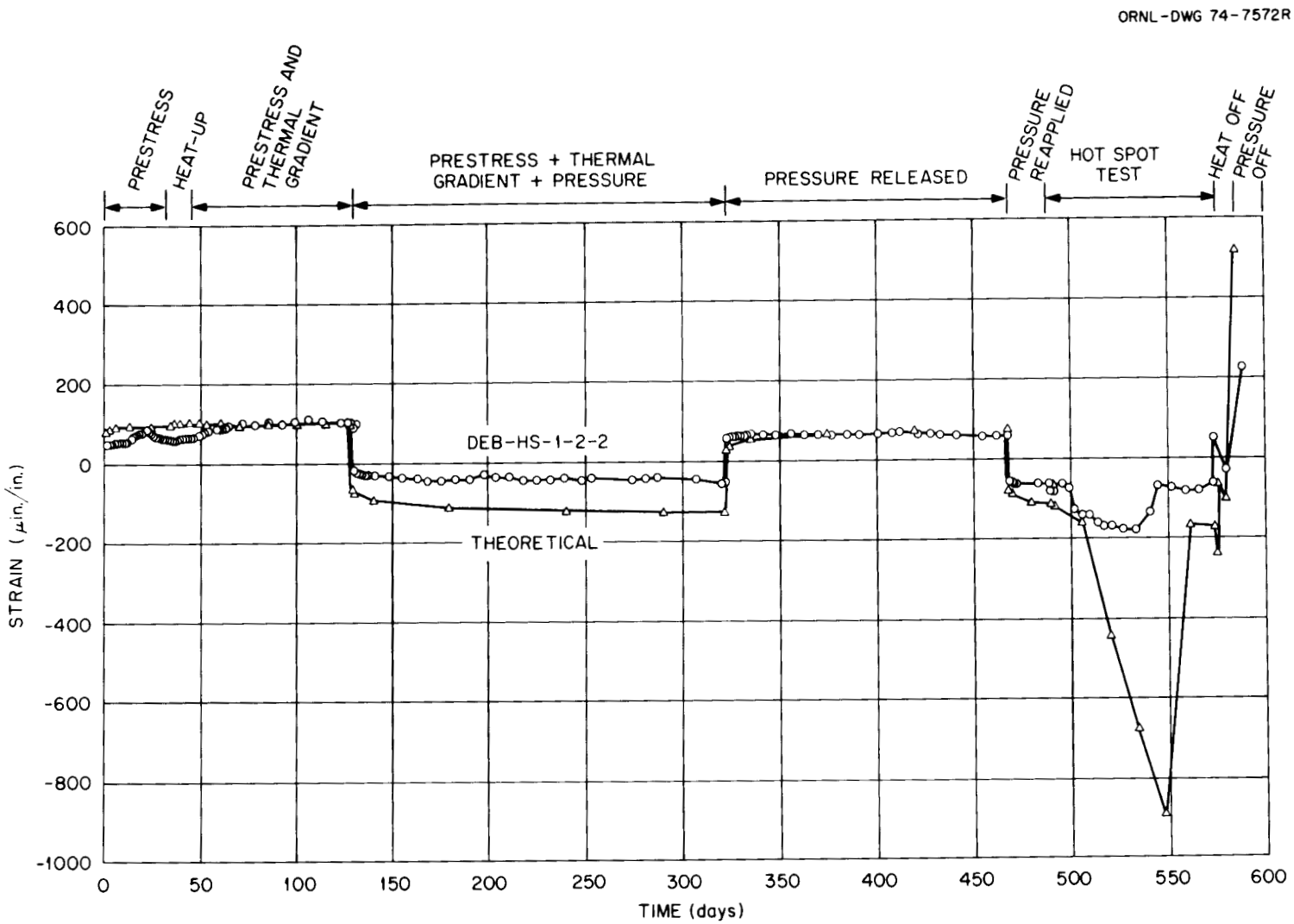

Fig. 8.8. Calculated and experimental results for hot-spot-position radial single-filament resistance strain gage.

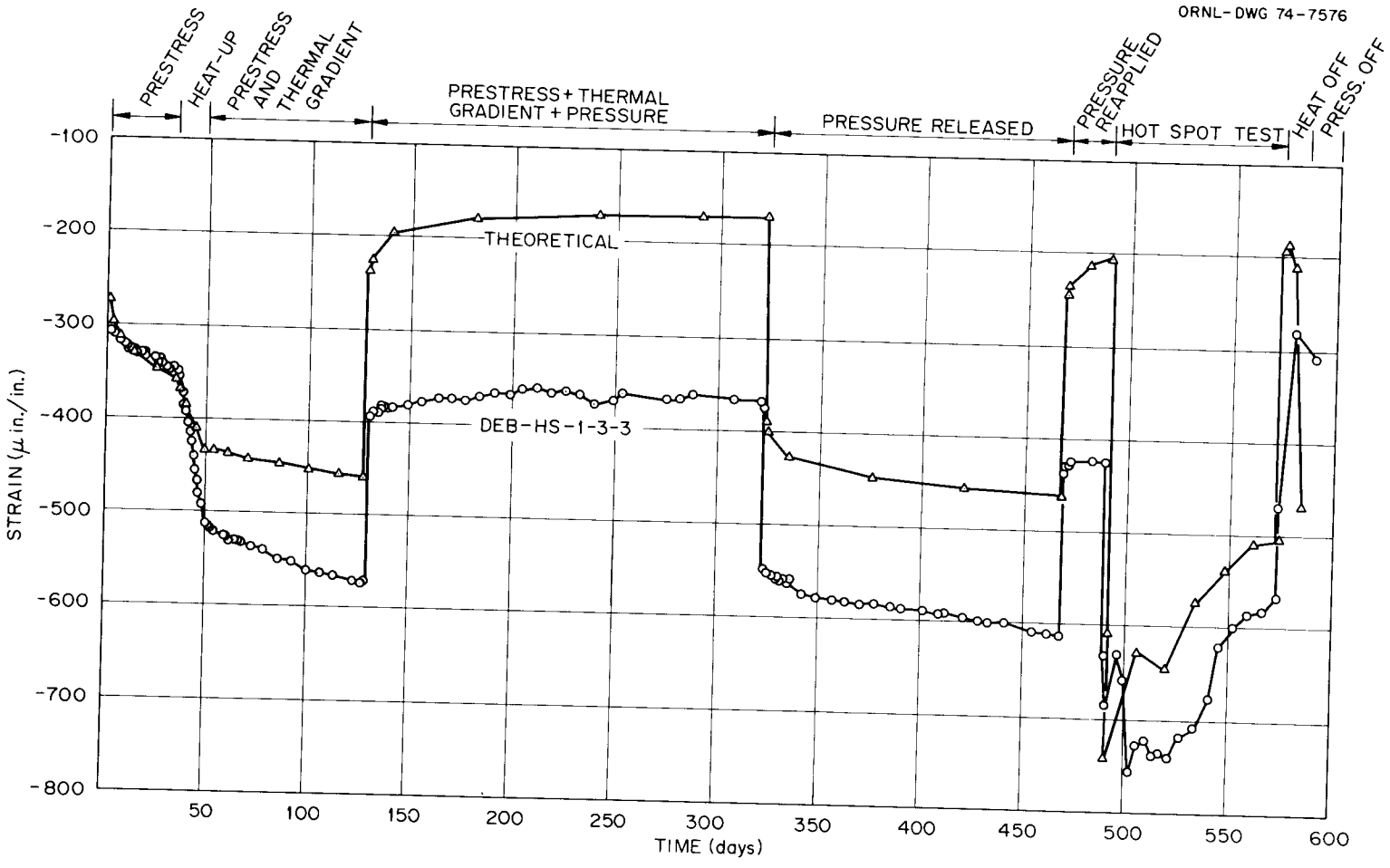

Fig. 8.9. Calculated and experimental results for hot-spot-position circumferential single-filament resistance strain gage.

analytical curves followed each other exceedingly well during the hot-spot test.

Average comparisons for the type A vibrating-wire strain gages in radial position 1 (see Fig. 8.2) are shown in Figs. 8.10 to 8.12 for axial, radial, and circumferential directions respectively. The same general trends discussed for the single-filament type gages shown in Figs. 8.3 and 8.4 were recorded by this entirely different type of concrete embedment strain gage that was cast directly into the thermal cylinder model concrete, that is, overestimation by the analyses of prestressing and pressurization strains and underestimation of heatup strains. Since the vibrating-wire strain gages will function satisfactorily only at temperatures less than about 150°F, the gages failed at the beginning of the hot-spot test. The missing data in Fig. 8.10 from 240 to 390 days was caused by problems with the gage readout equipment. Although four vibrating-wire gage positions were used across the test section, the position 3 gage results, shown in Fig. 8.13, can be compared from the behavioral standpoint with the single-filament gage data shown in Fig. 8.7, with the same basic differences between experimental and analytical results being seen for both gage types.

Of the nine type B vibrating-wire embedment strain gages used in the model, six continued to operate during the experiment; however, the readings in many cases were inconsistent because of problems with the readout equipment. The vibrating-wire gage frequency monitor used for the study was designed specifically for use with type A gages and frequently gave inconsistent readings when used with type B and C gages.

Comparisons for two circumferential type B gages are given in Figs. 8.14 and 8.15 for the first and second gage positions. Although better agreement occurred for prestressing strains, the same basic trends are again seen for this gage type; that is, the calculated strain during pressure steps are larger and heatup strains smaller than the experimental values.

Only one of the type C vibrating-wire strain gages was included in the model. Although this gage is far superior in basic design than the other two types of vibrating-wire gages, it requires precasting to insure satisfactory performance. (This was not done in this experiment.)

The wound-wire resistance embedment strain gages also failed to perform satisfactorily, although only one did not remain operational during the experiment. (However, the gages of this type included in the companion concrete specimens did function satisfactorily. The unsatisfactory performance of these gages is attributed to absence of bonding between gage and concrete. It is felt that the present gage deficiency could be corrected with only minor modifications of the bonding surfaces of the gage housing.

Experimental and calculated stresses for three circumferentially oriented titanium stress cells are shown in Figs. 8.16 to 8.18 for the first, second, and fourth positions of Fig. 8.2 respectively. These cells functioned satisfactorily until after the initial pressurization loading. Cell 253 performed spasmodically from that point until the pressure was released, and cell 4-11-3 monitored an unexplainable stress drop at 360 days. This test was the first attempt to use a stress cell of this particular design; further refinement will be required to insure reliability and long-term stability.

The pressure diaphragm type of stress cell consists of two single-filament embedment strain gages positioned in parallel in uniform stress locations, with one having a relatively thin sheet metal pressure diaphragm attached. The stress is determined by measuring the applied diaphragm pressure required to balance the strain readings of the two gages. Although this technique appeared capable of measuring stresses developed during short-term loading (see following discussion of companion specimen tests), it was incapable of determining time-dependent stresses in the thermal cylinder model. To do this would require individual diaphragm pressure control and strain gage readout systems.

The calculated and experimental strains for axial and circumferential weldable strain gages are shown in Figs. 8.19 and 8.20 for the concrete pressure annulus sides of the inside heat exchanger (B heat exchanger) respectively. The same general observation made for the embedment instrumentation also applies to these gages; that is, except for the hot-spot experiment, the strains produced by mechanical loadings were slightly overestimated by the analysis and those produced during heatup were underestimated. The sharp fluctuations in calculated results noted previously for the embedment gages during hot-spot heating were not seen on the liner, but the greatest disagreement occurred during the hot-spot part of the experiment. This was especially true in the case of the circumferential gage.

Comparisons for the weldable gages located on the annulus side of the heat exchanger or liner, Fig. 8.20, show considerably greater disagreement. This trend was consistent for all four sets of liner gages. The strains produced by heatup were distorted considerably; however, pressurization strains were consistent with the readings for the concrete side. A post-mortem examination of the annulus side gages, which did not have integral leads, showed that the resistance of the gages changed during the experiment while that of the gages on the concrete side, which were equipped with integral

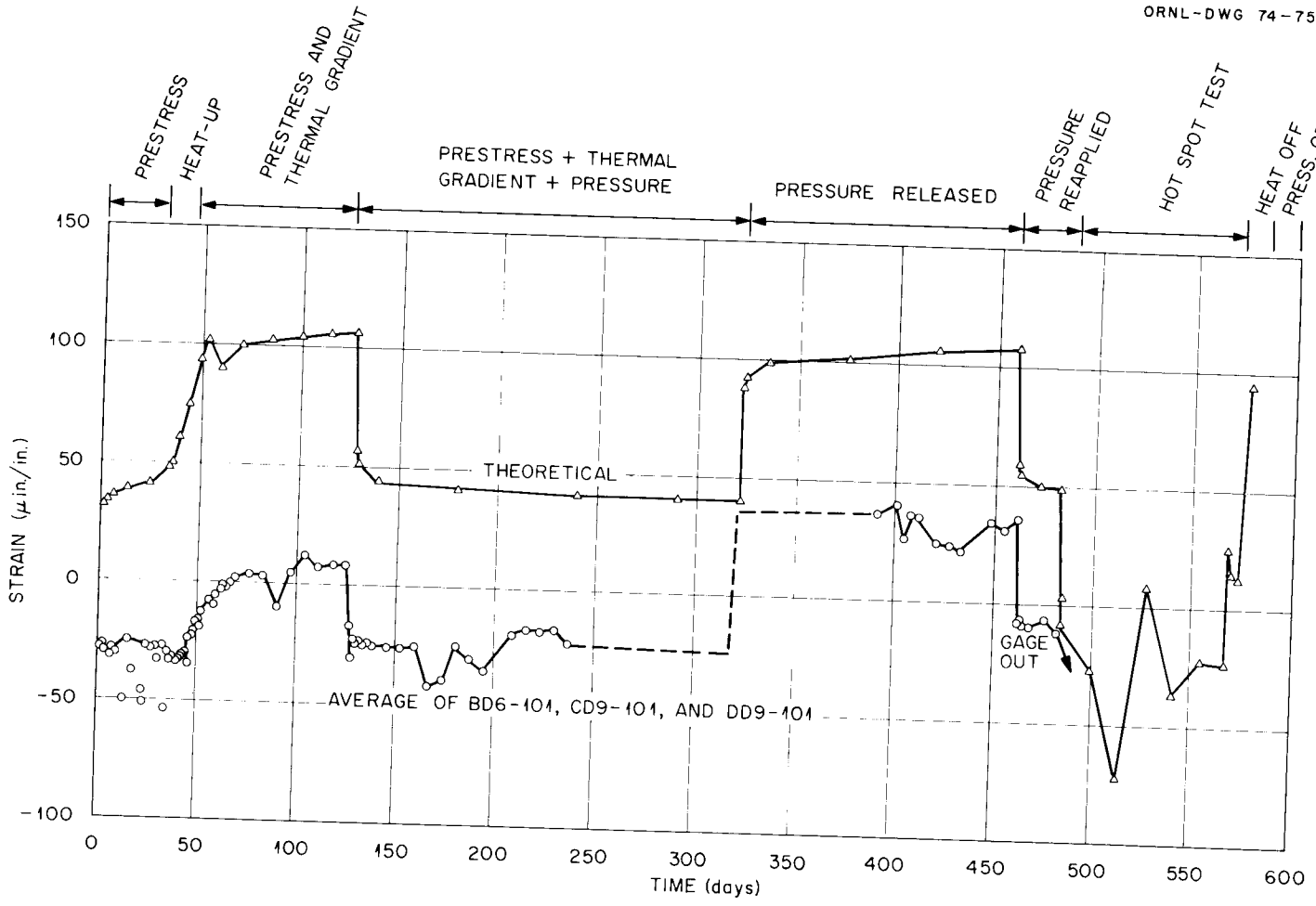

Fig. 8.10. Calculated and experimental results for first-position axial type A vibrating-wire strain gages.

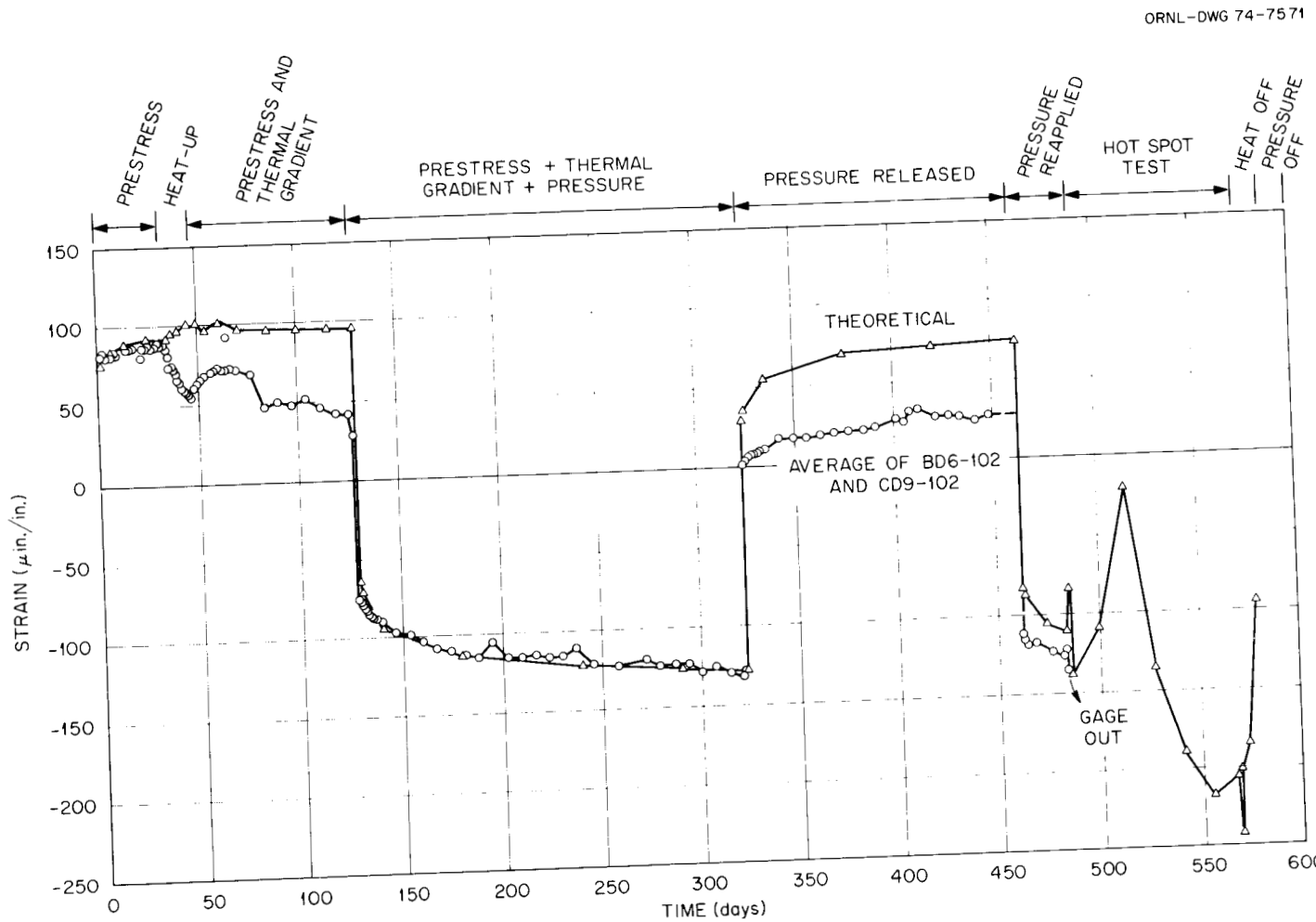

Fig. 8.11. Calculated and experimental results for first-position radial type A vibrating-wire strain gages.

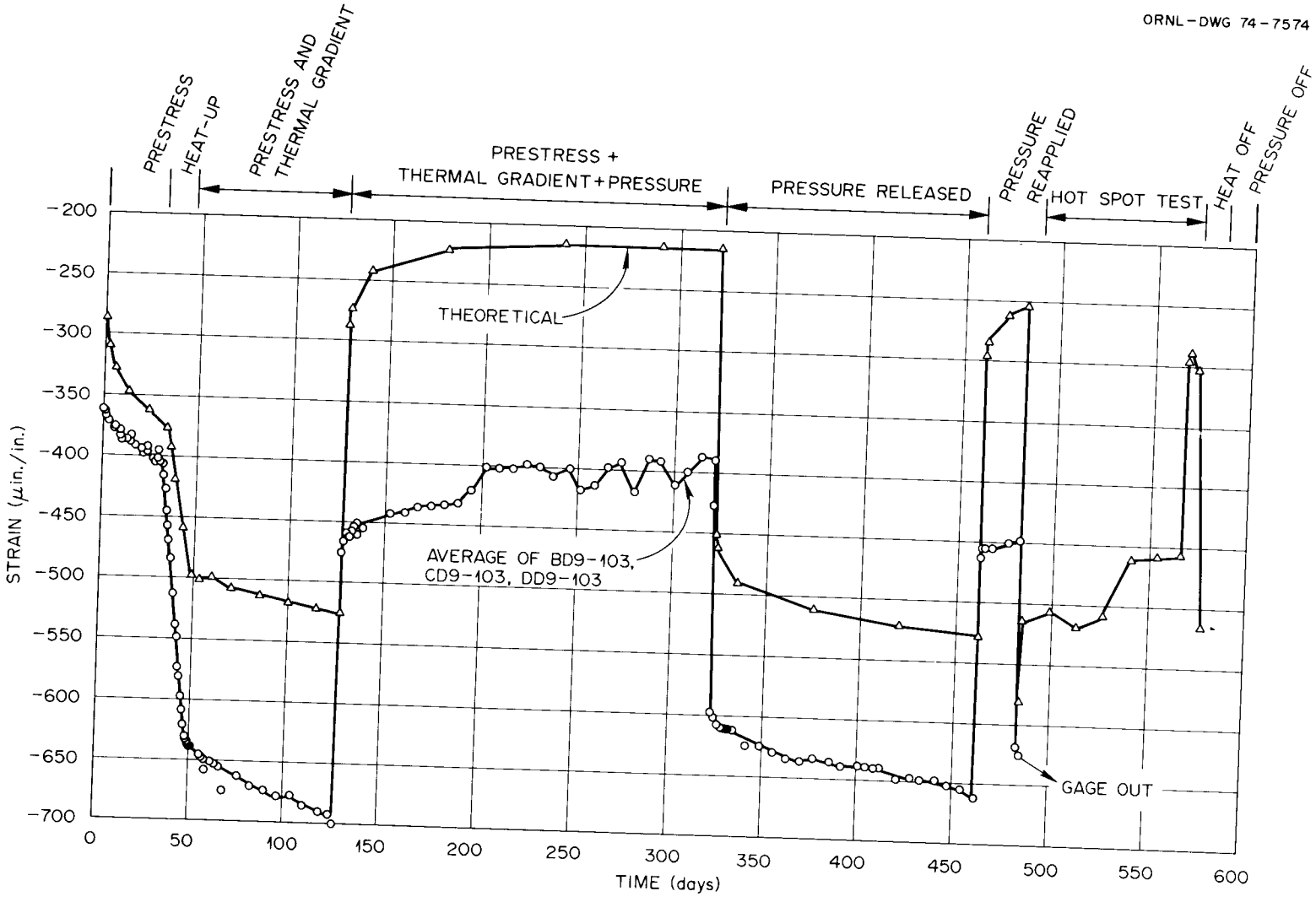

Fig. 8.12. Calculated and experimental results for first-position circumferential type A vibrating-wire strain gages.

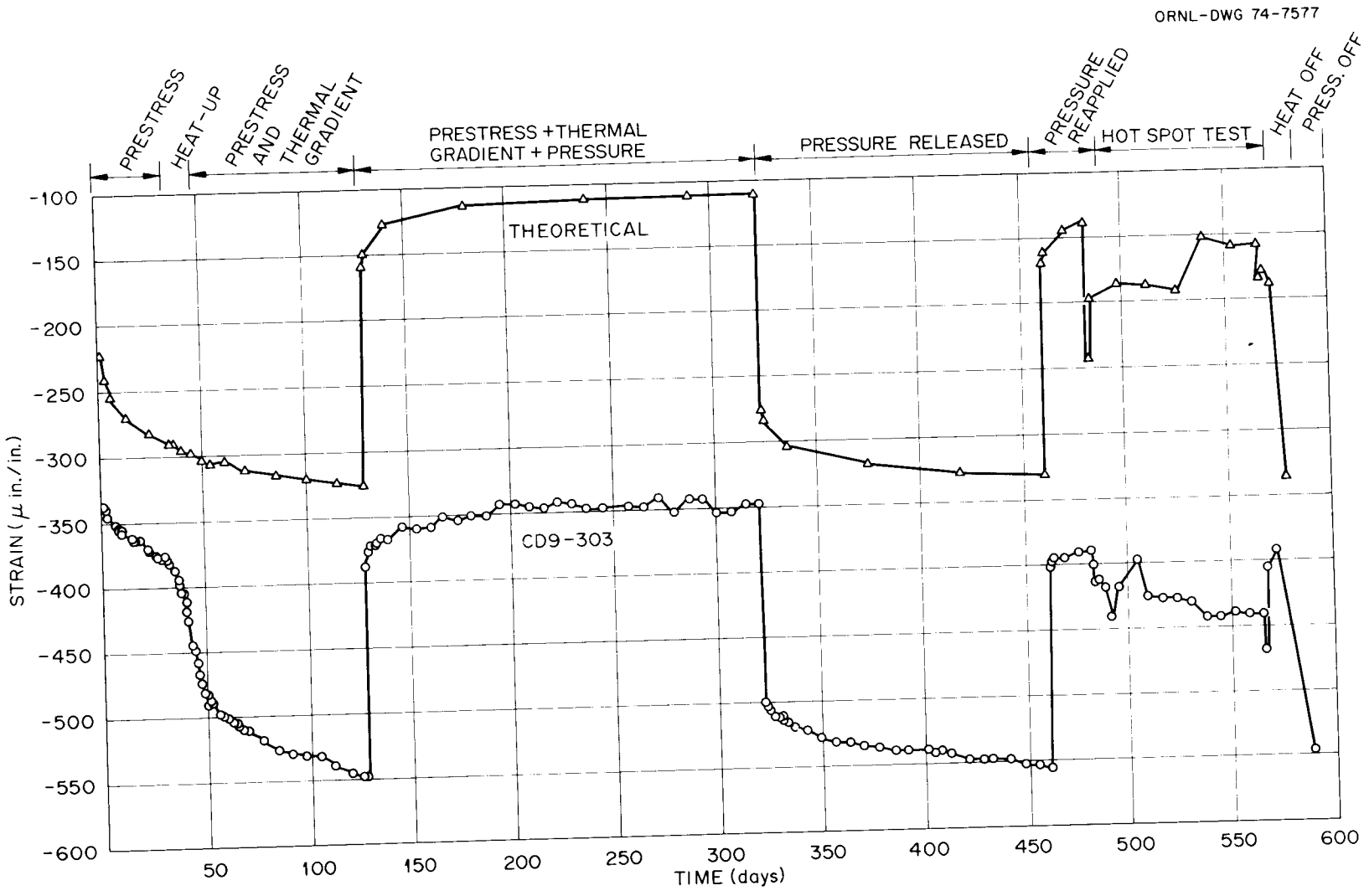

Fig. 8.13. Calculated and experimental results for the third-position circumferential type A vibrating-wire strain gage.

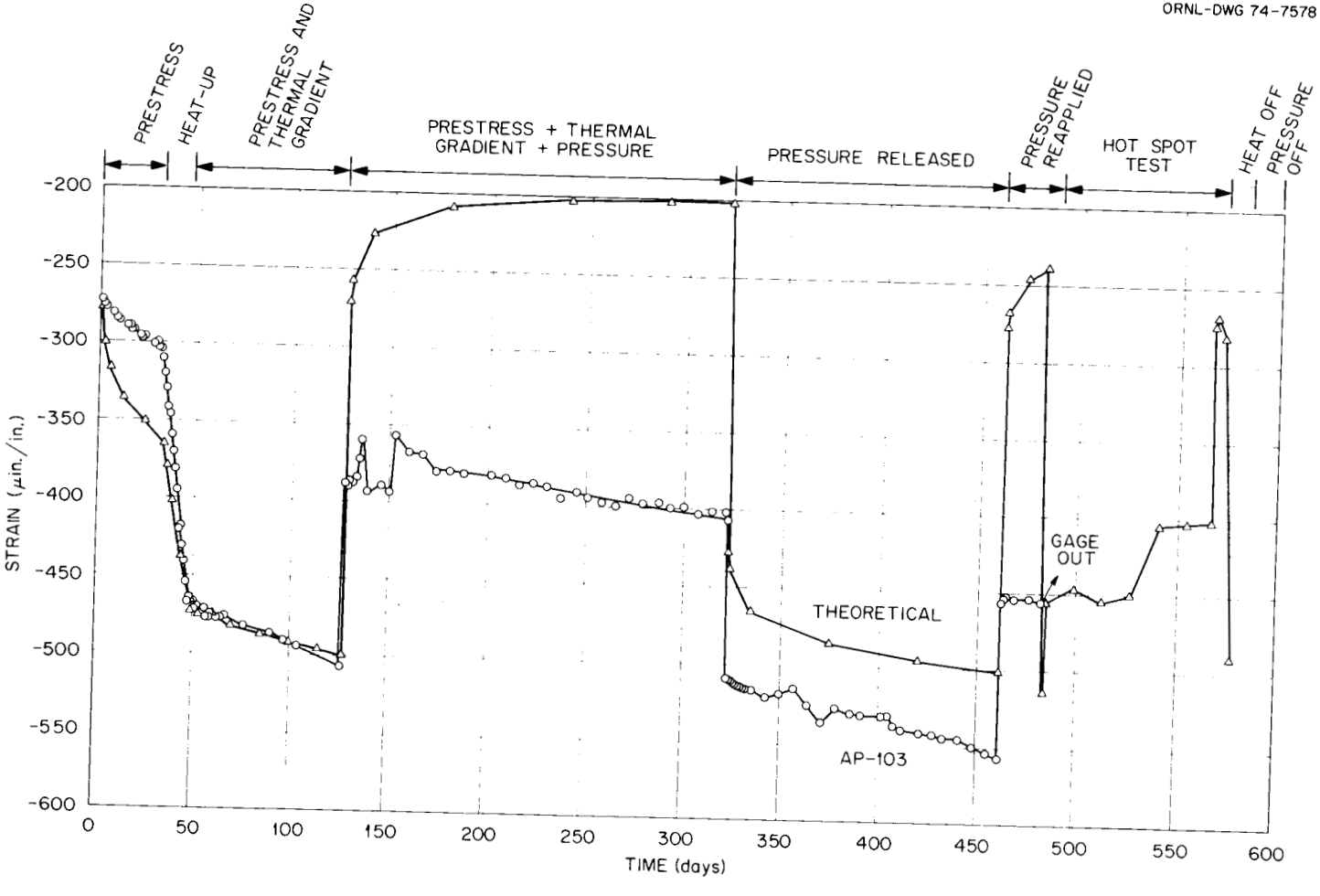

Fig. 8.14. Calculated and experimental results for first-position circumferential type B vibrating-wire strain gage.

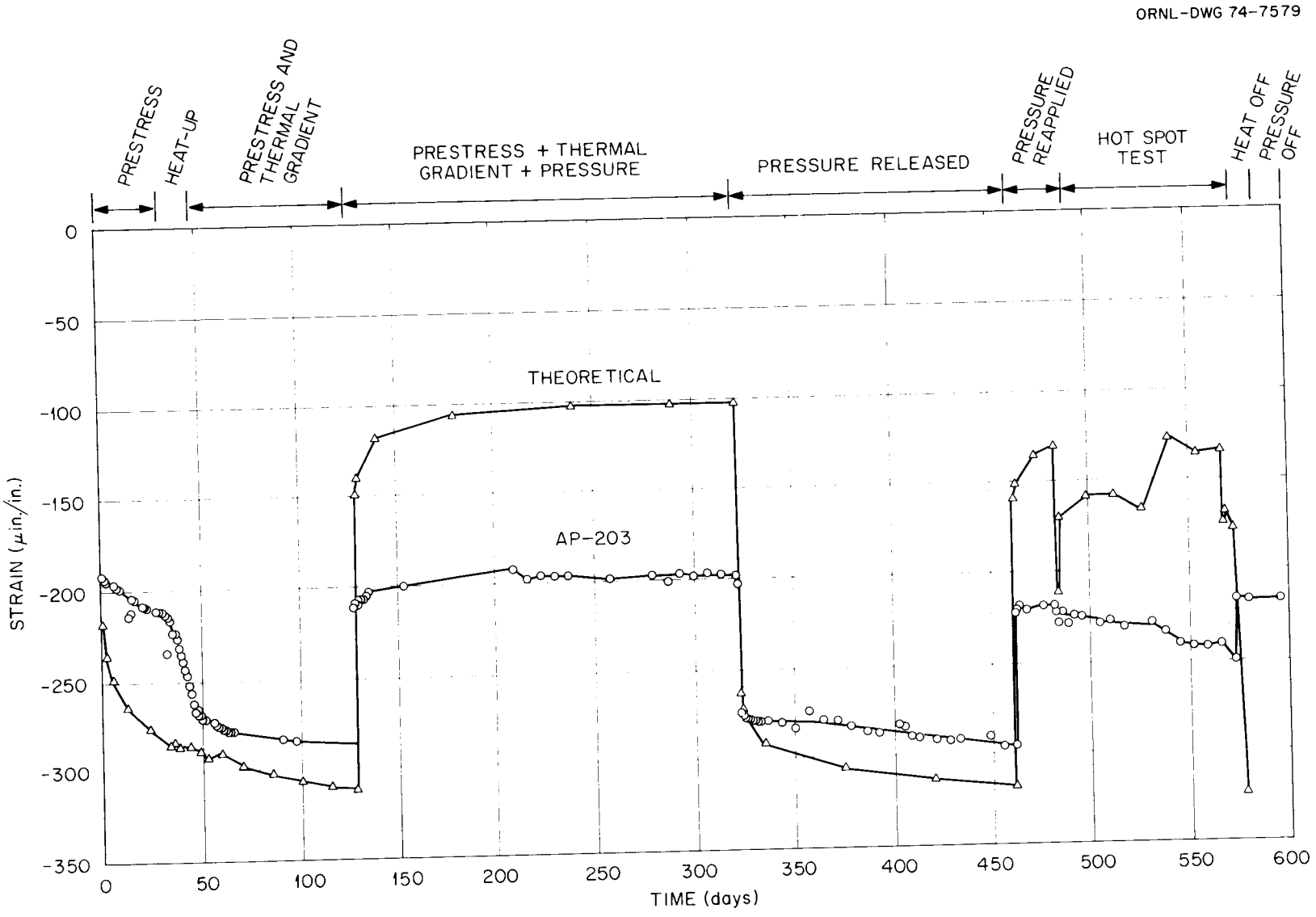

Fig. 8.15. Calculated and experimental results for second-position circumferential type B vibrating-wire strain gage.

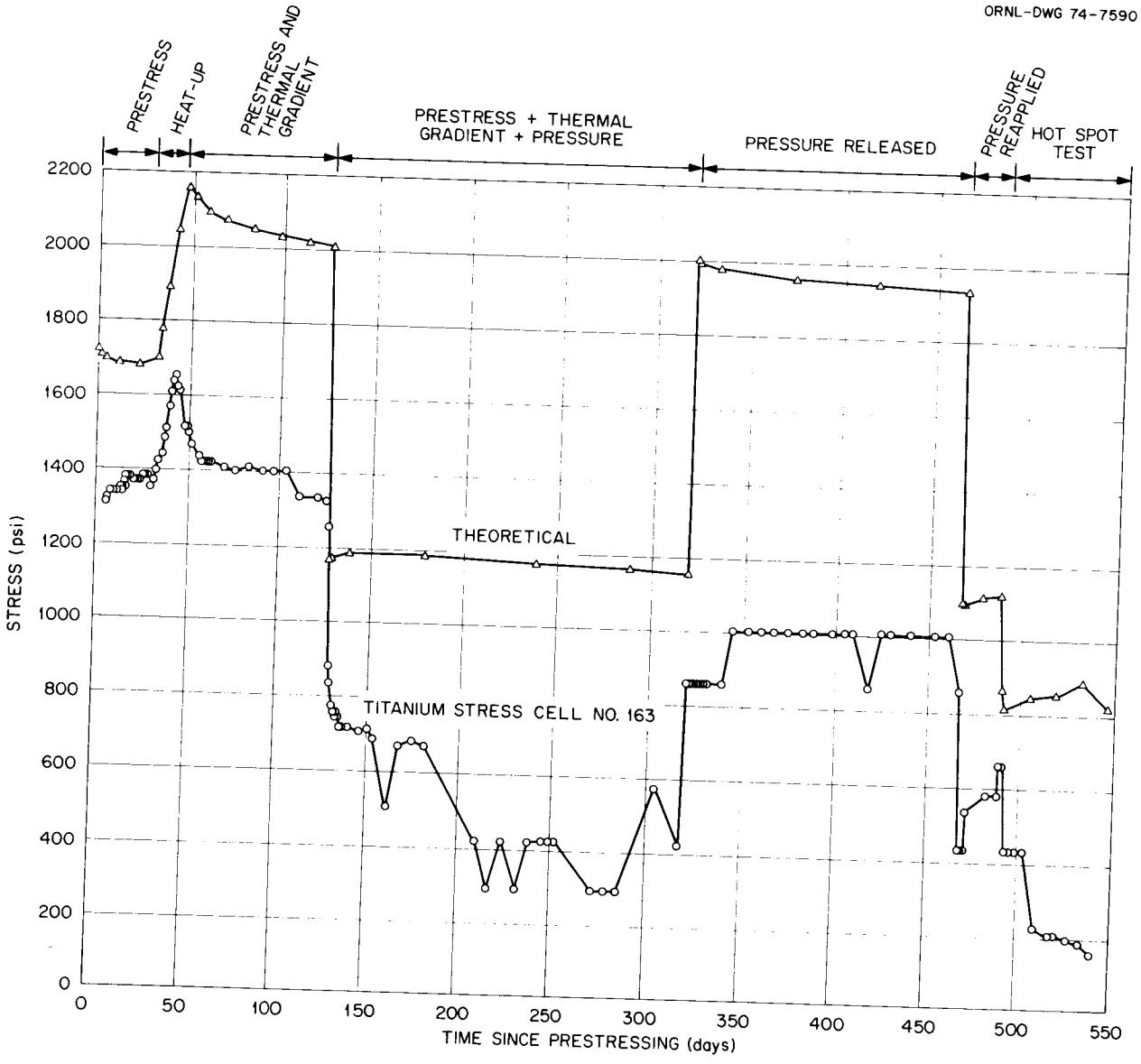

Fig. 8.16. Calculated and experimental results for first-position circumferential titanium stress cell.

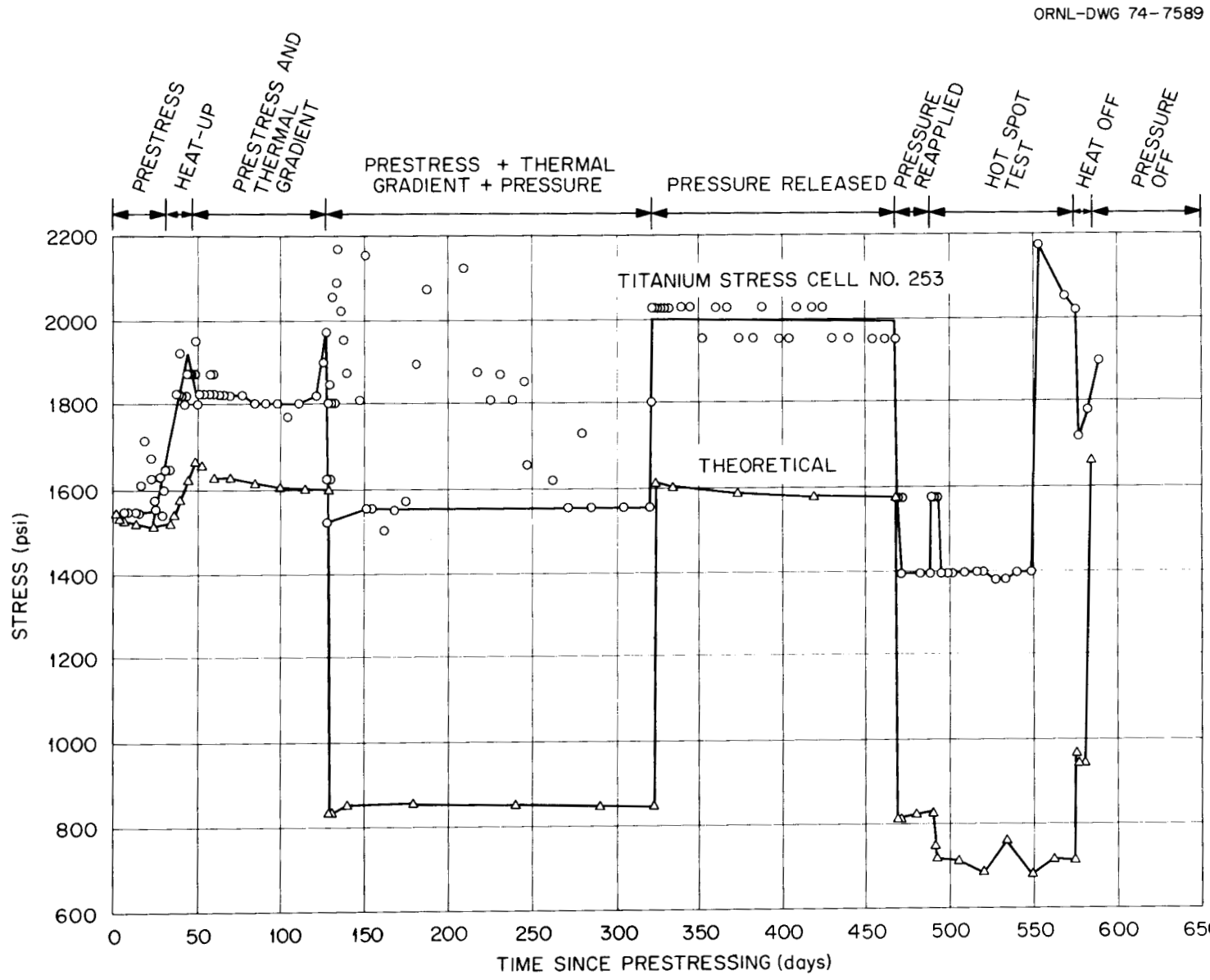

Fig. 8.17. Calculated and experimental results for second-position circumferential titanium stress cell.

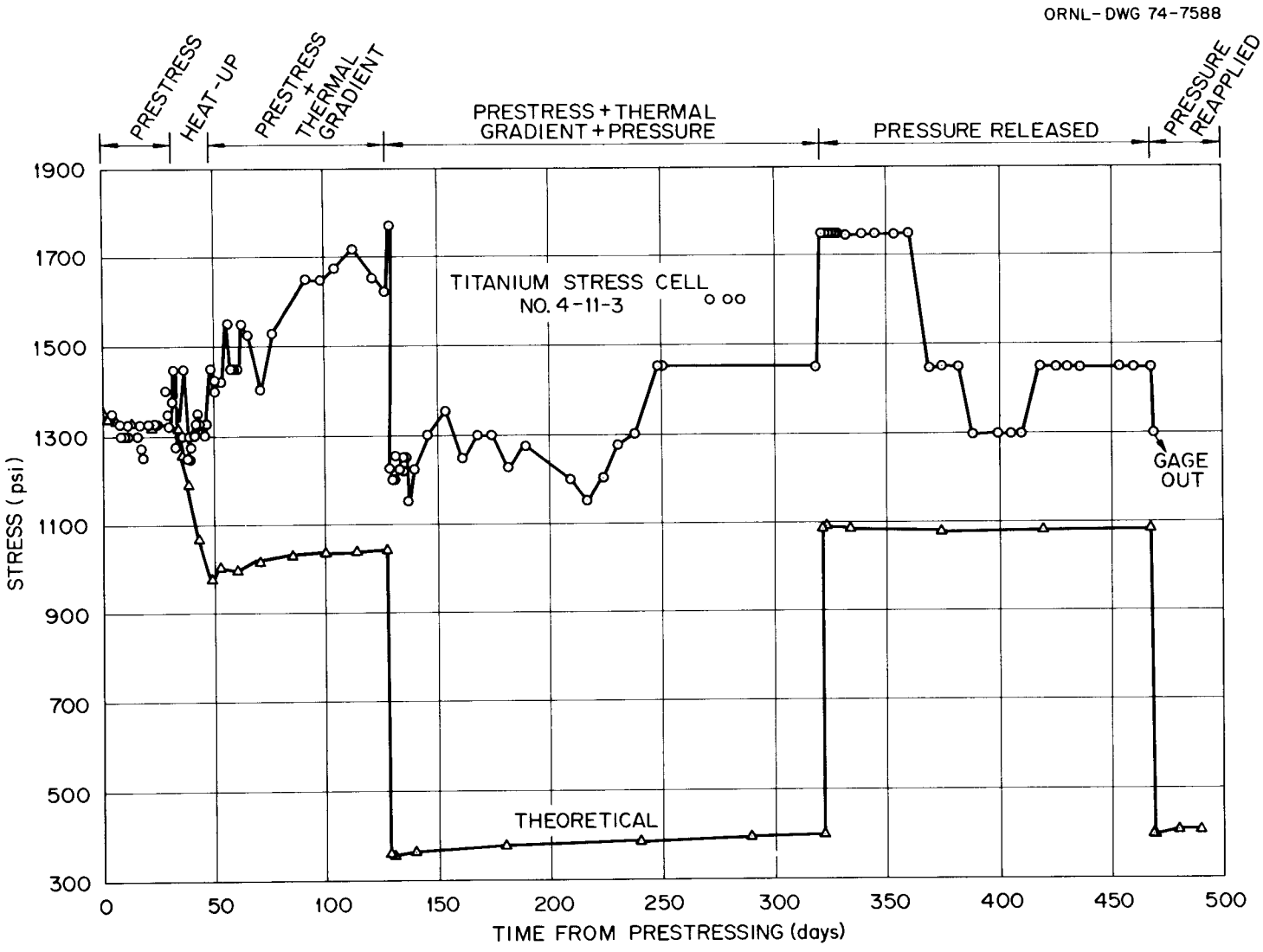

Fig. 8.18. Calculated and experimental results for fourth-position circumferential titanium stress cell.

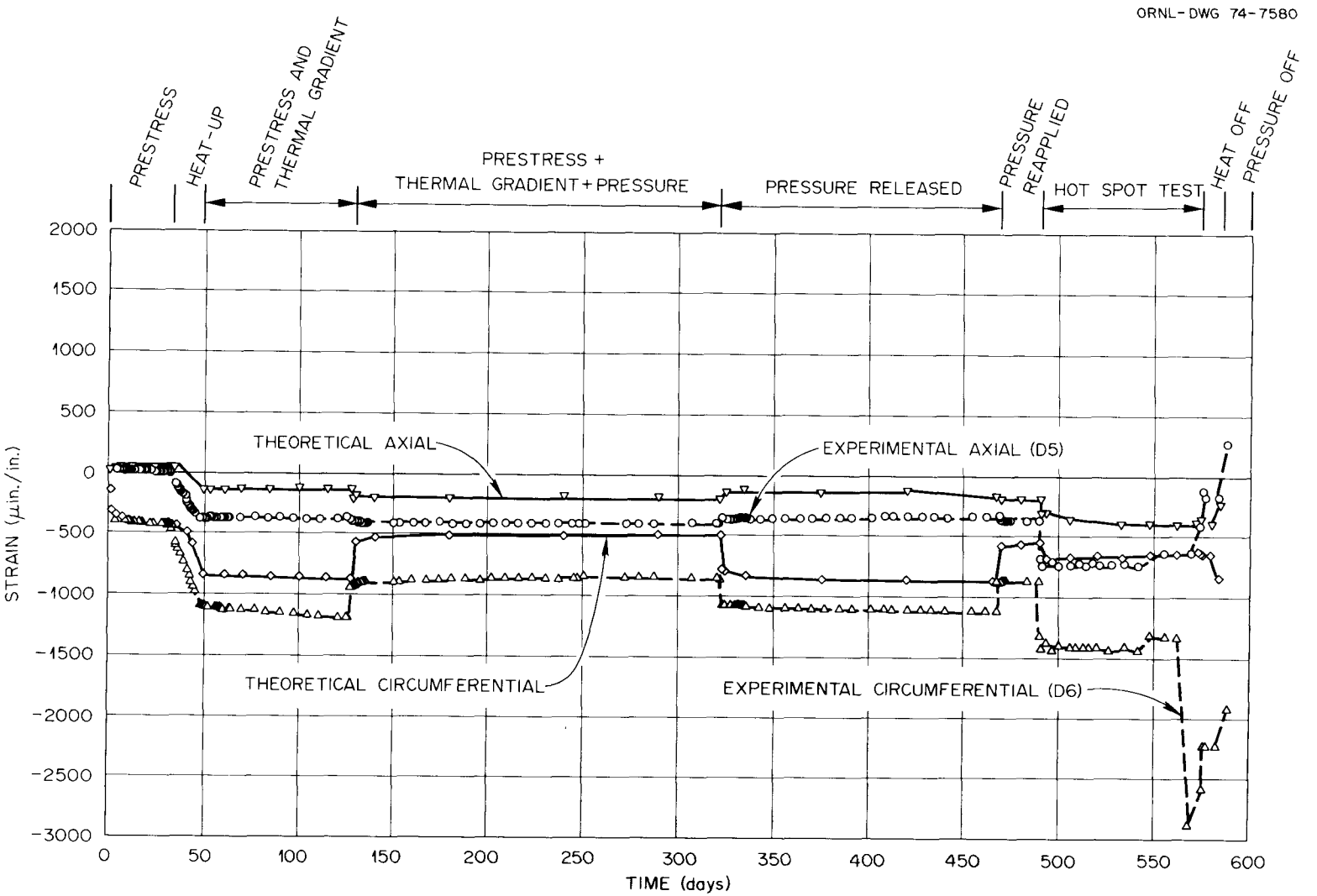

Fig. 8.19. Calculated and experimental results for axial and circumferential weldable strain gages attached to the concrete side of B heat exchanger.

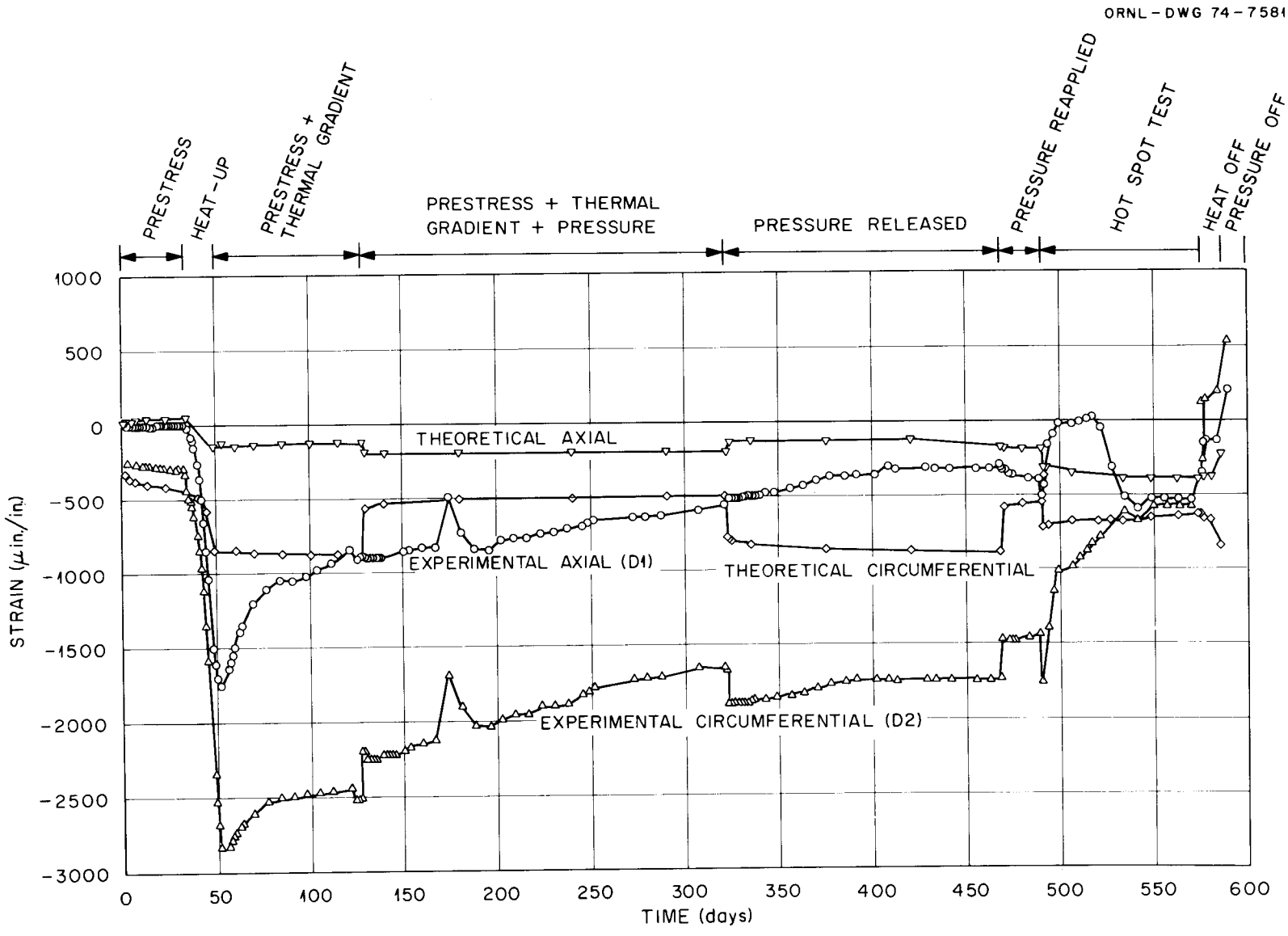

Fig. 8.20. Calculated and experimental results for axial and circumferential weldable strain gages attached to the annulus side of B heat exchanger.

leads, remained unchanged. It was thus concluded that the Fig. 8.19 gage data represented the behavior of the heat exchanger and that strain distortions seen in Fig. 8.20 resulted from instrumentation problems rather than liner behavior.

The results for weldable gages attached at the level of the hot-spot heaters are shown in Fig. 8.21. For comparison, the figure shows plots for circumferential gages attached to both sides of the heat exchanger. Although the hot-spot heating strains were much greater than those in Fig. 8.19, the same general trend in shown; however, in this case the circumferential gage did not exhibit the previously noted strain jump toward the end of the hot-spot heating period.

Individual strands of 12 axial and 8 circumferential prestressing tendons were instrumented with conventional foil resistance strain gages, and compression load cells were attached in series with the axial tendons. Results for three axial tendon strain gages are shown in Fig. 8.22. The inner row tendon gage CCB-3 apparently suffered a bonding failure prior to prestressing and must therefore be discounted. The two outer row tendon gages positioned as shown in the small inset of Fig. 8.22 indicated stable conditions until initiation of the hot experiment. At that time, gage CCB-2 showed a gradual strain decrease followed by a discrete jump. The load-vs-time plot of axial tendon load cell CTR-2 is shown in Fig. 8.23. This transducer, which was attached to the CCB-2 instrumented tendon, indicated a stable loading during the hot-spot heating period. It is therefore doubtful that the strain gage recorded a real tendon behavior. On the other hand, load transducers CTR-1 and CTR-3, which were coupled to inner row tendons, measured periodic step-load drops during the experiment. Recent post-mortem studies gave strong evidence that the load changes were produced by progressive corrosion failure of inner row tendons. The corrosion problem is discussed in Section 8.1.4.

Strain gage data for two circumferential tendons are shown in Fig. 8.24. In contrast to the axial tendons, these tendons were located outside the concrete test section and constrained as shown in Fig. 8.1. Based on the strain gage data, the circumferential tendons apparently performed satisfactorily.

Companion specimen tests. Two 18- by 40-in. concrete cylinders were instrumented with every type of embedment stress and strain measuring device employed in the thermal cylinder in order to provide a better understanding of basic gage behavior. These companion test cylinders were cast, sealed, and heated, and one was loaded uniaxially in accordance with the large-model time schedule. Both cylinders were maintained at 150°F temperature during the time-dependent portion of the study. Cylinder M-1 was subjected to a 3600-psi uniaxial loading 56 days from the time of thermal cylinder model prestressing, and cylinder M-2 remained unstressed during the model testing period. The unabridged strain history of the companion specimen single-filament resistance strain gages is shown in Fig. 8.25. The axial gages in both cylinders experienced excessive drift quite early in the experiment, and the unstressed M-2 cylinder lateral gage began drifting severely at 420 days. On the other hand, the stressed M-1 specimen lateral gage performed consistently for the duration of the experiment. The excessive number of gage failures was probably caused by the relatively high temperature seen by these gages.

In addition to the sustained testing period, the M-1 specimen was loaded and unloaded in steps both at 75 and 150°F; the M-2 specimen was also short-time load tested at 75°F to provide additional gage data. Typical stress-vs-strain plots for these short term tests are shown in Figs. 8.26 and 8.27 for axial single-filament resistance gage M1-SEB-111 and type B vibrating-wire gage M2-P-101 respectively. The concrete properties obtained for the operating gages of each type are shown in Table 8.2, where the final values are average 180-day strength test results for moist-cured 6- by 12-in. cylinders. Since the much larger companion specimens were sealed to prevent moisture loss and were at least 180 days of age, the 180-day compressive strength test data were used as the basis for comparison of gage performance. The 150°F data were obtained after approximately 550 days of heating; consequently, the modulus of elasticity should be slightly higher than the 180-day value. All the gages could not be evaluated because of premature failure of some of the companion specimen gages; however, based on the available data, certain conclusions can be made.

The single-filament resistance and type B vibrating-wire embedment gages gave the most accurate readings. The wound-wire resistance gages also performed satisfactorily at both temperatures, which was surprising since the thermal cylinder model gages of this type were unsatisfactory. The type C vibrating-wire gage gave reasonable results at room temperature, but the 150°F readings were significantly low.

The surface resistance gages listed in Table 8.2 were experimental gages developed as part of the ORNL biaxial creep test apparatus.[5] Three gages were attached to pairs of small steel posts protruding from the surface

5. R. F. Denkins, *GCR Program Semiannu. Progr. Rep. Mar. 31, 1969,* ORNL-4424, pp. 127–38.

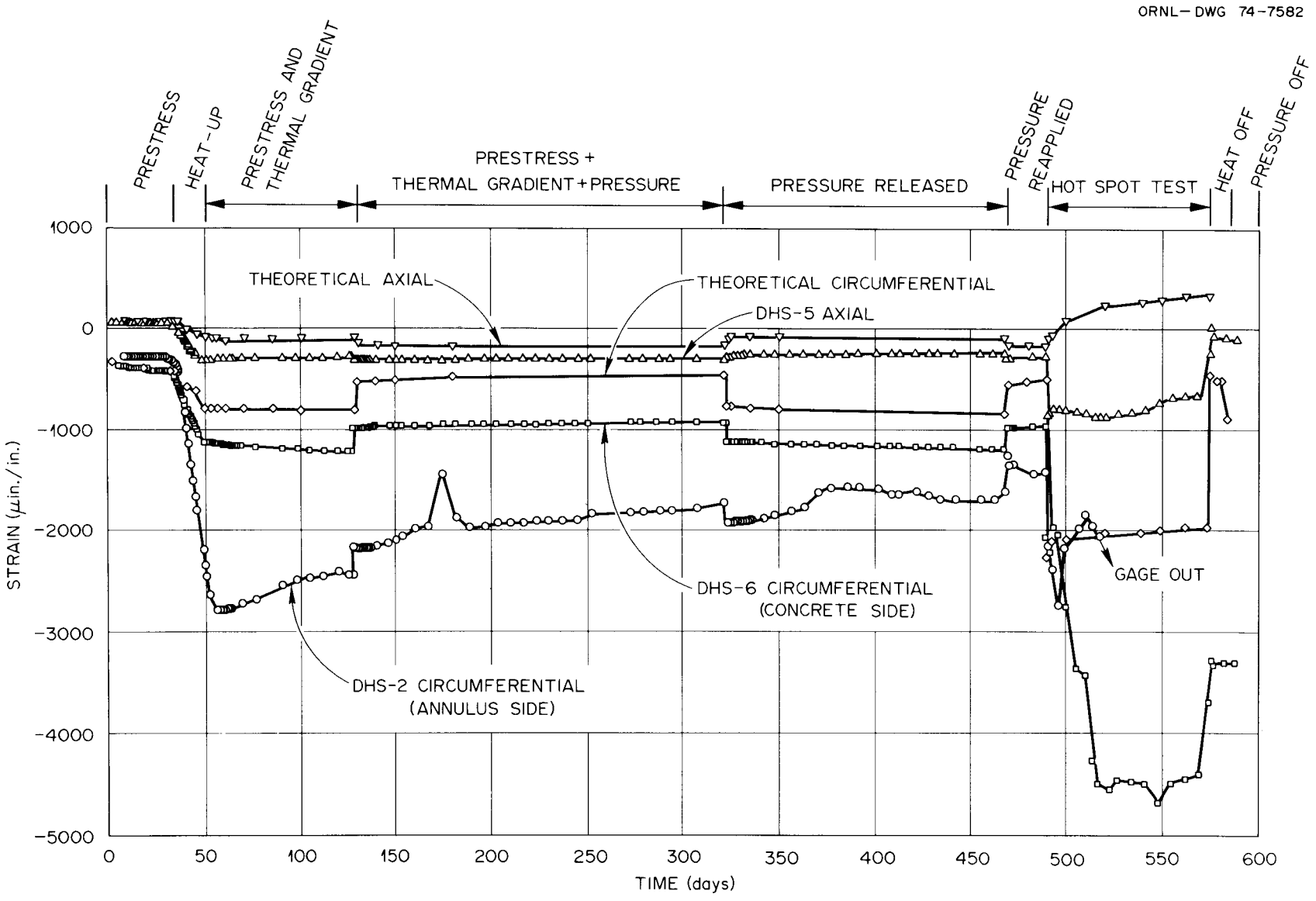

Fig. 8.21. Calculated and experimental results for axial and circumferential weldable strain gages attached to concrete side and for circumferential gage attached to annulus side of B heat exchanger.

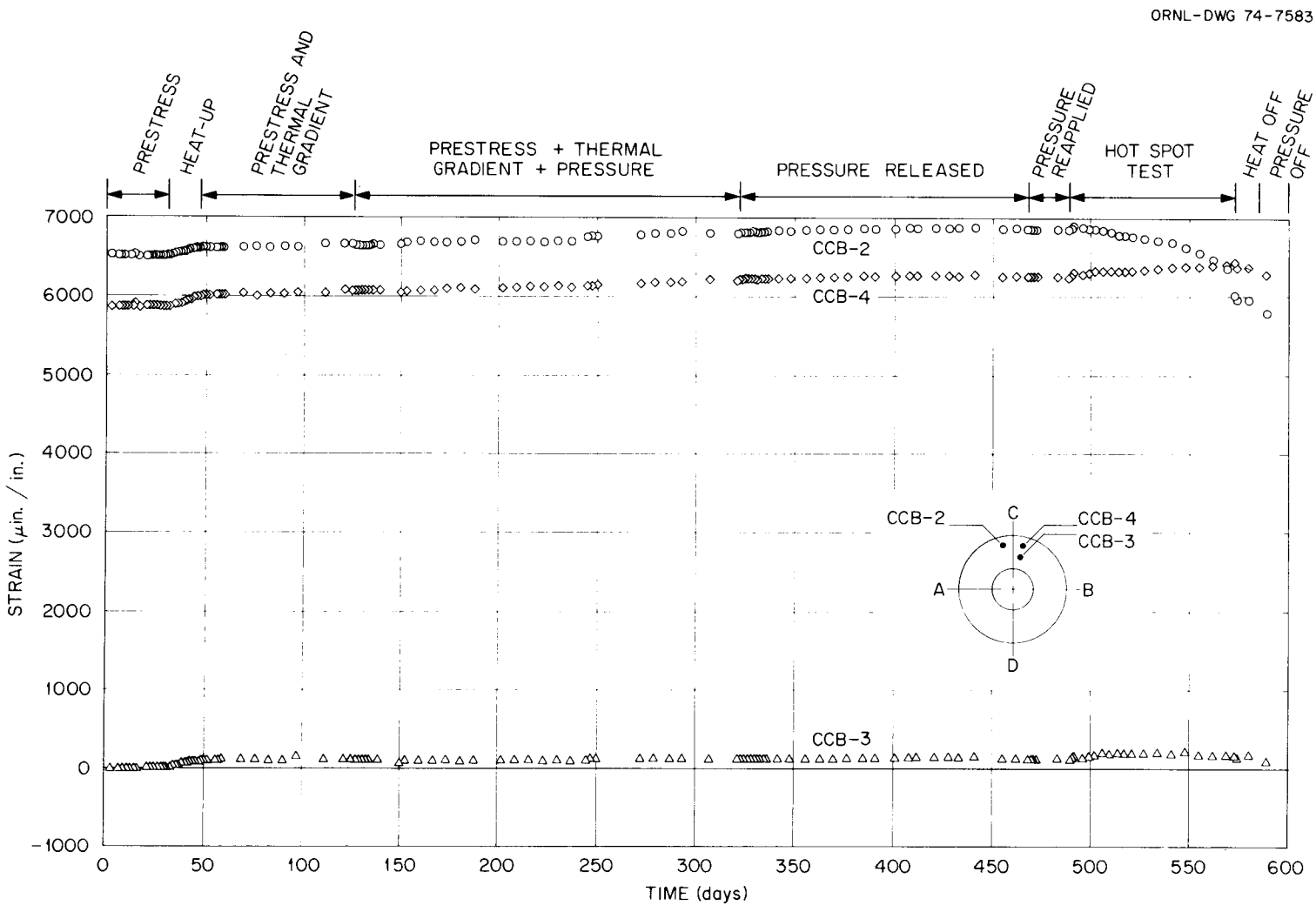

Fig. 8.22. Experimental results for foil-type strain gages attached to axial prestressing tendons.

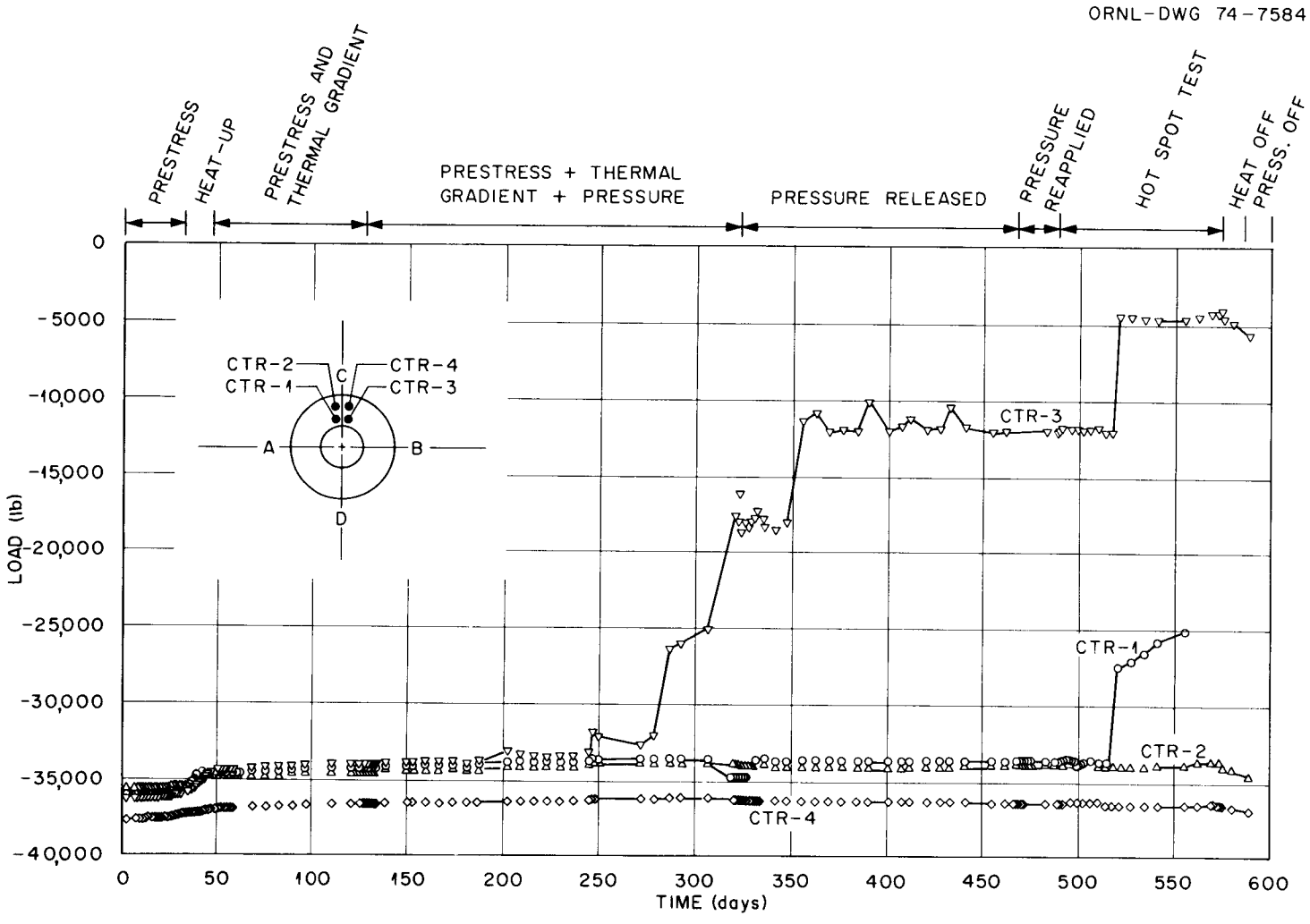

Fig. 8.23. Experimental results for load cells coupled to axial prestressing tendons.

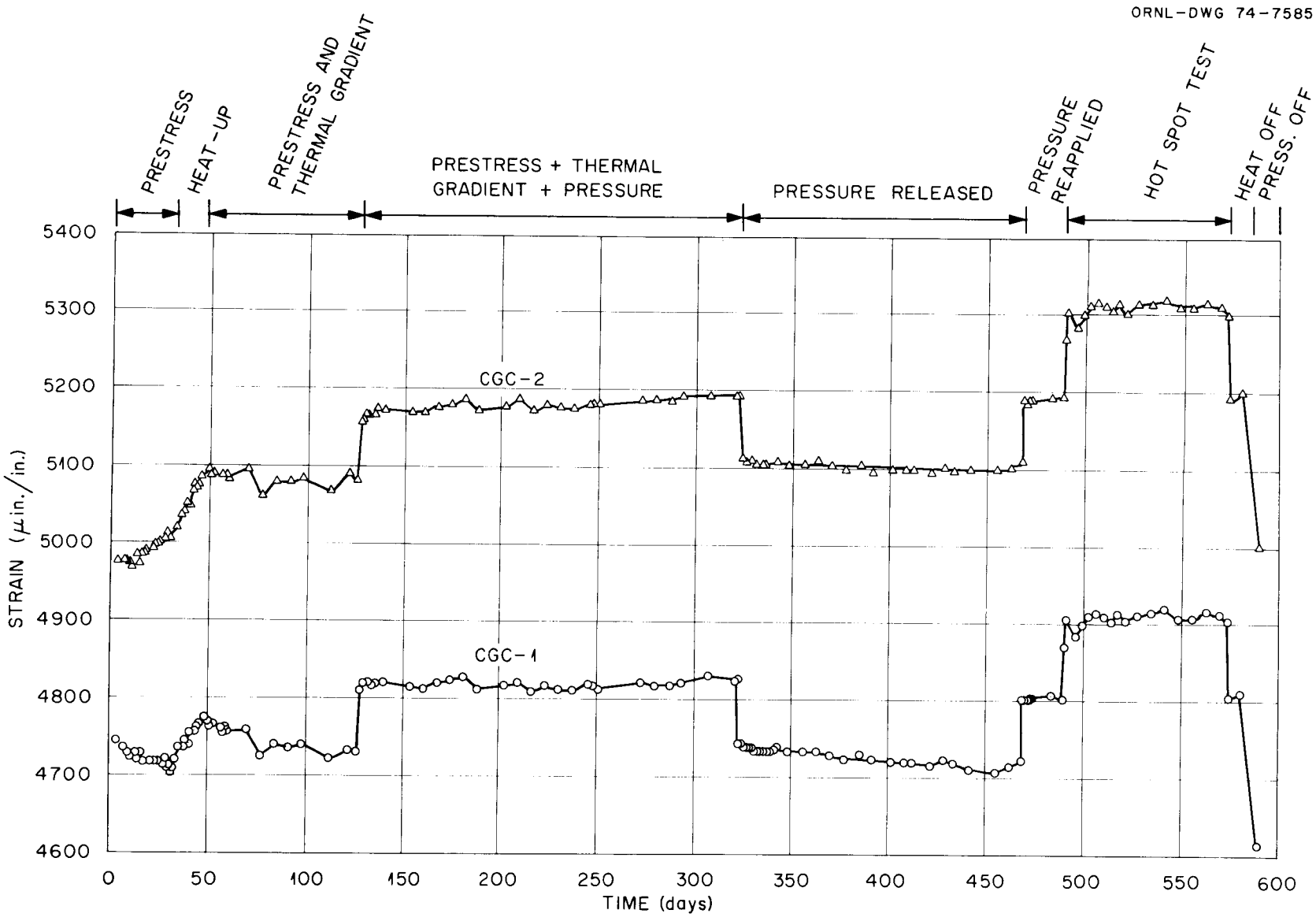

Fig. 8.24. Experimental results for foil-type strain gages attached to circumferential prestressing tendons.

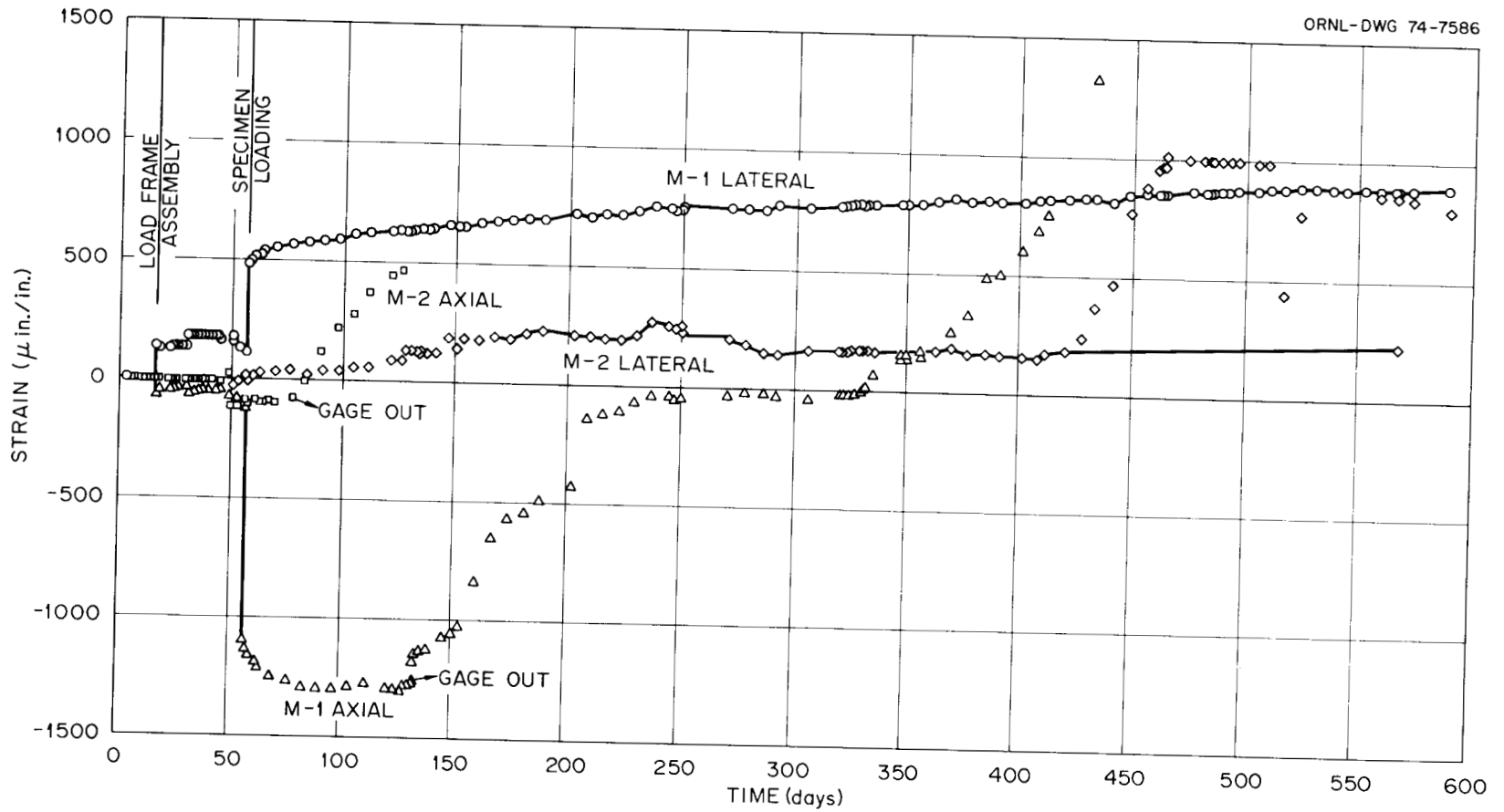

Fig. 8.25. Experimental results for axial and lateral single-filament resistance strain gages of stressed M-1 and unstressed M-2 companion concrete cylinders.

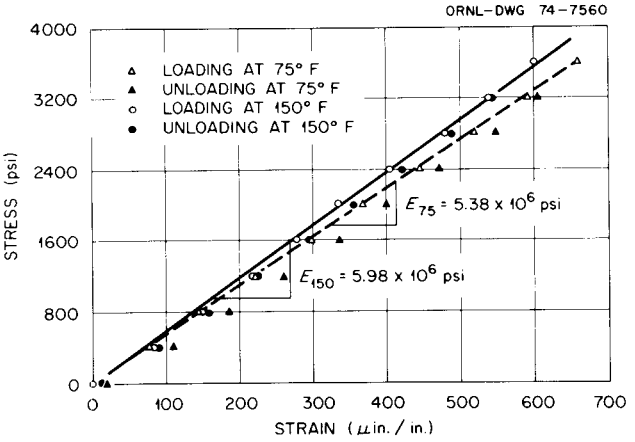

Fig. 8.26. Short-time M-1 specimen load test results for axial single-filament resistance strain gage.

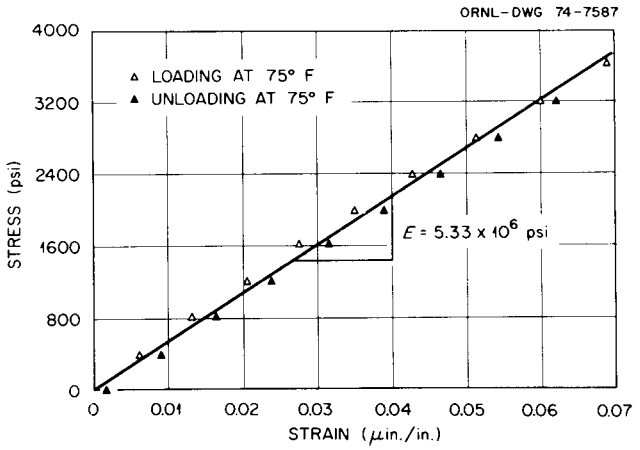

Fig. 8.27. Short-time M-2 specimen load test results for axial type B vibrating-wire strain gage.

of each cylinder at equal angular spacing. Although these gages were not operational during the room-temperature test, they performed satisfactorily at 150°F.

The results of the uniaxial compression testing of the titanium stress cell are shown in Fig. 8.28. In addition to the companion specimen tests of the embedded gages, each stress cell was load calibrated under uniaxial compression. The results indicated that the embedded stress cell readings must be multiplied by 1.19 to obtain the actual stress in the concrete.

We also attempted to monitor the embedded pressure type stress cells during the companion specimen tests

Table 8.2. Companion specimen compression test results

Gage type	Modulus of elasticity (psi)		Poisson ratio
	75°F	150°F	
	× 10^6	× 10^6	
Single filament resistance	5.38	5.98	
Type B vibrating wire	5.33		0.24
Type C vibrating wire	4.67	4.74	
Wound wire resistance	4.90	6.40	0.31
Surface resistance		5.80	
Concrete strength tests[a]	5.40		0.28

[a]See Table 7.1 in Ref. 1 for additional concrete strength data.

but, owing to a need for additional and more sophisticated instrumentation, were able to obtain only the following three readings:

Actual stress (psi)	Stress cell pressure (psi)	Percent deviation
402	700	74
795	1500	89
3666	4200	15

This device was able to determine the maximum specimen stress to within 15% but was unable to measure the lower stress levels to a reasonable accuracy.

Although both of the types of stress-measurement devices used in this experiment offer some promise, considerable work will be required to develop a satisfactory embedment stress cell that is capable of monitoring time-dependent stresses in prestressed concrete structures.

8.1.2 Disassembly of the Thermal Cylinder Model

The thermal cylinder model detensioning was completed on May 30, 1973, which was 771 days from the time of the original tensioning of the prestressing system. The circumferential tendons were completely detensioned first; then the axial tendons were detensioned in one step in sets of 13 in a quadrant at a time using a reverse of the original loading sequence. One significant system failure was revealed during the detensioning operation. The axial tendons shown in Fig. 8.29 were equally divided into an inner and an outer row of the model test section. Hydraulic pull rams were coupled to the tendons, and the loading was raised to 45,000 to 47,000 lb to lift off the restraining nut which was then loosened. The first inner row tendon was

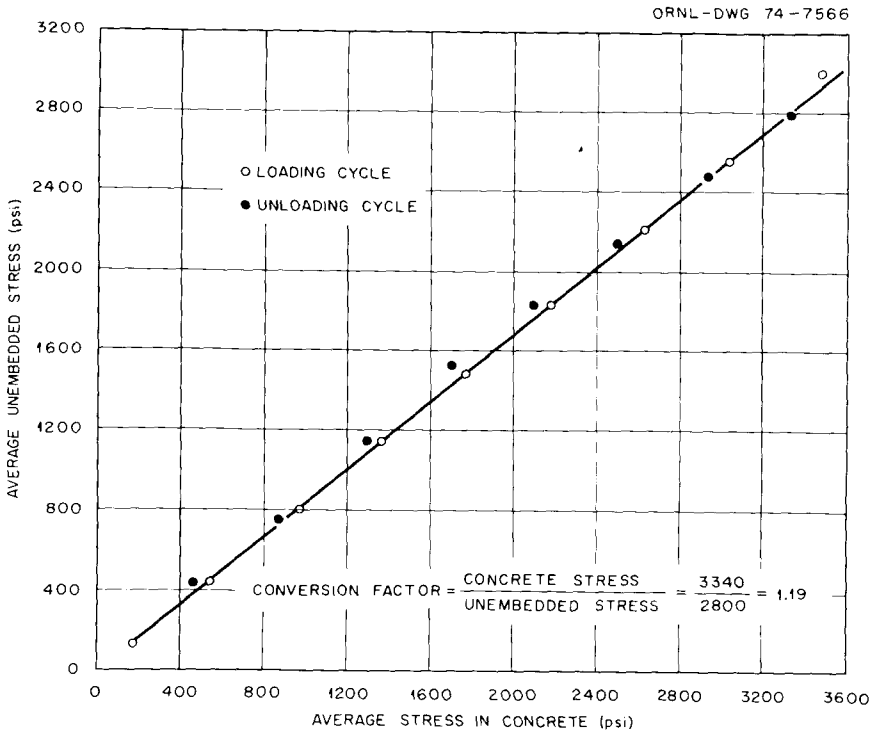

Fig. 8.28. Comparison of concrete embedment stress cell laboratory calibration for embedded and unembedded conditions.

pulled out excessively at ~20,000 lb, thereby indicating failure. All the outer tendons required at least a pressure of 45,000 lb to loosen the restraining nut, while all but two of the inner row tendons required only a low ram pressure to unseat the nut.

Upon completion of the detensioning operation, one of the failed tendons was removed. It appeared to have failed near the bottom anchor, and as indicated by the darkened appearance of some of the fracture surfaces, the wires had evidently failed prior to detensioning. The investigation of the mechanism of these tendon failures is discussed in Section 8.1.4.

After the circumferential prestressing assemblies were removed, the model was stripped and the inner concrete core (shown in Fig. 8.1) removed. A visual examination of the liner did not reveal any buckling, cracking, or other problems. Portions of the steel liners were removed at the six locations designated as cut sections in Fig. 8.30, and the exposed portions of the axial tendon assemblies were capped and sealed as shown in Fig. 8.31 to prevent contamination during sectioning of the concrete. The model outer ring was transported to a commercial marble company for sectioning. The ring was first cut in half using a water-cooled (nonchlorinated well water) diamond wire saw; additional sectioning was done using a diamond circular saw. The portion of the test section labeled as "moisture block" in Fig. 8.30 was further sectioned as shown in Fig. 8.32 to provide a 1 X 1 X 1 ft moisture test cube containing a stainless steel moisture probe access tube at the center. The use of this test cube in calibrating the moisture probe is described in Section 8.1.5.

Visual inspection of the exposed cross sections revealed no significant defects or structural cracks in the concrete. The slices made at the instrumentation section showed that a good bond existed between the various gages and the concrete.

The section produced by cut 15 (see Fig. 8.30) is shown in Fig. 8.33. The centermost gage label is to the right and below a precast three-gage rosette of single-filament resistance strain gages. A closeup of the excellent bond achieved between the precast gage rosette and the remaining concrete is shown in Fig. 8.34. The upper gage shown in Fig. 8.33 is an axially oriented type A vibrating-wire gage, and the lower gage is the activator coil housing and one end anchor of a radially oriented gage of the same type. The crack shown to the right of the upper gage occurred during

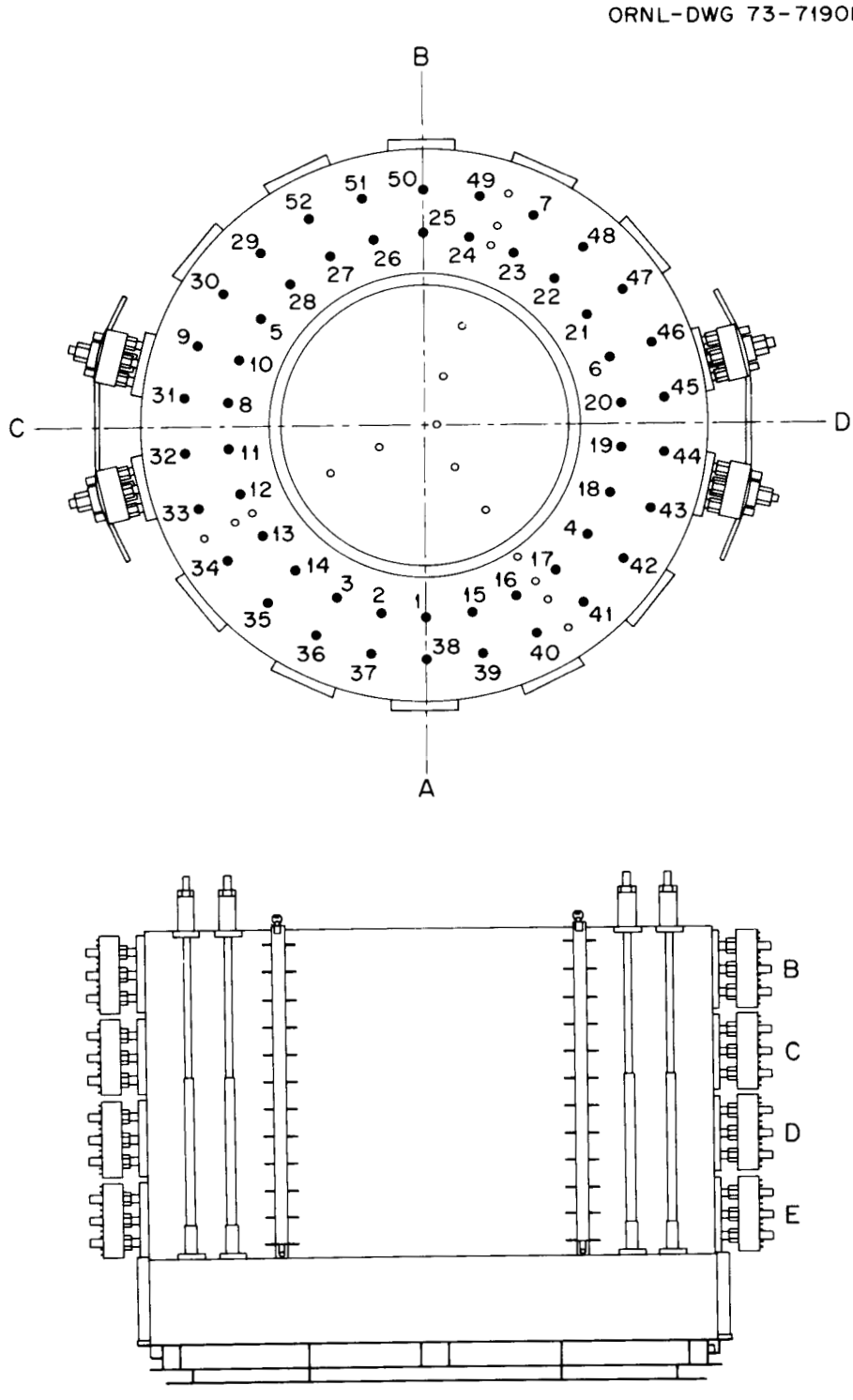

Fig. 8.29. Thermal cylinder prestressing system.

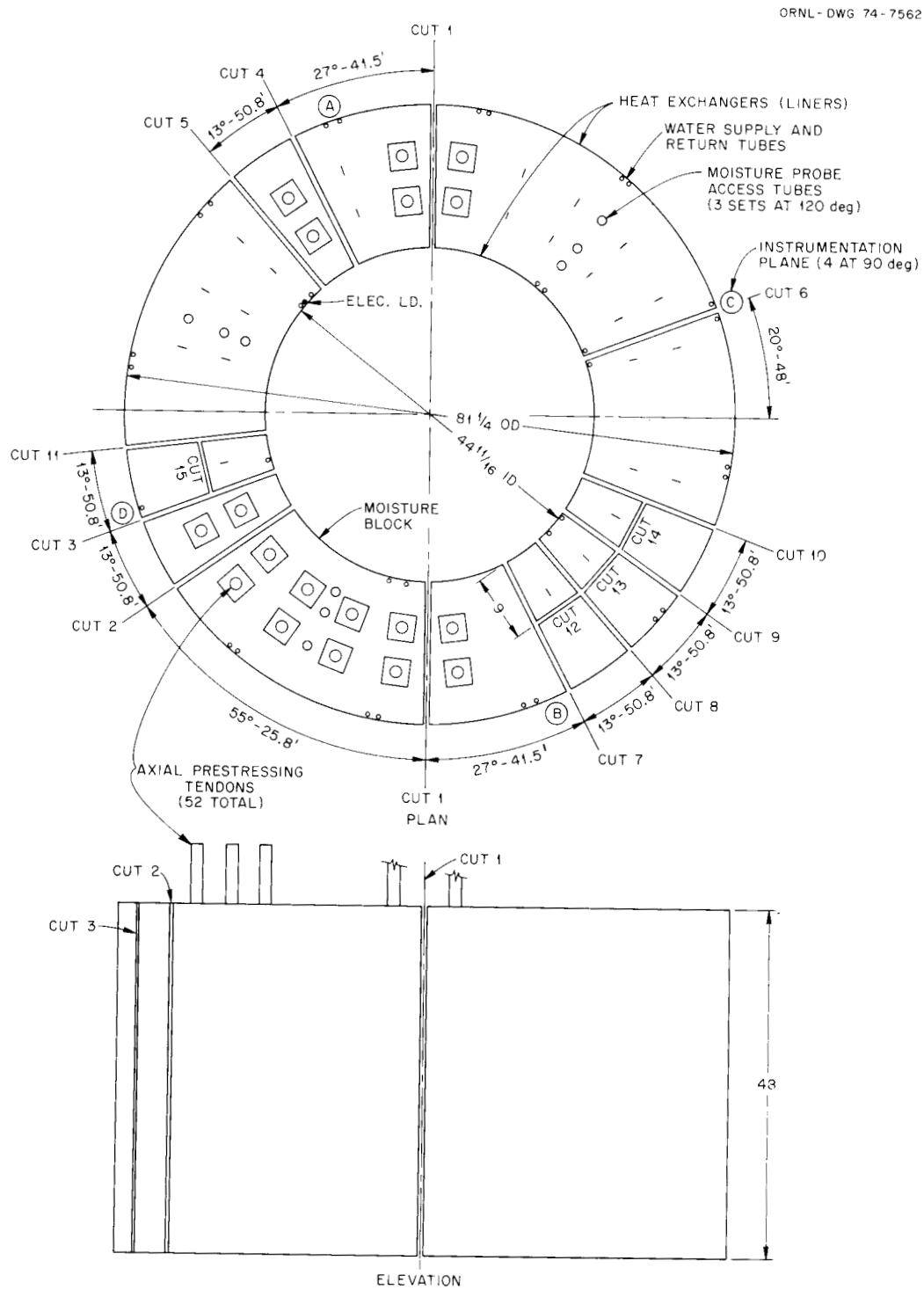

Fig. 8.30. Thermal cylinder model sectioning plan.

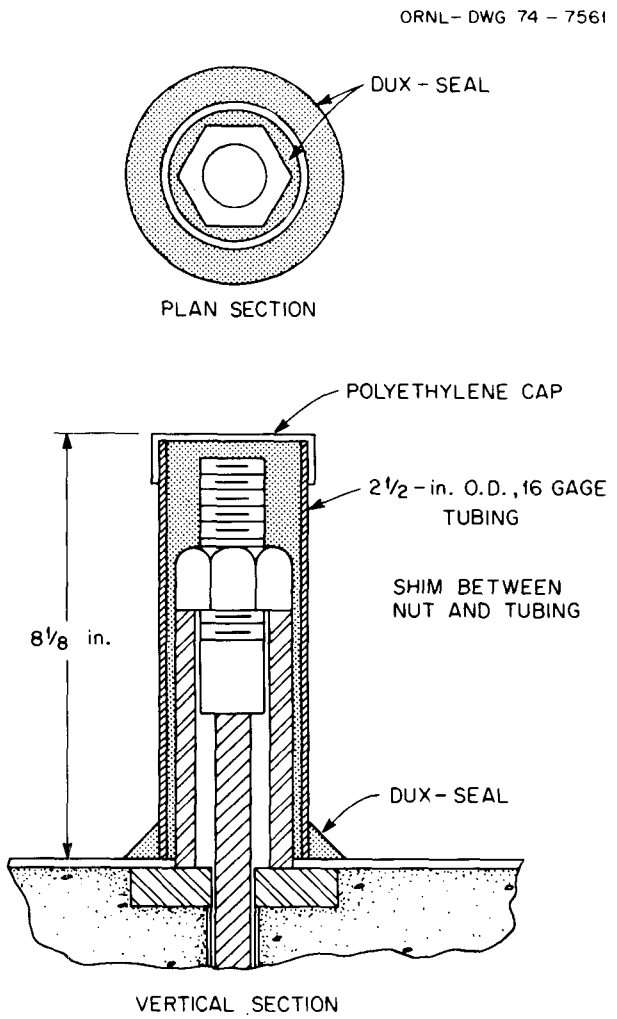

Fig. 8.31. Axial prestressing tendon assembly moisture seal for concrete sectioning.

the cutting operation, and the remaining inclusions seen in the concrete are primarily sectioned instrumentation leads.

8.1.3 Rebound Hammer Test Results

Although there were no significant defects seen in the cut surfaces, the concrete immediately surrounding the hot-spot heating elements was darkened as shown in Fig. 8.35, which indicates that some change occurred in the concrete due to the 450°F hot-spot heating. A series of readings were made on the concrete faces using an impact hammer (or sclerometer). This test is based on the principle that the rebound of an elastic mass depends on the hardness of the surface against which the mass impinges. Compressive strength of the material can be determined from this behavior. The test apparatus consists of a spring-loaded mass having a fixed amount of energy imparted to it by extending a spring to a predetermined compression. The mass is then released, and the distance traveled by the rebounding mass, expressed as a percentage of the initial extension of the spring, is called the rebound number. This number is an arbitrary measure, since it depends on the energy stored in the given spring and on the size of the mass.

The test is sensitive to local variations in the concrete; for example, the presence of a large piece of aggregate immediately beneath the plunger would result in an abnormally high rebound number. In contrast, the presence of a void in a similar position would result in a relatively low number. A correlation of rebound number with unconfined compressive strength is given in the textbook by Neville[6] for a concrete made with crushed limestone aggregate. Figure 8.36 is a reproduction of this curve with the straight line extended to include a compressive strength of 8000 psi.

The results of a rebound test of the sectioned thermal cylinder model are shown in Table 8.3. Rebound readings were taken on the four faces of the cross section at the A and B quadrants. Readings were made along lines constructed perpendicular to the inside surface of the cylindrical test sections at two elevations as shown in Fig. 8.37. One base set was taken in the upper part of the model approximately 1 ft from the top, and one was taken through the vertical center of the hot-spot heated zone. The distances shown in the table were taken from the inside surface of the section. The "at heater" readings were taken directly adjacent to the panel coil heaters. As can be seen on the right hand side of the table, considerable compressive strength reductions were measured in the local heat-affected zone. This zone was easily distinguished by the distinct color change when compared with the rest of the cross section. On the other hand, the base readings taken at a considerable distance from the heat-affected zone show very little strength variation. The average strength determined from the base readings was 7500 psi. There is little doubt that a significant strength decrease was experienced in the heat-affected zone. The thermal cylinder had a 28-day unconfined compressive strength of approximately 7000 psi, which might tend to indicate that the rebound reading strength correlation may be slightly low. However, these readings were

6. A. M. Neville, *Properties of Concrete*, Wiley, New York, 1963.

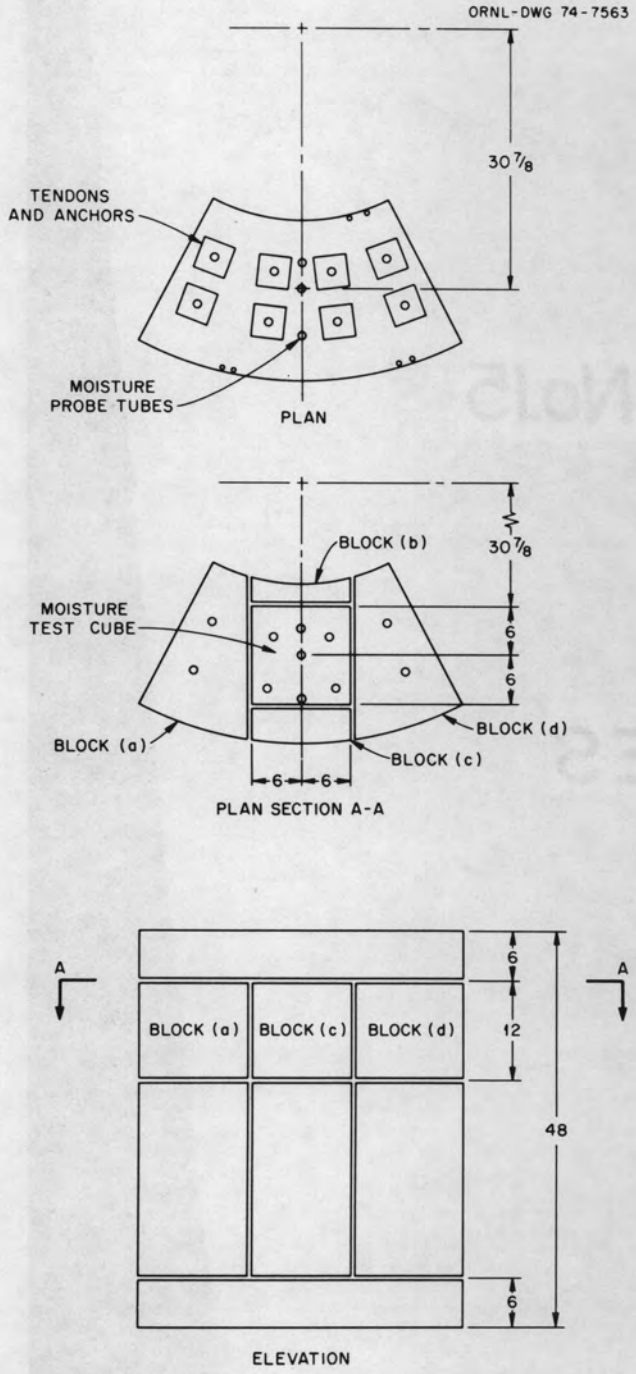

Fig. 8.32. Cutting plan for moisture block section of thermal cylinder model.

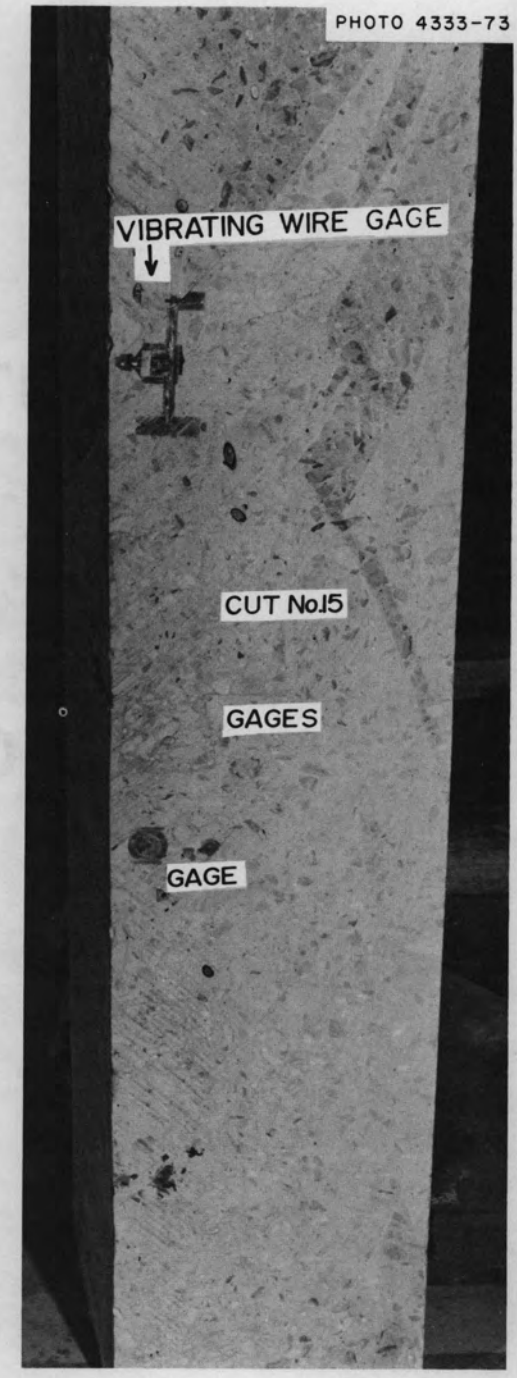

Fig. 8.33. Thermal cylinder model section produced by cut 15.

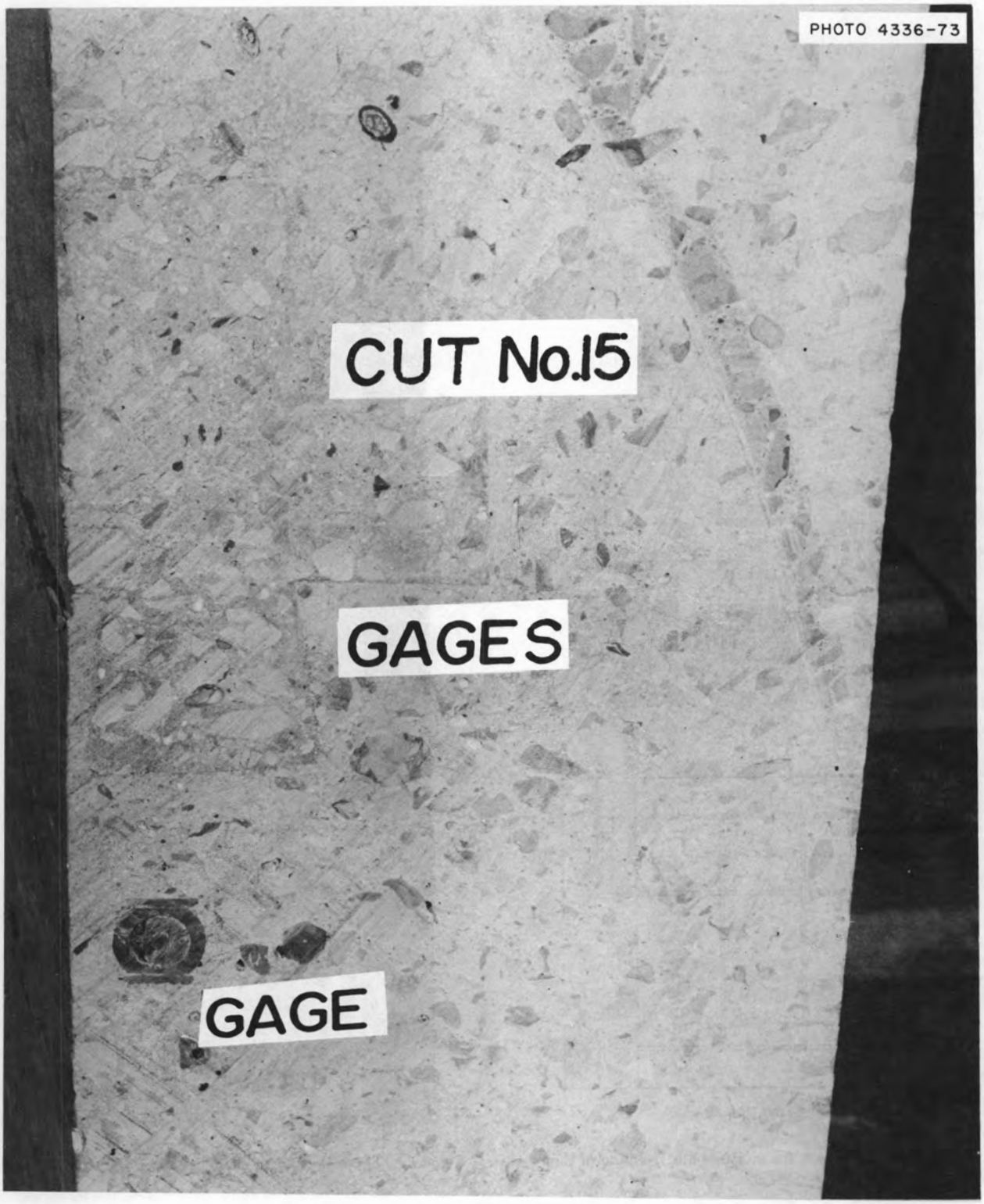

Fig. 8.34. Closeup of cut 15 showing bond between precast single-filament resistance gage rosettes and model concrete.

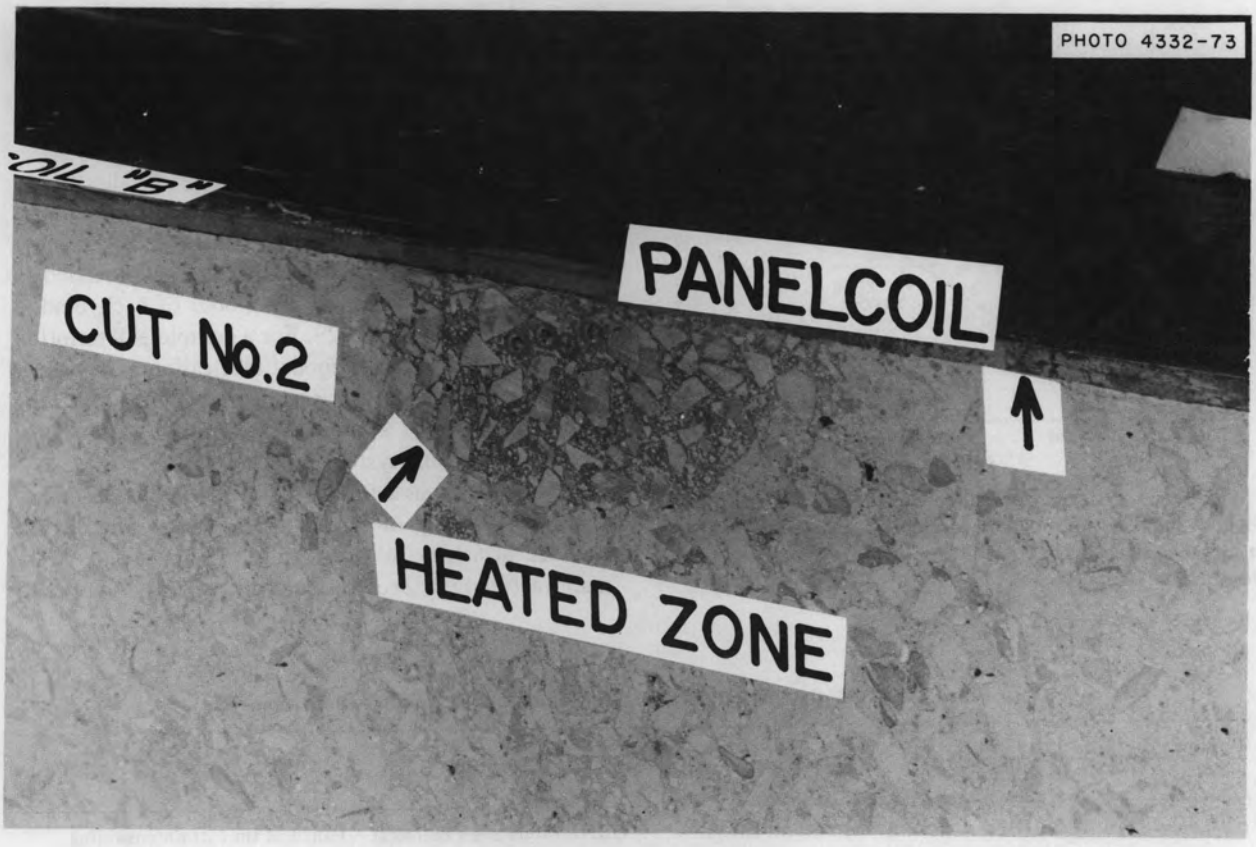

Fig. 8.35. Cross section of cut 2 showing discoloration in the vicinity of the hot-spot heating coils.

Table 8.3. Summary of impact hammer (or sclerometer) readings on thermal cylinder model cross sections

Distance (in.)	Base readings			Readings at hot-spot level					
				A section		B section		Average	Compressive strength (psi)
	A	B	Average	1	2	1	2		
At heater				31	23		30	28.00	4600
1	43	41	42	38	40	38	34	37.50	6300
3	43	44	43.5	42	40	43	39	41.00	6900
5	45	46	45.5	41	40	40	43	41.00	6900
7	43	43	43.0	41	41	43	43	42.00	7100
9	44	43	43.5	48	41	42	44	43.75	7500
11	43	44	43.5	43	43	43	45	43.50	7500
13	43	44	43.4	42	45	43	45	43.75	7500
15	44	45	44.5	49[a]	43	44	44	43.70	7500
17	43	45	44.5	42	47	42	44	43.75	7500

[a]Excessively high readings taken on aggregates not included in the average; readings for large aggregate inclusions were 50.

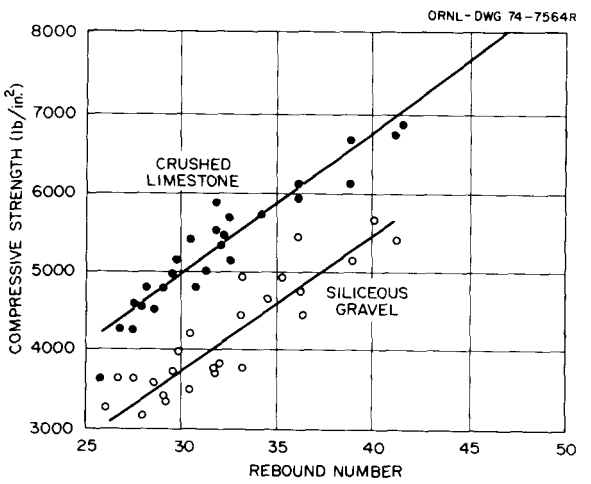

Fig. 8.36. Relation between compressive strength and rebound number for concrete cylinders made with different aggregates. (Readings taken on the side of a cylinder with the hammer horizontal.)

taken on the matrix rather than on the aggregates whenever possible. The rebound readings made on large aggregates were significantly higher.

8.1.4 Tendon Corrosion Study

A thorough investigation is being conducted to determine the cause of causes of the tendon failures described in Section 8.1.2. The status of the 26 inner row and 2 of the outer row tendons is summarized in Table 8.4. The location in the model of each tendon listed is shown in Fig. 8.29. For a complete description of the thermal cylinder model fabrication and testing, the reader is referred to Refs. 1 and 3. The following discussion provides a detailed description of the axial tendon prestressing system.

Each tendon was a 0.6-in.-diam LOK-STRESS monostrand consisting of seven wires and having SEEE anchors attached to both ends. These strands were manufactured in accordance with ASTM A416 and

Table 8.4. PCRV thermal cylinder model – status of axial tendon examination

Tendon No.	Row[a]	Load cell designation	Failure location	Disposition	Remarks
1	I	ATR-11	Broke near bottom anchor	ORNL (Metals & Ceramics)	Failed at time of detensioning
2	I	None	Broke near bottom anchor	Stressteel Corporation	Failed at time of detensioning
3	I	None	Broke near bottom anchor	General Atomic Company	Failed at time of detensioning
4	I	None	Broke near bottom anchor	ORNL (tested single wires)	Failed at time of detensioning
5	I	None	Broke near bottom anchor	ORNL	Failed at time of detensioning
6	I	None	Broke near bottom anchor	ORNL (Metals & Ceramics)	Failed at time of detensioning
7	O	None	Failed at top	ORNL (Metals & Ceramics)	Failed at 57,500 lb
8	I	CTR-3	Failed near center	ORNL (Metals & Ceramics)	Failed at 8400 lb
9	O	None	Wire pulled through top anchor (1/2-in. wire in anchor)	Left in concrete	Stopped at 60,000 lb, wire slipping in anchor
10	I	None		Left in concrete	Failed at time of detensioning
11	I	CTR-1		Left in concrete	Failed during test (see load cell data)
12	I	None	Broke near top anchor	ORNL (Metals & Ceramics)	Failed at 6200 lb
13	I	None		Left in concrete	Failed at time of detensioning
14	I	None		Left in concrete	Failed at time of detensioning
15	I	None		Left in concrete	Failed at time of detensioning
16	I	None		Left in concrete	Failed at 43,000 lb
17	I	None		Left in concrete	Failed at time of detensioning
18	I	None		Left in concrete	Failed at 23,000 lb
19	I	DTR-9	Failed near top anchor	ORNL	Failed at 60,000 lb
20	I	DTR-7		Left in concrete	No indication of failure
21	I	None	Failed near bottom anchor	ORNL	Failed at 57,000 lb (one wire shows cracks)
22	I	None		Left in concrete	Failed at time of detensioning
23	I	None		Left in concrete	Failed at 31,000 lb
24	I	None		Left in concrete	Failed at 29,000 lb
25	I	BTR-5		Left in concrete	Failed during test (see load cell data)
26	I	None		Left in concrete	Excessive yielding at 32,500 lb
27	I	None		Left in concrete	Failed at time of detensioning
28	I	None		Left in concrete	Excessive yielding at 33,000 lb

[a] I = inside row; O = outside row.

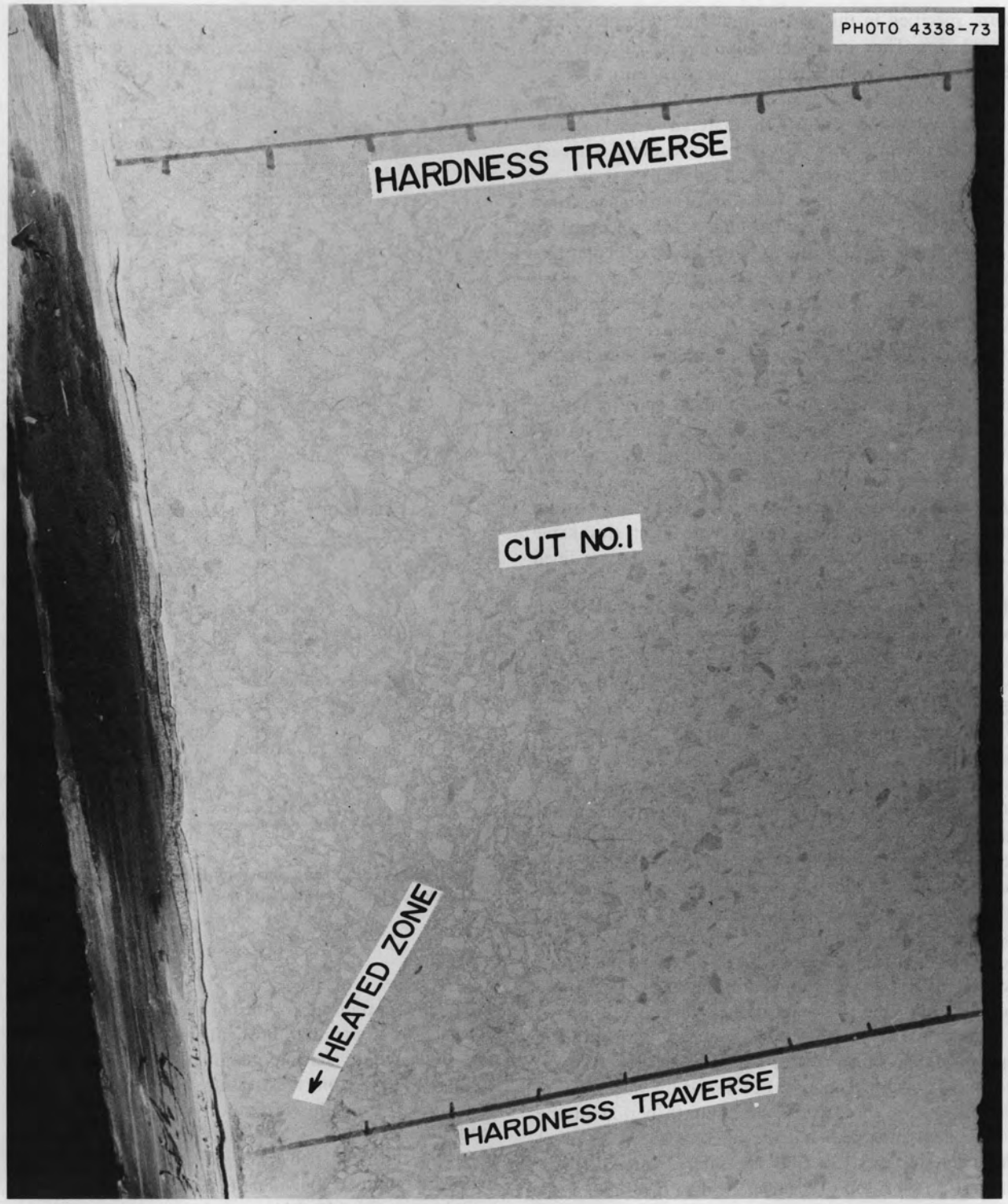

Fig. 8.37. Concrete rebound test traverse lines for concrete section of cut 1.

were specified in this case to minimize possible relaxation losses. They have a modulus of elasticity of 28 X 10^6 psi and a breaking strength of 250,000 psi.

The tendons were coated with a widely used commercial corrosion protection material when received from the manufacturer. A total of 12 tendons, 6 in each row, were instrumented with load cells at the top anchor and with foil-type electrical resistance strain gages on one wire of each strand. It was necessary to remove the original protective coating from an approximately 12-in. section of the instrumented wire to install the gage. These were the only tendons from which any of the original corrosion protection was removed. Once the strain gage application was completed, the tendon was waterproofed with a commercial wax using methods recommended by the Portland Cement Association.[7] The specific wax employed is generally recognized to provide effective corrosion protection. The tendons were housed in two-piece telescoping ducts in the manner shown in Fig. 8.38. The joint at the bottom anchor fitting was first sealed with heat shrinkable "flexite" tubing, and the lower duct section was filled with melted wax. The upper joint was then sealed with flexite tubing, and the upper duct section was filled with melted wax. The known volume of wax required to fill each tendon assembly was used to indicate whether it was completely filled. Also, when properly filled, the flexite tubing bulged slightly. Finally, the lower end of the bottom anchor fitting was sealed with melted wax.

The sealed tendon assemblies were positioned in the structure as shown in Fig. 8.1, and the bottom anchor plates were tack welded onto the bottom sheet metal seal. The assemblies were held in place at the top by a fixture, and a final epoxy seal was applied to the bottom anchor plates and lower tendon sleeves prior to casting. Upon completion of casting, the exposed concrete surface was sealed with an epoxy-copper layer. A final epoxy seal was applied to the top surface at the completion of the tendon posttensioning operation.

During the 15-month period simulating normal PCRV operation, the inner row of stressed axial tendons was subjected to approximately 125°F and the outer row to 100°F. During the subsequent 3-month period of the hot-spot test, the peak temperature was about 225°F at the inner row and 130°F at the outer. Figure 12.15 in the last progress report[1] shows the data for three of the axial tendon transducers during the period simulating normal vessel operation. In the figure transducer CTR-3 was indicated as having malfunctioned beginning at about 190 days from prestressing. Further examination of the data from this transducer in light of observed tendon failures has shown that the previously unexplainable shifts in load readings were apparently produced by failure of individual tendon wires. Figure 8.23 includes an unabridged history of the same transducer. Of the four transducers in this quadrant of the model for which load-time histories were obtained, CTR-3 was the only one exhibiting a substantial step change in loading prior to the hot-spot test. Although the data for

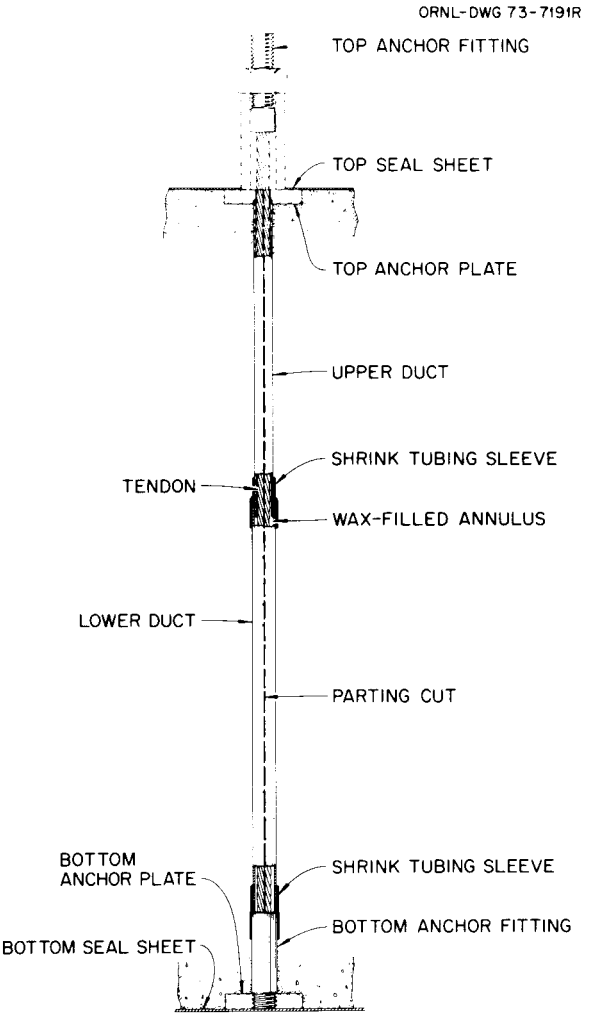

Fig. 8.38. Axial tendon assembly detail showing the parting cut employed in disassembly of ducts.

7. N. W. Hansen and O. A. Kurvits, "Instrumentation for Structural Testing," *J. PCA Res. Develop. Lab.* 7(2), 33 (May 1965).

CTR-3 indicate that some wires failed starting at 250 days, which was prior to the hot-spot experiment, the loss of tendon load appears to be generally associated with the period following the hot-spot test.

During the course of the experiment, noises were reported which appeared to have emanated from the model. During one of these incidents, an inspection was made of the circumferential prestressing system; however, no problem was discovered nor was the source of the noise identified. In retrospect, it could be concluded that the sounds were made by failing axial tendon wires.

During detensioning, which is described in Section 8.1.2, the outer row of tendons all required the full ram load of about 45,000 lb to unseat the restraining nut. In contrast, all but three of the inner row tendons indicated failure of some or all the wires in the strand by virtue of the low ram pressure required for detensioning.

Thus far, a total of 11 tendons, 10 from the inner row and 1 from the outer, have been removed from the thermal cylinder model. During a selective reloading of outer row tendon 6, the top anchor fitting shown schematically in Fig. 8.38 was pulled almost through the entire length of strand to which it was swaged without inducing wire failure.

Of the 10 inner row tendons thus far removed from the model, 7 failed near the bottom anchor, 1 failed near the middle of its length, and 2 failed near the top anchor. One of the tendons that failed near the bottom anchor is shown in Fig. 8.39; a closeup of the failed end is shown in Fig. 8.40. Figure 8.41 is a photomicrograph

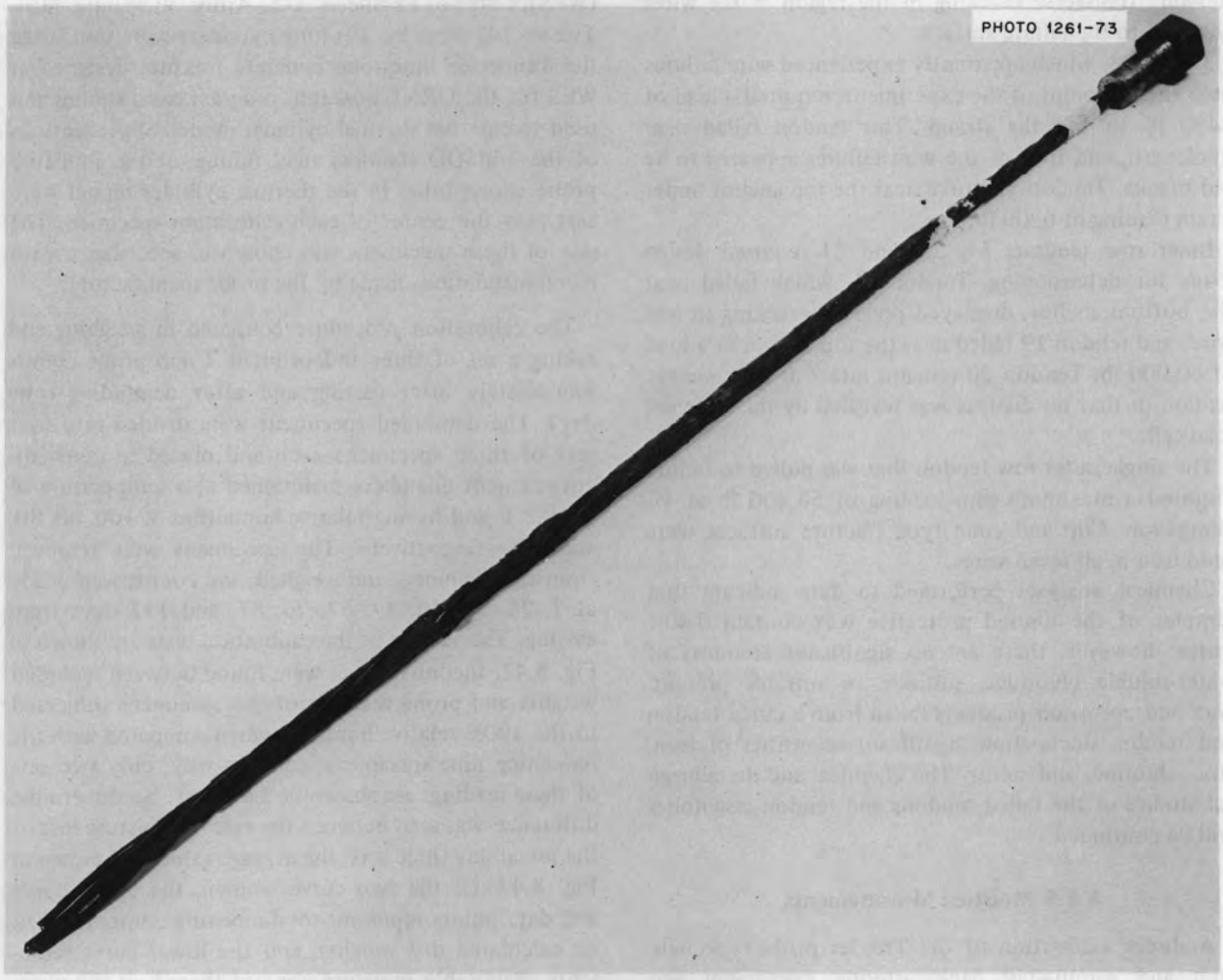

Fig. 8.39. Inner row tendon assembly exhibiting failure near bottom anchor.

Fig. 8.40. Closeup of failure surface of inner row tendon assembly.

showing transverse cracking in the region of the wires adjacent to the failure surface.

Tendon 8, which apparently experienced wire failures near the midpoint of the experiment, required a load of 8400 lb to fail the strand. This tendon failed near midlength, and four of the wire failures appeared to be old breaks. Tendon 12 broke near the top anchor under a ram loading of 6200 lb.

Inner row tendons 19, 20, and 21 required design loads for detensioning. Tendon 21, which failed near the bottom anchor, displayed previous cracking in one wire, and tendon 19 failed near the top anchor at a load of 60,000 lb. Tendon 20 remains intact in the concrete section in that no distress was revealed by the attached load cell.

The single outer row tendon that was pulled to failure required a maximum ram loading of 58,400 lb at 4% elongation. Cup and cone type fracture surfaces were produced in all seven wires.

Chemical analyses performed to date indicate that samples of the unused protective wax contain 0.40% sulfur; however, there are no significant amounts of water-soluble chlorides, sulfides, or nitrates present. Wax and corrosion products taken from a failed tendon and tendon ducts show significant quantities of iron, zinc, chlorine, and sulfur. The chemical and metallurgical studies of the failed tendons and tendon assemblies will be continued.

8.1.5 Moisture Measurements

A direct calibration of the Troxler probe-type neutron and gamma-ray backscattering instrument was conducted at the Waterways Experiment Station (WES), Corps of Engineers, U.S. Army, Vicksburg, Miss. Twelve 1-ft-diam by 1-ft-long cylinders were cast using the Tennessee limestone concrete mixture designed at WES for the ORNL concrete program basic studies and used to cast the thermal cylinder model. Short sections of the 1-in.-OD stainless steel tubing used as moisture probe access tubes in the thermal cylinder model were cast into the center of each calibration specimen. The size of these specimens was chosen in accordance with recommendations made by the probe manufacturer.

The calibration procedure consisted in weighing and taking a set of three independent 1-min probe counts immediately after casting and after demolding (one day). The demolded specimens were divided into four sets of three specimens each and placed in constant-environment chambers maintained at a temperature of 75 ± 2°F and having relative humidities of 100, 90, 80, and 70% respectively. The specimens were removed from the chambers and weighed, and counts were made at 7, 28, 35, 42, 49, 57, 76, 87, and 112 days from casting. The results of the calibration tests are shown in Fig. 8.42. Inconsistencies were found between recorded weights and probe readings of the specimens subjected to the 100% relative humidity when compared with the remaining nine specimens; consequently, only two sets of these readings are shown in the figure. No discernible difference was seen between the rate of moisture loss of the remaining three sets; the average values are shown in Fig. 8.42. Of the two curves shown, the upper curve and data points represent total moisture content (based on calculated dry weight), and the lower curve represents evaporable moisture content (based on the oven-dried specimen weights). The circled data points on

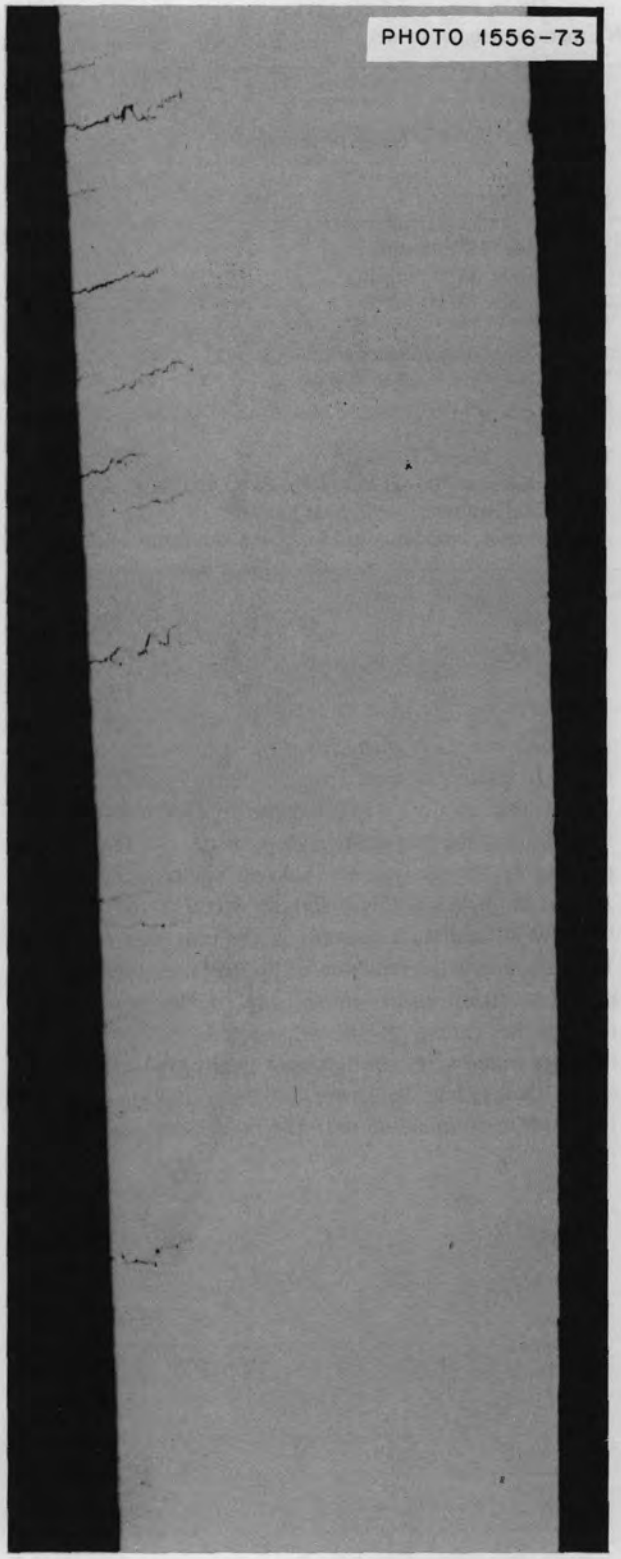

Fig. 8.41. Photomicrograph showing transverse cracking of axial tendon wire.

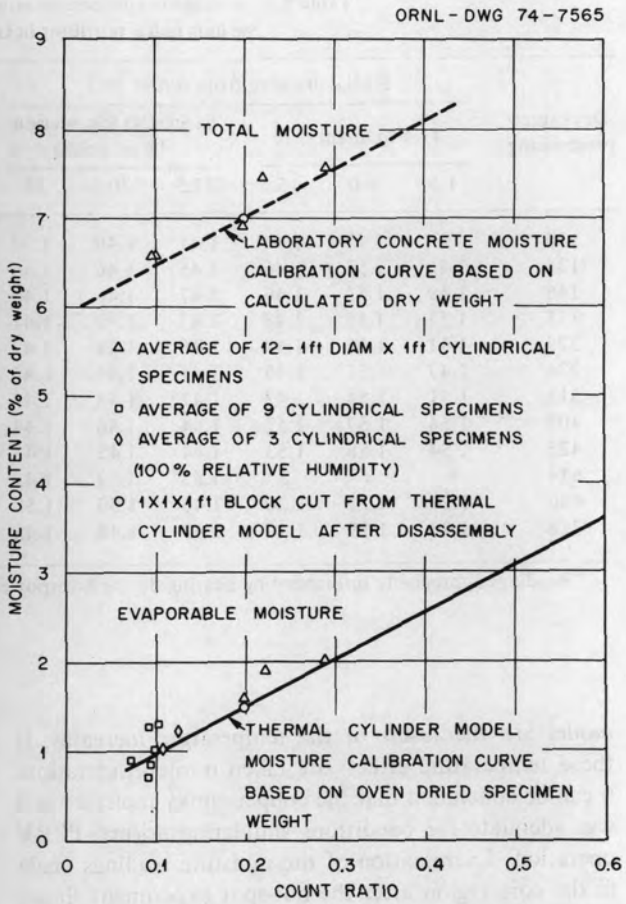

Fig. 8.42. Total and evaporable moisture content calibration curves for ORNL thermal cylinder concrete having 7.59% as-cast total moisture content.

both curves represent the moisture content measured using a 1 X 1 X 1 ft specimen.

This scaling factor was then used to reduce the thermal cylinder moisture probe data to the values shown in Table 8.5. Although it is difficult to make any meaningful comparison between the moisture contents of the model and the relatively small moisture calibration specimens, values can be used to provide an order of magnitude evaluation. At 28 days, the average moisture content of the specimens at 100% relative humidity was 1.89%, while the average of the specimens subjected to the three lower relative humidities was 1.30%. In comparison, the moisture content for the thermal cylinder model at 227 days (130 days after prestressing) was 1.42%.

Since the moisture probe was found to be slightly temperature sensitive, the slight increases in values coinciding with temperature changes applied to the

Table 8.5. Average evaporable moisture content (% of oven-dried weight) for various radial positions in ORNL thermal cylinder model

Days since prestressing	Radial distance from center (in.)						Status of test section
	41.5-in.-diam core			81-in.-OD test section (18 in. thick)			
	1.5	8.0	15.5	27.5	30.5	35	
130		1.47	1.44	1.41	1.40	1.37	75°F inside, 75°F outside
135	1.48	1.53	1.46	1.45	1.46	1.44	105°F inside, 75°F outside
146	1.49	1.53	1.46	1.47	1.46	1.45	150°F inside, 75°F outside
175	1.51	1.55	1.48	1.47	1.49	1.47	150–75°F
223	1.51	1.55	1.47	1.46	1.48	1.47	150–75°F, before pressurization
236	1.47	1.51	1.46	1.44	1.46	1.45	150–75°F, pressurized to 700 psi
318	1.51	1.54	1.47	1.47	1.48	1.47	Same as for 236 days
403	1.54	1.57	1.52	1.44	1.46	1.44	Same as for 236 days
425	1.54	1.58	1.53	1.44	1.45	1.43	150–75°F, pressure released
614	*a*	*a*	*a*	1.65[a]	1.52	1.48	Repressurized to 700 psi and subjected to 450° hot-spot heating
686	1.20	1.31	1.20	1.46	1.50	1.50	After cooldown to 150–75°F, at pressure
718	1.23	1.29	1.19	1.43	1.48	1.48	After complete cooldown to 75–75°F and pressure released

[a]Readings appreciably influenced by heating during hot-spot experiment.

model are the result of the temperature increases. If these temperature effects are taken into consideration, it can be concluded that the copper-epoxy moisture seal was adequate for conditions simulating normal PCRV operation. Examination of the moisture readings made in the core region after the hot-spot experiment shows that a small amount of moisture was lost during heating. This is a reasonable conclusion based on the measured temperature profiles, which show that a large portion of the core was subjected to temperatures of 175 to 200°F.

A similar examination of probe readings for the model test section indicates that the moisture content remained constant during or after the hot-spot experiment. It should be noted that a relatively small portion of this test section was subjected to elevated temperatures during the hot-spot heating; in fact, a fairly large portion of the section was cooled to temperatures of 100°F or lower, which should account for the differences of moisture content in the core and test ring. There is also little evidence of appreciable migration of moisture from inside to outside of the test section during the course of the experiment except for the readings made after the hot-spot heating which show a slight increase in moisture in the outer two probe positions in comparison with the innermost position.

9. HTGR Structural Materials Investigations

P. L. Rittenhouse

Many of the metallic components in the primary circuit of an HTGR are exposed to temperatures and environments of sufficient severity to result in time-dependent behavior (i.e., creep, corrosion, or long-term thermal stability may be the limiting factors in their use). The objectives of this program are to provide information to improve the bases for (1) determining the response of these materials to loading, (2) identifying the influence of environment on behavior, and (3) formulating structural design methods and failure criteria. The program was initiated and planning begun in the last two months of 1973.

9.1 MECHANICAL PROPERTIES OF HTGR STEAM-GENERATOR AND PRIMARY-CIRCUIT MATERIALS

C. R. Brinkman W. R. Martin P. L. Rittenhouse

The purpose of this work is to generate the elevated-temperature mechanical property data needed for validation of the structural design technology of the HTGR steam-generator and primary-circuit components. Creep behavior will be studied in stress-rupture and long-term creep tests conducted in helium atmospheres contaminated with H_2, H_2O, CO, CO_2, and CH_4 to levels consistent with those expected in the primary coolant. Fatigue, creep-fatigue interactions, stress relaxation, and crack-growth dynamics will also be investigated, and the effects of thermal aging on properties will be determined where appropriate. Materials currently scheduled to be studied – in approximate order of priority – are Incoloy 800, 2¼ Cr–1 Mo steel, Hastelloy X, 1010/1020 steel, Inconel 617, Hastelloy S, and high-alloy ferritic steels.

Work was initiated in December 1973 to study subcritical crack-growth rates in Incoloy 800 and 2¼ Cr–1 Mo steel in appropriate atmospheres at temperatures to 760°C (1400 °F).

9.2 WELDABILITY OF HTGR MATERIALS AND MECHANICAL PROPERTIES OF WELDMENTS

P. L. Rittenhouse G. M. Slaughter

This phase of the program will evaluate the weldability of HTGR primary-circuit materials. Weldments of Incoloy 800 to Incoloy 800 (with Inconel 82 and 182 filler metals) and Incoloy 800 to 2¼ Cr–1 Mo steel (with Inconel 82 filler metal) will receive emphasis early in the program. Later studies will be directed to the welding of 2¼ Cr–1 Mo steel to low-carbon steel and to the welding of the Hastelloy and Inconel 617. In all cases, the weldments (weld and heat-affected zones) will be evaluated by nondestructive examinations and through tensile and stress-rupture tests. Significant effort will be directed to this work beginning in mid-1974.

9.3 STRUCTURAL DESIGN METHODS FOR HTGR COMPONENTS

This segment of the program will develop design analysis methods for evaluation of the performance of HTGR primary-circuit components. Specifically, models will be formulated for predicting the behavior of materials under varying multiaxial loading and thermal conditions. Further, tests will be conducted to validate these models. This work will become active late in 1974.

9.4 CORROSION OF HTGR STEAM-GENERATOR MATERIALS

J. H. DeVan H. S. Isaacs P. L. Rittenhouse

One of the more critical components of the HTGR primary circuit is the steam generator, and, as in any steam supply system, the corrosion behavior of the steam-generator materials is of great importance. Plans are to evaluate the general, pitting, and stress corrosion of HTGR steam-generator materials through a series of steam-loop tests. Initially, Incoloy 800, 2¼ Cr–1 Mo steel, and appropriate weldments of these materials will be tested under superheat, evaporator, and alternating wet-dry steam conditions. Particular attention will be given to the performance of evaporator-section materials under conditions of boiling heat transfer. The reference water chemistry for the steam-corrosion tests will be typical of HTGR feedwater, but tests will also be conducted with additions of Cl^-, oxygen, and Na^+ to evaluate corrosion behavior under off-design conditions. Potential materials for future HTGR steam-generator application (e.g., ferritic steels with 9% and greater chromium and Inconel 617) will be examined as this program progresses.

During this report period plans were developed for the construction (through a subcontract with Southern Nuclear Engineering) of a high-temperature steam-corrosion loop at the Bartow steam plant in Florida. This loop is designed so that it will be possible to instrument the corrosion specimens. A maximum operating temperature capability of 621°C (1150°F) was selected to fulfill present and near-future requirements for the corrosion testing of HTGR steam-generator materials. This combination of high temperature and steam environment severely restricts the number of available applicable materials for construction of the loop. Inconel 617 was chosen because it (1) possesses the best balance of strength and thermal stability, (2) has equivalent or superior fabricability and weldability, and (3) is being considered for use in HTGR steam generators.

Since the Inconel 617 loop will not be available for operation until late 1974, initial corrosion tests of HTGR materials will be conducted in two existing loops operated by Southern Nuclear Engineering. One of these loops will be run under cyclic superheat–saturated steam conditions and the other with superheated steam. Fabrication of the constant-load pressurized-tube specimens to be employed in both of these loops is under way.

10. HTGR Fission Product Technology

H. J. de Nordwall

Fission product distribution studies enable HTGR designers to evaluate the cost of access to critical primary-circuit components during normal and accident conditions, to estimate the likely radiation doses from fission products released during normal operation, and to judge the consequences of fission product redistributions following accidents.

The guiding principle is that radiation exposure should be minimized to an extent determined by available technology, cost, and the likely benefits of nuclear power.[1] Quantitative definitions of this goal are still incomplete,[2] particularly with reference to the integrated dose that may be acquired during those rare maintenance operations that necessitate significant exposure of a larger than normal population of workers. Also, economic penalties associated with the presence of gamma emitters in the circuit have not been assessed. However, it would seem prudent to attempt to confine the maximum proportion of fission products to the core in order to simultaneously minimize potential demands on the outer fission product barriers of the plant such as the prestressed concrete reactor vessel (PCRV) liner and the secondary containment, economic and radiological impacts of the inventory of gamma emitters in the primary circuit, and the source term of the design-basis accident. At the same time, one would be maximizing inspectability and accessibility before and after accidents in which fission products may be distributed beyond the PCRV.

1. *The Safety of Nuclear Power Reactors (Light Water-Cooled) and Related Facilities*, WASH-1250 (July 1973).

2. R. H. Flowers, "Fission Product Control in the HTR," Paper 23 presented at the BNES International Conference on Nuclear Fuel Performance, London, Oct. 15–19, 1973 (proceedings to be published).

The current reference fuel is a Triso-Biso combination in which ~50% of the fissions occur in the less-retentive Biso fuel. We are currently concerned with determining the retentive ability of a low-temperature isotropic (LTI) Biso-coated ThO_2 fuel so that the cost-benefit equation can be more fully discussed.

Other work on fission product control is described in Chapter 13.

10.1 MATHEMATICAL ANALYSIS OF FISSION PRODUCT RELEASE FROM PYROCARBON-COATED FUEL PARTICLES

R. B. Evans III M. T. Morgan

The ultimate objective of this phase of the program is to devise a valid "source term" that will reflect the fission-product-release behavior of coated particles under reactor conditions. This requires consideration of various solutions of the heat equation, expressed in terms of selected mass transfer parameters, in order to select a suitable "diffusion model." If the model will describe release within a reactor, it should also describe release as it is measured under less complicated laboratory conditions. Our current approach has been to concentrate on release as it occurs under controlled laboratory conditions, with the realization that the results must be refined to include additional and more complicated factors associated with high-temperature irradiation.

Since a release-vs-time curve for a laboratory annealing experiment must eventually indicate depletion effects, our initial efforts concerned possible application of two integrated-rate equations that were characterized by a continuously decreasing driving potential.

One set of equations was expressed in spherical coordinates and the other in slab geometry. It was found that the results for a slab geometry, properly adjusted, gave amazingly good approximations to the results for a spherical geometry. This was gratifying because the simpler slab geometry results can be used for initial estimation of parameters. The major contribution of spherical coordinates is additional complexity. Comparisons of decreasing-potential equations with experimental data revealed no instance (to date) where decreases in driving forces started at the beginning of the experiment. In fact, it appeared that in most cases the driving force remained constant for a while before depletion effects took control. A third set of equations, to cover delayed depletion, were therefore derived, and the results appear promising. Consideration was also given to possible effects of external film resistances when constant-potential conditions prevailed. The sacrificial layers of pyrocarbon added to certain coatings function as high-resistivity films with some additional capacity.

Although only a limited amount of data was available for analyses, consideration of the equations demonstrated that internal parameters, such as long-term trapping of cesium in the kernel, driving forces, and partition coefficients, would govern the overall release behavior. The need for longer term experiments was established, and the mathematical exercises give considerable insight as to what we seek and how such long-term data might be handled. The experimental results obtained and the status of prediction of cesium release from fissioning fuel are discussed in the following sections.

10.2 POSTIRRADIATION MEASUREMENTS OF CESIUM RELEASE

M. T. Morgan R. B. Evans III
R. L. Towns L. L. Fairchild

Experimental work has concentrated on the behavior of cesium, because, of the metallic fission products cesium, strontium, and barium, cesium probably has the shortest residence time in the structural graphite surrounding the fuel. Cesium retention by the core is thus likely to be determined to a greater extent by the properties and temperature of fuel particles.

A distinguishing feature of our experimental technique for studying cesium release is the time required to perform the experiment at realistic temperatures. This, coupled with a desire for direct verification of the role of various parameters and components, prompted design of a special set of experiments with separated particle components as described below.

Several particles from a long-term annealing experiment were cracked, the components separated, and total cesium contents measured. A series of extended anneals with the separated components revealed that essentially all the cesium in the coating and buffer materials was released in a short time, while an appreciable fraction in the kernel could not be driven off. This ultimate retention value could never have been determined in the usual fashion. Since total cesium contents of the buffer and outer coating were obtained after an extended release-rate experiment, attempts were made to combine information from these related, but distinctly different, measurements. The combination was interesting, but it was clear that a complete appraisal would require cesium concentration profiles associated with both sets of information.

Such a combination with concentration profiles will provide verification of boundary conditions as well as the determination of the partition coefficient and the cesium solubility in the coating. Current plans are to obtain initial boundary conditions from the concentration profiles. Anneals of coated particle components suggest that a short (6-hr) anneal at 1250°C of as-irradiated coated particles will bring the source region to equilibrium.

A method of stripping small increments from the outer coating by grinding has been developed to obtain concentration profiles. Single particles are placed under a small copper piston that is constrained by a spinning steel cylinder. This array is swept back and forth across a rotating abrasive surface comprised of kerosene-wet emery paper (600 Å) cemented to a flat disk. The cylinder and abrasive surface are driven by separate motors. Unirradiated particles have been ground up to, and through, the outer coating/buffer layer interface, and sphericity has been maintained up to, but not beyond, this interface. However, it is sometimes possible to regain sphericity as the kernel/buffer interface is approached.

Another major part of our effort for the year was to assemble the data from previous experiments for review and publication; most of this task was completed.

None of the fuels annealed after irradiation at low temperatures released all their original cesium. Between 30 and 96% of the cesium was apparently being retained in sites from which release was either impossible or very slow, since these experiments lasted several thousand hours. This limiting release phenomenon is illustrated in Fig. 10.1, where the release-vs-time curve

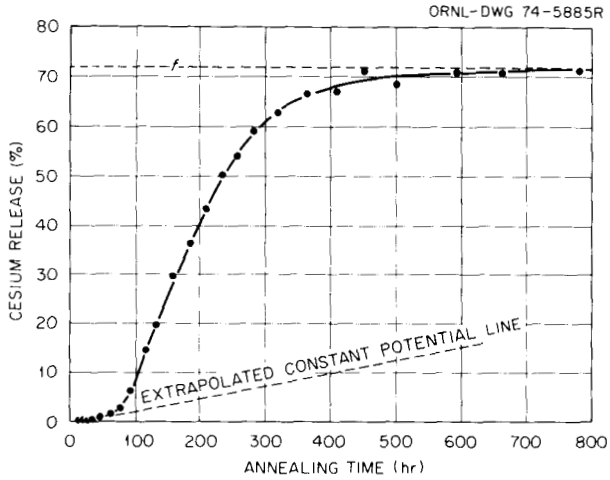

Fig. 10.1. Cesium release vs time for LTI Biso-coated ThO_2 particles irradiated to 3.5% FIMA and annealed at 1600°C.

approaches an asymptotic value indicating 73% release. No obvious correlation between $1 - f$, the fraction trapped, and the previous history of the particle or the annealing temperature has become apparent to date.

Figure 10.1 also illustrates a second feature of cesium release vs time that leads to uncertainty in generalizing our conclusions. Although the early part of the curve follows the form expected for a release driven by a constant cesium potential, which is a feature of all release curves measured to date, the rate of cesium release after the cesium has broken through the coating is very much greater than that predicted. This rapid rise in release could have been caused by a sudden release of some of the trapped cesium or a change in coating structure. Coating failure in the normal sense can be eliminated since krypton was retained.

Figure 10.2 is a more typical graph of cesium release vs dimensionless time Dt/ℓ^2, where D is the diffusion

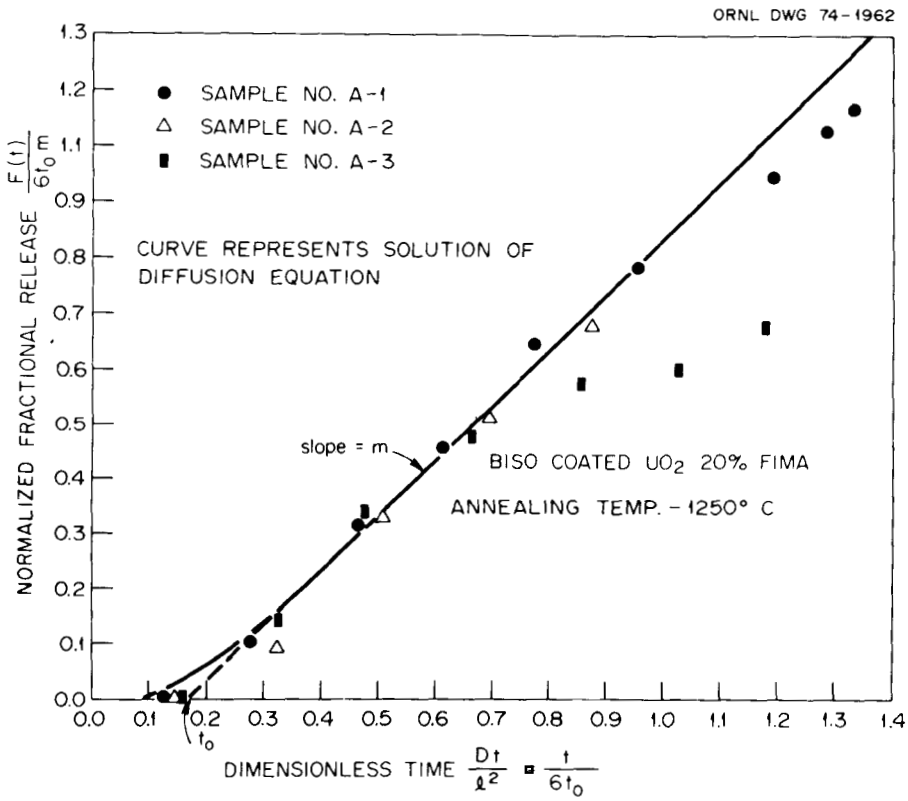

Fig. 10.2. Fractional release of cesium from Biso-coated UO_2 particles previously irradiated below 800°C to 20% FIMA. (Note the reproducibility of behavior in the early constant-potential region and later onset of depletion.)

coefficient of cesium in the coating and ℓ is the coating thickness. This release follows a constant-potential line for some time and then drops off as a result of depletion of the kernel. Mathematical description of this curve requires identification of the point at which depletion of the source region begins and the partition coefficient of cesium between the kernel and the coating when the cesium potential is not constant. Appropriately normalized release curves have been found to be quite reproducible in the constant-potential region.

The release of cesium from particles coated with high-temperature isotropic (HTI) pyrocarbon was substantially below that of low-temperature isotropic (LTI) pyrocarbon-coated fuels above 1250°C.

10.3 STATUS OF ESTIMATION OF CESIUM RELEASE FROM BISO-COATED FUELS DURING IRRADIATION

H. J. de Nordwall R. B. Evans III M. T. Morgan

It is clearly premature to argue that the ThO_2 kernel will play an important part in controlling cesium release from a Biso-coated ThO_2 fuel, since there is no published evidence to support the proposition that trapping will be maintained during high-temperature irradiation. Solid-state phenomena such as trapping are known to be sensitive to irradiation.

Second, we cannot yet define a conservative trapping fraction that would be significantly useful (i.e., greater than zero).

Therefore, one is forced to estimate cesium release using a model in which only the coating controls release. Combination of the complementary results obtained by Burnette[3] and the authors yields the following equation for D_{Cs} in LTI pyrocarbon:

$$D(\mathrm{Cs})_A = 0.538e^{-78{,}000/RT}\ \mathrm{cm}^2/\mathrm{sec}\ . \qquad (10.1)$$

The equation of the upper 95% confidence limit for this generic data collection is

$$D(\mathrm{Cs})_B = 5.38e^{-78{,}000/RT}\ \mathrm{cm}^2/\mathrm{sec}\ . \qquad (10.2)$$

Figure 10.3 shows the results of conservative estimates of cesium release from a Biso-coated fuel irradiated for one fuel cycle (3.2 years) at constant power and temperature. Releases were calculated using our best estimates of D_{Cs} in pyrocarbon [curve A, Eq. (10.1)] and upper-bound values [curve B, Eq. (10.2)].

Ratios of the release to total production R were computed in slab geometry using a corrected solution to the diffusion equation given by Jaeger and Clarke[4] in terms of the dimensionless variables $T = Dt/(b-a)^2$ and $L = 3(b-a)b/a^2\phi$:

$$R = 1 - \left(\frac{L+2}{2L}\right)\left[\frac{f_4\,(L,\,T)}{T}\right]\ ,$$

where f_4 is a tabulated function of L and T. The result for spherical geometry differs by <10% for $0.01 < R < 1$. The reference particle had the following geometrical characteristics: kernel diameter, 500 μm; buffer thickness, 85 μm; and pyrocarbon-coating thickness $(b-a)$, 75 μm. Since only the coating was controlling release, the source was represented as a well-stirred fluid of thickness a (335 μm) in which long-lived cesium was being generated at a constant rate. The partition coefficient (ϕ) for cesium between source and coating was taken as unity. A zero concentration was maintained at the outer boundary.

The nominal expected fuel temperature distribution is included in Fig. 10.3 for reference.[5] Using curve A, the release of cesium is expected to exceed 50% for fuel above 1210°C; using curve B lowers this temperature to 1090°C. The percentages of Biso-coated fuel above these temperatures under design conditions are 1.7 and 4.5% respectively. The average ^{137}Cs inventories[6] associated with these quantities of fuel are ~70,000 and ~190,000 Ci. The retention of cesium by the structural graphite surrounding this relatively hot fuel is expected to be significant, but calculational methods remain unproved.

Retention of cesium by the kernel could lower curves A and B in Fig. 10.3 by from 3 to 25 times based on our out-of-reactor observations. In addition, one must consider that real fuel particles do not spend 3.2 years at constant temperature. The beneficial effect of a reduction in the time spent at a given temperature may

3. R. D. Burnette, W. E. Bell, and N. L. Baldwin, "Fission Product Retention Characteristics of HTGR Fuel," *Proc. Brit. Nucl. Energy Soc. Conf. on Nuclear Fuel Performance, London, October 1973.*

4. J. C. Jaeger and M. Clarke, "Numerical Results for Some Problems on Conduction of Heat in Slabs with Various Surface Conditions," *Phil. Mag.* **38**, 504 (1947).

5. Delmarva Power & Light Co., Summit Power Station, *Preliminary Safety Analysis Report*, Chap. 4, Fig. 4.4.2-1, Docket 50-450 (1973).

6. Ibid., Chap. 11, Table 11.1.1-2.

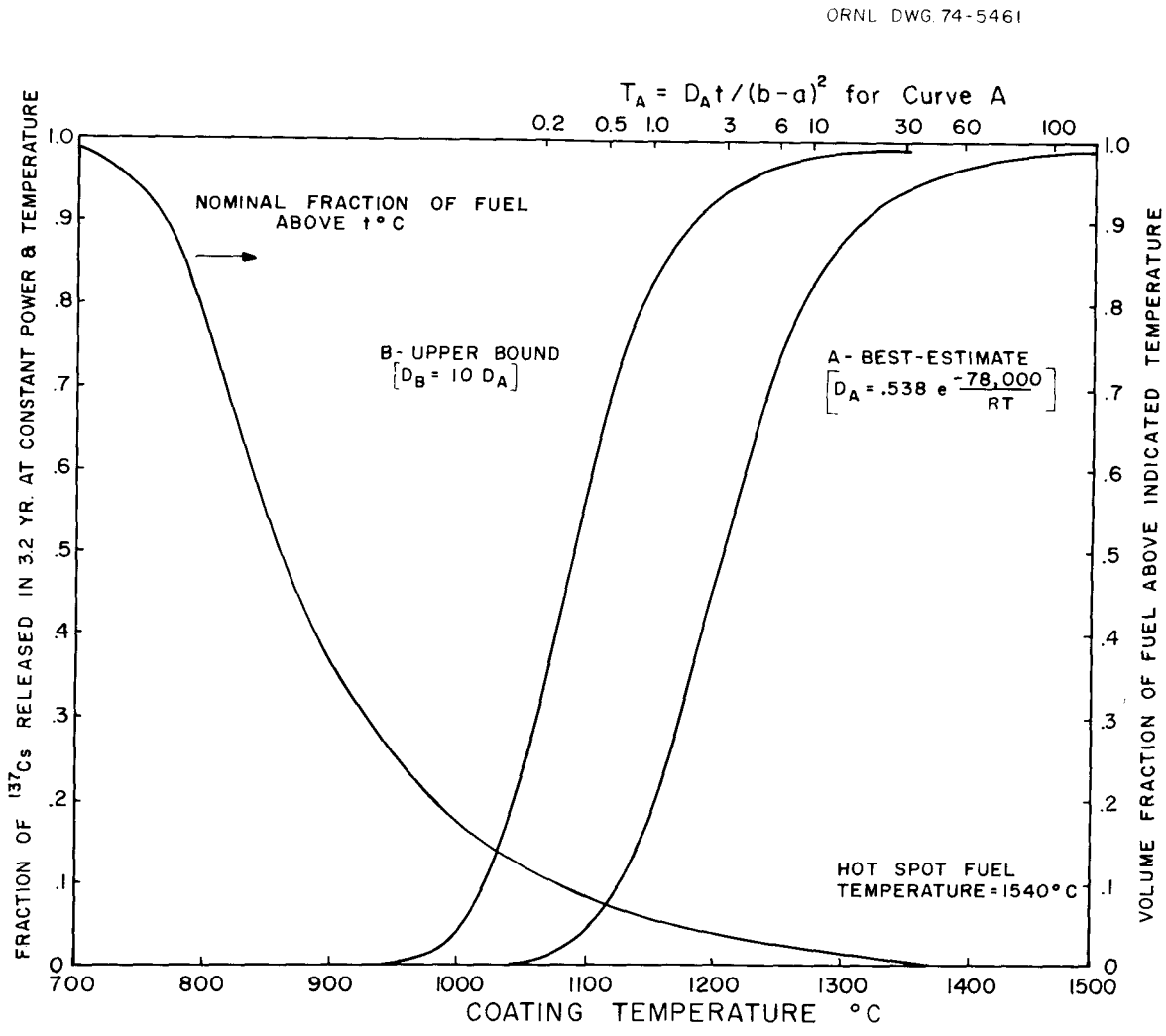

Fig. 10.3. Estimated fraction of ^{137}Cs released from a pyrocarbon-coated fuel particle operating at constant power and temperature for 3.2 years without resistance or trapping in the kernel.

be visualized using the values of Dt/a^2 at the top of Fig. 10.3. Second, constant-potential conditions that would prevent further increases in the cesium driving force with time may occur. Substitution of diffusion data for production coatings can be expected to reduce some of the gap between curves *A* and *B*. However, not enough data are presently available to determine whether Biso-coated ThO_2 fuel can control cesium release well enough to meet potential requirements for primary-circuit access.

The goals of current research and development are to determine the significance of the role of the $(Th,U)O_2$ kernel in cesium retention, to improve whole core release estimates, and to define realistic goals for the control of cesium release from the core. Other parts of the program are engaged in reducing thermal resistances in block-type elements which could lead to lower fuel temperatures.

11. HTGR Fuel Chemistry

H. J. de Nordwall

This task is devoted to the understanding, quantifying, and, where appropriate, developing techniques to mitigate the chemical effects that could limit the performance of HTGR fuel particles. The work year has dealt mainly with theoretical and experimental analyses of mass transport effects, such as kernel migration, in HTGR oxide fuels. These analyses were advanced significantly by the availability of experimental measurements of kernel migration from the fuels irradiation program described in Section 7.4. In-reactor experiments with carbide- or nitride-containing UO_2 particles were initiated to evaluate the possible mitigation of kernel migration by these means. A program for the measurement of gas pressure and oxygen potential in irradiated fuel particles was developed, and the experimental apparatus was constructed and tested. Literature surveys were performed to delineate potential chemical means for improving the retention of cesium, barium, and strontium by oxide kernels.

11.1 MASS TRANSPORT IN FUEL PARTICLES IN A TEMPERATURE GRADIENT

T. B. Lindemer

The phenomenon of fuel kernel migration in a thermal gradient is widely observed in the oxide and carbide fuel particles used in HTGRs. The rate of migration is generally observed to be sufficient to establish operational limits on the time–temperature–power-density relationships that can be specified in the design of an HTGR core. It has been difficult to establish the rate-controlling mechanism of migration and hence to propose reliable means of mitigation. During 1973, methods that can be used to establish experimentally the rate-controlling mechanism were developed and applied to the analysis of in-reactor kernel migration observed in coated particles of UO_2, $Th_{1-z}U_zO_2$, and ThO_2.

Three classes of migration mechanism were considered: gas-solid reactions, the widely proposed CO-CO_2 gaseous diffusion, and solid-state diffusion across the fuel kernel.[1] Expressions for their rates of migration were developed. All rate expressions had the Arrhenius form, but with temperature-dependent preexponential terms. All suffered from a practical insufficiency; that is, the values of many of the constants had not been measured. However, estimates of the rate of carbon transfer by CO-CO_2 diffusion in fission gas and by a reaction-controlled mechanism were made. Breachings of the carbon coatings were predicted at times that were orders of magnitude less than those observed experimentally.

Further theoretical analyses led to a general experimental method for establishing the rate-controlling mechanism. The ratio of the predicted kernel migration in a particle located at any radius in a fuel rod cross section to that at a reference position, conveniently the midradius, contains only the activation energy and the calculable temperature and temperature gradient; the preexponential constants cancel. The shape of a plot of this ratio vs radius turns out to be characteristic of a given mechanism and relatively insensitive to the activation energy. The plot may therefore be used to distinguish different mechanisms if sufficiently precise data are available.

---

1. T. B. Lindemer and H. J. de Nordwall, *An Analysis of Chemical Failure of Coated UO_2 and Other Oxide Fuels in the High-Temperature Gas-Cooled Reactor*, ORNL-4926 (January 1974).

The first set of in-reactor experimental kernel migration data for carbide and oxide fuel particles of the U.S. design became available in 1973;[2] these metallographically derived data were analyzed by the techniques described above.[3] The analyses for the carbide fuel rods, in which the carbide migration is known to be controlled by solid-state diffusion,[4,5] demonstrated that the ratio technique for analysis of kernel migration indeed yielded the theoretically predicted behavior. The subsequent analysis of the UO_2, $Th_{1-z}U_zO_2$, or ThO_2 oxide kernel migration established that the migration rate was definitely not controlled by the rate of $CO\text{-}CO_2$ diffusion as long as the pressure of carbon monoxide was not buffered by some specific chemical equilibrium. Furthermore, the data indicated that a solid-state diffusion mechanism was most likely controlling the kernel migration rate.

A solid-state "kernel migration coefficient" (KMC) was calculated for each particle in the several irradiation experiments. The KMC is defined as $(\Delta y/\Delta t)(T^2)(dT/dx)^{-1}$, in which Δy is the observed migration in time Δt. These coefficients, obtained from 900 to 2000°C, are shown in Figs. 11.1 to 11.3. The order of stability was $UO_2 < Th_{1-z}U_zO_2 < ThO_2$, with the KMC for ThO_2 being about the same as that published[3] for unirradiated ThC_2. The KMC for ThO_2 did not exhibit any burnup dependence in the burnup range 0.3 to 14% FIMA (fissions per initial heavy metal atom). Considerable additional in-reactor fuel testing is under way to improve the statistics of these correlations and to prove their applicability at irradiation times beyond the present range of 30 to 274 days.

Out-of-reactor studies of mass transport in unirradiated coated particles placed in a temperature gradient have just begun.

Another area of interest is the use of second-phase additions to oxide kernels to reduce the rate of kernel migration, particularly in UO_2. The basic, though unsubstantiated, working premise has been that lowering of the oxygen chemical potential (P_{CO}) within the oxide particles by chemical buffering will lead to lower carbon transfer rates. (It should be pointed out that this action may be in conflict with the requirements for retention of the fission products, which also varies with oxygen potential; there a higher P_{CO} is desirable.) Buffering additives such as CeO_2 or SiC have been proposed in the literature, while we have in-reactor tests (HRB-7 and HRB-8) of coated particles containing UO_2 and second-phase UC_2 or U_2N_3. Such testing is a basic requirement of these investigations because it is presently not possible to predict the chemical behavior of 75% FIMA oxide fuel, that is, fuel with a fission product to uranium ratio of 6 at the end of life.

11.2 GAS PRESSURE MEASUREMENTS IN COATED PARTICLES

T. B. Lindemer

An experimental program has been initiated to measure the oxygen release (as carbon monoxide) from irradiated oxide-coated particles as a function of fission density and temperature. The measurements will be unique for oxide fuels of the U.S. design and will provide a direct means for establishing the overall chemical behavior of the oxide-forming fission products. Such information is needed both for the theoretical analysis of mass transport and fission product in oxide fuels and for the hydraulic design of the particle coating. The release of krypton and xenon will also be measured.

An apparatus to measure the number of moles of carbon monoxide and krypton plus xenon released on crushing a hot irradiated coated particle has been built and tested. The corresponding particle internal pressure is determined using an estimate of the total accessible volume in the kernel and buffer regions made from particle dimensions.

A diagram of the apparatus is shown in Fig. 11.4. The various chambers were built from standard high-vacuum parts. A measurement is made by heating the particle in vacuo to the desired temperature, which may range up to 2000°C, allowing it to degas, and then simultaneously crushing and cooling it rapidly to a temperature at which no further reaction between oxides and carbon can take place. The heat from the small particle and the light graphite heater is dissipated by radiation or absorbed by the cool anvil and the crusher. The total quantity of released gas, now held in a 385-cm^3 calibrated volume, is determined by measuring the pressure with a sensitive capacitance manometer. Reactive gases are then removed using a titanium filament at

---

2. R. A. Olstad et al., *An Irradiation of Candidate HTGR Fuels in the H-1 and H-2 Capsules*, ORNL-TM-4397 (to be issued).

3. T. B. Lindemer and R. A. Olstad, *HTGR Fuel Kernel Migration Data for the Th-U-C-O System as of April 1, 1974*, ORNL-TM-4493 (to be issued).

4. T. D. Gulden, "Carbon Thermal Diffusion in the UC_2-C System," *J. Amer. Ceram. Soc.* **55**, 14–18 (1972).

5. C. B. Scott and O. M. Stansfield, *Stability of Irradiated Coated-Particle Fuels in a Temperature Gradient*, Gulf-GA-A12081 (1972).

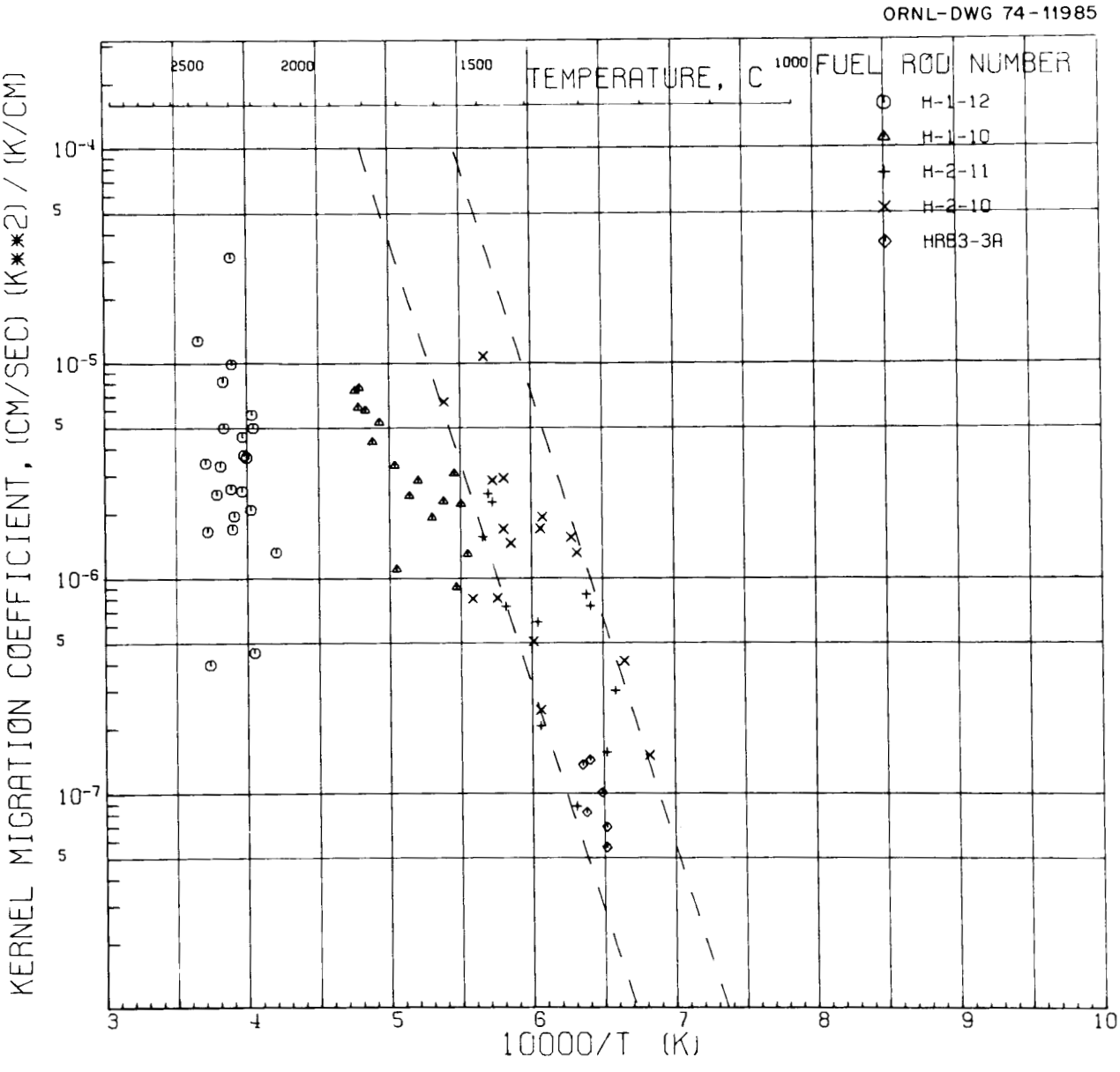

Fig. 11.1. In-reactor kernel migration coefficients for Biso-coated ThO_2 irradiated in the HFIR and ETR facilities. Also shown for comparison are the 95% confidence limits for out-of-reactor migration of unirradiated ThC_2 (Ref. 5).

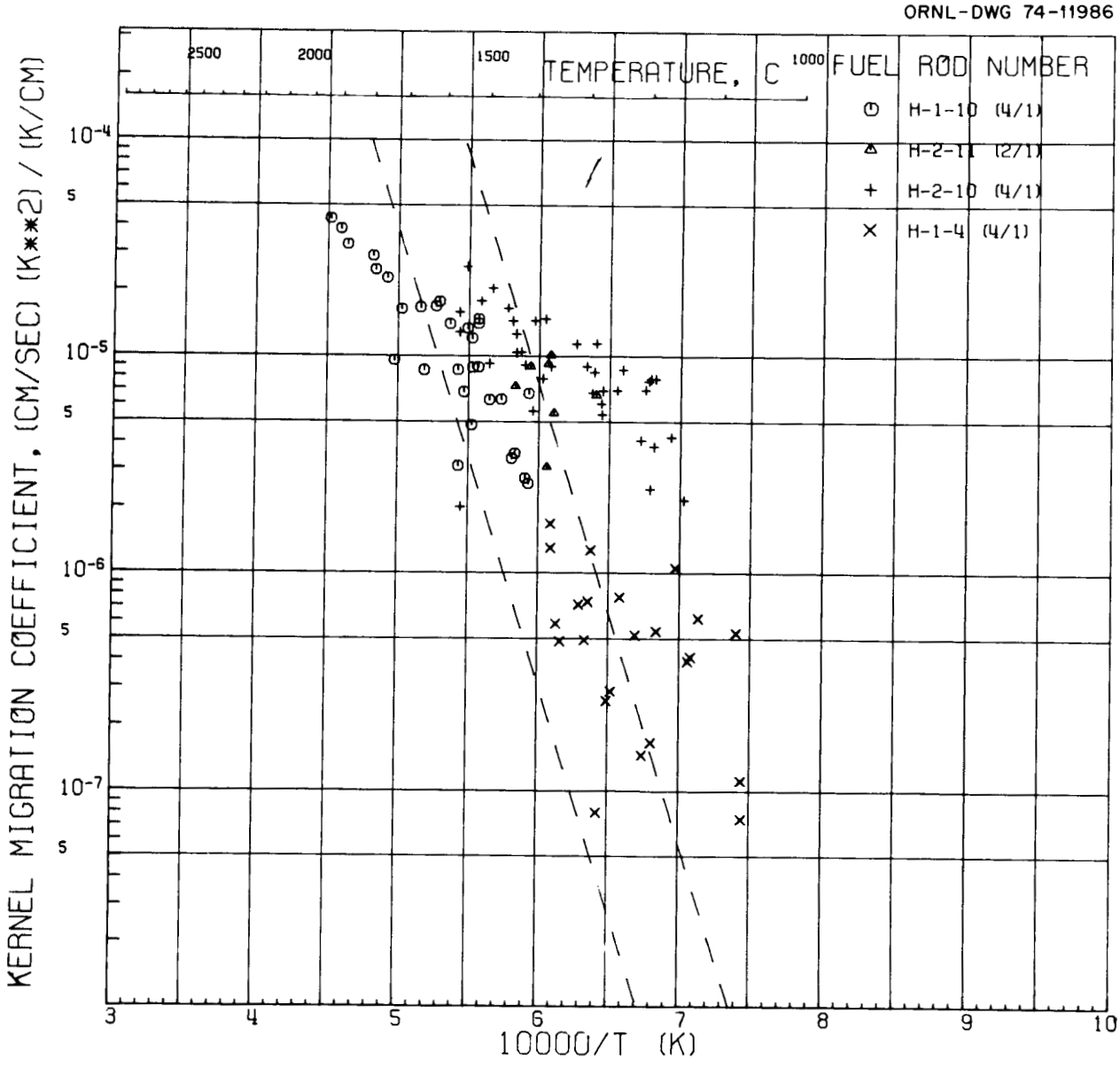

Fig. 11.2. In-reactor kernel migration coefficients for Biso-coated $Th_{1-z}U_zO_2$ irradiated in the ETR facility. The specific Th/U ratios are given in the legend with each fuel rod number. Also shown for comparison are the 95% confidence limits for out-of-reactor migration of unirradiated ThC_2 (Ref. 5).

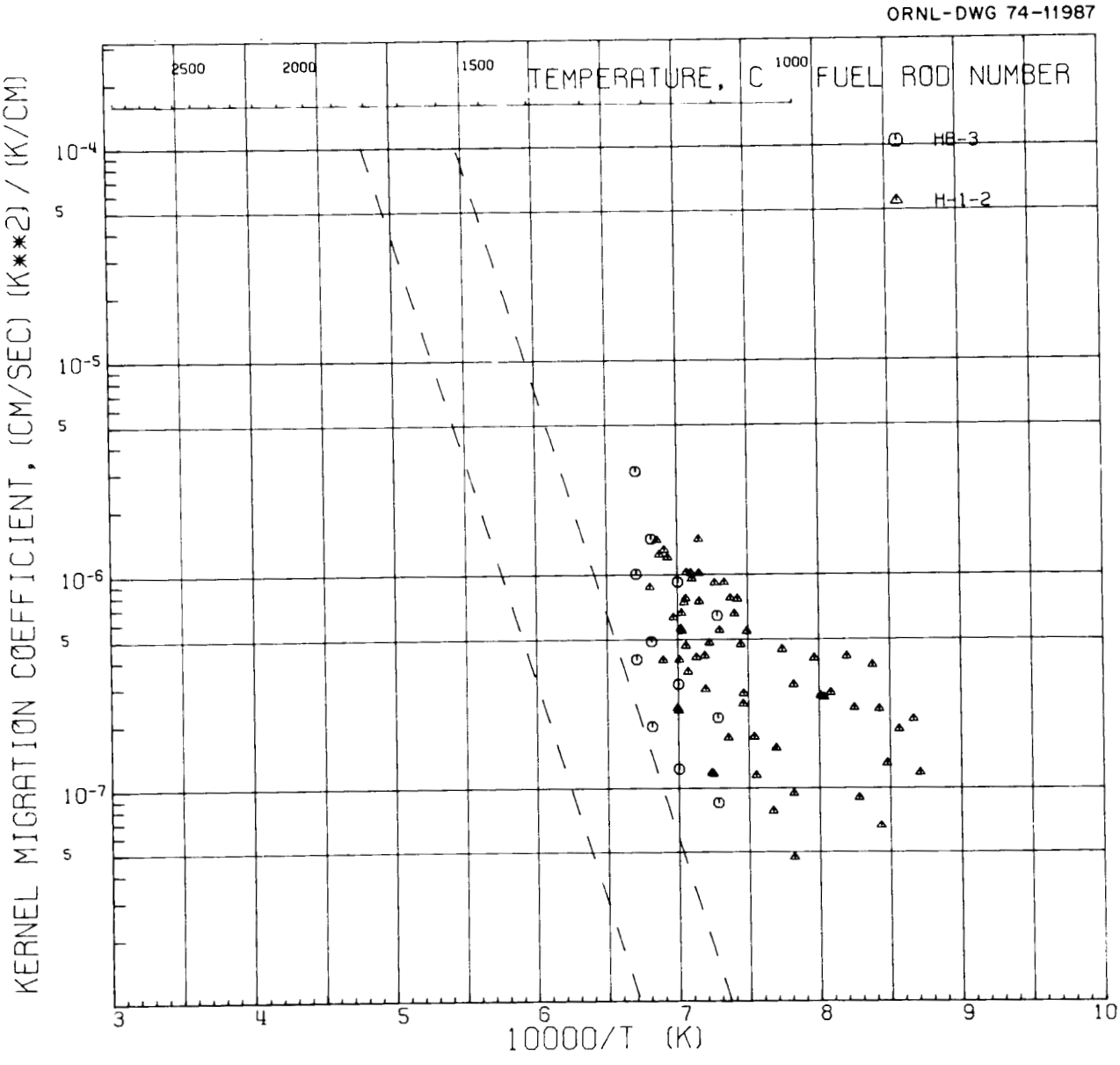

Fig. 11.3. In-reactor kernel migration coefficients for Biso-coated UO_2 irradiated in the ORR and ETR facilities. Also shown for comparison are the 95% confidence limits for out-of-reactor migration of ThC_2 (Ref. 5).

ORNL DWG 73-12780

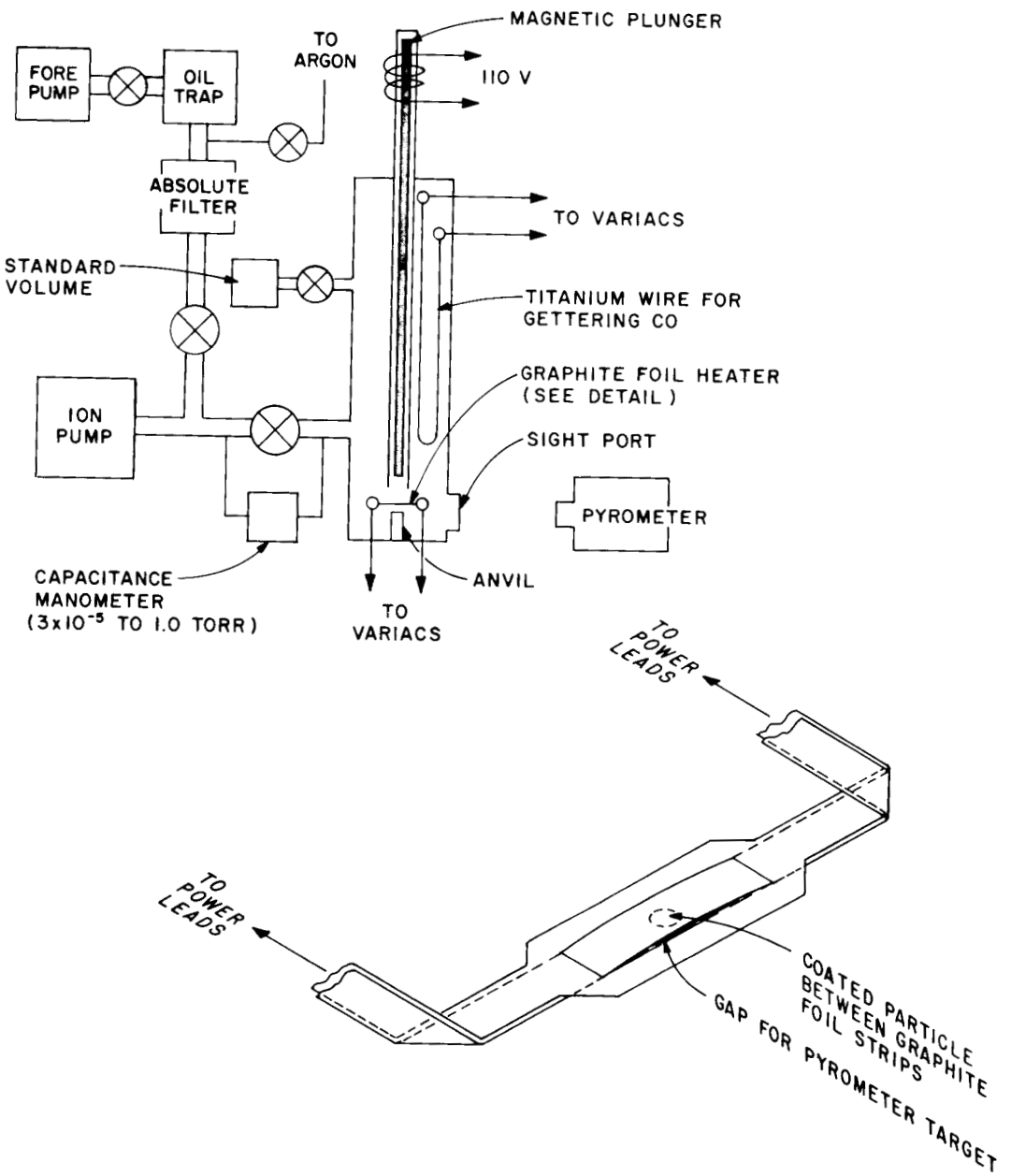

Fig. 11.4. Apparatus for measuring the gas content of coated fuel particles at high temperatures.

~1000°C as a getter, leaving krypton and xenon. The krypton and xenon are determined by a second pressure measurement. The number of fissions that have occurred in the particle, which is required to normalize gas release measurements, is measured by gamma spectroscopy.

Extensive testing has demonstrated that degassing can be adequately controlled, the separation of reactive gases from krypton and xenon is complete, cooling is rapid enough to prevent CO production after crushing, and the number of moles of gas in the system can be measured to ±5% accuracy.

11.3 CHEMICAL COMPATIBILITY OF FUEL AND FISSION PRODUCTS WITH COATINGS

T. B. Lindemer M. T. Morgan

Literature reviews have been performed to ascertain whether coating-kernel interaction can be reduced by chemical modification aimed toward confining reactive fission products within the kernel.

A complete survey of known phase equilibrium data indicated that additions of Al_2O_3 and/or possibly SiO_2 might combine effectively with cesium, strontium, and barium. Concurrent experimental work by German researchers indicated that these additions were indeed effective at reactor temperatures.[6] Large reductions in fission product release were also reported.

---

6. R. Förthmann et al., "Development of Coated Fuel Particles for Increased Safety Requirements," Paper IAEA SM-169/40 presented at the IAEA Symposium on Principles and Standards of Reactor Safety, February 1973. See also Report GERHTR-72.

Part III. HTGR Safety Program

12. HTGR Systems and Safety Analysis

J. R. Engel A. M. Perry

The systems and safety analysis task is the central, integrating task of the HTGR safety program, gathering and utilizing the information from other task areas in a combined analysis of postulated HTGR accidents and safety-related issues. During 1973, the principal activity in this program was the preparation of an overall HTGR Safety Program Plan. Work was also carried forward on a formal approach for the description, cataloging, and analysis of accident sequences. No quantitative overall accident analyses were undertaken during the year, but a method was implemented for calculation of fission product transport in HTGR cores, and fission product inventories in the Peach Bottom Reactor were calculated for comparison with measured values in discharged fuel.

12.1 NATIONAL HTGR SAFETY PROGRAM PLAN

J. R. Engel

A major activity for the HTGR safety program during 1973 was the preparation of a National HTGR Safety Program Plan. The plan was originally intended to include research, development, and analysis in all phases of HTGR technology that relate to the evaluation of HTGR safety. A program was laid out covering the ten-year period FY-1974 through FY-1983, a period expected to see the introduction of the first several commercial HTGRs. Planned levels of effort were heavily concentrated during the first part of the period, with more than 80% of the effort scheduled for completion by 1979. The plan was prepared by ORNL, with substantial assistance from the General Atomic Company (GAC), along lines approved by AEC's Division of Reactor Research and Development.

A preliminary draft of the plan was completed in July 1973 and submitted to AEC for review and comment. Following this review, an extensive revision and expansion of the document was undertaken, and a new draft was presented to the Commission in December.

The plan was organized into seven principal areas: (1) HTGR systems and safety analysis, (2) fission product technology, (3) primary-coolant technology, (4) seismic and vibration technology, (5) confinement components (reactor vessel and containment structures), (6) primary-system materials technology, and (7) safety instrumentation. These areas included an extensive program for surveillance of operating reactors (Peach Bottom and Fort St. Vrain) and postoperational observations of core and components. In each area, the current status of technology was reviewed and a detailed list of tasks developed, the successful completion of which would facilitate the analysis of postulated accident sequences and improve the evaluation of safety margins.

It has subsequently been determined that most of the research and development activities identified in the plan belong properly in the HTGR base program. In order to make generally available the detailed review of technology contained in the plan, while significantly

redefining the scope of the safety program itself, it was decided to divide the plan into two parts, to be published as a Planning Guide for HTGR Safety and Safety-Related Research and Development.[1] The guide was to be published in the first half of CY-1974.

12.2 SYSTEMS AND SAFETY ANALYSES

P. Rubel

A plan for organizing HTGR systems and safety analyses was described previously.[2] Briefly, it amounts to describing potential accident progressions by means of complementary models of event sequence logic, of reactor and plant transient behavior, of component damage mechanisms, and of fission product release and transport processes. Such analyses are subject to occasional revision and refinement so that they can represent the best available information from the various supporting technologies.

During 1973, additional work was done toward developing procedures and formats for describing accident sequences. Following the method of Nielsen,[3] the primary (coarse-structured) accident event logic is to be expressed in a few main decision trees, each of which proceeds from a major plant contingency condition toward various possible outcomes. As now envisioned, the initial contingencies will correspond to the categories of potentially serious accidents identified in safety discussions in the plant licensing documents;[4] each of these categories actually represents a class of events that may vary widely in degree and circumstance. A typical category is "water ingress," which could range from barely detectable to quantities causing prestressed concrete reactor vessel pressure-relief actuation. The advent of each initial contingency is to be traced to the originating causes by fault tree analyses.

Since each primary decision tree in this scheme is really a composite of a number of trees (i.e., one for each significant variant of the initial contingency), rigorous tree-logic expansions in detail would not only become very complex but would also introduce logic anomalies. The complexity would be greatly increased in any attempt to express conjecture, which is considered necessary in early tentative logic models. Accordingly, in order to achieve conciseness in describing wide ranges of events and conditions, a matrix format was devised as an interim aid in the first-stage expansion of accident event logic. The matrix lists system main functions and other major events that affect primary functional objectives (e.g., a component failure in the helium circuit may cause some coolant bypass flow around the core). These events are selected to represent discrete intervals of possible ranges (e.g., degree of heat removal deficiency) where appropriate and are grouped according to responsible subsystem or major component. Combinations of events are then selected; while the selection process could be both arbitrary and subjective, these objections can be overcome partly by concensus and partly through probability evaluations. In the interest of conciseness and ability of the diagrams to convey essential information, it may prove advantageous to divide the event sequence arrays into phases, either by time or at crucial decision points.

Further expansion of the accident events identified in the matrices is to be by subsidiary fault trees. These will interface with system reliability analyses, to which they will introduce specific accident circumstances that affect the equipment response prospects. Some of the earliest expansions, however, may be conjectural and merely indicate incentives and appropriate objectives for further investigation.

In close relation to, and in support of, the accident event sequence descriptions, it is planned to evaluate systems and component qualifications to meet specific challenges. Conventional reliability is one aspect of such investigations. More directly involved with the overall safety program, however, are the capabilities of components to withstand environment- and accident-induced stresses. The organization of the analysis is intended to highlight such matters and help define the associated accident conditions to which the component may be exposed.

A preliminary analysis of the event sequences in the cooling interruption class of accidents was conducted in conjunction with the methods development. This helped to identify the practical problems and requirements for event descriptions in general and to demonstrate the utility of the methods. Since so much of the analysis content is still speculative, it is not intended for publication in the near future.

---

1. Staffs of Oak Ridge National Laboratory and General Atomic Company, *Planning Guide for HTGR Safety and Safety-Related Research and Development,* ORNL-4968 (May 1974).
2. P. Rubel, "Systems and Safety Analysis," *GCR Programs Annu. Progr. Rep. Dec. 31, 1972,* ORNL-4911, pp. 179–80.
3. D. S. Nielsen, "The Cause/Consequence Diagram Method as a Basis for Quantitative Reliability Analysis," paper presented at the ENA/CREST meeting on Applicability of Quantitative Reliability Analysis of Complex Systems and Nuclear Plants in its Relation to Safety, Munich, May 26–28, 1971.
4. For example, *Summit Power Station Preliminary Safety Analysis Report,* Delmarva Power and Light Company.

12.3 FISSION PRODUCT TRANSPORT IN HTGR CORES

R. J. Kedl

Safety studies for HTGRs require an understanding of the behavior of fission products during normal operation as well as under accident conditions. In particular, the form and distribution of fission products within the core and throughout the primary circuit should be known at the beginning of an accident sequence to be analyzed. These distributions are obtained by theoretical calculations whose validity is tested by comparison with measured distributions in experimental loops and in operating reactors.

To develop the capability for performing such calculations and in preparation for the analysis and interpretation of observed fission product distributions in fuel elements removed from the Peach Bottom Reactor, we acquired from GAC the fission product transport code FIPER-Q, a version of the GAC code FIPER-X.[5] FIPER is designed to solve transient, one-dimensional diffusion problems in slab, cylindrical, or spherical geometry, with various optional boundary conditions to describe transfer of fission products from the solid graphite moderator to the helium coolant. In addition, a pseudo-two-dimensional capability is provided by allowing the coupling of successive axial regions of the reactor through the fission product concentrations in the helium coolant stream.

The code was designed for use on a UNIVAC 1108 computer. Considerable effort was devoted both to understanding the code in detail and to adapting it for operation on the IBM 360 computers at ORNL. From analysis of the FORTRAN programming and by application to test problems for which analytical solutions may be obtained, the basic mathematical treatment of the physical processes considered has been validated. Several additions to the program and to its output were made, including the printing of current release to birth rate ratios and fission product inventories in fuel particles, in graphite, and in coolant as absolute amounts (micromoles and curies) and as fractions of the total inventory. The program conversion was essentially completed and tested, with the exception of certain options not needed for our work.

A series of five bench-mark problems was composed, with which it is hoped to compare FIPER-Q with FIPDIG, a similar code used in the United Kingdom, as a general check on both codes. Computations for the five problems were completed at ORNL, but comparable FIPDIG calculations were not yet available at the end of the year.

5. B. Forutanpour and B. Roos, *FIPERX, A Fortran V Program for the Solution of One-Dimensional Linear and Nonlinear Diffusion Problems,* GA-9904 (September 1969).

12.4 CALCULATION OF FISSION PRODUCT INVENTORIES IN THE PEACH BOTTOM REACTOR

M. L. Tobias

The HTGR surveillance program includes measurements of the distributions of several important fission products in the Peach Bottom Reactor core and primary circuit. In support of this work, we calculated the nominal inventories of selected fission products in the fuel compacts of fuel element E06-01 making use of the ORIGEN code.[6] Consistent data for time-dependent neutron fluxes and for few-group cross sections of the principal fuel nuclides were obtained from two-dimensional fuel depletion calculations[7] by GAC for the actual power history of core 2 of the Peach Bottom Reactor. The purpose of the time-dependent inventory calculations, in conjunction with the related postirradiation inventory measurements, was to establish the source term for subsequent fission product release and transport calculations.

The measured and calculated activities in element E06-01 at the end of the irradiation period are compared in Table 12.1. The measured and calculated

6. M. J. Bell, *ORIGEN, The ORNL Isotope Generation and Depletion Code,* ORNL-4628 (May 1973).

7. Private communication from General Atomic Company.

Table 12.1. Comparison of measured[a] and calculated[b] fission product activities in fuel element E06-01 of the Peach Bottom Reactor core 2

Nuclide	Activity (Ci)[c]		Ratio
	Measured	Calculated	
^{95}Zr	5638	5180	0.92
^{103}Ru	2128	2660	1.25
^{106}Ru	230	196	0.85
^{125}Sb	9.7	6.5	0.67
^{134}Cs	129	161	1.25
^{137}Cs	186	168	0.91
^{144}Ce	3155	3180	1.01
^{154}Eu	3.1	3.3	1.07
Av			0.99

[a]See Sect. 13.2.

[b]ORIGEN code, actual irradiation history (power vs time).

[c]Normalized to 30 compacts, end of irradiation.

results are in reasonably good agreement; the average deviation is −1% and the largest deviation is −33%. We conclude that the calculated time-dependent fission product inventories in the fuel should be adequate for fission product transport calculations and that errors in the source terms will usually be small compared with those associated with measurements of the fission product transport itself.

13. Fission Product Technology

H. J. de Nordwall

The overall goals of the work described here are similar to those stated in Chapter 10. However, since support had been derived from the HTGR Safety Program, emphasis is on the behavior of iodine, the most toxic volatile fission product element, and on integral validation experiments that seek to determine whether mathematical models of fission product transport do in fact predict the distributions observed in operating reactors conservatively and adequately.

Iodine adsorption and desorption studies are aimed toward determining the capacity of the primary coolant circuit for iodine under normal operating conditions and the rates at which deposited iodine can be desorbed during accidents involving depressurization, steam ingress, or overheating of the steam generator. A knowledge of the capacity of the circuit for iodine is an important factor in determining whether the very useful decontamination of the primary coolant by "plate-out" can be sustained throughout reactor lifetimes. Knowledge of desorption rates permits the calculation of time-dependent iodine concentrations in the containment throughout the course of an accident. However, it should be pointed out that if the containment isolation valves close as designed and access to the containment for postaccident maintenance is not required, all the iodine that is anticipated to be present in the primary circuit, inclusive of the "design" safety margin, may be released without breaching federal regulations.

Our experiments using the Peach Bottom HTGR are aimed toward exploiting the unique characteristics of that reactor, namely, its accessible primary circuit and its relatively uniformly loaded core. Specifically, we seek to measure the rates of fission product release from the core as a function of time and to relate these measurements to the distribution of fission products within the core. Given adequate sampling of core components, one should then be able to test the FIPER code on a reasonable scale. In addition, measurements of the distributions of deposited fission products yield information about deposition and reentrainment.

13.1 IODINE ADSORPTION AND DESORPTION STUDIES

E. L. Compere M. F. Osborne

13.1.1 Factors Limiting Iodine Concentration in the Primary Coolant Circuit

The possible release of fission product iodine from an HTGR during normal operation or as a result of postulated accidents is directly dependent on the inventory in the primary coolant circuit, either in the gas phase or deposited on system surfaces. Limits on these inventories can be derived from the regulatory limits on radiation dose to the public resulting from any such releases. The inventory levels are a balance between production in fuel particles and release to the coolant, and removal from the coolant system by various processes. The factors affecting the chemical relationships between gas-borne iodine and that held on surfaces are of particular interest, both with respect to deposition and to desorption, or liftoff.

Derived release limits. The possible dose to the public as a result of a postulated accident is regulated by 10 CFR 100, which requires that an exclusion area boundary be located such that, in particular, the dose to the thyroid of any individual cannot exceed 300 rem.

The thyroid dose to an adult from ^{131}I, the dominant iodine nuclide, is 1.47×10^6 rem/Ci inhaled.[1,2] Assuming an accelerated breathing rate[3] of 5×10^{-4} m^3/sec and a worst case meteorological dispersion factor of 1×10^{-3} $(Ci/m^3)/(Ci/sec)$ at a representative distance of 500 m between the plant vent and the exclusion area boundary, we calculate a dose of 0.74 rem/Ci ^{131}I vented during an accident. Thus the derived plant release limit corresponding to 300 rem to the thyroid is $300 \times f'/0.74 = 410f'$ Ci ^{131}I, where f' is the fraction of total thyroid dose that results from ^{131}I inhalation. The coolant system inventory limit N_C depends then on the liftoff, or desorption, fraction L_C appropriate to the postulated accident and the fraction (L_S) that is released from the secondary containment system,

$$(N_C)_{max} = 410f'/(L_C L_S) ,$$

where N_C is the inventory of ^{131}I in the coolant system both on the surfaces and in the gas, and possibly that released to the coolant circuit in the course of the accident under consideration. Valves to isolate the secondary system should close promptly, and any iodine that is transported into the secondary containment will be removed by absorption in internal recirculating filters and deposition on the walls and floor of the containment. The isolated secondary containment leak rate is expected to be 0.25%/day.[4] For the 2-hr interval frequently employed, $L_S = 0.0025/12 = 0.0002$, which indicates that $(N_C)_{max}$ could be greater than 2×10^6 Ci even if $L_C = 1$. As will be shown below, such quantities of activity cannot occur in the primary coolant system. Thus the dose limits of 10 CFR 100 could not be exceeded if the isolation valves close as designed.

If the secondary isolation valves do not close, material released into the secondary could pass through ($L_S \sim 1$). However, it is possible that the desorption fraction L_C within the coolant system will be constrained to remain small, and the associated inventory limit of the primary coolant system would still be relatively high.

In the case of release under normal operating conditions, a thyroid dose limit of 15 mrem/year is indicated[1,5] if the proposed limits of 10 CFR 50, Appendix I (presently proposed for light-water reactors only), are applied. The air-grass-cow-milk-child pathway is limiting, and ^{131}I is the dominant nuclide. An average air concentration of 1.0 pCi/m^3 of ^{131}I will by this pathway result in a dose of 3620 mrem/year to a child using 1 liter of milk per day. An appropriate average meteorological dispersion factor of $(\bar{\chi}/Q) = 10^{-5}$ $(Ci/m^3)/(Ci/sec)$ will result in a derived emission limit for ^{131}I of $0.013f$ Ci/year, where f is the fraction of all thyroid dose that would be contributed by ^{131}I through the milk pathway.

The primary system leakage rate for the Summit Power Station HTGR was estimated to be 0.01%/day,[4] and the lumped decontamination factor for the prestressed concrete reactor vessel (PCRV) concrete and secondary containment was assumed[4] to be 100 for all iodine species, all paths, and all velocities.

On the basis of these assumptions, the derived limiting ^{131}I content of the primary coolant system gas during normal operation (assuming $f \approx 1$) is

$$(N_G)_{max} = 0.013 \times 100/(0.001 \times 365) \approx 36 \text{ Ci} .$$

This corresponds to 1.3×10^{18} atoms of ^{131}I or a partial pressure of 10^{-10} atm of ^{131}I.

Various other estimates of leakage rates and decontamination factors have been made for other reactors (subject to other limits). Leakage rates for HTRs have been taken as 100%/year[6] with no subsequent decontamination; however, a coolant content of 5×10^{-5} Ci was indicated, resulting from the implicit assumption of very rapid deposition on surfaces from the primary coolant gas.

Audebeau[7] and co-workers assumed a leakage rate of 0.2%/day and no further decontamination (factor = 1)

---

1. C. E. Easterly, ORNL Health Physics Division, personal communication.
2. F. J. Soldat, N. M. Robinson, and D. A. Baker, *Models and Computer Codes for Evaluating Environmental Radiation Doses*, BNWL-1754 (February 1974).
3. *Meteorology and Atomic Energy – 1968*, D. H. Seade, ed., TID-24190, p. 366.
4. Delmarva Power and Light Company, *Preliminary Safety Analysis Report for the Summit Power Station*, Docket 50-450, as amended through February 1974.
5. *Interim Licensing Policy on as Low as Practicable for Gaseous Radioiodine Releases from Light-Water-Cooled Nuclear Power Reactors*, AEC Regulatory Guide 1.42, June 1973.
6. H. Bonka and K. Brüssermann, *Iodine Release from Nuclear Power Plants and Reprocessing Plants as Well as Contamination of the Environment in the Future*, Jül-997-RG (August 1973).
7. J. P. Audebeau, R. L. R. Lefevre, and M. S. T. Price, "Quality Management for HTR Fuels," paper presented at British Nuclear Energy Society Conference, London, Oct. 15–19, 1973 (proceedings to be published).

in assessment of the effects of fuel quality control on iodine release from HTGRs. A "plate-out coefficient" of 10^3 was assumed, resulting in a coolant inventory of 0.68 Ci in their model.

The above transfer terms provide the relationship between primary system inventories and dose. We now turn to considerations of the factors serving to fix the inventory in the primary system coolant gas and on the system surfaces.

Iodine generation and release from fuel. If we ignore the details of precursor chains and assume that the various fission product nuclides of interest are produced directly, the birth rate B of any nuclide is related to power (MW) and yield through the expression

$$B = 3.12 \times 10^{16} \times \text{MW} \times \text{yield, atoms/sec} .$$

In the present case, the weighted yield is based on 60% ^{233}U fissions and 40% ^{235}U fissions.[4] Thus at a power of 2000 MW(t) and a ^{131}I yield of 0.031 there are 1.9×10^{18} atoms of ^{131}I generated in the core per second. The steady-state inventory of ^{131}I is thereby 1.9×10^{24} atoms, or 5.2×10^7 Ci.

Use of the procedures outlined in the Summit Power Station PSAR[4,8,9] permits us to assume an effective release-to-birth ratio (R/B) for ^{131}I of 1.7×10^{-4}. This result, and an estimated value of 0.0027 for the average fraction of fuel particles with cracked coatings, yield a diffusion rate coefficient D/a^2 of 4.4×10^{-10} sec^{-1} for iodine release from cracked fuel particles. Release/birth values for other short-lived iodine isotopes can be obtained by using this value of D/a^2 in the approximate Booth formula,[10]

$$R/B = 3\sqrt{D/a^2 \lambda} ,$$

where λ is the half-life of the particular isotope. In the case of long-lived or stable isotopes, the cumulative fractional release F at time t can be obtained from the relation

$$F = \frac{4}{\sqrt{\pi}} \sqrt{\frac{Dt}{a^2}} - \frac{3}{2}\frac{Dt}{a^2} .$$

It is necessary to account for the various annual fuel reload segments of the core separately for the long-lived and stable isotopes, noting also that older segments have lower power densities[4] and doubtless somewhat lower fuel temperatures.

An inventory of the amounts of various iodine nuclides released into the primary coolant system of a 2000-MW(t) HTGR is shown in Table 13.1. An 80% service factor was used for the stable isotopes.

At the end of one year of operation, for example, the inventory of iodine released into the primary system is about 1.9×10^{22} atoms; in three years it is about 8×10^{22} atoms, etc. At steady state the system contains

8. H. J. de Nordwall and W. E. Bell, "Fission Product Control in HTGR Plants," *Proceedings of ANS Topical Meeting, Gas-Cooled Reactors, HTGR and GCFBR, May 7–10, 1974, Gatlinburg, Tenn.*, CONF-740501.

9. R. D. Burnette, W. E. Bell, and N. L. Baldwin, "Fission Product Retention Characteristics of HTGR Fuel," paper presented at British Nuclear Energy Conference, London, Oct. 15–19, 1973 (proceedings to be published).

10. A. H. Booth, *A Method of Calculating Fission Gas Diffusion from UO_2 Fuel and Its Application to the X-2-f Loop Test*, CRDC-721 (September 1957: Cited in J. Belle, *Uranium Dioxide. Properties and Nuclear Applications*, 1961, p. 490, USAEC.

Table 13.1. Estimated inventory of iodine nuclides released into primary coolant system

2000-MW(t), 80% service factor for "stable" isotopes; 0.27% cracked particles

Iodine nuclide	127	129	131	132	133	134	135
Half-life	Stable	1.6×10^7y	193.5h	2.28h	20.8h	0.88h	6.7h
Yield,[a] %	0.411	1.358	3.140	4.495	6.290	6.412	5.371
Entry rate (one year), atoms/sec	2.0×10^{14}	6.8×10^{14}	3.2×10^{14}	5.0×10^{13}	2.2×10^{14}	4.6×10^{13}	9.5×10^{13}
Equilibrium	3.7×10^{14}	1.2×10^{15}	3.2×10^{14}	5.0×10^{13}	2.2×10^{14}	4.6×10^{13}	9.5×10^{13}
Released atom inventory							
1 year	4.3×10^{21}	1.4×10^{22}	3.2×10^{20}	6×10^{17}	2.4×10^{10}	2×10^{17}	2.7×10^{18}
3 years	1.8×10^{22}	6.1×10^{22}	3.2×10^{20}	6×10^{17}	2.4×10^{10}	2×10^{17}	2.7×10^{18}
40 years	3.0×10^{23}	1.0×10^{24}	3.2×10^{20}	6×10^{17}	2.4×10^{10}	2×10^{17}	2.7×10^{18}

[a] 60% ^{233}U fissions, 40% ^{235}U fissions.

about 8600 Ci ^{131}I, along with somewhat smaller but appreciable quantities of the other radioactive iodine nuclides. The entry rate of iodine into the primary coolant system is (at one year) 1.6×10^{15} atoms/sec, 20% of which is ^{131}I. The entry rate of stable isotopes increases as they build up in the elements; just prior to replacement the total iodine entry rate is 2.3×10^{15} atoms/sec, 14% of which is ^{131}I.

Primary coolant system. Iodine atoms entering the primary coolant system are rapidly circulated with the heated helium coolant gas through the steam generators and back through the core. Any of several forms of iodine removal by system surfaces may occur. Part of the circulating stream is passed through a helium purification system. Some parameters recently listed[4] for one of two reactors of the Summit Power Station of the Delmarva Power and Light Company are given below.

Power	Nominal 2000 MW(t)
Primary He inventory for mixing	9320 lb at 47 atm
Coolant circulation rate	2006 lb/sec
PCRV leak rate	0.01%/day
Helium purification plant flow rate	2070 lb/hr

The various rate constants for the removal of iodine from the primary coolant gas are

Decay (^{131}I)	$\lambda = 0.995 \times 10^{-6}$ sec^{-1}
Purification	$r_p = 6.17 \times 10^{-5}$ sec^{-1}
PCRV leak	$r_L = 1.16 \times 10^{-9}$ sec^{-1}
Surface deposition (plate-out)	$r_S = \frac{2006}{9320} \ln \frac{100}{100 - Z} \approx 0.0022Z$, sec^{-1}

The term Z is the percent removed per pass by plate-out. The lumped removal rate constant obtained from the above,

$$\Sigma(r, \lambda) = 6.27 \times 10^{-5} + r_S ,$$

is evidently strongly affected by the surface deposition rate.

At steady state the amounts of a given iodine nuclide in the gas (N_G) and on the surface (N_S) are given by

$$N_G = R'/\Sigma(r, \lambda)$$

and

$$N_S = N_G \frac{r_S}{\lambda} = \frac{R' r_S}{\lambda \, \Sigma(r, \lambda)},$$

where R' is the entry rate of the nuclide into the primary coolant, which is taken as equal to the release rate from fuel, as discussed earlier.

The leak rate from the primary system is then

$$L' = N_G r_L = \frac{R' r_L}{\Sigma(r, \lambda)} .$$

Using the entry rate of ^{131}I to the primary system of 3.2×10^{14} atoms/sec (8.6×10^{-3} Ci/sec) with no surface deposition, the ^{131}I content of the primary system gas at steady state is 140 Ci, above the derived limiting content of 36 Ci, whereas a value much below this is to be desired. Clearly some surface deposition (more than 0.1% per pass) is desirable and essential. As discussed later, deposition has been found to occur at ample rates (up to 40% per pass) in reactors where the surfaces had not become covered with iodine. Larger amounts of iodine will need to be deposited on unit primary system surfaces during the lifetime of power reactors. Consequently, it is necessary to evaluate the nature of surface deposition and the capacity of system surfaces for fission product iodine.

The nature of the deposition will strongly affect the rate of removal under accident conditions.

Iodine deposition. Surface deposition or plate-out may occur by (1) reaction with metal surfaces to produce a volatile iodide and subsequent permanent deposition of the reaction product at some point in the system or (2) adsorption on surfaces. The nature of the surfaces will require definition.

If the conditions for the first possibility – formation, vapor transport, and permanent deposition of a volatile iodide – are fulfilled, it is certainly possible to continue the plate-out indefinitely. On the other hand, if plate-out involves immobilizing the iodine on the surface by adsorption (or reaction), the extent of the system surfaces could produce a limit to the continuation of plate-out. Other options to control iodine release, not defined here, would then have to be exercised.

If a fairly rapid exchange of iodine between gas-borne and adsorbed phases occurs, a sufficient surface should provide a long enough holdup to permit adequate decay of radioactive iodine.

13.1.2 Surface Composition

The major materials of the primary coolant circuit that could contribute to iodine plate-out are heat exchanger surfaces, core and reflector graphite channels and pores, and system walls. (Interaction between

graphite and iodine will not be considered in this report.)

Iodine in the HTGR primary coolant may react with bare metal surfaces to form metal iodides, but this must compete with possible oxidation of the surface by impurities in the helium, largely the result of a slight water ingress. In the set of exploratory thermochemical calculations to be described, it was assumed that an impurity concentration corresponding to 10 (or 20) ppm of H_2O at 50 atm total coolant pressure existed in the circuit prior to equilibration with graphite at the temperatures considered.

Subject to this assumption, the thermochemical calculations[11,12] indicate that oxidation of iron to Fe_3O_4 can occur up to about 400°C, whereas Cr_2O_3 can form at all temperatures of interest. At temperatures up to about 500°C, iron can be oxidized in the presence of Cr_2O_3 to form $FeCr_2O_4$. Increase of the hydrogen-to-oxygen (H/O) ratio by a factor of 10 would reduce the temperature below which Fe_3O_4 is stable by about 50°C, with little effect on Cr_2O_3 or $FeCr_2O_4$ formation. Increase in water content, or reduction in the H/O ratio, slightly increases the temperature below which Fe_3O_4 is stable. Radiation reactions or other sources of hydrogen, such as oil leaks (not evaluated), might cause the gas to become more reducing. The relationships are presented graphically in Fig. 13.1. In this figure the proportionate excess or deficiency of free and combined hydrogen relative to free and combined oxygen in the gas phase is expressed in terms of a ratio

$$R = (P_{H_2} + P_{H_2O})/(P_{H_2O} + P_{CO} + 2P_{CO_2})$$

such that $R = 1$ if the only source of hydrogen or oxygen is water.

Based only on equilibrium considerations, there appear to be few if any combinations of metal composition and temperature in the primary system that would not be susceptible to metal oxide formation, particularly if enough time were available for sufficient chromium to diffuse to the metal surface in alloys containing low proportions of chromium. It is recognized that manganese, which is present in the alloys to 1% or less, also forms relatively stable oxides.

11. O. Kubachewski, E. Ll. Evans, and C. B. Alcock, *Metallurgical Thermochemistry*, 4th ed., Table E, Pergamon, 1967.

12. D. R. Stull, *JANAF Thermochemical Tables*, Thermal Research Laboratory, Dow Chemical Company, Midland, Mich., 1964.

13.1.3 Adsorption Equilibria and Surface Capacity for Iodine

Since some experimental data for the adsorption of iodine on iron already existed,[13] materials representative of oxidized surfaces were chosen for initial study.

Adsorption of iodine on Fe_3O_4. The determination of the adsorption coefficient of iodine on Fe_3O_4 by the bithermal equilibration method described previously[14] has been completed. Determinations at a particular sample temperature were generally made at iodine source vapor pressures of 10^{-11}, 10^{-10}, 10^{-9}, 10^{-8}, and 10^{-7} atm. The first sample used Fe_3O_4 prepared by Sweeton and Baes;[15] measurements were made at 200 and 300°C. A second sample of high-purity Fe_3O_4, obtained from Rocky Mountain Research Co., was used for determinations at 250, 350, 400, and 450°C. The first sample had a surface area (BET) of 0.16 m^2/g and a crystallite size of 222 Å; the second had a surface area of 0.25 m^2/g and a crystallite size of 216 Å.

The vapor pressure of iodine at low temperatures was obtained by interpolation from values listed by Honig and Hook.[16] The partial pressure of iodine at the sample was calculated taking into account the dissociation of I_2 into iodine atoms (which becomes dominant at the higher temperatures and lower pressures) and the thermal transpiration effect.[17]

Since the temperature and, correspondingly, the dissociation of I_2 varies around the HTGR circuit, while the pressure of helium remains effectively constant, the function $(P_I + 2P_{I_2})$, called the "iodine burden" and denoted by P_{burden}, is a more useful parameter than either P_I or P_{I_2} for plotting isotherms showing the amount of iodine adsorbed on unit surface. Such a plot is shown in Fig. 13.2.

It may be seen that a limiting value of adsorption in the vicinity of 2.0×10^{14} atoms/cm^2 is indicated, suggesting that this may represent monolayer saturation. A closely packed monolayer of iodine atoms (2.2

13. E. Hoinkis, *A Review of the Adsorption of Iodine on Metal and Its Behavior in Loops*, ORNL-TM-2916 (May 1970).

14. M. F. Osborne, "Iodine Adsorption and Desorption," *GCR Program Annu. Progr. Rep. Dec. 31, 1972*, ORNL-4911, pp. 168–70.

15. F. H. Sweeton and C. F. Baes, Jr., "The Solubility of Magnetite and Hydrolysis of Ferrous Iron in Aqueous Solutions at Elevated Temperatures," *J. Chem. Thermodyn.* **2**, 479–500 (1970).

16. R. E. Honig and H. O. Hook, *RCA Review*, pp. 360–68, September 1960.

17. C. E. Milstead, W. E. Bell, and J. H. Norman, "Deposition of Iodine on Low Chromium-Alloy Steels," *Nucl. Appl. Tech.* **7**, 361–66 (1969).

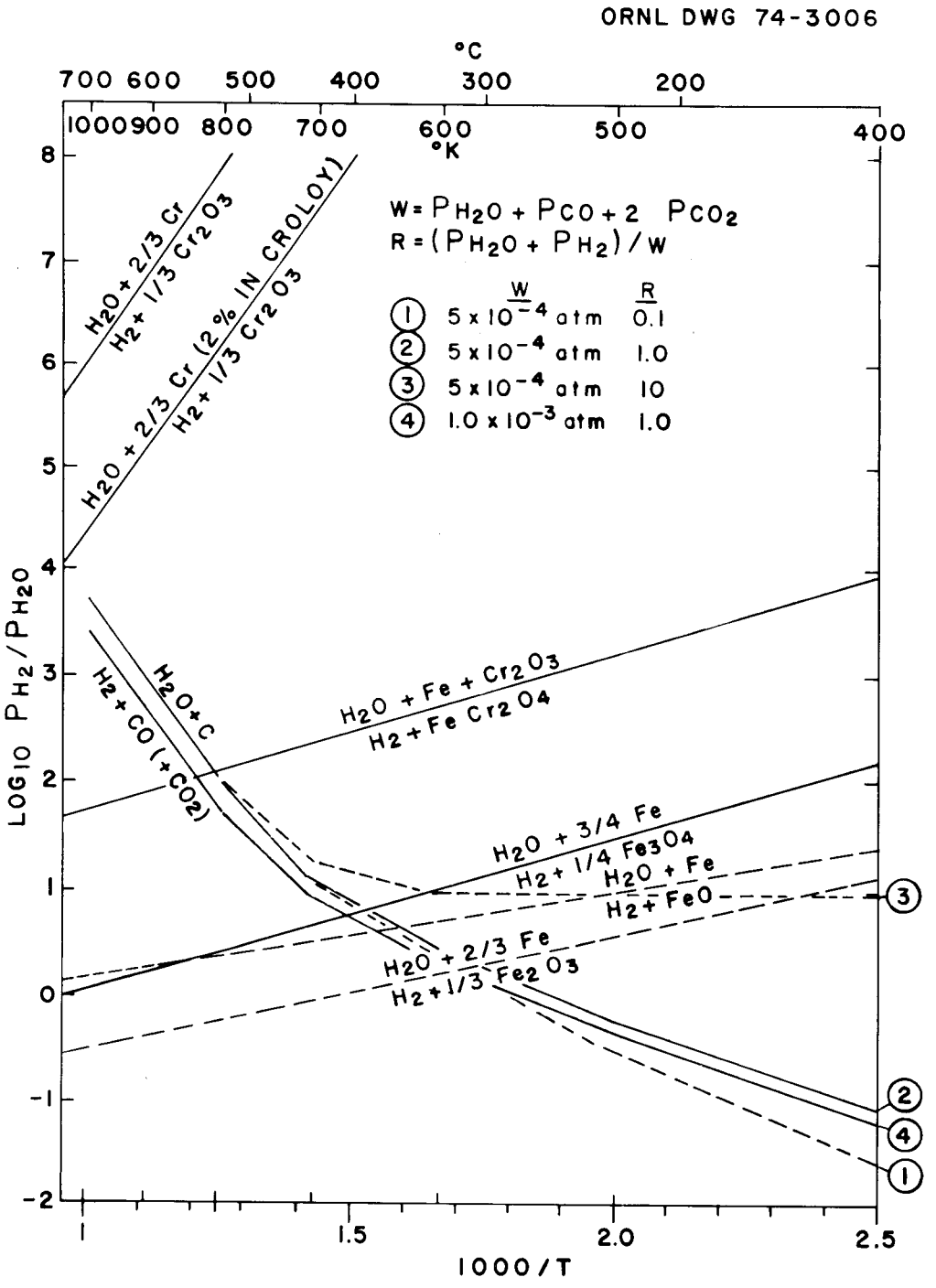

Fig. 13.1. Oxidation of iron and chromium vs temperature by ($H_2O + H_2 + CO + CO_2$) in equilibrium with carbon.

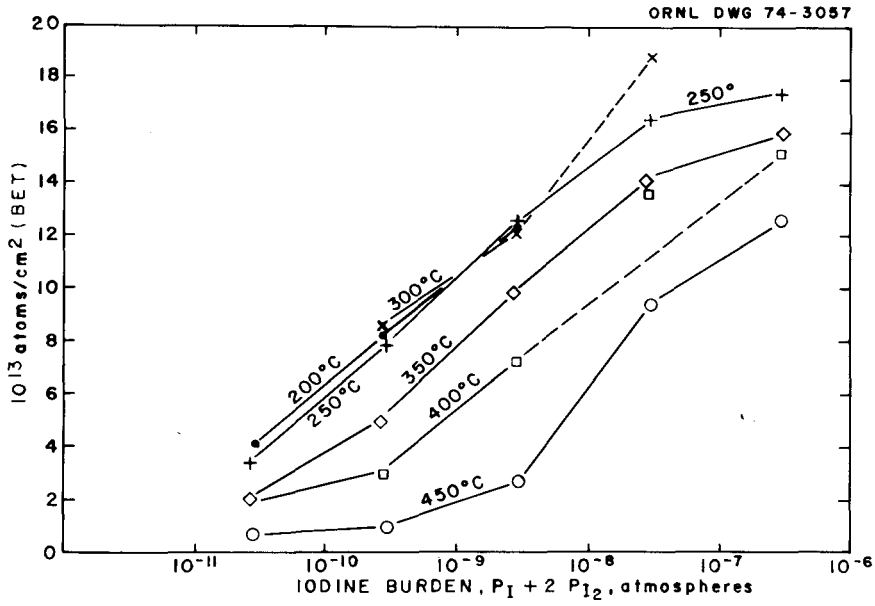

Fig. 13.2. Iodine adsorption on Fe_3O_4 vs concentration in gas.

Å ionic radius) would result in about 6×10^{14} sites/cm^2. However, chemisorption implies specific bonds to particular substrate atoms; thus the capacity would appear to be related to the spacing of iron atoms, possibly divalent iron, in the Fe_3O_4 surfaces. An Fe_3O_4 unit cell (a_0 = 8.394 Å) contains 8 molecules arranged[18] in an inverse spinel structure: $Fe^{3+}(Fe^{2+}\text{-}Fe^{3+})O_4$. The Fe^{2+} ions on this structure are indicated to be arranged in pairs with approximately 2.97 Å spacing between the two; this is too close to hold an iodine atom on each. The closest distance of adjacent pairs is indicated to be about 4.9 Å; there would be no more than about 2.8×10^{14} such sites per square centimeter, and quite possibly less, depending on exposure.

Chemisorption of iodine on all exposed atoms of elemental iron (bcc, a_0 = 2.8664 Å) again is not possible in any single plane. The closest feasible regular spacing of iodine chemisorption sites appears to be on alternate iron atoms in the 110 plane, permitting about 4.1×10^{14} sites/cm^2.

The inventory of iodine atoms released into the primary coolant system was indicated to be 1.9×10^{22} atoms at the end of the first year. The capacity of Fe_3O_4 surfaces for iodine at a partial pressure of 5×10^{-10} atm (previously indicated to be an upper limit) and at temperatures in the range 200 to 300°C is about 8×10^{13} atoms/cm^2. Thus, these data imply that if permanent adsorption on Fe_3O_4 were the only deposition mechanism, within a year the sites on about 2×10^8 cm^2 of microscopic surface would be needed. The superficial surface area of steam generator surface below such temperatures is of this magnitude.

Since the expected life of the reactor is 40 years, other means of removing ^{131}I and other shorter-lived iodine isotopes from the primary helium require consideration.

13.1.4 Iodine Deposition and Exchange

The existence of an adsorption equilibrium requires concurrent evaporation along with deposition, resulting in an exchange of isotopes between gas and surface phases. If the rates are adequate, the surface area needed to provide enough holdup for sufficient decay of radioactive species to occur could be considerably less than that required if adsorbed atoms were more or less permanently fixed to adsorption sites. The partial pressure of stable iodine at steady state would be determined by the rates of entry and of removal by the purification plant. The ensuing partial pressure would determine the fractional surface coverage; this, and the available surface area, would determine the average

18. H. Krebe (Tr. P. H. L. Walter), *Fundamentals of Inorganic Crystal Chemistry*, pp. 266–67, McGraw-Hill, London, 1968.

residence time, and the residence time would determine the reduction by decay of the system content, and consequently the gas content, of radioactive iodine.

A simple model for steady-state isothermal adsorption of a single radioactive species and a single stable species leads to the following expression for the area needed to maintain iodine isotope concentration in the coolant at a given level:

$$A\,n = \left[\frac{C_1^\circ}{C_1} - 1\right]\left[1 + \frac{r_P}{\lambda_1}\right]\left[1 + \frac{\lambda_1}{e}\right]\left[\frac{V}{k} + \frac{R_2'}{r_P}\right],$$

where

n = number of adsorption sites on unit microscopic area, sites/cm^2,

A = system microscopic area (BET), cm^2,

C_1 = radioactive isotope concentration in gas, atom/cm^3,

C_1° = radioactive isotope concentration in gas in absence of adsorption, atoms/cm^3,

r_p = rate constant for removal from primary system to purification system [6.17×10^{-5} sec^{-1}],

λ_1 = isotope decay constant [1×10^{-6} sec^{-1}],

e = surface evaporation rate constant, sec^{-1} (assume $e \gg \lambda$),

V = gas system volume [9.7×10^8 cm^3],

R_2' = ingress rate of stable atoms [9×10^{14} atoms/sec],

k = Langmuir coefficient in concentration units [$\theta = kC(1 - \theta)$] for stable nuclides [4.8×10^{-11} cm^3/atom, based on Fig. 13.2].

The values in brackets apply to the system discussed earlier; also, $C_1^\circ/C_1 = 140/36 \approx 3.9$. We then calculate $A\,n = 6.3 \times 10^{21}$ sites. If the value of n is 2×10^{14} atoms/cm^2 (Fig. 13.2), then $A \approx 3 \times 10^7$ cm^2 (BET).

Since the superficial area in the steam generators, in particular the economizer and evaporator regions, will be somewhat above 10^8 cm^2, it appears that iodine removal by adsorption on Fe_3O_4, with relatively rapid exchange, could be marginally sufficient to ensure an iodine pressure below 10^{-10} atm. Exchange rates have not been measured for iodine on Fe_3O_4. However, relatively rapid exchange was reported by General Atomic Company[19] at 400°C for iodine on mild steel surfaces loaded with iodine at relatively high iodine pressures ($\sim 10^{-7}$ atm).

13.1.5 Removal of Iodine from the Primary Coolant as Metal Iodides

It is possible that metallic areas will be available (particularly if the H_2/H_2O ratio is high for any reason) and that consequently gas-borne iodine could react with metals to form volatile iodides. Condensation of these iodides on the cooler parts of the circuit could provide an unlimited sink for iodine removal. They would also constitute a major localized source of iodine that would require consideration in the analysis of accidents involving fission product redistribution.

The thermodynamic data assembled by Hoinkis[13] have been used to calculate the equilibrium compositions at various temperatures for a constant iodine burden of 2×10^{-10} atm if elemental iron is always present. The results are presented in Table 13.2.

Steady circulation with equilibrium at all points around the circuit and with metallic iron available at all points will result in a Van Arkel type process.[20] (As the iodine-bearing gases are cooled, iron will react to form gaseous iron iodides; as the iodides are heated, iron will be precipitated.) Also, as the temperature approaches 500°K, iron diiodide partial pressure will exceed the vapor pressure and FeI_2 could deposit.

We have indicated earlier that Fe_3O_4 should exist in the system below 400°C (673°K). If elemental iron is not available to the gas below such a temperature, the iron burden at this temperature would limit the iron diiodide partial pressure at lower temperatures, and the gas temperature would have to increase to about 183°C (456°K) before condensation of iron diiodide could occur. (In this and other discussions the "burden," in atmospheres, of a given atom will be defined as the sum of the partial pressures of each gas-borne species containing it multiplied by the number of the given kind of atoms in the species. At constant system pressure it is independent of temperature and reactions in the gas phase, unless additions or removal from the gas phase occur.)

Two factors actually operate against deposition by condensation discussed above. First, metal surface temperatures are not believed to get as low as 183°C, and possibly not as low as 227°C, except behind the

---

19. "Sorption of Iodine on Metal Surfaces (Dynamic Method)," *Public Service Company of Colorado 330 MW(e) High-Temperature Gas-Cooled Reactor Research and Development Program Quart. Progr. Rep. Sept. 30, 1967*, GA-8270, pp. 143–55.

20. R. F. Rolsten, *Iodide Metals and Metal Iodides*, Wiley, New York, 1961.

Table 13.2. Equilibrium vapor composition at fixed iodine burden in the presence of elemental iron

	Temperature (°K)		
	1000	673	500
Vapor pressure of FeI_2(s), atm	2.5×10^{-2}	2.1×10^{-6}	7.22×10^{-11}
Iodine burden = $\Sigma N_I P$, atm (assigned)	2×10^{-10}	2×10^{-10}	2×10^{-10}
Iron burden = $\Sigma N_{Fe} P$, atm	3.9×10^{-16}	1.49×10^{-12}	7.76×10^{-11}
P_I, atm	2.00×10^{-10}	1.97×10^{-10}	1.98×10^{-11}
P_{I_2}, atm	1.14×10^{-17}	8.95×10^{-14}	1.25×10^{-11}
P_{FeI_2}, atm	3.9×10^{-16}	1.49×10^{-12}	7.74×10^{-11}
$P_{Fe_2I_4}$, atm	4.7×10^{-29}	7.3×10^{-20}	3.15×10^{-14}
P_{FeI_3}, atm	1.3×10^{-23}	2.6×10^{-17}	1.34×10^{-13}

thermal barrier, which is effectively inaccessible. Second, the reaction rates with high-temperature surfaces would have to be faster than is deemed likely, so that equilibrium concentrations may not develop around the circuit. Some data indicating iron iodide transport at higher iodine pressures ($\sim 10^{-8}$ to 10^{-7} atm) have been presented by the General Atomic Company.[19]

In addition to Fe, the metals of HTGR primary coolant circuits include Ni, Cr, Mn, and small proportions of other elements that are also capable of forming volatile iodides, principally the diiodides. Calculations related to the behavior of iron were reported by Hoinkis[13] and by Milstead et al.,[17] that of chromium has been reported by Osborne,[21] and the stability and volatility of various metal iodides have been discussed by Rolsten.[20] We have calculated equilibrium constants for the formation of FeI_2, NiI_2, CrI_2, and MnI_2, as gas and condensed phase, at 500 and 1000°K, using thermodynamic data presented by Brewer.[22,23] These values and their differences (which correspond to the logarithm of the vapor pressure of the condensed diiodide) are shown in Table 13.3.

The values indicate unambiguously that where manganese is available to form the iodide, it will be the

21. M. F. Osborne, "Iodine Adsorption and Desorption," *GCR Program Annu. Progr. Rep. Dec. 31, 1972,* ORNL-4911, pp. 168–72.

22. L. Brewer, G. R. Somayajulu, and E. Brackett, "Thermodynamic Properties of Gaseous Metal Dihalides," *Chem. Rev.* **1964,** 111–21.

23. G. N. Lewis and M. Randall, *Thermodynamics,* 2d ed., revised by K. S. Pitzer and L. Brewer, McGraw-Hill, New York, 1961.

Table 13.3. Logarithm of equilibrium constants for the reaction $M(s) + 2I(g) = MI_2$(s or g)

	Log K (condensed state)		Log K (gas)		Log VP (atm)[a]	
	500°K	1000°K	500°K	1000°K	500°K	1000°K
FeI_2	23.23	6.02[b]	12.72	5.15	−10.51	−0.87[b]
NiI_2	18.47	2.79	6.28	1.74	−12.19	−1.05
CrI_2	26.59	7.54	10.07	4.08	−16.52	−3.46
MnI_2	35.78	12.53[b]	24.04	10.50	−11.74	−2.03[b]
$2I = I_2$			21.11	5.76		

[a] Equal to log K(gas) − log K (condensed).
[b] Liquid.

dominant solid or vapor species (despite low concentration in the alloys); the associated log K value is much the highest. This is consistent with a statement by Rolsten[20] that the high stability of manganese iodide will prevent the production of manganese by the iodide process.

Because HTGR coolant systems are likely to contain much more oxygen (as H_2O, CO, and CO_2) than iodine, it is likely that both manganese and chromium will (where available at the surface) be bound as oxides.

13.1.6 Iodine Behavior under Accident Conditions

The effectiveness of deposition on primary circuit surfaces is best assessed in terms of the ratio of the amount of iodine deposited on surfaces to that in the gas phase at steady state, which, from equations presented in Section 13.1.3, can be seen to be r_s/λ for a system in which deposition is not limited by surface capacity. For the example employed, r_s/λ is ~2200, but values in excess of 20,000 have been measured in operating HTGRs with relatively clean circuits.[24,25] In assessing the release of iodine during an accident, one must therefore pay careful attention to the rate at which deposited iodine can become gas borne either by evaporation, as the result of chemical reaction, or because the surface itself is inherently mobile, as in the case of a dust film. To date, we have been concerned with physical desorption and desorption due to chemical reaction.

Four scouting experiments made with portions of a sample of iron powder on which iodine had been adsorbed at 400°C to a surface concentration of 7.4×10^{14} atoms/cm^2 (BET) are reported below. [The iron powder had a specific surface area of 0.14 m^2/g (BET).]

Isothermal desorption into a flowing helium stream containing 3% H_2O was examined at 250°C by placing one-fourth of the sample (about 0.4 g) in a heated 1-in.-diam tube and passing the helium-steam mixture over it at 1 liter (STP)/min. After 5 hr, about 13% of the original iodine was desorbed.

Three desorption experiments were conducted using the temperature-ramp technique. In two of these experiments, a helium–3% steam mixture was passed over a separate portion of the sample while the temperature was increased steadily at a rate of 2°C/min. Flows of 2.2 and 4.5 liters (STP)/min, respectively, were used. In the third experiment, pure helium flowing at 2.2 liters (STP)/min was used, with the same rate of temperature increase (2°C/min). The amount of iodine remaining on the specimen at any time (or temperature) was determined by in-situ gamma spectrometry. Figure 13.3 is a graph of the course of desorption in the respective experiments, which was consistent with first-order kinetics.

First-order desorption rate coefficients (k, sec^{-1}) obtained by differentiating the curves are shown in Table 13.4 for temperatures of 250, 400, and 550°C, along with the single value obtained from the isothermal experiment.

Neill[26] reported that at 400°C, iodine at a surface concentration of about 8×10^{15} atoms/cm^2 on bright steel was desorbed under vacuum with an initial rate constant of about 7×10^{-5} sec^{-1}, about twice what we observed into flowing helium. However, evaporation into vacuum and into a flowing gas stream may not be limited by the same factors.

It may be seen that in the experiments using moist helium, the desorption rate coefficients were proportional to flow. This suggests that desorption may depend on partition between the surface and gas phases. A partition coefficient Z (atoms/liter)/(atoms/cm^2) can be calculated through the use of the expression

$$Z = \frac{273.1kA}{TF},$$

where F is the rate of flow [liters (STP)/sec], T is the temperature (°K) at which the first-order rate coefficient k (sec^{-1}) is evaluated, and A is the BET surface area of the sample (cm^2). Values of Z for the various experiments and conditions are also shown in Table 13.4. It may be seen that values of Z at a given temperature are consistent for the moist helium experiments.

If we assume that the desorption rate into pure helium can be similarly treated, the partition coefficients are less than those for moist helium at 250 and at 400°C, indicating less desorption under the given conditions.

An equilibrium partition ratio can be calculated at 400°C for the static procedure in which the sample was

---

24. P. R. Rowland, W. E. Browning, and M. Carylyle, *Behavior of Iodine Isotopes in a High Temperature Gas Reactor Coolant Circuit,* D.P. Report 736 (November 1970).

25. H. J. de Nordwall, F. F. Dyer, J. O. Kolb, and W. J. Martin, Sect. 13.2, this report.

26. F. H. Neill, *Adsorption and Desorption of Iodine on Mild Steel,* ORNL-TM-2763 (April 1970).

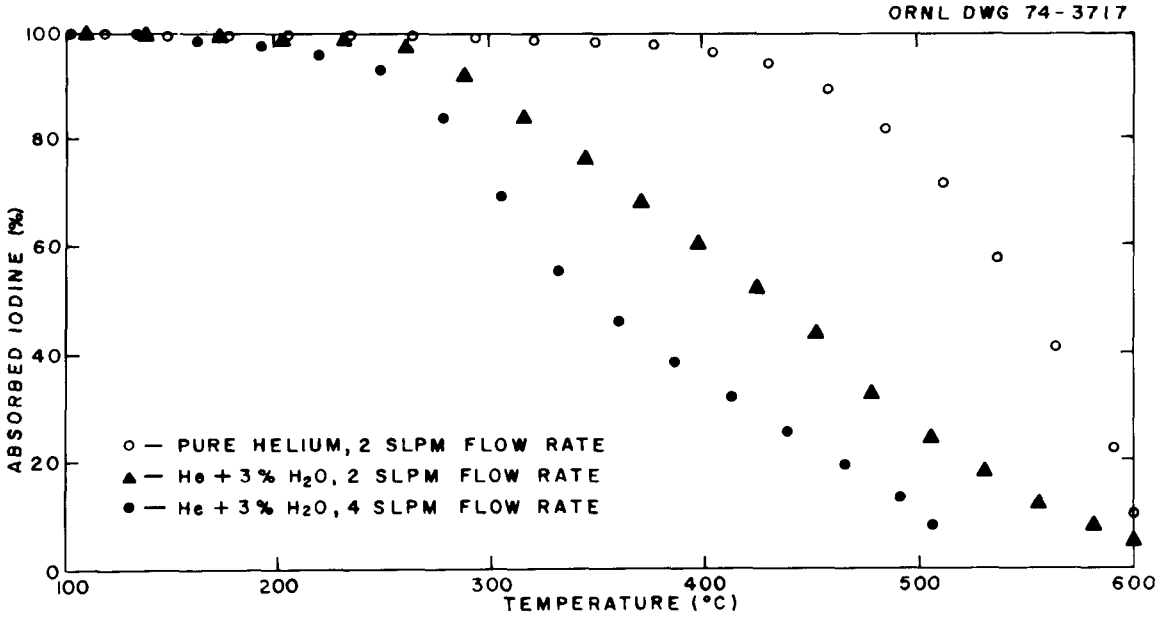

Fig. 13.3. Thermodesorption of iodine from iron powder into flowing helium, heated at 2°C/min.

Table 13.4. Desorption of iodine from iron into flowing moist or dry helium

Type	Flow [liters (STP)/min]	Fraction H_2O	Coefficient[a]	250°C	400°C	550°C
Isothermal	1.	0.03	k	8×10^{-6}		
			Z	0.14		
Ramp	2.4	0.03	k	2.0×10^{-5}	1.5×10^{-4}	5×10^{-4}
			Z	0.16	0.9	2.6
Ramp	4.3	0.03	k	4×10^{-5}	2×10^{-4}	1.1×10^{-3}
			Z	0.16	1.2	2.5
Ramp	2.2	0	k	2×10^{-6}	3×10^{-5}	4×10^{-3}
			Z	0.016	0.19	2.0

[a]Here k = first-order desorption rate coefficient (sec^{-1}) and Z = partition coefficient [(atoms/liter)/(atoms/cm^2)].

prepared by depositing iodine on the sample surfaces,

$$Z_{eq} = \frac{6.02 \times 10^{23} \times P}{SRT} = \frac{6.02 \times 10^{23} \times 2.5 \times 10^{-8}}{7.4 \times 10^{14} \times 0.082 \times 673}$$

$$= 0.37 \frac{\text{atom/liter}}{\text{atom/cm}^2},$$

where S is the original surface concentration (7.4×10^{14} atoms/cm^2), P is the iodine pressure at the sample ($\sim 2.5 \times 10^{-8}$ atm) after thermal transpiration and dissociation are taken into account, and T is the sample temperature (673°K).

Comparison with the experimental value at 400°C in the dry helium experiment, $Z = 0.19$, indicates that the values are in reasonable agreement, the value obtained by the kinetic method indicating a little less release than that derived using the static method. The closeness of the agreement indicates that the experiment with dry

helium probably did depend predominantly on partition equilibrium. Quite possibly this was also true for the experiments with moist helium, but mass transfer analysis (not attempted) appears desirable.

It may be shown that if a substance is partitioned between gas and surface phases with a partition ratio of M^* atoms on surfaces/atoms in gas, and the gas is isothermally bled off (depressurized), then

$$(M^* + 1) \ln\left(\frac{N_S^0}{N_S}\right) = \ln\left(\frac{P^0}{P_1}\right),$$

where N_S^0 and N_S are the number of atoms originally and later in the system and P^0 and P_1 are the corresponding system pressures. By definition,

$$M^* = (A/V)/Z ,$$

where A is the (microscopic) surface area of the system on which iodine is adsorbed and V is the effective volume of the gas in the system. In order to estimate the effects of full depressurization in an HTGR, we assume an area A holding iodine of 2×10^8 cm^2 and an effective volume equal to that occupied by 9320 lb of helium at 47.6 atm (P_0) (i.e., $V = 0.95 \times 10^6$ liters at 250°C, etc.). We thus calculate the fraction lost at the various temperatures to be 0.0003, 0.005, and 0.056 at 250, 400, and 550°C respectively.

The complete release to the environment of several percent of the primary coolant circuit inventory of ^{131}I may be required in order to exceed 10 CFR 100 limits. This material is likely to have been deposited in the cooler region of the steam generator. The above values suggest that in a dry system, a heatup of these regions would have to occur before potentially intolerable release of ^{131}I would occur, even in the case of complete depressurization completely released to the environment. In the moist system this may also be the case (as indicated by similarly calculated values), but mass transfer effects may need to be considered.

13.2 FISSION PRODUCT BEHAVIOR IN THE PRIMARY CIRCUIT OF THE PEACH BOTTOM HTGR

J. O. Kolb W. J. Martin
F. F. Dyer L. L. Fairchild

13.2.1 Experimental

The experimental measurements that were made as part of this program involve sampling the helium coolant leaving and returning to the core and measuring the surface concentrations of gamma-emitting fission products deposited on accessible portions of the primary coolant circuit.

The coolant samplers were designed to (1) permit helium to enter the sampler at reactor coolant velocity to minimize perturbation of particle flow paths (isokinetic sampling), (2) separate molecular species from particulate matter, and (3) separate and collect particulate matter according to size while avoiding agglomeration on collecting surfaces and consequent obscuring of particulate features.

Design and material limitations were imposed by the sizes of the available openings in the circuit boundary, the temperature of the helium being sampled, and the necessity for the upstream sampler to incorporate a thermocouple. Upstream and downstream (relative to the steam generator) samplers are therefore different in detail. The downstream sampler is shown schematically in Fig. 13.4.

Gas enters the sampler through an inlet nozzle and flows through three silver diffusion tubes in parallel, a five-stage cascade impactor, a silver membrane filter, a fiberglass "absolute" filter, and, finally, silver zeolite and treated charcoal traps to remove any remaining iodine and organic iodine compounds.[27] After the sampler is removed, each component is analyzed separately. External surfaces exposed to hot coolant are examined to determine the extent of any coolant-metal interactions.

The order of the active components in the sampler was determined by a desire to prevent condensable molecular species from passing through a filter. In a system containing a relatively large amount of dust, there are advantages in trying to remove dust first, particularly if the dust particles are large enough to be removed centrifugally. Where the dust particles are small, deposition of some dust in diffusion tubes is unavoidable. The resulting confusion depends on the relative proportions of a given nuclide present as dust and molecules. An ideal sampling station would include three samplers: (1) the type described above; (2) the type used in the Dragon Project, which is designed to remove heavy particles first; and (3) a short charcoal trap and filter to remove everything to permit easy and rapid analysis of the total inventory of the gas being sampled.

---

27. R. D. Ackley and Z. Combs, *Applicability of Inorganic Sorbents for Trapping Radioiodine from LMFBR Fuel Reprocessing Off-Gas*, ORNL-TM-4227 (May 1973).

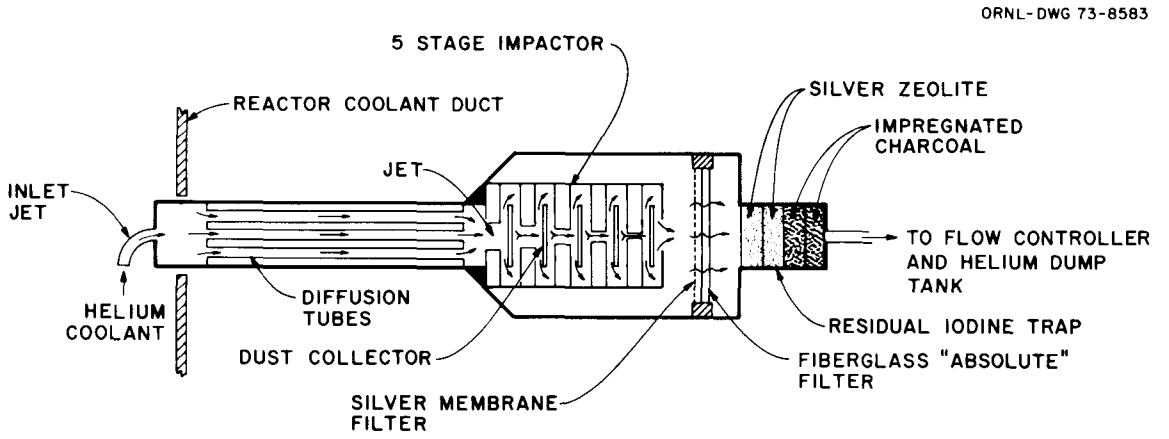

Fig. 13.4. Downstream coolant sampler used in the Peach Bottom HTGR.

In the downstream sampler, silver was chosen as the fabrication material for the diffusion tubes and the first filter element because (1) it would not tarnish in a reactor atmosphere, (2) stable silver is not sought in the coolant circuit dust, and (3) its electrical conductivity and bright metallic surface facilitates examination of deposits by electron and optical microscopy.

The upstream sampler consisted of two units, one containing diffusion tubes and one containing filters and absorbers. The filter unit was separated from the diffusion tube unit by a few feet of pipe; the diffusion tubes were made from stainless steel, partly because sufficiently small silver tubes were unavailable and partly to avoid risk of silver vapor entering the reactor.

Although the coolant samplers were in place throughout each entire reactor operating period, they were operated only toward the end of the cycle to minimize dust accumulation and to make the collected fission products relate as closely as possible to the reactor downtime at which the samplers were removed. Even so, the amount of dust collected caused agglomeration on the impactor plates and filter surfaces.

During reactor shutdown, deposition of gamma-ray-emitting radionuclides on different portions of the primary coolant ducting was measured by gamma-spectroscopy using a Ge(Li) detector surrounded by a shield designed to transmit gamma rays from only a limited area on the duct. The detector was moved manually around the primary circuit cavity, the analyzer remaining in the reactor air room. This exercise has been carried out three times: in June 1971 and 1972 and in September 1973.

In order to estimate the contributions of rare-gas decay in the primary circuit to observed activities of rare-gas daughters such as ^{137}Cs and ^{90}Sr, the concentrations of short-lived krypton and xenon isotopes were measured by flowing the coolant directly through a specially designed counting cell.

13.2.2 Iodine Behavior

The distribution of iodine between sampler components is given in Table 13.5 for the pair of samplers removed in May 1973.

Table 13.5. Iodine distributions in coolant samplers (May 1973)

Component	Iodine concentration (μCi)	
	Upstream	Downstream
Diffusion tubes	0.047	0.034
Dust	0.0014	<0.018[a]
Special traps	0.00014	0.0036
Total	0.048	0.038–0.056

[a]Upper limit; no ^{131}I peaks actually observed.

Since no ^{131}I was found in the last impregnated charcoal and silver zeolite traps, one has some assurance that a substantial fraction of the iodine entering the samplers was collected. The apportionment of the totals between different species was made using the observed distribution of ^{131}I between sampler components.

"Organic iodides," which are characterized by their ready passage through the diffusion tubes and dust filters and subsequent deposition on the adsorbers, were

present only at relatively low concentrations. The gas-borne iodine leaving the reactor at about 610°C was only 0.3% "organic iodide," whereas that leaving the steam generator at about 310°C contained between 6 and 9% of organic iodide. Approximately 90% of the organic iodide entering the core was apparently being destroyed by passage through the core. Since the filters in both samplers operated at similar ambient temperature, organic iodide generation in the samplers cannot account for all of the iodine found in the special traps. Organic iodide compounds were apparently being formed in the steam generator, probably by reactions between deposited iodine and carbon-containing materials on the steam generator surfaces.

The composition of the dust circulating in the Peach Bottom HTGR indicates that it does not have a single source.[28] During this sampling period, small quantities of oil from the purified helium compressor were known to be leaking into the primary coolant circuit. That this had raised the dust concentration was confirmed by a later experiment (when the oil leak had been stopped) in which almost no dust was detected in our samplers. May 1973 dust appeared to contain only traces of iodine.

The large fraction of iodine in the diffusion tubes was not entirely consistent with the observed flat-surface concentration profiles (Figs. 13.5 and 13.6) or the amount of dust visible. There was clearly not enough dust in the diffusion tubes to ascribe activity measured in that region to the type of dust collected on the filters. The temperature distribution in the sampler may also have influenced the iodine distribution. Unambiguous assignment of this iodine to definite molecular species must await the results of further experiments.

In spite of this uncertainty about the iodine-carrying species, between 38 and 58% of all ^{131}I leaving the core was being deposited on fixed surfaces between the samplers, which include the steam generator. If one excludes the organic iodide compounds from this estimate of the deposition rate, one obtains higher values (viz., 41 to 60%), but one must then describe the production of organic iodides separately. (This may be desirable anyway, since organic iodides may behave differently in PCRV concrete and do behave differently in the remainder of the chain leading to man.) We hasten to add that the translation of these conclusions to another reactor is only valid if residence times,

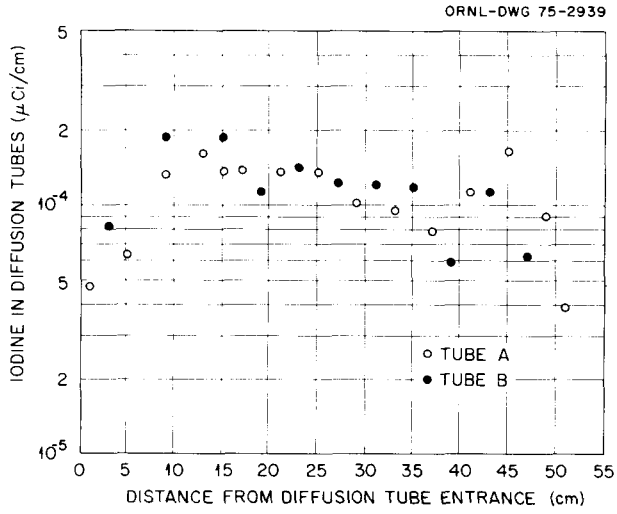

Fig. 13.5. Distribution of ^{131}I in diffusion tubes of upstream samplers.

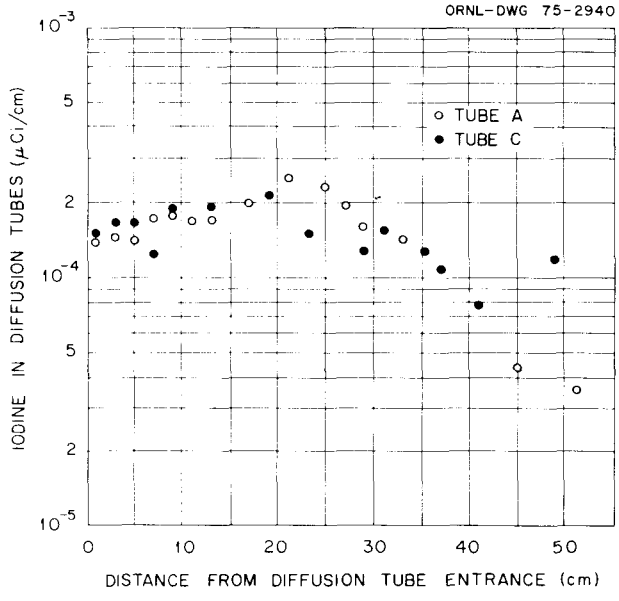

Fig. 13.6. Distribution of ^{131}I in diffusion tubes of downstream sampler (May 18, 1973).

temperatures, temperature distributions, and deposition rates are similar and if adsorption isotherms are linear.

The possible dependence of the deposition ratio on the iodine content of the primary circuit was discussed in Section 13.1. No attempt was made to measure ^{129}I and stable ^{127}I in our samplers. We expect that barely detectable amounts of these nuclides will be present on

28. F. F. Dyer et al., *GCR Program Annu. Progr. Rep. Dec. 31, 1972*, ORNL-4911, p. 172.

the surfaces of the steam generator and ducting after the reactor is decommissioned.

Surface concentrations of ^{131}I in the cold duct, as measured in September 1973 by gamma spectroscopy, are shown in Fig. 13.7. The concentration was found to vary exponentially with distance along the duct, indicating that deposition was irreversible. The mass transfer coefficient h for deposition was calculated to be 5.9 cm/sec by fitting the equation

$$a_s(x) = a_s(o)\, e^{-\left(h\frac{P}{A} + \lambda\right)\frac{x}{U}}$$

to our results. In this expression, a_s is the surface activity ($\mu Ci/cm^2$) at point x, h is the mass transfer coefficient, P is the duct perimeter, A is the cross-sectional area, and U is the velocity. The mass transfer coefficient calculated by Hanson[29] using the PAD code[30] to represent the deposition of an atom of similar size (Xe) was about 5.7 cm/sec; this tends to confirm that some elemental iodine [I + I_2] was present in the gas leaving the steam generator.

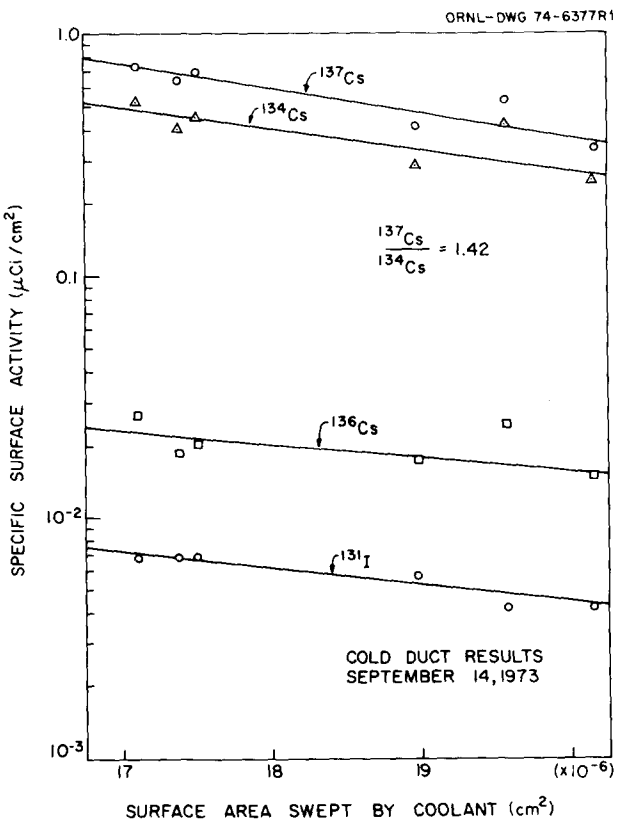

Fig. 13.7. Surface concentrations of ^{131}I in the cold duct (Sept. 14, 1973).

Integration of the expression above yielded an activity for the cold duct of a single coolant loop of 0.0097 Ci, 0.0045 Ci of which was deposited in the region between the steam generator and the downstream gas samplers.

No ^{131}I was detected on the hot duct. However, surface concentrations on the hot duct comparable to that found on the cold duct would have been detected.

The observed depletion of the coolant and the deposition in the cold duct were used to calculate the ^{131}I inventory of the steam generator surfaces and the accessible parts of the circuit (i.e., the region from the hot valve to the end of the cold return duct). The No. 1 steam generator and the loop were estimated to contain 0.025 and 0.035 Ci of ^{131}I respectively. Assuming that both loops contain the same amount of iodine, that the gas phase contains a negligible amount of iodine, and that the inaccessible regions of the coolant circuit contain insignificant amounts of deposited iodine, either because their surfaces are too hot or because deposition rates are too low, one calculates that $R'/B(^{131}I)$, the rate of release from the core into the coolant circuit to the birth rate, was 2.4×10^{-8}. To obtain the rate of ^{131}I release from the fuel, one must multiply the rate of release by the purge attenuation factor, which, when last measured, was about 6000. This higher release rate ($\sim 10^{-4}$) is the one that should be compared with the expected release rate for larger HTGRs.

Conclusions. Helium leaving the core contains very little CH_3I and dust-borne iodine. The organic iodine that enters the core from the steam generator is almost completely destroyed in the core, and temperatures are too high for iodine to adsorb appreciably on the circulating dust leaving the core and perhaps on the walls of the hot duct as well.

On entering the steam generator, the iodine divides itself between the gas phase and a two-component surface consisting of a dust layer and the metal structure. Between 35 and 58% of the iodine leaving the core leaves the region between the samplers in a similar molecular form, and 0.025%/hr of the iodine deposited

29. D. Hanson, General Atomic Company, unpublished work.
30. F. E. Vanslager and L. D. Mears, *PAD, A Computer Code for Calculating the Plateout Activity Distribution in a Reactor Circuit*, GA-10460 (January 1971).

between the samplers reenters the gas phase after an unknown delay as "organic iodine."

A further, less well-defined fraction of adsorbed iodine may become associated with a dust layer that coats the surfaces of the steam generator and reenter the gas phase on dust particles. Alternatively, iodine atoms may react with dust in the gas phase. We cannot distinguish the two processes. However, we prefer the former model, because it is kinetically more probable and because our results for cesium imply that some dust may remain on the steam generator and duct surfaces for years. Dust passing through the core would be almost completely freed of iodine.

We prefer to await results from our second set of samplers, which were not affected by oil decomposition products, before recommending how the concentration of different circulating species downstream of a steam generator should be calculated. Clearly a single deposition rate for all iodines must be selected with great care if the conversion of organic and dust-carried iodine in the core is to be conservatively described.

Finally, we would caution the reader that these data may only apply to Peach Bottom during a time when oil is leaking into the circuit. Their general applicability remains to be established by further measurements in this and other HTGRs.

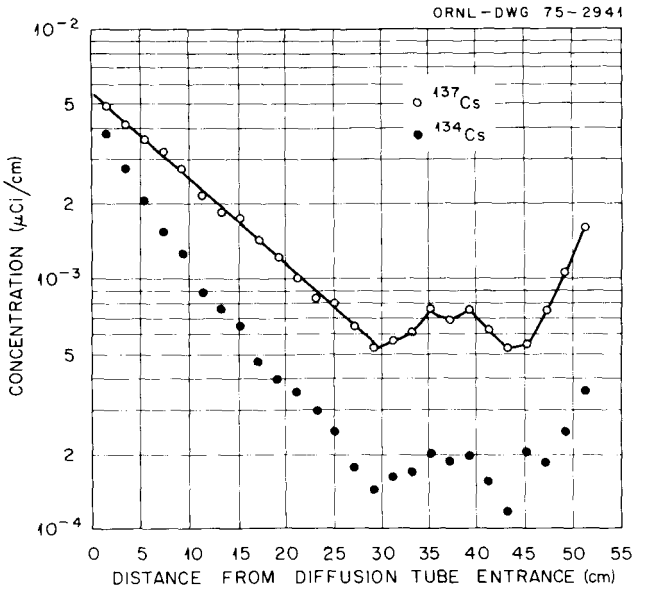

Fig. 13.8. Distribution of radiocesium on diffusion tube C upstream sampler (May 18, 1973).

13.2.3 The Behavior of Cesium

Cesium in the coolant circuit. The distribution of cesium between components of the upstream and downstream samplers is shown in Table 13.6. The axial surface concentration profiles measured in upstream and downstream diffusion tubes are shown in Figs. 13.8 and 13.9 respectively. These profiles exhibit an exponential distribution followed by a uniform distribution, with considerable scatter in the uniform values. We have ascribed the exponential distribution to the deposition of gaseous species that obey gas diffusion principles and the uniform distribution to the deposition of dust particles that contain radiocesium. We observed that the surface concentrations of cesium increased several centimeters from exit ends of all diffusion tubes. This anomaly remains to be explained. We assumed that the uniform dust-borne cesium was constant along the entire diffusion tube length and have subtracted this total dust-borne cesium from the total amount of cesium found on the diffusion tubes to obtain a net fractional amount of gaseous cesium in the coolant. The concentration of cesium isotopes in the coolant derived from these observations are presented in Table 13.7.

Table 13.6. Observed distribution of cesium activities (μCi) in Peach Bottom gas samplers on May 17, 1973

Component	Upstream				Downstream[a]		
	^{134}Cs	^{136}Cs	^{137}Cs	^{137}Cs/^{134}Cs	^{134}Cs	^{137}Cs	^{137}Cs/^{134}Cs
Diffusion tubes	0.28	0.0083	0.55	1.9	0.12	0 38	3.1
Impactor					0.50	1.81	3.6
Filters	0.33	0.0064	1.17	3.6	0.26	1.10	4.2
Total	0.61	0.012	1.72		0.88	3.29	

[a]No ^{136}Cs was found in the downstream samplers.

Table 13.7. Adjusted cesium concentrations (μCi/lb) in the Peach Bottom HTGR coolant in May 1973[a]

Assigned species	Upstream			Adjusted $^{137}Cs/^{134}Cs$	Downstream[b]		Adjusted $^{137}Cs/^{134}Cs$
	^{134}Cs	^{136}Cs	^{137}Cs		^{134}Cs	^{137}Cs	
Cs (gas)	1.94N4	7.05N5	2.32N4	1.2	1.19N5	4.76N5	4.0
Cs (dust)	3.82N4	5.47N5	1.26N3	3.3	7.95N4	2.83N3	3.6
Total	5.76N4	1.25N4	1.49N3		8.07N4	2.88N3	

[a]A number expressed as 2.32N4 denotes, for example, a value of 2.32×10^{-4}.
[b]No ^{136}Cs was detected in downstream sampler.

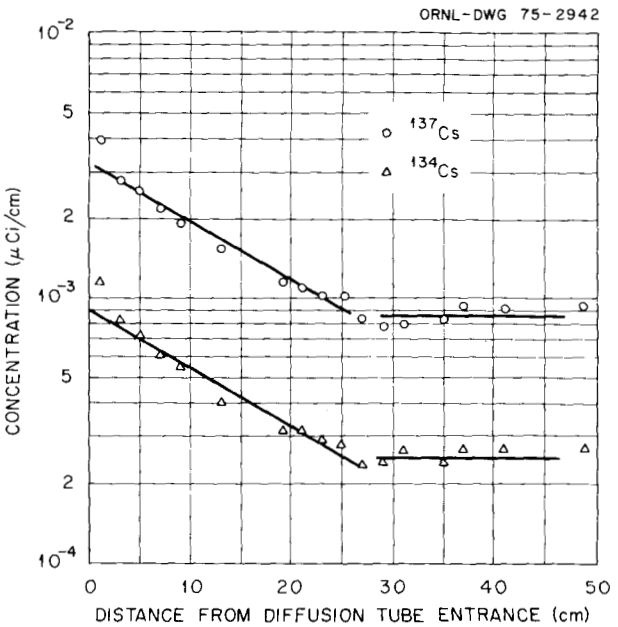

Fig. 13.9. Distribution of ^{134}Cs-^{137}Cs in diffusion tube C of downstream sampler (May 18, 1973).

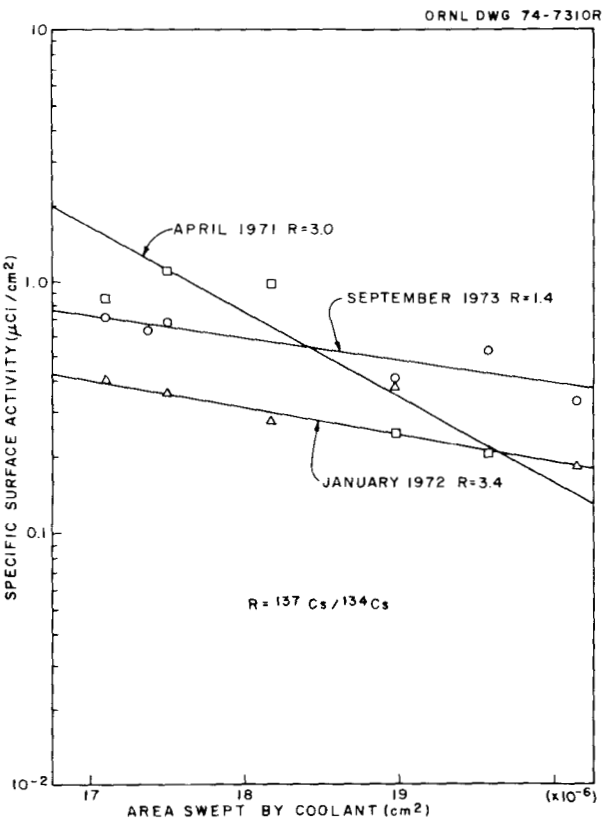

Fig. 13.10. Distribution of ^{137}Cs on cold duct.

Cesium was also measured in the cold return duct during the September 1973 shutdown. These results are shown in Fig. 13.7 and Table 13.8. Figure 13.10 compares the ^{137}Cs distributions measured in 1971, 1972, and 1973 at approximately one-year intervals.

Only an upper limit of 0.2 μCi/cm^2 could be measured on the hot duct upstream of the steam generator.

As for iodine, the duct surface concentration data were fitted to an exponential equation of the form

$$a_s(x) = a_s(o)\, e^{-\left(h\frac{P}{A} + \lambda\right)\frac{x}{U}},$$

which was then integrated to yield A_s, the activity on the loop No. 1 cold duct surfaces. Values of h and A_s

Table 13.8. Activities (μCi/cm^2) on the cold return duct, Sept. 4, 1973[a]

Position	^{134}Cs	^{137}Cs	^{136}Cs	^{137}Cs/^{134}Cs
Steam generator exit	0.527	0.726	2.65×10^{-2}	1.38
Compressor entry downstream of HC-203 valve	0.404	0.644	1.88×10^{-2}	1.59
Compressor entry by cavity entry	0.459	0.699	2.05×10^{-2}	1.52
Compressor exit by cavity entry	0.132	0.182	7.7×10^{-3}	1.38
Compressor exit line near steam generator	0.289	0.415	1.72×10^{-2}	1.44
Vertical return duct	0.422	0.538	2.44×10^{-2}	1.27
Compressor return before joining concentric duct	0.246	0.338	1.48×10^{-2}	1.37

[a]Results are based on the assumption that the walls of ducts consisted of 7/16 in. of steel plus 3.75 in. of thermal insulation.

are given below:

	h (cm/sec)	A_s (Ci)
^{134}Cs	4.1	0.69
^{136}Cs	2.9	0.035
^{137}Cs	5.8	0.96

Discussion. The description of the behavior of cesium is complicated by the fact that fuel, cesium-containing graphite, and cesium vapor were deposited in the steam generator and other parts of the primary circuit during the operation of the first core. This has resulted in the steam generator functioning as a net source of cesium rather than a sink. For example, the total concentration of ^{137}Cs at the upstream sampler was 1.49×10^{-3} μCi per pound of helium and that at the downstream sampler was 2.88×10^{-3} μCi/lb. Second, dust was clearly playing an important role in cesium distribution. This difficulty is partially resolvable by utilizing the fact that it has been $3\frac{1}{2}$ years since core I ceased operation. Cesium from core I is relatively richer in ^{137}Cs than that being generated after some 600 days of core II operation. We expect core I cesium to have a ^{137}Cs/^{134}Cs ratio of about 5, while the ^{137}Cs/^{134}Cs ratios found in May 1973 were as low as 0.7 on the inlet jet and 0.8 on the external surface of the upstream sampler.

The variation of the cesium ratio in the diffusion tubes, shown in Fig. 13.11, indicates that the molecular

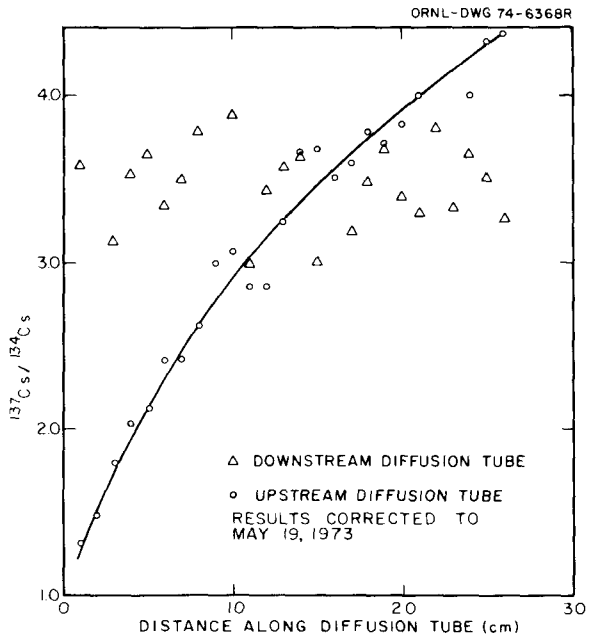

Fig. 13.11. Cesium ratio in the diffusion tubes (May 19, 1973).

cesium deposited in the early parts of the upstream diffusion tubes was predominantly new. However, all cesium in the downstream tube had about the same high isotopic ratio, indicating that the cesium was much older than that in the upstream sampler and that partial

isotopic exchange was occurring in the steam generator between Cs(gas) and Cs(dust). There was also some interference from dust.

The dust samples contained cesium of similar apparent age to that in the large ducts in 1972, with a cesium ratio of about 3.5. The $^{137}Cs/^{134}Cs$ ratio for cesium collected in both of the 1973 samplers is lower than that found earlier in the same locations.

In the cold duct downstream of the steam generator, the mean $^{137}Cs/^{134}Cs$ ratio fell from 3.4 in 1972 to 1.4 in 1973 after rising from 3.0 to 3.4 during the previous year.[28] These ratios are given in Fig. 13.10. These changes indicate that cesium is now being released by core II and that new cesium is now being carried to all parts of the circuit, including the region downstream of the steam generator. Both the slope of the deposition profile in the cold duct and the distribution of cesium in the downstream diffusion tube sampler indicate that not all the cesium in this region is associated with dust.

Finally, the rate of deposition of cesium in the cold duct now exceeds the rate of the reentrainment observed between 1971 and 1972. The ultimate cesium sink has not been definitely identified, but cesium released from core I, as determined by isotopic ratio, has been found on the external surfaces of the E06-01 element and in the purge inlet channel.

The percentages of atomic cesium [Cs(gas)] deposited per pass in the steam generator are 94 and 79% for ^{134}Cs and ^{137}Cs, respectively, the difference being ascribable to the steam generator being richer in ^{137}Cs than ^{134}Cs and able to exchange cesium with the coolant. Clearly the steam generator is not a perfect sink even for cesium vapor.

Finally, it is interesting to assess the rate at which cesium is leaving the core. In order to do this one must know δ, the fraction deposited per pass. While δ can be assessed for Cs(gas), it cannot be estimated for Cs(dust). Using the data in Table 13.7, we have calculated $A_s(1)/\delta$, the annual increase in the primary circuit activity, assuming that all molecular cesium in the circuit is from core II. Using the relationship

$$\frac{A_s(1)}{\delta} = 8.766 \times 10^{-3}\, a_g(0) F\,,$$

where F is the flow rate and $a_g(0)$ represents the gas phase concentration, we calculate the following upper limit estimate for the annual increase in cesium activity for both loops: 0.82 Ci/year for ^{134}Cs and 0.98 Ci/year for ^{137}Cs. These core release rates will be compared with calculated estimates when a whole core release calculation using realistic temperatures can be performed.

Cesium in the core. A fuel element was withdrawn from the reactor after 384 days of operation, and axial and radial distributions of cesium, strontium, and tritium were measured in the graphite components. Radiochemical analysis is approaching completion. Detailed interpretation of observations is being deferred until similar information is available from a 701-day element. The most significant observations for cesium are given below.

1. Cesium deposited on the top graphite reflector was able to penetrate below the surface, thus increasing the capacity of the reflector as a sink for cesium. Figure 13.12 shows radial concentration profiles for ^{134}Cs and ^{137}Cs. Analysis of the lower reflector awaits disassembly of the fission product trap.

2. The axial distributions of ^{137}Cs in the fuel, sleeve, and spine are shown in Fig. 13.13. Although these radially averaged concentrations tend to follow the fuel temperature distribution, there are two indications that cesium is being swept down the purge channel. First, the peak cesium activity in the spine and sleeve is further downstream than in the fuel, and second,

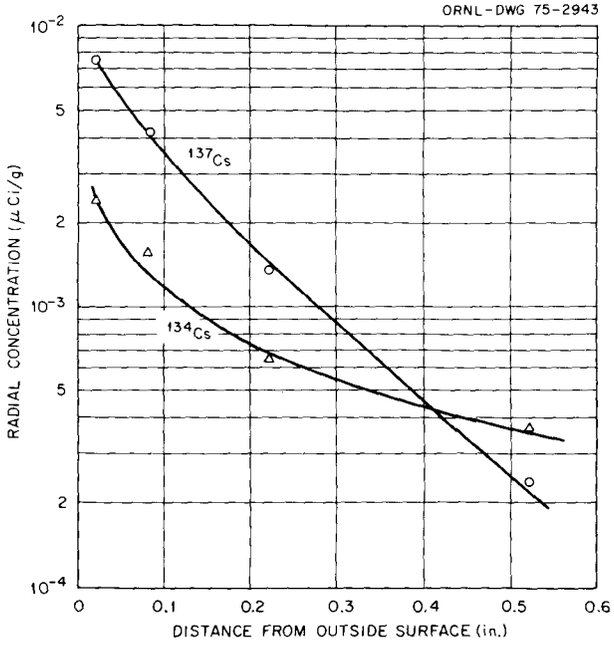

Fig. 13.12. Radial concentration of ^{137}Cs and ^{134}Cs in upper reflector fuel element E06-01.

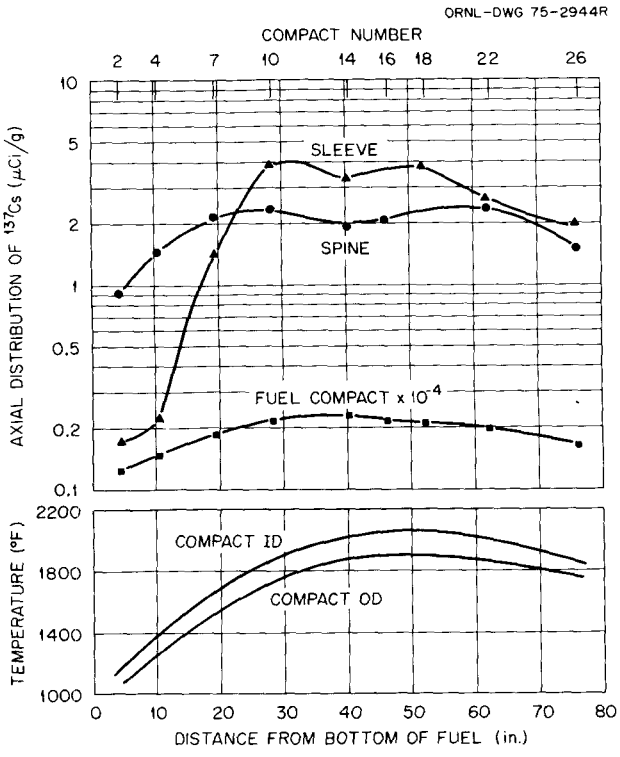

Fig. 13.13. Axial distribution of ^{137}Cs (Jan. 6, 1972).

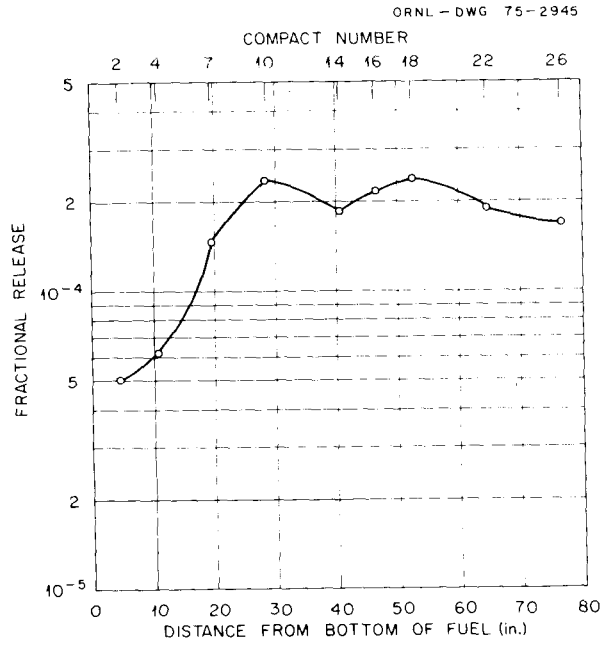

Fig. 13.14. Fractional release of ^{137}Cs from fuel to spine and sleeve of fuel element E06-01 (Jan. 6, 1972).

cesium appears to be piling up about 25 in. from the bottom of the active core. This conclusion is reinforced by preliminary observations on the 701-day element. The fraction of the cesium generated in the fuel that is residing in the fuel sleeve and spine is shown in Fig. 13.14. An average fractional release of ^{137}Cs derived from these results is 1.6×10^{-4}. Measurements have shown that very little of the released cesium is in the fission product trap.

The observed radial concentration profiles for ^{137}Cs in the sleeve at three axial positions are shown in Fig. 13.15. The concave shape of the plot of concentration vs radius is inconsistent with a single simple diffusion process, although the steep concentration gradients imply a substantial attenuation and hence delay of cesium during passage from the fuel to the coolant. The exponential concentration profile could indicate that the helium being sucked through the fuel sleeve by the purge was influencing the transport process, but only if a steady state had been attained.

Conclusions. Cesium from core II appears to be entering the primary coolant circuit at about 1 Ci/year after about 600 effective full-power days of operation. The significance of this observation in relation to the behavior of a large reactor will depend to a great extent on a detailed comparison of the temperature history of a Peach Bottom element and that of a large HTGR.

Once in the circuit, a cesium atom has the same options as an iodine atom, although the adsorption on both carbonaceous and metallic surfaces are larger (not so large that a perfect sink deposition model can be used over the whole temperature range).

The relative role of surface dust, oxide films, and base metals in retaining deposited cesium and other fission product metals cannot be identified at present but will be examined when samples of circuit materials are available.

Integration of the total amount of cesium in the circuit requires analyses of steam generator parts.

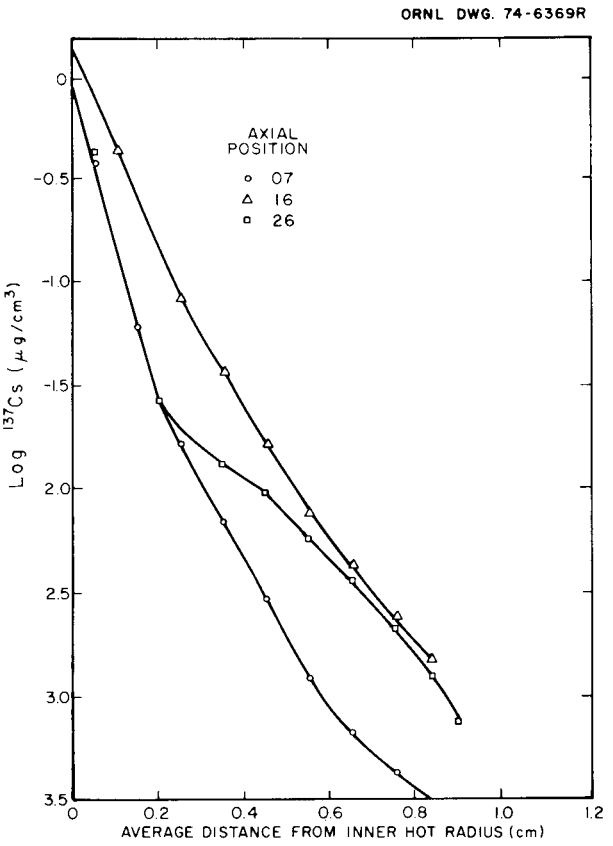

Fig. 13.15. Radial profiles for E06-01 sleeve.

14. Primary Coolant Technology

A. P. Malinauskas

The carbon and graphite that are employed in the reactor as neutron moderator, fuel cladding, and core structural material are acceptably stable at the elevated temperatures and radiation intensities involved. However, at the temperatures of operation, the materials can be readily oxidized; therefore, some attention must be given to maintaining the chemically inert coolant helium free from oxidizing impurities.

Because of the operating conditions involved, the most likely oxidant of significance is steam, and the most probable occurrences leading to steam ingress involve either continuous inleakage from small leaks in the steam generator or the sudden introduction of a large amount of steam through the rupture of a steam generator tube.

Establishing the consequences of continuous but minor steam inleakage involves considerations of long-term effects, whereas large, sudden steam ingresses result in effects of more immediate concern. Both long- and short-term effects of steam inleakage are being investigated and, to focus on the analytical aspects of the problem more directly, activity in this area has been concentrated on the development and use of computational programs as aids in analyses of the consequences of steam ingresses.

14.1 EVALUATION OF COOLANT-CORE INTERACTIONS AND COOLANT COMPOSITION DURING FORT ST. VRAIN STARTUP

G. L. Tingey[1]

To establish the effects of steam ingress on the physical properties of the graphite components, as well as the effects of resultant alterations of coolant composition on the performance of metallic components, it is necessary to consider the kinetics of the chemical processes involved. These are quite complex and are further complicated by the constant mixing and recirculation of the gases through zones of varying temperature, effects of radiation on the chemical reactions, and the nature of the sources (inleakage) and sinks (e.g., the purification system) for the impurity species involved. Thus, rather sophisticated computational programs, such as GOP (for steady-state conditions) or OXIDE (for transient conditions) are required for systems analyses.

Considerable effort has been expended both in code development and in providing experimentally derived input data for use in the codes, but few opportunities have been provided to test the codes and the input data against actual measurements from an operating HTGR. Initial startup of the Fort St. Vrain Reactor will provide a unique opportunity, not only in this regard but also in the evaluation of the significance of radiolytic reactions in an operational system. Because the GOP code is the only computational program presently available that includes radiolytic reactions, this code is to be used as both an aid in identifying parameters of particular significance and as a mechanism for startup data analysis.

Most of the effort during the current reporting period has been expended in updating and modifying the code for use on a CDC CYBER 74 system. (The code had previously been used on a UNIVAC 1108 system.) Several test cases have also been run to identify parameters that are particularly sensitive to radiolytic reactions. In this manner, we have observed that radiation effects cause a substantial increase in the H_2/H_2O ratio and at least an order of magnitude decrease in the CO/CO_2 ratio at the temperatures of interest. Moreover, although not treated quantitatively,

1. Battelle Pacific Northwest Laboratories.

the formation of methane appears to result primarily from radiation-induced processes.

14.2 COMPUTER ANALYSIS OF THE EFFECTS OF STEAM INGRESS INTO THE COOLANT CIRCUIT

D. S. Joy

As indicated above, emphasis during this reporting period has been on the development and use of computational programs for analysis of effects of steam ingress into the primary coolant circuit. For this purpose, the OXIDE-2 code, which had been developed for use on a UNIVAC 1108 computational system, has been obtained from General Atomic Company and adapted for use on the IBM 360/91 system.

Further work is to proceed in two directions; one of these will use the code, in its present or only slightly modified form, as an aid in the indentification of components that are particularly vulnerable to oxidative attack and to the sensitivity of the results to the input data employed. The second direction will critically examine the mathematical aspects, assumptions, and physical phenomena that form the structure of the OXIDE-2 code.

15. Confinement Components

J. P. Callahan

The initial effort under this new task area consisted of a preliminary review of recent literature on prestressed concrete reactor vessels and reactor containment structures to provide background material for preparation of Chapter 12 of the HTGR Safety Program planning guide.[1] Chapter 12 of the report briefly summarizes the present status of confinement component technology and outlines a comprehensive research and development program. This initial review of the literature will be expanded to provide the information required for preparing an in-depth technology assessment of HTGR confinement components.

[1] *Planning Guide for HTGR Safety and Safety Related Research and Development*, ORNL-4968 (May 1974).

16. Primary Systems Materials Technology

P. L. Rittenhouse

This program is concerned with the materials used in the construction of the primary systems of HTGRs. Its objective is to develop information that will permit more precise definition of material response and behavior under abnormal reactor conditions and thereby provide improved bases for the evaluation of safety.

16.1 NATIONAL HTGR SAFETY PROGRAM PLAN

R. G. Donnelly W. P. Eatherly P. L. Rittenhouse

During the final quarter of 1973, we developed a plan for work on the safety-related aspects of primary-system materials. The categories of materials covered in this plan are (1) primary loop metallic components (ducting, steam generator, circulator, etc.); (2) graphite components (support blocks, reflectors, etc.); and (3) control components (absorber materials and burnable poisons).

In each of these categories, the primary emphasis is to study mechanical properties, failure criteria, and environmental effects (temperature, atmosphere, irradiation, etc.) as they relate to the assurance of safety during off-design reactor conditions.

16.2 TECHNOLOGY STATUS REPORT

W. R. Martin P. L. Rittenhouse

The preparation and publication of a report evaluating HTGR metallic structural materials technology has been authorized under the HTGR Safety Program. This report, to be completed during FY 1974, will (1) identify all HTGR structural alloys of interest, their applications, and their environments under accident conditions; (2) describe the status of technology, including existing information on properties and ongoing programs; and (3) identify specific areas in which additional study could lead to a better understanding of materials behavior and therefore to quantification of margins of safety. During the latter part of the year, we identified the scope of the information required for this report and have pursued this in detail through discussions with the General Atomic Company (GAC) and through literature review.

16.3 PEACH BOTTOM METALLURGICAL POSTMORTEM

P. L. Rittenhouse

The Peach Bottom 40-MW(e) prototype HTGR has been in operation since 1968, and its planned decommissioning (to begin late in 1974) offers a unique opportunity to establish the effects of extended exposure to primary- and secondary-coolant environments on HTGR structural materials. The results of such studies would be relevant to both safety and design aspects of current and future gas-cooled reactor systems.

General Atomic Company and ORNL have cooperated with Philadelphia Electric Company (the Peach Bottom operator) and Suntac Nuclear Corporation (the decommissioning agent) to identify the desirability, feasibility, and cost of removing various components from the reactor primary system for examination. It is now proposed to remove one of the steam generators essentially intact (i.e., tubesheet, tubing bundle, and shroud); samples of the concentric (hot) ducting including the hot valve; selected parts of the helium circulator; and two sections of the cold ducting. Procedures and precautions needed in component removal, handling, and shipping have been identified and agreed upon by GAC and ORNL. Disassembly, sectioning, and metallurgical examination of these components will allow us to obtain evidence related to wear, erosion, corrosion, carburization, and metallurgical stability and integrity.

17. HTGR Safety Studies for the Directorate of Licensing

J. P. Sanders

Support for this effort was initiated in late November 1972 and continued throughout the year. The initial structure of the work was designed to place certain ORNL personnel in a position to act as consultants to the Gas-Cooled Reactors Branch (GCRB) of the Directorate of Licensing (DOL) in support of their response to licensing applications for commercial HTGR plants.

As a foundation for this task, work was initiated in collecting and evaluating certain basic property data and performance criteria for materials and components. In September 1973, the first licensing topical report[1] was received together with a request from the General Atomic Company (GAC) that it be reviewed so that it could be used as the basis for future license applications.

Upon the receipt of this request, the GCRB staff asked that the efforts at ORNL be devoted mainly to the evaluation of specific sections of the report. This task composed the major effort during the remainder of the year. The Summit PSAR[2] and later the Fulton PSAR[3] were used to provide details concerning the system design and operation in this evaluation effort.

17.1 AN ADIABATIC HEATUP MODEL

W. D. Turner I. I. Siman-Tov

17.1.1 Definition of Problem

One of the first problems to be studied was the development of temperatures in the core of an HTGR following simultaneous loss of forced cooling (LOFC) and reactor trip. Under these conditions, the afterheat remaining in the fuel is distributed by conduction throughout the large mass of graphite in the active core and in the reflector. Historically, this computation was of interest, since it had been determined that, for the Fort St. Vrain (FSV) design, this ultimate accident would result in maximum temperatures that would cause the insulation on the prestressed concrete reactor vessel (PCRV) liner to fail and allow all the afterheat to be conducted to the PCRV liner cooling system without catastrophic damage to the containment vessel.

Natural convection loops within the central core cavity would be formed among the higher power and the lower power refueling regions under normal conditions. The formation of these loops would tend to redistribute the heat within the central core cavity. This effect has been omitted from this series of calculations because the operating specifications, at least for the commercial plants, require that the primary system be depressurized within a limited time following the LOFC accident. Depressurization of the primary system essentially eliminates the effectiveness of the natural convection loops.

The sequence of the task was to evaluate existing general heat conduction computer programs to determine their applicability for this problem, to evaluate the appropriate model for the composite core, to determine the appropriate physical property values for the core components, and to determine the most appropriate specifications for the boundary conditions and the initial conditions for the computation.

The task commenced with a study of the concept of the HTGR and included a review of the thermal analysis

1. V. Joksimovic et al., *An Analysis of HTGR Core Cooling Capability,* Gulf-GA-A12504 (GA-LTR-1) (Mar. 30, 1973).
2. Delmarva Power and Light Company, Summit Power Station, *Preliminary Safety Analysis Report.*
3. Philadelphia Electric Company, Fulton Generating Station, *Preliminary Safety Analysis Report.*

presented in the Fort St. Vrain FSAR.[4] Existing heat transfer codes from Oak Ridge as well as other installations were surveyed, and HEATING4, a modification of the generalized heat conduction code HEATING3, was chosen as the basic tool to be used in the analysis.[5] It was selected due to its flexibility to handle a wide variety of problems, its ease of input data preparation, its ready adaption to other problems, and the experience and knowledge that the staff at ORNL possessed in its development and use. It was felt that this latter aspect would greatly facilitate making modifications in the code to adapt it to a specific application.

17.1.2 Representation of the Nonhomogeneous Core Structure

In developing a model to predict the temperature distribution in the HTGR during a LOFC accident, it is impractical to represent the reactor core in detail since the model must be presented to the heat transfer code as a combination of regions where each region contains a homogeneous material. This is a particularly difficult problem in describing the core of the reactor due to its nonhomogeneous nature.

Figure 17.1 shows the geometry of one-twelfth of the single regular hexagonal element used in the FSV core, and Fig. 17.2 illustrates the complete arrangement of these elements in the core. It is obvious from these figures that a detailed "point-by-point" analysis would require excessive computer core and time; as shown later, this detailed analysis is not necessary. An accurate representation of the effective thermal properties which appropriately depict the transient heat flow must be obtained in order to evaluate their effect on the temperatures of interest. The effective density, specific heat, and volumetric heat generation rate are relatively easy to evaluate, since they depend only upon the volume fraction of each material in the zone. The effective conductivity of the core is more difficult to evaluate, since it involves both parallel and series heat flow by conduction as well as radiation across the coolant channels and the gaps separating fuel elements. As an additional complication, the thermal properties for each material may vary with temperature. For various HTGR core designs, the diameters of the fuel rods and the forced-coolant channels may differ and the fuel-coolant pitch may change from one calculation to another, resulting in a change in the heat flow network.

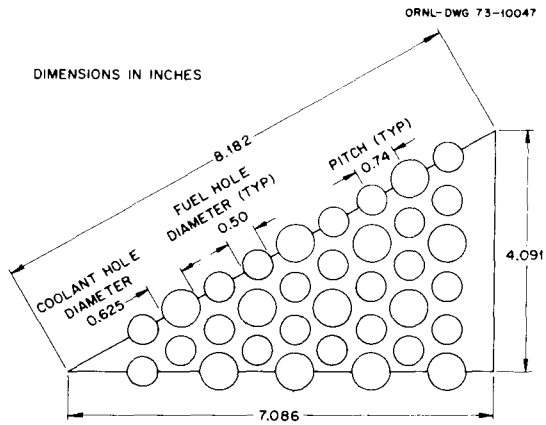

Fig. 17.1. View of one-twelfth of a hexagonal fuel element.

Thus, a study was made to determine the effects of the radial thermal conductivity on the temperatures of interest in the HTGR core during a LOFC accident. First, the technique developed by Gulf General Atomic (GGA) to calculate the effective radial thermal conductivity of the active core of the reactor was evaluated. The unit cell depicted in Fig. 17.3 was devised as an independent check on this technique. The model consisted of a rectangle of graphite containing one-half of a coolant channel and a fuel rod. The ends of the rectangle were insulated, and one side of the rectangle was maintained at a fixed temperature while a constant heat flux was assumed at the other. This defines a typical unit cell at the horizontal midplane of the core of the reactor. The one-half coolant channel was approximated by three rectangles of decreasing size, and the fuel rod was approximated by five rectangles of varying sizes. The area of the approximated regions was equal to the actual areas. One-dimensional radiation parallel to the long axis of the approximating rectangles was considered across the regions defining the coolant channel. The steady-state solution was obtained using the HEATING3 code, and the effective conductivity of the unit cell was calculated by

$$k_e = q' \frac{\Delta L}{\Delta T} \quad , \tag{1}$$

where q is the constant heat flux, ΔL is the thickness of the unit cell in the direction of heat flow, and ΔT is the average temperature drop across the unit cell.

Calculations were made for a boundary temperature T_b of 1500°F, and comparisons were made with the results presented in the Fort St. Vrain FSAR. Calculations could have been made for several values of the

4. Fort St. Vrain Nuclear Generating Station, Final Safety Analysis Report, Public Service Company of Colorado, Denver, Colo.

5. W. D. Turner and M. Siman-Tov, *HEATING3 – An IBM 360 Heat Conduction Program,* ORNL-TM-3208 (February 1971).

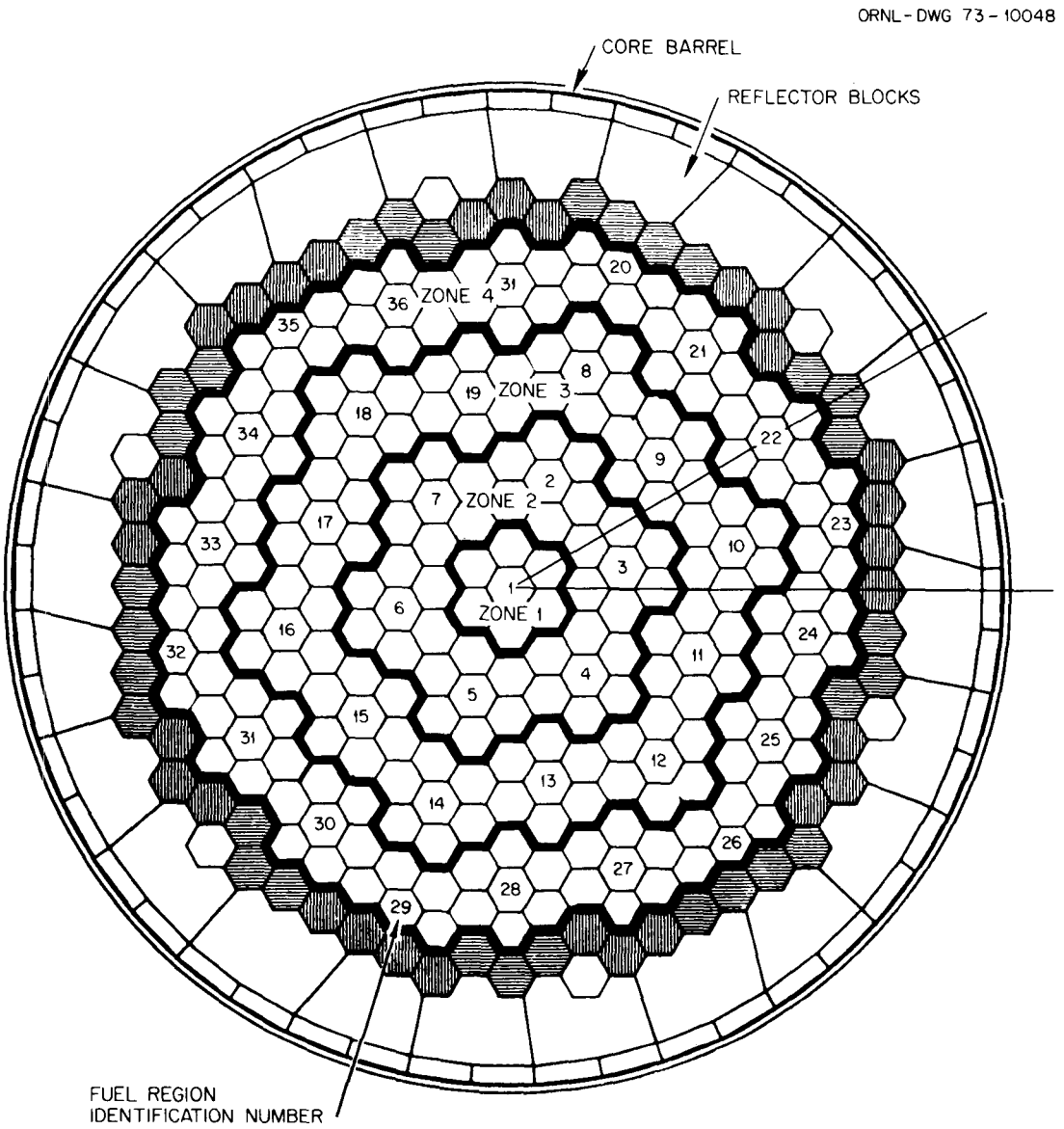

Fig. 17.2. Cross-sectional view of all the elements. Arrangement in the core.

boundary temperature to obtain the temperature-dependent effective radial thermal conductivity, but it was determined in the study that this was unnecessary. By considering both parallel and series heat flow, the following analytical expression was also obtained for the model depicted in Fig. 17.3:

$$K_r = \frac{1}{W} \sum_{i=1}^{7} W_i K_i \,, \qquad (2)$$

where

K_r = effective radial thermal conductivity,
W_i = width of the ith heat flow path,
K_i = effective thermal conductivity of the ith heat flow path,

$$W = \sum_{i=1}^{7} W_i,$$

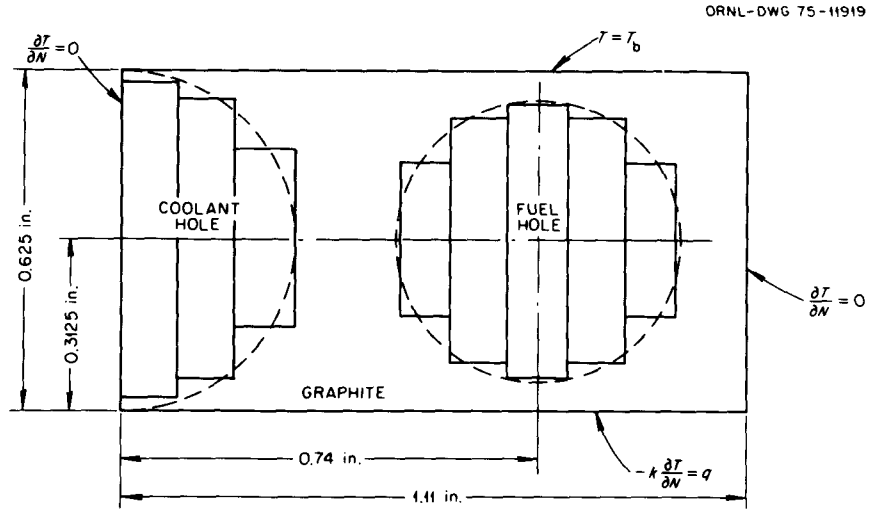

Fig. 17.3. Unit cell for evaluating radial thermal conductivity in HTGR.

$$K_i = \frac{L}{(L_i/k_r) + (L - L_i/k_g)} \qquad i = 1 \text{ to } 3,$$

$$K_i = \frac{L}{(L_i/k_f) + (L - L_i/k_g)} \qquad i = 4 \text{ to } 6,$$

$$K_7 = k_g,$$

L = total length of each of the seven heat flow paths,

L_i = length of the heat flow path in either the coolant or fuel,

k_f, k_g = thermal conductivities of the fuel and graphite respectively,

k_r = effective thermal conductivity across the coolant due to radiation.

The expression derived by Loeb[6] was used for k_r. Effective thermal conductivities as a function of temperature were calculated from Eq. (2) and compared with the curve in Fig. D.1-5 of the Fort St. Vrain FSAR.[4] The two curves have the same general shape. However, the conductivity as calculated from Eq. (2) was 37% lower at 1500°F and 94% higher at 7000°F. The curves crossed at about 5000°F.

6. A. L. Leob, "Thermal Conductivity: VIII, A Theory of Thermal Conductivity of Porous Materials," *J. Am. Ceram. Soc.* **37**, 96–99 (1954).

17.1.3 Evaluation of Effective Thermal Conductivity

Calculations were performed on a series of rather detailed one-dimensional radial models to determine the effects of the radial thermal conductivity on the temperatures obtained in an HTGR core during a LOFC.[7] The one-dimensional models (Fig. 17.4) assumed that the active core was infinite in the vertical direction (or that the vertical extent of the active core was large compared with its radius) and that the active core was homogeneous in the axial and angular directions. The model depicted the reactor from its radial center line to the outer diameter of the PCRV liner, which was assumed to be at a constant temperature of 130°F.

The core is shown divided into regions consisting of composite active elements, side reflectors, spaces between elements, core barrel, gas space separations between the barrel and the liner insulation, and a heat sink at the outer boundary (representing the temperature of the water-cooled PCRV liner).

The active core regions were divided into four radial zones that were used to represent the radial power distribution. The average power levels in each radial zone were taken from Fig. D.1-10 of the Fort St. Vrain

7. I. I. Siman-Tov and J. P. Sanders, personal communication (October 1973).

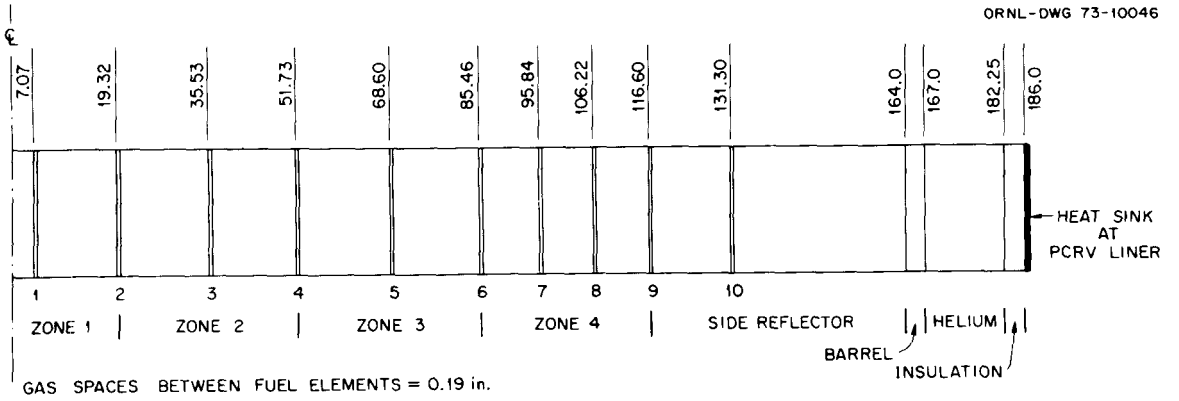

Fig. 17.4. One-dimensional radial model of the HTGR core.

FSAR.[4] An axial midplane power factor of 1.36 was used with these radial power levels; this value was extrapolated from Fig. 3.5-9 of the Fort St. Vrain FSAR. The power decay function following the reactor trip is introduced into the computation as a tabular function derived from Fig. D.1-9 of this FSAR. In the one-dimensional radial model, consideration was given to the relative importance of representing the respective core volumes correctly as opposed to a correct representation of the heat transfer surface. Study led to the choice of the accurate representation of the core volumes. The regions were then constructed in such a way that their volumes were equal to the actual volumes of the elements represented.

This choice ensured the correct representation of the average power concentration and heat capacity of the reactor core. Most of the material properties, including those of the composite fuel elements, were obtained from Table D.3-15 of the Fort St. Vrain FSAR[4] with the exception of the thermal properties of helium.[8] Heat was transferred across the helium spaces between fuel elements both by radiation and conduction.

The first calculation using the geometric representation shown in Fig. 17.4 was divided into four related cases that were tested. For purposes of identification these cases will be denoted I through IV, as follows.

Case I The basic case with effective conductivities derived analytically as described by Eq. (2) with all the spaces between elements represented.

Case II The same calculation with effective conductivities taken from Fig. D. 1-5 of the Fort St. Vrain FSAR.[4]

Case III The same calculation using an effective thermal conductivity of 0.0 for the composite core elements.[9]

Case IV This case is similar to case I, but with no representation of the spaces between the fuel elements.

Three additional models were introduced to evaluate the temperature drop across the fuel rod and to evaluate the composite effective thermal conductivities by using the HEATING4 code. These cases were labeled as follows.

Case V This case is similar to case I; in addition, one fuel rod and the surrounding graphite were represented at the center of the core.

Case VI This case[10] was an entirely different model as shown in Fig. 17.5. It is initiated by using a steady-state calculation of temperatures under normal operating conditions, but neglects further loss of heat to the coolant following LOFC and reactor trip.

Case VII This case, which models a typical conduction radiation heat transfer element in the active core as described by Eq. (1), is used to calculate numerically the effective thermal conductivity in the active core.

8. H. Peterson, *The Properties of Helium; Density, Specific Heats, Viscosity, and Thermal Conductivity at Pressures from 1 to 100 bar and from Room Temperature to about 1800K,* Riso Report No. 224 (September 1970).

9. Since the numerical technique does not allow a conductivity of zero to be put in, a conductivity of 10^{-7} Btu hr^{-1} $in.^{-1}$ $(°F)^{-1}$ was used.

10. This model was not a part of the study, but the results of the calculation pertaining to LOFC are shown here to reinforce the results obtained from case V.

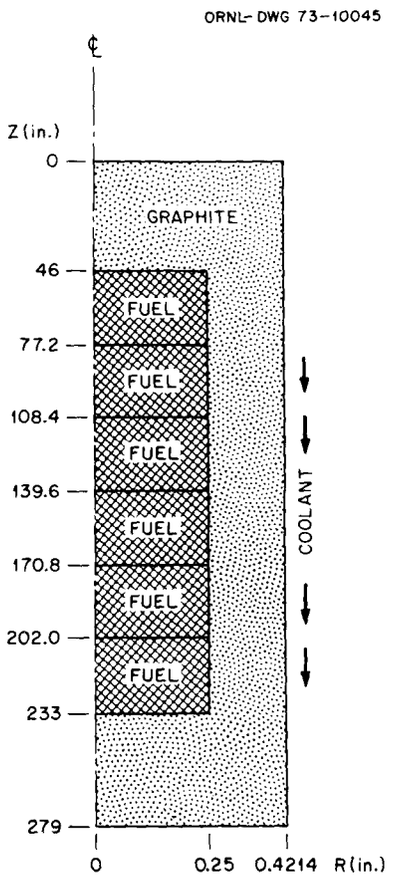

Fig. 17.5. Two-dimensional model of a unit cell for consideration of flow.

17.1.4 Results of Evaluation of Effective Thermal Conductivity

The results of cases I through IV are given in Fig. 17.6. The temperature of the hottest region in the core (at R = 60.3 in.) shows very little dependence on the effective conductivity. For the first 5 hr after LOFC and reactor trip, the temperatures are essentially the same for the first three cases, and within the first 10 hr the difference is within less than 5% of the overall temperature change. At the center line, cases I and II still indicate good agreement within the first 10 hr; but for the case with the thermal conductivity equal to zero, the center-line temperature is lower since no heat is being transferred to it from the hotter regions. The same effect is seen at the interface between the active core and the side reflector.

The best agreement is observed between cases I and IV. At the center line and at the hottest region, these two lines actually coincide (they are within a few degrees of each other); while at the side reflector the temperature of case IV is slightly lower due to the slightly better conduction to the sink through the side reflector.

The results of cases V and VI are given in Figs. 17.7 and 17.8 respectively. Case V demonstrates the temperature changes in a fuel rod situated in the center of the core surrounded by graphite and the composite core as in case I. Within 2 min, the temperatures of the fuel, graphite, and core converge essentially to the same temperature.[11] Case VI uses a different model to calculate the fuel, graphite, and coolant temperatures. For this case, the initial temperature for the transient calculation due to LOFC and reactor trip is determined from a steady-state calculation for the normal operating conditions. The results of this case also demonstrate that within 2 min following the reactor trip, the temperatures of the center line, the fuel-graphite interface, and the graphite-coolant interface approach the same value.

Comparisons between cases I, II, and III imply that the effective radial thermal conductivity has very little effect on the maximum temperatures during the first 10 hr following a LOFC accident with subsequent reactor trip. The results of cases I and II indicate that the temperature distributions in the first 10 hr are not sensitive to a detailed representation of the effective thermal conductivity. A comparison of the results of cases I and IV indicates that the gaps between fuel elements have little effect on heat transport in the core during the first 10 hr and that they are not the principal resistance in the heat transfer of the generated heat to the sink.

The results of cases V and VI indicate that as soon as fission power in the fuel rods is reduced, the temperatures of these rods approach that of the surrounding graphite, allowing one to treat the active core as a homogeneous material with composite properties. This is due to the relative heat capacity and the graphite conductivity. No contact resistance has been considered, but a value of 3 Btu hr^{-1} ft^{-2} $(°F)^{-1}$ was used for the fuel conductivity. This value is lower than experimental thermal conductivities measured for the fuel rods.

11. This case has initial temperatures based on Fig. 3.6-2 of the Fort St. Vrain FSAR. It is not clear that this is realistic but, since the effect of the initial temperature distribution is very quickly dissipated, the results are still valid for the time shortly after the initiation of a reactor trip.

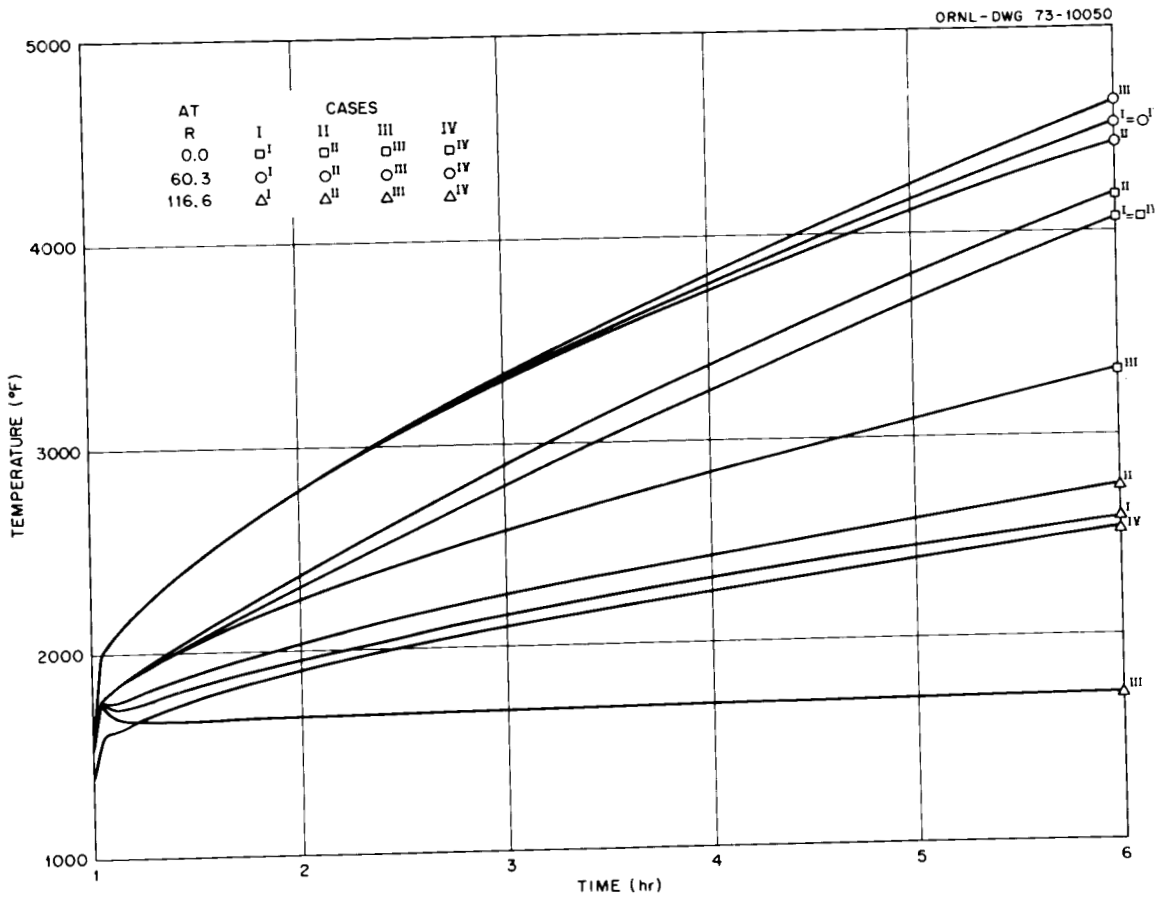

Fig. 17.6. Comparative representation of results for cases I through IV.

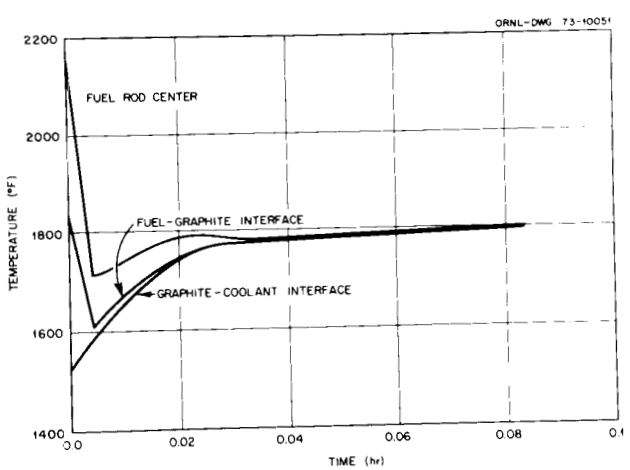

Fig. 17.7. Results for case V.

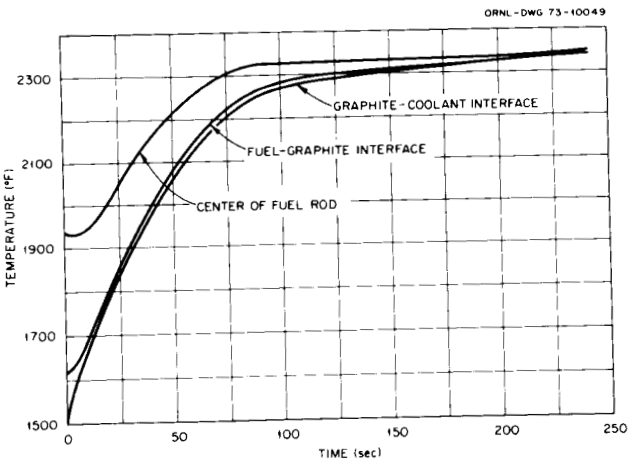

Fig. 17.8. Results for case VI.

Because the heat generation is distributed throughout the core and because of the effect of the annular gas return duct in the FSV design and the PCRV liner insulation, little heat is transported through or out of the core during the first few hours after LOFC and reactor trip. Therefore, the temperature changes are mainly dependent on the heat capacity of the core and the heat generated in it. Although the heat leaving the active core during this time period is small, the thermal properties of the core are such that the transients are small and do not result in any immediate degradation of the core materials.

In evaluating the conclusions made by GGA in the FSAR[4] concerning these transients, it was not necessary to have detailed and very accurate values for the effective thermal conductivities of the composite core. For calculations representing a longer period, when high temperature gradients will be developed or when the PCRV liner insulation fails, this conclusion does not apply.

17.1.5 Development of Two-Dimensional Adiabatic Heatup Model

The one-dimensional radial model was extended to the two-dimensional RZ model depicted in Fig. 17.9.

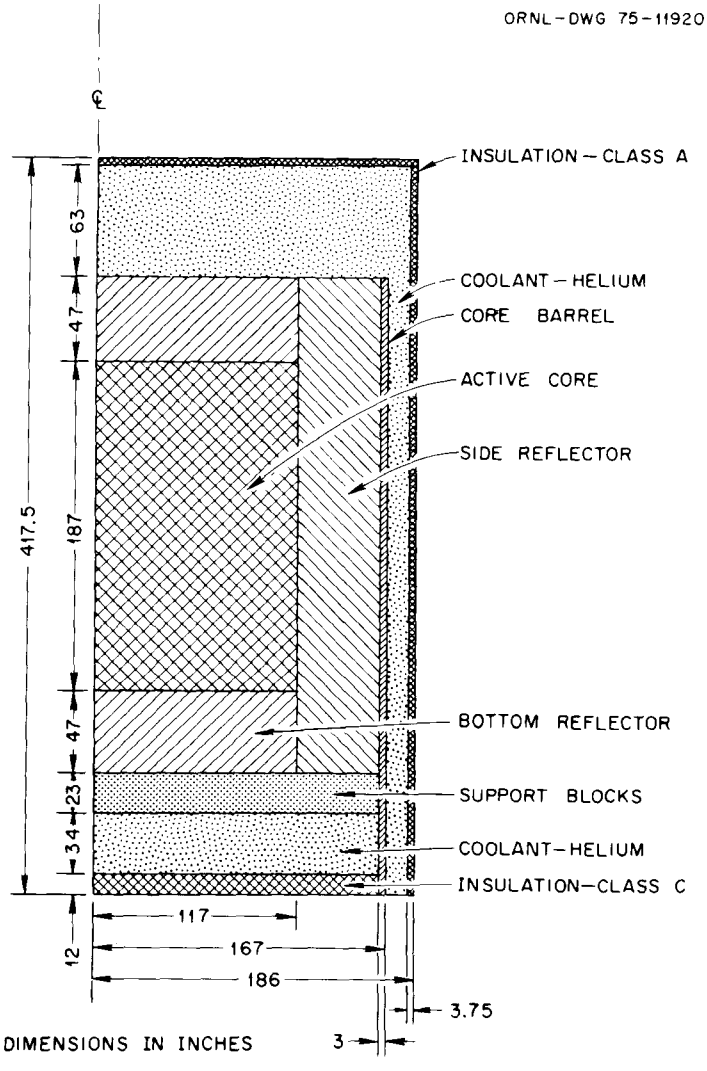

Fig. 17.9. Preliminary RZ model for analyzing LOFC accident.

This model was similar to the one presented in the FSAR for the Fort St. Vrain HTGR.[4]

The model included the active core with spatially distributed fission product decay generation; the top, bottom, and side graphite reflectors; the graphite core support blocks and posts; the steel core barrel surrounding the side reflector; the thermal insulation coversheets; and the helium-filled zones. The thermal conductivity in the active core and graphite reflectors was anisotropic. The temperature-dependent radial thermal conductivity was calculated by Eq. (2), while the temperature-dependent axial thermal conductivity was calculated by

$$k_a = \sum_{i=1}^{3} P_i k_i \quad , \tag{3}$$

where k_a is effective axial thermal conductivity; P_i is percentage of axial cross-sectional area associated with the fuel, graphite, and helium respectively; and k_i is temperature-dependent thermal conductivity for the fuel, graphite, and helium respectively. The composite densities and specific heats in the active core and graphite reflectors are calculated by a volumetric average of the properties of the materials involved. The active core was modeled in the radial direction in the same manner as the one-dimensional radial model presented earlier. Heat was transferred by both conduction and radiation across the helium gaps. The boundary along $r = 0$ was a no-flux surface, whereas the remaining boundaries were held at a constant sink temperature of 130°F on the side wall and top head and 200°F on the bottom.

Results were compatible with the results from the one-dimensional radial model as well as those reported in the Fort St. Vrain FSAR.[4]

17.2 COUPLED CONDUCTION-CONVECTION MODEL (CCCM)

W. D. Turner

17.2.1 Addition of Convection Algorithm to CCCM

One problem that must be addressed during the safety studies of an HTGR involves the determination of the transient temperatures in the active core and along the coolant channels during the system transients that would follow a reactor trip or an abnormal transient condition. A model depicting this type of transient requires an analysis of the total heat transferred to the gas by convection.

A version of the heat transfer code[5] HEATING was modified to include the flow of fluid in a coolant channel. The analysis is restricted to a two-dimensional RZ model or a three-dimensional ROZ model and assumes that the fluid flow is one dimensional along the Z axis. The code yields the steady-state or transient temperature distribution in both the solid materials and the coolant; the calculation requires the mass flow rate and inlet temperature, pressure, and composition of the coolant as input. The equation which determines the temperatures in the coolant for the steady-state problem is

$$\begin{cases} GC_pA_c \dfrac{\partial T(z)}{\partial z} = 2\pi rq \qquad 0 \leqslant z \leqslant L \\ T(0) = T_o \end{cases} , \tag{4}$$

where

G = mass flow rate of the coolant,
C_p = specific heat of the coolant,
A_c = cross-sectional area of the coolant channel,
r = radius of the coolant channel,
q = heat flux normal to the surface of the coolant channel,
T_o = inlet temperature,
L = length of the coolant channel.

For the transient calculations, the governing equation for the temperatures in the coolant channel is

$$\begin{cases} \rho C_pA_c \dfrac{\partial T(z,t)}{\partial t} = 2\pi rq - GC_pA_c \dfrac{\partial T(z,t)}{\partial z} \\ \qquad\qquad 0 \leqslant z \leqslant L,\ t > 0 \\ T(z,0) = f(z) \qquad 0 \leqslant z \leqslant L \\ T(0,t) = T_{\text{in}}(t)\ t > 0 \end{cases} \tag{5}$$

where ρ is the density of the coolant, $f(z)$ is the initial temperature distribution, and $T_{\text{in}}(t)$ is the time-dependent inlet temperature.

These equations were written in finite-difference form compatible with the numerical technique used in HEATING. The calculation of the film heat transfer coefficient to the helium flowing inside the coolant

channels is determined by

$$h = \begin{cases} 0.0196\mathrm{Re}^{0.8}k/d & 4000 \leqslant \mathrm{Re} \\ 0.004GC_p + \left(\dfrac{14.9k}{d} - 0.004GC_p\right)\left(\dfrac{\mathrm{Re} - 2100}{1900}\right) & 2100 < \mathrm{Re} < 4000 \\ 0.656GC_p/\mathrm{Re}^{2/3} & \mathrm{Re} \leqslant 2100 \end{cases} \quad (6)$$

where

h = film heat transfer coefficient [Btu hr^{-1} ft^{-2} $(°F)^{-1}$],
Re = Reynolds number (dimensionless),
k = temperature-dependent thermal conductivity of the helium [Btu hr^{-1} ft^{-1} $(°F)^{-1}$],
d = diameter of the coolant channel (ft),
G = mass velocity of the helium (lb_m hr^{-1} ft^{-2}),
C_p = heat capacity of the helium [Btu lb_m^{-1} $(°F)^{-1}$].

The second part of Eq. (6) is a linear interpolation, based on the Reynolds number, between the first relationship evaluated at Re = 4000 and the third evaluated at Re = 2100.

17.2.2 Addition of Implicit Transient Algorithm to CCCM

Preliminary calculations indicated that the models which would be necessary in the thermal analysis of the HTGR safety studies would require an excessive amount of computing time on the HEATING code to determine the transient temperature distribution over the periods of interest. Many implicit numerical techniques exist which are capable of solving most transient problems faster then the classical explicit procedure which is used in HEATING. However, the adaption of most of them in the code would require extensive revisions as well as curtailments of important features.

It was determined that both the Crank-Nicolson and the classical implicit (backwards Euler) procedures could be incorporated into the current framework of the HEATING computer code without drastically changing the structure of the program. Thus, both techniques were added to the code. The resulting system of equations is solved by point successive overrelaxation iteration, and procedures were incorporated into the code for estimating the optimum acceleration parameter. An iterative procedure based on Carre's analysis[12] was included to estimate the optimum acceleration parameter for problems involving constant coefficients and a constant time increment. For other problems, an empirical procedure was developed which monitors the number of iterations necessary to satisfy the convergence criterion. The acceleration parameter is then updated based on the change in the number of iterations as a function of time.

The implicit procedure incorporated in the HTGR version of HEATING makes this code considerably more efficient than the previous version. For example, the older version required over an order of magnitude more CPU time than the revised code to calculate the transient temperatures for a typical HTGR heat transfer problem. No attempt was made to optimize the time increment for the solution using the implicit procedure, whereas the explicit procedure used the maximum time increment allowed for a stable solution. Comparison of calculations indicated that the solution obtained using the implicit procedure was as accurate as the one obtained using the older version of the code.

This version of the HEATING4 code, which includes both the coupled conduction-convection calculations and the implicit procedure for transient problems as well as other refinements, has been denoted as the Coupled Conduction-Convection Model (CCCM).

17.2.3 Development of CCCM

One of the models that has been developed to analyze the transient temperatures in the active core and coolant channels of an HTGR during an accident condition involving a reduced mass velocity is presented below.

A typical unit cell in an active core during normal operation and reduced flow of coolant is depicted in Fig. 17.10. The three vertical sides are considered to be no-flux surfaces since they represent lines of symmetry. This three-dimensional model can be approximated by the two-dimensional RZ model depicted in Fig. 17.5. Since the heat capacity is the dominant feature in the heat transfer characteristics of the active core, the outer radius of the graphite was chosen so that the volume of the graphite is accurately represented. The six fuel zones are used to approximate the axial power distribution. The bottom of the cylinder and the boundary

12. B. A. Carre, "The Determination of the Optimum Accelerating Factor for Successive Over-relaxation," *Comp. J.* **4**, 73–78 (1961).

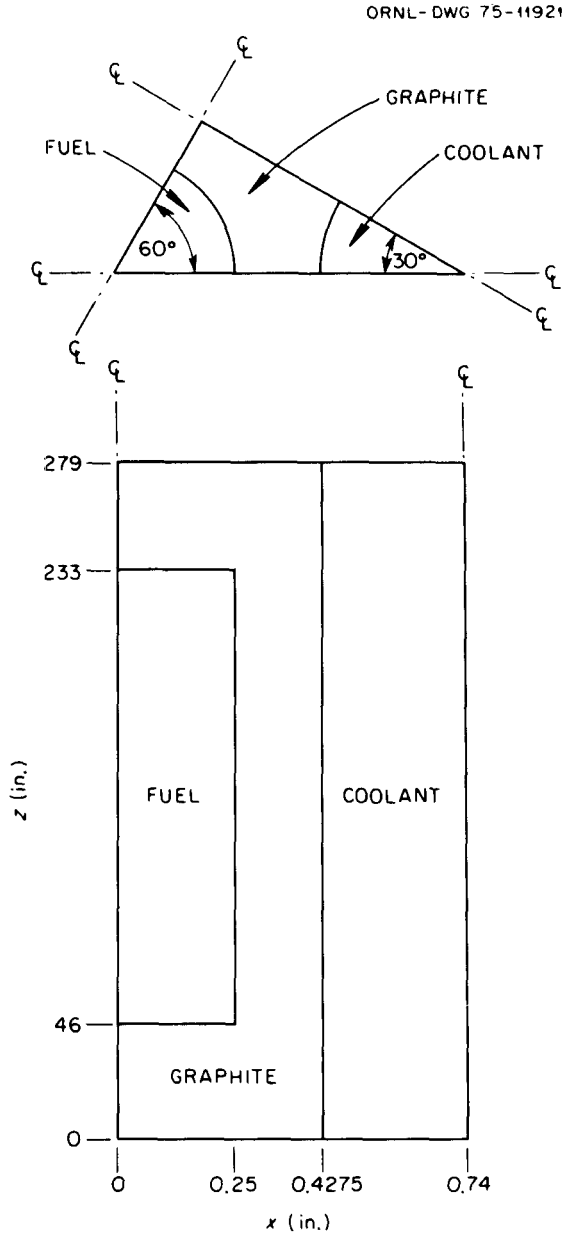

Fig. 17.10. Three-dimensional unit cell in active core during normal operation and reduced coolant flow.

along R = 0 are considered to be no-flux surfaces. At the top of the cylinder, heat is transferred to the coolant by convection and to the superstructure above the active core by radiation. The inlet temperature, the mass velocity, the pressure, and the composition of the coolant and the axial power distribution are represented as functions of time.

17.2.4 Calculations Using CCCM

Based on data received from GGA at our request, we made calculations to predict the transient response of the maximum fuel temperature and coolant exit temperature using GGA's flow rates and inlet temperatures for the following cases involving the 2000-MW(t) Delmarva Power and Light reactor:

A. Reactor trip from 100% power (Fig. 4.3 in Ref. 1).

B. Immediate loss of main loop cooling (LOMLC) followed by shutdown on one core auxiliary cooling system (CACS) loop with a 40-min delay and one main loop helium shutoff valve failed in open position (Fig. 4.20 in Ref. 1).

C. Design base depressurization accident (DBDA) with cooling on the main loops for 12 min and then cooling with one CACS loop 17 min after reactor trip (Fig. 4.28 in Ref. 1).

D. DBDA and a LOMLC with cooldown by one CACS after 5-min delay (Fig. 4.33 in Ref. 1).

Axial temperature profiles for normal operating conditions are presented in Fig. 17.11. The temperature profiles are based on the axial power distribution given by GGA[13] and on a radial power peaking factor of 1.6.

Transient temperature responses for cases A through D are presented in Figs. 17.12 through 17.15 respectively. The maximum fuel temperature and the coolant exit temperature from the ORNL calculations are drawn as a continuous function of time in each of the figures. Data at selected points from the appropriate figures from Gulf-GA-A12504 are also included.[1]

Results for case A

Figure 17.12 shows the temperature for a reactor trip from 100% power with a radial power peaking factor of 1.6. The volume *average* fuel temperature and the average core outlet helium temperature from Fig. 4.3 of Gulf-GA-A12504 are also included. The results agree quite well through the 1-hr time period. Note that the calculated fuel temperatures are for the highest power region and therefore should represent the maximum fuel temperatures as compared with average fuel temperatures presented in Fig. 4.3 of Ref. 1. (Note: The calculations of GGA determine both maximum and average fuel temperatures and these values are dumped on magnetic tape. It is the choice of the person who makes the plots from these tapes as to which values will be presented.) The same distinction is made between

13. R. A. Clark, letter to J. P. Sanders, Sept. 17, 1973.

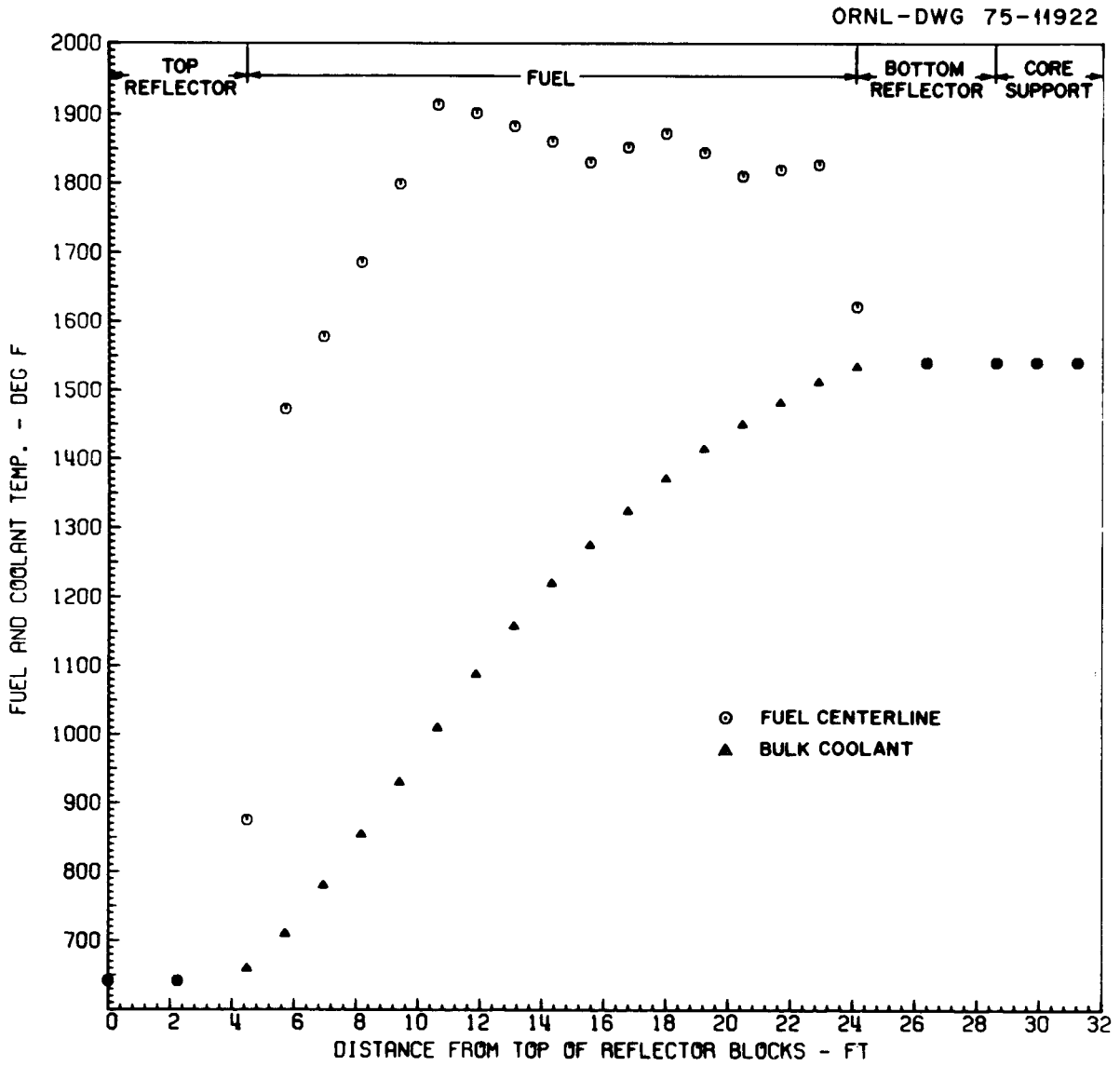

Fig. 17.11. Axial temperature profiles, normal operating conditions, with radial power peaking factor of 1.6.

the two exit coolant temperatures shown in Fig. 17.12; however, if the flow orifices are still effective at the lower flow rates, the exit temperatures of the coolant from all channels should be about the same.

Results for case B

The temperatures for an immediate LOMLC followed by shutdown on one CACS loop after a 40-min delay with one main loop helium shutoff valve failed open are presented in Fig. 17.13. The maximum fuel temperature and the core maximum coolant outlet temperature from Fig. 4.20 of Gulf-GA-A12504 are indicated in the figure. For times less than 2.75 hr, the Reynolds number was determined to be less than 4000. The ORNL calculations indicate that the maximum fuel temperature is 1914°F at normal operating conditions; 30 sec after LOMLC, this maximum fuel temperature drops to a value of 1708°F and then increases to a maximum value of 2622°F at 40 min when operation of the CACS loop is initiated. After 6 hr, the maximum fuel temperature is 510°F.

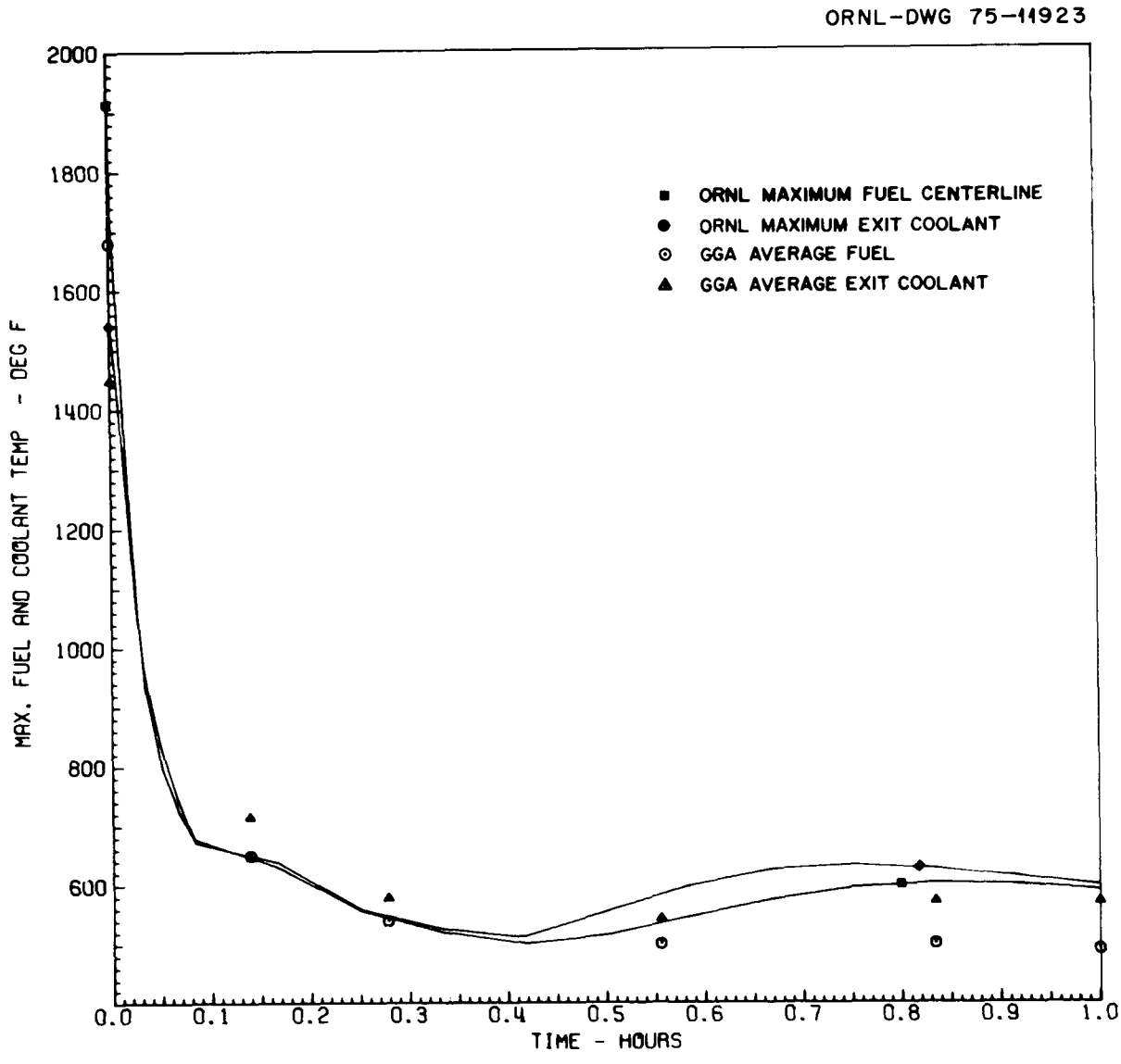

Fig. 17.12. Partial comparison of GGA and ORNL plant transients following reactor trip from 100% power (see Fig. 4.3 of Gulf-GA-A12504) with radial power peaking factor of 1.6.

Both the maximum fuel temperature and the maximum outlet coolant temperature are below values calculated by GGA for most of the transient. This is due to the fact that the GGA calculations include the buoyancy effect of the hot gas in the channel with a higher power density compared with cooler gas in channels with lower power density. This effect, which is not presently included in the ORNL calculations, will be most prominent for those cases where the gas pressure is higher, the gas flow rate is very low, and the delay time to start of forced convective flow is long. All these characteristics are found in case B.

Note that even though reverse flow is prohibited by the relatively low gas flow in this case, there is a "tendency" toward the formation of a natural convection loop that impedes forced convective flow in the hotter channels and enhances it in the cooler channels.

Results for case C

The temperatures for DBDA with cooling on the main loops for 12 min followed by cooling with one CACS

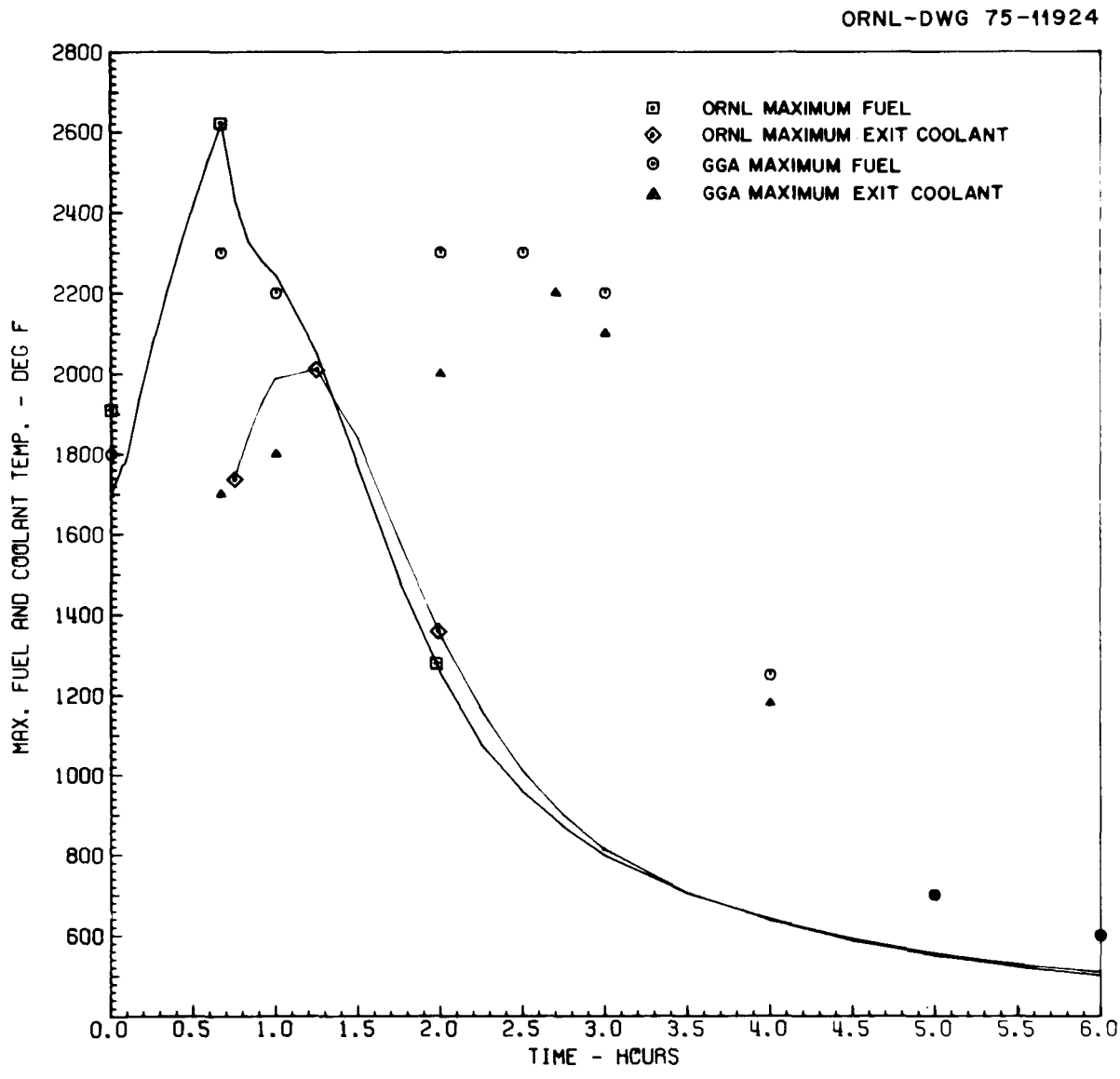

Fig. 17.13. Partial comparison of GGA and ORNL plant transient responses for immediate LOMLC with shutdown on one CACS loop after a 40-min delay and one main loop shutoff valve failed in open position (see Fig. 4.20 of Gulf-GA-12504) with radial power peaking factor of 1.6.

loop 17 min after reactor trip are presented in Fig. 17.14. The maximum fuel temperature and the core maximum coolant outlet temperature, taken from Fig. 4.28 of Gulf-GA-A12504, are identified. The maximum fuel temperature during normal operating conditions as calculated by ORNL is 1903°F. The Reynolds number drops below 4000 at about 2 min after initiation of the depressurization accident. The maximum fuel temperature drops to a minimum of 1347°F at 10 min and then increases to a maximum of 1727°F at 1.5 hr. Ten hours after reactor trip, the maximum fuel temperature is 989°F and is decreasing.

The general curve indicated by the ORNL calculations is quite similar to that presented by GGA. Again, the temperatures calculated by ORNL are lower because the effect of reduced flow in the hot channel due to the buoyancy of the hotter gas is not included in the ORNL calculations at present. This effect is less than in case B

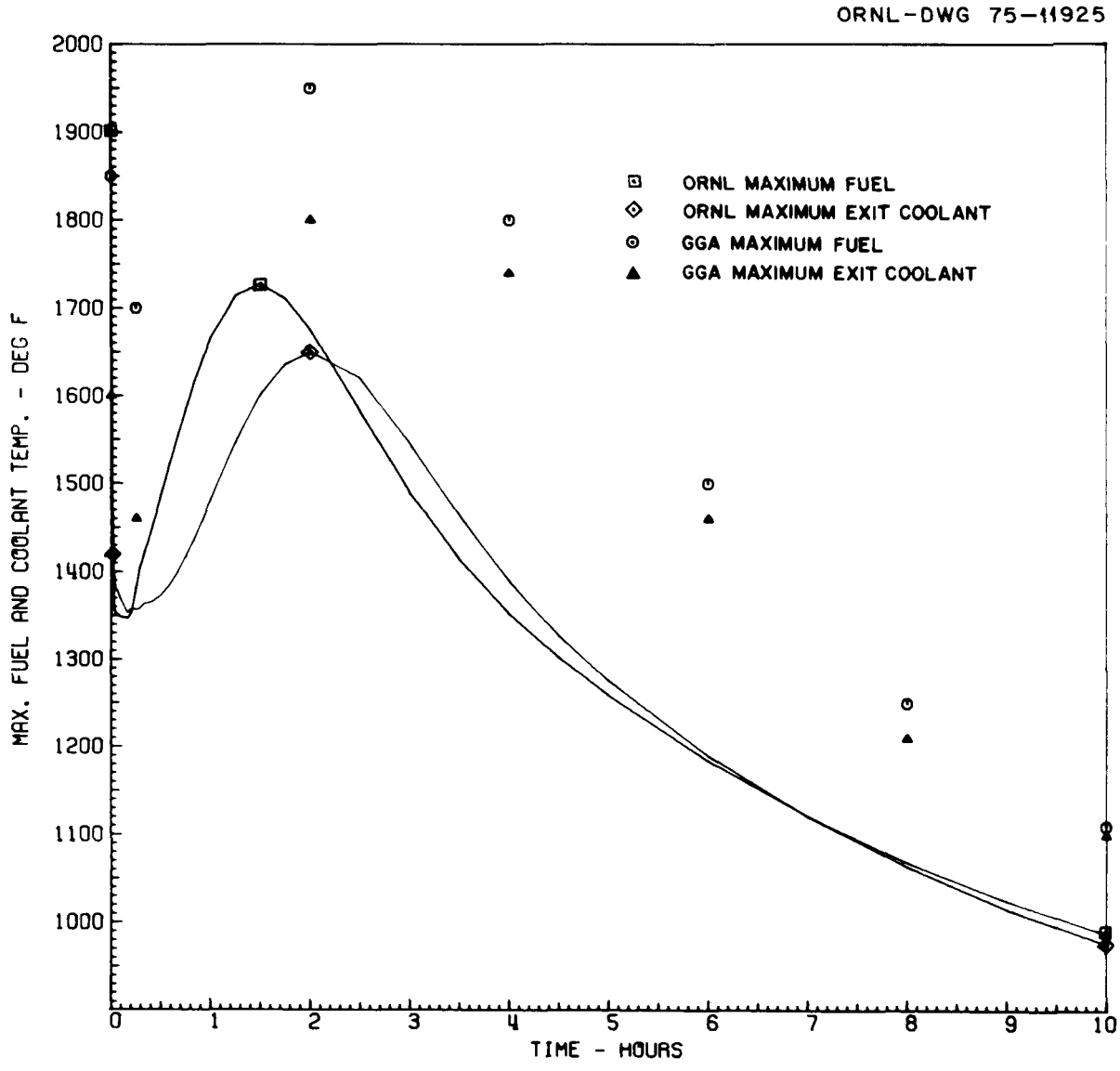

Fig. 17.14. Partial comparison of GGA and ORNL plant transient responses for DBDA with cooling on main loops for 12 min and cooling with one CACS loop 17 min after reactor trip (see Fig. 4.28 of Gulf-GA-A12504) with radial power peaking factor of 1.6.

due to the fact that the pressure is much lower, the gas density is lower, and therefore the density difference is less.

Results for case D

The temperatures for DBDA and LOMLC with cooldown by one CACS after a 5-min delay are presented in Fig. 17.15. The maximum fuel temperature and the core maximum coolant outlet temperature, as presented by GGA in Fig. 4.33 of Gulf-GA-A12504, are indicated. The ORNL calculations show the maximum fuel temperature during normal operating conditions as 1914°F. The maximum fuel temperature drops to a minimum of 1708°F at 30 sec after initiation of the accident, increases to a maximum of 2095°F at 1 hr, and drops to 1403°F at 6 hr. When the CACS is activated, the Reynolds number is below 4000.

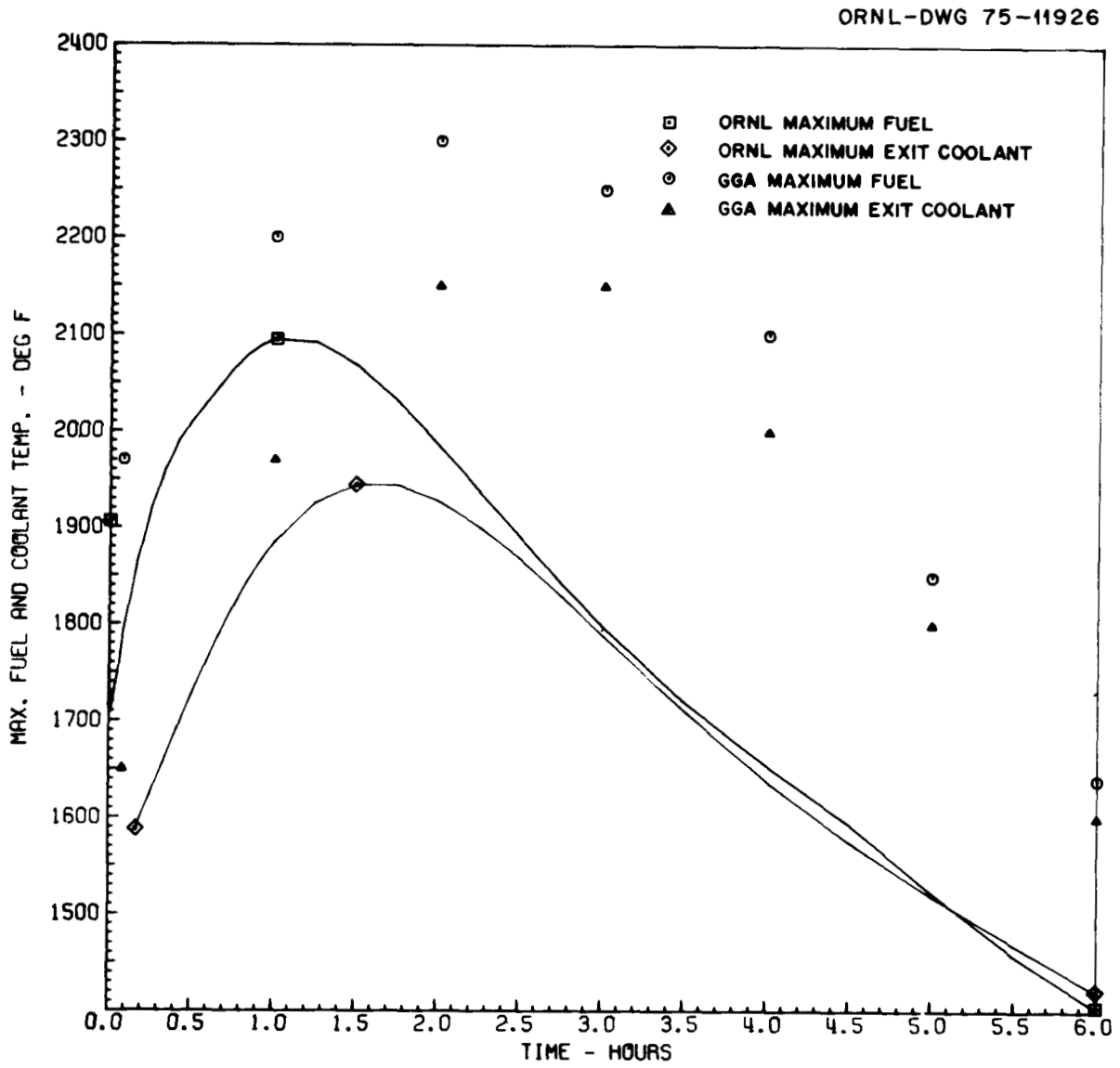

Fig. 17.15. Partial comparison of GGA and ORNL plant transient responses for DBDA and a LOMLC with cooldown by one CACS loop after 5-min delay (see Fig. 4.33 of Gulf-GA-A12504) with radial peaking factor of 1.6.

As with case C, the values calculated at ORNL for the coolant and fuel temperatures in case D are lower than those presented by GGA. Again, the difference arises from the absence of the buoyancy effect in the hot channel in the ORNL calculations. The effect is more pronounced for case D than for case C due to the absence of the short period of operation on the main loop, which cooled down the entire core at the beginning of the accident.

Further code developments

In addition to the exclusion of the natural convection buoyancy effects in the ORNL calculations, the effect of the orifice settings at the reduced flow rates have not been included. It is assumed that the orifices have been positioned to appropriately distribute flow during full-power operation. Under these full-flow conditions, the pressure losses over the orifice plus entrance and

exit effects are proportional to the velocity squared, while the pressure loss due to friction in the channels is proportional to the velocity to the 1.8 power. In the laminar range, the same type of relationship holds for the contraction and expansion losses, but the frictional losses are now proportional to the velocity squared. At the same time, the relative losses due to contraction and expansion and friction are changing as the flow decreases.

These two effects, which are to some degree interrelated, must be included to modify the distribution of total coolant flow stipulated by GGA for the core. An additional subroutine will be inserted in the ORNL calculations to provide the proper amount of coolant flow to the channel with the higher power density.

It was noted in the ORNL calculations that the maximum fuel temperature shifted axially downward after scram of the reactor and subsequent reduced flow of coolant. This is due to the fact that the peak axial power occurs in the upper third of the core. During the transient, heat is convectively transported from this axial position to the cooler lower portions of the core, and thus, the maximum fuel temperature migrates downward. This effect is also evident in the curves presented by GGA and confirmed by discussion with George Malek.

The required modifications will be made in the ORNL computations to reflect these requirements to accurately represent the conditions at these low coolant flows.

Development of plotting package to aid in analysis of results from heat transfer codes

A computer code has been developed to create graphical output to facilitate interpretation of the results from the HTGR models which are solved on the HEATING code. The graphical output includes the transient response of the maximum fuel temperature and the coolant exit temperature as well as axial temperature profiles through the fuel and the coolant channel. However, the plotting code is not fully operational.

17.3. FAILURE OF FUEL PARTICLES UNDER HTGR OPERATING CONDITIONS

T. B. Lindemer F. J. Homan

In establishing the temperature links for the operation of the fuel in the HTGR, basic studies were initiated relative to two failure mechanisms. The first was the mass transport, or "Amoeba," effect that results for the thermal gradient across the fuel particle during operation. The second was directed toward an evaluation of the stresses that develop in the particle coating due to irradiation damage and changes in temperature levels.

17.3.1 Failure of Particles by Mass Transport in a Temperature Gradient

The work represented by this phase of the study was documented in a topical report that developed the model for chemical failure of coated particle fuels. The work was based on the model that in HTGR fuels, failure can occur as the result of irradiation damage, high internal pressure, or chemical reaction. Failure is aggravated by increases in temperature (or power density), which can occur in nuclear reactor accidents. Coating failure constitutes removal of a protective boundary and results in increases in fission product release rates from coated particles. This release could result in a gradual increase in the coolant circuit fission product inventory providing that this failure rate is appreciable. This inventory is the major source of radioactive material that must be considered in the analysis of a hypothetical depressurization accident.

Definition of failure temperatures with respect to operating temperature allows assessment of the necessary rate of response of protective systems and the description of the consequences of cooling accidents.

Codes exist for the analysis of performance under normal conditions, but they do not emphasize chemical phenomena such as mass transport involved in fuel failure. Therefore, this subtask will concentrate on such chemical phenomena.

Carbide fuels

Descriptions of carbon or fuel transport under nonisothermal conditions across coated (U, Th)C_2 and ThC_2 kernels by a solid-state thermal diffusion process appear to be adequate and can be obtained from existing reports.[14] We will use this information to predict particle failure during the next several months as abnormal conditions of temperature and temperature gradient under accident conditions become available to us from other tasks within this study.

Oxide fuels

Other less well understood mechanisms involving transport of carbon by its gaseous oxides appear to be

14. C. B. Scott and O. M. Stansfield, *Stability of Irradiated Coated-Particle Fuels in a Temperature Gradient,* Gulf-GA-A12081 (September 1972).

associated with failure of oxide fuels. The irradiation behavior of urania-bearing particles is observed to include the eventual release of fission gas from the particle when a temperature gradient exists across the particle. An empirical correlation for this release is available from the results from the Dragon project.[15] This failure of the coating of the particle is associated with the transport of carbon from the hot to the cold side of the particle and with the movement of the kernel up the temperature gradient. Mechanisms that may produce the transport of carbon have been proposed in the literature, but prior to our recent work, no mathematical model has been available to predict the behavior observed in the studies from the Dragon project.

Recently we have developed a model that is based on the transport of carbon by the interdiffusion of CO and CO_2 across the temperature gradient. This model assumes a uniform total pressure of all gases in the particle and local equilibrium in the C-CO-CO_2 system; the latter condition establishes a gradient in the partial pressure of CO and CO_2 and the conditions necessary for transport of carbon. Three forms of the model have been developed and are given below.

SiC-containing (Triso) particles. The analysis of the Dragon project data[15] led us to the conclusion that the SiC layer was chemically buffering the pressure of carbon monoxide in the particle to that for the SiC-CO-C-SiO_2 equilibrium. Under these conditions, the mathematical form of the carbon-transport equation appears to be

$$M = \frac{t(P_{CO} + P_{CO_2})}{F_f(nRT/a\theta)} \frac{\epsilon'}{q'} \frac{dT}{dz} k P_{CO} \times \ln \left[1 + \frac{(nRT/a\theta)F_f}{P_{CO} + P_{CO_2} + P_i} \right] , \quad (7)$$

where

a = ratio of the void space in the buffer layer/kernal volume;
F = fissions per initial heavy metal atom (FIMA), %;
f = final;
ϵ'/q' = geometrical factor, ~0.017;
i = initial;
M = thickness of carbon removed, μm;
n = moles of fission gas per mole of fuel per % FIMA, ≈0.003;
P_{CO} = average partial pressure of CO;
P_{CO_2} = average partial pressure of CO_2;
P_i = partial pressure of the coating gas entrained in the buffer layer;
R = 82.06 atm cm^{-3} $mole^{-1}$ $(°C)^{-1}$;
k = rate of carbon transport via interdiffusion in the CO-CO_2 system, $\mu m\ hr^{-1}$ $(°C/cm)^{-1}$ atm^{-1} (see Fig. 17.16);
T = average temperature, °K;
t = time at temperature, sec;
dT/dz = temperature gradient, °C/cm;
θ = molar volume of the fuel, cm^3/mole.

This model appeared to adequately describe the behavior of the Dragon project fuel within their temperature range of 1425 to 1900°C and may be useful for calculation of failure of Triso fuels under the conditions defined in this DRL work. However, it should be cautioned that the present mathematical model has not been tested on Triso fuels designed and operated under conditions prevalent in the U.S. gas-cooled reactors. Therefore, the results obtained from such calculations should be considered tentative.

Biso (pyrocarbon coatings only) particles in reactor. In the absence of the SiC coating, no chemical system is apparent for maintaining P_{CO} at a fixed value; it may therefore vary with burnup because the consumption of oxygen by oxide-forming fission products does not exactly equal that released by UO_2 upon fissioning. A model has been developed to accommodate the variation of P_{CO} with burnup; this model is based on a linear release of CO with burnup and is

$$M = \frac{t(dT/dz)(\epsilon'/q')k}{F_f \frac{RT}{a\theta}(m+n)} \left\{ \left[b^2 - \frac{mb(b+P_g)}{m+n} + \frac{m^2(b+P_g)^2}{(m+n)^2} \right] \ln \left[1 + \frac{(m+n)\frac{RTF_f}{a\theta}}{b+P_g} \right] + \frac{mRT}{a\theta} \left[b - \frac{m(b+P_g)}{m+n} \right] F_f + \tfrac{1}{2} \left(\frac{mRT}{a\theta} \right)^2 F_f^2 \right\} , \quad (8)$$

in which b is initial pressure of P_{CO} (atm) and m is moles of carbon monoxide generated as a result of burnup per mole of fuel oxide per % FIMA. It is evident

15. L. W. Graham, "The Development and Performance of HTR Core Materials," pp. 494–517 in *Proceedings of Gas-Cooled Reactor Information Meeting, Oak Ridge National Laboratory, Apr. 27–30, 1970*, CONF-700401.

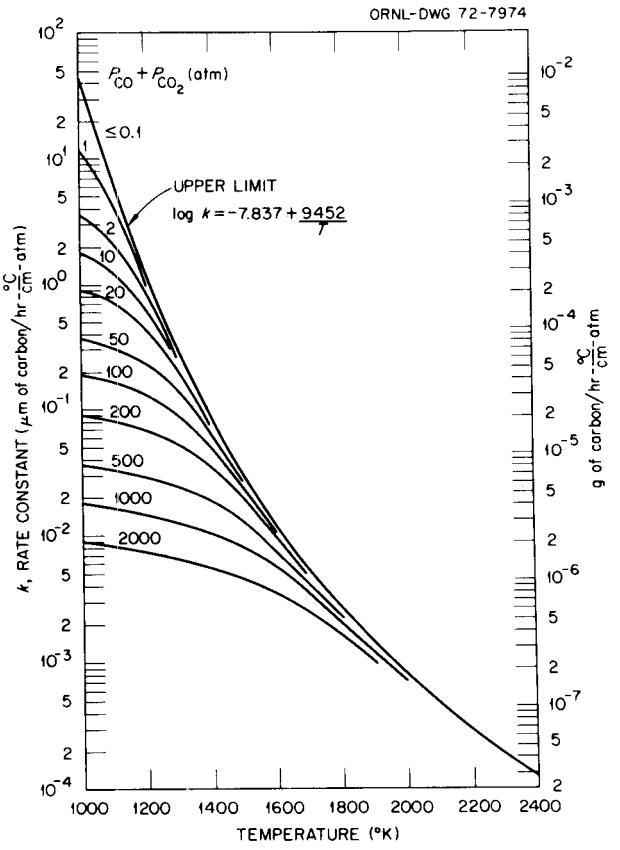

Fig. 17.16. Temperature and pressure dependence of the rate constant k for carbon transport via interdiffusion in the CO-CO_2 system.

that if m = 0, Eq. (8) reduces to Eq. (7). Again, this equation has not been applied to interpretation of actual irradiation results because such results are just becoming available under conditions where the values of m, temperatures, and temperature gradients are sufficiently known. Therefore, any predictions made with the model must be considered tentative.

Out-of-reactor Biso model. Here the pressures of CO and other gases in a coated particle are invariant at a given temperature, and the model for carbon transport becomes

$$M = \frac{\epsilon'}{q'} kt \frac{dT}{dz} P_{CO} \frac{P_{CO} + P_{CO_2}}{P_{CO} + P_{CO_2} + P_g} \quad . \tag{9}$$

Present calculations indicate that this model predicts failure of as-coated Biso coatings in out-of-reactor tests under conditions where actual experiments do not demonstrate failure. Since the out-of-reactor model is based on well-known simple theories and well-defined experimental data, there is no clear reason why the model calculations and experimental results disagree. Either the failure mode is controlled by a slower process, such as a chemical reaction of CO, CO_2, and carbon, or the experimental data were not taken with techniques sensitive enough to reveal failure of the coatings.

In this reporting period, computer codes for the calculation of the rate of thinning of the pyrocarbon coatings by CO-CO_2 interdiffusion in the buffer layer of the oxide-fueled particles have been under development. These results are compared with observed behavior in oxide fuels and with rates of the decomposition reaction $2CO \rightarrow CO_2 + C$ in an attempt to test the validity of the model. We are currently attempting to resolve this out-of-reactor discrepancy because of its pertinence to the in-reaction Biso model.

We are continuing to interpret the very minimal available experimental data for carbon transport by the CO-CO_2 mechanism in oxide particles. Some data are available from a KFA report[16] for carbon transport and subsequent kernel movement in as-coated UO_{2+x} particles. For such a system our mathematical model[17] suggests

$$M = \frac{\epsilon'}{q'} kt \frac{dT}{dz} P_{CO} \frac{P_{CO} + P_{CO_2}}{P_{CO} + P_{CO_2} + P_g} \quad , \tag{10}$$

where

M = carbon transported (μm),
ϵ'/q' = ratio of observed diffusion coefficient to that in free space (dimensionless),
k = rate constant for the C-CO-CO_2 system,
$\log k = -7.837 + 9452/T$ (Ref. 17),
t = time (hr),
dT/dz = temperature gradient (°C/cm),
P_{CO}, P_{CO_2} = pressure of CO or CO_2 (atm),
P_g = pressure or residual coating gases, usually 1 atm.

In the KFA experiments at 1700°C the as-coated value of O/U was 2.005; upon subsequent heating, the

16. A Nauomidis, R. Rotterdam, and B. T. Thiele, Tech. Rept. KFA-IRW-IB 2/72, pp. 13–16 (January 1972).

17. T. B. Lindemer and H. J. de Nordwall, *An Analysis of Chemical Failure of Urania Fuel Particles in the High-Temperature Gas-Cooled Reactor,* to be published as an ORNL-TM report.

O/U would be reduced to 2.000 and the hyperstoichiometric oxygen would react with carbon to form CO. The value of P_{CO} can be calculated from the ideal gas law; the ratio of free volume in the buffer layer to the superficial volume of the kernel calculated from the photomicrographs in the report, assuming a 50%-dense buffer layer, was 0.82. The value of P_{CO} was therefore 40.0 atm. In the KFA experiments, they observed metallographically that M = 70 μm at 1700°C in 480 hr at dT/dz = 200°C/cm. We can predict what M should be from the above equation with ϵ'/q' = 0.017 obtained from our analysis of the Dragon Project empirical correlation.[15] We calculate M = 58 μm, which is in good agreement with the observed behavior.

The KFA work with kernels having an O/U of 2.000 in the as-coated condition was performed over the temperature range of 1400 to 1800°C for times up to 720 hr at dT/dz = 200°C/cm. The value of P_{CO} is not known, but values of 1 to 10 atm are indicated from the measurements of Bildstein and Strigl.[18] At 1400°C, Eq. (10) would give 8 to 160 μm of carbon transported, depending on whether the low or high value of P_{CO} is used; while at 1800°C, 0.6 to 6.0 μm is predicted. It is doubtful whether <10 μm of transported carbon would be observable metallographically because the carbon transported to the cold side would probably just densify the buffer layer. In view of the uncertainty in the value of P_{CO}, it would appear that the lack of observable transport is not inconsistent with the predictions of the above equation.

We are currently applying the mathematical model to three different situations: to Triso and Biso particles during irradiation and to as-coated particles out of reactor. To date, the Triso model used for the Dragon Project data[15] and the as-coated model analyzed above appear to agree with experimental work. The Biso in-reactor particle model does not agree at present, and work is continuing on this calculation as information becomes available.

17.3.2 Coated-Particle-Performance Modeling

The objective of this work is to provide evaluations of fuel degradation (stress analysis) for the U.S. AEC Directorate of Licensing. During the present reporting period, the three coated-particle-performance codes available to us have been obtained and made operational on our computers. These codes, STRETCH,[19-21] TRISO,[22,23] and STRESS-2,[24-26] each have unique capabilities and characteristics. STRETCH is capable only of analysis of Biso particles, TRISO of Triso particles, and STRESS-2 of any combination of coatings up to a total of six.

Of the three codes, STRESS-2 is potentially the most useful. In addition to its flexibility in being able to model both Biso and Triso particles, it is substantially more sophisticated than the other two codes. It considers such events as gap formations between layers and subsequent closing of the gaps, failures of the inner layers, and the subsequent changes in stresses and displacement of the outer layers. Since the various coatings are deposited at different temperatures, stresses can arise before irradiation begins from thermal sources. STRESS-2 has an option which permits inclusion of the fabrication stages in the performance history of the coated particle.

All the codes require relatively small amounts of computer time (about 30 sec for a single case of an IBM 360/91 computer) and require modest core storage (less than 200 K bytes).

All three codes have certain limitations, and the limitations are similar. In each case the properties of the kernel and coating are dose dependent but not temperature dependent. This implies that the coated particle will operate at one temperature during irradiation and precludes accurate evaluation of the consequences of temperature changes.

Of the three codes, only STRETCH calculates the operating temperature of the kernel and coatings from

18. H. Bildstein and A. Strigl, *Determination of Gases in Low Enriched Coated Oxide Particles,* Dragon Project Report 728 (August 1970). Reference used with permission of Dragon Project.

19. J. W. Prados and J. L. Scott, *Mathematical Model for Predicting Coated Particle Behavior,* ORNL-TM-1405 (March 1966).

20. J. W. Prados and T. G. Godfrey, *STRETCH, A Computer Program for Predicting Coated-Particle Irradiation Behavior, Modification IV,* ORNL-TM-2127 (April 1968).

21. J. W. Prados and J. L. Scott, "Mathematical Model for Predicting Coated Particle Behavior," *Nucl. Appl.* **2**, 402–14 (October 1966).

22. J. L. Kaae, "A Mathematical Model for Calculating Stresses in a Pyrocarbon- and Silicon Carbide-Coated Fuel Particle," *J. Nucl. Mater.* **29**, 249 (1969).

23. J. L. Kaae, "A Mathematical Model for Calculating Stresses in a Four-Layer Carbon-Silicon Carbide-Coated Fuel Particle," *J. Nucl. Mater.* **32**, 322 (1969).

24. H. Walther and P. G. Novario, *Stress Analysis in Coated Particle Fuels, Part I: Theory and Examples, Part II: Computer Programme Stress I,* D. P. Report 604 (August 1968) (Part II, July 1969).

25. K. Bongartz, *Theoretical Investigations of Coated Particle Fuel Performance by Stress Analysis,* D. P. Report 648 (May 1969).

26. H. Walther, *A Model for Stress Analysis in Coated Fuel Particles,* D. P. Report 683 (October 1969).

the cross section and neutron fluxes input. Thus, it appears that STRETCH would be the easiest to modify for cyclic irradiation histories, but the problem of introducing temperature-dependent properties would still remain. STRETCH and TRISO do not have failure models included, and failure of the coatings must be implied from the stresses calculated. As indicated, STRESS-2 calculates coating failures directly and, in addition, calculates the consequences of the failure on the remaining unfailed layers during subsequent irradiation.

Comparison of STRESS-2 and TRISO

In performing the comparison of these two codes, we have selected a Triso particle described in a recent paper by Gulden et al.[27] The particle design characteristics and performance predictions (determined by GGA using TRISO) presented by Gulden are shown in Fig. 17.17. Unfortunately, the materials properties assumed

27. T. D. Gulden et al., "The Mechanical Design of TRISO-Coated Particle Fuels for the Large HTGR," *Nucl. Technol.*, **16**(1), 100–9 (October 1972).

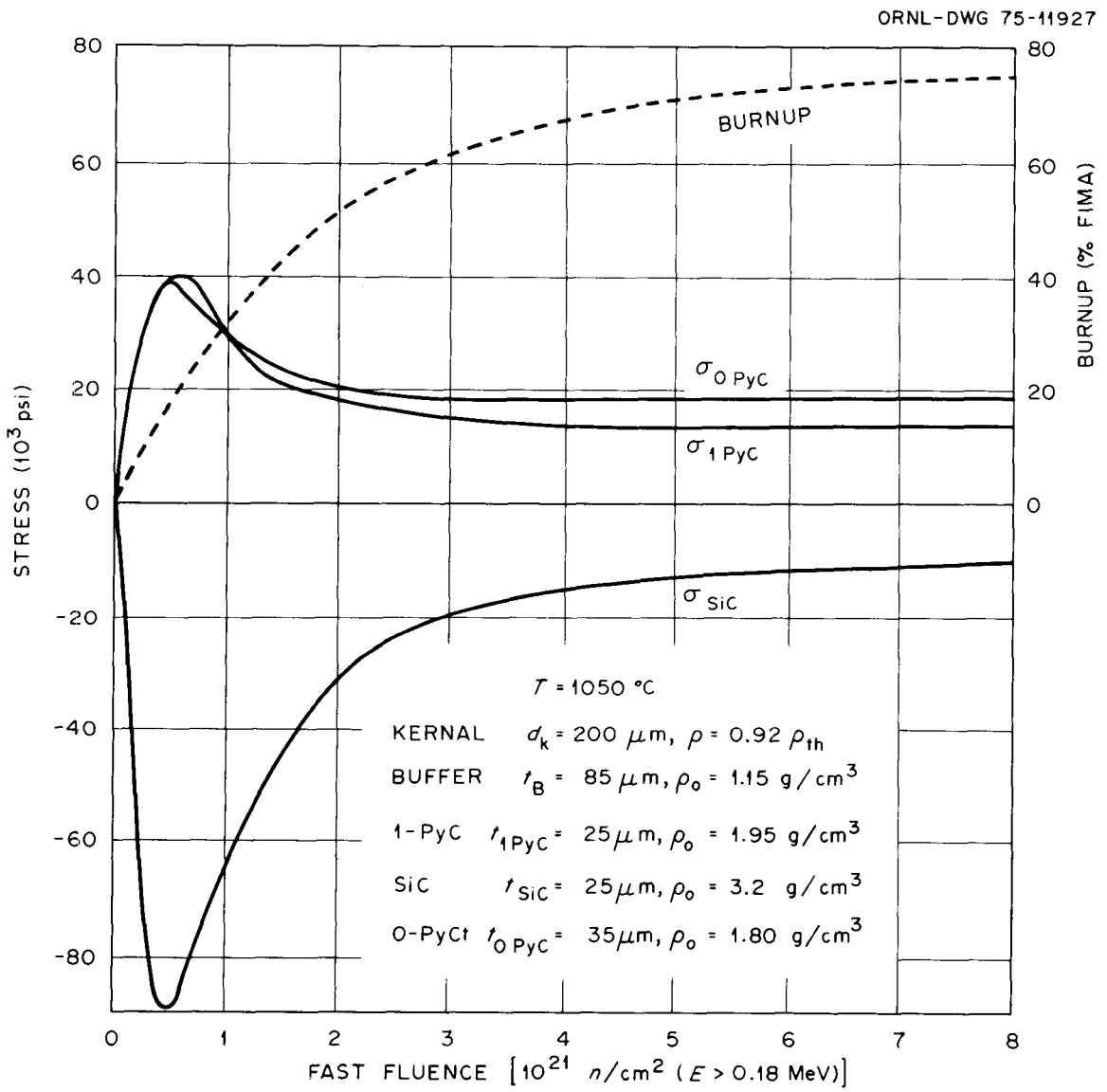

Fig. 17.17. Coating stresses in Triso fissile particle.

for the kernel and coatings were not described in the paper, so property values extracted from the literature were used. The two most important properties in the predictions of performance under irradiation are the creep constant and the irradiation-induced deformation characteristics of the PyC layers. We used a creep constant of 1.0×10^{-27} $(psi)^{-1}$ $(neutrons/cm^2)^{-1}$ and irradiation deformation characteristics described by the broken curve in Fig. 17.18. The data of Kaae et al.[28] were applied to both PyC layers even though there was a slight difference in density between the inner and outer PyC layers. Using these data in both codes, the predicted performances shown in Fig. 17.19 were obtained. The very high densification rates derived from the data shown in Fig. 17.18 (broken curve) resulted in failure predicted for the inner PyC layer by STRESS-2; TRISO does not indicate failure.

To continue the comparison, the failure stress used in the input to STRESS-2 was increased, and the case was rerun to obtain a valid comparison. As can be seen from Fig. 17.19, the two codes compare very well. The gas pressures predicted by TRISO are slightly higher than those predicted by STRESS-2, but this can be partially explained in the differences in burnup used. STRESS-2 does not calculate burnup, and a burnup-vs-fluence relationship must be included in the input. We used the curve shown in Fig. 17.17. TRISO computes the burnup relationship, and for the case studied, this burnup was slightly higher than that used in the input for STRESS-2. The burnup curve comparison is shown in Fig. 17.20.

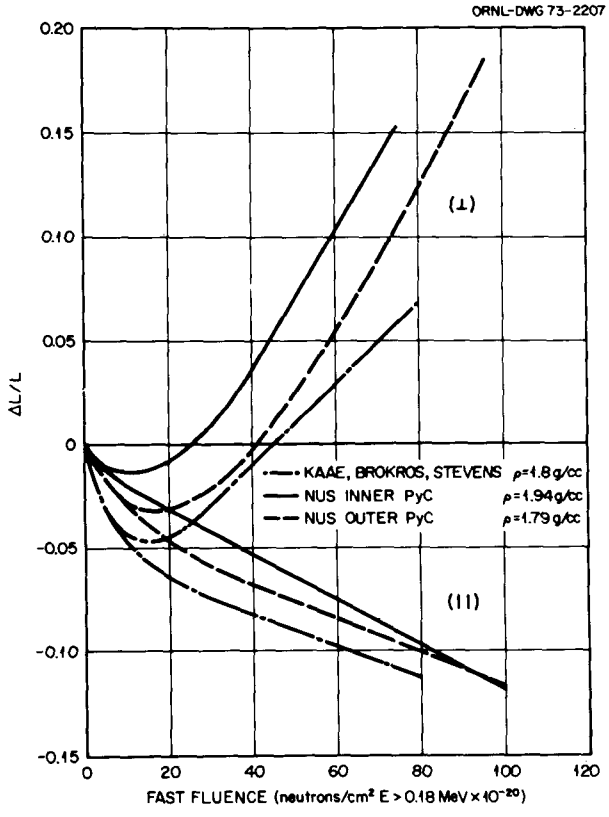

Fig. 17.18. Irradiation-induced dimensional changes of PyC.

A comparison of Fig. 17.17 and Fig. 17.19 shows that the predicted stresses for the inner PyC and SiC layers are somewhat different. We found this to be due to the irradiation-induced deformation data used. By using the data[29] from the solid curve in Fig. 17.18 for the inner PyC and the dashed curve in Fig. 17.18 for the outer PyC, we were able to duplicate the performance predictions presented by Gulden et al.[27] with both codes. These results are shown in Fig. 17.21.

From this comparison, we have concluded that TRISO and STRESS-2 are mathematically equivalent, although TRISO is somewhat simpler. For example, TRISO assumes the SiC layer does not creep and is dimensionally stable under irradiation. Thus, it is not necessary (or possible) to introduce creep or irradiation-induced deformation data for this layer. The same is true for the buffer layer, although for different reasons. TRISO assumes that the buffer layer is weak and cannot impart loads to the other layers except through the mechanism of fuel swelling. With STRESS-2 it is possible to study the effect of failure of one or more layers on the stresses developed in the remaining unfailed layers; this is not possible with TRISO.

Comparison of STRESS-2 and STRETCH

For this comparison we selected the Biso fissile particle presently planned for the OF-1 capsule (irradiation test currently being fabricated for the Oak Ridge Research Reactor). This particle, a 4.2:1 $(Th:U)O_2$ kernel that is 350 μ in diameter, is coated with a 100-μ buffer and 100-μ LTI layer. The kernel, buffer, and LTI densities were assumed to be 95, 50, and 86.4% of

28. J. L. Kaae, J. C. Bokros, and D. W. Stevens, "Dimensional Changes and Creep of Poorly Crystalline Isotropic Carbons and Carbon-Silicon Alloys During Irradiation," *Carbon* **10**, 571–85 (1972).

29. Private communication, J. C. Scarborough, NUS Corp., with F. J. Homan, ORNL, Feb. 6, 1973.

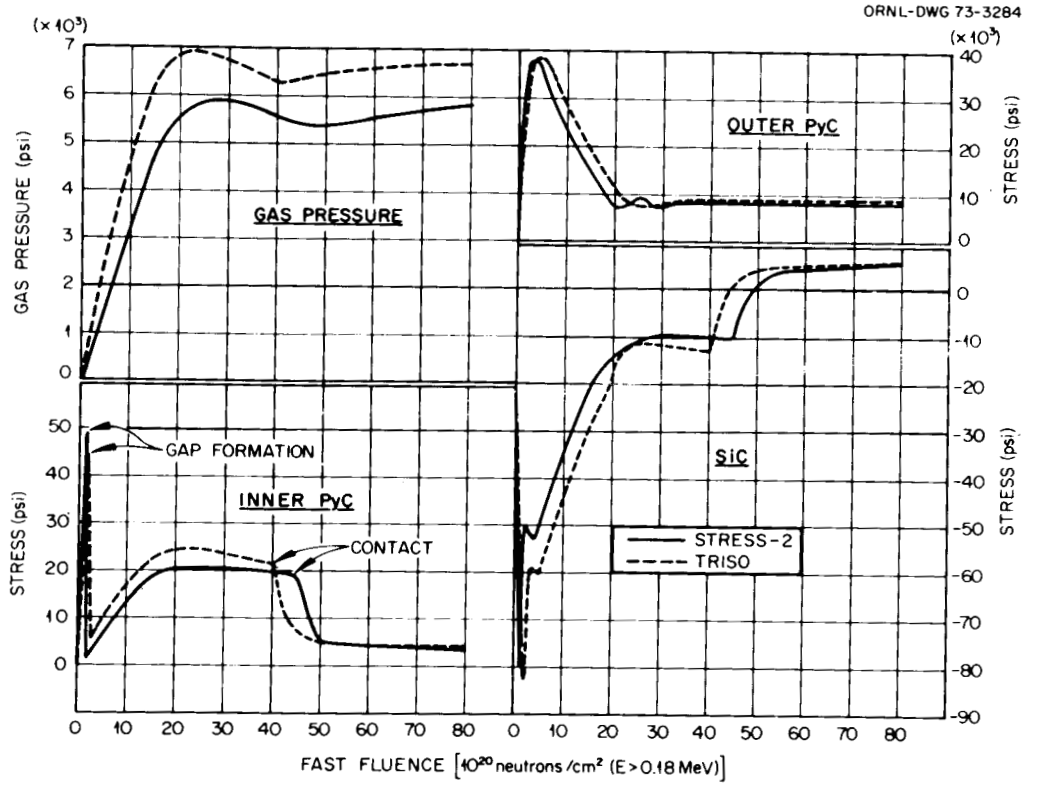

Fig. 17.19. Comparison of STRESS-2 and TRISO performance codes.

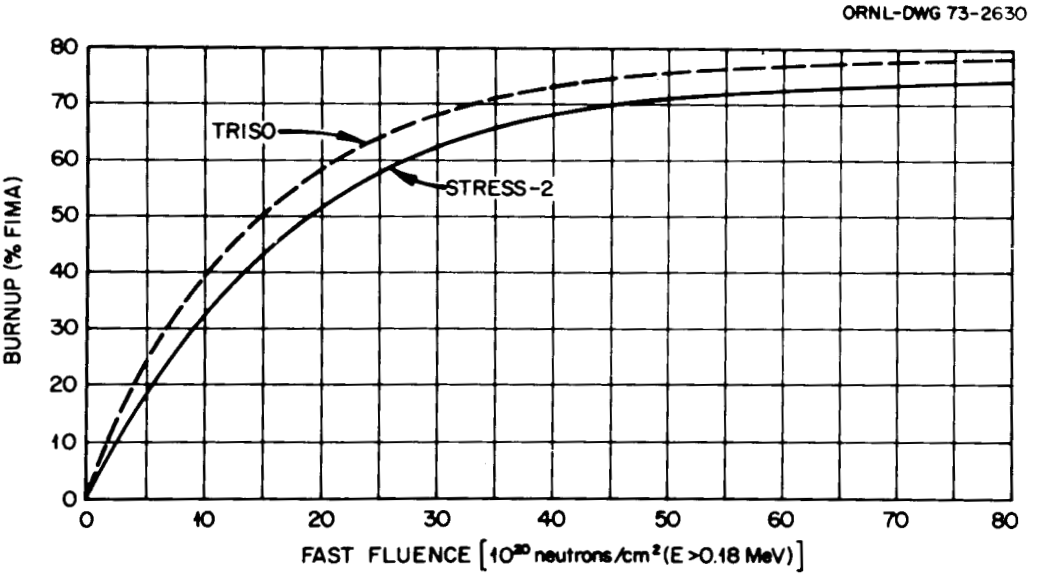

Fig. 17.20. Burnup curves used for TRISO–STRESS-2 comparison.

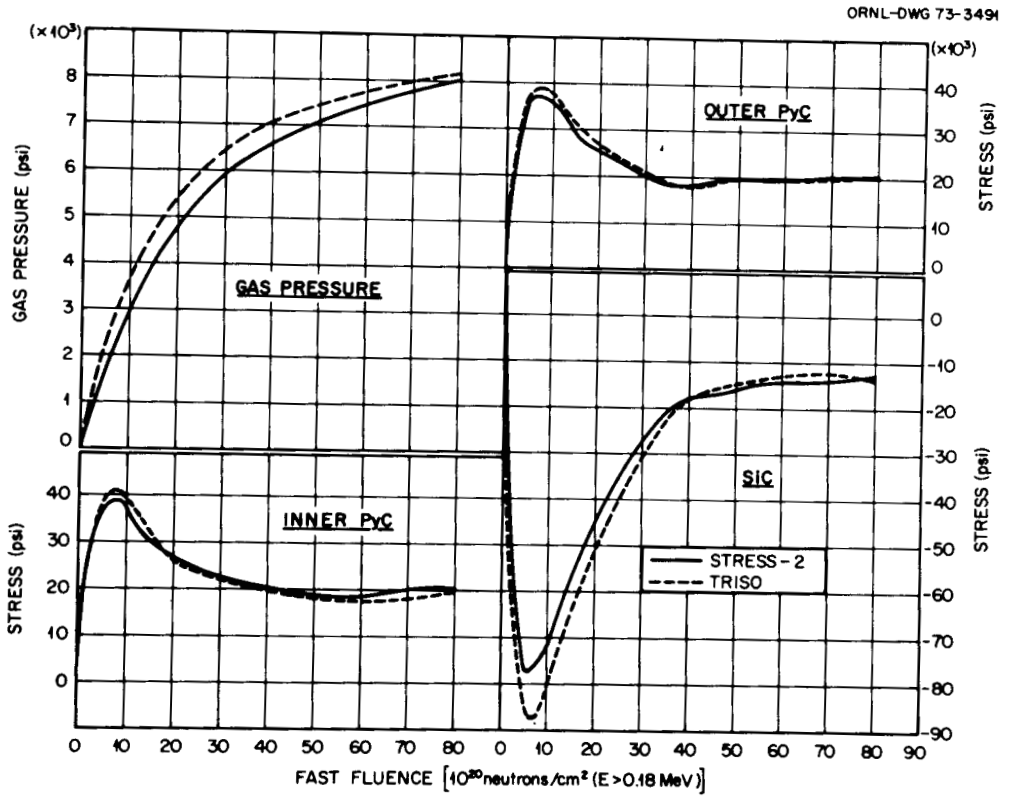

Fig. 17.21. TRISO–STRESS-2 comparison for GGA particle.

theoretical density respectively. The deposition temperatures of the buffer and the LTI were 1470 and 1375°C, respectively, and the irradiation temperature was assumed to be 1300°C. Because STRESS-2 required the relationship between burnup and fluence as input, such a curve was computed with STRETCH and used in STRESS-2. This curve is shown in Fig. 17.22.

Calculations of fission gas pressure and LTI tangential stresses as functions of fast fluence are shown in Fig. 17.23 for both codes. Notice there is little difference in the two curves at the left of the figure below a fluence of about 60 X 10^{20} neutrons/cm^2. At that point, the pressure calculated by STRESS-2 begins to flatten compared with the pressure calculated by STRETCH. The reason for this can be demonstrated by examining the curves at the right of the figure, which show the tangential stresses calculated in the PyC. STRETCH considers the buffer layer to be very weak and incapable of supporting loads either in tension or compression. Therefore, no loads are transmitted from the buffer to the PyC during any phase of the

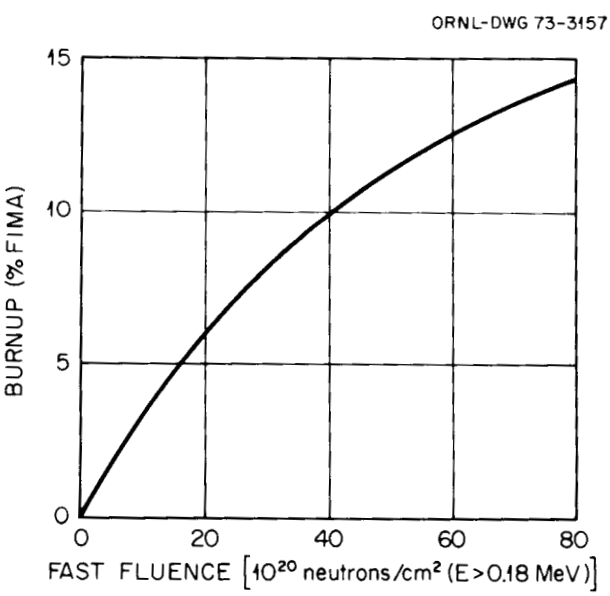

Fig. 17.22. Burnup vs fluence for STRESS-2 vs TRISO comparison.

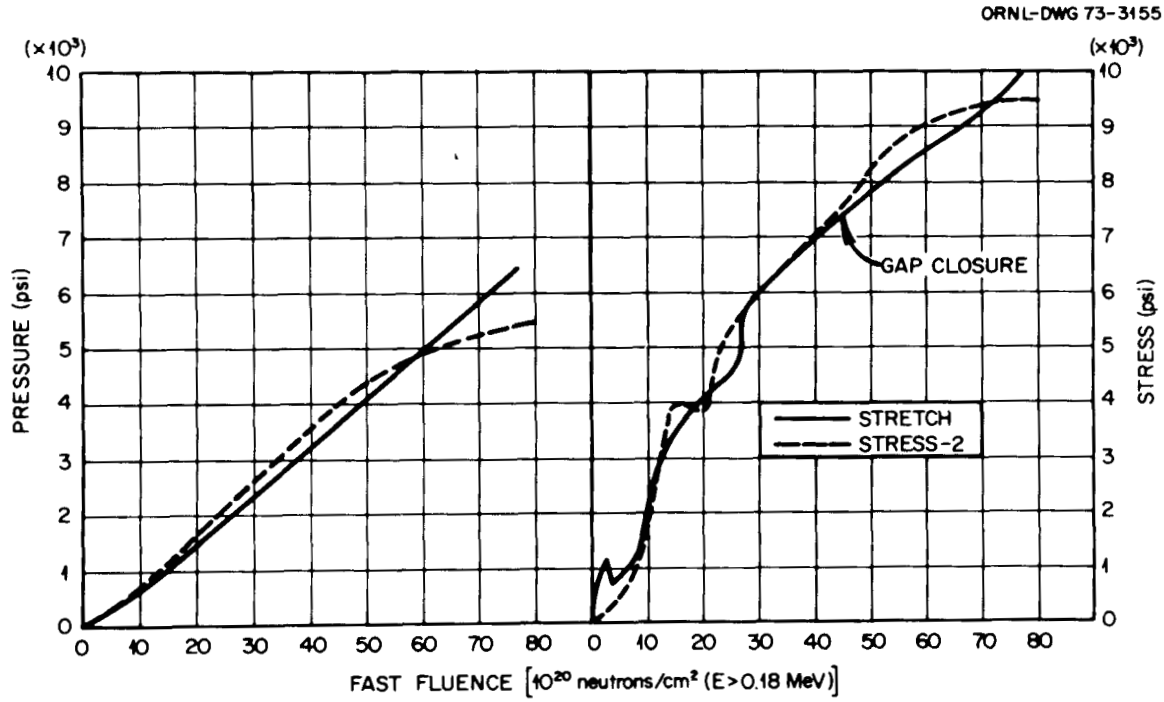

Fig. 17.23. Comparison of STRETCH and STRESS-2 codes.

irradiation history. On the other hand, the buffer properties in STRESS-2 are described in detail in the input.

In the case being studied, the input densification characteristics of the two layers are as shown in Fig. 17.24. The buffer layer densifies very rapidly at first, but by 40×10^{20} fast fluence the densification rate has decreased to zero. The PyC densifies more slowly at first, but continues to densify throughout the entire irradiation history. At about 45×10^{20} fast fluence the gap between the buffer and PyC closes (the gap formed very early in life because of the difference in coating temperatures), and the stresses in the PyC layer increases slightly due to the continued densification and shrinkage down upon the buffer. The presence of the buffer prevents the PyC from shrinking as much as it would if there were no restraint, and this provides more space for the fission gas; this explains the observation noted earlier from the left portion of Fig. 17.23.

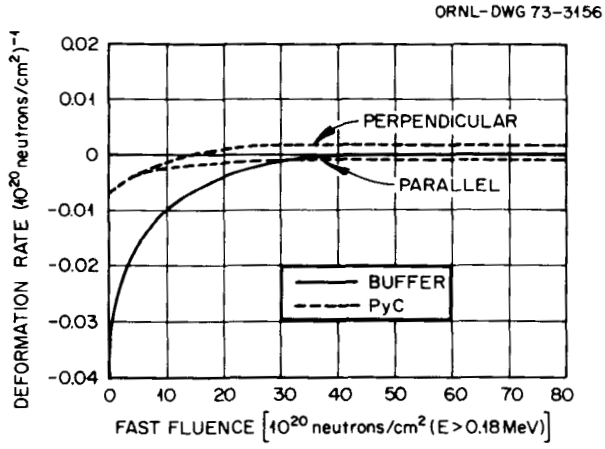

Fig. 17.24. Densification rates of buffer and PyC layers.

Conclusion

The differences noted in predicted performance of the two codes are minor, and we have concluded that STRESS-2 and STRETCH are mathematically equivalent.

17.4 SENSITIVITY OF HTGR FUEL PERFORMANCE TO MATERIAL PROPERTIES AND PARTICLE DESIGN

F. J. Homan

17.4.1 Introduction

The three coated particle performance models and their associated computer programs as currently used at ORNL and GGA were shown to give equivalent results for identical cases. The STRESS-2 code was selected as the most potentially useful because of its flexibility and mathematical sophistication. We then investigated the sensitivity of STRESS-2 performance predictions to materials properties and particle design for a Triso fuel.

The materials properties for the kernel and each coating required as input to STRESS-2 are listed below. Each property can be represented as a function of fluence, and properties must be supplied for planes both parallel and perpendicular to the plane of coating deposition. The properties are:

1. elastic modulus
2. Poisson's ratio,
3. irradiation creep coefficient,
4. thermal creep coefficient,
5. irradiation-induced densification rate,
6. thermal expansion coefficient,
7. temperature-independent expansion (time-dependent effects).

Thermal creep (item 4) is assumed to be at zero at the irradiation temperatures of interest for HTGR fuel. Temperature-dependent expansion (item 7) is not well understood and is usually set to zero in the input. These two properties will not be included in the sensitivity analysis.

Particle design characteristics required as input to STRESS-2 are listed as follows:

1. burnup-fluence relationship,
2. kernel diameter,
3. coating thicknesses,
4. fractional density of kernel and each coating,
5. temperature at which coatings are deposited,
6. molecular weight of fuel kernel,
7. number of fissile plus fertile atoms per fuel molecule,
8. theoretical density of fuel kernel,
9. irradiation temperature,
10. fission gas release fraction.

17.4.2 Sensitivity of Predicted Performance to Materials Properties

The sensitivity of predicted performance to materials properties and design parameters was determined by establishing a base case, varying the properties and parameters one at a time, and recording the deviation of predicted performance from the base case. Properties and design parameters for the base case are shown in Table 17.1. This is basically the same particle described earlier by Gulden et al.[27] It should be recalled that properties in planes both parallel and perpendicular to the coating deposition plane are required. For this study it was assumed that all coatings were isotropic at the beginning of the irradiation, so that numerical values would be equal in both planes. It has been established that the coatings become more anisotropic with increased irradiation; this is due, in part, to the irradiation-induced deformation. This aspect of performance can be modeled with STRESS-2 by using fluence-dependent properties. However, for this study it was assumed that the properties remained constant throughout the irradiation. Irradiation-induced dimensional changes for the buffer and PyC are not given in Table 17.1. The behavior assumed for both the inner and outer PyC coatings is shown in Fig. 17.25. To compute stresses in the coatings, STRESS-2 requires the *rate* of dimensional change at any point in time, which is computed from the raw data, such as shown in Fig. 17.25. The dimensional change rates for both buffer and PyC coatings used in this study were shown in Fig. 17.24.

Kernel and coating property data have been increased and decreased by factors of 2 and 10 from the base case values (except for Poisson's ratio, which has been varied by only a factor of 2). Results for the kernel, buffer, PyC, and SiC coatings are given in Tables 17.2 through 17.5 respectively. Basically, three categories of information are contained in these tables: the peak stresses in the PyC and SiC coatings, the relative deviation of these stresses from base case values, and the fluence at which the peak stresses occurred. The sensitivity of a given property can be found quickly by looking at the portion of the tables where the relative deviations are tabulated. No sensitivity for a given property would be indicated by a value of unity under "relative deviation from base case." Greater sensitivity is indicated by greater deviation from unity.

From Tables 17.2 through 17.5, it is clear that predicted performance is insensitive to properties input for the kernel and buffer and that the irradiation-induced creep constants are the most important

Table 17.1. Base case properties and design parameters

	Kernel	Buffer	Inner PyC	SiC	Outer PyC
		Properties			
E, elastic modulus (psi)	2.8×10^7	1×10^5	4×10^6	6×10^7	4×10^6
μ, Poisson's ratio	0.302	0.300	0.25	0.18	0.25
α, thermal expansion coefficient ($^\circ C^{-1}$)	8.2×10^{-6}	5×10^{-6}	5.4×10^{-6}	5.5×10^{-6}	5.4×10^{-6}
k, irradiation creep coefficient	0	1×10^{-27}	1×10^{-27}	0	1×10^{-27}
ℓ, thermal creep coefficient	0	0	0	0	0
s, irradiation-induced shrinkage	0	See text	See text	0	See text
β, temperature-independent expansion	0	0	0	0	0
		Design parameters			
d, kernel diameter (μm)	200				
t, coating thickness (μm)		85	25	25	35
ρ, coating density (% of theoretical)	92	52.3	86.6	99	82
D_t, coating deposition temperature ($^\circ$C)		1250	1250	1650	1250
F, gas release fraction	1.0				
M, kernel molecular weight (g/mole)	259				
I_t, irradiation temperature ($^\circ$C)	1050				
ρ, kernel theoretical density (g/cc)	11.68				
A, metal atoms/molecule	1.0				

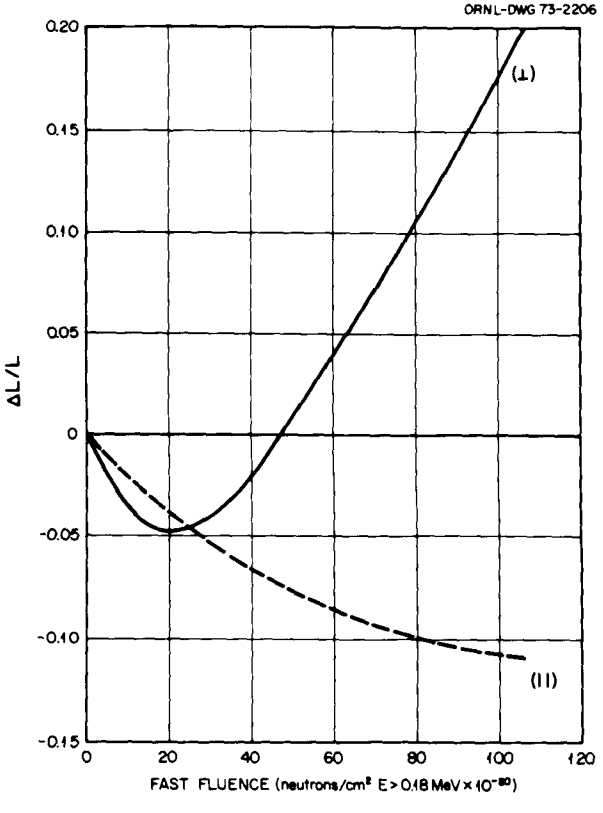

Fig. 17.25. Irradiation-induced dimensional changes of PyC.

Table 17.2. Sensitivity of performance predictions to kernel properties[a]

		Maximum $\sigma\theta$ (psi)			Relative deviation from base case			Fluence at which maximum stress is reached [10^{20} neutrons/cm^2 ($E>0.18$ MeV)]		
		Inner PyC	SiC	Outer PyC	Inner PyC	SiC	Outer PyC	Inner PyC	SiC	Outer PyC
Base case		30,686	13,601	16,700				6	80	6
E	1/2	No change from base case								
	2									
	1/10									
	10									
μ	1/2	No change from base case								
	2									
α	1/2	30,610	13,591	16,699	1.00	1.00	1.00	6	80	6
	2	30,742	13,460	16,704	1.05	0.99	1.00	6	80	6
	1/10									
	10	31,213	12,273	16,739	1.02	0.70	1.00	6	80	6

[a]Designation of parameters shown in Table 17.1.

Table 17.3. Sensitivity of performance predictions to buffer properties[a]

		Maximum $\sigma\theta$ (psi)			Relative deviation from base case			Fluence at which maximum stress is reached [10^{20} neutrons/cm^2 ($E > 0.18$ MeV)]		
		Inner PyC	SiC	Outer PyC	Inner PyC	SiC	Outer PyC	Inner PyC	SiC	Outer PyC
Base case		30,686	13,601	16,700				6	80	6
E	1/2	30,681	13,611	16,700	1.00	1.00	1.00	6	80	6
	2	30,696	13,580	16,701	1.00	1.00	1.00	6	80	6
	1/10	30,675	13,624	16,699	1.00	1.00	1.00	6	80	6
	10	30,732	13,444	16,703	1.00	0.99	1.00	6	80	6
μ	1/2	30,687	13,598	16,700	1.00	1.00	1.00	6	80	6
	2	29,432	20,164	16,714	0.06	1.48	1.00	6	80	6
α	1/2	30,686	13,601	16,700	1.00	1.00	1.00	6	80	6
	2	30,686	13,601	16,700	1.00	1.00	1.00	6	80	6
	1/10	30,686	13,601	16,700	1.00	1.00	1.00	6	80	6
	10	31,725	12,728	16,700	1.00	0.94	1.00	6	80	6
k	1/2	30,686	13,603	16,700	1.00	1.00	1.00	6	80	6
	2	30,686	13,603	16,700	1.00	1.00	1.00	6	80	6
	1/10	30,686	13,601	16,700	1.00	1.00	1.00	6	80	6
	10	30,686	13,601	16,700	1.00	1.00	1.00	6	80	6

[a]Designation of parameters shown in Table 17.1.

Table 17.4. Sensitivity of performance predictions to PyC coating properties[a]

		Maximum $\sigma\theta$ (psi)			Relative deviation from base case			Fluence at which maximum stress is reached [10^{20} neutrons/cm^2 ($E > 0.18$ MeV)]		
		Inner PyC	SiC	Outer PyC	Inner PyC	SiC	Outer PyC	Inner PyC	SiC	Outer PyC
Base case		30,686	13,601	16,700				6	80	6
E	1/2	26,618	12,810	15,257	0.87	0.94	0.91	10	80	10
	2	33,711	14,179	17,674	1.10	1.04	1.06	4	80	4
	1/10	13,930	7,099	10,189	0.45	0.52	0.61	20	80	25
	10	36,622	14,694	18,547	1.19	1.08	1.11	2	80	2
μ	1/2	29,697	13,398	16,517	0.97	0.99	0.99	8	80	6
	2	33,045	14,025	17,021	1.08	1.03	1.02	4	80	4
α	1/2	29,975	14,029	16,594	0.98	1.03	0.99	6	80	6
	2[b]									
	1/10	29,692	14,414	16,508	0.97	1.06	0.99	8	80	6
	10[c]									
k	1/2[d]									
	2	16,825	20,533	8,923	0.55	1.51	0.53	4	80	4
	1/10[e]									
	10	3,630	25,840	1,910	0.12	1.90	0.11	1	80	1

[a]Designation of parameters shown in Table 17.1.
[b]Inner PyC layer broken during fabrication.
[c]Inner and outer PyC layers broken during fabrication.
[d]Inner PyC broken at 6×10^{20} neutrons/cm^2.
[e]Inner PyC layer broken at 4×10^{20} neutrons/cm^2; outer PyC layer broken at 6×10^{20} neutrons/cm^2.

Table 17.5. Sensitivity of performance predictions to SiC coating properties[a]

		Maximum $\sigma\theta$ (psi)			Relative deviation from base case			Fluence at which maximum stress is reached [10^{20} neutrons/cm^2 ($E > 0.18$ MeV)]		
		Inner PyC	SiC	Outer PyC	Inner PyC	SiC	Outer PyC	Inner PyC	SiC	Outer PyC
Base case		30,686	13,601	16,700				6	80	6
E	1/2	29,984	13,474	16,421	0.98	0.99	0.98	8	80	6
	2	31,036	13,740	16,812	1.01	1.01	1.01	6	80	6
	1/10	26,550	11,653	15,056	0.87	0.86	0.90	10	80	10
	10	31,298	13,856	16,885	1.02	1.02	1.01	6	80	6
μ	1/2	30,615	13,575	16,670	1.00	1.00	1.00	6	80	6
	2	30,825	13,653	16,758	1.00	1.00	1.00	6	80	6
α	1/2	31,500	12,943	16,813	1.03	0.95	1.01	6	80	6
	2	29,525	15,043	16,470	0.96	1.11	0.99	8	80	6
	1/10	32,153	12,422	16,904	1.05	0.91	1.01	6	80	6
	10[b]									
k	10^{-26}	11,859	−2,311	14,359	0.39		0.86	40	80	50
	10^{-27}	10,219	2,404	13,720	0.33	0.18	0.82	45	80	45
	10^{-28}	25,404	12,284	14,544	0.83	0.90	0.87	6	80	6
	10^{-29}	30,080	14,393	16,451	0.98	1.06	0.99	6	75	6

[a]Designation of parameters shown in Table 17.1.
[b]SiC layer broken during fabrication.

materials properties for the PyC and SiC coatings (except for irradiation-induced deformation, which will be discussed in greater detail later). Of course, the information in the tables only tells part of the story. The complete coating stress and gas pressure histories are plotted in Fig. 17.26 for different irradiation creep constants in the PyC coatings. The base case situation is designated by a (1) next to the curve. It can be seen from Fig. 17.26 that the maximum stress in the SiC coating occurs at the end of the irradiation, while the maximum stress in the PyC coatings occurs quite early.

It is relatively easy to vary the materials properties shown in Tables 17.2 through 17.5 around the base case values because the property is described by a pair of numbers for each coating when fluence-related changes in the property are not considered. For irradiation-induced deformation, the task is not quite so easy. Length change values, or deformation rate values as a

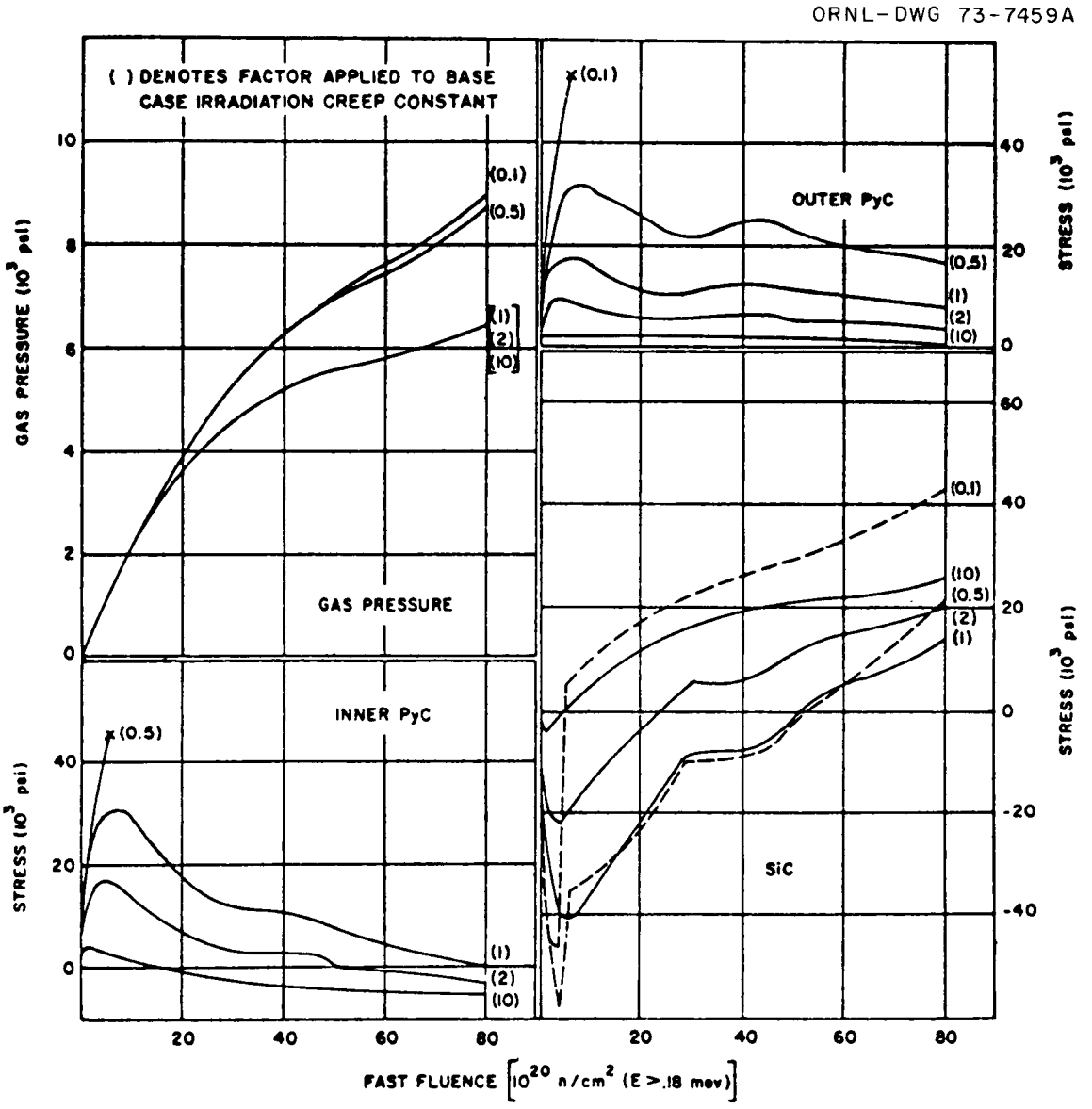

Fig. 17.26. Influence of creep coefficient assumed for PyC on calculated coating stresses.

function of fluence, are required for the entire span of irradiation history of the particle. The sensitivity of the predicted performance to this material property has been studied by using three distinct sets of data to describe irradiation-induced deformation. One set of data is shown in Fig. 17.25, and the other two are shown in Fig. 17.18. The sensitivity of predicted performance to changes in this property is shown in Fig. 17.27. The variability among the three sets of irradiation-induced dimensional change data is quite small when compared with the variability considered for the other materials properties. And, as shown in Fig. 17.27, this small amount of variability produces fairly significant changes in predicted performance.

17.4.3 Discussion of Materials Property Sensitivity

Irradiation-induced dimensional changes. Pyrolytic carbon changes dimensions under irradiation, with material having preirradiation densities of less than 2.0 g/cc generally becoming more dense and materials with preirradiation densities greater than 2.0 g/cc becoming less dense.[30] The manner in which the density changes are distributed in directions parallel and perpendicular to the deposition plane (as shown in Fig. 17.25) is important to the performance of the coating under irradiation. A greater rate of shrinkage (corresponding to a less dense coating) causes the outer PyC coating to shrink more rapidly upon the SiC coating, generated high compressive stresses in the SiC and high tensile stresses in the outer PyC. The inner PyC will shrink away from the SiC coating and form a gap. The difference in the rates of dimensional change in the parallel and perpendicular directions is itself a source

30. *HTGR Base Program Quarterly Progress Report for the Period Ending May 31, 1972,* Gulf-GA-A12150, pp. 97–104.

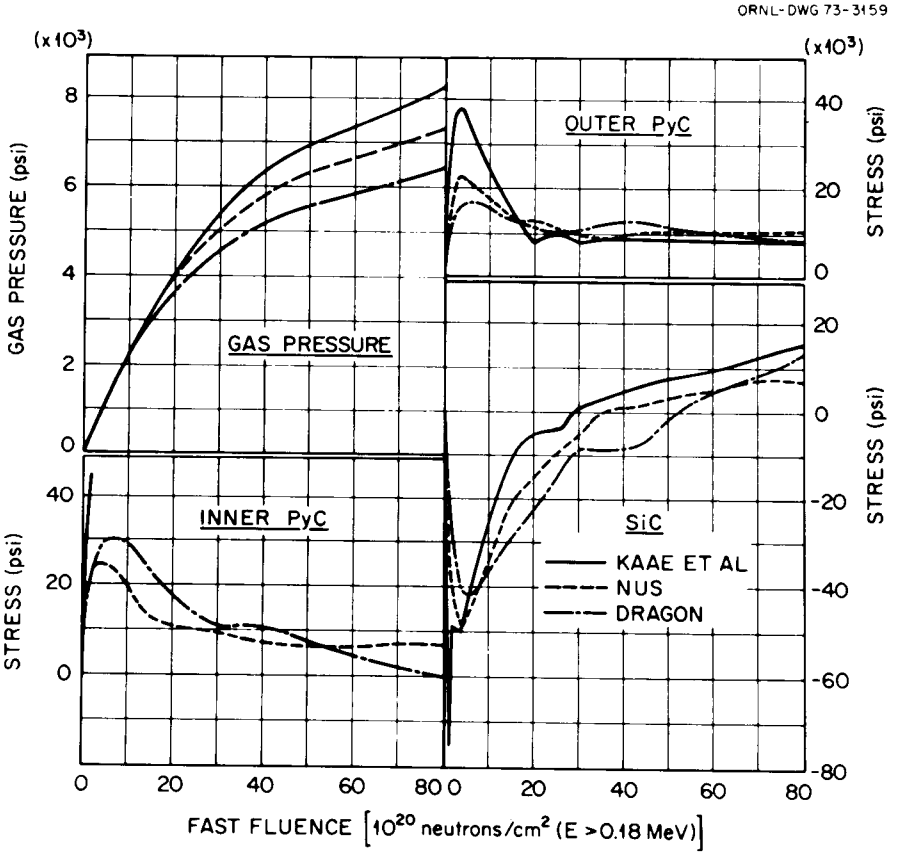

Fig. 17.27. Influence of irradiation-induced deformation of PyC on calculated coating stresses.

of stress-producing failure in the unrestrained inner coatings if the deformation rates are suitably high.

Irradiation-induced creep. Irradiation-induced creep serves to relieve the stresses caused by irradiation-induced deformation, thermal sources, and fission gas pressure. Low PyC creep rates lead to failure of the coatings, as shown in Fig. 17.26, due to inability to relieve the stresses. High PyC creep rates result in substantially lower stresses in the PyC coatings due to rapid stress relaxation but increased stresses in the SiC coating, which must now support the pressure loads, due to the decreased strengths of the PyC coatings. The SiC coatings are generally thought to be dimensionally stable and have a very low creep rate. Higher creep rates in the SiC results in lower stresses in all layers, as shown in Table 17.5.

Thermal expansion. Variation in thermal expansion coefficient values for the various coatings about the base case values does not significantly change the predicted coating stresses (Tables 17.2 through 17.5). Thermal stresses are relieved fairly quickly by creep during irradiation of the particle. However, during the fabrication phase of the history, where the coatings are applied at different temperatures and the particle eventually brought down to room temperature prior to irradiation, some severe thermal stresses can develop which cannot be relieved by creep. As shown in Table 17.4, increasing the PyC thermal expansion coefficient significantly from the base case value resulted in broken coatings during fabrication.

Elastic modulus and Poisson's ratio. It is somewhat surprising that changes in these properties do not influence the coating stresses more extensively than shown in Tables 17.2 through 17.5. This question is resolved somewhat by Prados' observation[19] that the stress equations for a hollow sphere reduce the classical Lame equation (stresses dependent only on internal pressure and geometry) for an isotropic material when creep is not considered. When creep is considered, the dependence on elastic modulus and Poisson's ratio is present but weak.[20]

17.4.4 Sensitivity of Predicted Performance to Design Parameters

The base case design parameters for Triso particles have been varied in similar fashion to the properties to determine sensitivity. The results are summarized in Table 17.6, which is similar to Tables 17.2 through 17.5, except that maximum gas pressure is considered. Several observations can be made from the table.

1. The relationship between the kernel and the buffer volumes appears to be the most significant design consideration. The particle failed completely when the diameter of the kernel was doubled; when the diameter of the kernel was halved, the gas pressure was reduced to a very low level. Layer stresses were not significantly influenced by the low gas pressure, indicating that irradiation-induced deformation must account for most of the coating stresses in this situation. Reducing the thickness of the buffer by a factor of 2 resulted in very high gas pressures and failure of the SiC layer.

2. Changes in the input fractional densities for the kernel and buffer influenced the SiC stresses. However, no influence resulted from changing the input fractional densities of the other layers. This indicates that input densities for these layers are inoperative, and density changes must be reflected in the property library, in particular the irradiation-induced deformation characteristics.

3. Changes in the thickness of the PyC and SiC layers had some impact on computer stresses, with the impact being greatest for the SiC layer.

4. There is no significant influence of coating deposition temperatures on predicted performance.

5. Kernel molecular weight and particle irradiation temperature changes produced small performance variations. Gas release fractions strongly influenced fission gas pressures and stresses in the SiC coating. The shape of the burnup curve is not especially important.

17.4.5 Conclusion

The sensitivity analysis presented here for a Triso particle has indicated that, with the exception of the PyC irradiation creep and deformation characteristics, the influence of materials properties on predicted performance is relatively small. In addition, of the design considerations, the relationship of kernel volume to buffer volume was most important. The influence of coating thickness changes was greatest for the SiC layer.

17.5 ANALYSES OF TRITIUM DISTRIBUTION AND RELEASE IN HTGR

E. L. Compere C. W. Nestor

A mathematical model of the generation and distribution of tritium in high-temperature gas-cooled reactors was previously described by Freid.[31] This model was incorporated in a computer code, TRITGO, which

31. S. H. Freid, "Tritium in HTGR," in *ORNL Nuclear Safety Research and Development Program Bimonthly Report for March–April 1972, Non-LMFBR Programs,* ORNL-TM-3831, pp. 72–73; *ORNL Nuclear Safety Research and Development Program Bimonthly Report for May–June 1972, Non-LMFBR Programs,* ORNL-TM-3900, pp. 76–78.

Table 17.6. Sensitivity of performance predictions to design characteristics[a]

	Maximum $\sigma\theta$ (psi)			Relative deviation from base case			Fluence at which maximum stress is reached [10^{20} neutrons/cm^2(E>0.18 MeV)]			Maximum gas pressure (psi)
	Inner PyC	SiC	Outer PyC	Inner PyC	SiC	Outer PyC	Inner PyC	SiC	Outer PyC	
Base case	30,686	13,601	16,700				6	80	6	6,452
Kernel										
2d	[b]									32,214
$\frac{1}{2}d$	35,626	−8,034	15,849	1.16		0.95	8	80	6	1,315
ρ + 5%	30,629	16,517	16,707	1.00	1.21	1.00	6	80	6	7,120
ρ − 5%	30,733	11,663	16,695	1.00	0.86	1.00	6	80	6	5,986
Buffer										
2t	27,701	−4,732	17,551	0.90		1.05	6	80	6	1,395
$\frac{1}{2}t$	32,697	Broken	43,938	1.07		2.63	6	55	55	51,584
ρ + 5%	30,597	18,406	16,710	1.00	1.35	1.00	6	80	6	7,572
ρ − 5%	30,758	10,169	16,692	1.00	0.75	1.00	6	80	6	5,620
D_t + 100°C	30,677	13,557	16,699	1.00	1.00	1.00	6	80	6	6,441
D_t − 100°C	30,685	13,654	16,700	1.00	1.00	1.00	6	80	6	6,465
Inner PyC										
2t	25,034[c]	−8,525	17,713	0.82		1.06	4	80	2	6,102
$\frac{1}{2}t$	25,303	15,362	16,642	0.82	1.13	1.00	8	80	6	6,900
ρ + 5%	30,686	13,601	16,700	1.00	1.00	1.00	6	80	6	6,452
ρ − 5%	30,686	13,601	16,700	1.00	1.00	1.00	6	80	6	6,452
D_t + 100°C	30,680	13,758	16,700	1.00	1.01	1.00	6	80	6	6,490
D_t − 100°C	30,679	13,457	16,699	1.00	0.99	1.00	6	80	6	6,417
SiC										
2t	31,004	6,758	17,129	1.01	0.50	1.03	6	80	6	6,462
$\frac{1}{2}t$	30,009	27,521	16,243	0.98	2.02	0.97	8	80	6	6,433
ρ − 5%	30,686	13,601	16,700	1.00	1.00	1.00	6	80	6	6,452
D_t + 100°C	30,684	13,603	16,700	1.00	1.00	1.00	6	80	6	6,452
D_t − 100°C	30,688	13,601	16,700	1.00	1.00	1.00	6	80	6	6,451
Outer PyC										
2t	30,503	2,481	14,321	0.99	0.18	0.86	6	80	6	6,468
$\frac{1}{2}t$	30,833	18,715	18,586	1.00	1.38	1.11	6	80	6	6,445
ρ + 5%	30,686	13,601	16,700	1.00	1.00	1.00	6	80	6	6,452
ρ − 5%	30,686	13,601	16,700	1.00	1.00	1.00	6	80	6	6,452
D_t + 100°C	30,685	13,600	16,699	1.00	1.00	1.00	6	80	6	6,452
D_t − 100°C	30,687	13,602	16,701	1.00	1.00	1.00	6	80	6	6,452
M										
269	30,716	12,110	16,697	1.00	0.89	1.00	6	80	6	6,093
249	30,655	15,159	16,704	1.00	1.11	1.00	6	80	6	6,827
IT										
1150°C	30,638	15,628	16,707	1.00	1.15	1.00	6	80	6	6,937
950°C	30,735	11,551	16,693	1.00	0.85	1.00	6	80	6	5,961
F, 0.5	31,056	−276	16,660	1.01		1.00	6	80	6	3,126
F, 2.0	29,938	45,661	16,783	0.98	3.36	1.00	6	80	6	14,025
Linear burnup	31,226	13,370	16,640	1.02	0.98	1.00	6	80	6	6,472
A, 2	29,822	96,627	16,813	0.97	7.10	1.01	6	80	6	23,291

[a]Designation of property or parameter shown in Table 17.1.
[b]Failure at 25 × 10^{20} neutrons/cm^2.
[c]Gap formed.

calculated the amounts of tritium in various regions resulting from the various sources. This code was used as a starting point in the analysis of tritium distribution and release in HTGRs for the Directorate of Licensing. Results from this analysis were documented in a topical report[32] which also described the code and discussed possible extension and refinement of the calculational model. An abstract of the report is given below.

32. E. L. Compere, S. H. Freid, and C. W. Nestor, *Distribution and Release of Tritium in High-Temperature Gas-Cooled Reactors as a Function of Design, Operational, and Material Parameters,* ORNL-TM-4303 (June 1974).

Abstract

Tritium will be produced in high-temperature gas-cooled reactors not only by fission, but also to a significant extent by reactions of neutrons with boron in burnable poison and control rods, with trace lithium impurity, and with ^{3}He occurring naturally in the helium coolant flowing through the core. A portion of the tritium that is formed in solids or fuel may be released to the coolant. This tritium mingles with the hydrogen in the coolant and will, in part, chemisorb on graphite. In addition, it may leak with the coolant from the reactor vessel, be removed in the helium purification system, or permeate system walls into the steam generator, where as a result of removal (blowdown) or losses it is subject to release to the environment.

The differential equations describing the above behavior are developed. Assumption of steady conditions, including hydrogen concentration, for a period makes it possible to express the distribution as well as the production in the form of coupled sets of linear first-order ordinary differential equations. A generalized analytical solution of these is presented.

The above tritium generation and distribution model has been incorporated in a computer code, TRITGO. An illustrative calculation using parameters taken from the PSAR description of the Fort St. Vrain Reactor has been made. This indicates that most of the tritium emerging from the primary coolant will have been generated by the $^{3}He(n,p)T$ reaction. A significant fraction enters the steam generator. The tritium in the steam generator blowdown, after proper dilution, may be considered for release to the environment. The effects of varying a number of system parameters are considered.

Part IV. Gas-Cooled Fast Reactor Program

18. GCFR Irradiation Experiments

A. W. Longest J. A. Conlin

A series of fuel-rod irradiation tests have been conducted at ORNL in support of fuel development for the Gas-Cooled Fast Breeder Reactor (GCFR). The GCFR is being developed at General Atomic Company (GAC) with support from the U.S. Atomic Energy Commission (USAEC) and a number of electric utility companies. The fuels-irradiation program for the GCFR consists of both thermal- and fast-flux testing in capsule and loop experiments. Thermal-flux tests are being performed at ORNL in a series of capsule tests in the Oak Ridge Research Reactor (ORR) poolside facility. These tests, supported by the USAEC, represent the combined efforts of GAC, ORNL, and Argonne National Laboratory (ANL).

Two fuel-rod concepts for the GCFR have been investigated in the ORNL thermal-flux tests: a sealed fuel rod and a vented-and-pressure-equalized fuel rod. Earlier tests of 20 fuel rods of the sealed type (ORR capsules P-1 through P-8) indicated this concept to be a feasible backup design; however, cladding temperatures and dimensions must be carefully specified and controlled to insure that cladding ovality and subsequent failure by localized cladding collapse do not occur under the high coolant pressure (1250 psig) in the GCFR.

The current irradiation test, capsule GB-10, and the preceding one, capsule GB-9, were designed to permit an initial evaluation of the overall performance of the vented-and-pressure-equalized fuel rod, which is the reference fuel-rod design for the GCFR. Various aspects of the GCFR pressure-equalization system[1] are also being studied in these tests. Postirradiation examination of the GB-9 fuel rod, which was irradiated at 14.8 kW/ft peak power to a fuel burnup of approximately 54,000 MWd/metric ton of heavy metal, continued at ANL and GAC into calendar year 1973. The GB-9 experiment provided substantial information[2-9] on the

1. R. J. Campana, "Pressure Equalization System for Gas-Cooled Fast Breeder Reactor Fuel Elements," *Nucl. Technol.* **12,** 185 (October 1971).
2. A. W. Longest et al., "Irradiation of GCFR-ORR Capsule GB-9," *GCR-TU Programs Annu. Progr. Rep. Sept. 30, 1971,* ORNL-4760, pp. 149–63.
3. A. W. Longest et al., "Irradiation of GCFR-ORR Capsule GB-9," *GCR-TU Programs Annu. Progr. Rep. Dec. 31, 1972,* ORNL-4911, pp. 213–15.
4. A. W. Longest et al., "Fission-Gas Release Measurements from Fast Breeder (U,Pu)O_2 Fuel," *Trans. Amer. Nucl. Soc.* **13,** 604 (1970).
5. A. W. Longest, R. B. Fitts, and J. A. Conlin, "Fission Gas Release Behavior in a Vented (U,Pu)O_2 GCFR Fuel Pin," *Trans. Amer. Nucl. Soc.* **15,** 197 (1972).
6. R. B. Fitts and E. L. Long, Jr., "Postirradiation Examination of GCFR-ORR Capsule GB-9," *GCR Programs Annu. Progr. Rep. Dec. 31, 1972,* ORNL-4911, pp. 215–20.
7. S. Langer et al., "Volatile Fission Product Migration and Plateout in GCFR Rod Irradiations," *Trans. Amer. Nucl. Soc.* **15,** 850 (1972).
8. R. J. Campana et al., "The Effect of Irradiation Results on the GCFR Pressure Equalization System (Venting) Design," *Trans. Amer. Nucl. Soc.* **16,** 109 (1973).
9. J. R. Lindgren et al., *Irradiation Testing in the Development of Gas-Cooled Fast Breeder Reactor Fuel Elements,* GA-A12657 (1973).

fission-product-release behavior to be expected from the GCFR vented fuel rod, and the results have been used in many aspects of the GCFR pressure-equalization system design. The GB-10 fuel rod, similar to GB-9 but designed with even greater capability for measuring fission product release and transport, is being operated in three successive peak power steps: 12, 13.5, and 14.8 kW/ft. Capsule GB-10 is unique in that it is providing, for the first time, direct measurements of the release and transport of fission products from the mixed-oxide fuel pellets of an operating fast breeder reactor fuel rod.

18.1 DESCRIPTION OF GCFR-ORR CAPSULE GB-10

Thermal-flux irradiation capsule GB-10, which contains a $(U,Pu)O_2$-fueled stainless-steel-clad vented rod with a charcoal trap, has operated successfully in the ORR poolside facility to a fuel burnup of 35,000 MWd/metric ton of heavy metal; it is scheduled for a $2\frac{1}{2}$-year irradiation to a burnup of approximately 75,000 MWd/metric ton. The fuel rod was operated initially at a peak power level of 12 kW/ft (565°C peak cladding OD temperature) to a burnup of approximately 27,000 MWd/metric ton and is currently operating at an intermediate power level of 13.5 kW/ft (630°C peak cladding OD temperature). Following the completion of the 13.5-kW/ft operation, the power will be increased to 14.8 kW/ft (685°C peak cladding OD temperature) for the remainder of the irradiation. Other operating conditions include a 300°C rod trap temperature and cladding internal and external pressures of 1000 and 975 psig respectively. The test conditions are typical of those expected for a GCFR fuel rod except for the absence of significant fast-neutron exposure.

The GB-10 fuel rod is a shortened prototype of the GCFR rod with a 9-in.-long region of $(U,Pu)O_2$ solid pellet fuel, a 2-in.-long upper blanket region of depleted UO_2, and a 1-in.-long charcoal trap. Sweep line connections to the rod (Fig. 18.1) permit fission product release measurements under as many as ten different sweep flow modes, including passage of the sweep through the entire rod, which simulates a leak in the cladding of a GCFR fuel pin.

Measurement of fission product release to date has consisted in continuous monitoring of the effluent sweep line activity and of analyzing, by gamma-ray spectrometry, sweep-gas samples taken on a periodic basis. In calendar year 1974, we plan to add to the effluent sweep system an on-line Ge(Li) detector system, a sampling system for taking large gas samples

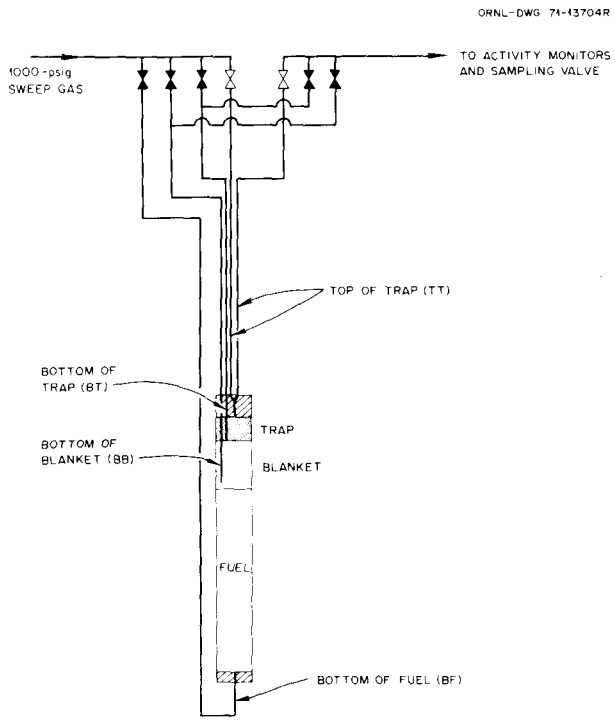

Fig. 18.1. Sweep lines for GCFR-ORR capsule GB-10.

for the determination of stable noble-gas release rates, and a system for semicontinuous monitoring of tritium release.

Capsule GB-10 was designed to provide the more detailed fission product release and transport information needed for both the GCFR and the liquid-metal-cooled fast breeder reactor (LMFBR) development programs. A major objective of capsule GB-10, in addition to providing information on the gaseous fission product release behavior, is to obtain additional needed information on the release, transport, and trapping of the volatile fission products.

The GB-10 capsule and fuel-rod design, planned operating conditions, and experimental results obtained early in the irradiation have been reported in detail previously.[9-11] However, for the sake of completeness, some of this information will be repeated in the following sections.

---

10. A. W. Longest and J. A. Conlin, "Design and Operation of GCFR-ORR Capsule GB-10," *GCR Programs Annu. Progr. Rep. Dec. 31, 1972,* ORNL-4911, pp. 220–33.

11. J. R. Lindgren et al., *Planned Thermal Irradiation of Manifold-Vented $(U,Pu)O_2$-Fueled Rod in ORR Capsule GB-10,* GA-A12123 (1973).

18.2 RESULTS FROM IRRADIATION TESTING OF CAPSULE GB-10

18.2.1 Steady-State Fission-Gas Release Rates vs Burnup

Steady-state fission-gas release rates have been measured as a function of time at power levels of 12 and 13.5 kW/ft under all the planned sweep flow modes. Typical fractional release data (R/B) are shown in Figs. 18.2 and 18.3 for sweep flow modes TT-TT and BF-BB respectively. The various GB-10 sweep flow modes are designated by two letters indicating the entrance point followed by two more letters indicating the exit point from the fuel rod. Referring to Fig. 18.1, BF = bottom of fuel, TT = top of charcoal trap, BT = bottom of charcoal trap, and BB = bottom of upper blanket.

Relatively high initial fission-gas release rates decreased by a factor of 10 during the first approximately 2500 MWd/metric ton burnup and then started an increasing trend that continued to approximately 6000 MWd/metric ton. The release rates continued to increase, but at a very slow rate, during the remainder of the 12-kW/ft operation. When the fuel-rod power was increased from 12 to 13.5 kW/ft at a burnup of approximately 27,000 MWd/metric ton, the release rates increased sharply, peaked, and then started a decreasing trend.

During the fuel-rod power increase from 12 to 13.5 kW/ft, the sweep flow was directed through the fuel rod under mode BF-TT. Two gas samples were taken under steady-state conditions prior to the power increase, one was taken soon after the power increase, and two were taken the following day. The results of these samples, together with the response of the ionization chamber on the high-pressure section of the effluent sweep line, described the mixed-oxide-fuel release behavior during the power increase period fairly well. These release data and pertinent operating conditions during and following the power increase are plotted in Fig. 18.4. The spikes in line activity upon changing the flow mode from

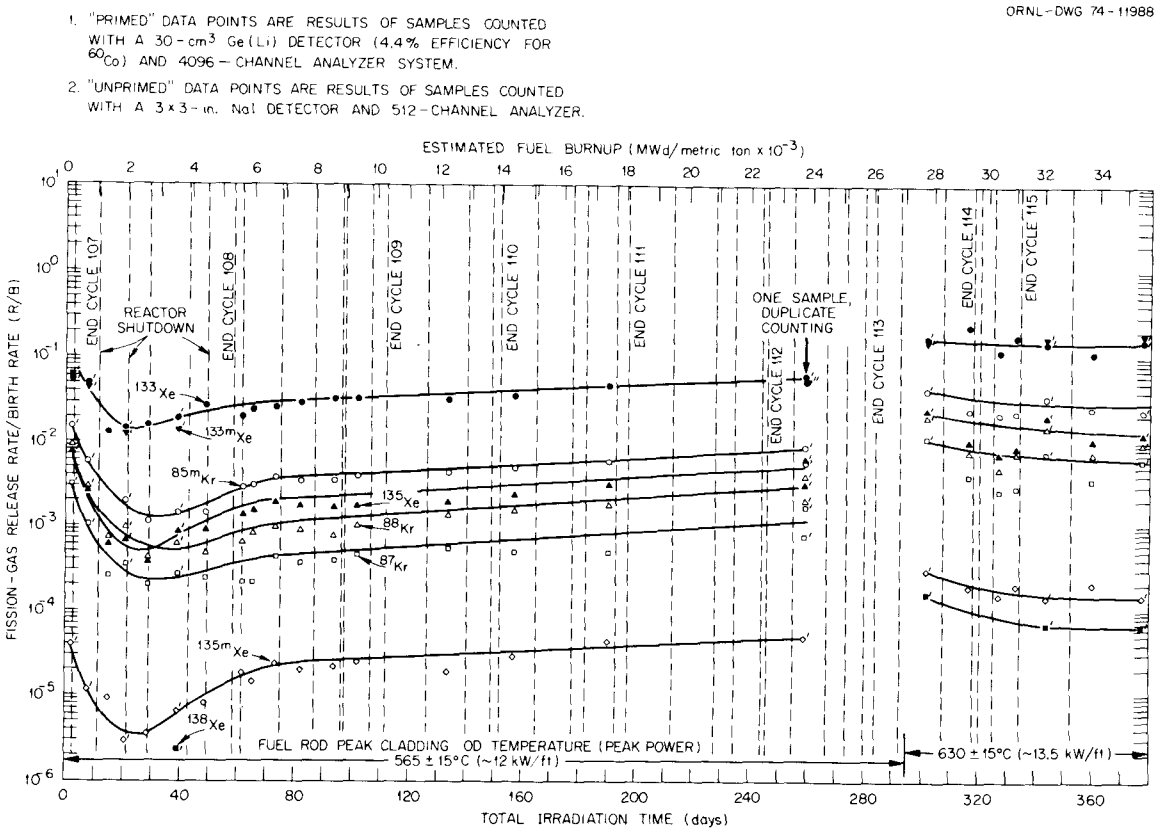

Fig. 18.2. Steady-state fission-gas release from GB-10 fuel rod vs time for case of sweep flow mode TT-TT.

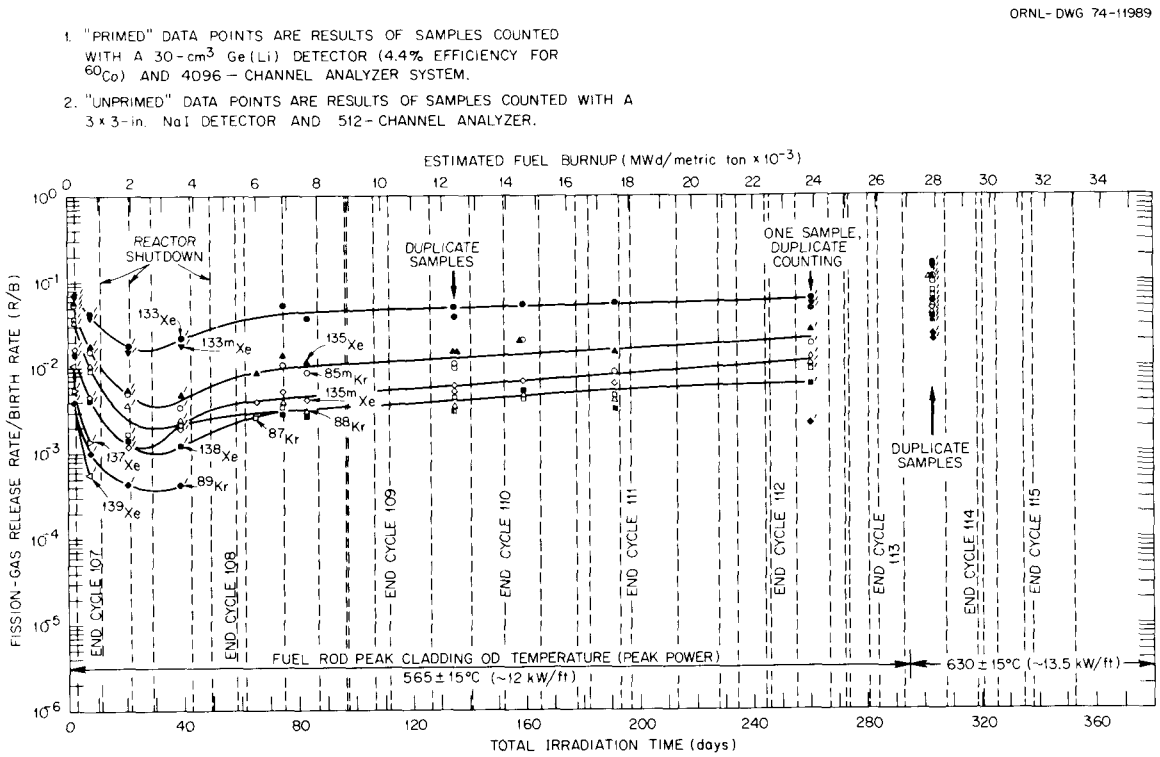

Fig. 18.3. Steady-state fission-gas release from GB-10 fuel rod vs time for case of sweep flow mode BF-BB.

TT-TT to BF-TT occurred as the inventory of fission gases that accumulated in the rod under the TT-TT flow mode was swept from the rod and passed by the ionization chamber on the effluent sweep line.

The fission-gas release behavior observed during the operation of GB-10 to date has been consistent with that observed during the operation of capsule GB-9 in that there is a strong continuous release during the operation that is quite sensitive to power level and temperature changes.

18.2.2 Fission-Gas Release Behavior During Startup and Shutdown

There has been no evidence of significant bursts of activity release from the initially solid pellet fuel in GB-10 during startup or shutdown periods. When no bursts were observed from the hollow-pellet fuel in GB-9, it was thought that perhaps activity pulses from the fuel might disperse and not be detected because of the limitations of the sweep line arrangement. In GB-10, however, it has been possible to sweep the fuel region directly while monitoring the effluent sweep line activity for activity bursts.

18.2.3 Fuel-Rod Flow Resistance vs Burnup

Pressure drop measurements are routinely obtained under several GB-10 sweep flow modes by means of two 0- to 1500-psig pressure transducers located in the sweep system on the inlet side of the fuel rod. Because of their locations, the two elements should indicate the same pressure when the TT inlet line is being used; thus, a check of their agreement is obtained under this flow condition. When one of the alternate inlet flow lines is used, a pressure drop (ΔP) measurement that includes the fuel region resistance to flow is obtained. However, the ΔP measurement always includes the pressure drop in the ~70 ft of 0.027-in.-ID inlet line used for all but the TT inlet line. Pressure drop calculations indicate that ~70 ft of 0.027-in.-ID inlet sweep line accounts for about 4 to 5 psi of the total measured ΔP for the conditions of 1000 psig pressure and 1000 cm^3 STP/min flow rate. In addition, operation under the various flow modes has shown that the upper blanket and charcoal trap sections of the rod offer negligible resistance to flow compared with the 70 ft of 0.027-in.-ID inlet line. Thus, measurements that are much greater than 5 psi indicate fuel region resistance

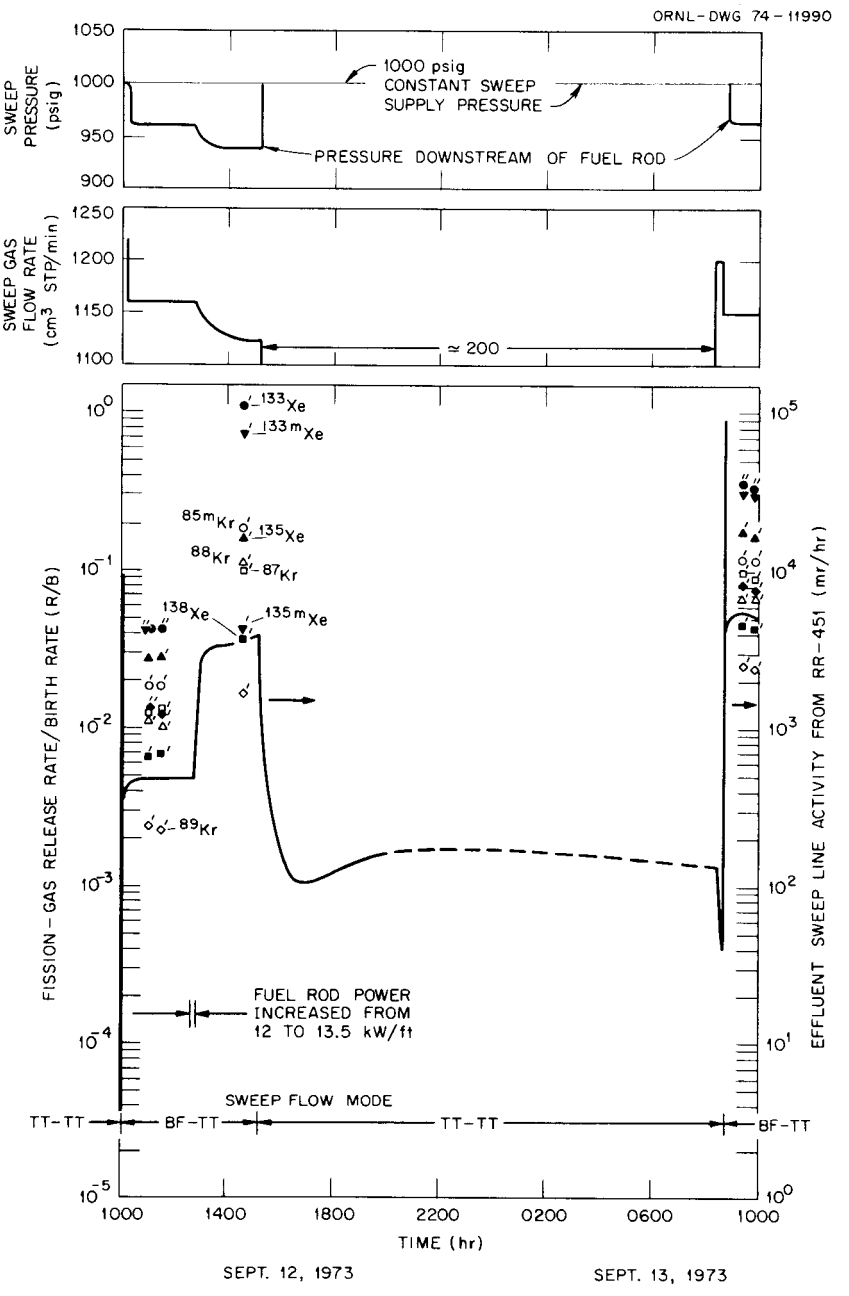

1. "PRIMED" DATA POINTS ARE RESULTS OF SAMPLES COUNTED WITH A 30-cm³ Ge(Li) DETECTOR (4.4% EFFICIENCY FOR ^{60}Co) AND 4096-CHANNEL ANALYZER SYSTEM.
2. "UNPRIMED" DATA POINTS ARE RESULTS OF SAMPLES COUNTED WITH A 3×3-in. NaI DETECTOR AND 512-CHANNEL ANALYZER.

Fig. 18.4. Activity release from capsule GB-10 during and following fuel rod power increase from 12 to 13.5 kW/ft on Sept. 12, 1973.

to flow and/or possible plugging of the inlet sweep line to the bottom of the rod.

The pressure drop indications to date, although limited to no better than ±5 psi with the present instrumentation, showed the flow resistance of the inlet line and fuel column in the "cold condition" to be ~65 psi at a flow rate of ~1000 cm^3 STP/min prior to the initial startup and about 3 to 6 psi at the same flow rate at a point where the fuel burnup was ~18,100 MWd/metric ton and where the corresponding indication under the "hot condition" was ~10 psi. Pressure differential indications under the hot condition and flow rates close to 1000 cm^3 STP/min showed fluctuations between 25 and 70 psi during the initial startup, a decrease to ~10 psi the first week of irradiation, ~10 psi to a fuel burnup ~18,100 MWd/metric ton, and a later increase to ~40 psi by the end of the 12.5-kW/ft operation. When the peak fuel-rod power was increased from ~12 to 13.5 kW/ft at 27,000 MWd/metric ton burnup, the pressure differential increased from 40 to 60 psi, as shown by the pressures plotted in Fig. 18.4. By the next day, the differential had dropped back to 40 psi. Subsequent data obtained at 13.5 kW/ft operation showed a decrease to ~30 psi at ~29,300 MWd/metric ton fuel burnup followed by an increase to ~60 psi at 35,600 MWd/metric ton (Jan. 15, 1974).

18.2.4 Iodine-Deposition Measurements at 12 kW/ft

Capsule GB-10 was fully retracted on Apr. 17, 1973, at an estimated fuel burnup of 18,100 MWd/metric ton to measure shutdown xenon release rates following operation at 12 kW/ft. A series of sweep gas samples were taken under carefully controlled flow conditions in an attempt to determine the equilibrium deposition of ^{135}I and ^{133}I in the various regions of the fuel rod and in the effluent sweep line during the preceding period of normal steady-state operation under flow mode TT-TT. Three sets of samples were taken, and in each case the sampling order was BF-TT, BF-BT, BF-BB, TT-BB, TT-BT, and TT-TT. All samples were taken with the charcoal trap and upper blanket regions of the rod electrically heated to a charcoal temperature of 235°C, except for the TT-TT samples, which were taken with the heaters off. Samples were taken approximately 5 min following the flow mode changes, or 5 min following cutoff of the heaters in the case of the TT-TT samples. All the samples were counted using the NaI detector system described previously (see Fig. 18.2 for detector system description).

The ^{135}Xe and ^{133}Xe release data obtained are plotted in Figs. 18.5 and 18.6 respectively. Also shown in these figures are the extrapolations (broken lines) of the xenon release rates back to the time of shutdown that were used to estimate the iodine-deposition results given in Table 18.1. In the calculations, the shutdown deposition activities (or decay rates) of ^{135}I and ^{133}I in each flow path were assumed to be equal to the "extrapolated shutdown release rates" of their xenon daughters. This assumption is subject to some question, since the xenon release data departed from the expected straight-line behavior on the semilog plots and, instead, showed an initial buildup. We do not have a satisfactory explanation for the curvature of the xenon release data in Figs. 18.5 and 18.6. In making iodine-deposition measurements at the 13.5- and 14.8-kW/ft power levels, we hope to be able to follow the shutdown xenon release for a longer period of time than we were able to at the 12-kW/ft level. Perhaps these later results will help explain the 12-kW/ft results.

18.2.5 Long-Lived Activity Deposition in Effluent Sweep System

A radiation survey of the GB-10 effluent lines in the reactor pool was made on Oct. 8, 1973, during a reactor shutdown period (fuel burnup of ~29,500 MWd/metric ton). The survey showed 300 to 700 mR/hr of long-lived activity on the conduit containing the effluent lines and ~12 R/hr at a junction box near the pool dam (about midway between capsule and valve box) where welded couplings exist in the lines. A subsequent survey during a reactor shutdown period in January 1974 indicated lower activities by a factor of about 2. We plan to continue surveying these lines and, if necessary, curtail sampling as required to prevent much higher buildup of activity on the lines.

The irradiation of capsule GB-10 was interrupted on Oct. 14, 1973, when a slow leak developed in a downstream low-pressure section of the sweep-gas effluent system at a needle valve (HCV-110, Dwg. 1-10040-QG-124) used to regulate the sweep flow rate. This valve was replaced during a reactor shutdown on Nov. 6–9, 1973. In replacing the needle valve, we had to open the valve box and remove the 4 in. of lead shielding from the vicinity of the effluent sweep line valves. While the lead shielding was removed, we installed several tees and valves in the high-pressure section of the effluent sweep line to facilitate later hookup of the loop with the on-line Ge(Li) gamma-ray detector. In doing this work, we removed a 5-in.-long segment of the old line. The line segment was cut on one end and had a fitting on the other end.

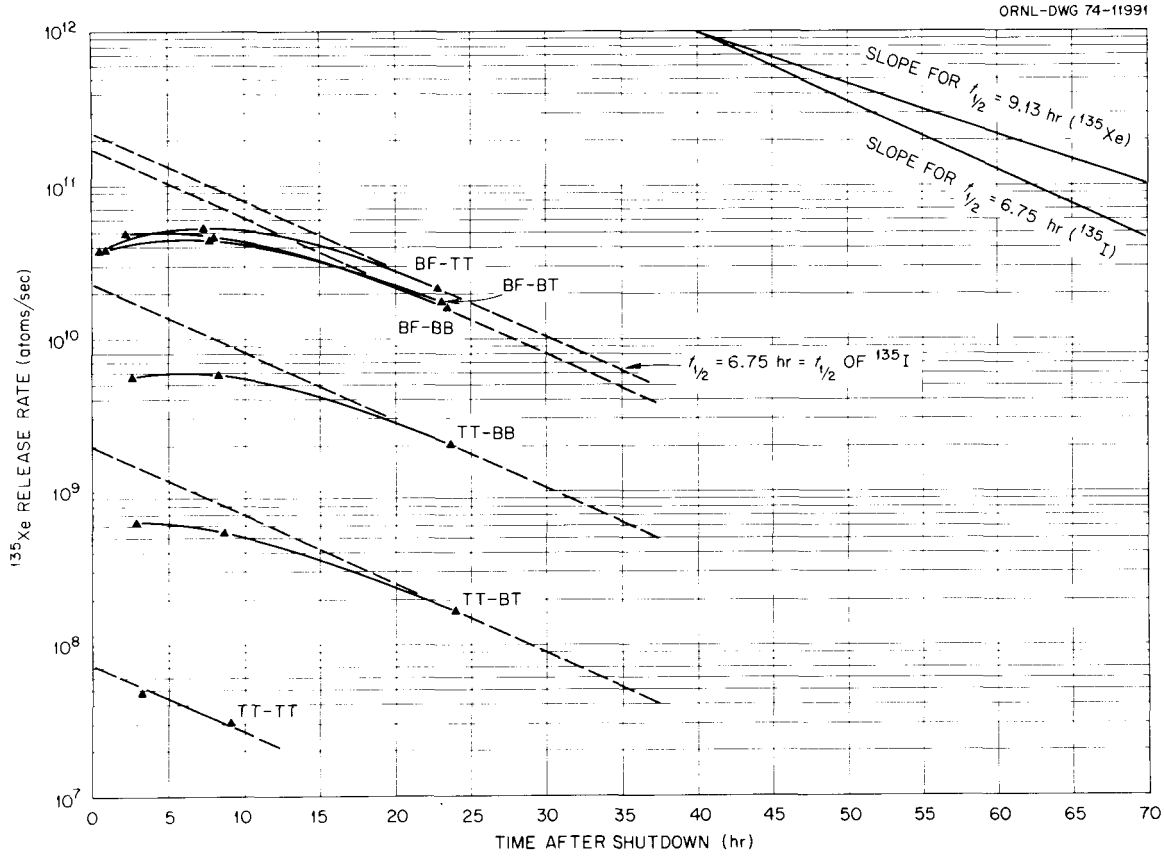

Fig. 18.5. Measured ^{135}Xe release rates following full retraction of capsule GB-10 on Apr. 17, 1973.

Table 18.1. Iodine-deposition results[a] obtained for 12-kW/ft operation of capsule GB-10

Region of GB-10 sweep system	Sweep[b] flow mode	Estimated iodine deposition in indicated flow path (upper half of table) or in region indicated (lower half of table) at time of shutdown			
		^{135}I		^{133}I	
		Curies	Fraction of total inventory[c]	Curies	Fraction of total inventory[d]
	TT-TT	0.0020	4.5×10^{-6}	0.0124	2.4×10^{-5}
	TT-BT	0.0541	1.2×10^{-4}	0.114	2.2×10^{-4}
	TT-BB	0.622	1.4×10^{-3}	1.24	2.4×10^{-3}
	BF-TT	5.95	1.3×10^{-2}	13.0	2.5×10^{-2}
TT-TT lines		0.0020	4.5×10^{-6}	0.0124	2.4×10^{-5}
Fuel-rod charcoal trap		0.0541	1.2×10^{-4}	0.114	2.2×10^{-4}
Upper blanket		0.568	1.3×10^{-3}	1.13	2.1×10^{-3}
Fuel region surfaces		5.33	1.2×10^{-2}	11.8	2.2×10^{-2}

[a]Based on ^{135}Xe and ^{133}Xe release measurements made following capsule retraction on Apr. 17, 1973, at an estimated fuel burnup of 18,100 MWd/metric ton.

[b]Flow modes are designated by two letters indicating the entrance point followed by two more letters indicating the exit point from the fuel rod. BF = bottom of fuel, TT = top of charcoal trap, BT = bottom of charcoal trap, BB = bottom of upper blanket.

[c]Estimated ^{135}I inventory at shutdown assuming no release = 441 Ci.

[d]Estimated ^{133}I inventory at shutdown assuming no release = 527 Ci.

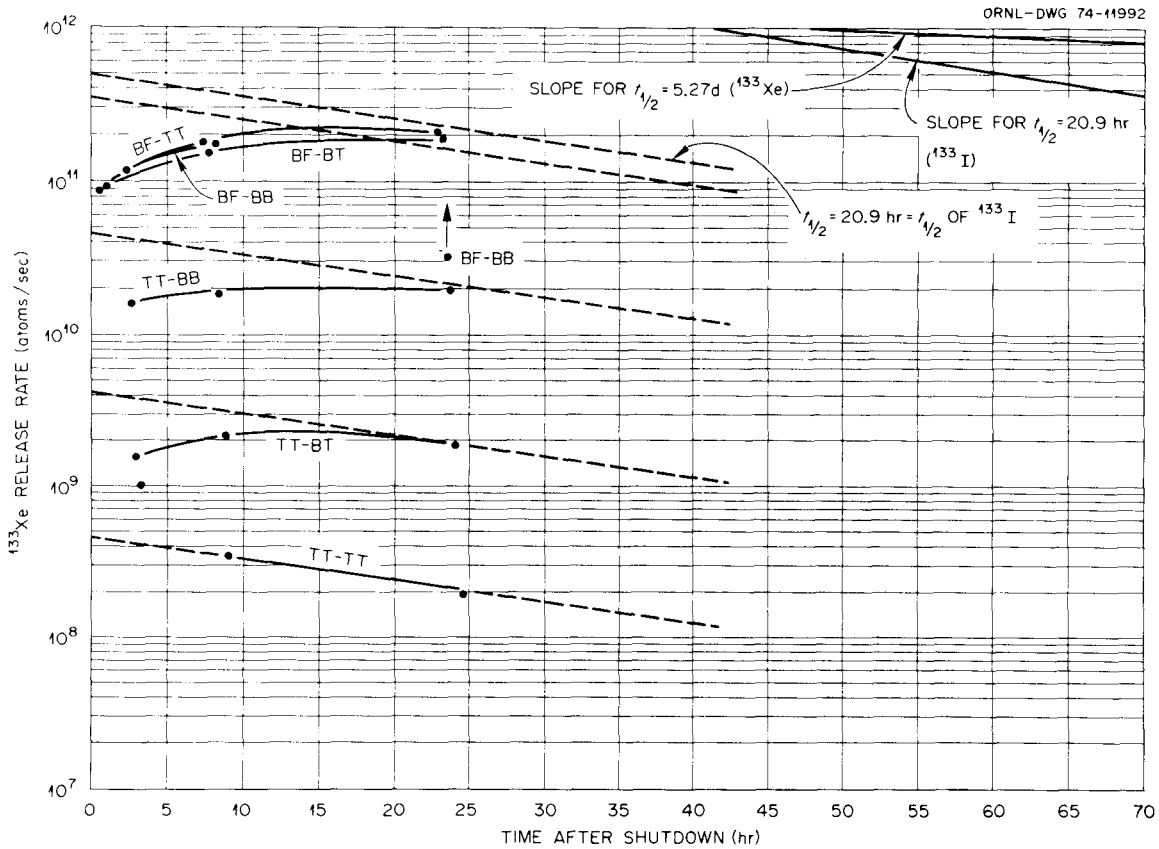

Fig. 18.6. Measured ^{133}Xe release rates following full retraction of capsule GB-10 on Apr. 17, 1973.

With the lead shielding removed from the effluent sweep line valving, the activity level was approximately 500 mR/hr near the valves and lines. This long-lived activity was due to fission product deposition on the effluent sweep system surfaces. The needle valve (HVC-110) read ~7 mR/hr after removal. The 5-in.-long segment of $\frac{1}{8}$-in.-OD X 0.027-in.-ID effluent sweep line after removal read ~300 mR/hr; the activity was much higher on the end with the fitting than on the cut end.

Both the needle valve and the segment of sweep line were counted using the NaI detector system (see Fig. 18.2). The capsule was shut down on Oct. 14, 1973. The activity on the needle valve was counted on Nov. 7, 1973, and that on the line segment was counted on Nov. 8, 1973. The following activities were found to be present.

Isotope	Half-life	Activity at time of counting			
		Needle valve HCV-110		Segment of sweep line	
		dis/sec	μCi	dis/sec	μCi
^{131}I	8.05 d	2.4×10^3	0.064	6.77×10^4	1.83
^{134}Cs	2.1 y	7.4×10^2	0.02	2.3×10^5	6.3
^{137}Cs	26.6 y	1.4×10^4	0.37	3.5×10^6	95.0
^{140}Ba	12.8 d	4.8×10^3	0.13	8.1×10^4	2.2
^{140}La	40.2 h	6.3×10^3	0.17	9.3×10^4	2.5
^{141}Ce	32 d	7.4×10^1	0.002		

When the on-line Ge(Li) detector loop is placed in operation, we may be able to obtain further information on line deposition. Initially, at least, we plan to use

this loop only under TT effluent conditions (i.e., flow modes TT-TT, BT-TT, BB-TT, or BF-TT) and to determine if the fuel-rod charcoal trap effectively removes ^{131}I from the gas stream. The radionuclides ^{137}Cs, ^{140}Ba, and ^{140}La have radioactive gaseous precursors (^{137}Xe and ^{140}Xe), whereas ^{131}I and ^{134}Cs do not. Later, similar observations could be made using the BT effluent line and perhaps the BB effluent line.

18.2.6 Neutron Radiography at 12 kW/ft

Neutron radiographs were taken of the GB-10 capsule near the end of the 12-kW/ft operating period. These radiographs, taken on Aug. 9, 1973, at an estimated fuel burnup level of ~26,100 MWd/metric ton, were compared with preirradiation neutron radiographs. The radiographs showed that the approximately 9-in.-long mixed-oxide fuel column had settled about $^{5}/_{32}$ in. Numerous cracks, especially in the longitudinal direction, could be seen in the fuel pellets, but there was no evidence that a central hole had developed during operation at 12 kW/ft. A small central hole, up to about 0.020 in. in diameter, probably would not be detectable in the radiographs. The fuel column settling, or densification, observed in GB-10 did not occur in the GB-9 test rod. However, the GB-9 rod contained hollow fuel pellets having an initial density of 91%, and the rod was operated at 14.8 kW/ft (685°C peak cladding OD temperature) throughout its irradiation. The initial density of the solid fuel pellets in GB-10 was lower (87%), giving about the same initial fuel column smear density as in GB-9 (84% of theoretical density in GB-10 vs 85% in GB-9). The test pellets in both rods had 0.006-in. dished ends. A central hole large enough to be detected by neutron radiography is expected to form in the GB-10 fuel column as the fuel-rod power level is increased.

The as-fabricated central hole in the lower two enriched-UO_2 half-pellets [below the $(U,Pu)O_2$ column] had become slightly funnel shaped, with the smaller diameter of the funnel at the bottom. The central hole in the upper two enriched-UO_2 half-pellets could not be seen clearly because of instrumentation leads. The remainder of the fuel rods and capsule parts appeared normal, and no other changes from the preirradiation radiographs were detected.

18.2.7 Decay Heating in the Charcoal Trap

So far in the irradiation of capsule GB-10 at the reduced fuel-rod power levels of 12 and 13.5 kW/ft, we have observed no significant fission product decay heating in the rod trap. The capsule has been operated under the BF-TT sweep flow mode numerous times for up to several hours at a time, but little or no trap decay heating has been detected. The BF-TT flow mode simulates the GCFR "leaking rod" condition and is the GB-10 flow mode in which transport of volatile fission products to the rod trap and resultant decay heating are expected to be the greatest. Decay heating in the trapping system of the GCFR would be of concern if a large fraction of the volatile fission products generated in the fuel were transported to the charcoal traps. We plan to conduct additional trap decay heat tests after the fuel-rod power level is increased to 14.8 kW/ft.

18.2.8 Operating Plans for Remainder of 13.5-kW/ft Operation

The acquisition of experimental data will continue at the present power level of 13.5 kW/ft as well as at the final power level of 14.8 kW/ft. In addition, we expect our capability for studying the fission-product-release behavior to be improved by the three additions to the GB-10 effluent sweep system: the on-line Ge(Li) gamma-ray detector system, a sampling system for taking large gas samples (~1 liter) for the determination of stable noble-gas release rates using mass spectrometry, and a system for semicontinuous measurement of the tritium content in the effluent stream. The on-line Ge(Li) detector system is expected to be operational in March 1974, the stable-gas sampling system in June 1974, and the tritium monitoring system before the end of calendar year 1974.

Before the fuel-rod power is increased to 14.8 kW/ft for the remainder of the irradiation to ~75,000 MWd/metric ton, we plan to conduct several special tests. Some of these will be easier to perform at the present lower-activity release levels than at those expected at 14.8 kW/ft. In addition to obtaining iodine-deposition measurements and neutron radiography, special tests planned at 13.5 kW/ft include (1) steady-state operation at lower sweep pressures (200 and 300 psig) to determine release behavior as a function of pressure, (2) measurement of the sweep-gas gamma spectrum as a function of sweep flow rate over a wide flow rate range (wide range of travel times from fuel rod) using the on-line Ge(Li) detector system, (3) power cycling tests between 13.5 and 9–12 kW/ft, and (4) pressure cycling tests (either at 13.5 or 14.8 kW/ft). We expect to complete these tests and be ready for 14.8-kW/ft operation by about September 1974.

19. GCFR Steam-Generator Modeling

O. W. Burke J. P. Sanders

This chapter covers the continuation of a task that was initiated on July 1, 1972. The purpose of this task was to develop a hybrid computer model of the steam generator for a gas-cooled fast breeder reactor (GCFR) and to use this model to simulate various system transients as well as steady-state operations. As a first objective, the results obtained from running certain prescribed transients using this model would be compared with those obtained by the General Atomic Company (GAC) from their computer model of the overall nuclear steam supply system. This would hopefully validate the steam-generator portion of their model that has been extensively used in system transient analyses.

19.1 COMPUTER DESCRIPTION

The ORNL hybrid computer being used in this task consists of a solid-state analog computer interfaced to a digital computer. The analog computer is a state-of-the-art computer with a ±100-V reference. The analog computer console also contains the components for interfacing with the digital computer, which has a 36-bit word length, 32,000 words of fast memory, and a cycle time of about 1.45 μsec. It accepts either assembly language or FORTRAN IV programs. Communication with the analog computer is accomplished through FORTRAN callable subroutines.

19.2 DESCRIPTION OF SYSTEM TO BE MODELED

The portion of the overall system modeled in this task includes the feedwater flow control valve, the steam generator (economizer, evaporator, and superheater), the helium circulator turbine control valve, and the piping interconnecting these units. Since input signals to the control valves are required from other parts of the system in order for them to operate in an automatic mode and since these signals are not available in this model, the control valves, as simulated, were manually operated.

The steam generator is a once-through type with helically wound tubes. Heat is transferred from helium in the shell section to water-steam in the tube section.

19.3 MATHEMATICAL MODEL OF STEAM GENERATOR

The computer model of the steam generator was developed from a set of coupled, nonlinear, partial differential equations derived from the laws of conservation of mass, momentum, and energy pertaining to the primary and secondary fluids. The equations, written in one space dimension x (the direction of water flow) and time t, are the following:

Conservation of mass (water):

$$\frac{\partial \rho}{\partial t} + \frac{\partial}{\partial x}(\rho v) = 0 . \tag{1}$$

Conservation of momentum (water):

$$\frac{\partial(\rho v)}{\partial t} + \frac{\partial}{\partial x}(\rho v^2) = -\frac{k\,\partial p}{\partial x} - cv^2 . \tag{2}$$

Conservation of energy (water):

$$\frac{\partial(\rho h)}{\partial t} + \frac{\partial(\rho h v)}{\partial x} = k_1 H(\theta - T) . \tag{3}$$

Conservation of energy (helium):

$$\frac{\partial\theta}{\partial t} + V_s \frac{\partial\theta}{\partial x} = \frac{Hk_2}{\rho_s c_p}(T - \theta) . \tag{4}$$

The equations of state for water are

$$T = T(p, h) ,$$

$$\rho = \rho(p, h) .$$

The variables used in the above equations are defined as follows:

T = water temperature, °F,

ρ = water density, lb/ft^3,

v = water velocity, fps,

p = water pressure, psi,

c = coefficient of friction,

k = constant used to make units consistent,

h = specific enthalpy of water, Btu/lb,

H = heat transfer coefficient of helium to water, Btu sec^{-1} ft^{-2} (°F)$^{-1}$,

k_1 = ratio of the surface area of a tube to the water volume in the tube, ft^{-1},

k_2 = ratio of the surface area of a tube to the helium volume adjacent to the tube, ft^{-1},

ρ_s = helium density (assumed constant), lb/ft^3,

c_p = specific heat of helium at constant pressure, Btu lb^{-1} (°F)$^{-1}$ (assumed constant),

θ = helium temperature, °F,

V_s = helium velocity, fps.

19.4 COMPUTER MODEL DEVELOPMENT

The decision was made to solve for the water pressure, the water enthalpy, the water velocity, and the helium temperature in terms of the other variables. The partial differential equations were differenced in time, so that the resulting model is a continuous-space, discrete-time model. The resulting differential equations are

$$\frac{dp}{dx} = -\frac{\rho \mathrm{v}}{k}\frac{d\mathrm{v}}{dx} - \frac{c\mathrm{v}^2}{k} - \frac{\rho}{k}\frac{\mathrm{v} - \mathrm{v}_k}{\Delta t} ,$$

$$\frac{dh}{dx} = \frac{1}{\rho \mathrm{v}}[k_1 H(\theta - T)] - \frac{h - h_k}{\mathrm{v}\,\Delta t} ,$$

$$\frac{d\mathrm{v}}{dx} = -\frac{\mathrm{v}}{\rho}\frac{d\rho}{dx} - \frac{\rho - \rho_k}{\rho\,\Delta t} ,$$

$$\frac{d\theta}{dx} = +\frac{Hk_2(T - \theta)}{\rho_s c_p V_s} - \frac{\theta - \theta_k}{V_s\,\Delta t} .$$

The subscript k represents the value of that variable at the preceding time step; the time step length Δt was arbitrarily set at 1 sec.

When implementing these equations on the hybrid computer, care must be exercised in assigning tasks to the digital and analog portions so that each machine performs the tasks that by nature it does best. The tasks were assigned as follows:

Analog computer:

1. integrate differential equations,
2. set coefficient values on coefficient devices,
3. generate functions of one variable,
4. provide simulation control logic devices.

Digital computer:

1. control simulation operation,
2. provide storage,
3. generate functions of two variables.

The pressure and enthalpy of the water are known at the feedwater end (left end) of the steam generator, the helium temperature is known at the right end, and the water velocity can be calculated at the right end using circulator turbine control valve relationships. Thus we can have an "initial value" problem by alternately integrating the water pressure and enthalpy equations from left to right and integrating the helium temperature and water velocity equations from right to left. One iteration consists of one left-to-right integration and one right-to-left integration, each using the latest information obtained by integrating in the opposite direction.

19.5 STATUS OF TASK

The program has been written and "debugged," and the full-power steady-state case has been run.

Since one of the first objectives in the use of this model was to compare its performance with that of the corresponding portion of a complete system model developed by GAC, a transient had to be specified that could be simulated on either model. The "simulated" load-reduction transient, agreed on by ORNL and GAC, is one that is used for model performance comparisons only and does not imply a "real life" system transient. The transient was implemented in the following manner.

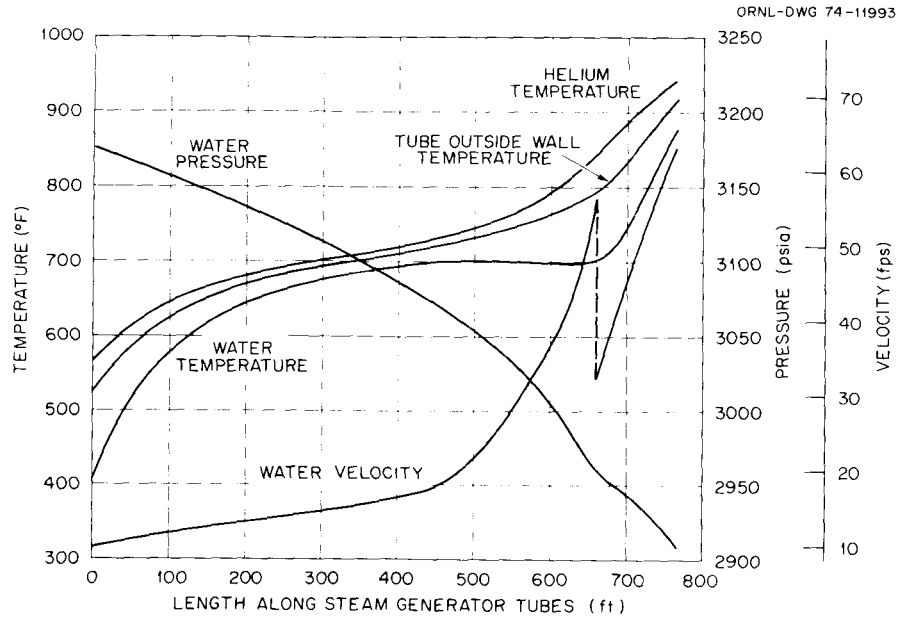

Fig. 19.1. Steady-state profiles of temperature and other parameters at full design load.

The system is initially operating at full design load in a steady state. At transient time zero, the following actions are initiated:

1. The feedwater flow control valve opening area is decreased from its initial full load value to 10% of that value on a 2-min ramp.
2. The circulator turbine control valve area is changed as in item 1 except that the ramp duration is $2\frac{1}{2}$ min.
3. The water conditions at the feedwater pump discharge remain constant at design full-load conditions.
4. The helium coolant mass flow rate is ramped from the design full-load value to 10% of that value in $2\frac{1}{2}$ min.

It must be pointed out that this is not truly a load-reduction transient. Since this simulation model simulates only a portion of the complete steam system and since no automatic controllers are simulated, a true load reduction cannot be simulated with it.

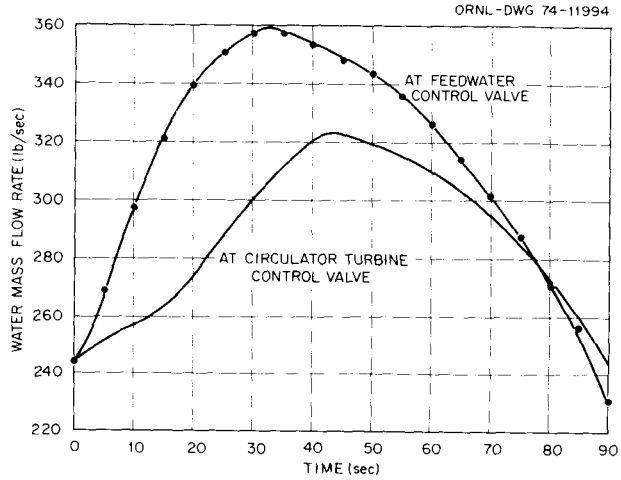

Fig. 19.2. Effects of simulated load reduction transient on mass flow rate of water in system.

19.6 RESULTS AND DISCUSSION

The spatial plots of the interesting variables for the steady-state full-load run are shown in Fig. 19.1. The time plots of the variables for the simulated load-reduction run are shown in Figs. 19.2 to 19.4.

The steady-state results were essentially the same as those from the GAC model. The shapes of the curves for the simulated load-reduction transient were very similar to those obtained by GAC. However, there was some time displacement in the peaks, etc., which was attributed to the fact that the ORNL model had no provision for the heat capacity of the tube wall metal. This oversight will be corrected. Except for the above-mentioned oversight, it appears that the two models give essentially the same results for the same transients.

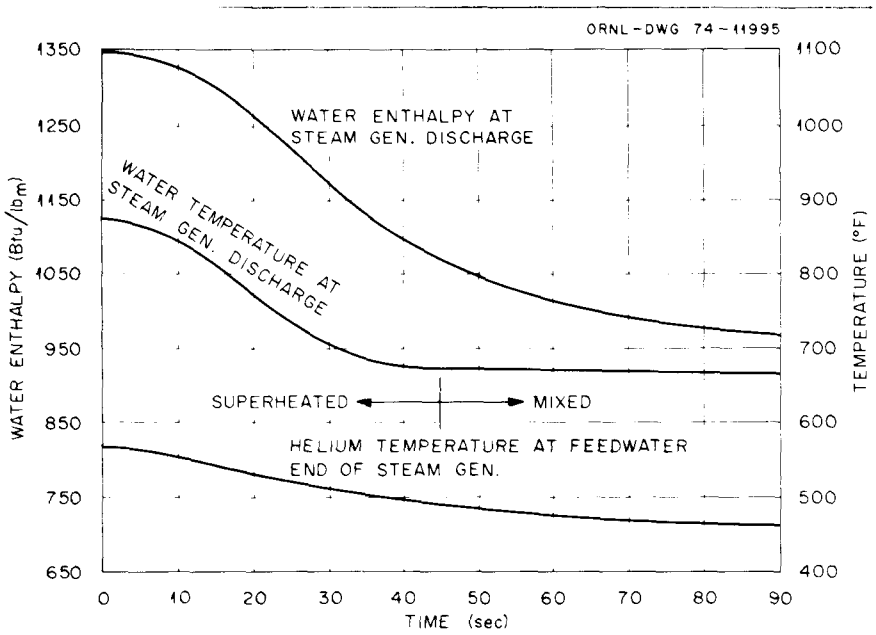

Fig. 19.3. Effects of simulated load reduction transient on water temperature and enthalpy in system.

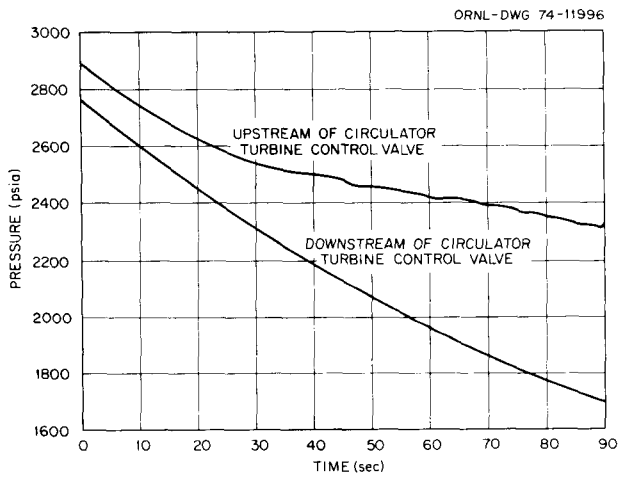

Fig. 19.4. Effects of simulated load reduction transient on system pressure at circulator turbine control valve.

20. GCFR Core Flow Test Facility

R. E. MacPherson A. G. Grindell

The Core Flow Test Facility (CFTF) for the gas-cooled fast reactor (GCFR) development program is being planned as an out-of-reactor facility to supply helium at appropriate flow, temperature, and pressure conditions to a multipin test bundle that simulates a portion of a GCFR core. The bundle will consist of electric cartridge heaters that simulate the configuration of individual GCFR fuel and blanket pins. The facility will be used for experimental studies of the structural and thermal responses of GCFR fuel-pin assemblies to thermal and gas dynamic conditions associated with steady-state and transient operation for comparison with predictions made with analytical models.

During the first two quarters of FY-1974, two planning meetings were held with General Atomic Company personnel to initiate the definition of the test facility requirements. An increase in operating expense funding in the third quarter permitted us to start organizing a conceptual design effort. Studies were initiated of the electrical power supply and control and helium coolant flow control.

Before the end of FY-1974, we plan to produce a conceptual design of the facility and to initiate preparation of the conceptual design description in accordance with the planning chronology for FY-1976 construction budget projects.

GAS-COOLED REACTOR PROGRAMS

DECEMBER 31, 1974

P. R. KASTEN, DIRECTOR — CMO
JUNE ZACHARY, SECY — CMO
J. H. COOBS,* ASSOC. DIR. — M&C
(VACANT) SECY. — M&C
A. L. LOTTS,* ASSOC. DIR. — M&C
PATRICIA VILES, SECY — M&C

DIVISION MANAGERS AND COORDINATORS

D. COSTANZO* — AC
A. L. LOTTS* — M&C
R. E. MACPHERSON* — R
A. P. MALINAUSKAS* — CT
K. J. NOTZ — CT
T. N. WASHBURN — M&C
J. P. CALLAHAN — R

THORIUM UTILIZATION PROGRAM

A. L. LOTTS,* MGR. — M&C

REPROCESSING

K. J. NOTZ,* MGR. — CT
MILDRED PAYNE, SECY — CT

REPROCESSING DEVELOPMENT (1110)

K. J. NOTZ* — CT

GENERAL DEVELOPMENT (1100)

K. J. NOTZ* — CT

HEAD-END PROCESSING (1101)

V. C. A. VAUGHEN — CT
C. L. FITZGERALD — CT
D. J. KINGTON — CT

SOLVENT EXTRACTION PROCESSING (1102)

R. H. RAINEY* — CT

OFF-GAS CLEANUP (1103)

R. W. GLASS — CT
R. D. ACKLEY — CT
T. M. GILLIAM — CT
H. W. R. BEAUJEAN† — CT
D. M. LEVINS† — CT

PRODUCT PREPARATION (1104)

J. W. SNIDER* — CT

WASTE TREATMENT AND DISPOSAL (1105)

K. J. NOTZ,* ACTG. — CT

REPROCESSING PROTOTYPE FACILITY (120)

J. W. SNIDER* — CT

GENERAL PLANT REQUIREMENTS (1200)

J. W. SNIDER* — CT

HEAD-END PROCESSING SYSTEM (1201)

J. W. SNIDER* — CT

SOLVENT EXTRACTION PROCESSING (1202)

R. H. RAINEY* — CT

OFF-GAS CLEANUP SYSTEM (1203)

K. H. LIN — CT
W. L. CARTER — CT

PRODUCT PREPARATION SYSTEM (1204)

J. W. SNIDER* — CT

SUPPORT FACILITIES (1206)

J. W. SNIDER* — CT

REFABRICATION PROCESS DEVELOPMENT (210)

J. D. SEASE* — M&C

GENERAL DEVELOPMENT (2100)

R. A. BRADLEY* — M&C
A. R. OLSEN — M&C
S. R. MCNEANY — M&C
H. R. LIVESEY — M&C

URANIUM FEED PREPARATION (2101)

F. E. HARRINGTON* — CT

RESIN LOADING (2102)

P. A. HAAS — CT
J. P. DRAGO — CT
J. H. SHAFFER — CT
C. W. GREENE — CT
C. F. KECK — CT
W. E. SHOCKLEY — CT
K. LADD — CT
R. D. ARTHUR — CT

RESIN CARBONIZATION (2103)

W. J. LACKEY* — M&C
D. R. JOHNSON — M&C
R. M. WEST — M&C
W. M. BRADLEY — M&C
W. B. STINES — M&C

MICROSPHERE COATING (2104)

W. J. LACKEY* — M&C
D. P. STINTON — M&C
C. E. DEVORE — M&C
J. B. FLYNN — M&C
W. I. MASON — M&C

FUEL ROD FABRICATION (2105)

R. L. HAMNER* — M&C
J. D. JENKINS — M&C
J. E. RUSHTON — M&C
S. W. COOK — M&C
J. C. MCLAUGHLIN — M&C
A. G. MASON — M&C

FUEL ELEMENT ASSEMBLY (2106)

R. L. HAMNER* — M&C
A. J. CAPUTO — M&C
W. H. MILLER — M&C

SAMPLE INSPECTION (2107)

W. H. PECHIN — M&C
J. E. MACK — M&C
D. L. REED — M&C
L. J. TURNER — M&C
C. E. ZACHARY — M&C
D. A. COSTANZO* — AC
J. L. BOTTS — AC
D. E. LAVALLE — AC

PROCESS CONTROL AND DATA HANDLING (2108)

R. A. BRADLEY* — M&C
W. R. HAMEL — I&C
A. F. JOHNSON — E
B. C. DUGGINS — I&C

WASTE HANDLING (2109)

J. O. JENKINS — R
R. J. BRAATZ — E

MATERIALS HANDLING (2110)

R. A. BRADLEY* — M&C

REFABRICATION PROTOTYPE PLANT (220)

J. W. HILL, PROJ. ENGR. — E
F. C. DAVIS, DESIGN MGR. — E

PROJECT STAFF

J. W. HILL, PE — E
J. P. JARVIS, ASSOC. PE — E
D. P. REID, ASSOC. PE — E
T. F. SCANLAN, QA MGR. — E

DESIGN STAFF

F. C. DAVIS, PE – MECH. — E
G. RENFRO, PE – GE (ACTG.) — E
B. LIEBERMAN, PE – INSTR. & ELECTRICAL (ACTG.)
C. C. HAWS, PE – CHEM. PROC. — CT

GENERAL PLANT (2200)

J. P. JARVIS — E
J. E. VAN CLEVE (ACTG.) — M&C

U FEED PREPARATION (2201)

F. E. HARRINGTON* — CT

RESIN LOADING (2202)

C. C. HAWS — CT

RESIN CARBONIZATION (2203)

M. K. PRESTON* — CT

MICROSPHERE COATING (2204)

M. K. PRESTON* — CT

FUEL ROD FABRICATION (2205)

R. I. DEADERICK — E

FUEL ELEMENT ASSEMBLY (2206)

W. G. COBB — E

SAMPLE INSPECTION (2207)

D. A. DYSLIN — E

PROCESS CONTROL AND DATA HANDLING (2208)

B. C. DUGGINS, ACTG. — I&C

WASTE HANDLING (2209)

F. HENSLEY* — E

MATERIALS HANDLING (2210)

F. HENSLEY* — E

RECYCLE FUEL IRRADIATIONS AND EXAMINATIONS (230)

F. J. HOMAN* — M&C

FUEL PERFORMANCE ASSESSMENT (2300)

E. L. LONG, JR.* — M&C

CAPSULE IRRADIATION TESTS (2301)

M. J. KANIA* — M&C

PEACH BOTTOM IRRADIATION TESTS (2302)

K. H. VALENTINE* — M&C

LARGE-SCALE RECYCLE TEST ELEMENTS (2303)

E. L. LONG, JR.* — M&C

REFABRICATED FUEL IRRADIATION TESTS (2304)

K. H. VALENTINE* — M&C

ENGINEERING AND ECONOMIC STUDIES (310)

F. J. HOMAN* — M&C

FUEL CYCLE SYSTEMS ANALYSIS (3100)

W. E. THOMAS — R

REPROCESSING TECHNIQUES (3101)

J. W. SNIDER* — CT
D. C. WATKIN — CT

REFABRICATION TECHNIQUES (3102)

M. S. JUDD — M&C

ENVIRONMENTAL, SAFEGUARDS, AND SAFETY ANALYSIS (3103)

M. L. TOBIAS — R

HTGR BASE PROGRAM

J. H. COOBS,* MGR. — M&C

PCRV DEVELOPMENT

J. P. CALLAHAN* — R
W. G. DODGE — R
D. N. FANNING* — R
M. N. RAFTENBURG* — R
D. A. CANONICO* — M&C
R. K. NANSTAD — M&C
J. E. SMITH* — R
C. C. HURTT — R

HTGR FUEL AND FISSION PRODUCT CHEMISTRY

A. P. MALINAUSKAS* — CT
R. B. EVANS* — CT
T. B. LINDEMER* — CT
M. T. MORGAN — CT
R. L. PEARSON — CT
R. L. TOWNS — CT

HTGR FISSION PRODUCT SURVEILLANCE

R. P. WICHNER* — CT
F. F. DYER** — AC
W. J. MARTIN — CT
L. L. FAIRCHILD — CT

STEAM-GRAPHITE REACTION RATE STUDIES

A. P. MALINAUSKAS* — CT
D. S. JOY* — CT
G. L. TINGEY† — BPNL

HTGR STRUCTURAL MATERIALS EVALUATIONS

P. L. RITTENHOUSE — M&C
C. R. BRINKMAN* — M&C
W. R. CORWIN — M&C
J. H. DEVAN* — M&C
J. C. GRIESS — M&C

ANALYTICAL CHEMISTRY DEVELOPMENT

D. A. COSTANZO* — AC
J. L. BOTTS — AC
L. G. FARRAR — AC
D. E. LAVALLE — AC
F. L. LAYTON — AC
W. F. ROGERS — AC
L. B. YEATTS — AC

HTGR FUEL DEVELOPMENT

W. P. EATHERLY* — M&C
R. L. BEATTY — M&C
E. S. BOMAR — M&C
J. I. FEDERER — M&C
O. J. HORNE — M&C
J. M. ROBBINS — M&C
V. J. TENNERY — M&C
G. W. WEBER — M&C
J. T. EAST — M&C
J. W. GEER — M&C
C. HAMBY, JR. — M&C
H. KEATING — M&C
D. PITTMAN** — NP
W. W. PROAPS — M&C
D. E. ROSSON — M&C

HTGR FUEL IRRADIATION TESTING

J. A. CONLIN* — R
K. R. THOMS — R
C. R. HYMAN* — R
R. M. FLANDERS — R
B. H. MONTGOMERY — R
L. J. SHERSKY — R
C. A. WALLACE — R

HTGR REACTOR ANALYSIS

J. D. JENKINS* — R
E. J. ALLEN — R
H. T. KERR — R
R. W. KNOLL* — R

POSTIRRADIATION EXAMINATION AND EVALUATION OF HTGR FUEL

F. J. HOMAN* — M&C
M. J. KANIA* — M&C
E. L. LONG, JR.* — M&C
K. H. VALENTINE* — M&C

GRAPHITE CREEP IRRADIATIONS

W. P. EATHERLY* — M&C
W. H. COOK — M&C
C. R. KENNEDY — M&C
J. A. CONLIN* — R
R. L. SENN — R

HTGR SAFETY PROGRAM

HTGR SAFETY STUDIES FOR RRD

T. E. COLE, MGR. — R
SUE BEGLEY,* SECY — R

SYSTEMS AND SAFETY ANALYSIS

DUNLAP SCOTT, JR. — R
S. J. BALL* — I&C
N. E. CLAPP, JR.* — I&C
J. C. CLEVELAND* — R
J. G. DELENE* — R
I. T. DUDLEY — R
R. C. GWALTNEY — R
R. A. HEDRICK* — I&C
PAUL RUBEL* — I&C

FISSION PRODUCT TECHNOLOGY

A. P. MALINAUSKAS* — CT
E. L. COMPERE — CT
R. J. KEDL — R

PRIMARY COOLANT TECHNOLOGY

A. P. MALINAUSKAS* — CT
D. S. JOY* — CT
R. P. WICHNER* — CT

SEISMIC AND VIBRATION TECHNOLOGY

J. P. CALLAHAN* — R
T. G. CARLEY† — UT
H. A. NELMS* — R

CONFINEMENT COMPONENTS

J. P. CALLAHAN* — R
E. G. BURDETTE† — UT
D. N. FANNING* — R
D. W. GOODPASTURE† — UT

PRIMARY SYSTEM MATERIALS TECHNOLOGY

P. L. RITTENHOUSE* — M&C
R. G. DONNELLY* — M&C
W. P. EATHERLY* — M&C

SAFETY INSTRUMENTATION

J. L. ANDERSON* — I&C
J. B. BULLOCK* — I&C
W. R. HAMEL* — I&C

HTGR SAFETY STUDIES FOR DOL AND RSR

J. P. SANDERS, MGR. — R
SUE BEGLEY,* SECY — R

HTGR SAFETY STUDIES FOR DOL

THERMAL ANALYSIS

I. I. SIMANTOV — CS
W. D. TURNER* — CS

TRANSIENT SYSTEM RESPONSE

R. M. DEVAULT* — CS
G. E. GILES, JR.* — CS

COMPONENT ANALYSIS

D. D. PAUL — R
R. L. REID† — UT
J. R. TALLACKSON — R

STRESS ANALYSIS

C. W. COLLINS* — E
S. K. ISKANDER* — CS

HTGR SAFETY STUDIES FOR RSR

S. J. BALL,* COORDINATOR — I&C

CORE THERMAL RESPONSE

S. J. BALL* — I&C
J. C. CLEVELAND — R

SYSTEM DYNAMICS

N. E. CLAPP, JR.* — I&C
J. G. DELENE* — R
R. A. HEDRICK* — I&C

SYSTEM RESPONSE

T. W. KERLIN† — UT

GCFR PROGRAM

URI GAT, ACTG. MGR. — R
JUDY JARNIGAN,* SECY — R

FUEL IRRADIATION

J. A. CONLIN* — R
A. W. LONGEST — R
L. J. SHERSKY* — R
R. M. FLANDERS* — R

PRESSURE VESSELS AND CLOSURES

J. P. CALLAHAN* — R
G. C. ROBINSON* — R
M. N. RAFTENBERG* — R

SHIELDING STUDIES

C. E. CLIFFORD* — NP
F. R. MYNATT* — NP
D. E. BARTINE* — NP
M. B. EMMETT* — NP
J. R. KNIGHT* — NP
J. V. PACE III* — NP
L. R. WILLIAMS — NP

CORE FLOW TEST LOOP

R. E. MACPHERSON* — R
A. G. GRINDELL — R
D. L. GRAY* — E
T. L. HUDSON* — E
H. J. METZ* — I&C
R. L. MOORE* — I&C
H. C. YOUNG* — R
D. L. CLARK* — R
W. K. FURLONG* — R
W. P. HUNTLEY* — R
M. J. ROBERTS* — I&C

SYSTEM RESPONSE STUDIES, GCFR AND CFTL

S. J. BALL* — I&C
O. W. BURKE* — I&C
T. W. KERLIN† — UT

* PART TIME/DUAL CAPACITY
† SUBCONTRACT
‡ GUEST SCIENTIST, KFA JÜLICH, WEST GERMANY
| GUEST SCIENTIST, AUSTRALIAN AEC
AC ANALYTICAL CHEMISTRY DIVISION
CMO CENTRAL MANAGEMENT OFFICE
CS COMPUTER SCIENCES DIVISION
CT CHEMICAL TECHNOLOGY DIVISION
E UCC-ND ENGINEERING
I&C INSTRUMENTATION AND CONTROLS DIVISION
M&C METALS AND CERAMICS DIVISION
NP NEUTRON PHYSICS DIVISION
R REACTOR DIVISION
** ON LOAN

ORNL 4975
UC-77 – Gas Cooled Reactor Technology

INTERNAL DISTRIBUTION

1. J. A. Auxier
2. S. J. Ball
3. D. E. Bartine
4. R. L. Beatty
5. A. L. Boch
6. C. J. Borkowski
7. R. A. Bradley
8. J. P. Callahan
9. D. A. Canonico
10. T. E. Cole
11. J. A. Conlin
12–13. J. H. Coobs
14. D. A. Costanzo
15. F. L. Culler
16. F. C. Davis
17. J. R. DiStefano
18. B. C. Duggins
19. F. F. Dyer
20. W. P. Eatherly
21. G. G. Fee
22. D. E. Ferguson
23. Uri Gat
24. R. W. Glass
25. A. G. Grindell
26. P. A. Haas
27. W. R. Hamel
28. R. L. Hamner
29. W. O. Harms
30. F. E. Harrington
31. R. F. Hibbs (UCC)
32. M. R. Hill
33. R. M. Hill, Jr.
34. F. J. Homan
35. J. D. Jenkins
36. D. R. Johnson
37–76. P. R. Kasten
77. H. T. Kerr
78. W. J. Lackey
79. K. H. Lin
80. T. B. Lindemer
81. E. L. Long, Jr.
82. A. W. Longest
83–87. A. L. Lotts
88. R. E. MacPherson
89. F. C. Maienschein
90. A. P. Malinauskas
91. W. R. Martin
92. D. L. McElroy
93. B. H. Montgomery
94. C. S. Morgan
95. M. T. Morgan
96. F. H. Neill
97. K. J. Notz
98. A. R. Olsen
99. W. H. Pechin
100. H. Postma
101. R. H. Rainey
102. D. P. Reid
103. P. L. Rittenhouse
104. A. D. Ryon
105. J. P. Sanders
106. Dunlap Scott
107. J. D. Sease
108. J. H. Shaffer
109. M. R. Sheldon
110. R. L. Shepard
111. J. W. Snider
112. M. L. Tobias
113. D. B. Trauger
114. V. C. A. Vaughen
115. T. N. Washburn
116. J. R. Weir
117. G. D. Whitman
118. R. P. Wichner
119. R. G. Wymer
120. ORNL Patent Office
121. Y-12 Document Reference Section
122–124. Central Research Library
125–130. Laboratory Records Department
131. Laboratory Records, RC

EXTERNAL DISTRIBUTION

132–133. Director, Division of Reactor Research and Development, Energy Research and Development Administration, Washington, D.C. 20545
134. Director, Reactor Division, ERDA, ORO
135. Director, Research and Technical Support Division, ERDA, ORO
136–302. Given distribution as shown in TID-4500 under category UC-77, Gas Cooled Reactor Technology (25 copies – NTIS)

☆ U.S. GOVERNMENT PRINTING OFFICE: 1976-748-189/312